

NORTHWESTERN UNIVERSITY

Measurement of the W Boson Branching Fractions in Proton-Proton
Collisions at 13 TeV Center-of-mass Energy with the CMS Experiment

A DISSERTATION

SUBMITTED TO THE GRADUATE SCHOOL
IN PARTIAL FULFILLMENT OF THE REQUIREMENTS

for the degree

DOCTOR OF PHILOSOPHY

Field of Physics

By

Ziheng Chen

EVANSTON, ILLINOIS

September 2021

© Copyright by Ziheng Chen 2021

All Rights Reserved

ABSTRACT

Measurement of the W Boson Branching Fractions in Proton-Proton Collisions at 13 TeV
 Center-of-mass Energy with the CMS Experiment

Ziheng Chen

The leptonic and inclusive hadronic decay branching fractions of the W boson are studied using 35.9 fb^{-1} of proton-proton collision data collected at $\sqrt{s} = 13 \text{ TeV}$ during the 2016 run of the CMS experiment. Events characterized by the production of pairs of W bosons from $t\bar{t}$ and tW processes are selected. Multiple event categories sensitive to the signal processes are defined based on the presence of energetic isolated charged leptons, the number of hadronic jets, and the number of b tagged jets.

Two analysis approaches are developed in parallel for a cross-check. One (referred to as the shape analysis) performs a maximum likelihood estimation of the W branching fractions based on a fit to the distribution of the lepton transverse momentum in each data category simultaneously. The other (referred to as the counting analysis) constructs ratios of yields in channels with the same trigger and solves the branching fractions from a set of quadratic equations. In terms of precision, the shape analysis is about three times more precise than the counting analysis. This is because the shape analysis exploits extra data regions to control systematic uncertainties and acquires extra sensitivity with the shape information, while the counting is limited by the tau identification systematic uncertainties.

In shape analysis, the branching fractions of the W boson decaying into electron, muon, and tau lepton final states are determined as 10.83(10)%, 10.94(08)%, 10.77(21)%, respectively; in counting analysis they are measured as 11.16(27)%, 11.13(22)%, 10.64(65)%, respectively. Both support the hypothesis of lepton flavor universality for the weak interaction.

The shape analysis is currently the most precise measurement of the three individual leptonic branching fractions of W boson decays.

Under the assumption of lepton flavor universality, the shape analysis further determines the inclusive leptonic and hadronic decay branching fractions as $(10.89 \pm 0.08)\%$ and $(67.32 \pm 0.23)\%$, respectively. From these results, three standard model quantities are derived: the sum square of elements in the first two rows of the Cabibbo–Kobayashi–Maskawa (CKM) matrix $\sum |V_{ij}|^2 = 1.991 \pm 0.019$, the CKM element $|V_{cs}| = 0.969 \pm 0.011$, and the strong coupling constant at the W mass scale, $\alpha_S(m_W) = 0.094 \pm 0.033$.

Acknowledgements

First and foremost, I would like to express my deepest and most sincere gratitude to my supervisor *Mayda Velasco*, Professor in the Physics Department, Northwestern University, who provides me with excellent guidance and training to explore and research the wonderful world of particle physics.

Next, I would like to thank *Nathaniel Odell*, a postdoc fellow in the Physics Department, Northwestern University, and the colleague I collaborate the most closely with on this thesis, for providing me enormous support and advice during the studies in this thesis. Without him, this thesis would not be completed.

Also, many people within the CMS have given me beneficial guidance. I could not appreciate more the ARC committee members and the SMP colleagues for sharing their constructive suggestions and insights about our analysis work. Besides, I also want to acknowledge my HGCAL DPG colleagues and BRIL BCM1F colleagues for providing me with marvelous opportunities and experiences on the detector research and developing.

Finally, I would like to thank my family members, including my wife *Shuyuan Hu*, who is currently studying for her Ph.D. in Heidelberg, Germany, as well as my parents in China. Despite the long distance, the love, joy, happiness, and support they brought to me during my doctoral journey is one of the most invaluable and beautiful things that ever happen to me.

Table of Contents

ABSTRACT	3
Acknowledgements	5
Table of Contents	6
List of Tables	11
List of Figures	15
Chapter 1. Introduction	37
1.1. Overview	37
1.2. Related Experimental Results	42
1.2.1. Tests of Lepton Flavor Universality	42
1.2.2. Measurements of V_{cs}	56
Chapter 2. Physics Foundations	59
2.1. Standard Model Particles	59
2.1.1. Fermions	60
2.1.2. Bosons	62
2.2. Physics in the Hadron Colliders	62
2.2.1. Parton Distribution Functions	63
2.2.2. Hard Processes	66
2.2.3. Jet Forming	68
2.3. Beyond the Standard Model for Lepton Flavor Universality Violation	69

2.3.1. Kinematics of Top Quark Decay	71
2.3.2. Standard Model Top Width	72
2.3.3. Models with W'	76
2.3.4. Models with H^+	86
2.3.5. Models with Leptoquark	94
2.4. Derivation of V_{cs} from W leptonic branching fraction	95
 Chapter 3. The CMS Experiment	98
3.1. The Large Hadron Collider	98
3.2. Detector Apparatus	100
3.2.1. Magnet	102
3.2.2. Inner Tracking System	102
3.2.3. Electromagnetic Calorimeter	105
3.2.4. Hadronic Calorimeter	106
3.2.5. Muon System	107
3.3. Trigger System	108
3.3.1. Level-1 Trigger	109
3.3.2. High Level Trigger	110
3.4. Object Reconstruction	111
3.4.1. Muons	113
3.4.2. Electrons and Photons	114
3.4.3. Hadrons	116
3.4.4. Jets	117
3.4.5. b Jet Tagging	118
3.4.6. Hadronic Tau Identification	119
3.5. Simulation	124

Chapter 4. Measurements of W Branching Fractions and Test of Lepton Flavor Universality with the CMS 2016 Dataset	127
4.1. Dataset and Simulated Events	127
4.1.1. Data	127
4.1.2. Simulated Dataset	128
4.2. Selection	129
4.2.1. Object Selection	129
4.2.2. Event Selection	135
4.3. Calibrations and Corrections	145
4.3.1. Generator-Level Reweighting	145
4.3.2. Corrections for Physics Objects	149
4.3.3. Corrections for Trigger Efficiencies	150
4.3.4. Corrections for Jets Faking Hadronic Taus	156
4.3.5. Corrections for b Tag Efficiency and Mistag Probability	160
4.4. Background Estimation	162
4.4.1. QCD background in the $e\tau_h$ and $\mu\tau_h$ channels	163
4.4.2. QCD background in the eh and μh channels	168
4.5. Statistical Analysis	171
4.5.1. Modeling the Decays of WW Pairs	172
4.5.2. Shape Analysis	174
4.5.3. Counting Analysis	188
4.6. Systematic Uncertainties	195
4.6.1. Sources of Systematic Uncertainties	196
4.6.2. Shape Analysis	208
4.6.3. Counting Analysis	211

4.7. Results	215
4.7.1. W branching fractions	215
4.7.2. Ratios of Branching Fractions and Derived Quantities	218
Chapter 5. Clustering Algorithms for the Reconstruction of the CMS High Granularity Calorimeter (HGCAL)	221
5.1. Design and Reconstruction of HGCAL	222
5.2. Cluster of Energy (CLUE) Clustering Algorithm	224
5.2.1. Algorithm Description	225
5.2.2. GPU Implementation	230
5.2.3. Performance Evaluation	231
5.3. CLUE in the CMS Software Framework (CMSSW)	237
5.3.1. Integration in the CMSSW	237
5.3.2. Performance in the CMSSW	240
Chapter 6. Conclusion	242
Appendix A. An Outline of the Quantum Field Theory of the Standard Model	244
A.1. Yang-Mills Gauge Theory	248
A.1.1. U(1) Gauge Symmetry	249
A.1.2. SU(2) Gauge Symmetry	250
A.1.3. SU(3) Gauge Symmetry	251
A.2. The Higgs Mechanism	253
A.2.1. U(1) Spontaneous Symmetry Breaking	254
A.2.2. SU(2) Spontaneous Symmetry Breaking	257
A.3. Glashow-Weinberg-Salam Electroweak Model	259
A.3.1. Electroweak Mixing Angle	260

	10
A.3.2. Gauge Boson Mass	262
A.3.3. Fermion Mass and Fermion Mixing	265
A.4. Quantum Chromodynamics	268
Appendix B. Plots for the Analysis of W Branching Fractions	272
B.1. Kinematics Plots in Counting Analysis	272
B.2. Kinematics Plots in Shape Analysis	289
Appendix C. Supplement Materials for CLUE clustering algorithm	324
C.1. Pseudocode	324
C.2. Extra Performance Tests	325
References	333

List of Tables

1.1	Standard model quantities can be derived from the measured $\mathcal{B}(W \rightarrow h)$.	42
1.2	The measurement of $\sigma_{p\bar{p} \rightarrow W} \times \mathcal{B}(W \rightarrow \ell\nu)$ for $\ell \in \{e, \mu, \tau\}$ and the ratios between leptonic channels by UA1 and UA2 at the CERN SPS.	44
1.3	The measurement of $\sigma_{p\bar{p} \rightarrow W} \times \mathcal{B}(W \rightarrow \ell\nu)$ for $\ell \in \{e, \mu, \tau\}$ and the ratios between leptonic channels by CDF and D0 at the Fermilab Tevatron.	45
1.4	Three individual leptonic branching fractions from the four LEP experiments and the combined result [16].	51
1.5	Standard Model predictions and the experimental measurements of the leptonic or semi-leptonic branching ratios of the pseudoscalar mesons [37].	54
1.6	World average of the experimental measurements of the nine elements in the CKM matrix in the PDG [27].	56
2.1	The electroweak quantum number of the first generation leptons and quarks. The second and third generation have the same electroweak quantum number as the first generation. The listed quantum numbers are isospin T , the third component of isospin T^3 , charge Q and hypercharge Y .	60

2.2	There are four possibilities of 2HDM if imposing flavor conservation. The four types differ from each other by the specific ways fermion masses are generated with Φ_1, Φ_2 . The second and third column show the fermion masses which Φ_1, Φ_2 are responsible for in the four types. The last three columns show the coupling constants A, B, C in the interaction Lagrangian in Equation 2.37.	88
4.1	Data samples produced by CMS in 2016.	128
4.2	Simulated datasets.	130
4.3	Tight muon identification criteria as provided by muon Physics Object Group (POG).	131
4.4	Tight electron identification criteria as provided by the EGamma Physics Object Group (POG).	132
4.5	Jet ID requirements for 2016.	134
4.6	Summary of object selection. For τ_h , sh ape (counting) analysis uses Tight (VTight) working points of τ_h isolation MVA.	135
4.7	Baseline categorization of events based on the triggering electron or muon, the presence of isolated reconstructed charged leptons.	136
4.8	Categorization of the events with electron, muon, and/or tau leptons passing the reconstruction criteria, based on their jet and b-tagged jet multiplicities. The yellow cells are the regions Incorporated in the shape analysis only. Also shape analysis splits $n_j = 2$ and $n_j \geq 3$ regions for $e\tau_h$ and $\mu\tau_h$ channels, shown as the yellow lines.	137
4.9	Composition of accepted $t\bar{t}$ and tW events, breakdown by 21 WW decay modes. Values are in percent.	141

4.10	Estimates of the yields for various processes in the ee, $\mu\mu$, e μ and eh, μh final states broken down by the number of b tags. The estimate of the expected yield is compared to the yield observed from data. Uncertainties are statistical plus variation from luminosity and normalization uncertainties.	142
4.11	Estimates of the yields for various processes in the e τ_h and μh categories broken down by the number of b tags. The estimate of the expected yield is compared to the yield observed from data. Uncertainties are statistical only.	143
4.12	Estimates of the yields. The estimate of the expected yield is compared to the yield observed from data. Uncertainties are statistical only.	144
4.13	Scale factors of ($j \rightarrow \tau_h$) with Tight and Very Tight τ_h working point.	159
4.14	Efficiency of $t\bar{t}+tW$ events, breakdown by 21 WW decay. Values are in percent.	189
4.15	Coefficients of quadratic equations c_{lk} in terms of efficiency matrix E and normalized yields $\{X_e, X_\mu, X_\tau\}$, where the index $l \in \{e, \mu, \tau\}$ and the index $k \in \{0, 1, 2, \dots, 9\}$. In the table, $\Delta_{ij} \equiv E_{ij}^{tl} - X_l \times (E_{ij}^{te} + E_{ij}^{tm} + E_{ij}^{t\tau_h} + E_{ij}^{th})$ is a 6×6 matrix, where the lower index i, j are for the 6×6 elements.	193
4.16	Statistical and systematic uncertainties in counting analysis.	214
4.17	Values of branching fractions determined in both analysis approaches and the PDG values. The errors include statistical (first) and systematic (second) uncertainties.	215
4.18	Correlation matrix of leptonic branching fractions.	216

4.19	Ratios of branching fractions.	218
4.20	SM quantities can be derived from the CMS measured $R_{h/l}^W$.	220
5.1	Kernels and Parallelism	231
5.2	Decomposition of CLUE execution time in the case of 10^4 points per layer with 100 layers. The time of sub-processes on GPU is measured with NVIDIA profiler, while on CPU is measured with <code>std::chrono</code> timers in the C++ code. The uncertainties are the standard deviations of 200 trial runs of the same event (10000 trial runs if GPU). The uncertainties of sub-processes on GPU are neglectable given that the maximum and minimum kernel execution time measured by NVIDIA Profiler are very close. With respect to the single-threaded CPU, the speed up factors of the multi-threaded CPU with TBB and the GPU are given in the bracket. “other” represents the difference between total execution time and the sum of the execution time of CLUE steps, and major CUDA API calls in the case of GPU.	234

List of Figures

1.1	Measurement of $\sigma_{p\bar{p} \rightarrow W} \times \mathcal{B}(W \rightarrow \ell\nu)$ for $\ell \in \{e, \mu, \tau\}$ by the SPS [1] and Tevatron [5, 6, 7, 8, 9, 10, 11] experiments.	43
1.2	g_τ^W/g_e^W measured by the SPS and Tevatron experiments [11]. In all the four experiments, the ratio of the weak coupling constant between electron and tau was extracted by the ratio of $\sigma_{p\bar{p} \rightarrow W} \times \mathcal{B}(W \rightarrow \tau\nu)$ and $\sigma_{p\bar{p} \rightarrow W} \times \mathcal{B}(W \rightarrow e\nu)$. The average was combined by D0 collaboration [11], the last published result among the four.	44
1.3	The LEP measurement of WW production cross-section. The measurement was a combine of the four LEP experiments, with a total 3 fb^{-1} data. The WW production at LEP was mainly induced by exchanging neutrinos in the t-channel and quark annihilation to Z/γ in the s-channel. The measured cross-section agreed with the theoretical calculation.	48
1.4	W leptonic and hadronic branching fractions from the four LEP experiments [16].	50
1.5	The measurement of $\frac{\mathcal{B}(W \rightarrow \tau\nu)}{\mathcal{B}(W \rightarrow \mu\nu)}$ by ATLAS using the full LHC run-2 dataset [23].	52
1.6	Anomaly of lepton flavor universality in the semi-leptonic decays of B meson [55]. The world average of $R_{D,\tau/l}^B$ and $R_{D^*,\tau/l}^B$ shows a four sigma deviation from the Standard Model prediction.	55

1.7	The $ V_{cs} $ measurements [27]. The 2020 PDG average [27] combines the results from D and D_s decay.	58
2.1	Particles in the Standard Model. Fermions include three generations of quarks and leptons, while bosons include four gauge bosons and one Higgs boson.	59
2.2	PDF of valence quark, sea quark and gluon at $\mu^2 = 10 \text{ GeV}^2$ and $\mu^2 = 10^4 \text{ GeV}^2$ [27]. The valence quarks dominate the high-x region and in total only account for about 38% of the proton momentum. The low-x region is dominated by the sea quarks and gluons, forming a “soft cloud” around the valence quarks. Gluons are the major components of the “soft cloud”, and in total carry over 40% of the proton momentum. Comparing PDF in (<i>left</i>) and (<i>right</i>), the increasing of the energy scale dramatically populates the soft gluons and soft sea quarks. Intuitively speaking, more and more “soft cloud” of sea quarks and gluons are revealed as the probing energy increases.	65
2.3	Summary of the cross-sections of the SM processes in the LHC. The grey bar shows the theoretical predictions. The red, blue and green points indicate the CMS measurements or the exclusion limits at 7, 8, 13 TeV.	66
2.4	The tree-level processes of $t\bar{t}$ production in the LHC. In all three diagrams, $t\bar{t}$ is produced with the QCD interaction. In the LHC, the dominant production processes are the two diagrams on the right, with two incoming gluons colliding in the s-channel and t-channel, respectively. The top quark decays into one W boson and one b quark immediately after the production.	67

2.5	The tree-level processes of tW production. The incoming b quark scatters off a gluon with QCD interaction and gets excited into a top quark via the electroweak interaction.	67
2.6	The tree-level process of WW production. These two diagrams are both induced by electroweak interactions.	68
2.7	Beyond-the-standard-Models that could enhance the tau channel in the top decay.	70
2.8	Top quark decay in the Standard Model.	71
2.9	The Standard Model $\overline{ \mathcal{M} ^2}$ as a function on the (E_1, E_3) plane. It shows a sharp peak at $E_3 = \frac{m_t^2 - m_W^2}{2m_t} = 67.8 \text{ GeV}$. $\Gamma_{t \rightarrow b\tau\nu}^{\text{SM}}$ is proportional to the integral of $\overline{ \mathcal{M} ^2}$ within a triangle region on the (E_1, E_3) plane.	75
2.10	The branching fraction of W' in the nonuniversal gauge interaction model (NUGIM) as a function of \cot_E [73], where \cot_E is the parameter controlling the degree of nonuniversality.	81
2.11	$ \mathcal{M} ^2_W$, $ \mathcal{M} ^2_{W'}$ and $ \mathcal{M} ^2_{\text{int}}$ on the (E_1, E_3) plane, shown as orange, blue and green surface, respectively. Changing the two model parameters $(\cot_E, m_{W'})$ leads to different scenarios. Upper left, upper right and lower plots illustrate $(\cot_E = 1, m_{W'} = 140 \text{ GeV})$, $(\cot_E = 1, m_{W'} = 300 \text{ GeV})$, and $(\cot_E = 4, m_{W'} = 300 \text{ GeV})$ cases.	84
2.12	The relative tau enhancement $\Gamma_{t \rightarrow b\tau\nu}^{\text{BSM}}/\Gamma_{t \rightarrow b\tau\nu}^{\text{SM}}$ in the NUGIM parameter space $(\cot_E, m_{W'})$. $\Gamma_{t \rightarrow b\tau\nu}^{\text{BSM}}$ is calculated from integrating $ \mathcal{M} ^2_{W'} + \mathcal{M} ^2_{\text{int}}$. Our analysis confirms LFU with 2% uncertainty, excluding the $\Gamma_{t \rightarrow b\tau\nu}^{\text{BSM}}/\Gamma_{t \rightarrow b\tau\nu}^{\text{SM}} > 2\%$ with one sigma, shown as the left side of the green contour.	85

2.13	Direct Search of W' on the Atlas and CMS.	85
2.14	$ \overline{\mathcal{M}} ^2_{H^+}$ and $ \overline{\mathcal{M}} ^2_{int}$ are 2D functions of (E_1, E_3) with two parameters $(m_{H^+}, \tan \beta)$. The $ \overline{\mathcal{M}} ^2_W$, $ \overline{\mathcal{M}} ^2_{H^+}$ and $ \overline{\mathcal{M}} ^2_{int}$ are shown as orange, blue and green surface, respectively. The valid kinematics is a triangle area on the (E_1, E_3) plane. The first, second, and third row uses model parameters $(m_{H^+} = 140 \text{ GeV}, \tan \beta = 10)$, $(m_{H^+} = 140 \text{ GeV}, \tan \beta = 40)$, and $(m_{H^+} = 200 \text{ GeV}, \tan \beta = 40)$. The right column is zoom-in views of the left column to show the small interference term $ \overline{\mathcal{M}} ^2_{int}$.	92
2.15	$\Gamma_{t \rightarrow b\tau\nu}^{\text{BSM}} / \Gamma_{t \rightarrow b\tau\nu}^{\text{SM}}$ in the 2D parameter space $(m_{H^+}, \tan \beta)$. Our analysis confirms the LFU with a relative uncertainty of 2%. The contours correspond to one and two experimental sigma, $\Gamma_{t \rightarrow b\tau\nu}^{\text{BSM}} / \Gamma_{t \rightarrow b\tau\nu}^{\text{SM}} = 2\%$ and $\Gamma_{t \rightarrow b\tau\nu}^{\text{BSM}} / \Gamma_{t \rightarrow b\tau\nu}^{\text{SM}} = 4\%$, are shown as the green and blue dash line, the left side of which is excluded.	93
2.16	Result of the direct search for H^+ in the CMS Run-I [101].	93
2.17	The real and virtual diagram of W decay at the next-to-leading order of α_S .	96
3.1	Schematic overview of the LHC and the related accelerator complex. The accelerator chain, from the beginning to the end, includes the proton source, radio frequency quadrupole (RFQ), LINAC, proton synchrotron booster (PSB), proton synchrotron (PS), super proton synchrotron (SPS), and finally the LHC [114]. Around the ring path of the LHC locate four LHC experiments: CMS [109] at point-5, ATLAS [110] at point-1, LHCb [111] at point-8 and Alice [112] at point-2.	99
3.2	The layout of the CMS detector [120].	101

3.3	The layout of the CMS inner tracking system [109]. It is consist of pixel detector and silicon strip tracker, covering regions with $ \eta < 2.5$.	103
3.4	The material thickness of the inner tracking system.	103
3.5	The layout of the CMS detector on the z-r plane [123]. The full coverage of pseudorapidity is up to $ \eta = 5$. The detector includes the tracker, electromagnetic calorimeter, hadronic calorimeter, magnet, and muon system. The details of tracker is shown in Figuge 3.3.	104
3.6	The logic structure of level-1 trigger (L1T).	109
3.7	The behaviors of different kinds of particle-flow candidates in the detector.	112
3.8	The resolution of muon transverse momentum as a function of eta with different muon energies [131] . The left and right plots show the result of the standalone and global reconstruction, respectively.	114
3.9	The energy resolution of the electron (<i>left</i>) and photon (<i>right</i>) [131].	114
3.10	The jet energy resolution [129] with and without Charged Hadron Subtraction (CHS) in three pileup scenarios $\langle \mu \rangle = 0, 15, 25$. The improvement from CHS is more prominent at higher pile-ups.	117
3.11	The distribution of the b tag score from the combined multivariate analysis (cMVA) b tagger [21].	120
3.12	The τ_h identification efficiency and $j \rightarrow \tau_h$ misidentification probability in the QCD multijets events [26]. Different working points are shown in different colors.	123
3.13	Physics processes happening in a proton-proton collision. The lower purple blob represents underline events. The upper purple blob shows the	

hard process with initial state radiation (ISR) before it, and with final state ratio (FSR), parton shower (PS), hadronization, meson/baryon decay after it. All of these processes are handled properly in the GEN stage by the generator and PYTHIA.

125

- 4.1 The distributions of the tailing muon p_T (*upper left*) and impact parameter (*upper right*). The ratios between $t\bar{t}/tW \rightarrow \mu\tau \rightarrow \mu\mu$ and other simulations are shown as orange dots, while the ratios between $t\bar{t}/tW \rightarrow \mu\mu$ and other simulations are shown as blue dots, as function of the tailing muon p_T (*lower left*) and impact parameter (*lower right*). 139

- 4.2 trailing lepton p_T in the $\mu\mu, ee, \mu e, e\mu$ channel. Data and MC events channel are split based on the trigger test of leading and trailing lepton: blue for both leptons firing trigger, orange for only leading lepton firing trigger, green for only trailing lepton firing trigger, red for neither leptons firing trigger. The lines are for data and the filled areas are for simulation. 140

- 4.3 (*top*) Pileup distribution in data and simulation including the $\pm\sigma$ variation of the data pileup distributions. (*bottom*) The weights parameterized by number of simulated pileup resulting from taking the ratio of the pileup distribution in data and simulation. 146

- 4.4 Comparison of the trailing lepton p_T distribution in $e\mu$ events with at least two jets and at least one b tag with top p_T weights applied and without the weights. 147

- 4.5 (*top*) Comparison of weighted and unweighted dilepton p_T spectrum for dimuon events with two jets and no b tags. (*bottom*) Comparison

	between ration of distributions in the top distribution and the analytical function for generating weights.	148
4.6	(<i>left</i>) Weights for the $\text{qq} \rightarrow \text{WW}$ process as a function of the $\text{WW} p_T$ and the two components of systematic variation. (<i>right</i>) Trailing lepton p_T from the $\text{qq} \rightarrow \text{WW} \rightarrow e\mu\nu\nu$ simulated sample when there are no reconstructed jets.	148
4.7	Scale factors for the single muon trigger efficiencies in run periods 2016 BCDEF (<i>left</i>) and GH (<i>right</i>). The uncertainties displayed are only statistical uncertainties.	151
4.8	The m_{ee} distribution of the selected events for the measurement of the scale factors of single-electron trigger efficiencies.	151
4.9	The 2D maps of ϵ_{data} , ϵ_{MC} and scale factors in run period 2016 BCDEF (<i>upper</i>) and 2016 GH (<i>lower</i>).	153
4.10	Scale factors in each 2016 data taking period.	153
4.11	Scale factors and uncertainties in the 2016 BCDEFF. Total uncertainties (<i>upper right</i>) combines the “two shifts” (<i>lower</i>) and statistical uncertainties.	154
4.12	Scale factors and uncertainties in the 2016 GH. Total uncertainties (<i>upper right</i>) combines the “two shifts” (<i>lower</i>) and statistical uncertainties.	155
4.13	Prefiring probabilities $\epsilon_i(p_T, \eta)$ for photons (<i>left</i>) and jets (<i>right</i>).	156
4.14	The kinematics distribution of $e\mu + \tau_h$, $\mu\mu + \tau_h$, $ee + \tau_h$ channels with Tight τ_h working point.	158
4.15	The kinematics distribution of $e\mu + \tau_h$, $\mu\mu + \tau_h$, $ee + \tau_h$ channels with Very Tight τ_h working point.	159

4.16	The correlation matrix and the pulls of the fitting parameters for Tight (<i>left</i>) and Very Tight (<i>right</i>) τ_h working point.	160
4.17	Distribution of the b tag score of the b, c and light quark jets in the Z+jets and t <bar>t} simulated dataset.</bar>	162
4.18	The b tag efficiencies for jets originating from b quark (<i>left</i>), c quark (<i>middle</i>), and light quark (<i>right</i>).	162
4.19	The $m_{e\tau_h}$ and $m_{\mu\tau_h}$ distributions in the same-sign and opposite-sign regions of e τ_h (on the right) and $\mu\tau_h$ (on the left) channel with the anti-isolated lepton and zero jets.	165
4.20	The $m_{\mu\tau_h}$ distributions in the same-sign and opposite-sign regions of $\mu\tau_h$ channel (<i>left two columns</i>). The $m_{e\tau_h}$ spectrum in the same-sign and opposite-sign regions of e τ_h channel (<i>right two columns</i>). Three rows correspond to $n_j = 0, n_b = 0, n_j = 1, n_b = 0, n_j = 1, n_b = 1$, respectively.	166
4.21	The $m_{\mu\tau_h}$ distributions in the same-sign and opposite-sign regions of $\mu\tau_h$ channel (<i>left two columns</i>). The $m_{e\tau_h}$ spectrum in the same-sign and opposite-sign regions of e τ_h channel (<i>right two columns</i>). Three rows correspond to $n_j \geq 2, n_b = 0, n_j \geq 2, n_b = 1, n_j \geq 2, n_b \geq 2$, respectively.	167
4.22	isolated and anti-isolated lepton plus jet regions with $1 \leq n_j < 4$ and $n_b \geq 1$, μh in the left two columns and eh in the right two columns.	169
4.23	The $SF^{\overline{\text{iso}} \rightarrow \text{iso}}$ measured in the lepton plus jet regions with $1 \leq n_j < 4$ and $n_b \geq 1$.	170

4.24	Fully data-driven QCD estimation in μh and eh signal regions with $n_j \geq 4$ and $n_b \geq 1$ based on the anti-isolation region with $SF^{\text{iso} \rightarrow \text{iso}}$.	170
4.25	The isolated and anti-isolated regions of eh and μh channels with $n_j \geq 4$ and $n_b \geq 1$. The left and right two columns are for the μh channel and eh channel, respectively	171
4.26	The QCD estimation in μh and eh signal regions with $n_j \geq 4$ and $n_b \geq 1$ based on data-driven shape and simulation-based normalization.	172
4.27	Templates used as inputs to the fit for the ee and $\mu\mu$ channels.	175
4.28	Templates used as inputs to the fit for the $e\mu$ channel.	176
4.29	Templates used as inputs to the fit for the $e\tau_h$ channel.	177
4.30	Templates used as inputs to the fit for the $\mu\tau_h$ channel.	177
4.31	Templates used as inputs to the fit for the eh and μh channels.	178
4.32	Results of bias test showing the value of each of the four branching fractions determined from the fit versus the value used to generate the pseudo-dataset. The red dashed line indicates a line of slope one passing through the origin.	181
4.33	Histogrammed values of the bias measured for each of the scan points. The values of μ and σ denote the mean and standard error for each distribution.	182
4.34	Pulls for nuisance parameters based on toy data while scanning the W boson leptonic branching fractions. The black dots indicate the values for individual trials, the blue bars show the standard error estimated from those trials, and the orange bar are the values estimated from the Hessian of the negative log-likelihood NLL .	183

4.35	Values for the negative log-likelihood while scanning over the leptonic branching fractions of the W.	184
4.36	Bin-by-bin sensitivity for the electronic branching fraction.	185
4.37	Bin-by-bin sensitivity for the muonic branching fraction.	186
4.38	Bin-by-bin sensitivity for the tauonic branching fraction.	187
4.39	Channels are organized into four groups based on trigger type and b tag multiplicity. Counting analysis extracts W branching fractions from the yields of grouped channels.	188
4.40	Efficiency matrices of eight channels with $n_b = 1$ and $n_b \geq 2$. The channels are grouped based on trigger types and b tag multiplicities.	190
4.41	Visualization of Equation 4.19 in the $\{\beta_e, \beta_\mu, \beta_\tau\}$ parameter space. Each equation is a hyperbolic plane, while their intersection is the solution. Mathematically, there are 8 possible solutions. However, only one solution is physical, located with $\beta \in (0, 1)$.	192
4.42	Distribution of $\{\beta_e, \beta_\mu, \beta_\tau\}$ extracted from 2000 toy MC datasets. The curves are Gaussian fit to the distributions.	195
4.43	Distribution of gen-level τ_h decay modes of $t\bar{t} \rightarrow \mu\tau_h$ simulated events selected in the $\mu\tau_h$ channel.	199
4.44	Effect of final state radiation on the τ_h identification and $j \rightarrow \tau_h$ misidentification obtained from the dedicated and the nominal $t\bar{t}$ samples. The Tight and VTight WP are shown on the left and right, respectively.	202
4.45	ISR, MEPS, UE effect on the τ_h identification and $j \rightarrow \tau_h$ misidentification obtained from the dedicated and the nominal $t\bar{t}$	

	samples. The Tight and VTight WP are shown on the left and right, respectively.	203
4.46	envelops on 21 efficiencies due to final state radiation (FSR) uncertainty. Vtight WP is shown.	204
4.47	Envelops on 21 efficiencies due to initial state radiation (ISR) uncertainty. Vtight WP is shown.	205
4.48	Envelops on 21 efficiencies due to parton shower matching (ME-PS) uncertainty. VTight WP is shown.	206
4.49	Envelops on 21 efficiencies due to underline event (UE) uncertainty. Vtight WP is shown.	207
4.50	Pulls and constrain of all non-MC statistic nuisance parameters after minimizing the likelihood.	209
4.51	Correlation matrix for branching fractions and nuisance parameters. This does not include the nuisance parameters associated with bin-by-bin MC statistical uncertainty.	210
4.52	The statistical and systematic part of the V matrix.	212
4.53	Statistical uncertainties and impacts of systematic parameters in counting analysis.	213
4.54	Summary of measured values of leptonic branching fractions.	216
4.55	Two dimensional comparisons of leptonic branching fractions. For each pair shown in the panels, the branching fraction that is not shown has been marginalized over. The dashed lines correspond to 68% and 95% contour levels for the resulting two dimensional Gaussian distribution.	217

4.56	Two dimensional distributions of the ratios $\mathcal{B}(W \rightarrow \tau\nu)/\mathcal{B}(W \rightarrow e\nu)$ vs $\mathcal{B}(W \rightarrow \tau\nu)/\mathcal{B}(W \rightarrow \mu\nu)$ with comparisons of the CMS result to LEP and ATLAS measurements.	219
4.57	The $ V_{cs} $ derived from the $\mathcal{B}(W \rightarrow \ell\nu)$ measurement by CMS, LEP and CMS+LEP, in comparison with the direct measurements [27].	220
5.1	The design of HGCAL [31]. (<i>left</i>) Sketch of HGCAL endcap. (<i>mid-left</i>) The internal structure on the longitudinal-radial (z-r) plane. Red and blue rectangles indicate regions of CE-E (for calorimeter endcap electromagnetic) and CE-H (for calorimeter endcap hadronic), respectively, where CE-E has 28 full Si layers and CE-H has 8 full Si layers plus 14 Si-scintillators hybrid layers. (<i>mid-right, right</i>) Layouts of CE-E and CE-H layer. Silicon wafers are shown as yellow and green hexagons and scintillators are shown as red mesh. Darker, medium and lighter shades of hexagons represent silicon wafers with thickness of 120, 200 and 300 μm , respectively.	222
5.2	2D points are indexed with a grid for fast neighborhood query in CLUE. Construction of this spatial index only involves registering the indices of points into the bins of the grid according to points' 2D spatial positions. To query d-neighborhood $N_d(i)$ defined in Equation 5.2, taking the red point for example, we first locate its $\Omega_d(i)$ defined in Equation 5.1, a set of all points in the bins touched by a square window $[x_i \pm d, y_i \pm d]$. The $[x_i \pm d, y_i \pm d]$ window is shown as the orange square while $\Omega_d(i)$ is shown as orange points. Then we examine points in $\Omega_d(i)$ to identify	

those within a distance d from point i , shown as the ones contained in the red circle.

227

5.3

Demonstration of CLUE algorithm. Points are distributed inside a 6×6 2D area and CLUE parameters are set to $d_c = 0.5, \rho_c = 3.9, \delta_c = \delta_o = 1$.

Before the clustering procedure starts, a fixed-grid spatial index is constructed. In the first step, shown in Fig. 5.3 (a), CLUE calculates the local density ρ for each point, defined in Equation 5.3. The color and size of points represent their local densities. In the second step, shown in Fig. 5.3 (b), CLUE calculates the nearest-higher (nh) and the separation (δ) for each point, defined in Equation 5.4. The black arrows represent the relation from the nearest-higher of a point to the point itself. If the nearest-higher of a point is -1, there is no arrow pointing to it. In the third step, in as Fig. 5.3 (c), CLUE promotes a point as a seed if ρ, δ are both large, or demote it to an outlier if ρ is small and δ is large. Promoted seeds and demoted outliers are shown as stars and grey squares, respectively. In the fourth step, shown in Fig. 5.3 (d), CLUE propagates the cluster indices from seeds through their chains of followers defined in Equation 5.5. Noise points, which are outliers and their descendant followers, are guaranteed not to receive any cluster indices from any seeds. The color of points represents the cluster indices. A grey square means its cluster index is undefined and the point should be considered as noise.

229

5.4

Examples of CLUE clustering on synthetic datasets. Each sample includes 1000 2D points with the same weight generated from certain distributions, including uniform noise points. The color of points

represent their cluster indices. Black points represent outliers detached from any clusters. The links between pairs of points illustrate the relationship between nearest-higher and follower. The red stars highlight the cluster seeds.

232

5.5

Noise rejection using different values of δ_o . Noise is either an outlier or a descendant follower of an outlier. In this dataset [173], 4000 points are distributed in 500×500 2D square area. Figure 5.5 (a) represents the decision plot on the $\rho - \delta$ plane, where fixed $\rho_c = 80$ and $\delta_c = 40$ values are shown as vertical and horizontal blue lines, respectively. Three different values of δ_o (10,20,60) are shown as orange dash lines. Figures 5.5 (b), (c) and (d) show the results with $\delta_o = 10, 20, 60$, respectively, illustrating how increasing δ_o loosens the continuity requirement and helps to demote outliers. The level of noise rejection should be chosen according to the user's needs.

232

5.6

(upper) Execution time of CLUE on the single-threaded CPU, multi-threaded CPU with TBB and GPU scale linearly with number of input points, ranging from 10^5 to 10^6 in total. Execution time on single-threaded CPU is shown as blue circles and on 10 multi-threaded CPU with Thread Building Blocks (TBB) is shown as blue squares, while the time on GPU is shown as green circles. The stacked bars represent the decomposition of execution time. The green and blue narrower bars are latency for data traffic between host memory and device memory; wider bars represent time of essential CLUE steps; light grey narrower bars labelled as "other" are the difference between the total execution time and the sum of major CLUE steps (and major CUDA API calls

if GPU). (*lower*) Comparing with the single-threaded CPU, the speed up factors of the GPU range from 48 to 112, while the speed up factors of the multi-threaded CPU with TBB range from 1.2 to 2.0, which is less than the number of concurrent threads on CPU because of atomic pushing to the data containers discussed in Section 5.2.2. Table 5.2 shows the details of the decomposition of the execution time in the case of 10^4 points per layer.

235

5.7 Workflow of CLUE-GPU in CMS Software framework (CMSSW). Hits are offloaded from CPU to GPU after energy calibration. Then CLUE process are carried out on GPU. In the end, the cluster indices of all hits are transported back to CPU for post processing.

238

5.8 Example of clustering result from previous algorithm in CMSSW version 10.6.X (*left*) and CLUE-CPU (*middle*) and CLUE-GPU (*right*). The example shows a small region on the 12th layer of a simulated of $t\bar{t}$ event.

239

5.9 Average execution time of HGCAL clustering for PU200 events. The testing platform is based on Intel i7-4770K CPU and NVIDIA GTX 1080 GPU. Blue, orange and green bars represent execution time of CMSSW_10_6_X, CLUE-CPU and CLUE-GPU respectively. Both CMSSW_10_6_X and CLUE-CPU use a single CPU thread. Three green bars are three evolving versions of CLUE-GPU.

240

A.1 Spontaneous symmetry breaking of the scalar field ϕ with a $U(1)$ global symmetric potential. The shape of potential on the complex plane looks like a Mexican hat. The scalar field's minimum potential shifts from the

origin by the amount of Higgs vacuum expectation value, forming a ring of positions with minimal potential. The scalar field has to choose one of the positions on the ring to settle down. Such a choice is so-called spontaneous symmetry breaking. The radial and lateral perturbation mode around this minimal position gives rise to the Higgs field and the Goldstone field.

254

A.2	Vertices of SM electroweak Triple-Gauge-Couplings. WW pairs couple to Z/γ because of the electroweak mixing θ_W . The Triple-Gauge-Couplings is one of the major process of WW pair production in the electron-positron collider $e^-e^+ \rightarrow Z/\gamma \rightarrow W^+W^-$ such as LEP2 which is discussed in Section ??.	262
A.3	Vertices of SM electroweak Quatic-Gauge-Couplings.	262
A.4	Vertices of SM Higgs-gauge couplings and Higgs-fermion coupling. The coupling strength is proportional to the mass of the coupled gauge boson or fermion.	264
A.5	Vertices of the SM QCD interaction. Quarks and gluons both carry colors allowing quark-gluon interaction and gluon self-interaction.	268
B.1	μe channel with $n_j \geq 2, n_b = 1$.	273
B.2	μe channel with $n_j \geq 2, n_b \geq 2$.	274
B.3	$\mu\mu$ channel with $n_j \geq 2, n_b = 1$.	275
B.4	$\mu\mu$ channel with $n_j \geq 2, n_b \geq 2$.	276
B.5	$\mu\tau$ channel with $n_j \geq 2, n_b = 1$.	277
B.6	$\mu\tau$ channel with $n_j \geq 2, n_b \geq 2$.	278

B.7	μ jet channel with $n_j \geq 4, n_b = 1$.	279
B.8	μ jet channel with $n_j \geq 4, n_b \geq 2$.	280
B.9	ee channel with $n_j \geq 4, n_b = 1$.	281
B.10	ee channel with $n_j \geq 2, n_b \geq 2$.	282
B.11	$e\mu$ channel with $n_j \geq 4, n_b = 1$.	283
B.12	$e\mu$ channel with $n_j \geq 2, n_b \geq 2$.	284
B.13	$e\tau$ channel with $n_j \geq 4, n_b = 1$.	285
B.14	$e\tau$ channel with $n_j \geq 2, n_b \geq 2$.	286
B.15	e jet channel with $n_j \geq 4, n_b = 1$.	287
B.16	e jet channel with $n_j \geq 2, n_b \geq 2$.	288
B.17	p_T and η distributions for leading (top) and trailing (bottom) electrons in the ee channel with $N_j \geq 2, N_b = 1$, and Z boson veto.	289
B.18	Dielectron mass, p_T , and ΔR in the ee channel with $N_j \geq 2, N_b = 1$, and Z boson veto.	290
B.19	p_T and η distributions for leading (top) and trailing (bottom) electrons in the ee channel with $N_j \geq 2, N_b \geq 2$, and Z boson veto.	290
B.20	Dielectron mass, p_T , and ΔR in the ee channel with $N_j \geq 2, N_b \geq 2$, and Z boson veto.	291
B.21	Multiplicity of b tagged jets, non-tagged jets, and MET in ee channel with $N_j \geq 2$.	291
B.22	p_T and η distributions for leading (top) and trailing (bottom) electrons in the $\mu\mu$ channel with $N_j \geq 2, N_b = 1$, and Z boson veto.	292

B.23	Dielectron mass, p_T , and ΔR in the $\mu\mu$ channel with $N_j \geq 2$, $N_b = 1$, and Z boson veto.	292
B.24	p_T and η distributions for leading (top) and trailing (bottom) electrons in the $\mu\mu$ channel with $N_j \geq 2$, $N_b \geq 2$, and Z boson veto.	293
B.25	Dielectron mass, p_T , and ΔR in the $\mu\mu$ channel with $N_j \geq 2$, $N_b \geq 2$, and Z boson veto.	293
B.26	Multiplicity of b tagged jets, non-tagged jets, and MET in $\mu\mu$ channel with $N_j \geq 2$.	294
B.27	p_T and η distributions for leading (top) and trailing (bottom) electrons in the $e\mu$ channel with $N_j = 0$.	295
B.28	Dielectron mass, p_T , and ΔR in the $e\mu$ channel with $N_j = 0$.	295
B.29	p_T and η distributions for leading (top) and trailing (bottom) electrons in the $e\mu$ channel with $N_j = 1$ and $N_b = 0$.	296
B.30	Dielectron mass, p_T , and ΔR in the $e\mu$ channel with $N_j = 0$ and $N_b = 0$.	296
B.31	p_T and η distributions for leading (top) and trailing (bottom) electrons in the $e\mu$ channel with $N_j = 1$ and $N_b = 1$.	297
B.32	Dielectron mass, p_T , and ΔR in the $e\mu$ channel with $N_j = 1$ and $N_b = 1$.	297
B.33	p_T and η distributions for leading (top) and trailing (bottom) electrons in the $e\mu$ channel with $N_j \geq 2$ and $N_b = 0$.	298
B.34	Dielectron mass, p_T , and ΔR in the $e\mu$ channel with $N_j \geq 2$ and $N_b = 0$.	298
B.35	p_T and η distributions for leading (top) and trailing (bottom) electrons in the $e\mu$ channel with $N_j \geq 2$ and $N_b = 1$.	299
B.36	Dielectron mass, p_T , and ΔR in the $e\mu$ channel with $N_j \geq 2$ and $N_b = 1$.	299

B.37	p_T and η distributions for leading (top) and trailing (bottom) electrons in the $e\mu$ channel with $N_j \geq 2$ and $N_b = 1$.	300
B.38	Dielectron mass, p_T , and ΔR in the $e\mu$ channel with $N_j \geq 2$ and $N_b = 1$.	300
B.39	Multiplicity of b tagged jets, non-tagged jets, and MET in $e\mu$ channel.	301
B.40	p_T and η distributions for leading (top) and trailing (bottom) electrons in the $e\tau$ channel with $N_j = 0$.	302
B.41	Dielectron mass, p_T , and ΔR in the $e\tau$ channel with $N_j = 0$.	302
B.42	p_T and η distributions for leading (top) and trailing (bottom) electrons in the $e\tau$ channel with $N_j = 1$ and $N_b = 0$.	303
B.43	Dielectron mass, p_T , and ΔR in the $e\tau$ channel with $N_j = 0$ and $N_b = 0$.	303
B.44	p_T and η distributions for leading (top) and trailing (bottom) electrons in the $e\tau$ channel with $N_j = 1$ and $N_b = 1$.	304
B.45	Dielectron mass, p_T , and ΔR in the $e\tau$ channel with $N_j = 1$ and $N_b = 1$.	304
B.46	p_T and η distributions for leading (top) and trailing (bottom) electrons in the $e\tau$ channel with $N_j \geq 2$ and $N_b = 0$.	305
B.47	Dielectron mass, p_T , and ΔR in the $e\tau$ channel with $N_j \geq 2$ and $N_b = 0$.	305
B.48	p_T and η distributions for leading (top) and trailing (bottom) electrons in the $e\tau$ channel with $N_j = 2$ and $N_b = 1$.	306
B.49	Dielectron mass, p_T , and ΔR in the $e\tau$ channel with $N_j = 2$ and $N_b = 1$.	306
B.50	p_T and η distributions for leading (top) and trailing (bottom) electrons in the $e\tau$ channel with $N_j = 2$ and $N_b = 2$.	307
B.51	Dielectron mass, p_T , and ΔR in the $e\tau$ channel with $N_j = 2$ and $N_b = 2$.	307

B.52	p_T and η distributions for leading (top) and trailing (bottom) electrons in the $e\tau$ channel with $N_j \geq 3$ and $N_b = 1$.	308
B.53	Dielectron mass, p_T , and ΔR in the $e\tau$ channel with $N_j \geq 3$ and $N_b = 1$.	308
B.54	p_T and η distributions for leading (top) and trailing (bottom) electrons in the $e\tau$ channel with $N_j \geq 3$ and $N_b \geq 2$.	309
B.55	Dielectron mass, p_T , and ΔR in the $e\tau$ channel with $N_j \geq 3$ and $N_b \geq 2$.	309
B.56	Multiplicity of b tagged jets, non-tagged jets, and MET in $e\tau$ channel.	310
B.57	p_T and η distributions for leading (top) and trailing (bottom) electrons in the $\mu\tau$ channel with $N_j = 0$.	311
B.58	Dielectron mass, p_T , and ΔR in the $\mu\tau$ channel with $N_j = 0$.	311
B.59	p_T and η distributions for leading (top) and trailing (bottom) electrons in the $\mu\tau$ channel with $N_j = 1$ and $N_b = 0$.	312
B.60	Dielectron mass, p_T , and ΔR in the $\mu\tau$ channel with $N_j = 0$ and $N_b = 0$.	312
B.61	p_T and η distributions for leading (top) and trailing (bottom) electrons in the $\mu\tau$ channel with $N_j = 1$ and $N_b = 1$.	313
B.62	Dielectron mass, p_T , and ΔR in the $\mu\tau$ channel with $N_j = 1$ and $N_b = 1$.	313
B.63	p_T and η distributions for leading (top) and trailing (bottom) electrons in the $\mu\tau$ channel with $N_j \geq 2$ and $N_b = 0$.	314
B.64	Dielectron mass, p_T , and ΔR in the $\mu\tau$ channel with $N_j \geq 2$ and $N_b = 0$.	314
B.65	p_T and η distributions for leading (top) and trailing (bottom) electrons in the $\mu\tau$ channel with $N_j = 2$ and $N_b = 1$.	315
B.66	Dielectron mass, p_T , and ΔR in the $\mu\tau$ channel with $N_j = 2$ and $N_b = 1$.	315

B.67	p_T and η distributions for leading (top) and trailing (bottom) electrons in the $\mu\tau$ channel with $N_j = 2$ and $N_b = 2$.	316
B.68	Dielectron mass, p_T , and ΔR in the $\mu\tau$ channel with $N_j = 2$ and $N_b = 2$.	316
B.69	p_T and η distributions for leading (top) and trailing (bottom) electrons in the $\mu\tau$ channel with $N_j \geq 3$ and $N_b = 1$.	317
B.70	Dielectron mass, p_T , and ΔR in the $\mu\tau$ channel with $N_j \geq 3$ and $N_b = 1$.	317
B.71	p_T and η distributions for leading (top) and trailing (bottom) electrons in the $\mu\tau$ channel with $N_j \geq 3$ and $N_b \geq 2$.	318
B.72	Dielectron mass, p_T , and ΔR in the $\mu\tau$ channel with $N_j \geq 3$ and $N_b \geq 2$.	318
B.73	Multiplicity of b tagged jets, non-tagged jets, and MET in $\mu\tau$ channel.	319
B.74	p_T and η distributions for the muon in the $e +$ jets channel with $N_j \geq 4$ and $N_b = 1$.	319
B.75	Multiplicity of b tagged jets, non-tagged jets, and MET in $e +$ jets channel with $N_j \geq 4$ and $N_b = 1$.	320
B.76	p_T and η distributions for the muon in the $e +$ jets channel with $N_j \geq 2$ and $N_b \geq 2$.	320
B.77	Multiplicity of b tagged jets, non-tagged jets, and MET in $e +$ jets channel with $N_j \geq 4$ and $N_b \geq 2$.	320
B.78	p_T and η distributions for the muon in the $\mu +$ jets channel with $N_j \geq 4$ and $N_b = 1$.	322
B.79	Multiplicity of b tagged jets, non-tagged jets, and MET in $\mu +$ jets channel with $N_j \geq 4$ and $N_b = 1$.	322
B.80	p_T and η distributions for the muon in the $\mu +$ jets channel with $N_j \geq 2$ and $N_b \geq 2$.	323

B.81	Multiplicity of b tagged jets, non-tagged jets, and MET in $\mu + \text{jets}$ channel with $N_j \geq 4$ and $N_b \geq 2$.	323
C.1	Execution time of CLUE on CPU and GPU both scale linearly with number of input points, ranging from 10^5 to 10^6 in total on 100 layers. Mean and standard deviation are based on 200 trial runs. AMD Ryzen 2700X and NVIDIA GTX 1080Ti.	326
C.2	Stability during 200 trial runs	326
C.3	Execution time of CLUE on CPU and GPU both scale linearly with number of input points, ranging from 10^5 to 10^6 in total on 100 layers. Mean and standard deviation are based on 200 trial runs. (10000 trial runs if GPU of Patatrack02) Intel Xeon Silver 4114 and NVIDIA Tesla V100	329
C.4	Stability during 200 trial runs	330
C.5	On GPU of Patatrack02, 10000 trials are performed	330

CHAPTER 1

Introduction

1.1. Overview

In the standard model (SM) of particle physics, the interaction between the charged weak bosons and the leptons is expressed by the Lagrangian term $\bar{\chi}_L \gamma^\mu (g T_a W_\mu^a + g' Y B_\mu) \chi_L$, where the coupling constant g is the same for all three lepton generations. Namely,

$$g_e = g_\mu = g_\tau \equiv g.$$

This property is part of a fundamental SM assumption, known as lepton flavor universality (LFU). Therefore, a test of LFU for the W boson's interaction is an important aspect to examine the SM and probe new physics. It has been performed by many particle physics experiments, approaches of which primarily include using the decay of W boson produced in colliders, using the weak decay of mesons, and using the weak decay of leptons. Section 1.2 in this introduction briefly reviews these activities. Among them, the most related experiments to this thesis are performed with the decay of W bosons produced in high-energy particle colliders.

The earliest LFU test of this kind can be traced back to the experiments at the Super Proton Synchrotron (SPS), UA1 [1] and UA2 [2, 3, 4], at CERN in the 1980s. The measurements were then improved by the Tevatron experiments, CDF [5, 6, 7, 8] and D0 [9, 10, 11], at Fermilab during Tevatron's run-1 from 1985 to 1995. Both SPS and Tevatron produced W bosons from p- \bar{p} collisions. One of the common features of these experiments was that the primary measured quantities were the cross-sections of the inclusive W production in

three W leptonic decay channels, $\sigma_{p\bar{p} \rightarrow W} \times \mathcal{B}(W \rightarrow \ell\nu)$ for $\ell \in \{e, \mu, \tau\}$. Then LFU were tested by taking the ratios of the measured $\sigma_{p\bar{p} \rightarrow W} \times \mathcal{B}(W \rightarrow \ell\nu)$ between two different lepton generations. For W coupling to the electron and tau, the combined SPS and Tevatron result [11] showed

$$g_\tau^W / g_e^W = 0.988 \pm 0.025 \quad (\text{SPS+Tevatron}).$$

Overall, the SPS and Tevatron results did not show any clear sign of LFU violation related to the W boson.

The most precise measurements of the three W leptonic branching fractions came from the four LEP experiments, ALEPH [12], DELPHI [13], OPAL [14], L3 [15] during the LEP's run-2 (1995-2000) which produced W W pairs from the electron-positron collisions. By the time of this thesis, the four LEP experiments are still the only W leptonic branching fraction measurements included in the world average by the Particle Data Group (PDG). The combined LEP result [16] gave 10.71(16)%, 10.63(15)%, 11.38(21)% for the electronic, muonic and tauonic branching fractions, respectively. Assuming partial universality between electron and muon, ratio between the tauonic and the combined electronic and muonic branching fractions was reported [16] as

$$R_{\tau/(e,\mu)}^W = \frac{2 \times \mathcal{B}(W \rightarrow \tau\nu)}{\mathcal{B}(W \rightarrow e\nu) + \mathcal{B}(W \rightarrow \mu\nu)} = 1.066 \pm 0.025 \quad (\text{LEP}).$$

In comparison, the SM predictions [17, 18, 19] for $R_{\tau/(e,\mu)}^W$ is 0.99912, taking into account the next-to-leading order electroweak corrections and the effect of lepton mass in the W decay phase space. LEP's $R_{\tau/(e,\mu)}^W$ shows a 2.6 standard deviation [16] from the SM prediction. This moderate deviation motivates the measurement of the branching fractions more precisely.

Opportunities arrive in the LHC era. During the LHC run-2, proton and proton collision at $\sqrt{s} = 13 \text{ TeV}$ allows an unprecedentedly large cross-section for $t\bar{t}$ production. Since a

top quark decays almost exclusively into one W boson and one b quark, with the help of b tagging techniques [20, 21, 22], it is possible to select a large and high-purity sample of $t\bar{t}$ events with two W bosons, which can then be used to study W boson decays. A recent measurement by the ATLAS Collaboration [23] has exploited such a strategy to measure $R_{\tau/\mu}^W = \frac{\mathcal{B}(W \rightarrow \tau\nu)}{\mathcal{B}(W \rightarrow \mu\nu)}$ by fitting the impact parameter distribution of the final state muons. The resulting value is $R_{\tau/\mu}^W = 0.992 \pm 0.013$, suggesting that lepton flavor universality is preferred.

In CMS, there has been a significant improvement on the identification of the hadronic tau leptons [24, 25, 26], which further opens the door to efficiently select W decays with τ_h final states in addition to electron and muon final states, and therefore to measure all the three leptonic branching fractions simultaneously. The CMS analysis in this thesis is performed under this context.

Motivations:

- The measurements of three W leptonic branching fractions have not been improved for more than a decade since LEP;
- LEP's $R_{\tau/(e,\mu)}$ shows a 2.6σ deviation from the SM prediction.

Opportunities:

- LHC 13 TeV p-p collisions produce a large number of $t\bar{t}$ events giving WW pairs;
- The improved b tagging allows to select $t\bar{t}$ events with a high purity;
- The improved τ_h identification enables to efficiently select W tauonic decays.

We have performed a simultaneous measurement of $\mathcal{B}(W \rightarrow e\nu)$, $\mathcal{B}(W \rightarrow \mu\nu)$, $\mathcal{B}(W \rightarrow \tau\nu)$ and the inclusive hadronic branching $\mathcal{B}(W \rightarrow h)$. 35.9 fb^{-1} of data collected by the CMS at $\sqrt{s} = 13 \text{ TeV}$ during the 2016 run of the LHC are analyzed by selecting events consistent with the decay of $t\bar{t} \rightarrow WW + bb$ and $tW \rightarrow WW + b$. The final states resulting from either one or both of the W bosons decaying leptonically are considered. To collect these events, single electron and single muon triggers are used, thus requiring that the final state must

contain at least one prompt electron or muon. Based on the presence of final state objects, data sample are split into a few channels, including μe , $\mu\mu$, $\mu\tau_h$, μh channel based on the single muon trigger and ee , $e\mu$, $e\tau_h$, eh channel based on the single electron trigger. The estimation of the W branching fractions is carried out based on two separately-developed approaches:

Shape analysis	template fit the p_T distribution of the sensitive leptons in all different channels simultaneously.
Counting analysis	construct ratios of yields for channels with the same trigger and solve three leptonic branching fractions from a set of quadratic equations.

The shape analysis is designed to push forward the precision of W branching fractions beyond LEP. It makes the most advantage of the shape information of the lepton p_T spectrum to discriminate the electron and muon coming from W boson decay and from the decay of taus from W boson. Comparing with the lepton impact parameters, p_T can be calibrated more conveniently using the energy correction provided by the CMS physics object group (POG), and systematics uncertainty associated to p_T is also expected to be smaller. To achieve better precision, shape analysis includes extra orthogonal regions besides the $t\bar{t}$ enriched regions, thus constraining some of the most offending systematics such as those related to τ_h reconstruction.

The counting analysis is designed to cross-check the shape analysis, with more emphasis on the robustness over precision. It eliminates the shape information of the kinematics distribution and uses only $t\bar{t}$ concentrated regions. By constructing ratios of yields for channels with the same trigger, it has the benefit of canceling some systematics uncertainties related to $t\bar{t}$ cross section, trigger efficiency and luminosity, and being robust with the lepton

energy calibration. However, its precision is significantly limited by the τ_h identification systematics, ultimately being less sensitive than the shape analysis.

This thesis describes both the approaches and their results. For $\mathcal{B}(W \rightarrow \tau\nu)$, the shape analysis achieves an absolute uncertainty of 2.1%, while the uncertainty of counting analysis is about 6.7%. The final result of shape and counting analysis agree with each other within one sigma. In the CMS publication, the more precise result from the shape analysis is reported as the official CMS result, and are compared and combined with the LEP result.

With the simultaneously measured three individual leptonic branching fractions and their correlations, the pairwise ratios between two branching fractions are calculated to test the SM LFU predictions. Furthermore, the leptonic and inclusive hadronic branching fraction under the lepton flavor universality assumption are also estimated by repeating the shape analysis, which alternatively uses the same parameter for three leptonic branching fractions. From the measured $\mathcal{B}(W \rightarrow h)$, some SM quantities can be derived, as listed in Table 1.1. Assuming the unitarity of the CKM matrix, the strong coupling constant $\alpha_S(m_W)$ can be calculated; alternatively, using the latest experimental measurement of $\alpha_S(m_W)$, the square sum of the six CKM elements in the first two rows can be calculated and compared with the unitarity. Among the six elements in the square sum $\sum_{d,s,b}^{u,c} |V_{ij}|^2$, $|V_{cs}|$ has the least experimental precision, currently at percent level. So we can take a step further to determine $|V_{cs}|$ using the experimental values of five other CKM elements. The mathematics and physics related to these derivations are covered in Section 2.4.

For the outlook of this measurement in the LHC run-3 and high luminosity LHC (HL-LHC) [28] runs, the further precision improvement can be contributed from the advancement of the τ_h identification, as well as the improvement of the impact parameter resolution if it is included in the future as additional discriminating observables or additional categorization dimensions. In the era of HL-LHC, a few exciting upgrades of the CMS detector will have

Table 1.1. Standard model quantities can be derived from the measured $\mathcal{B}(W \rightarrow h)$.

Assumption		Derived quantity
CKM Unitarity $\sum_{d,s,b}^{u,c} V_{ij} ^2 = 2$	\implies	$\alpha_S(m_W)$
PDG $\alpha_S(m_W) = 1.1200 \pm 0.010$ [27]	\implies	$\sum_{d,s,b}^{u,c} V_{ij} ^2$
PDG $\alpha_S(m_W) = 1.1200 \pm 0.010$ [27]	\implies	$ V_{cs} $
PDG $ V_{ud} ^2 + V_{us} ^2 + V_{ub} ^2 + V_{cd} ^2 + V_{cb} ^2 = 1.0490(18)$ [27]		

been accomplished after the phase-2 upgrade [29]. A new tracker system [30] will improve the resolution of the impact parameter. A new endcap calorimeter, the high granularity calorimeter (HGCAL) [31], is expected to improve the τ_h identification by allowing novel deep learning algorithms based on its high-resolution jet images. This thesis also describes a new clustering algorithm developed for the HGCAL reconstruction and the corresponding high-performance computing using GPUs.

The rest of this introduction covers a brief review of the related LFU tests and $|V_{cs}|$ measurements. Chapter 2 and 3 describe the related SM/BSM physics and the key aspects of the CMS experiment, respectively. Chapter 4 presents the method and the result of the measurement of the W branching fractions, followed by the supplement studies in Chapter 5. Chapter 6 shows the clustering algorithm developed for the HGCAL reconstruction and its high performance computing using GPUs.

1.2. Related Experimental Results

This section gives a brief review of two groups of related experiments: the LFU tests in the charged weak decays and the measurements of $|V_{cs}|$.

1.2.1. Tests of Lepton Flavor Universality

1.2.1.1. Test with W Boson Decay.

SPS and Tevatron

Both SPS and Tevatron collide protons and anti-protons. SPS operated at CERN from 1981 to 1991 at a center-of-mass energy of 0.546 TeV and 0.630 TeV. The SM electroweak bosons, W and Z, were first discovered in the SPS in 1983 [32, 33]. In 1985, Tevatron at Fermilab began operations at a higher center-of-mass energy at 1.8 TeV, which was later upgraded to 1.96 TeV in its second run since 2001. Tevatron was in service for more than 20 years until 2010 to give way to the LHC.

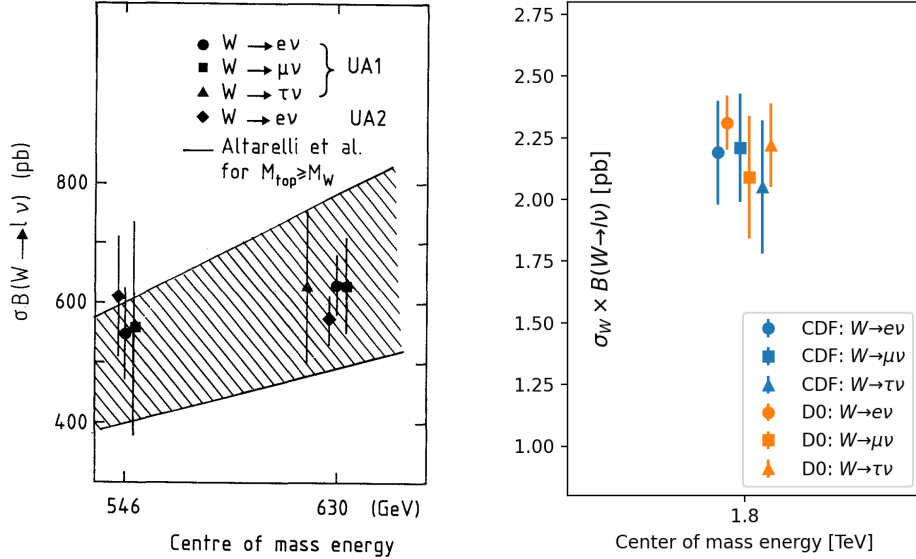


Figure 1.1. Measurement of $\sigma_{p\bar{p}} \times \mathcal{B}(W \rightarrow \ell\nu)$ for $\ell \in \{e, \mu, \tau\}$ by the SPS [1] and Tevatron [5, 6, 7, 8, 9, 10, 11] experiments.

The UA1, UA2 at the CERN SPS and the CDF, D0 at the Fermilab Tevatron measured $\sigma_{p\bar{p}} \times \mathcal{B}(W \rightarrow \ell\nu)$ for $\ell \in \{e, \mu, \tau\}$, shown in Figure 1.1. The LFU test is performed by taking the ratios of two different leptonic channels. Figure 1.2 from [11] summarizes the results of g_τ^W/g_e^W derived by the SPS and Tevatron experiments. The combined average was calculated by the D0 collaboration [11], which was the last published result among the four. The average assumed uncorrelated systematical and statistical uncertainties. All

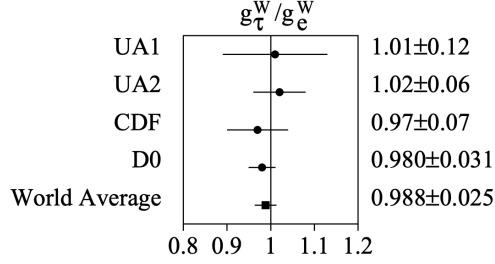


Figure 1.2. g_τ^W/g_e^W measured by the SPS and Tevatron experiments [11]. In all the four experiments, the ratio of the weak coupling constant between electron and tau was extracted by the ratio of $\sigma_{p\bar{p} \rightarrow W} \times \mathcal{B}(W \rightarrow \tau\nu)$ and $\sigma_{p\bar{p} \rightarrow W} \times \mathcal{B}(W \rightarrow e\nu)$. The average was combined by D0 collaboration [11], the last published result among the four.

four measurements confirmed consistency with the SM lepton flavor universality within one experimental uncertainty.

Table 1.2. The measurement of $\sigma_{p\bar{p} \rightarrow W} \times \mathcal{B}(W \rightarrow \ell\nu)$ for $\ell \in \{e, \mu, \tau\}$ and the ratios between leptonic channels by UA1 and UA2 at the CERN SPS.

UA1 [1]		
	$p\bar{p}$ at $\sqrt{s} = 0.546$ TeV	$p\bar{p}$ at $\sqrt{s} = 0.630$ TeV
$\sigma_{p\bar{p} \rightarrow W} \times \mathcal{B}(W \rightarrow e\nu)$ [nb]	0.55 ± 0.08 (stat) ± 0.09 (syst)	0.63 ± 0.06 (stat) ± 0.10 (syst)
$\sigma_{p\bar{p} \rightarrow W} \times \mathcal{B}(W \rightarrow \mu\nu)$ [nb]	0.56 ± 0.18 (stat) ± 0.12 (syst)	0.63 ± 0.08 (stat) ± 0.11 (syst)
$\sigma_{p\bar{p} \rightarrow W} \times \mathcal{B}(W \rightarrow \tau\nu)$ [nb]		0.63 ± 0.13 (stat) ± 0.12 (syst)
$\mathcal{B}(W \rightarrow \mu\nu)/\mathcal{B}(W \rightarrow e\nu)$		1.00 ± 0.14 (stat) ± 0.08 (syst)
$\mathcal{B}(W \rightarrow \tau\nu)/\mathcal{B}(W \rightarrow e\nu)$		1.02 ± 0.20 (stat) ± 0.10 (syst)

UA2		
	$p\bar{p}$ at $\sqrt{s} = 0.546$ TeV	$p\bar{p}$ at $\sqrt{s} = 0.630$ TeV
$\sigma_{p\bar{p} \rightarrow W} \times \mathcal{B}(W \rightarrow e\nu)$ [nb] [2]	0.50 ± 0.09 (stat) ± 0.05 (syst)	0.53 ± 0.06 (stat) ± 0.05 (syst)
$\mathcal{B}(W \rightarrow \tau\nu)/\mathcal{B}(W \rightarrow e\nu)$ [4]	-	1.04 ± 0.08 (stat) ± 0.08 (syst)

UA1 was a general-purpose particle detector at the CERN SPS, consisting of the inner tracker, electromagnetic calorimeter, hadronic calorimeter, and a muon system, sequentially from the inside to the outside. It took 0.546 TeV and 0.63 TeV data during 1982-1983 and

Table 1.3. The measurement of $\sigma_{p\bar{p} \rightarrow W} \times \mathcal{B}(W \rightarrow \ell\nu)$ for $\ell \in \{e, \mu, \tau\}$ and the ratios between leptonic channels by CDF and D0 at the Fermilab Tevatron.

CDF with p \bar{p} at $\sqrt{s} = 1.8$ TeV	
$\sigma_{p\bar{p} \rightarrow W} \times \mathcal{B}(W \rightarrow e\nu)$ [nb] [6]	2.19 ± 0.04 (stat) ± 0.21 (syst)
$\sigma_{p\bar{p} \rightarrow W} \times \mathcal{B}(W \rightarrow \mu\nu)$ [nb] [7]	2.21 ± 0.07 (stat) ± 0.21 (syst)
$\sigma_{p\bar{p} \rightarrow W} \times \mathcal{B}(W \rightarrow \tau\nu)$ [nb] [8]	2.05 ± 0.27
$\mathcal{B}(W \rightarrow \mu\nu)/\mathcal{B}(W \rightarrow e\nu)$ [7]	1.02 ± 0.08
$\mathcal{B}(W \rightarrow \tau\nu)/\mathcal{B}(W \rightarrow e\nu)$ [8]	0.94 ± 0.14

D0 with p \bar{p} at $\sqrt{s} = 1.8$ TeV	
$\sigma_{p\bar{p} \rightarrow W} \times \mathcal{B}(W \rightarrow e\nu)$ [nb] [9]	2.31 ± 0.01 (stat) ± 0.05 (syst) ± 0.10 (lum)
$\sigma_{p\bar{p} \rightarrow W} \times \mathcal{B}(W \rightarrow \mu\nu)$ [nb] [10]	2.09 ± 0.23 (stat) ± 0.11 (syst)
$\sigma_{p\bar{p} \rightarrow W} \times \mathcal{B}(W \rightarrow \tau\nu)$ [nb] [11]	2.22 ± 0.09 (stat) ± 0.10 (syst) ± 0.10 (lum)
$\mathcal{B}(W \rightarrow \mu\nu)/\mathcal{B}(W \rightarrow e\nu)$ [10]	0.89 ± 0.10
$\mathcal{B}(W \rightarrow \tau\nu)/\mathcal{B}(W \rightarrow e\nu)$ [11]	0.961 ± 0.061

1984-1985, respectively. Its W boson measurement is summarized in [1]. $W \rightarrow e\nu$ events were selected based on single electron plus missing transverse energy (E_T^{miss}). The QCD and $W \rightarrow \tau_e \nu$ background were estimated by the data-driven approach and simulation, respectively. In total, 59 and 240 $W \rightarrow e\nu$ events were selected from the 0.546 TeV and 0.63 TeV dataset, respectively. $W \rightarrow \mu\nu$ events were selected based on single muon plus E_T^{miss} trigger. The background involving muons from tau and meson decays was estimated by simulations. In total, 10 and 57 $W \rightarrow \mu\nu$ events were selected from 0.546 TeV and 0.63 TeV dataset. $W \rightarrow \tau\nu$ sample was selected with a single hadronic tau plus E_T^{miss} selection. The hadronic taus were identified as highly collimated narrow jets with low charged-track multiplicities. A τ -likelihood was calculated for each jet candidate based on its shape and charged tracks. In total, 32 events were selected from the combined 0.546 TeV and 0.63 TeV dataset. Based on the yields, UA1 reported the $\sigma_{p\bar{p} \rightarrow W} \times \mathcal{B}(W \rightarrow \ell\nu)$ for $\ell \in \{e, \mu, \tau\}$ at

0.546 TeV and 0.63 TeV center-of-mass energy. Pair-wise ratios were calculated to test the lepton flavor universality. Table 1.2 lists the measurements by UA1.

UA2 was a particle detector at the CERN SPS, consisting of a tracking system surrounded by a calorimetry system with electromagnetic and hadronic compartments. Unlike UA1, UA2 was not a multipurpose detector; its focus was on the calorimeters and did not have a muon detector. Therefore, lepton flavor universality test on UA2 mainly involved the $W \rightarrow e\nu$ and $W \rightarrow \tau\nu$. [2] summarized the $\sigma_{p\bar{p} \rightarrow W} \times \mathcal{B}(W \rightarrow e\nu)$ measurements from the UA2 using 0.546 TeV and 0.63 TeV dataset collected during 1982-1983 and 1984-1985. The measurement was based on single-electron plus E_T^{miss} trigger. After the UA2 upgrade during 1985-1987, tau channel was added and a test of the lepton flavor universality between electrons and taus was performed [3, 4], using the 0.63 TeV data collected during 1988-1990. The hadronic taus were reconstructed from jet candidates with requirements on the relative hadronic energy and the lateral energy profile. The data was triggered with E_T^{miss} trigger in 1988-1989 and a dedicated hadronic tau trigger in 1990. [3] analyzed the former dataset, while [4] combined the two datasets. The result [4] for the ratio between tauonic decay and electronic decay is shown in the Table 1.2.

CDF was an azimuthally and forward-backward symmetric general-purpose detector at the Fermilab Tevatron. It was consist of several subdetector layers, including a silicon tracker, a gas chamber as the central outer tracker, solenoid magnet, electromagnetic and hadronic calorimeters, and muon detector. CDF began taking its first data in 1985 and started its run-1 data taking after its first upgrade in 1989. For $W \rightarrow e\nu$, [6] presented a measurement of $\sigma_{p\bar{p} \rightarrow W} \times \mathcal{B}(W \rightarrow e\nu)$ using the single-electron trigger. For $W \rightarrow \mu\nu$, [7] presented a measurement of $\sigma_{p\bar{p} \rightarrow W} \times \mathcal{B}(W \rightarrow \mu\nu)$ and the ratio of muon and electron channels. This measurement used the single-muon trigger. Citing the previous CDF result on $\sigma_{p\bar{p} \rightarrow W} \times \mathcal{B}(W \rightarrow e\nu)$ [6], it obtained the ratio of the muonic and electronic weak coupling

as $g_\mu^W/g_e^W = 1.01 \pm 0.04$, consistent with the lepton flavor universality. Both electron and muon channels required E_T^{miss} to target the W+jets events. For $W \rightarrow \tau\nu$, [8] measured the $\sigma_{p\bar{p} \rightarrow W} \times \mathcal{B}(W \rightarrow \tau\nu)$ and its ratio to the previously obtained electronic channel [6]. The tau channel was based on two triggers, E_T^{miss} trigger and single-tau trigger (presence of a tau jet with a lower threshold of E_T^{miss}), which yielded 132 and 47 final events respectively. The tau identification required 0-3 tracks with no tracks in the $10^\circ - 30^\circ$ region separate from the seeding track. Combining the two triggers, the ratio between tau channel and electron channel was reported as $g_\tau^W/g_e^W = 0.97 \pm 0.07$, consistent with the SM lepton flavor universality. Table 1.3 lists the CDF results.

D0 was consist of a hybrid tracking system with silicon inner tracker and scintillator fiber outer tracker, superconducting solenoid, electromagnetic and hadronic calorimeter, and muon system. The detector was completed in 1991 and was placed in the Tevatron in February 1992. D0 collected 1.8 TeV data during 1992-1995. With data collected in 1992-1993, D0 presented a measurement of $\sigma_{p\bar{p} \rightarrow W} \times \mathcal{B}(W \rightarrow e\nu, \mu\nu)$ and their ratio [10]. Later, in the year 1994-1995, about 6 times more data was collected, and accordingly $\sigma_{p\bar{p} \rightarrow W} \times \mathcal{B}(W \rightarrow e\nu)$ was updated with a better precision [9]. It is worth noticing that this update [9] also reported the electronic branching fraction as $\mathcal{B}(W \rightarrow e\nu) = (10.66 \pm 0.15 \pm 0.21 \pm 0.11 \pm 0.11)\%$, where the uncertainties were for statistics, systematics, theory, and undetermined next-to-leading order theoretical calculation. Also, with the 1994-1995 data, D0 measured $\sigma_{p\bar{p} \rightarrow W} \times \mathcal{B}(W \rightarrow \tau\nu)$ and test the lepton flavor universality between tau and electron [11], shown in Figure 1.2. For $W \rightarrow e\nu$ and $W \rightarrow \mu\nu$, the event selection was based on single-electron plus E_T^{miss} and single-muon plus E_T^{miss} . For $W \rightarrow \tau\nu$, D0 used a dedicated hadronic tau trigger, which included requirements on E_T^{miss} , p_T of the leading narrow jet, and no jet opposite to the leading narrow jet. For each jet candidate, the energy in the leading two towers over the total energy was used to identify τ_h . Table 1.3 lists the D0 results.

LEP

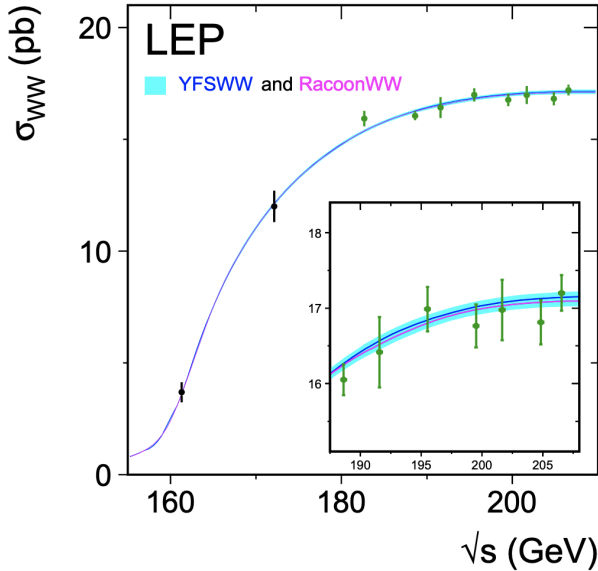


Figure 1.3. The LEP measurement of WW production cross-section. The measurement was a combine of the four LEP experiments, with a total 3 fb^{-1} data. The WW production at LEP was mainly induced by exchanging neutrinos in the t-channel and quark annihilation to Z/γ in the s-channel. The measured cross-section agreed with the theoretical calculation.

The LEP at CERN collided electrons and positrons at the center-of-mass energy of Z pole during its first running phase (1989-1995). Then the collision energy was increased to a maximum of 209 GeV during its second running phase (LEP-2 1995-2000). In some parts of 1995 and 1997, LEP was operated at center-of-mass energies below the WW resonance at 130.3 GeV, 136.3 GeV, and 140.2 GeV. The later runs of LEP-2 scanned at ten different energies above the WW resonance ranging from 161.3 GeV to 209 GeV. During the full scanning the center-of-mass energy from 130 GeV to 209 GeV, the four LEP experiments ALEPH, DELPHI, L3, and OPAL, collected a total data of 3 fb^{-1} integrated luminosity.

ALEPH was a cylindrical symmetric detector with a tracking system (drift chamber and TPC) and electromagnetic calorimeter, super conducting solenoid, streamer tubes inserted

in the iron return yokes for the hadron and muon detection. DELPHI was also a cylindrical general-purpose detector consisting of vertex detector, time projection chamber (TPC) tracker, Ring-Imaging Cherenkov detector, electromagnetic calorimeter, solenoid, hadroinc calorimeter, muon chamber. OPAL's structure was formed by vertex detector, tracker, magnetic solenoid, crystal ECAL/HCAL, and muon detector. Unlike the other 3 detectors, L3 had its magnetic solenoid as the outmost layer; inside were trackers (silicon strip micro vertex detector and time expansion chamber), electromagnetic/hadronic calorimeters, and muon chamber.

The WW production in the electron positron collision was primarily induced by the electroweak process in the t-channel exchanging ν_e , and the triple gauge boson coupling process in the s-channel mediated by Z boson or photon. The measurement of WW production cross-section from the four LEP experiments combined is shown in Figure 1.3. There is a clear turn-on for the WW production at the 161.3 GeV. The combined result of WW cross-section is consistent with the theoretic prediction by YFSWW and RACOONWW.

Each experiment determined the three W leptonic decay branching fractions from the WW cross-sections measurement [16]. The hadronic branching fraction was determined from the leptonic ones based on the unitarity. When combining the four experiments, the theoretical uncertainties of signal and background, as well as the theoretical uncertainties of the luminosity, were treated as correlated; the experimental uncertainties on the luminosity, detector effects, and simulation statistics are treated as uncorrelated. The details of the $\mathcal{B}(W \rightarrow \ell\nu)$ results and the correlations are summarized in Table 1.4 and in Figure 1.4. A suspicious excess of the lepton flavor universality was observed in the result. While the electronic and muonic branching fractions agree well with each other, the tauonic branching fraction is significantly larger than the average of the other two. The ratio between the

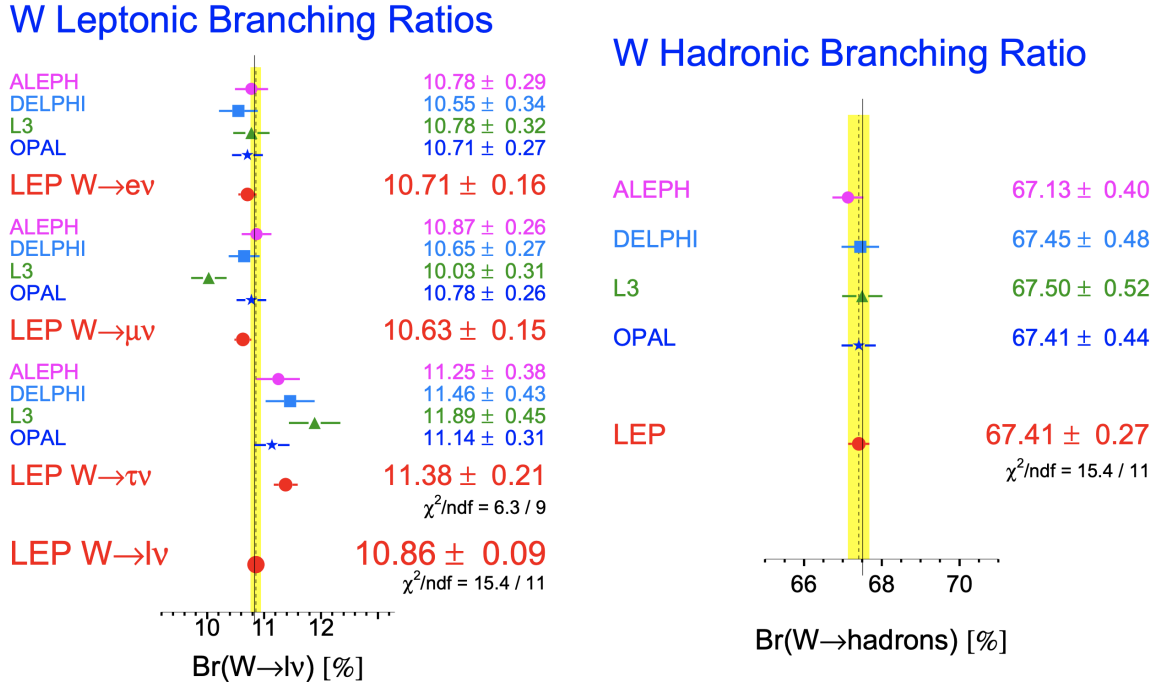


Figure 1.4. W leptonic and hadronic branching fractions from the four LEP experiments [16].

$\mathcal{B}(W \rightarrow \tau\nu)$ and the average of $\mathcal{B}(W \rightarrow e\nu)$ and $\mathcal{B}(W \rightarrow \mu\nu)$ was reported as [16] 1.066 ± 0.025 , showing a 2.6 standard deviation from the lepton flavor universality.

Table 1.4. Three individual leptonic branching fractions from the four LEP experiments and the combined result [16].

ALEPH [12]			
$\mathcal{B}(W \rightarrow e\nu)$	10.78 ± 0.27 (stat) ± 0.10 (syst)	$[+1.000 \quad -0.009 \quad -0.332]$	
$\mathcal{B}(W \rightarrow \mu\nu)$	10.87 ± 0.25 (stat) ± 0.08 (syst)	$[-0.009 \quad +1.000 \quad -0.268]$	
$\mathcal{B}(W \rightarrow \tau\nu)$	11.25 ± 0.32 (stat) ± 0.20 (syst)	$[-0.332 \quad -0.268 \quad +1.000]$	

DELPHI [13]			
$\mathcal{B}(W \rightarrow e\nu)$	10.55 ± 0.31 (stat) ± 0.14 (syst)	$[+1.000 \quad +0.030 \quad -0.340]$	
$\mathcal{B}(W \rightarrow \mu\nu)$	10.65 ± 0.26 (stat) ± 0.08 (syst)	$[+0.030 \quad +1.000 \quad -0.170]$	
$\mathcal{B}(W \rightarrow \tau\nu)$	11.46 ± 0.39 (stat) ± 0.19 (syst)	$[-0.340 \quad -0.170 \quad +1.000]$	

L3 [15]			
$\mathcal{B}(W \rightarrow e\nu)$	10.78 ± 0.29 (stat) ± 0.13 (syst)	$[+1.000 \quad +0.136 \quad -0.201]$	
$\mathcal{B}(W \rightarrow \mu\nu)$	10.03 ± 0.29 (stat) ± 0.12 (syst)	$[+0.136 \quad +1.000 \quad -0.122]$	
$\mathcal{B}(W \rightarrow \tau\nu)$	11.89 ± 0.40 (stat) ± 0.20 (syst)	$[-0.201 \quad -0.122 \quad +1.000]$	

OPAL [14]			
$\mathcal{B}(W \rightarrow e\nu)$	10.71 ± 0.25 (stat) ± 0.11 (syst)	$[+1.000 \quad +0.135 \quad -0.303]$	
$\mathcal{B}(W \rightarrow \mu\nu)$	10.78 ± 0.24 (stat) ± 0.10 (syst)	$[+0.135 \quad +1.000 \quad -0.230]$	
$\mathcal{B}(W \rightarrow \tau\nu)$	11.14 ± 0.31 (stat) ± 0.17 (syst)	$[-0.303 \quad -0.230 \quad +1.000]$	

LEP Average [16]			
$\mathcal{B}(W \rightarrow e\nu)$	10.71 ± 0.14 (stat) ± 0.07 (syst)	$[+1.000 \quad +0.136 \quad -0.201]$	
$\mathcal{B}(W \rightarrow \mu\nu)$	10.63 ± 0.13 (stat) ± 0.07 (syst)	$[+0.136 \quad +1.000 \quad -0.122]$	
$\mathcal{B}(W \rightarrow \tau\nu)$	11.38 ± 0.17 (stat) ± 0.11 (syst)	$[-0.201 \quad -0.122 \quad +1.000]$	

LHC

During the LHC run-1 at a center-of-mass energy of 7 TeV and 8 TeV, the lepton flavor universality was studied in the electron and muon channels of $W+jets$ events. Two such measurements were published by the ATLAS and LHCb. ATLAS measured the $\sigma_{pp \rightarrow W} \times \mathcal{B}(W \rightarrow e\nu, \mu\nu)$ [34] with 7 TeV data collected in 2011 corresponding to 4.6 fb^{-1} integrated luminosity. The events were triggered with single-lepton triggers and selected with several lepton isolation and identification cuts, as well as E_T^{miss} cuts. The ratio $\frac{\mathcal{B}(W \rightarrow \mu\nu)}{\mathcal{B}(W \rightarrow e\nu)}$ was determined as 1.003 ± 0.010 . LHCb measured the $\sigma_{pp \rightarrow W} \times \mathcal{B}(W \rightarrow e\nu)$ [35] and $\sigma_{pp \rightarrow W} \times \mathcal{B}(W \rightarrow \mu\nu)$ [36] in two separate analysis with 8 TeV data corresponding to 2 fb^{-1} integrated luminosity. The events were also triggered with the single-lepton triggers, and the selections required on lepton quality and E_T^{miss} . To test universality, the second analysis [35] compared its electron channel to the muon channel published in the first analysis [36], taking into account the experimental correlations. The comparison included both the total cross-section and the differential cross-section with respect to pseudorapidity. The differential cross-section agreed well between the electron channel and muon channel. Their ratio led to $\frac{\mathcal{B}(W \rightarrow \mu\nu)}{\mathcal{B}(W \rightarrow e\nu)} = 0.980 \pm 0.018$.

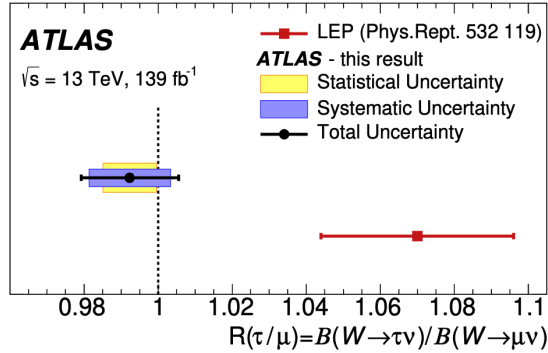


Figure 1.5. The measurement of $\frac{\mathcal{B}(W \rightarrow \tau\nu)}{\mathcal{B}(W \rightarrow \mu\nu)}$ by ATLAS using the full LHC run-2 dataset [23].

During the LHC run-2 at a center-of-mass energy of 13 TeV, W bosons from the $t\bar{t}$ events are treated as the major signal for the LFU test, thanks to the high $t\bar{t}$ cross-section at 13 TeV. ATLAS [23] measured the ratio between the tauonic and the muonic branching fractions

$\frac{\mathcal{B}(W \rightarrow \tau\nu)}{\mathcal{B}(W \rightarrow \mu\nu)}$ using the LHC run-2 data at 13 TeV collected during 2016-2018 corresponding to 139 fb^{-1} integrated luminosity. The analysis selects $t\bar{t}$ events in the $\mu\mu$ and $e\mu$ final states using single-muon and single-electron trigger, respective, requiring two b tagged jets for better $t\bar{t}$ purity. Tau is probed with tau's muonic decay, which is about 17% of the total tau decay width. The measurement fits to the distribution of the transverse impact parameter D_0 of the selected muons (in three p_T bins) to discriminate $W \rightarrow \mu$ and $W \rightarrow \tau \rightarrow \mu$, where the templates of prompt $W \rightarrow \mu$ are derived in a data-driven manner from a calibration region of $Z \rightarrow \mu\mu$ events without jet requirements. Also with this calibration region, the calibrations for the D_0 resolution are derived. The backgrounds of non-prompt muons from the hadron decay $h \rightarrow \mu$ and prompt muons from Z decay $Z \rightarrow \mu\mu$ are calibrated by control regions with $m_{\mu\mu}$ in the Z window and with same-sign muons, respectively (keeping same muon, jet and b tag requirements as signal regions). Probing taus with the muonic decay helps cancel the systematical uncertainties related to the muon reconstruction and trigger. Also, the systematical uncertainties concerning hadronic tau identification is avoided. The reported result of the branching ratio is

$$\frac{\mathcal{B}(W \rightarrow \tau\nu)}{\mathcal{B}(W \rightarrow \mu\nu)} = 0.992 \pm 0.013 [\pm 0.007 \text{ (stat)} \pm 0.011 \text{ (stat)}]$$

Table 1.5. Standard Model predictions and the experimental measurements of the leptonic or semi-leptonic branching ratios of the pseudoscalar mesons [37].

	SM Prediction	World Average	Included measurements
$R_{e/\mu}^\pi [10^{-4}]$	1.2352 ± 0.0001 [38]	1.2327 ± 0.0023	TRIUMF [39, 40], PiENu [41], BGO-OD [42]
$R_{e/\mu}^K [10^{-5}]$	2.477 ± 0.001 [38]	2.488 ± 0.009	NA62 [43], KLOE [44]
$R_{\tau/\mu}^{D_s}$	9.76 ± 0.10 [45]	9.95 ± 0.61	HFLAV [46] ave of CLEO, BASIII, BELLE, BABAR
$R_{D,\tau/\ell}^B$	0.299 ± 0.003 [37]	0.340 ± 0.030	BABAR [47, 48], Belle [49]
$R_{D^*,\tau/\ell}^B$	0.258 ± 0.005 [37]	0.295 ± 0.014	BABAR [47, 48], Belle [49, 50, 51], LHCb[52, 53, 54]

1.2.1.2. Test with Meson Decay. The charged weak current decays of mesons mediated by W bosons also provide tests of LU. The most stringent constraints come from the study of fully-leptonic decay of the charged pions or kaons, which are helicity suppressed in the SM depending on the lepton mass. Pions and kaons are kinematically allowed to decay into electrons and muons. The ratio between the electronic and muonic branching fractions of pion is measured by TRIUMF [39, 40], PiENu [41] and BGO-OD[42], while that of kaon is measured by NA62 [43] and KLOE [44], shown in Table 1.5. The measured ratios are consistent with the SM LFU predictions. For D_s meson, tauonic decay is possible, and the ratio between tauonic and muonic branching fraction $R_{\tau/\mu}^{D_s}$ is measured in the charm factories including CLEO, BASIII, Belle, and BaBar. Table 1.5 shows these experimental measurements and the comparison to the SM theoretical calculations, where the agreement to LFU is indicated.

Additionally, the tests of LFU can be performed by taking ratios between the semi-leptonic charged weak decays of mesons, such as $D \rightarrow K\ell\nu$. The Heavy Flavor Averaging Group (HFLAV) [55] provides a summary of the LFU test using the semi-leptonic charged weak decays of the D meson and the B meson. An anomaly is observed in the $B \rightarrow D^{(*)}\ell\nu$ semi-leptonic decay in the tau channel versus the electron and muon channel. $R_{D^{(*)},\tau/\ell}^B$ is measured in the Belle [49, 50, 51], BaBar [47, 48] and LHCb [52, 53, 54]. Ratios are defined as $R_{D^{(*)},\tau/\ell}^B = \frac{\mathcal{B}(B \rightarrow D^{(*)}\tau\nu)}{\mathcal{B}(B \rightarrow D^{(*)}\ell\nu)}$ where $\ell = e, \mu$. The experimental results are listed in Table 1.5. Figure 1.6 illustrates this anomaly in the B meson semi-leptonic decays. The world average of Belle, BaBar and LHCb is about four sigma deviated from the SM theoretical prediction.

1.2.1.3. Test with Tau Decay. The LFU involving the charged weak current can also be tested by the tau precision measurements [55, 56]. In the SM, the only expected difference between $\tau^- \rightarrow e^- \bar{\nu}_e \nu_\tau$ and $\tau^- \rightarrow \mu^- \bar{\nu}_\mu \nu_\tau$ decay is due to the decay kinematic phase space. g_μ/g_e can be obtained by precision measurements of tau's electronic and muonic decay

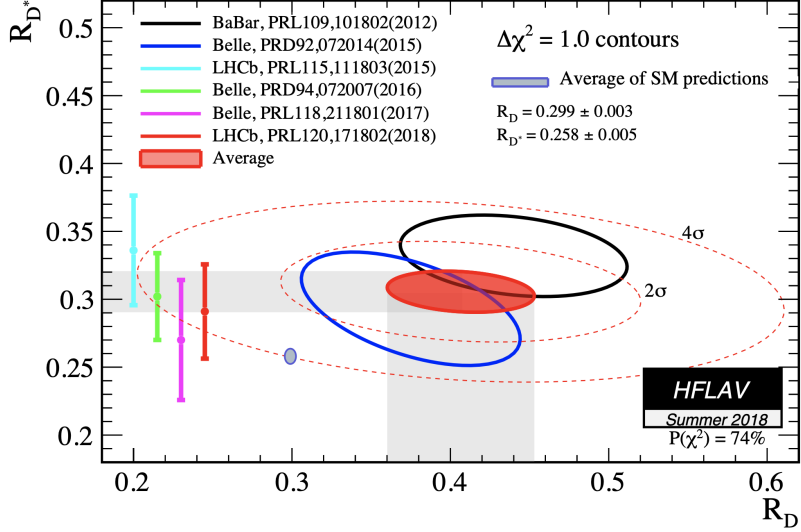


Figure 1.6. Anomaly of lepton flavor universality in the semi-leptonic decays of B meson [55]. The world average of $R_{D,\tau/l}^B$ and $R_{D^*,\tau/l}^B$ shows a four sigma deviation from the Standard Model prediction.

widths. Similarly, g_τ/g_μ can be obtained by precision measurement of tau's electronic decay $\tau^- \rightarrow e^- \bar{\nu}_e \nu_\tau$ and muon's electronic decay $\mu^- \rightarrow e^- \bar{\nu}_e \nu_\mu$. The ratio of the weak couplings to the third and first generation leptons can be obtained from the measurements of the width of $\tau^- \rightarrow \mu^- \bar{\nu}_\mu \nu_\tau$ and $\mu^- \rightarrow e^- \bar{\nu}_e \nu_\mu$. These represent one of the most stringent experimental tests for LFU in the electroweak sector. By global fitting to the tau precision measurements, HFLAV [55] determines the ratios of electroweak coupling constant among the three leptons as

$$g_\tau/g_\mu = 1.0010 \pm 0.0014$$

$$g_\tau/g_e = 1.0029 \pm 0.0014$$

$$g_\mu/g_e = 1.0018 \pm 0.0014$$

1.2.2. Measurements of V_{cs}

The CKM matrix represents the mixing between quarks' mass eigenstates and the flavor eigenstates. When physical quarks in their mass eigenstates participate in the weak interaction, they are projected to the flavor eigenstates by the CKM matrix. More details about the quantum field theory of the CKM matrix in the standard model are discussed in Appendix A.3.

Table 1.6. World average of the experimental measurements of the nine elements in the CKM matrix in the PDG [27].

$ V_{ud} = 0.97370 \pm 0.00014$	$ V_{us} = 0.2245 \pm 0.0008$	$ V_{ub} = 0.00382 \pm 0.00024$
$ V_{cd} = 0.221 \pm 0.004$	$ V_{cs} = 0.987 \pm 0.011$	$ V_{cb} = 0.0410 \pm 0.0014$
$ V_{td} = 0.0080 \pm 0.0003$	$ V_{ts} = 0.0388 \pm 0.0011$	$ V_{tb} = 1.013 \pm 0.030$

The current experimental measurements of the nine elements in the CKM matrix [27] are shown in Table 1.6. Among the six elements in the first two rows, the measurement of $|V_{cs}|$ shown in Figure 1.7 has the least precision. Currently, there are two direct approaches to measure $|V_{cs}|$, using the D meson decay in the charm factories and using the on-shell $W \rightarrow cs$ with jet tagging in the collider experiments.

The best direct determination of $|V_{cs}|$ is from the semi-leptonic decay of D meson and the leptonic decay of D_s meson produced in the charm factory. For D_s meson, the branching fraction of $D_s^+ \rightarrow \mu^+\nu$ and $D_s^+ \rightarrow \tau^+\nu$ are both measured in the Belle [57], CLEO [58, 59, 60], BaBar [61] and BESIII [62, 63]. Using the experimental value of the mass and lifetime of D_s meson, as well as the lattice QCD calculation of the form factor f_{D_s} , $|V_{cs}|$ can be determined from the D_s leptonic decay and yields a world average of $|V_{cs}| = 0.992 \pm 0.012$ [55], where the dominating uncertainty is from the experimental error. For D meson, the branching fraction of $D \rightarrow K\ell\nu$ is measured by CLEO-c [64], Belle [65], BaBar [66] and BESIII [67, 68], which leads to an average of $|V_{cs}|$ of $|V_{cs}| = 0.939 \pm 0.038$ [55] in the D

meson decay. The dominant uncertainty is from the theoretical calculations of the D meson form factor with lattice QCD. Combining the results from the D and D_s meson decays, the charm factories produce $|V_{cs}| = 0.987 \pm 0.011$ [55]. This is also the value considered as the world average by the PDG [27].

The second direct measurement of $|V_{cs}|$ is from the on-shell $W \rightarrow cs$ decays in the collider experiments. This approach relies on jet tagging to identifies the jets originating from the c and s quarks, which is relatively difficult, especially in the LHC with a more complex hadron environment. Therefore, this approach is less explored comparing with the D/D_s approach. So far, the only published result based on the $W \rightarrow cs$ approach is from the DELPHI [69] in the LEP. DELPHI identified the charged mesons based on their ionization energy losses while traversing through the TPC tracking system. Since s and c jets tend to include energetic kaons, they were first tagged by the p_T and the particle identity (π or K) of the leading meson in the jet. Then the impact parameters of the tracks in the jet were considered to discriminate c quark jets against other jets. The result from DELPHI was reported as $|V_{cs}| = 0.94^{+0.32}_{-0.26} \pm 0.13$.

In addition, LEP published one indirect result. LEP measures the $\mathcal{B}(W \rightarrow \ell\nu) = (10.83 \pm 0.07 \pm 0.07)\%$ [16], based on which calculates the sum of all six CKM element in the first two rows as $\sum_{d,s,b}^{u,c} |V_{ij}|^2 = 2.002 \pm 0.027$. Since $|V_{cs}|$ is the least precisely measured element, LEP subtract other five elements from $\sum_{d,s,b}^{u,c} |V_{ij}|^2$ and produces an indirect measurement of $|V_{cs}| = 0.969 \pm 0.013$. With the latest CKM values for the other five elements, repeating LEP's calculation gives $|V_{cs}| = 0.972 \pm 0.013$. The same calculation can be done with the $\mathcal{B}(W \rightarrow \ell\nu)$ measurement by the CMS presented in this thesis.

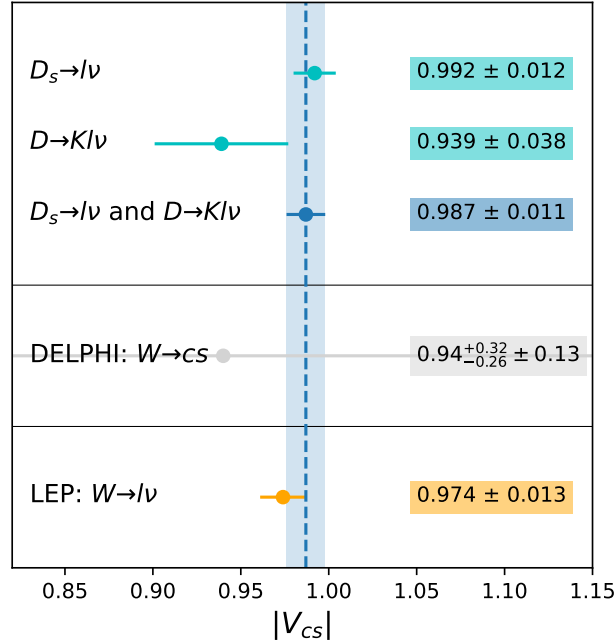


Figure 1.7. The $|V_{cs}|$ measurements [27]. The 2020 PDG average [27] combines the results from D and D_s decay.

CHAPTER 2

Physics Foundations

2.1. Standard Model Particles

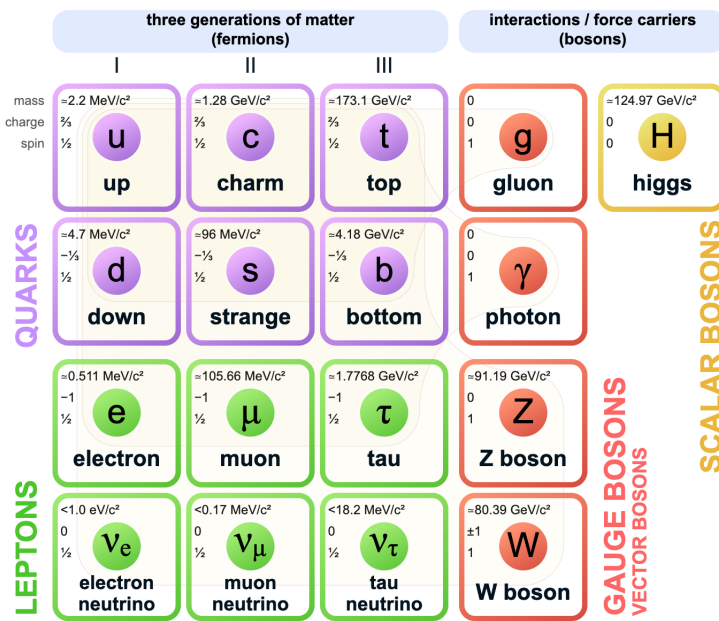


Figure 2.1. Particles in the Standard Model. Fermions include three generations of quarks and leptons, while bosons include four gauge bosons and one Higgs boson.

The standard model treats matter and the force as a set of quantum fields, excited states of which correspond to different fundamental particles. Figure 2.1 shows the table of the SM particles. The “matter particles” are spin- $\frac{1}{2}$ fermions including three generations of quarks and leptons. The “force particles” are spin-1 gauge bosons accounting for the electromagnetic, strong, weak forces. Additionally, there is a spin-0 Higgs boson that generates mass for fermions and gauge bosons. The theoretical foundation of the SM particles in Figure 2.1

is the quantum field theory (QFT), a theory joining quantum mechanics and special relativity. Appendix A summarizes the backbone of the quantum field theory for SM, covering Yang-Mills Gauge Theory, Higgs Mechanism, Glashow-Weinberg-Salam (GWS) electroweak model and Quantum Chromodynamics (QCD). This section provides an overall description of the SM particles.

2.1.1. Fermions

Table 2.1. The electroweak quantum number of the first generation leptons and quarks. The second and third generation have the same electroweak quantum number as the first generation. The listed quantum numbers are isospin T , the third component of isospin T^3 , charge Q and hypercharge Y .

lepton	T	T^3	Q	Y	quark	T	T^3	Q	Y
$\nu_{e,L}$	$\frac{1}{2}$	$\frac{1}{2}$	0	-1	u_L	$\frac{1}{2}$	$\frac{1}{2}$	$\frac{2}{3}$	$\frac{1}{3}$
e_L	$\frac{1}{2}$	$-\frac{1}{2}$	-1	-1	d_L	$\frac{1}{2}$	$-\frac{1}{2}$	$-\frac{1}{3}$	$\frac{1}{3}$
-	-	-	-	-	u_R	0	0	$\frac{2}{3}$	$\frac{4}{3}$
e_R	0	0	-1	-2	d_R	0	0	$-\frac{1}{3}$	$-\frac{2}{3}$

Quarks. Three generations of quarks have been discovered: up (u) and down (d) being the first generation, charm (c) and strange (s) being the second generation, top (t) and bottom (b) being the third generation. The terminology “generation” is often referred to as “family” as well. The up, charm and top quarks have electric charge of $\frac{2}{3}$, while the electric charge of down, strange and bottom quark is $-\frac{1}{3}$. Other than electric charge, quark also carries color quantum number and thus participates in the strong interaction. The color quantum number (red, green, and blue) is analogous to the electric charge in the electromagnetic force. Each quark has its corresponding antiquark carrying an opposite electric charge and anti-color. However, neither the fractional charge nor individual color charge is observed in nature, because quarks never exist alone. Quarks and their properties only reveal during the high-energy short-distance local interactions. In the low energy scale, they are

always combined in two-quark or three-quark bounded states, called mesons and baryons respectively, which are color-neutral and integer-charged. This phenomenon is known as “quark confinement”. Quarks not only couple to the electromagnetic and strong force, but are also involved in the weak interaction. The weak hypercharge and isospin of quarks are listed in the Table 2.1. The masses of quarks arrange from a few MeV to 173 GeV. The heavy quarks decay into light quarks via the weak force with quark mixing. Therefore, the matter in our everyday life includes only the first generation light quarks. The most massive quark t quark decays almost instantaneously to one b quark and one W gauge boson upon its production before hadronizing into bounded states. Quark model has been successful in the classification of mesons and baryons, and explaining the observations in many experiments such as the lepton-nucleon deep-inelastic scattering, electron-positron annihilation and proton-proton hard collision.

Leptons. Three generations of leptons have been discovered: electrons (e) and electron neutrino (ν_e) being the first generation, muon (μ) and muon neutrino (ν_μ) being the second generation, tau (τ) and tau neutrino (ν_τ) being the third generation. Electron, muon and tau have negative one electric charge and couple to the electromagnetic force, while all neutrinos are not charged and do not interact electromagnetically. Charged leptons can be both left-handed and right-handed, while the neutrinos can only be left-handed because right-handed neutrinos have not been experimentally observed so far. Due to the chiral nature of weak interaction, the left-handed leptons couples to both W and Z weak gauge bosons, while right-handed charged leptons do not couple to the W bosons. The quantum number of leptons are also shown in the Table 2.1. The masses of the charged leptons increases with the lepton generations. Charged leptons in the second and third generations have finite lifetimes. Therefore, electrons are the only charged lepton in our everyday matter. Neutrinos in the SM had been thought as massless until the discovery of neutrino oscillation.

The neutrino masses were then added to the SM. But the exact values of neutrino masses are still not fully determined yet.

2.1.2. Bosons

The bosons in the SM consist of four spin-1 gauge bosons and one spin-0 Higgs boson. Four gauge bosons are responsible for the forces between fermions: the electromagnetic force is mediated by the photon γ ; the strong nuclear force is propagated by gluons g , the weak force is carried by the W and Z bosons. In the QFT, the existence of gauge boson originates from engaging the local symmetries for the fermions Lagrangian. In other words, force is modelled as a consequence of “gauging” the matter. Among the four gauge bosons, photon and gluon are massless while the W and Z boson are massive with $m_W = 80.385 \pm 0.015$ GeV and $m_Z = 90.183 \pm 0.002$ GeV [27], respectively. The non-zero mass of the gauge boson breaks the gauge symmetry and causes renormalization issues, unless the mass of gauge boson is generated by the Higgs mechanism. The Higgs boson is a spin-0 boson predicted in the 1960s to solve the problems related to the gauge boson mass. It was finally confirmed exist at $m_H = 125.09 \pm 0.24$ GeV by the CMS [70] and the ATLAS [71] experiment at LHC in 2012. It was the last missing piece added in the SM particles. Besides the mass of gauge bosons, Higgs boson also generates fermions’ masses via Yukawa couplings.

2.2. Physics in the Hadron Colliders

When protons collide in hadron collider, it is actually the quarks and gluons inside the protons, called partons, that collide at the high center-of-mass energies. This high energy collision between partons is called the hard process and can be calculated perturbatively with the quantum field theory. However, the experimental observables from the proton-proton

collision not only involves the physics in the hard process, but also includes many low-energy QCD processes happening before and after the hard process that cannot be treated with perturbative QCD (pQCD). Therefore, to properly make predictions to experiments, efforts are made to understand how partons distribute in the collided protons before the hard process, and how outgoing particles evolve in the long-distance range after the hard process. These studies yield the topics of the parton distribution function (PDF) and jet physics. In this section, brief descriptions of the PDF, hard process, and jet physics are presented. This provides a basic picture to understand event generators described in Section 3.5. Also, it helps understand the sources of some theoretical uncertainties in the W branching fraction analysis.

2.2.1. Parton Distribution Functions

A proton can be pictured as three valence quarks surrounded by a cloud of soft gluon and sea quarks. For a proton with a given momentum, the probability distribution of finding a certain type of parton is described by the parton distribution functions $f_i(x)$, where x denotes the fraction of the total proton momentum p carried by the parton. When colliding protons, partons are actually participating in the high energy collision. As a result, the cross-section of the collision is a convolution of the cross-section of the hard process and the PDFs of the two collided partons:

$$\sigma_{pp \rightarrow X} = \sum_{ij} \int dx_1 dx_2 f_i(x_1, \mu^2) f_j(x_2, \mu^2) \hat{\sigma}_{ij \rightarrow X}(x_1 p_1, x_2 p_2, \mu^2). \quad (2.1)$$

This factorizes the total cross-section into the hard collision and PDFs, where μ is the factorization scale. To make theoretical predictions in the LHC, the PDFs are one of the necessary inputs. The measurements of PDFs are primarily accomplished by the lepton-hadron deep inelastic scattering (DIS) experiments. The DIS cross-section yields the structure functions

of the hadrons $F_2(x)$, which theoretically equals to the sum of PDFs weighted by the quark momentum and charge squared: $F_2(x) = \sum_i xQ_i^2 f_i(x)$. The PDFs of different quarks $f_i(x)$ are extracted from the electron DIS off protons and neutron targets, using the quark symmetries between the proton and neutron. The PDFs of anti-quarks are extracted from the DIS experiments with the neutrino and anti-neutrino beams, since the intermediatelying W^\pm bosons are capable of probing specific charge conjugated states. However, the gluon distribution is not directly measured in the DIS experiments because both the mediating photon and W bosons in the DIS process do not carry color charge and thus do not probe the gluons. Instead, the information about the gluon distribution is indirectly extracted from the evolution of quark PDFs in different energy scales based on the DGLAP equation:

$$\mu \frac{d}{d\mu} \begin{bmatrix} f_i(x, \mu^2) \\ f_g(x, \mu^2) \end{bmatrix} = \sum_j \frac{\alpha_s}{\pi} \int_x^1 \frac{dy}{y} \begin{bmatrix} P_{q_i q_j}(\frac{x}{y}) & P_{q_i g}(\frac{x}{y}) \\ P_{g q_j}(\frac{x}{y}) & P_{gg}(\frac{x}{y}) \end{bmatrix} \begin{bmatrix} f_j(y, \mu^2) \\ f_g(y, \mu^2) \end{bmatrix}, \quad (2.2)$$

where P_{ab} is the DGLAP splitting function, representing the probability of parton a radiating another parton b with a fraction momentum $z = \frac{p_b}{p_a}$. The splitting function P_{ab} is calculated by considering the tree-level Feynman diagram and reads as

$$\begin{aligned} P_{qq}(z) &= \frac{4}{3} \left[\frac{1+z^2}{1-z} \right]_+, \quad P_{qg}(z) = \frac{1}{2} \left[z^2 + (1-z)^2 \right], \quad P_{gq}(z) = \frac{4}{3} \left[\frac{1+(1-z)^2}{z} \right] \\ P_{gg}(z) &= 6 \left[\frac{z}{1-z} + \frac{1-z}{z} + z(1-z) \right] + (11 - \frac{n_f}{3}) \delta(1-z). \end{aligned} \quad (2.3)$$

The DGLAP equation is a renormalization group equation (RGE) for the scale-dependent evolution of PDFs, similar to the RGE for the running of couplings in Equation A.60. The driving for the PDF evolution is the splitting functions in Equation 2.3, analogous to the role of beta function in the running of coupling constants. An intuitive understanding of the PDF evolution is that as the probing energy increases, more and more “soft cloud” of sea quarks and gluons are revealed. As a result, the PDFs of sea quarks and gluons increase

in the low x region. The DGLAP equation in Equation 2.2 is a set of two first-order linear differential equations, and the solution is

$$\begin{bmatrix} f_i(x, \mu^2) \\ f_g(x, \mu^2) \end{bmatrix} = \begin{bmatrix} f_i(x, \mu_0^2) \\ f_g(x, \mu_0^2) \end{bmatrix} + \frac{\alpha_s}{2\pi} \log\left(\frac{\mu^2}{\mu_0^2}\right) \sum_j \int_x^1 \frac{dy}{y} \begin{bmatrix} P_{q_i q_j}(\frac{x}{y}) & P_{q_i g}(\frac{x}{y}) \\ P_{g q_j}(\frac{x}{y}) & P_{g g}(\frac{x}{y}) \end{bmatrix} \begin{bmatrix} f_j(y, \mu_0^2) \\ f_g(y, \mu_0^2) \end{bmatrix}, \quad (2.4)$$

where the μ^2 is the variable factorization scale in Equation 2.1, and μ_0^2 is the reference scale of the renormalization group. The measured PDFs at two different energy scales $\mu^2 = 10 \text{ GeV}^2$ and $\mu^2 = 10^4 \text{ GeV}^2$ are shown in Figure 2.2

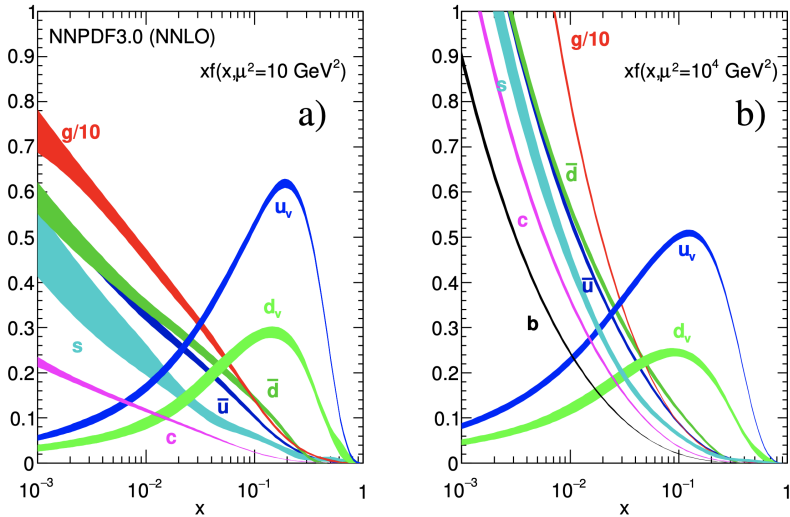


Figure 2.2. PDF of valence quark, sea quark and gluon at $\mu^2 = 10 \text{ GeV}^2$ and $\mu^2 = 10^4 \text{ GeV}^2$ [27]. The valence quarks dominate the high- x region and in total only account for about 38% of the proton momentum. The low- x region is dominated by the sea quarks and gluons, forming a “soft cloud” around the valence quarks. Gluons are the major components of the “soft cloud”, and in total carry over 40% of the proton momentum. Comparing PDF in (*left*) and (*right*), the increasing of the energy scale dramatically populates the soft gluons and soft sea quarks. Intuitively speaking, more and more “soft cloud” of sea quarks and gluons are revealed as the probing energy increases.

2.2.2. Hard Processes

The hard processes between partons happen in the short-distance range and can be calculated perturbatively with quantum field theories. In the LHC, the hard processes allowed by the SM include the electroweak, QCD, and Higgs interactions. Figure 2.3 shows a summary of the total cross-section of the SM processes in the LHC measured by the experiments and predicted by the SM. For this thesis, the signal processes producing a pair of W bosons include $t\bar{t}$, tW and WW .

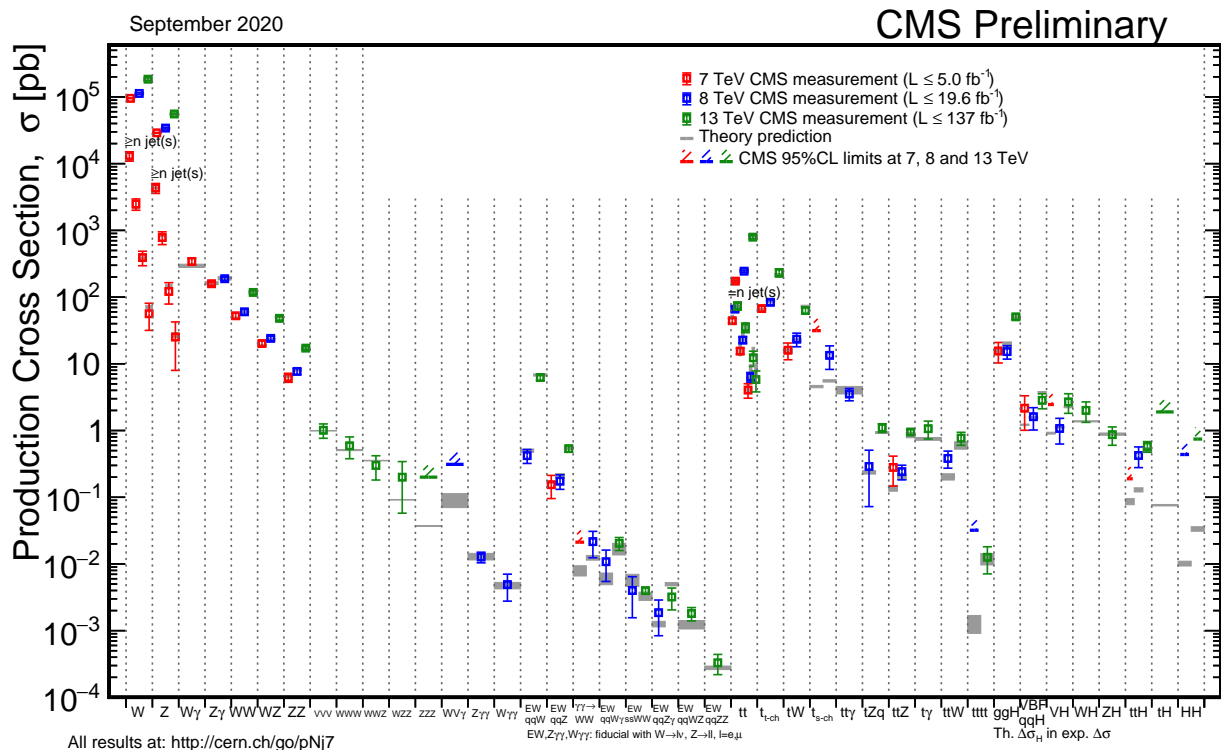


Figure 2.3. Summary of the cross-sections of the SM processes in the LHC. The grey bar shows the theoretical predictions. The red, blue and green points indicate the CMS measurements or the exclusion limits at 7, 8, 13 TeV.

For $t\bar{t}$, the top quark pairs are produced with the QCD interaction. The tree-level diagrams for the $t\bar{t}$ production is shown in Figure 2.4. The quark-antiquark annihilation, shown as Figure 2.4 left, was the dominant process in the Tevatron, where the quark and antiquark

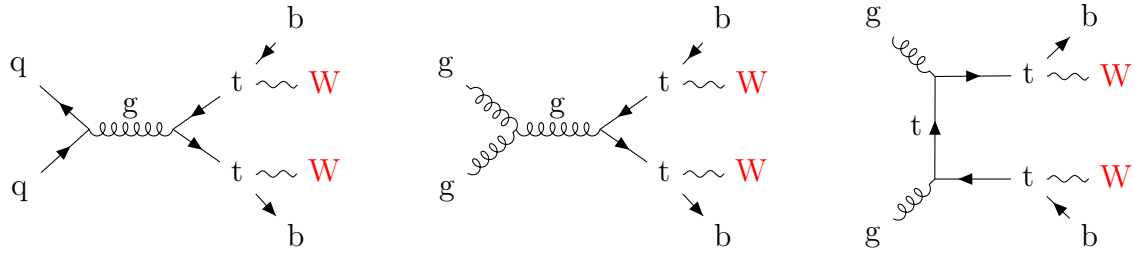


Figure 2.4. The tree-level processes of $t\bar{t}$ production in the LHC. In all three diagrams, $t\bar{t}$ is produced with the QCD interaction. In the LHC, the dominant production processes are the two diagrams on the right, with two incoming gluons colliding in the s-channel and t-channel, respectively. The top quark decays into one W boson and one b quark immediately after the production.

are the valence quark in the proton and anti-proton. But in the LHC, which collides proton-proton at a higher center-of-mass energy, gluon-gluon fusion in the s channel and t channel, shown as Figure 2.4 middle and right, are the dominant diagrams. The top quark decays into one b quark and one W boson instantly after being produced. The resulting pair of W bosons are used to measure W branching fractions in this thesis. Meanwhile, the outgoing b quarks are used to tag the $t\bar{t}$ events.

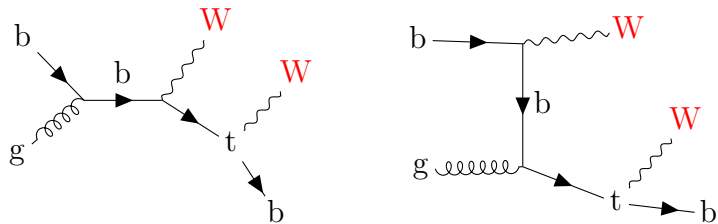


Figure 2.5. The tree-level processes of tW production. The incoming b quark scatters off a gluon with QCD interaction and gets excited into a top quark via the electroweak interaction.

The tW production is induced via weak interactions and has smaller cross-section compared to $t\bar{t}$ production. The tree-level tW processes are shown in Figure 2.5. One W boson is produced associated with top quark. The outgoing top quark decays into one b quark and another W boson. The two W bosons are used for W measurements, while the b quarks is used to tag the tW event.

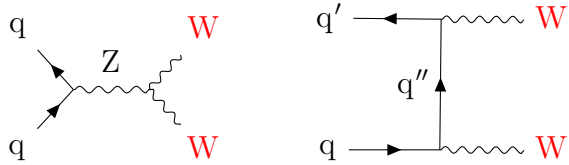


Figure 2.6. The tree-level process of WW production. These two diagrams are both induced by electroweak interactions.

The WW events are produced by electroweak interactions. Figure 2.6 shows two major tree-level processes of the WW production. In the first diagram, quark and antiquark annihilate into a virtual Z/γ , which then decays into WW via the electroweak triple-gauge-coupling (TGC). In the second diagram, WW is produced in the t-channel of quark-quark scattering. The WW processes contribute at small cross-sections to the event selection with $n_b = 0$. The treatment of the WW process is different between the shape analysis and the counting analysis: the shape analysis treat it as a signal process, while the counting analysis which does not have any $n_b = 0$ category treats it as a background.

2.2.3. Jet Forming

A few processes take place between the hard process and the particle reaching the detectors. These processes mainly include the parton shower, hadronization, and meson/baryon decay. In addition, final state radiations (FSR) of isolated photons and gluons are also possible.

In an energy scale larger than Λ_{QCD} , quarks emit gluons, and subsequently, gluons convert into quark-antiquark pairs. Therefore, an initial parton ends up to be a bunch of secondary partons. And the initial momentum is split among all the secondary partons. This process is called the parton shower. The differential phase space of the gluon emission is

$$dS = \frac{2\alpha_s C_F}{\pi} \frac{dE}{E} \frac{d\theta}{\sin \theta} \frac{d\phi}{2\pi}. \quad (2.5)$$

The gluon emission cross-section diverges at a small θ and a small energy E , often referred to as “inferred colinear” divergence. Therefore the parton shower tends to soft and colinear within a narrow cone of the initial parton. When the energy scale drops below Λ_{QCD} , the partons start to group together and form mesons and baryons. This process is called hadronization or fragmentation. There are two popular models for hadronization, the cluster approach and the string approach, both of which contain a few algorithm parameters derived from the experimental data. For example, PYTHIA uses the string model for hadronization [72]. After hadronization, unstable mesons and baryons decay into stable particles like π , K, γ , e, μ based on the corresponding life-times and certain decaying matrix elements, such as electroweak decaying. The decay processes can be also handle by PYTHIA. More details about the simulation of these processes in the CMS simulated events are discussed in Section 3.5.

After parton shower, hadronization, meson/baryon decay, as well as possible FSR, a parton from the hard process finally ends up to be a narrow cone of stable particles, including charge hadrons, neutral hadrons, photons, and leptons. This cone of particles can be clustered together to represent the initial seeding parton. This cluster of colinear particles is called a jet. A jet is defined by a clustering algorithm (e.g. anti- k_T) and scale parameter (e.g. $\delta R = 0.4$). To reliably represent the seeding parton, a jet algorithm has to be insensitive to the soft-colinear parton showering, so-called “inferred colinear safe”. The jet algorithm in the CMS reconstruction is discussed in Section 3.4.

2.3. Beyond the Standard Model for Lepton Flavor Universality Violation

The primary signal process for the measurement of W branching fractions is $t\bar{t}$. If any beyond the standard model (BSM) physics leads to a small amount of lepton flavor universality violation (LFUV) in the top decay, it will be observed as a non-universality of

the $\mathcal{B}(W \rightarrow \ell\nu)$ result. Besides mediating top quark decay, it is possible for the BSM to affect the experimental observables in other ways. For example, BSM particle X could be produced on-shell in association with t and b quark in the t-channel $pp \rightarrow tbX$, where X is usually at TeV scale and decays with a non-universality manner. In this circumstance, the heavy on-shell X decay gives rise to highly boosted leptons. However, since this $\mathcal{B}(W \rightarrow \ell\nu)$ measurement is primarily based on the trailing leptons in the dilepton channels and low energy taus in the lepton-plus-tau channels, the observables in our analysis are insensitive to such scenario. Thus when estimating the sensitivity of our measurement to BSMs, we focus on BSMs' LFUV effects in the top decay.

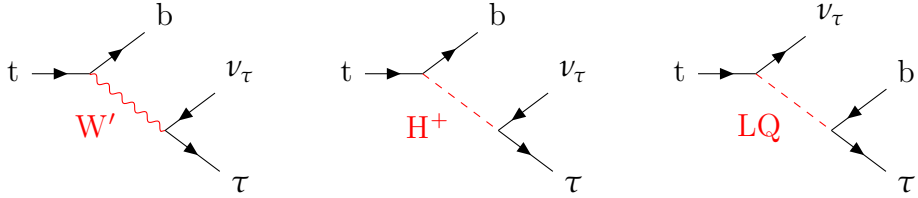


Figure 2.7. Beyond-the-standard-Models that could enhance the tau channel in the top decay.

The BSMs, which can cause LFUV in the top decay, are shown in the Figure 2.7. These models include but are not limited to the W' with a non-universal gauge coupling, H^+ in the two higgs doublets model (2HDM), and leptoquark or LQ in many grand unification models. The underline mechanism to induce LFUV in these BSMs are different: for W' , the coupling to the third generation lepton is elevated by the special structure of the gauge symmetry extension; for H^+ , the coupling to tau is stronger due to tau's heavier mass comparing with electron and muon; for leptoquark, LQ can be generation-conserved and thus the third generation LQ from the top decay tends to produce the third-generation fermions. This section first defines the model-independent top decay kinematics, followed by a QFT calculation of the SM top decay width. Then it discusses the three LFUV BSMs

in Figure 2.7 and estimates the sensitivity of the CMS $\mathcal{B}(W \rightarrow \ell\nu)$ measurement to these BSMs.

2.3.1. Kinematics of Top Quark Decay

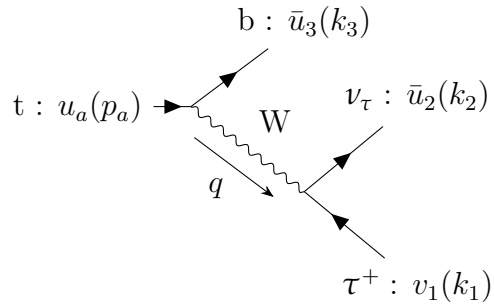


Figure 2.8. Top quark decay in the Standard Model.

Figure 2.8 is the tree-level diagram of the SM top quark decay. The incoming top quark is denoted as a u-type spinor $u_a(p_a)$ with four-momentum p_a ; the outgoing anti-tau is denoted as a v-type spinor $v_1(k_1)$ with four-momentum k_1 ; the outgoing ν_τ and b are represented by the \bar{u} -type spinors $\bar{u}_2(k_2)$ and $\bar{u}_3(k_3)$ with four-momentum k_2 and k_3 , respectively. Note that this correspondence between the spinors $\{\bar{u}_2(k_2), \bar{u}_3(k_3)\}$ and particles $\{\nu_\tau, b\}$ are the same when W' or H^+ mediates the top decay, but are swapped for the leptoquark. The four-momentum exchanged between the fermion currents is denoted as $q = k_1 + k_2 = p_a - k_3$. Using the spinor representation in Figure 2.8, the pair-wised inner products of the four-momentums in the center-of-mass frame can be calculated based on the energy-momentum

conservation:

$$\begin{aligned}
q^2 &= m_t^2 + m_3^2 - 2m_t E_3 \\
p_a \cdot k_1 &= m_t E_1 \\
p_a \cdot k_2 &= m_t^2 - m_t E_3 - m_t E_1 \\
p_a \cdot k_3 &= m_t E_3 \\
k_1 \cdot k_2 &= m_t^2/2 - m_1^2/2 + m_3^2/2 - m_t E_3 \\
k_2 \cdot k_3 &= m_t^2/2 + m_1^2/2 - m_3^2/2 + m_t E_1 \\
k_1 \cdot k_3 &= -m_t^2/2 - m_1^2/2 - m_3^2/2 + m_t E_1 + m_t E_3,
\end{aligned} \tag{2.6}$$

where all terms related to m_2 are neglected because neutrino is massless, and all the inner products are represented in terms of (E_1, E_3) with mass constants. It is equivalent to use (E_2, E_3) or (E_1, E_2) as variables. The top total width is proportional to the integral of the matrix element $|\mathcal{M}|^2$ over the three-body decay phase space PS_3

$$\Gamma = \frac{1}{2m_t} \int |\mathcal{M}|^2 d\text{PS}_3 = \frac{1}{64\pi^3 m_t} \int_0^{m_t/2} dE_3 \int_{m_t/2-E_3}^{m_t/2} dE_1 |\mathcal{M}|^2, \tag{2.7}$$

where the integral over PS_3 is parametrized by (E_1, E_3) .

2.3.2. Standard Model Top Width

In the SM, the total decay width of top quark in Figure 2.8 can be calculated in two ways: the narrow width approximation and the $|\mathcal{M}|^2$ integral in Equation 2.7. With narrow width approximation (NWA), the top width approximately equals to the product of top width

$\Gamma_{t \rightarrow bW}$ and W tauonic branching fraction $\mathcal{B}(W \rightarrow \tau\nu)$.

$$\Gamma_{t \rightarrow b\tau\nu}^{\text{NWA}} = \Gamma_{t \rightarrow bW} \times \mathcal{B}(W \rightarrow \tau\nu) = \frac{g^2 m_t}{64\pi} \cdot \frac{m_t^2}{m_W^2} \left[1 + 2 \frac{m_W^2}{m_t^2} \right] \left[1 - \frac{m_W^2}{m_t^2} \right]^2 \times 10.8\% = 0.157 \text{ GeV}$$

$$(2.8)$$

Because the width of W is indeed relatively small, the NWA provides a good approximation to top tauonic width. But for the BSMs, the propagator's narrow width condition does not necessarily hold. Thus, it is useful to calculate tree-level diagram using the $\overline{|\mathcal{M}|^2}$ integral in the SM case and then repeat it for BSMs. In the $\overline{|\mathcal{M}|^2}$ integral, the finite non-zero width of W is taken into account. At tree-level, the W width is

$$\Gamma_W = 9 \times \frac{g^2 m_W}{48\pi} = 2.07 \text{ GeV},$$

$$(2.9)$$

where the factor $9 = 3 + 2 \times 3$ is the multiplicity of the three lepton generations plus two possible quark generations with three colors. The next leading order width Γ_W^{NLO} due to QCD corrections is discussed in the next section. In Feynman rule, the propagator of massive gauge vector boson has a gauge parameter ξ . Under the unitary gauge, ξ is set to infinity $\xi \rightarrow \infty$ and the Feynman rule for the massive vector propagator is $\frac{g^{\mu\nu} - q^\mu q^\nu/M^2}{q^2 - M^2}$. The propagator has a pole on the real axis at the boson mass M . When the massive vector is not stable and thus has a total decay width of Γ , its self-energy induces a finite but non-zero imaginary part of the pole which is proportional to the propagator's mass M and the total width Γ . This leads to the Breit–Wigner propagator:

$$\overbrace{\overrightarrow{W}}_q = -i \frac{g^{\mu\nu} - (1 - \xi) \frac{q^\mu q^\nu}{q^2 - \xi m_W^2}}{q^2 - m_W^2 + im_W \Gamma_W} \stackrel{\xi \rightarrow \infty}{=} -i \frac{g^{\mu\nu} - q^\mu q^\nu/m_W^2}{q^2 - m_W^2 + im_W \Gamma_W}$$

$$(2.10)$$

Now we can build the full matrix element with the Feynman rule. The amplitude takes the form of a Breit–Wigner propagator sandwiched by two fermion currents and scaled by the

coupling constant squared. The amplitude and its complex conjugate read as

$$\mathcal{M} = -i\left(\frac{g}{\sqrt{2}}\right)^2 \cdot [\bar{u}_3 \gamma_\mu P_L u_a] \frac{g^{\mu\nu} - q^\mu q^\nu/M_W^2}{q^2 - m_W^2 + im_W \Gamma_W} [\bar{u}_2 \gamma_\nu P_L v_1] \quad (2.11)$$

$$\mathcal{M}^* = i\left(\frac{g}{\sqrt{2}}\right)^2 \cdot [\bar{v}_1 P_R \gamma_\rho u_2] \frac{g^{\rho\sigma} - q^\rho q^\sigma/M_W^2}{q^2 - m_W^2 - im_W \Gamma_W} [\bar{u}_a P_R \gamma_\sigma u_3] \quad (2.12)$$

The amplitude squared is the product of \mathcal{M} and \mathcal{M}^* :

$$\begin{aligned} |\mathcal{M}|^2 &= \frac{g^4}{4} \frac{1}{(q^2 - m_W^2)^2 + m_W^2 \Gamma_W^2} \cdot (g^{\mu\nu} - q^\mu q^\nu/M_W^2) (g^{\rho\sigma} - q^\rho q^\sigma/M_W^2) \cdot \\ &\quad [\bar{u}_3 \gamma_\mu P_L u_a] [\bar{u}_a P_R \gamma_\sigma u_3] \cdot [\bar{u}_2 \gamma_\nu P_L v_1] [\bar{v}_1 P_R \gamma_\rho u_2] \\ &= \frac{g^4}{4} \frac{1}{(q^2 - m_W^2)^2 + m_W^2 \Gamma_W^2} \cdot \\ &\quad (g^{\mu\nu} - (p_a^\mu - k_3^\mu)(k_1^\nu + k_2^\nu)/M_W^2) (g^{\rho\sigma} - (k_1^\rho + k_2^\rho)(p_a^\sigma - k_3^\sigma)/M_W^2) \cdot \\ &\quad [\bar{u}_3 \gamma_\mu P_L u_a] [\bar{u}_a P_R \gamma_\sigma u_3] \cdot [\bar{u}_2 \gamma_\nu P_L v_1] [\bar{v}_1 P_R \gamma_\rho u_2]. \end{aligned} \quad (2.13)$$

The top quarks produced in the LHC shown in Figure 2.4 can be treated as unpolarized. So for the average of $|\mathcal{M}|^2$, we average over initial state spins and sum over final state spins. This step uses some properties of the spinors and the trace calculation of gamma matrices, including trace for swapping spinors $\bar{u}u = Tr[u\bar{u}]$, the spin completeness relation for spin sum $\sum_s u(p, s)\bar{u}(p, s) = \not{p} + m$ and $\sum_s v(p, s)\bar{v}(p, s) = \not{p} - m$. The average amplitude squared reads as

$$\begin{aligned} \overline{|\mathcal{M}|^2} &= \frac{1}{2} \sum_s \mathcal{M}^* \mathcal{M} = \frac{g^4}{8} \frac{1}{(q^2 - m_W^2)^2 + m_W^2 \Gamma_W^2} \left\{ \right. \\ &\quad 16(k_2 \cdot k_3)(k_1 \cdot p_a) + \frac{8}{m_W^2} [m_1^2 m_3^2 (k_2 \cdot p_a) - m_1^2 m_t^2 (k_2 \cdot k_3)] \\ &\quad \left. + \frac{4}{m_W^4} [(m_1^2 m_t^2 + m_1^2 m_3^2)(k_1 \cdot k_2)(k_3 \cdot p_a) - 2m_1^2 m_3^2 m_t^2 (k_1 \cdot k_2)] \right\}. \end{aligned} \quad (2.14)$$

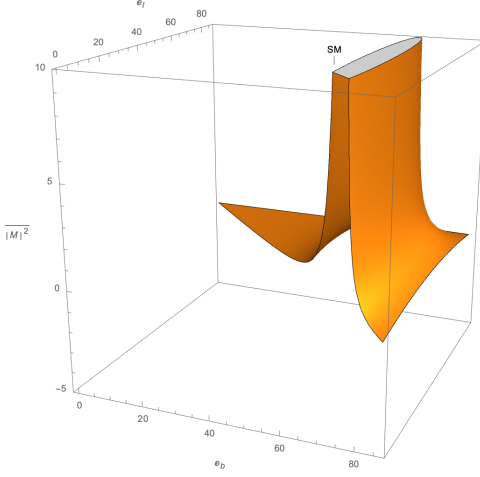


Figure 2.9. The Standard Model $\overline{|\mathcal{M}|^2}$ as a function on the (E_1, E_3) plane. It shows a sharp peak at $E_3 = \frac{m_t^2 - m_W^2}{2m_t} = 67.8$ GeV. $\Gamma_{t \rightarrow b\tau\nu}^{\text{SM}}$ is proportional to the integral of $\overline{|\mathcal{M}|^2}$ within a triangle region on the (E_1, E_3) plane.

Since tau and b quark mass are much less than the top mass, $m_1 \ll m_t$ and $m_3 \ll m_t$, the terms with m_1 and m_3 can be neglected. Eventually, the average amplitude squared becomes

$$\overline{|\mathcal{M}|^2} = g^4 \frac{2(k_2 \cdot k_3)(k_1 \cdot p_a)}{(q^2 - m_W^2)^2 + m_W^2 \Gamma_W^2} \quad (2.15)$$

where the inner products $(k_2 \cdot k_3)$ and $(k_1 \cdot p_a)$ can be represent in terms of (E_1, E_3) using Equation 2.6, which essentially parametrizes $\overline{|\mathcal{M}|^2}$ as a function on the (E_1, E_3) plane shown in Figure 2.9. The decay kinematic constraint corresponds to a triangle area on the (E_1, E_3) plane. The top total width is obtained from the $\overline{|\mathcal{M}|^2}$ integral within this triangle area

$$\Gamma_{t \rightarrow b\tau\nu}^{\text{SM}} = \frac{g^4}{64\pi^3 m_t} \int_0^{m_t/2} dE_3 \int_{m_t/2 - E_3}^{m_t/2} dE_1 \frac{m_t^3 E_1 - 2m_t^2 E_1^2}{(-2m_t E_3 + m_t^2 - m_W^2)^2 + m_W^2 \Gamma_W^2}, \quad (2.16)$$

where one can plug in $m_t = 173.1$ GeV, $m_W = 80.6$ GeV, $g = 0.64$ and $\Gamma_W = 2.07$ GeV and evaluate the numerical value of the integral:

$$\Gamma_{t \rightarrow b\tau\nu}^{\text{SM}} = 0.154 \text{ GeV}. \quad (2.17)$$

This result from the tree-level QFT calculation with Feynman rule $\Gamma_{t \rightarrow b\tau\nu}^{\text{SM}} = 0.154 \text{ GeV}$ agrees well with the one calculated with the narrow width approximation.

2.3.3. Models with W'

2.3.3.1. Model Overview. W' is a hypothetical massive gauge boson that couples to the electroweak charge current in many BSMs. Many direct searches for W' boson have been conducted in the CMS and ATLAS at the LHC, including searches in the $W' \rightarrow \tau\nu$ channel (tau plus E_T^{miss}) [73, 74, 75], $W' \rightarrow \ell\nu$ channel (electron or muon plus E_T^{miss}) [76, 77], $W' \rightarrow WZ$ channel[78, 79], $W' \rightarrow q_1q_2$ channel [80, 81], and $W' \rightarrow tb$ channel [82, 83]. The direct searches for W' are usually model-independent, where an excess of data with respect to the SM prediction is searched in the corresponding mass spectrum. Then the limits of the W' mass are set in the context of Sequential Standard Model (SSM), in which no specific assumption is made on the BSM gauge structures, and W' coupling to fermions is the same as W coupling to fermion in the SM. So SSM is the most generic W' BSM with the least extra assumption on top of SM. The ATLAS experiment has excluded an SSM W' for masses below 3.7 TeV in the $\tau + E_T^{\text{miss}}$ channel. The CMS experiment has excluded an SSM W' for masses below 5.2 TeV in the combination of electron and muon channels. The current PDG combined limit of the $m_{W'}$ is also 5.2 TeV in the context of SSM. In contrast to the direct search, interpreting the potential LFUV in the W' -mediated top decay is more model-dependent. This subsection presents an overview of the W' BSMs and then focuses on the most relevant W' models, the Nonuniversal G221 model.

One of the most common ways to model the new physics is to extend the structure of the SM gauge symmetry. The extension of the gauge symmetry consequently introduces new gauge bosons, such as W' . Though there are many possible ways to extend the SM $SU(2)_L \times U(1)_Y$ to a larger symmetry group, such as the grand unification models with a

$SU(5)$ symmetry, one of the simplest and the most widely studied extension is $SU(2)_1 \times SU(2)_2 \times U(1)_X$. Models based on such gauge extension are commonly called G221 models [84]. Though having the same underline gauge structure, different G221 models can embed different fermion doublets in the $SU(2)_1$ and $SU(2)_2$ groups, thus predicting different physics. Depending on the physical contents assigned to the $SU(2)_1 \times SU(2)_2 \times U(1)_X$ group, the G221 models are classified into three types: Left-Right [85], Ununified [86, 87] and Nonuniversal [88, 89, 90].

- Left-Right. The $SU(2)_1$ and $SU(2)_2$ in the left-right G221 describe the left-handed and right-handed fermion doublets, respectively. The fermion doublets involve both lepton and quarks. There are variations in which the right-handed fermion doublets are comprised of only leptons or quarks. The left-handed fermion doublets in the $SU(2)_1$ group are the same as those in the SM; the right-handed fermion doublet in the $SU(2)_2$ assumes the existence of right-handed neutrinos with masses beyond the TeV scale. In the low energy domain, the combination of the $SU(2)_2$ and the BSM $U(1)_X$ symmetry spontaneously breaks into the SM hypercharge symmetry $U(1)_Y$. Namely, the BSM breaking step is $SU(2)_2 \times U(1)_X \rightarrow U(1)_Y$, which gives masses to the new gauge bosons like W' . While the W couples to left-handed doublets like SM, W' couples to the right-handed doublets. Besides, W' could have a suppressed coupling to the left-handed doublets via the W - W' mixing.
- Ununified. The $SU(2)_1$ and $SU(2)_2$ in the ununified G221 describe the lepton doublets and quark doublets, respectively. The $U(1)_X$ is the same as the SM hypercharge symmetry, $U(1)_X = U(1)_Y$. The name “ununified” highlights that leptons and quarks have separate $SU(2)$ symmetries. The two separate quark and lepton symmetries break into a single symmetry, the SM $SU(2)_L$, in the low energy domain. Namely, the BSM breaking step is $SU(2)_1 \times SU(2)_2 \rightarrow SU(2)_L$, which gives

masses to the new gauge bosons like W' . The coupling of W' is mainly to the quark currents, which leads to a potential enhancement in the quark-involved processes.

- Nonuniversal. The $SU(2)_1$ and $SU(2)_2$ in the nonuniversal G221, sometimes referred to as nonuniversal gauge interaction models (NUGIM), describe the fermion doublets in the first two generations and fermion doublets in the third generation, respectively. The $U(1)_X$ is the same as the SM hypercharge symmetry, $U(1)_X = U(1)_Y$. The name “nonuniversal” implies that the first two generations and the third generation are embedded into separate $SU(2)$ groups. The BSM breaking is the same as the ununified G221, $SU(2)_1 \times SU(2)_2 \rightarrow SU(2)_L$. There is a mixing angle θ_E between the $SU(2)_1$ and $SU(2)_2$ groups. Thus, W' couplings to the third generation and the first two generations are scaled by $\cot \theta_E$ and $\tan \theta_E$ respectively, leading to potential nonuniversal effects in the weak processes.

Among the three types, the most relevant model is NUGIM which is intended to violate the universality in the weak sector. Now, we focus on our sensitivity to this model. The interaction Lagrangian in the NUGIM originates from the covariant derivatives for light ($gen=1,2$) and heavy ($gen=3$) fermions. Denoting the coupling constants in the $SU(2)_1, SU(2)_2, U(1)_X$ as g_1, g_2, g' , the covariant derivatives are

$$\begin{aligned} D_\mu \psi_{gen=1,2} &= [\partial_\mu - ig_1 W_{1\mu}^a T^a P_L - ig' Y B_\mu] \psi_{gen=1,2} \\ D_\mu \psi_{gen=3} &= [\partial_\mu - ig_2 W_{2\mu}^a T^a P_L - ig' Y B_\mu] \psi_{gen=3} \end{aligned} \tag{2.18}$$

Given the mixing angle θ_E between the $SU(2)_1$ and $SU(2)_2$ group, the underlying coupling constants g_1, g_2 are related to the SM weak coupling constant g by

$$g_1 = g / \cos \theta_E, \quad g_2 = g / \sin \theta_E. \tag{2.19}$$

And the SM W^a triplet fields and new BSM triplet fields W'^a are the mixing states of W_1^a and W_2^a :

$$W^a = \frac{g_1 W_1^a + g_2 W_2^a}{\sqrt{g_1^2 + g_2^2}} \quad W'^a = \frac{-g_1 W_1^a + g_2 W_2^a}{\sqrt{g_1^2 + g_2^2}} \quad (2.20)$$

NUGIM employs two higgs doublets to generate mass for gauge bosons, including W and W' . Different from the standard two higgs doublets model (2HDM) which is discussed in Section 2.3.4, here the two higgs doublets are responsible for the first two generations and the third generation fermions. A large Higgs vacuum expectation value (VEV) ratio between the two doublets, $\tan \beta$, can explain the relative smallness of masses in the first two generations compared to the top quark, whereas it does not explain the hierarchy $m_t > m_b$. This is in contrast to the 2HDM type-II models where large $\tan \beta$ can explain the hierarchy $m_b \ll m_t$, but not $m_u, m_c \ll m_t$. Given the covariant derivatives in Equation 2.18 and the mixing angle θ_E , the Feynman rule for W' couplings [91] to the light and heavy fermion currents are

$$\begin{aligned} \bar{t} b W'^+, \bar{\tau} \nu_\tau W'^+ &\implies -\frac{ig}{\sqrt{2}} \cot_E \gamma^\mu P_L \\ \bar{u} d W'^+, \bar{e} \nu_e W'^+ &\implies -\frac{ig}{\sqrt{2}} \tan_E \gamma^\mu P_L \end{aligned} \quad (2.21)$$

and the Feynman rule for the propagator W' takes a similar form to the SM W in Equation 2.10:

$$\overbrace{\overbrace{W'}^{q}}^q = -i \frac{g^{\mu\nu} - q^\mu q^\nu / m_{W'}^2}{q^2 - m_{W'}^2 + im_{W'} \Gamma_{W'}}. \quad (2.22)$$

In Equation 2.21, the larger is the parameter \cot_E , the more enhancement to the third generation and more suppression to the first two generations there would be. So \cot_E is the key parameter in the NUGIM to control the degree of “nonuniversality”. Also based on Equation 2.21, the total width and the branching fraction of W' can be calculated [91]. If we denote the decay rate of SM W to one generation of lepton and neutrino in Equation 2.9 as $\Gamma_\ell = \frac{g^2 m_W}{48\pi}$, the partial widths of W' to the first two generations and the third generation

fermion are

$$\begin{aligned}
 \Gamma_{W' \rightarrow tb} &= 3 \cot_E^2 \frac{W'}{W} \Gamma_\ell = 3 \cot_E^2 \frac{g^2 m_{W'}}{48\pi}, \\
 \Gamma_{W' \rightarrow ud} &= 3 \tan_E^2 \frac{W'}{W} \Gamma_\ell = 3 \tan_E^2 \frac{g^2 m_{W'}}{48\pi}, \\
 \Gamma_{W' \rightarrow \tau \nu_\tau} &= \cot_E^2 \frac{W'}{W} \Gamma_\ell = \cot_E^2 \frac{g^2 m_{W'}}{48\pi}, \\
 \Gamma_{W' \rightarrow e \nu_e} &= \tan_E^2 \frac{W'}{W} \Gamma_\ell = \tan_E^2 \frac{g^2 m_{W'}}{48\pi}.
 \end{aligned} \tag{2.23}$$

It is also allowed that W' decays into SM Higgs and W boson, $W' \rightarrow H + W$, width of which is $\Gamma_{W' \rightarrow HW} = \frac{1}{4} \Gamma_{W' \rightarrow \tau \nu_\tau}$ in the limit of large $\tan \beta$ corresponding to the SM fermion hierarchy [92]. Thus the total width of W' sums up the hadronic, leptonic and Higgs emitting width;

$$\Gamma_{W'} = \frac{g^2 m_{W'}}{48\pi} \left[(3 + 1 + \frac{1}{4}) \cot_E^2 + (6 + 2) \tan_E^2 \right]. \tag{2.24}$$

where the width is proportional to the \cot_E^2 or $1/\cot_E^2$ when $\cot_E^2 \gg 1$ or $1 \gg \cot_E^2 > 0$, respectively. So NUGIM has a built-in upper and lower boundaries for \cot_E , constrained by the width of W' . The parameter space beyond these boundaries predicts a W' with a width too wide to be physical. Take a conservatively large width as an example. If the width is smaller than half of the W' mass, then

$$0.21 < \cot_E < 6.48. \tag{2.25}$$

The branching fraction of W' is shown in Figure 2.10. When $\cot_E > 2$, W' decays dominantly to the third family fermions and the branching ratio to the first two generation is neglectable. The situation is reversed when $\cot_E < 0.5$.

2.3.3.2. Enhancement of Tauonic Decay. The total $|\mathcal{M}|^2$ in the NUGIM consists of the SM contribution in Section 2.3.2, plus contributions from W' propagator (denoted as

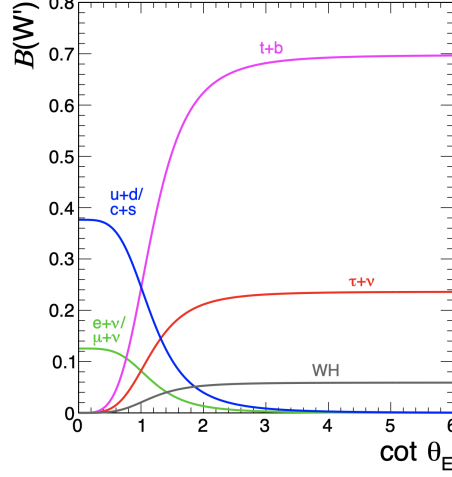


Figure 2.10. The branching fraction of W' in the nonuniversal gauge interaction model (NUGIM) as a function of \cot_E [73], where \cot_E is the parameter controlling the degree of nonuniversality.

$|\overline{\mathcal{M}}|^2_{W'}$) and the interference between W and W' (denoted as $|\overline{\mathcal{M}}|^2_{\text{int}}$). Namely,

$$|\overline{\mathcal{M}}|^2 = |\overline{\mathcal{M}}|^2_W + |\overline{\mathcal{M}}|^2_{W'} + |\overline{\mathcal{M}}|^2_{\text{int}}. \quad (2.26)$$

where the SM term $|\overline{\mathcal{M}}|^2_W$ has been calculated in Equation 2.15, while $|\overline{\mathcal{M}}|^2_{W'} + |\overline{\mathcal{M}}|^2_{\text{int}}$ is the new BSM contribution to evaluate. This BSM contribution enhances the tau channel in the top decay. Eventually, the ratio of this BSM contribution over the SM contribution will be estimated and compared with our experimental precision. Now consider $\cot_E > 2$ where the BSM branching fraction to first and second generation of leptons are neglectable. With Feynman rule, the matrix element of top quark's tauonic decay mediated by W' , similar to Equation 2.11, is spelt as the W' propagator sandwiched by two fermion currents and scaled by the coupling constant squared:

$$i\mathcal{M}_{W'} = \left(\frac{g \cot_E}{\sqrt{2}}\right)^2 \cdot [\bar{u}_3 \gamma_\mu P_L u_a] \frac{g^{\mu\nu} - q^\mu q^\nu / M_{W'}^2}{q^2 - m_{W'}^2 + i m_{W'} \Gamma_{W'}} [\bar{u}_2 \gamma_\nu P_L v_1]. \quad (2.27)$$

The calculation of the average amplitude squared $\overline{|\mathcal{M}|^2}_{W'}$ and $\overline{|\mathcal{M}|^2}_{\text{int}}$ has the same mathematical process as that in Section 2.3.2. First sum the spins; then evaluate the traces of gamma matrices. The result of such calculation reads as

$$\overline{|\mathcal{M}|^2}_{W'} = g^4 \cot_E^4 \frac{2(k_2 \cdot k_3)(k_1 \cdot p_a)}{(q^2 - m_{W'}^2)^2 + m_{W'}^2 \Gamma_{W'}^2} \quad (2.28)$$

and

$$\begin{aligned} \overline{|\mathcal{M}|^2}_{\text{int}} &= 2\overline{\text{Re}[\mathcal{M}_W^* \mathcal{M}_{W'}]} \\ &= 2g^4 \cot_E^2 \cdot [2(k_2 \cdot k_3)(k_1 \cdot p_a)] \cdot \\ &\quad \frac{(q^2 - m_W^2)(q^2 - m_{W'}^2) + m_W^2 m_{W'}^2 \Gamma_W^2 \Gamma_{W'}^2}{[(q^2 - m_W^2)^2 + m_W^2 \Gamma_W^2][(q^2 - m_{W'}^2)^2 + m_{W'}^2 \Gamma_{W'}^2]}, \end{aligned} \quad (2.29)$$

where the inner products $(k_2 \cdot k_3)$ and $(k_1 \cdot p_a)$ can be represented in terms of (E_1, E_3) using Equation 2.6. Then $\overline{|\mathcal{M}|^2}_{W'}$ and $\overline{|\mathcal{M}|^2}_{\text{int}}$ become 2D functions on the (E_1, E_3) plane. Figure 2.11 shows a visualization of the $\overline{|\mathcal{M}|^2}_W$, $\overline{|\mathcal{M}|^2}_{W'}$ and $\overline{|\mathcal{M}|^2}_{\text{int}}$ on the (E_1, E_3) plane, overlapped with the SM $\overline{|\mathcal{M}|^2}_W$ from Section 2.3.2. The $\overline{|\mathcal{M}|^2}_W$, $\overline{|\mathcal{M}|^2}_{W'}$ and $\overline{|\mathcal{M}|^2}_{\text{int}}$ are shown as orange, blue and green surface, respectively. The upper left plot in Figure 2.11 shows the scenario of $\cot_E = 1, m_{W'} = 140, where W' is light enough to be on-shell from the top decay and $\overline{|\mathcal{M}|^2}_{W'}$ has a clear peak at $E_3 = (m_t^2 - m_{W'}^2)/2m_t$. Due to this on-shell peak, $\overline{|\mathcal{M}|^2}_{W'}$ is much larger than the interference term $\overline{|\mathcal{M}|^2}_{\text{int}}$ and is the dominating BSM contribution. As $m_{W'}$ increases, the on-shell W' peak moves to left towards smaller E_3 and eventually disappear in the triangle area when $m_{W'} > m_t$. Upper right plot in Figure 2.11 shows the scenario of $\cot_E = 1, m_{W'} = 300, where the blue peak is out side the triangle area and the leading BSM contribution is from the interference. The lower plot in Figure 2.11 increases the \cot_E with $\cot_E = 4, m_{W'} = 300, where W' width is wider and the interference becomes stronger.$$$

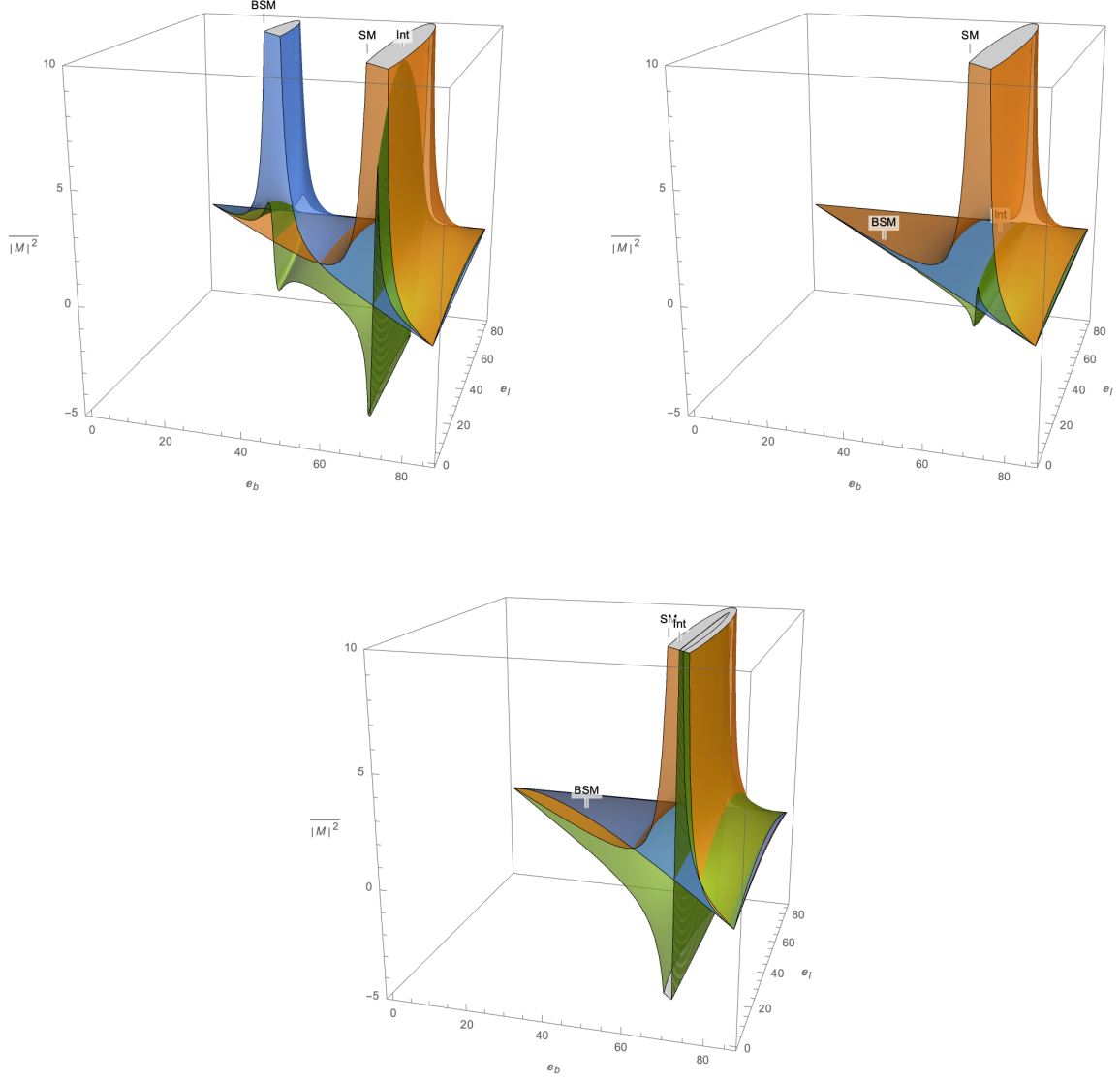


Figure 2.11. $|\mathcal{M}|^2_{W'}$, $|\mathcal{M}|^2_{W'}$ and $|\mathcal{M}|^2_{\text{int}}$ on the (E_1, E_3) plane, shown as orange, blue and green surface, respectively. Changing the two model parameters ($\cot_E, m_{W'}$) leads to different scenarios. Upper left, upper right and lower plots illustrate $(\cot_E = 1, m_{W'} = 140 \text{ GeV})$, $(\cot_E = 1, m_{W'} = 300 \text{ GeV})$, and $(\cot_E = 4, m_{W'} = 300 \text{ GeV})$ cases.

Upon integrating $|\mathcal{M}|^2_{W'} + |\mathcal{M}|^2_{\text{int}}$ on the (E_1, E_3) plane using Equation 2.7, one gets the BSM width of the taunic decay $\Gamma_{t \rightarrow b\tau\nu}^{\text{BSM}}$.

$$\Gamma_{t \rightarrow b\tau\nu}^{\text{BSM}} = \frac{1}{64\pi^3 m_t} \int_0^{m_t/2} dE_3 \int_{m_t/2 - E_3}^{m_t/2} dE_1 \left\{ |\mathcal{M}|^2_{W'} + |\mathcal{M}|^2_{\text{int}} \right\}, \quad (2.30)$$

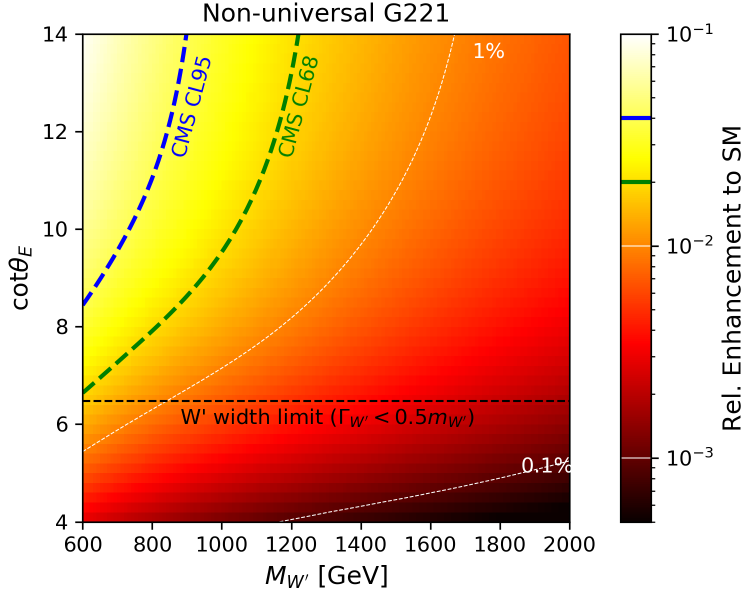


Figure 2.12. The relative tau enhancement $\Gamma_{t \rightarrow b\tau\nu}^{\text{BSM}}/\Gamma_{t \rightarrow b\tau\nu}^{\text{SM}}$ in the NUGIM parameter space ($\cot_E, m_{W'}$). $\Gamma_{t \rightarrow b\tau\nu}^{\text{BSM}}$ is calculated from integrating $\overline{|\mathcal{M}|^2}_{W'} + \overline{|\mathcal{M}|^2}_{\text{int}}$. Our analysis confirms LFU with 2% uncertainty, excluding the $\Gamma_{t \rightarrow b\tau\nu}^{\text{BSM}}/\Gamma_{t \rightarrow b\tau\nu}^{\text{SM}} > 2\%$ with one sigma, shown as the left side of the green contour.

Then the relative tau enhancement from the BSM with respect to SM can be obtained by $\Gamma_{t \rightarrow b\tau\nu}^{\text{BSM}}/\Gamma_{t \rightarrow b\tau\nu}^{\text{SM}}$. For example, when $\cot_E = 6$ and $m_{W'} = 1 \text{ TeV}$, $\overline{|\mathcal{M}|^2}_{W'} + \overline{|\mathcal{M}|^2}_{\text{int}}$ integral yields $\Gamma_{t \rightarrow b\tau\nu}^{\text{BSM}} = 0.86 \text{ MeV}$ and tau enhancement is

$$\frac{\Gamma_{t \rightarrow b\tau\nu}^{\text{BSM}}}{\Gamma_{t \rightarrow b\tau\nu}^{\text{SM}}} \sim 0.55\%, \quad (\cot_E = 6, m_{W'} = 1 \text{ TeV}). \quad (2.31)$$

In addition to this example, the tau enhancement $\Gamma_{t \rightarrow b\tau\nu}^{\text{BSM}}/\Gamma_{t \rightarrow b\tau\nu}^{\text{SM}}$ can be calculated in the model parameters space ($\cot_E, m_{W'}$), shown as Figure 2.12. The relative enhancement decreases as $m_{W'}$ increases and as \cot_E approaches to 1. Our analysis confirms lepton flavor universality with a 2% uncertainty, which translates to exclusion of $\Gamma_{t \rightarrow b\tau\nu}^{\text{BSM}}/\Gamma_{t \rightarrow b\tau\nu}^{\text{SM}} > 2\%$ shown as the left side of the green contour. For $m_{W'} > 600 \text{ GeV}$, this exclusion region is beyond the model's upper boundary of \cot_E and not as competitive as the direct searches, shown in Figure 2.13.

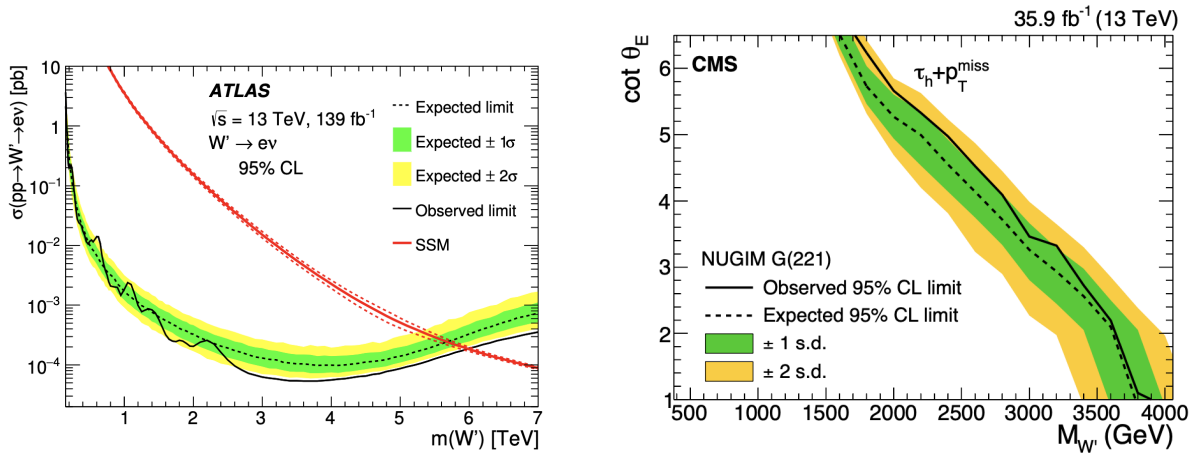


Figure 2.13. Direct Search of W' on the ATLAS and CMS.

2.3.4. Models with H^+

2.3.4.1. Model Overview. The charged Higgs boson H^+ is a hypothetical particle in the BSMs with extended scalar field structures. In the SM, the scalar sector has the simplest possible structure, one SU(2) doublet. Meanwhile the fermion structure with three mixing generations is not simple. It is possible that the scalar structure can have some more complex form. Two Higgs Doublet Model (2HDM) provides the next simplest structure for the SM scalar sector. It assumes one more scalar doublet in addition to that in the SM. The two scalar doublets are responsible for the masses of upper and lower fermions separately. There are three major motivations to 2HDM [93]: generating mass in the Minimal Supersymmetric Standard Model (MSSM) [94], explaining the strong CP in the QCD [95, 96], and adding extra CP-violation source for the baryon asymmetry [97, 98, 99].

The direct searches for H^+ have been conducted in two parts of the phase space, $m_{H^+} < m_t$ and $m_{H^+} > m_t$ [27]. For $m_{H^+} < m_t$, LEP [100], CMS [101] and ATLAS [102] have exclude H^+ with mass below 80 GeV, 155 GeV, and 140 GeV with 95% confidence level respectively. For $m_{H^+} > m_t$, ATLAS has provide a $\tan \beta$ -dependant exclusion of m_{H^+} [103], more explicitly $m_{H^+} > 181$ GeV, 129 GeV, 390 GeV, 894 GeV, 1017 GeV, 1103 GeV at

$\tan \beta = 10, 20, 30, 40, 50, 60$, respectively. Here in this section, we explore the effect of 2HDM H^+ in the top decay and evaluate the corresponding ‘tau enhancement’ with respect to SM.

In 2HDMs, there are two complex scalar doublets with eight fields:

$$\Phi_1 = \begin{bmatrix} \phi_1^+ \\ \frac{\nu_1}{\sqrt{2}} + \frac{\rho_1+i\eta_1}{\sqrt{2}} \end{bmatrix}, \Phi_2 = \begin{bmatrix} \phi_2^+ \\ \frac{\nu_2}{\sqrt{2}} + \frac{\rho_2+i\eta_2}{\sqrt{2}} \end{bmatrix} \quad (2.32)$$

where the ratio of the VEV of the two doublets are

$$\tan \beta = \frac{\nu_2}{\nu_1}, \quad (2.33)$$

and $\tan \beta$ is an important parameter in the model. The potential for the two scalar doublets reads as

$$\begin{aligned} V = & m_{11}^2 \Phi_1^\dagger \Phi_1 + m_{22}^2 \Phi_2^\dagger \Phi_2 - m_{12}^2 (\Phi_1^\dagger \Phi_2 + \Phi_2^\dagger \Phi_1) \\ & + \frac{\lambda_1}{2} (\Phi_1^\dagger \Phi_1)^2 + \frac{\lambda_2}{2} (\Phi_2^\dagger \Phi_2)^2 + \lambda_3 \Phi_1^\dagger \Phi_1 \Phi_2^\dagger \Phi_2 + \lambda_4 \Phi_1^\dagger \Phi_2 \Phi_2^\dagger \Phi_1 + \frac{\lambda_5}{2} [(\Phi_1^\dagger \Phi_2)^2 + (\Phi_2^\dagger \Phi_1)^2] \end{aligned} \quad (2.34)$$

which is minimized when choosing the vacuum expectation value $\Phi_1 = [0, v_1/\sqrt{2}]^T$ and $\Phi_2 = [0, v_2/\sqrt{2}]^T$.

Out of the eight fields in Equation 2.32, three are ‘eaten’ to give mass to the W and Z gauge bosons; the remaining five are physical scalar fields. These are a charged scalar, two neutral scalars, and one pseudoscalar [93]. The Lagrangian for the mass of the charged scalars is given by

$$\mathcal{L}_{H^\pm mass} = (m_{12}^2 - (\lambda_4 + \lambda_5)v_1v_2) \begin{bmatrix} \phi_1^- & \phi_2^- \end{bmatrix} \begin{bmatrix} \frac{v_2}{v_1} & -1 \\ -1 & \frac{v_1}{v_2} \end{bmatrix} \begin{bmatrix} \phi_1^+ \\ \phi_2^+ \end{bmatrix}, \quad (2.35)$$

which implies $m_{H^\pm} = \sqrt{[m_{12}^2/(v_1 v_2) - \lambda_4 - \lambda_5][v_1^2 + v_2^2]}$ and the mass eigenstate of the charged Higgs is a linear mixing of ϕ_1^\pm and ϕ_2^\pm :

$$H^\pm = \phi_2^\pm \cos \beta - \phi_1^\pm \sin \beta. \quad (2.36)$$

There are several types of 2HDM. If imposing flavor conservation, there are four possibilities (type I–IV) for the two Higgs doublets to couple to the SM fermions. Each of the four types gives rise to rather different phenomenology. In these four types of 2HDM, the generic form of the coupling between H^+ and SM fermions can be expressed as a superposition of right- and left-chiral coupling components [104]. The related Lagrangian term mediating the top decay is given by

$$\mathcal{L}_I = \frac{g}{\sqrt{2}m_W} H^+ \left[\bar{t}(A P_R + B P_L)b + \bar{\nu}(C P_L)l \right] \quad (2.37)$$

In the first possibility (type-I), the Φ_2 doublet gives masses to all quarks and leptons, so the other one, doublet Φ_1 , essentially decouples from fermions. In the second scenario (type-II), the Φ_2 doublet gives mass to the right-handed up-type quarks, and the Φ_1 -doublet gives mass to the right-handed down-type quarks and charged leptons. In the type-III, both up- and down-type quarks couple to the second doublet Φ_2 , and all leptons couple to the first one Φ_1 . In the fourth scenario (type-IV), the roles of two doublets are reversed with respect to type-II. The explicit arrangements to generate fermion mass with Φ_1, Φ_2 in the four types are listed in Table 2.2. Also the coupling constants A, B, C in Equation 2.37 are shown in Table 2.2 for the four types. Among these four types, the most interesting one is type-II because it is the 2HDM for the MSSM. So here as an example, we provide a interpretation of our result in the context of type-II 2HDM. Other types could be easily explored by using the corresponding A, B, C coefficients and going through the same process.

Table 2.2. There are four possibilities of 2HDM if imposing flavor conservation. The four types differ from each other by the specific ways fermion masses are generated with Φ_1, Φ_2 . The second and third column show the fermion masses which Φ_1, Φ_2 are responsible for in the four types. The last three columns show the coupling constants A, B, C in the interaction Lagrangian in Equation 2.37.

Type	Φ_1 Doublet	Φ_2 Doublet	A	B	C
I	—	u, d, e	$m_t \cot \beta$	$-m_b \cot \beta$	$-m_\tau \cot \beta$
II	d, e	u	$m_t \cot \beta$	$m_b \tan \beta$	$m_\tau \tan \beta$
III	e	u, d	$m_t \cot \beta$	$m_b \tan \beta$	$-m_\tau \cot \beta$
IV	u	d, e	$m_t \cot \beta$	$-m_b \cot \beta$	$m_\tau \tan \beta$

In type-II 2HDM, given the interaction Lagrangian in Equation 2.37 and coupling constants in Table 2.2, the total width of H^+ can be calculated as [105]

$$\Gamma_{H^+} = \frac{g^2 m_{H^+}}{32\pi} \frac{1}{m_W^2} \times \begin{cases} m_\tau^2 \tan^2 \beta + 3m_s^2 \tan^2 \beta + 3m_c^2 \cot^2 \beta, & m_{H^+} < m_t \\ m_\tau^2 \tan^2 \beta + 3(m_s^2 + m_b^2) \tan^2 \beta + 3(m_c^2 + m_t^2) \cot^2 \beta, & m_{H^+} > m_t \end{cases}, \quad (2.38)$$

where $H^+ \rightarrow sc, \tau\nu_\tau$ are considered when $m_{H^+} < m_t$ and $H^+ \rightarrow tb, sc, \tau\nu_\tau$ are considered when $m_{H^+} > m_t$. The Feynman rule for the H^+ propagator takes into account its mass and width:

$$\frac{\overset{H^+}{\text{---}}}{q} = \frac{1}{q^2 - m_{H^+}^2 + im_{H^+}\Gamma_{H^+}} \quad (2.39)$$

2.3.4.2. Enhancement of Tauonic Decay. The relative tau enhancement with respect to SM, $\Gamma_{t \rightarrow b\tau\nu}^{\text{BSM}}/\Gamma_{t \rightarrow b\tau\nu}^{\text{SM}}$, can be calculated in the context of type-II 2HDM. This is done by evaluating the tree-level Feynman diagram for the H^+ mediated top decay in the tau channel. For $t \rightarrow b\tau\nu$, the total $|\mathcal{M}|^2$ not only has the contributions from the SM W propagator discussed in Section 2.3.2, but also includes the H^+ part $|\mathcal{M}|^2_{H^+}$ and the W- H^+ interference

part $\overline{|\mathcal{M}|^2}_{\text{int}}$. Namely,

$$\overline{|\mathcal{M}|^2} = \overline{|\mathcal{M}|^2}_{\text{W}} + \overline{|\mathcal{M}|^2}_{\text{H}^+} + \overline{|\mathcal{M}|^2}_{\text{int}}, \quad (2.40)$$

where $\overline{|\mathcal{M}|^2}_{\text{H}^+} + \overline{|\mathcal{M}|^2}_{\text{int}}$ is the new BSM contribution to evaluate. This BSM contribution enhances tau channel in the top decay because of much heavier tau mass. In contrast, the muon and electron receives neglectable enhancement due to their much lighter masses. The calculation of $\overline{|\mathcal{M}|^2}_{\text{H}^+} + \overline{|\mathcal{M}|^2}_{\text{int}}$ is similar to that in Section 2.3.3. The differences are: the propagator is now a scalar; the masses of b, τ cannot be neglected because they are origins of the H^+ couplings in the 2HDM. With the Feynman rule, we spell the tree-level amplitude and its conjugate for the H^+ mediated tauonic top decay:

$$\mathcal{M} = \left(\frac{g}{\sqrt{2}}\right)^2 \frac{1}{m_W^2} \cdot \frac{[\bar{u}_2(C P_R) v_1] [\bar{u}_3(A P_R + B P_L) u_a]}{q^2 - m_{H^+}^2 + i m_{H^+} \Gamma_{H^+}} \quad (2.41)$$

and

$$\mathcal{M}^* = \left(\frac{g}{\sqrt{2}}\right)^2 \frac{1}{m_W^2} \cdot \frac{[\bar{u}_a(A P_L + B P_R) u_3] [\bar{v}_1(C P_L) u_2]}{q^2 - m_{H^+}^2 - i m_{H^+} \Gamma_{H^+}} \quad (2.42)$$

Then the average amplitude squared can be obtained by summing spins and evaluating the trace of gamma matrices. This process is the same as Section 2.3.2 and 2.3.3. So the middle steps are not shown here. The final result reads as

$$\overline{|\mathcal{M}|^2}_{\text{H}^+} = \frac{g^4}{2m_W^4} \frac{1}{(q^2 - m_{H^+}^2)^2 + m_{H^+}^2 \Gamma_{H^+}^2} C^2(k_1 \cdot k_2) \left[(A^2 + B^2)(k_3 \cdot p_a) + 2AB m_3 m_t \right] \quad (2.43)$$

and for the interference between the vector W and scalar H⁺

$$\begin{aligned}
\overline{|\mathcal{M}|^2}_{\text{int}} &= 2\overline{\text{Re}[\mathcal{M}_W^* \mathcal{M}_{H^+}]} \\
&= \frac{g^4}{m_W^4} \frac{(q^2 - m_W^2)(q^2 - m_{H^+}^2) + m_W^2 m_{H^+}^2 \Gamma_W^2 \Gamma_{H^+}^2}{[(q^2 - m_W^2)^2 + m_W^2 \Gamma_W^2][(q^2 - m_{H^+}^2)^2 + m_{H^+}^2 \Gamma_{H^+}^2]} \\
&\quad \left\{ m_W^2 C m_1 [A m_t(k_2 \cdot k_3) - B m_3(k_2 \cdot p_a)] + \right. \\
&\quad \left. [A m_t - B m_3] C m_1 (k_1 \cdot k_2)(k_3 \cdot p_a) + [B m_t - A m_3] C m_1 m_3 m_t (k_1 \cdot k_2) \right\}
\end{aligned} \tag{2.44}$$

The inner products, such as $(k_3 \cdot p_a)$, can be rewritten in terms of E_1, E_3 using Equation 2.6, such that $\overline{|\mathcal{M}|^2}_{H^+}$ and $\overline{|\mathcal{M}|^2}_{\text{int}}$ become 2D functions of (E_1, E_3) with two model parameters $(m_{H^+}, \tan \beta)$. Figure 2.14 shows the $\overline{|\mathcal{M}|^2}_{H^+}$ and $\overline{|\mathcal{M}|^2}_{\text{int}}$ as well as the SM $\overline{|\mathcal{M}|^2}_W$ on the (E_1, E_3) plane. The valid decay phase space is a triangle area on the (E_1, E_3) plane. When H^+ is lighter than top quark, $\overline{|\mathcal{M}|^2}_{H^+}$ has a peak at $E_3 = (m_t^2 - m_{H^+}^2)/2m_t^2$ for on-shell H^+ propagator. The peak moves left towards smaller E_3 as the m_{H^+} approaches m_t . When m_{H^+} exceeds m_t , the on-shell H^+ peak moves outside the valid kinematic triangle region. In this case, H^+ impacts the matrix element via its width; the wider, the larger $\overline{|\mathcal{M}|^2}_{H^+}$ and $\overline{|\mathcal{M}|^2}_{\text{int}}$ becomes.

Finally, using Equation 2.7, the extra top width due the BSM H^+ equals the integral of $\overline{|\mathcal{M}|^2}_{H^+} + \overline{|\mathcal{M}|^2}_{\text{int}}$

$$\Gamma_{t \rightarrow b\tau\nu}^{\text{BSM}} = \frac{1}{64\pi^3 m_t} \int_0^{m_t/2} dE_3 \int_{m_t/2-E_3}^{m_t/2} dE_1 \left\{ \overline{|\mathcal{M}|^2}_{H^+} + \overline{|\mathcal{M}|^2}_{\text{int}} \right\}, \tag{2.45}$$

Upon integrating over the triangle area on (E_1, E_3) plane, we get the BSM effect as a function of model parameters, $\Gamma_{t \rightarrow b\tau\nu}^{\text{BSM}}(m_{H^+}, \tan \beta)$. Take $m_{H^+} = 140$ GeV and $\tan \beta = 8$ as an example, $\Gamma_{t \rightarrow b\tau\nu}^{\text{BSM}} = 14.6$ MeV – 2.1 keV, where 14.6 MeV and -2.1 keV correspond the $\overline{|\mathcal{M}|^2}_{H^+}$ and

$\overline{|\mathcal{M}|^2}_{\text{int}}$ integral, respectively. When the charged Higgs is lighter than top quark, the absolutely dominant term is the $\overline{|\mathcal{M}|^2}_{H^+}$ integral and the $W - H^+$ interference is neglectable. Take $m_{H^+} = 200 \text{ GeV}$ and $\tan \beta = 8$ as another example: $\Gamma_{t \rightarrow b\tau\nu}^{\text{BSM}} = 0.6 \text{ keV} - 0.8 \text{ keV}$, which is extremely small comparing with the $\Gamma_{t \rightarrow b\tau\nu}^{\text{SM}} = 154 \text{ MeV}$. The relative tau enhancement $\Gamma_{t \rightarrow b\tau\nu}^{\text{BSM}} / \Gamma_{t \rightarrow b\tau\nu}^{\text{SM}}$ can be calculated at different model parameters $(m_{H^+}, \tan \beta)$. Figure 2.15 shows $\Gamma_{t \rightarrow b\tau\nu}^{\text{BSM}} / \Gamma_{t \rightarrow b\tau\nu}^{\text{SM}}$ in the 2D parameter space $(m_{H^+}, \tan \beta)$. Our analysis confirms the LFU with 2% uncertainty. In Figure 2.15, the contours correspond to one and two experimental sigma, $\Gamma_{t \rightarrow b\tau\nu}^{\text{BSM}} / \Gamma_{t \rightarrow b\tau\nu}^{\text{SM}} = 2\%$ and $\Gamma_{t \rightarrow b\tau\nu}^{\text{BSM}} / \Gamma_{t \rightarrow b\tau\nu}^{\text{SM}} = 4\%$, are shown as green and blue dash line. Generally, $m_{H^+} < 150 \text{ GeV}$ is excluded for all $\tan \beta$. But our analysis does not probe the $m_{H^+} > m_t$ parameter space, which is more suitable for a direct search with boosted tau. As a comparison, the run-I CMS direct search [101] is shown in Figure 2.16.

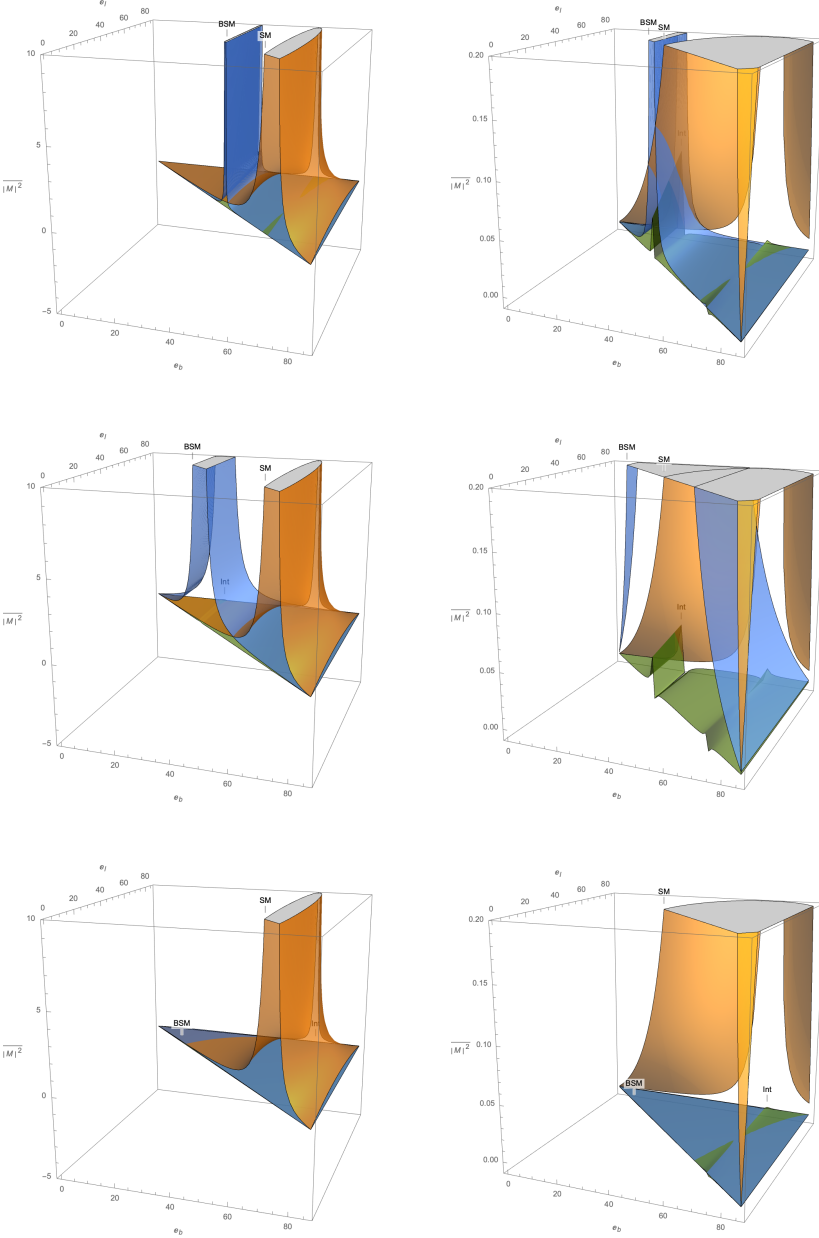


Figure 2.14. $|\mathcal{M}|^2_{H+}$ and $|\mathcal{M}|^2_{int}$ are 2D functions of (E_1, E_3) with two parameters $(m_{H+}, \tan \beta)$. The $|\mathcal{M}|^2_W$, $|\mathcal{M}|^2_{H+}$ and $|\mathcal{M}|^2_{int}$ are shown as orange, blue and green surface, respectively. The valid kinematics is a triangle area on the (E_1, E_3) plane. The first, second, and third row uses model parameters $(m_{H+} = 140 \text{ GeV}, \tan \beta = 10)$, $(m_{H+} = 140 \text{ GeV}, \tan \beta = 40)$, and $(m_{H+} = 200 \text{ GeV}, \tan \beta = 40)$. The right column is zoom-in views of the left column to show the small interference term $|\mathcal{M}|^2_{int}$.

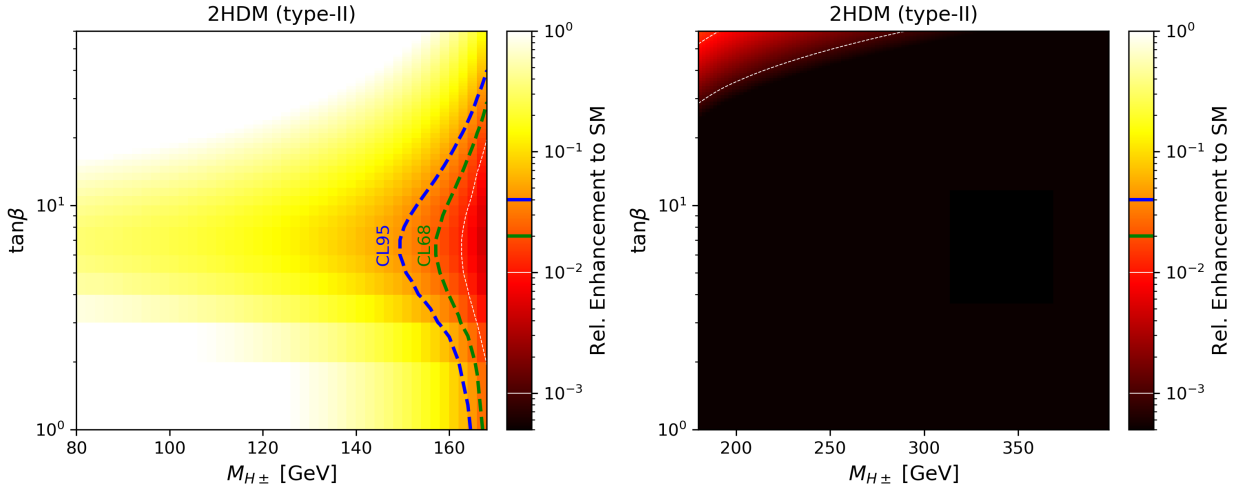


Figure 2.15. $\Gamma_{t \rightarrow b\tau\nu}^{\text{BSM}} / \Gamma_{t \rightarrow b\tau\nu}^{\text{SM}}$ in the 2D parameter space (m_{H^\pm} , $\tan\beta$). Our analysis confirms the LFU with a relative uncertainty of 2%. The contours correspond to one and two experimental sigma, $\Gamma_{t \rightarrow b\tau\nu}^{\text{BSM}} / \Gamma_{t \rightarrow b\tau\nu}^{\text{SM}} = 2\%$ and $\Gamma_{t \rightarrow b\tau\nu}^{\text{BSM}} / \Gamma_{t \rightarrow b\tau\nu}^{\text{SM}} = 4\%$, are shown as the green and blue dash line, the left side of which is excluded.

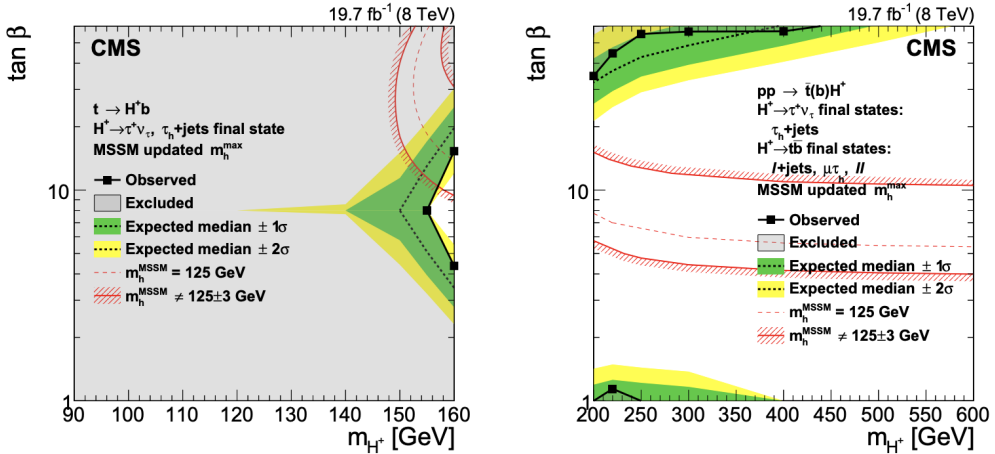


Figure 2.16. Result of the direct search for H^+ in the CMS Run-I [101].

2.3.5. Models with Leptoquark

Leptoquarks (LQ) is a hypothetical particle with both the lepton number and baryon number, motivated by the GUT and predicted by many theories unifying quarks and leptons. In some GUT, such as Georgi–Glashow SU(5) unification, Pati-Salam model with SU(4) color, leptoquark is a gauge vector boson to mediate forces between the lepton-quark current. In some models, such as extended technicolor models, leptoquark states appear as the bound scalar of techni-fermions. So LQ can be either a scalar or vector boson, which interacts with fermions via $\lambda \cdot (\bar{q}\gamma^\mu\ell)LQ_\mu$ if $s_{LQ} = 1$ or via Yukawa interaction $\lambda \cdot (\bar{q}\ell)LQ$ if spin $s_{LQ} = 0$. If the leptoquark couples both to left and right fermions, it is non-chiral. Otherwise, it is possible to couple only to the left- or right-handed fermions and be chiral. There are also possibilities that it couples to only one the fermion generation or couples to different fermion generations simultaneously.

There are many direct searches for the leptoquark at the LHC. A pair of leptoquarks could be produced via quark-quark annihilation and gluon-gluon fusion. Meanwhile, single leptoquark production may be possible via gluon-quark scattering. CMS and ATLAS have searched leptoquark decaying into the first, second, or third generation of fermions. The search with pair production of leptoquarks excludes $m_{LQ} < 1.05$ TeV, while the search with single produced leptoquark gives a slightly higher mass limit at 1.755 TeV.

Besides direct search, leptoquark would also cause BSM effective four-point interactions, allowing indirect searches. Searches for flavor-changing neutral current (FCNC) put a strong constraint on the leptoquark that simultaneously involves different lepton generations. Besides, pion's electronic decay and electron anomalous magnetic moment are also sensitive to non-chiral scalar leptoquarks. Electron-positron collider producing quark pairs in the t-channel also highly constrains LQ. Currently, with these indirect limits, it is believed that

the leptoquark is more likely to be a chiral scalar or vector coupling to a single family of fermions.

However, the interpretation of our results in the context of LQ is very model dependent. So here, we do not provide a interpretation specific to any LQ models. But in principle, the interpretation could follow the same process as that in Section 2.3.3 and 2.3.4, where BSM vector and scalar propagator are considered, respectively.

2.4. Derivation of V_{cs} from W leptonic branching fraction

The coupling strength between W boson and the fermion current is g . However, due to the quark mixing, the vertex between W boson and quark current is further scaled by a CKM element $|V_{ij}|$. Namely,

$$\begin{array}{ccc} \text{W} \sim \sim \sim \text{---} & \begin{array}{c} \nu \\ \text{---} \\ e \end{array} & = ig\gamma^\mu, \\ & \text{W} \sim \sim \sim \text{---} & \begin{array}{c} q_j \\ \text{---} \\ q_i \end{array} = ig|V_{ij}|. \end{array} \quad (2.46)$$

Denoting the partial width of W decaying into one generation of lepton current as Γ_ℓ , the tree-level calculation gives

$$\Gamma_\ell \equiv \Gamma_{W \rightarrow \ell\nu} = \frac{g^2 m_W}{48\pi}. \quad (2.47)$$

The NLO electroweak correction of Γ_ℓ is at 10^{-5} relative level [106]. The hadronic W width decaying into q_i, q_j at the leading order of QCD correction can be expressed in terms of Γ_ℓ

$$\Gamma_{W \rightarrow q_i q_j}^{\text{LO}} = 3|V_{ij}|^2 \frac{g^2 m_W}{48\pi} = 3|V_{ij}|^2 \Gamma_\ell, \quad (2.48)$$

where the factor 3 accounts for the three colors. The ratio between the total hadronic and the total leptonic W width, at the tree-level, then equals to the square sum of the CKM

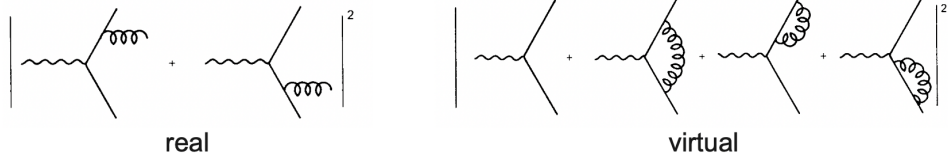


Figure 2.17. The real and virtual diagram of W decay at the next-to-leading order of α_S .

elements in the first two rows:

$$\frac{\Gamma_{\text{had}}^{\text{LO}}}{\Gamma_{\text{lep}}} = \frac{\sum_{ij=(uc)(dsb)} \Gamma_{W \rightarrow q_i q_j}^{\text{LO}}}{\sum_{e,\mu,\tau} \Gamma_\ell} = \frac{\sum_{ij=(uc)(dsb)} 3|V_{ij}|^2 \Gamma_\ell}{3\Gamma_\ell} = \sum_{\substack{\text{u,c} \\ \text{d,s,b}}} |V_{ij}|^2. \quad (2.49)$$

At next-to-leading order (NLO) in α_S , the QCD corrections related to the quark current are taken into account. More specifically, the real and virtual diagram shown in Figure 2.17 add extra contributions to the leading order width $\Gamma_{W \rightarrow q_i q_j}^{\text{LO}}$. The real diagram corresponds to the gluon final state radiation from the outgoing quarks. The virtual diagram corresponds to the interference between the tree level diagram and the virtual gluon bubbles in the quark current and at the vertex. The calculations of the real and virtual contribution can be expressed as a factor multiplied on the tree-level width $\Gamma_{W \rightarrow q_i q_j}^{\text{LO}}$.

$$\Gamma_{W \rightarrow q_i q_j}^{\text{V}} = \Gamma_{W \rightarrow q_i q_j}^{\text{LO}} \times \frac{\alpha_S}{2\pi} \frac{4}{3} \left\{ -\ln^2 \frac{m_g}{Q} - 3 \ln \frac{m_g}{Q} + \frac{\pi^2}{3} - \frac{7}{2} \right\} \quad (2.50)$$

$$\Gamma_{W \rightarrow q_i q_j}^{\text{R}} = \Gamma_{W \rightarrow q_i q_j}^{\text{LO}} \times \frac{\alpha_S}{2\pi} \frac{4}{3} \left\{ +\ln^2 \frac{m_g}{Q} + 3 \ln \frac{m_g}{Q} - \frac{\pi^2}{3} + 5 \right\} \quad (2.51)$$

where Q is the energy of the W boson and $m_g = 0$ is the mass of the gluon, which makes both the real and virtual width diverge. But the divergences in the real and virtual width exactly cancel each other, leading to a finite total contribution. This QCD correction turns out to be a factor of $k = (1 + \frac{\alpha_S}{\pi})$:

$$\Gamma_{W \rightarrow q_i q_j}^{\text{NLO}} = \Gamma_{W \rightarrow q_i q_j}^{\text{LO}} + \Gamma_{W \rightarrow q_i q_j}^{\text{V}} + \Gamma_{W \rightarrow q_i q_j}^{\text{R}} = \Gamma_{W \rightarrow q_i q_j}^{\text{LO}} \left(1 + \frac{\alpha_S(M_W)}{\pi} \right). \quad (2.52)$$

Therefore at NLO in α_S , the ratio between the hadronic and leptonic W widths also includes the $k = (1 + \frac{\alpha_S}{\pi})$ factor:

$$\frac{\Gamma_{\text{had}}^{\text{NLO}}}{\Gamma_{\text{lep}}} = \underbrace{(1 + \frac{\alpha_S}{\pi})}_{k} \sum_{\substack{\text{u,c} \\ \text{d,s,b}}} |V_{ij}|^2. \quad (2.53)$$

For higher order α_S corrections of the hadronicW width, the state-of-art factor has been calculated by considering additional QCD loops. At N³LO, the ratio between the hadronic and leptonicW width reads as

$$\frac{\Gamma_{\text{had}}^{\text{N}^3\text{LO}}}{\Gamma_{\text{lep}}} = \underbrace{\left[1 + 1.045(\frac{\alpha_S}{\pi}) + 0.94(\frac{\alpha_S}{\pi})^2 - 15(\frac{\alpha_S}{\pi})^3 \right]}_{k} \sum_{\substack{\text{u,c} \\ \text{d,s,b}}} |V_{ij}|^2. \quad (2.54)$$

Finally, the sum square of the CKM elements in the first two rows can be calculated by the experimental measurement of $\mathcal{B}(W \rightarrow h)$

$$\sum_{\substack{\text{u,c} \\ \text{d,s,b}}} |V_{ij}|^2 = \frac{1}{k} \times \frac{\mathcal{B}(W \rightarrow h)}{1 - \mathcal{B}(W \rightarrow h)} \quad (2.55)$$

where α_S at the W pole can be calculated with $\alpha_S(\mu_R = m_Z) = 0.1178 \pm 0.0010$ [27] and the QCD renormalization: $\alpha_S(m_W) = \alpha_S(\mu_R) - \alpha_s^2(\mu_R) \frac{\beta_0}{2\pi} \ln \frac{m_W}{\mu_R} = 0.1199 \pm 0.0010$. The square sum of the five more precisely measured CKM elements can be calculated from the latest experimental results [27] shown in Table 1.6. $SS_5 = |V_{ud}|^2 + |V_{us}|^2 + |V_{ub}|^2 + |V_{cd}|^2 + |V_{cb}|^2 = 1.0490 \pm 0.0018$, which leads to the expression for $|V_{cs}|$:

$$|V_{cs}| = \sqrt{\frac{1}{k} \times \frac{\mathcal{B}(W \rightarrow h)}{1 - \mathcal{B}(W \rightarrow h)} - SS_5}. \quad (2.56)$$

CHAPTER 3

The CMS Experiment

3.1. The Large Hadron Collider

The Large Hadron Collider (LHC) [107] is a 27km circular particle collider located at the European Organization for Nuclear Research (CERN) across the border between France and Switzerland. The LHC was constructed during 1998-2008 in a 100-meter-deep underground tunnel previously occupied by the Large Electron–Positron Collider (LEP) [108]. Inside the LHC, two proton beams collide at a maximum center-of-mass energy of $\sqrt{s} = 14 \text{ TeV}$ with a designed instant luminosity of $10^{34} \text{ cm}^{-2} \text{ s}^{-1}$. Around the ring path of the LHC, four collision positions are designed for the four LHC experiments: CMS [109] at point-5, ATLAS [110] at point-1, LHCb [111] at point-8 and Alice [112] at point-2.

The main components of the LHC include two tubes with ultrahigh vacuum and about ten thousand superconducting magnets with various sizes installed along the ring. The magnets include 1232 dipole magnets with a length of 15m to bend the beams and 392 quadrupole magnets with a length of 5m-7m to focus the beams [113]. Magnets of higher multipole orders are also used for corrections of the magnetic field. A liquid helium cooling system is used to cool the superconducting electromagnets at a cryogenic temperature of -271.3°C.

Before injected into the LHC, protons are accelerated to 450 GeV by a few existing accelerator facilities at CERN. Figure 3.1 shows a schematic overview of the LHC with its related accelerator complex [114]. First, protons are produced by the ionization of the hydrogen gas and extracted by a 90 keV voltage to inject into the radio frequency quadrupole (RFQ), which divides protons into bunch crossings and accelerates them to 750 keV. A linear

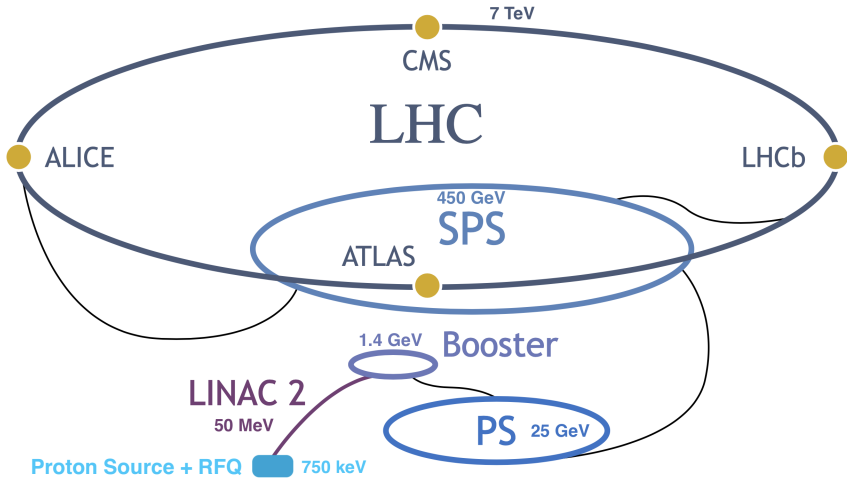


Figure 3.1. Schematic overview of the LHC and the related accelerator complex. The accelerator chain, from the beginning to the end, includes the proton source, radio frequency quadrupole (RFQ), LINAC, proton synchrotron booster (PSB), proton synchrotron (PS), super proton synchrotron (SPS), and finally the LHC [114]. Around the ring path of the LHC locate four LHC experiments: CMS [109] at point-5, ATLAS [110] at point-1, LHCb [111] at point-8 and Alice [112] at point-2.

accelerator (Linac) then energizes them to 50 MeV. The proton synchrotron booster (PSB), which has four superimposed synchrotron rings, brings the proton energy further to 1.4 GeV for the injection to the proton synchrotron (PS), a 628 m synchrotron outputting beams with an energy of 25 GeV. The super proton synchrotron (SPS) further boosts the protons to 450 GeV in its 7 km ring and delivers the beam to LHC. When the LHC accelerates the protons from 450 GeV at their injection to 6.5 TeV for the physics collision in the run-2, the dipole magnetic field is increased from 0.54 T to 7.7 T to enhance the banding power to circulating energized beams. During a physics run, luminosity of LHC decays with a lifetime of about 14.9 h [107] due to losses from physics collisions, photon emittances alone the circular path, and the scattering at the air remains. Therefore, new bunches of protons are injected into the LHC every one or two days.

The operation of the LHC from 2010 to 2035 consists of 6 runs with shutdown periods during the run intervals for upgrade and maintenance . In the run-1 from 2010 to 2013, LHC delivered about 6 fb^{-1} proton-proton collision at $\sqrt{s} = 7 \text{ TeV}$ in 2010-2011 and 23.3 fb^{-1} proton-proton collision at $\sqrt{s} = 8 \text{ TeV}$ in 2012 [115]. The discovery of the Higgs boson was made by the ATLAS [116] and the CMS [117] during the run-1. In the run-2 from 2016 to 2018, LHC produced 144 fb^{-1} proton-proton collisions at $\sqrt{s} = 13 \text{ TeV}$ [115]. Currently in 2020, the LHC is in its second long shutdown period, expecting Run-3 to start in 2021, operating at the maximum collision energy of $\sqrt{s} = 14 \text{ TeV}$. After run-3, LHC will be upgraded to a higher luminosity or the High-Luminosity LHC (HL-LHC), reaching an instant luminosity of $5 \times 10^{34} \text{ cm}^{-2} \text{ s}^{-1}$, five times as much as the current value. In the era of HL-LHC, three extra runs are scheduled during 2026-2035. In the long term future beyond the HL-LHC era, the Future Circular Collider (FCC) [118] plan is proposed to build a 100km hadron collider next to the LHC, further increasing the collision energy to a level of 100 TeV.

3.2. Detector Apparatus

The CMS [109] detector is a general-purpose apparatus located about 100 m underground at Point 5 of the LHC. It is close to the French village of Cessy, between Lake Geneva and the Jura mountains. As a general-purpose detector, the CMS detector is designed to observe new physics phenomena that the LHC might reveal [119]. At the designed LHC luminosity of $10^{34} \text{ cm}^{-2} \text{ s}^{-1}$, about 20 inelastic collisions on average are superimposed on the event of interest every collision of bunch crossings, leading to a large flux of particles originating from the collision point to enter the detector every 25 ns. To discern them and trigger the interested events within 25 ns latency over the LHC run period until 2035, the CMS detector is designed to be highly-segmented, radiation-hard and with good timing resolution [109].

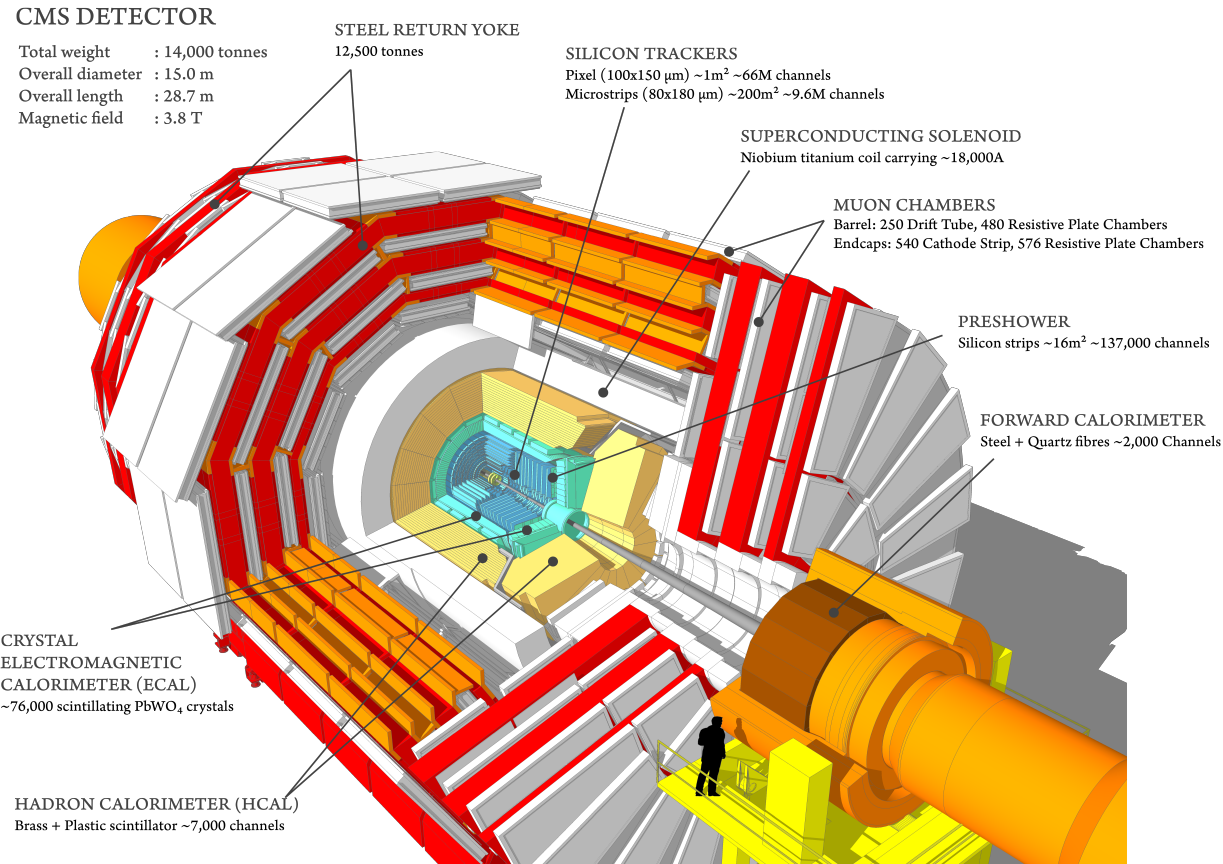


Figure 3.2. The layout of the CMS detector [120].

The apparatus layout of the CMS detector is shown in Figure 3.2 [120]. The central feature of the CMS apparatus is a superconducting solenoid of 6 m internal diameter, providing a magnetic field of 3.8 T. Within the superconducting solenoid volume are a silicon pixel and strip tracker, a lead tungstate crystal electromagnetic calorimeter, and a brass and scintillator hadron calorimeter, each composed of a barrel and two endcap sections. Muons are measured in gas-ionization detectors embedded in the steel flux-return yoke outside the solenoid. Additional forward calorimetry complements the coverage of the barrel and endcap detectors. More details of these sub-systems are discussed in this section.

3.2.1. Magnet

The CMS superconducting magnet [121] is used to provide bending to the charged particles as they traverse, which is crucial to both particle identification and momentum measurement. The internal magnetic field is 4 T with 2.6 GJ stored energy generated by a superconducting solenoid. The solenoid is 12.5 m in length, 6.3 m in diameter, and 200 ton in weight, consist of 41.7 MA-turn of wire. The radiation thickness of the solenoid is $4.9\chi_0$, which further prevents hadrons from entering the muon system. The solenoid is surrounded and mechanically supported by the iron return yoke, which directs the outer magnetic field in the muon system. The yoke, consisting of five barrel wheels and two endcaps, has an outer diameter of 14 m and a weight of 10000 ton. Both barrel and endcap return yoke have three iron layers with thicknesses of 300/630/630 mm and 250/600/600 mm, respectively.

3.2.2. Inner Tracking System

The inner tracking system [122] is used to measure the trajectories of charged particles. It consists of two major parts: pixel detector and Silicon strip tracker, and covers the region with $|\eta| < 2.5$. The layout of the inner tracking system is shown in Figure 3.3. The material thickness of the tracking system is shown in Figure 3.4.

The pixel detector, shown in the center of Figure 3.3, is consist of three cylindrical layers of pixel detector modules at radii of 4.4, 7.3, and 10.2 cm, totaling 66 million pixels with an area of 1 m². It is capable of producing three high precision 3D hits for each charged particle.

The silicon strip tracker system is immediately outside the pixel detector in the region of $20 < r < 116$ cm and $|z| < 282$ cm. The tracker system has three parts: Tracker Inner Barrel and Disk (TIB/TID), Tracker Outer Barral (TOB) and Tracker Endcaps (TEC), with a total of 9.3 million channels and 198 m² active silicon area. The silicon strip modules in

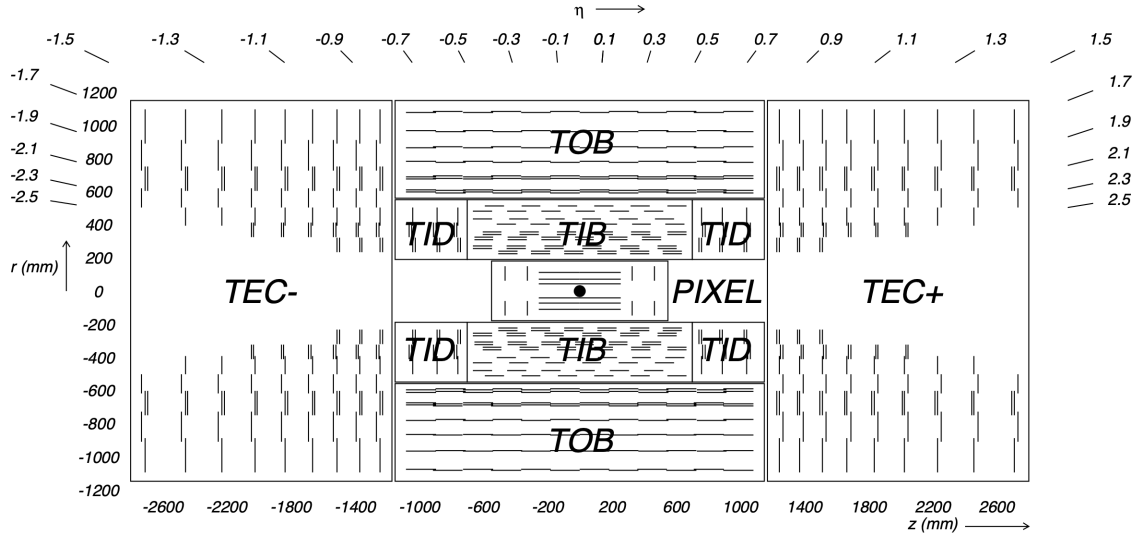


Figure 3.3. The layout of the CMS inner tracking system [109]. It is consist of pixel detector and silicon strip tracker, covering regions with $|\eta| < 2.5$.

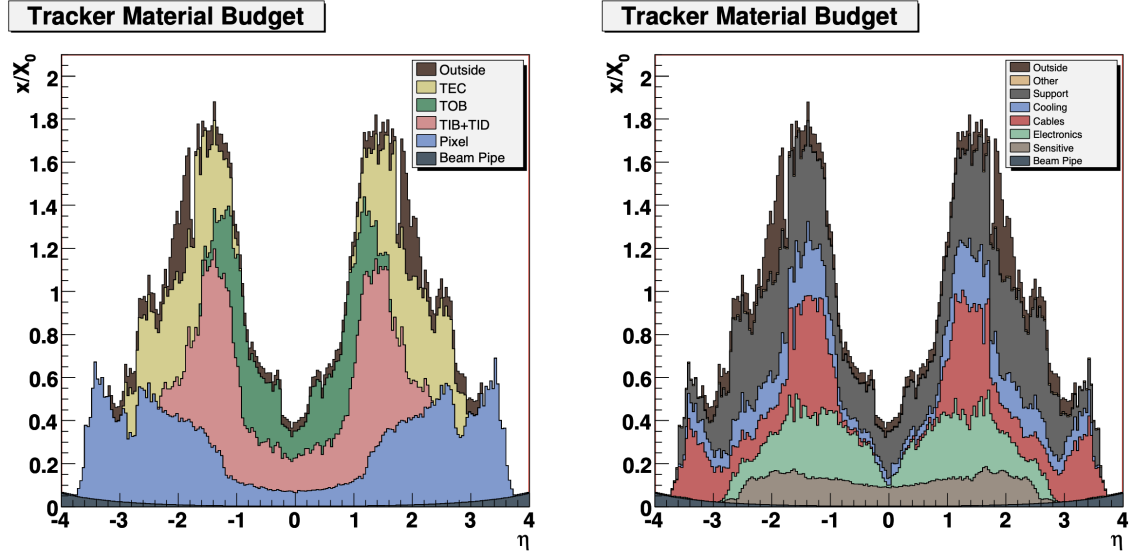


Figure 3.4. The material thickness of the inner tracking system.

the barrel are laid out in cylindrical shapes with their strips parallel to the z direction to measure $r - \phi$ coordinates. Meanwhile, those in the endcap region are in the shape of disks and place their strips in the radial direction to measure the $z - \phi$ coordinates. In addition

to the measurement of the 2D coordinates, the first two cylindrical layers of TIB and TOB, the two innermost rings of TID and TEC, as well as the fifth ring of TEC, are double-sided by placing a second micro-strip module back-to-back to the first with a stereo angle of 100 mrad. The double-sided modules can be seen in Figure 3.3. This small stereo angle allows the measurement of the third spacial coordinates: z in the barrel (TIB and TOB) and r on the endcap (TID and TEC). Such tracker design ensures to acquire at least nine hits in the silicon strip tracker with at least four being stereo measurements.

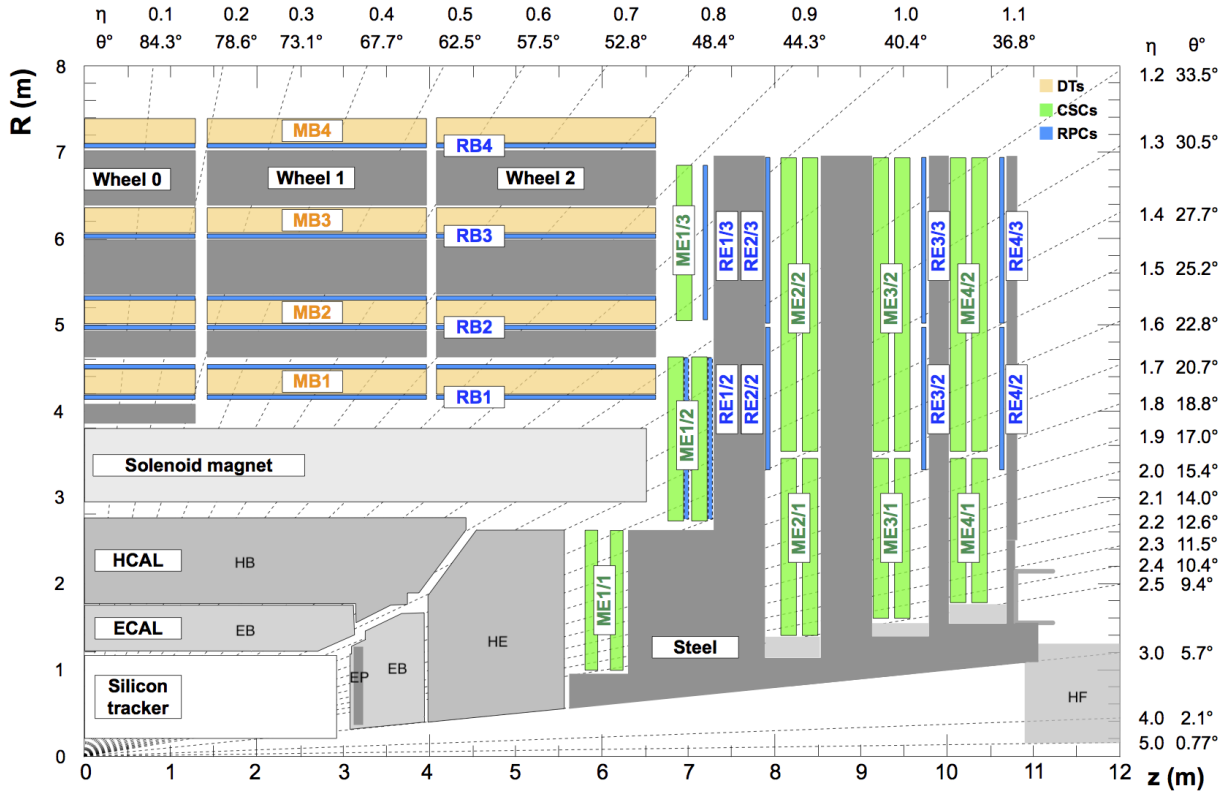


Figure 3.5. The layout of the CMS detector on the z - r plane [123]. The full coverage of pseudorapidity is up to $|\eta| = 5$. The detector includes the tracker, electromagnetic calorimeter, hadronic calorimeter, magnet, and muon system. The details of tracker is shown in Figure 3.3.

3.2.3. Electromagnetic Calorimeter

The CMS electromagnetic calorimeter (ECAL) [124] is used to measure the energy of electromagnetic showers. As shown in Figure 3.5, ECAL is located immediately outside the tracking system. ECAL consists of the barrel part (EB), the endcap part (EE), and a preshower system (PS) in front of EE. EB and EE are hermetic homogeneous calorimeter made of lead tungstate crystals with avalanche photodiode (APD) and vacuum phototriode (VPT) as readout sensors respective. The PS is a thin sampling calorimeter with lead-silicon alternating layers to enhance the spatial resolution in the endcap region. The total ECAL material thickness is larger than $25\chi_0$ and about $1.1\lambda_I$.

The barrel part of the ECAL (EB) covers the pseudorapidity range of $|\eta| < 1.479$ and consists of 61200 crystals arranged in a 170×360 $\eta - \phi$ grid, with 8.14 m^3 of total crystal volume and 67.4 ton of weight. The crystals have a tapered shape mounted in a quasi-projective distribution, in which the crystal axis has small angle with respect to the vector from the origin to minimize chances of cracks aligned with the particle trajectories. The crystal cross-section corresponds to approximately $\Delta\eta \times \Delta\phi = 0.0174 \times 0.0174$, or $22 \times 22\text{ mm}^2$ at the front face of crystal and $26 \times 26\text{ mm}^2$ at the rear face. The crystal length is 230 mm, corresponding to $25.8\chi_0$.

The endcaps (EE) cover the rapidity range $1.479 < |\eta| < 3.0$ and consist of 7324 identically shaped crystals grouped in mechanical units of five-by-five crystals (supercrystals, or SCs), with 2.90 m^3 of total crystal volume and 24.0 ton of weight. The crystals are arranged in a rectangular x-y grid, with the crystals pointing at a focus 1300 mm beyond the interaction point, giving 2° - 8° off-pointing angles. The crystals have a front face cross-section $28.62 \times 28.62\text{ mm}^2$, a rear face cross-section $30 \times 30\text{ mm}^2$ and a length of 220 mm, corresponding to $24.7\chi_0$.

A preshower detector (EP) is placed in front of EE in $1.479 < |\eta| < 2.6$ to increase the space resolution of electromagnetic showers and better identify neutral pions $\pi^0 \rightarrow \gamma\gamma$ in the endcap. EP is a sampling calorimeter of two lead-silicon layers with a total mechanical thickness of 20 cm. On each layer, the lead radiators initiate electromagnetic showers from incoming photons and electrons, while silicon strip sensors placed after each radiator measure the deposited energy and the transverse shower profiles. The directions of silicon strips on the two layers are orthogonal to each other. The material thickness of the first and second layer are $2 \chi_0$ and $1 \chi_0$ respective.

3.2.4. Hadronic Calorimeter

The CMS Hadron Calorimeter [125] is used to measure the energy of hadrons and determine the missing transverse energy. HCAL consists of four parts: the HCAL in the barrel region (HB), HCAL in the endcap region (HE), the forward hadronic calorimeter (HF), and a small section outside the magnetic (HO) in the barrel region. The purpose of HO is to catch the rare hadronic punch through in front of the muon system. As shown in Figure 3.5, HB and HE are designed right outside the ECAL, while FH is in the high pseudorapidity region outside the whole CMS endcap.

HB and HE are a sampling calorimeter covering $|\eta| < 1.3$ and $1.3 < |\eta| < 3.0$, respectively. They use brass absorbers (70% Cu and 30% Zn) and plastic scintillators for readout. HO covers the same $|\eta| < 1.3$ range as HB but uses iron as the absorber to enhance the material thickness of HB, especially in the low η region. With HO, the total material thickness of the HCAL is about $11.8 \lambda_I$, making sure the hadronic leakage to muon is very rare. Totally, HCAL has about 7000 scintillators channels. The spatial granularity is $\Delta\eta \times \Delta\phi = 0.087 \times 0.087$ in the HB, OB and the $1.3 < |\eta| < 1.6$ part of HE. In the rest part of HE, a

higher granularity of $\Delta\eta \times \Delta\phi = 0.017 \times 0.017$ is designed to increase the spatial resolution near the beam pipe.

HF is a sampling calorimeter covering $3.0 < |\eta| < 5$. It is essentially a cylindrical steel structure with fibers piecing from the back in z direction at two different depths. Its outer radius is 130.0 cm. The front face of the calorimeter is located at 11.2 m from the interaction point. The absorber is made of steel installed perpendicular to beam pipe with a total material depth of $10\lambda_I$. The active material is quartz fibers (fused-silica core and polymer hard-cladding) installed in parallel with the beam pipe. When particle showers in the HF, a small part of Cherenkov light generated at the quartz fibers' surface is captured. The two different penetration depths of fibers distinguish the electromagnetic shower and the hadronic shower. The long fibers span the entire HF, while short fibers start from 22 cm behind the HF front surface and extend to the back. These fibers are bundled to form $\Delta\phi \times \Delta\eta = 0.175 \times 0.175$ towers.

3.2.5. Muon System

The CMS muon system [126] is mounted in the return yoke outside the solenoid to measure the tracks of muons. The system consists of barrel detector (MB) covering $|\eta| < 1.2$ and endcap detectors (ME) covering $0.9 < |\eta| < 2.4$.

The barrel detector has 250 chambers in total which hosts 250 drift tube (DT) and 480 resistive plate chambers (RPC). The chambers are arranged in 4 concentric stations in the yoke, each of which is divided into five wheels with twelve sectors on each wheel. The two innermost stations, labeled as MB1 and MB2 in Figure 3.5, has two RPCs sandwiching a DT, while the two outermost stations, MB3 and MB4 in Figure 3.5, consist of a DT coupled to a layer of RPCs on the inner side.

Each DT in MB1, MB2, and MB3 has twelve layers of drift tubes divided into three groups of four consecutive layers, called superlayers. Two superlayers with wire parallel to z direction measure $r - \phi$ coordinates, the middle one with wire perpendicular to z direction measures $r - z$ coordinates. DTs in MB4 only have two superlayers for measurement of $r - \phi$ coordinates. RPCs are attached to DTs to improve the responding time, which is necessary for triggers. Each RPC detector has a bakelite chamber with two 2 mm wide gaps and operates in avalanche mode biased by a high voltage.

The endcap detectors (ME) on the two sides have 469 cathode strip chamber (CSC)s and 432 RPCs and are placed in the yokes that close the solenoid. The ME consists of four stations ME1-ME4. The disk of ME1 is divided into three concentric rings, while disks of ME2-ME4 have two rings. The details of the layout of the CSCs and RPCs in ME are shown in Figure 3.5. Each CSC is trapezoidal in shape and consists of 6 gas gaps. Each gap has a plane of radial cathode strips and a plane of anode wires running almost perpendicularly to the cathode strips, measuring hits with 3D coordinates.

3.3. Trigger System

CMS applies a two-tiered trigger system [127] to select the events of interest. The Level-1 Trigger (L1T), composed of custom hardware processors, uses information from the calorimeters and muon detectors to reduce the event rate from 40 MHz to 100 kHz, within a latency less than $4\ \mu\text{s}$. The second level, known as the High Level Trigger (HLT), consists of a farm of processors running a version of the full event reconstruction software optimized for fast processing. The HLT further reduces the event rate from 100 kHz to 1 kHz and output for data storage.

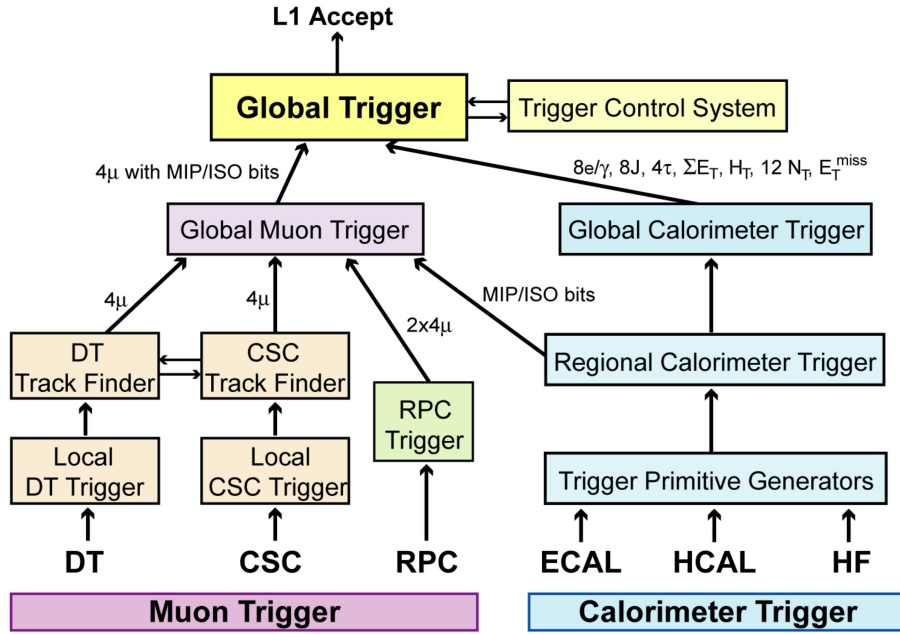


Figure 3.6. The logic structure of level-1 trigger (L1T).

3.3.1. Level-1 Trigger

L1 Trigger is designed to cope with the high collision frequency in the LHC, reducing the event rate from 40 MHz to 100 kHz, keeping only potential events of physics interest. To achieve this, the L1 trigger is designed with three components: local, regional, and global trigger. The logic structure is shown in Figure 3.6. The local triggers, also called Trigger Primitive Generator (TPG), are based on energy deposits in the calorimeter trigger towers as well as the track segments or hit patterns in muon chambers. Regional triggers combine the information from the local triggers in limited regions. They use pattern logic to determine the sorted trigger objects, such as electron or muon candidates. The Global Calorimeter Trigger (GCT) and Global Muon Trigger (GMT) determine the highest-rank calorimeter and muon objects across the entire experiment and transfer them to the Global Trigger (GT), the top entity of the Level-1 hierarchy. GT decides to reject an event or to accept it

for further evaluation by the HLT. The Level-1 Accept decision is communicated to the sub-detectors through the Timing Trigger and Control (TTC) system. Before decisions reach the front-end, the raw data are stored in FIFO pipelined memories in the front end electronics. Limited by the memory size, the latency between a given bunch crossing and the distribution of the L1T decision to the detector front-end electronics is limited to less than $4\mu\text{s}$ [128]. The L1T electronics are housed partly on the detectors, partly in the underground control room located at approximately 90 m from the experimental cavern.

3.3.2. High Level Trigger

The event selection at the HLT is performed similarly to that used in the offline processing. For each event, objects such as electrons, muons, jets are reconstructed, and a menu of identification criteria is applied to select the events of physics interest.

The HLT hardware consists of a CPU processor farm composed of commodity computers, the Event Filter Farm (EVF), running Scientific Linux operating system. The event filter farm consists of thousands of builder-filter units. In the builder units, individual event fragments from the detector are assembled to form complete events. Upon request from a filter unit, the builder unit ships an assembled event to the filter unit. The filter unit then unpacks the raw data into detector-specific data structures and performs the event reconstruction and selection. The associated builder unit and filter unit are located in a single multi-core machine and communicate via a shared memory. In total, the EVF was executed on approximately 13,000 CPU cores at the end of 2012 and the average HLT processing time per event is about 200 ms [128], about two orders of magnitude less than the offline reconstruction. EVF with 13,000 CPU cores allows the L1T output rate up to 100 kHz. With a fixed L1T rate, increasing CPU cores allows HLT to have more time budget per event. The output rate of the HLT is about 1 kHz. The output rate is an optimal

choice based on the event size, as well as the computing and storage capacity of the offline system.

The HLT filtering process uses the full precision of the data from the detector. The selection is based on offline-quality reconstruction algorithms. It works by computing a menu of the HLT paths, in each of which a predefined process of object reconstruction and event selection is executed. If at least one of the HLT paths get past, the event will be accepted and sent to storage and offline processing. Upon the HLT accept decisions are made, the events are sent to the storage manager for archival storage. The event data are stored locally on disk and eventually transferred to the CMS Tier-0 computing center for offline processing and permanent storage. Events are grouped into a set of non-exclusive streams according to the HLT decisions.

3.4. Object Reconstruction

The structure design of the CMS detector is ideal for the particle-flow reconstruction, which uses information from all subdetector systems to reconstruct each of the final state particles, including muons, electrons, photons, and hadrons. Based on the reconstructed particles, also known as the particle-flow candidates, jets are computed and then tagged by the b jet tagger and hadronic tau tagger.

Fig 3.7 illustrates the behaviors of different kinds of particle-flow candidates in the detector. Starting from the beam interaction region, particles first enter the tracker, where the charged-particles leave trajectories while neutral particles do not. The tracker is immersed in a magnetic field that bends the trajectories. Electrons and photons are then absorbed in the ECAL. The corresponding electromagnetic showers are detected as clusters of energy depositions. Charged and neutral hadrons may initiate showers in the ECAL as well, which are subsequently fully absorbed in the HCAL. The corresponding clusters are used to estimate

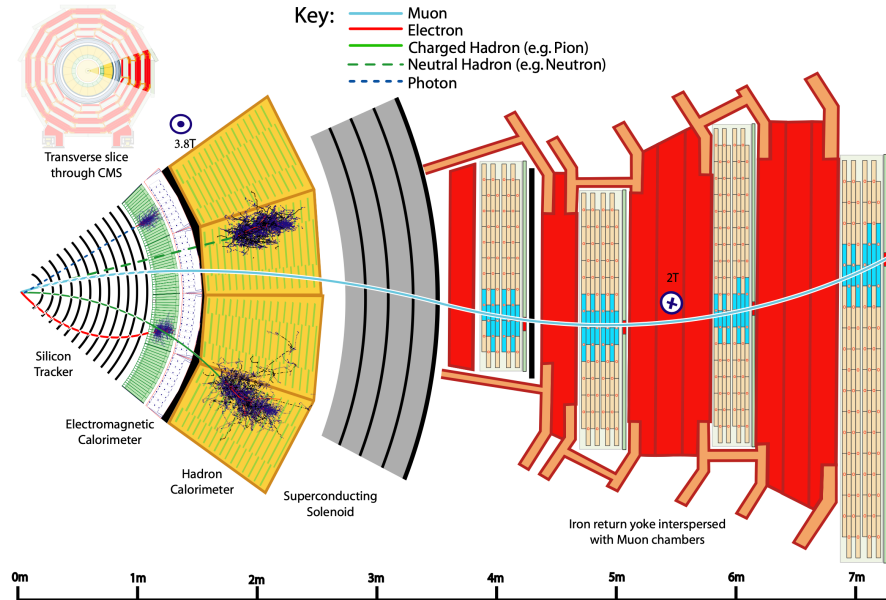


Figure 3.7. The behaviors of different kinds of particle-flow candidates in the detector.

their energies and directions. Muons and neutrinos traverse the calorimeters with little or no interactions. While neutrinos escape undetected, muons produce tracks in the muon detector located outside the solenoid. So, muons are characterized by the tracks in the tracker and muon detector with MIP in ECAL and HCAL. Electrons and photons deposit energy in the ECAL with and without track correspondence, respectively. Charged and neutral hadrons deposit energy in both ECAL and HCAL with and without track correspondence, respectively.

Regarding the algorithm process, the FPA begins with computing particle-flow elements in each subdetector, involving tracks in the tracker and the muon detector, clusters in the ECAL and the HCAL. Then PF elements in different subdetectors are linked to create PF Blocks via a linking process, such that a PF Block summarizes the activities of a potential particle candidate in all subdetectors. The details of reconstruction and linking of the PF elements can be found in [129]. In the end, PF candidates are identified from the PF blocks.

PFA combines information from the entire detector to achieve the best possible energy resolution and particle identification, significantly outperforming the standalone reconstruction of individual subdetectors.

3.4.1. Muons

The reconstruction of muon involves a standalone reconstruction in the muon detector followed by a global reconstruction which combines the trajectories in the tracker.

The standalone reconstruction starts with the track segments in the individual muon chambers. The state vectors (track position, momentum, and direction) associated with the segments found in the innermost chambers are used to seed the muon trajectories, working from inside out, using the Kalman Filter (KF) technique [130]. The track parameters and the corresponding errors are updated at each step. The procedure is iterated until the outermost measurement surface of the muon system is reached. A backward Kalman-filter is then applied, working from outside-in. Finally, the track is extrapolated to the nominal interaction point, and a vertex-constrained fit to the track parameters is performed.

The global muon reconstruction involves extending the muon trajectories to include hits in the silicon tracker. Starting from a standalone reconstructed muon, the trajectory is extrapolated from the innermost muon station to the outer tracker surface, taking into account the muon energy loss in the material and the effect of multiple scattering. This extrapolation and the associated uncertainty defines a region of interest in the tracker, where tracks are seeded by hit doublets and reconstructed using Kalman-filter. A final trajectory fit to the global hits is carried out to exact the muon momentum and impact parameters. This retains both prompt muons and muons from displaced vertices with the best possible efficiency and resolution. Figure 3.8 shows the resolution of muon transverse momentum as a function of eta at different muon energies. The left plot is the result of the standalone

reconstruction algorithm. The right is from the global reconstruction algorithm. A significant improvement is achieved when going from standalone to global muon reconstruction.

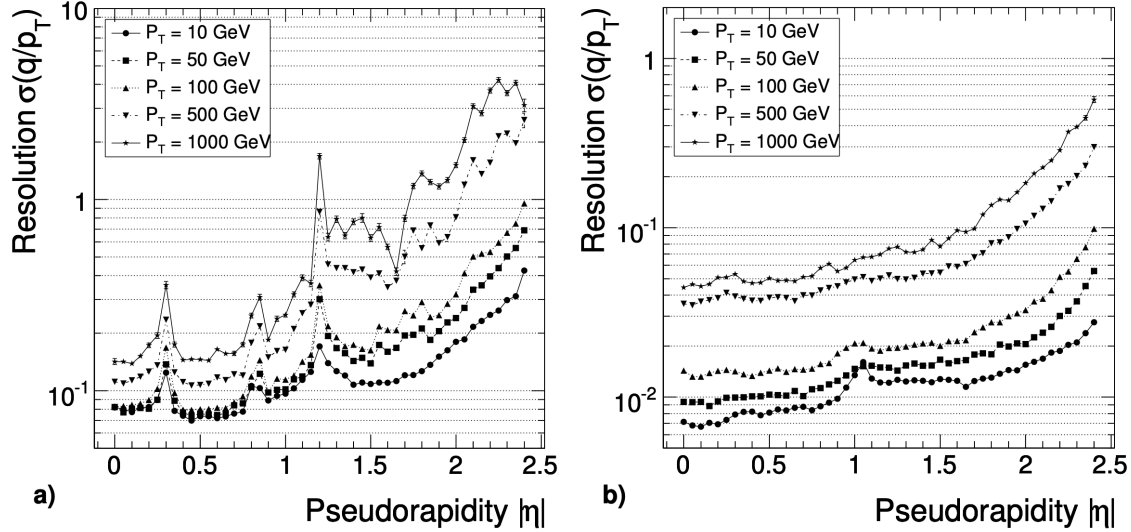


Figure 3.8. The resolution of muon transverse momentum as a function of eta with different muon energies [131]. The left and right plots show the result of the standalone and global reconstruction, respectively.

3.4.2. Electrons and Photons

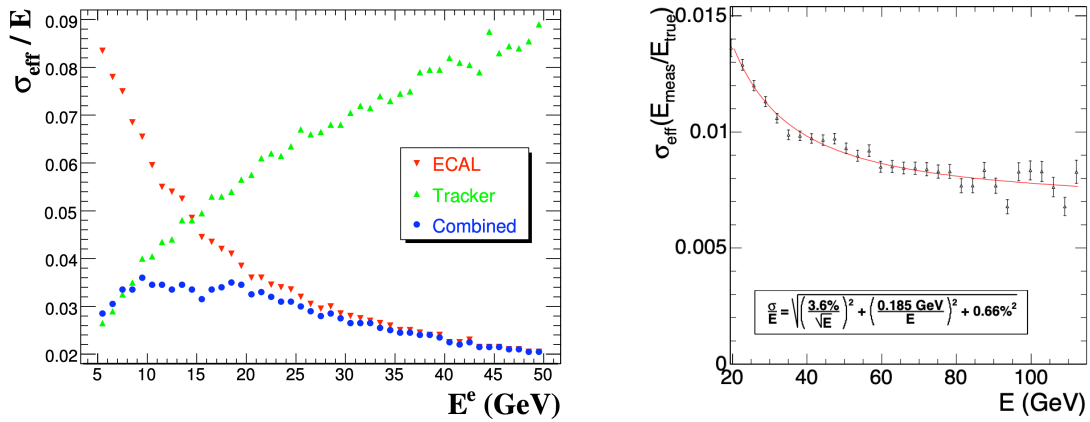


Figure 3.9. The energy resolution of the electron (left) and photon (right) [131].

The electron reconstruction in CMS is hampered by the amount of tracker material in front of the ECAL. The tracker material thickness varies strongly with η , as shown in Figure 3.4. When electrons traverse the tracker's silicon layers, they radiate collections of bremsstrahlung photons, and thereby the energy reaching the ECAL spreads along the ϕ direction. [131] provides a good illustration – "For electrons at $p^T = 10$ GeV, about half of the electrons radiate away more than half of their energy before reaching the surface of the ECAL. In about 10% of the cases, more than 95% of the initial electron energy is radiated!" Furthermore, the radiated photon can again convert into electron-positron pairs, usually soft and trapped in the magnetic field, losing all the energy in the end undetected.

The reconstruction of electron starts with making superclusters from the ECAL energy deposits. The superclustering algorithm is optimized for the scenarios of energy spread along ϕ direction. The supercluster helps the finding of track seeds, which are hit doublets in the pixel detector. If a seed compatible with the supercluster is found, the track building begins inside-out with a nonlinear filter called Gaussian Sum Filter (GSF) [132]. For superclusters successfully linked with GFS tracks, an electron candidate is made. A fit to the GSF tracks and ECAL superclusters is used to extract the four-momentum under the electron assumption. This combines the advantages of the tracker in the low energy region and the ECAL in the high energy region. The energy resolution of electrons using tracker-only, ECAL-only and the combined is shown in Figure 3.9 (left). For a supercluster not linked to any GFS tracks, a photon candidate is made. The energy is obtained from the sum of energy deposited in a supercluster of crystals. To quantify the photon shower's lateral spread, a variable called R9 is defined for the supercluster. It equals to the 3x3 crystals' energy around the leading crystal divided by the total supercluster energy. It is used as a quantity for photon identification. The energy resolution of photons with $R9 > 0.943$ is shown in Figure 3.9 (right).

3.4.3. Hadrons

Once muons, electrons, and isolated photons are identified, the remaining particles are neutral and charged hadrons. The calorimeter clusters not linked to any tracks suggest the non-isolated photons and neutral hadrons. Within the tracker acceptance ($|\eta| < 2.5$), all such ECAL clusters are turned into non-isolated photons, and all such HCAL clusters are turned into neutral hadrons.

Then the charged hadron reconstruction becomes the last step. Charge hadrons are made from the remaining calorimeter clusters and tracks. Each of the remaining HCAL clusters is linked to one or several tracks, which may in turn also link to some of the remaining ECAL clusters. It is possible that these remaining calorimeter clusters contain not only the charged hadrons but also the unresolved FSR photons and close-by non-isolated neutral hadrons around the charged hadrons. To identify these unresolved neutral components, a match of calorimeter energy and tracker momentum is carried out:

- If the calorimetric energy is compatible with the linked track momenta, no neutral particle is identified. The charged hadron's kinematics are redefined by a global calibration taking into account both the tracker and the calorimeters.
- If the calorimetric energy excesses the sum of the tracks momenta by an amount larger than the expected calorimetric energy resolution for hadrons, the excess may be interpreted as the presence of near-by photons and neutral hadrons. Such excess energy is in priority treated as a non-isolated photon and subtracted from the ECAL energy. In the case that the ECAL energy alone is not enough to account for the excess, the remaining excess is treated as a non-isolated neutral hadron.

- If the calibrated calorimeter energy is smaller than the tracking momentum, an additional search for non-isolated muon is carried out with a relaxed muon reconstruction standard. The momentum of the looser reconstructed muons is then subtracted before a re-compare.

3.4.4. Jets

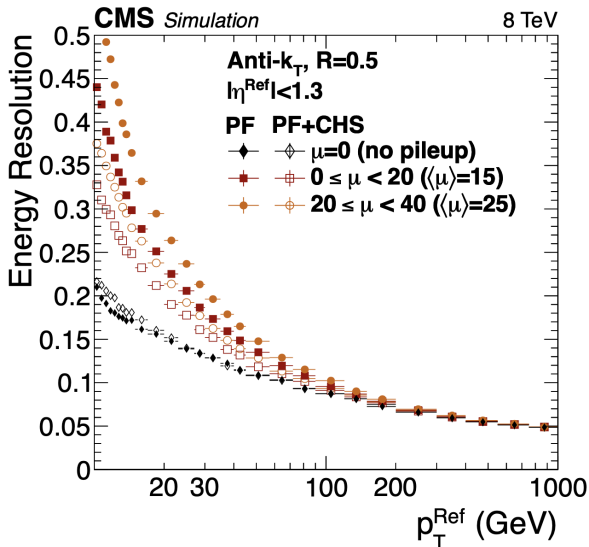


Figure 3.10. The jet energy resolution [129] with and without Charged Hadron Subtraction (CHS) in three pileup scenarios $\langle\mu\rangle = 0, 15, 25$. The improvement from CHS is more prominent at higher pile-ups.

With the PF candidates reconstructed, including muons, electrons, photons, charged and neutral hadrons, jets are produced by a clustering algorithm that groups colinear PF candidates to represent the particle originating from the hard process. The popular jet clustering algorithms include k_T , anti- k_T and Cambridge/Aachen algorithm [133], among which the key difference lies with the definitions of the distances. More specifically, if we denote the distance between two objects i and j as d_{ij} , the distance between the object i

and the beam as d_i , the general form of the distances d_{ij} and d_i can be written as

$$d_{ij} = \min(k_{T,i}^{2p}, k_{T,j}^{2p}) \frac{(\eta_i - \eta_j)^2 + (\phi_i - \phi_j)^2}{R^2}, \quad d_i = k_{T,i}^{2p}, \quad (3.1)$$

where R is a algorithm parameter related to the cone size of the jets and p is the power of k_T^2 . The k_T , anti- k_T and Cambridge/Aachen algorithm adopt $p = \{1, -1, 0\}$, respectively. The clustering algorithm used in the CMS is the anti- k_T algorithm. The parameter R is set to be 0.4 for slim jets and 0.8 for fat jets. During the anti- k_T clustering process, the shortest distance is searched among all the d_{ij} and d_i in the collection of PF candidates. If the minimal distance is d_{ij} , the two object i and j are merged into a new object. Otherwise, the minimal distance is d_i and the object i is output as a jet. This process is repeated until all objects are output.

The PF candidates in a jet may include the hadrons from the pile-up activities. The pile-up constituents in a jet become more relatively significant for the low p_T in the barrel region [129]. Hence a pile-up subtraction is designed to clean up the PF candidates from the pile-up. It removes charged hadrons not associated with the primary vertex. This step is called Charged Hadron Subtraction (CHS). Figure 3.10 shows the jet energy resolution with and without CHS for three pileup scenarios $\langle\mu\rangle = 0, 15, 25$. As the pile-up increases, the improvement from the CHS becomes more significant.

3.4.5. b Jet Tagging

To identify the jets originating from the b quarks, several tagging algorithms have been developed [20, 21, 22].

The first tagger is Jet Probability (JP) and Jet B Probability (JBP). JP computes the likelihood for each track to come from the primary vertex, given the track's impact parameter and the spatial resolution of the primary vertex. Such likelihoods for all tracks in the jet

are combined to indicate the probability of the jet coming from a non-prompt particle. JBP is a variation of JP. JBP assigns larger weights to the four tracks with the largest impact parameter.

The second tagger is Combined Secondary Vertex (CSV). Compared with JP/JBP, which focuses on tracks' impact parameters, CSV also performs a searching and fitting for tracks' secondary vertices. Then, it computes several kinematic and topology variables about the secondary vertices, such as the number of SV, the distance of SV, the corrected SV mass, the relative SV energy ratio, and the number of tracks in the SV. The full list of the input variables of the CSV version-1 and version-2 used during the LHC run-1 and run-2 can be found in [21]. Finally, all the jet and jet's secondary vertex variables are fed into a multivariate model to obtain a single b tag score. In the full run-2 dataset, with the same set of jet and jet's SV variables, the multivariate model is improved by a more flexible classifier, a fully-connected neural network (nn) with a few hidden layers. This nn-based tagger is called DeepCSV [22].

The third tagger is the combined multivariate analysis (cMVA). When electrons and muons present in a jet, the information related to the charged lepton is used to construct a soft-electron (SE) tagger and a soft-muon (SM) tagger, which are both boosted decision trees (BDT) trained with 2D and 3D lepton impact parameters and a few kinematic variables about the lepton's angular separation and relative k_T . Then an MVA combines the JP, JBP, CSV, SE, SM taggers into a final comprehensive b tag score. Figure 3.11 shows the distributions of the b tag score from the cMVA b tagger for the simulated light, c and b jets.

3.4.6. Hadronic Tau Identification

About 64.8% of taus decay hadronically. The major decay modes of hadronic taus include $B(\tau^- \rightarrow h^-\nu_\tau) = 11.5\%$, $B(\tau^- \rightarrow h^-\pi^0\nu_\tau) = 25.9\%$ (where the mass of $h^-\pi^0$ system is

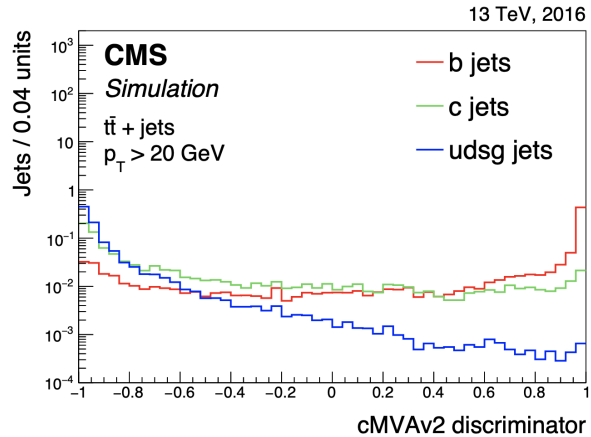


Figure 3.11. The distribution of the b tag score from the combined multivariate analysis (cMVA) b tagger [21].

resonant at $\rho(770)$), $B(\tau^- \rightarrow h^-\pi^0\pi^0\nu_\tau) = 9.5\%$ and $B(\tau^- \rightarrow h^-h^+h^-\nu_\tau) = 9.8\%$ (where mass of $h^-\pi^0\pi^0$ and $h^-h^+h^-$ system is resonant at $a_1(1260)$). The tau reconstruction at the CMS relies on these hadronic decay modes.

For each reconstructed jet, the tau reconstruction first attempts to match the jet constituents to the patterns of the common hadronic decay modes. The matching, also known as mode finding, is performed with the hadrons-plus-strips (HPS) algorithm. If the jet structure is found compatible with a decay mode and the decay mode involves certain meson resonances like $\rho(770)$ and $a_1(1260)$, HPS further checks consistency between visible mass of the tau candidate and the expected meson resonance. After the mode finding, a τ_h score based on the structure and isolation of the candidate's constituents is computed to discriminate against fakes from the quark or gluon jets, which could otherwise be significant due to the complex QCD environment in the LHC. Besides, discriminators against the electron and muon are also developed.

3.4.6.1. The τ_h Mode Finding. Starting from the constituents of the reconstructed jets, the hadrons-plus-strips (HPS) algorithm is used to match the jet structure to the expected τ_h pattern.

The π^0 mesons from the τ_h decay promptly decay into pairs of photons, which are highly likely to convert into $e + e^-$ pairs as they traverse the tracker material. The CMS magnetic field bends the $e + e^-$ and leads to a spatial separation of the $e + e^-$ pairs on the $\eta - \phi$ plane. The electron and photon candidates within a certain region of $\Delta\eta \times \Delta\phi$ are clustered together to reconstruct the neutral pions. The resulting cluster is referred to as a “strip”. The strip’s four-momentum is defined as the sum of all its constituent four-momenta. The clustering process defines a $\Delta\eta \times \Delta\phi = 0.20p_T^{-0.66} \times 0.35p_T^{-0.71}$ window for each of the strips, electrons, photons. The steps of the strip clustering process work as follows: the leading e/γ in the jet not yet included in any strips is used to seed a new strip; then, in order of decreasing p_T , the nearby e/γ whose window touches the strip window is merged with the strip, and the strip’s position and four-momentum are updated accordingly. These two steps of seeding and merging are repeated until all qualified e/γ are processed. Comparing with a fixed window size employed during the run-1, the window size of this strip clustering algorithm depends dynamically on the object’s p_T and better accounts for the different bending effects of different p_T .

Charged particles, often called prong, used in the reconstruction of τ_h candidates are required to have $p_T > 0.5$ GeV and must be compatible with the primary vertex. Due to the tau lifetime, when imposing primary vertex association, the transverse impact parameter is relaxed to $d_{xy} < 0.1$ cm. The requirement of $p_T > 0.5$ GeV on the charged particles ensures that the corresponding tracks have sufficient quality.

Based on the reconstructed strips and qualified tracks in a jet, the HPS algorithm generates all possible combinations of hadrons for the following decay modes: h^\pm , $h^\pm\pi^0$, $h^\pm\pi^0\pi^0$, $h^\pm h^\mp h^\pm$. For $h^\pm\pi^0$ decay mode, the total hadronic elements should be from $\rho(770)$ resonance. For $h^\pm\pi^0\pi^0$ and $h^\pm h^\mp h^\pm$, the total hadronic elements should be from $a_1(1260)$ resonance. So if $h^\pm\pi^0$ or $h^\pm\pi^0\pi^0$ or $h^\pm h^\mp h^\pm$ mode is found, the total visible mass of the

tau candidate is checked to be compatible with corresponding resonance. Last but not least, for each τ_h candidate, a signal cone is defined as

$$\Delta R_{sig} = \frac{3.0 \text{ GeV}}{p_T(\text{hadronic system})}, \quad \text{with } 0.05 \leq \Delta R_{sig} \leq 0.1. \quad (3.2)$$

If any charged particles or strip is located outside the signal cone, the τ_h candidate is rejected.

3.4.6.2. Discriminator against jets. To reduce the fakes from gluon or quark jets, discriminators are designed against $j \rightarrow \tau$ fakes for the τ_h candidates. Comparing with the quark and gluon jets, the τ_h tends to have a cleaner calorimeter environment in its near-by region. Base on this principle, an isolation quantity in a $\Delta R = 0.3$ cone is calculated. Two discriminators have been developed for 2016 analysis. They are isolation sum discriminator and MVA-based discriminator. For Run-2, the MVA classifier is improved by a more flexible classifier model, deep neural networks.

The isolation of τ_h candidate is computed by summing the p_T of charged particles and photons in a $\Delta R = 0.3$ cone around the τ_h candidate. The summing does not include the charged particle and photons of the τ_h candidate in the τ_h signal cone defined in Equation 3.2. The τ_h isolation is defined as

$$I_{\tau_h} = \sum p_T^{\text{charged}}(d_z < 0.2\text{cm}) + \max \left(0, \sum p_T^\gamma - \Delta\beta \sum p_T^{\text{charged}}(d_z > 0.2\text{cm}) \right) \quad (3.3)$$

where $d_z < 0.2$ cm requirement reduces the PU contributions in the $\sum p_T^{\text{charged}}$. Meanwhile, PU contributions in the $\sum p_T^\gamma$ is subtracted by the term $\Delta\beta \sum p_T^{\text{charged}}(d_z > 0.2 \text{ cm})$, where the parameter $\Delta\beta = 0.2$ scales the PU charged component to estimate the PU neutral component. The isolation sum discriminator requires I_{τ_h} to be less than some working point. In addition to I_{τ_h} cut, the p_T of the partial strip located outside the τ_h signal cone,

denoted as $p_T^{\text{strip, outer}}$, is calculated and requirement

$$p_T^{\text{strip, outer}} < 0.1 p_T^{\tau_h} \quad (3.4)$$

is imposed to further reduce $j \rightarrow \tau_h$ fakes given that the strip window in the strip clustering is dynamically p_T dependent. This additional cut on $p_T^{\text{strip, outer}}$ approximately reduces $j \rightarrow \tau_h$ fakes by another 20% without impacting the τ_h efficiency.

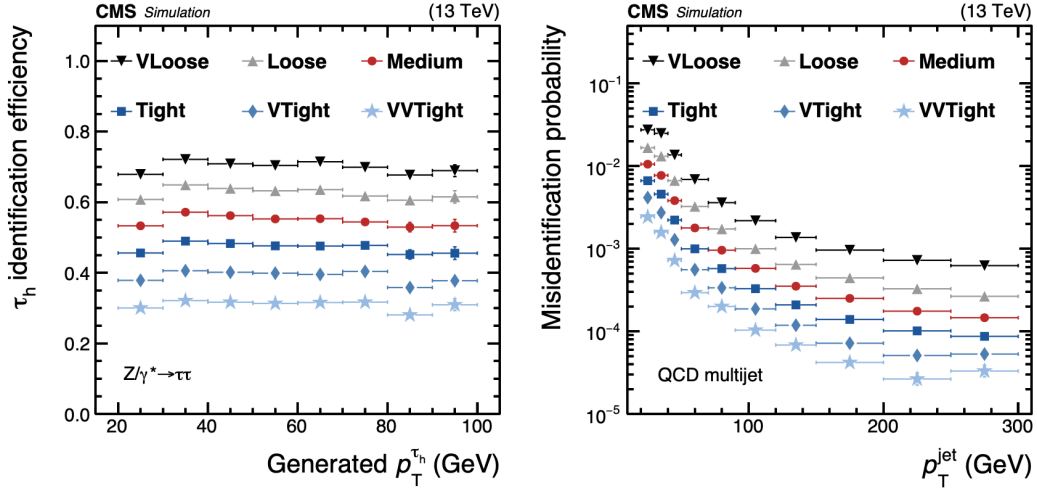


Figure 3.12. The τ_h identification efficiency and $j \rightarrow \tau_h$ misidentification probability in the QCD multijets events [26]. Different working points are shown in different colors.

MVA-based τ_h discriminator combines the isolation and other topology variables sensitive to the τ lifetime [26] to provide the best possible discrimination between τ_h and quark or gluon jets. The MVA classifier is a boosted decision tree (BDT). The input variables to the MVA includes I_{τ_h} in Equation 3.3, $p_T^{\text{strip, outer}}$ in Equation 3.4, spatial separations among e/ γ in the strips, significance of the 3D impact parameter (SIP3D) of the leading tracks, tau flight length for 3 prong $\tau_h \rightarrow h^\pm h^\mp h^\pm$ calculated by the secondary vertices. The full list of the input variables can be found in [24, 25]. Based on the MVA result, the isolation variable provides the most discriminating power. The next important variables are SIP3D and tau

flight length. The MVA combines all sensitive variables and outputs a single number for the τ_h identification score, which can be cut at different working points. Using different MVA working points, the τ_h identification efficiency and $j \rightarrow \tau_h$ misidentification probability in the QCD multijets events are shown in Figure 3.12. The τ_h identification is relatively constant with respect to p_T . In contrast, the misidentification probability drops significantly with the increase of p_T .

In addition to the isolation discriminator and MVA-based discriminator, Deep Tau Identification is also developed for the Run-2 analysis. The deep tau ID is similar to the MVA-based ID in the sense of combining a set of sensitive variables to a single τ_h score with a non-linear classification model. The difference is that the deep tau ID uses deep neural networks instead of BDTs for a more flexible classification.

3.5. Simulation

The Monte Carlo simulated events are produced via a pipeline which can be divided into three main stages, the event generation (GEN), the detector simulation (SIM), and the digitization (DIGI). Then the same reconstruction and triggering algorithms used for data are applied to simulated events.

The GEN stage generates a set of final-state particles for each event according to the interested QFT physics model. The involved software can be summarized as “Generator+PYTHIA”. Common generators include MADGRAPH, POWHEG, HERWIG, SHERPA. The event generation starts with initiating the generator with a configuration of the key input information, such as the beam parameters, the parton distribution functions (PDFs), and the corresponding QFT models. Upon initialized, the generator calculates the matrix element and cross-section of the hard processes at some perturbative order according to the provided QFT models. Then it outputs Monte Carlo events from the calculated differential cross-section.

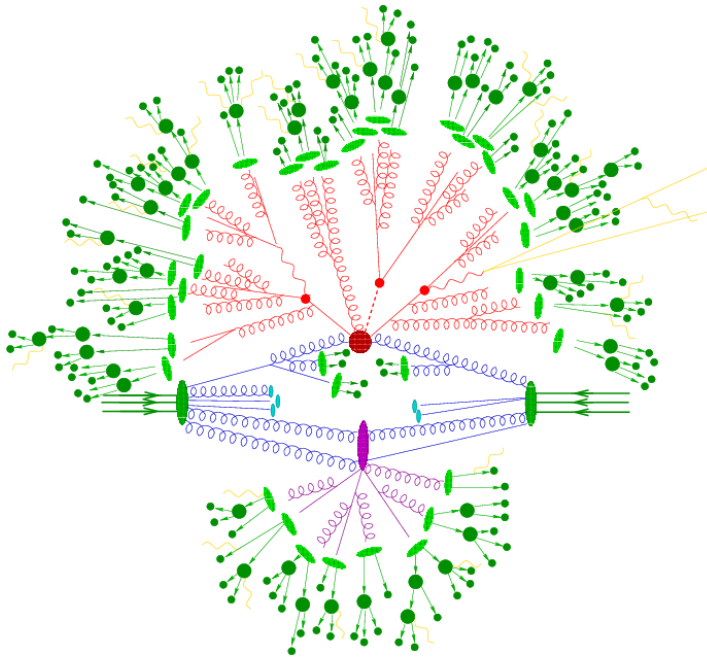


Figure 3.13. Physics processes happening in a proton-proton collision. The lower purple blob represents underline events. The upper purple blob shows the hard process with initial state radiation (ISR) before it, and with final state ratio (FSR), parton shower (PS), hadronization, meson/baryon decay after it. All of these processes are handled properly in the GEN stage by the generator and PYTHIA.

Possible QCD and QED ISR/FSR are also included in the generated events. Next, for all particles from the generator, PYTHIA is used to perform the potential parton showering, hadronization, and decay of unstable particles. In addition, PYTHIA also adds underline events (UE) to the generated events according to certain UE tuning [134]. The underline events are QCD scatterings at the same proton-proton vertex as the hard process. Figure 3.13 illustrates the physics processes happening during a proton-proton collision, all of which are properly treated in the GEN stage with the “Generator+PYTHIA” setup.

The SIM stage uses GEANT4 to simulate the energy deposits, known as hits, of the final state particles in the CMS detector. To achieve this, a detailed geometry model of the CMS detector, including the information about the detector layout, the magnetic field, the electronics, the cables, and the supporting mechanics, is created in the GEANT4. With this

geometry modelling, GEANT4 simulates the hits based on the physics for the interaction between the particles and the materials. After GEN-SIM, the pile-up events, often referred to as MinBias (MB) events and separately produced beforehand with the same GEN-SIM pipeline, are mixed with the signal events according to the instant luminosity and expected average number of PUs.

The DIGI stage simulates the response of the detector readout electronics to hits. The purpose is to simulate the best realism of the collected digitized signal as close as possible to the real CMS detector. After the DIGI stage, the same reconstruction and triggering software as the data events are used for the MC events. Finally, the MC events are output and stored in the same format as the experimental data as well.

CHAPTER 4

Measurements of W Branching Fractions and Test of Lepton Flavor Universality with the CMS 2016 Dataset

This chapter presents a precision measurement of W branching fractions with the CMS 2016 dataset. Lepton flavor universality is tested by taking the ratio of W leptonic branching fractions of different lepton generations. This measurement is done in collaboration with Nathaniel Odell, postdoctoral fellow at Northwestern University, who is in charge of the shape analysis.

This chapter is structured as follows:

- (1) A description of the analyzed datasets and simulation;
- (2) The selection of physics objects and events;
- (3) The calibrations and corrections;
- (4) The estimation of backgrounds;
- (5) The methods for extracting the branching fractions;
- (6) Estimation of systematic uncertainties;
- (7) Results of measured W branching fractions and a test of lepton flavor universality.

4.1. Dataset and Simulated Events

4.1.1. Data

In this analysis, data is selected based on the presence of at least one muon or one electron. The single muon dataset requires that events contain at least one muon with transverse momentum $p_T > 25 \text{ GeV}$ and passing the loose track isolation criterion, $\text{Iso}_{\text{track}} < 0.1$. The

single electron dataset requires that there be at least one electron satisfying the requirement that $p_T > 30 \text{ GeV}$ and that it passes the tight identification requirements as defined by the CMS Physics Object Group for electron and photon (EGamma POG). The specific dataset names and the associated integrated luminosities are listed in Table 4.1.

Table 4.1. Data samples produced by CMS in 2016.

Sample	Run ranges	$\int L(\text{ fb}^{-1})$
SingleMuon/Run2016B-03Feb2017_ver2-v2	272007-275376	5.33
SingleMuon/Run2016C-03Feb2017-v2	275657-276283	2.4
SingleMuon/Run2016D-03Feb2017-v2	276315-276811	4.26
SingleMuon/Run2016E-03Feb2017-v2	276831-277420	4.1
SingleMuon/Run2016F-03Feb2017-v2	277772-278808	3.2
SingleMuon/Run2016G-03Feb2017-v2	278820-280385	7.8
SingleMuon/Run2016H-03Feb2017_ver*-v1	281613-284044	9.2
SingleElectron/Run2016B-03Feb2017_ver2-v2	272007-275376	5.33
SingleElectron/Run2016C-03Feb2017-v2	275657-276283	2.4
SingleElectron/Run2016D-03Feb2017-v2	276315-276811	4.26
SingleElectron/Run2016E-03Feb2017-v2	276831-277420	4.1
SingleElectron/Run2016F-03Feb2017-v2	277772-278808	3.2
SingleElectron/Run2016G-03Feb2017-v2	278820-280385	7.8
SingleElectron/Run2016H-03Feb2017_ver*-v1	281613-284044	9.2

Run ranges where data quality is determined to be insufficient are removed from the dataset by applying a luminosity mask. The following file is provided in JSON format from the CMS Physics Performance and Dataset (PPD) group:

`Cert_271036-284044_13TeV_23Sep2016ReReco_Collisions16_JSON.txt`

The full dataset consists of 35.9 fb^{-1} of integrated luminosity [135]

4.1.2. Simulated Dataset

Simulated datasets are used for modelling the major SM processes, including SM diboson, $W/Z/\gamma$ associated with jets, single-top and $t\bar{t}$. The background from multijet QCD is estimated by a data-driven approach discussed in Section 4.4. The simulated samples used in

modelling the background and signal are shown in Table 4.2. The production of the samples was carried during the Summer 2016 campaign and the production of the mini Analysis Oriented Data format (miniAOD) was done using CMSSW release 8_0_26_patch2. The same release was used for processing both the data and the simulated samples. Lepton flavor universality is assumed for the simulated datasets, namely $\mathcal{B}(W \rightarrow \ell\nu) = 10.8\%$. To account for the deviation from the data, some corrections and reweightings of the simulated dataset are applied, which are discussed in Section 4.3.

4.2. Selection

4.2.1. Object Selection

The event topologies of interest will require reconstructing electrons, muons, hadronically decaying tau leptons, hadronic jets, b tagged jets, and missing transverse energy (E_T^{miss} or MET). In this section, the reconstruction and selection of these physics objects is described.

4.2.1.1. Primary vertex. Primary vertices (PV) are reconstructed based on information from the tracking subsystem, mainly through the inner pixel detector. Quality cuts are applied to reconstructed PVs to guarantee they come from a proton-proton hard scattering event. These cuts are as follows,

$$N_{\text{d.o.f.}} > 4; \quad |z| < 24 \text{ cm}; \quad \sqrt{x^2 + y^2} < 2 \text{ cm}.$$

The PVs are ordered based on the sum p_T of their reconstructed tracks. Selected physics objects are associated to the PV with the greatest sum p_T .

4.2.1.2. Muon. Muon candidates are reconstructed using both the muon and tracker systems. The coverage of these two detector systems allows reconstruction of muons within $|\eta| < 2.4$ and p_T as low as 5 GeV [136]. The details of particle-flow muon reconstruction are described in Section 3.4.1. In the analysis, selected muons are required to be reconstructed

Table 4.2. Simulated datasets.

Process	Generator	$\sigma \times \text{BR}$ (pb)
t̄t	POWHEG +PYTHIA	831.76
t̄t (leptonic)	POWHEG +PYTHIA	87.32
t̄t (semi-leptonic)	POWHEG +PYTHIA	364.35
tW	POWHEG +PYTHIA	35.6
t (t-channel)	POWHEG +PYTHIA	136.02
̄t (t-channel)	POWHEG +PYTHIA	80.95
Z+jets		
10 < $m_{\ell\ell} < 50$ GeV	MC@NLO +PYTHIA	18610
$m_{\ell\ell} > 50$ GeV	MC@NLO +PYTHIA	5765
$m_{\ell\ell} > 50$ GeV, $N_j = 0$	MC@NLO +PYTHIA	4757
$m_{\ell\ell} > 50$ GeV, $N_j = 1$	MC@NLO +PYTHIA	884.4
$m_{\ell\ell} > 50$ GeV, $N_j = 2$	MC@NLO +PYTHIA	338.9
W + 1 jet	MADGRAPH +PYTHIA	11486.5
W + 2 jet	MADGRAPH +PYTHIA	3775.2
W + 3 jet	MADGRAPH +PYTHIA	1139.8
W + 4 jet	MADGRAPH +PYTHIA	655.82
γ+jets		
40 < $H_T < 100$ GeV	MADGRAPH +PYTHIA	17410
100 < $H_T < 200$ GeV	MADGRAPH +PYTHIA	5363
200 < $H_T < 400$ GeV	MADGRAPH +PYTHIA	1178
400 < $H_T < 600$ GeV	MADGRAPH +PYTHIA	131.8
$H_T > 600$ GeV	MADGRAPH +PYTHIA	44.27
qq → WW → 2ℓ2ν	POWHEG	12.13
gg → WW → 2ℓ2ν	POWHEG	0.588
W Z → 3ℓν	POWHEG +PYTHIA	5.29
W Z → 2ℓ2q	MC@NLO +PYTHIA	5.595
Z Z → 2ℓ2ν	POWHEG +PYTHIA	0.564
Z Z → 2ℓ2q	MC@NLO +PYTHIA	3.22
Z Z → 4ℓ	MC@NLO +PYTHIA	1.21

using both the *global* muon and *tracker* muon reconstruction algorithms. The former begins with tracker information and extrapolates to find consistency with hits in the muons system,

while the latter inverts the reconstruction steps starting from the muon system and finding tracks that are consistent. The combination of these two algorithms makes for a muon reconstruction that is accurate in predicting muon momentum and efficient in detecting muons within the detector acceptance.

In the interest of detecting muons decaying from vector bosons, a set of identification and isolation requirements are applied [137]. The muon identification requirements are designed to have high selection efficiency and a low probability of misidentifying non-prompt muons originating from non-bosonic decays. The selection criteria provided by the muon Physics Object Group (POG) are listed in Table 4.3.

Table 4.3. Tight muon identification criteria as provided by muon Physics Object Group (POG).

variable	cut value
isGlobal	True
isPF	True
χ^2	< 10
number of matched stations	> 1
number of pixel hits	> 0
number of track layers	> 5
number of valid hits	> 0
$ d_{xy} $	< 0.2
$ d_z $	< 0.5
Iso_{PF}/p_T (ρ corrected)	< 0.15

To increase the likelihood of selecting muons produced by the prompt decay of vector bosons, an isolation requirement is placed on all muons. The isolation of the muon is calculated by summing the p_T of all charged hadronic, neutral hadronic, and photon particle flow candidates in a cone of radius $\Delta R = 0.4$ about the muon candidate. This quantity is corrected to remove the contamination of the neutral component due to pileup by subtracting

off the average energy deposited by pileup. It is defined as,

$$Iso_{\text{PF}} = Iso_{\text{ch.had}} + \max(0, Iso_{\text{neu.had}} + Iso_{\gamma} - 0.5Iso_{\text{pileup}}) .$$

4.2.1.3. Electron. Electrons are reconstructed by combining information from the electromagnetic calorimeter and the tracking system using a gaussian-sum filter (GSF) method [138]. The details of the particle-flow electron reconstruction are described in Section 3.4.2. All electrons are required to have $p_{\text{T}} \geq 20 \text{ GeV}$ and $|\eta| < 2.5$. Electrons are identified using a tight cut-based scheme. The requirements for this selection are listed in Table 4.4.

Table 4.4. Tight electron identification criteria as provided by the EGamma Physics Object Group (POG).

variable	$ \eta < 1.4446$	$ \eta \geq 1.566$
$\sigma_{i\eta}\sigma_{i\eta}$	< 0.00998	0.0394
$ d\eta $	< 0.00308	0.0292
$ d\phi $	< 0.0816	0.00605
H/E	< 0.0414	0.0641
$ \frac{1}{E} - \frac{1}{p} $	< 0.0129	0.0129
missing hits	≤ 1	≤ 1
$ d_0 $	< 1.	< 1.
conversion rejection	true	true
$Iso_{\text{PF}}/p_{\text{T}}$ (EA corrected)	< 0.0588	< 0.0571

The electrons are also required to pass a tight isolation criteria. The isolation variable is constructed by summing the energy of charged and neutral particle flow objects within a cone of radius $\Delta R = 0.4$ about the electron candidate and subtracting off the contribution from pileup. The combined particle flow isolation with the pileup correction is,

$$Iso_{\text{comb}} = Iso_{\text{ch.had.}} + \max(0, Iso_{\text{neu.had.}} + Iso_{\gamma} - \rho A_{\text{eff}}(|\eta_e|)) ,$$

The pileup correction is dependent on the parameter ρ which correlates with the average energy due to pileup, and the effective area which changes depending on the $|\eta|$ value of the electron.

4.2.1.4. Hadronic Tau. Hadronically decaying tau leptons are reconstructed using the hadron-plus-strips algorithm [139]. This algorithm constructs candidates seeded by a PF jet that are consistent with either a single or triple charged pion decay of the tau lepton. In the single charged pion decay mode, the presence of neutral pions is detected by reconstructing their photonic decays. The details of the hadronic tau identification is described in Section 3.4.6.

Reconstructed hadronic taus are required to have $p_T > 20 \text{ GeV}$ and $|\eta| < 2.3$ unless noted otherwise. If the hadronic tau candidate is found to overlap ($\Delta R < 0.3$) with either an electron or muon passing the analysis selections listed above, the tau candidate is rejected. To reduce fakes from electrons and muons that do not pass the analysis selections listed above, MVA discriminators are applied, which requires VTight electron rejection working point and Tight muon rejection working point. Jets originating from non-tau decays are rejected with a MVA discriminator that takes into account the pileup contribution to the neutral component of the tau decay [140]. It is observed that the counting analysis is more sensitive to contamination from by hadronic jets. So while the tight working point is used in the shape analysis, the very tight working point is used for the counting analysis.

4.2.1.5. Jet. Jets are reconstructed from particle-flow (PF) candidates [141]. PF candidates combine information from all of the detector subsystems to facilitate the reconstruction and identification of individual particles. These PF candidates are clustered using the anti- k_T algorithm [142] with a cone size of $\Delta R = 0.4$. Once reconstructed, a number of

corrections are applied to the jets to correct for pileup contamination, differing absolute response in jet p_T , and relative response in η [143]. To reduce contamination from photons and prompt leptons, several ID requirements are placed on the jets and are listed in Table 4.5.

Table 4.5. Jet ID requirements for 2016.

	$ \eta < 2.4$	$2.4 < \eta \leq 3.0$	$3.0 < \eta \leq 4.7$
number of constituents	> 1	> 1	–
neutral hadronic fraction	< 0.99	< 0.99	–
neutral EM fraction	< 0.99	< 0.99	< 0.9
charged hadronic fraction	> 0	–	–
charged EM fraction	< 0.99	–	–
number of charged constituents	> 0	–	–
number of neutrals	–	–	> 10

In addition to the above requirements, it is required that all jets have $p_T > 30\text{ GeV}$ and $|\eta| < 4.7$. Jets are vetoed if they overlap with a muon, electron, or tau passing the identification requirements described above within a cone size of $\Delta R = 0.3$.

4.2.1.6. b Tag. The identification of jets originating from the decay of b quarks is done using the CSV b tagging algorithm [144] is used to optimize the efficiency for identifying b jets while reducing the misidentification from jets originating from light quarks. Details of the b tagging algorithms are described in Section 3.4.5. In this analysis, the recommended medium working point ($\text{CSV} > 0.8484$) supplied by the b tag POG is used.

4.2.1.7. Summary. Table 4.6 gives a summary of the selection of physics objects, including electrons, muons, taus, jets and b tags. The corrections and calibrations of the physics objects are described in Section 4.3.2.

Table 4.6. Summary of object selection. For τ_h , sh ape (counting) analysis uses Tight (VTight) working points of τ_h isolation MVA.

	kinematic space	reconstruction quality	overlapping veto
e	$p_T > 20 \text{ GeV}, \eta < 2.5$	Tight identification Tight isolation	
μ	$p_T > 10 \text{ GeV}, \eta < 2.4$	Tight identification Tight isolation	
τ_h	$p_T > 20 \text{ GeV}, \eta < 2.3$	Decay mode matching (V)Tight isolation Tight μ rejection VTight e rejection	$\Delta R(\tau_h, e/\mu) > 0.3$
jet b tag	$p_T > 30 \text{ GeV}, \eta < 2.5$	Loose identification Medium CSV for b tag	$\Delta R(j, e/\mu/\tau_h) > 0.4$

4.2.2. Event Selection

The event selection begins by requiring an event pass the lowest p_T threshold single electron or muon trigger that is not prescaled. From these datasets it is possible to select events based on the number of WW-like final states originating from $t\bar{t}$ and tW production. These final states are constructed based on the number of reconstructed leptons, jet multiplicity, and b tag multiplicity. The categorization of these events differs between the counting and shape analysis. The common definition of the categories are listed in Table 4.7. There are eight channels defined by the multiplicities of leptons:

- ee, $e\mu$, $e\tau_h$, eh channels based on single electron trigger;
- μe , $\mu\mu$, $\mu\tau_h$, μh channels based on the single muon trigger.

In addition, n_j and n_b requirements are applied to further partition these eight channels, which are illustrated in Table 4.8. These selections are designed primarily to target $t\bar{t}$ production and specific W decay modes. The final states will tend to contain only events

Table 4.7. Baseline categorization of events based on the triggering electron or muon, the presence of isolated reconstructed charged leptons.

trigger	label	N_e	N_μ	N_τ	p_T	other
e	ee	2	0	0	$p_T^{e(e)} > 30(20) \text{ GeV}$	$ m_{ee} - m_Z > 15 \text{ GeV}$
	e μ	1	1	0	$p_T^{e(\mu)} > 30(10) \text{ GeV}$	OS
	e τ_h	1	0	1	$p_T^{e(\tau_h)} > 30(20) \text{ GeV}$	OS
	eh	1	0	0	$p_T^e > 30 \text{ GeV}$	
μ	μe	1	1	0	$p_T^{\mu(e)} > 25(20) \text{ GeV}$	OS
	$\mu\mu$	0	2	0	$p_T^{\mu(\mu)} > 25(10) \text{ GeV}$	$ m_{\mu\mu} - m_Z > 15 \text{ GeV}$
	$\mu\tau_h$	0	1	1	$p_T^{\mu(\tau_h)} > 25(20) \text{ GeV}$	OS
	μh	0	1	0	$p_T^\mu > 25 \text{ GeV}$	

from a single datastream except for the $e\mu$ selection which has non-negligible overlap between the electron and muon datastreams. Any overlap in events between the two datastreams are removed by only taking the events from single muon datastream. The shape analysis merges $e\mu$ and μe channel, while the counting analysis keeps the two separated, requiring additionally $p_T^e > (<)p_T^\mu$ in $e\mu$ (μe) if an event satisfies both channel.

The additional subdivisions of the dataset in the shape analysis are illustrated as yellow cells and lines in Table 4.8. These lower jet multiplicity and lower b tag multiplicity regions function as control regions to constrain systematic uncertainties, thus takes some special event selection requirement than Table 4.7. As described in the list above, the ee and $\mu\mu$ categories have a Z veto applied in the case that there are one or more b tags; this requirement is not applied in the zero b tag case. There is also a set of requirements to enhance the proportion of Drell-Yan in the $e\tau_h$ and $\mu\tau_h$ categories in the case that the number of jets is zero or one and there are no b tags. The requirements are designed to

Table 4.8. Categorization of the events with electron, muon, and/or tau leptons passing the reconstruction criteria, based on their jet and b-tagged jet multiplicities. The yellow cells are the regions Incorporated in the shape analysis only. Also shape analysis splits $n_j = 2$ and $n_j \geq 3$ regions for $e\tau_h$ and $\mu\tau_h$ channels, shown as the yellow lines.

	$N_j = 0$	$N_j = 1$	$N_j = 2$	$N_j = 3$	$N_j \geq 4$
$N_b = 0$	$e\tau_h, \mu\tau_h,$ $e\mu$	$e\tau_h, \mu\tau_h,$ $e\mu$	$e\tau_h, \mu\tau_h$	$ee, \mu\mu, e\mu$	
$N_b = 1$		$e\tau_h, \mu\tau_h, e\mu$	$e\tau_h, \mu\tau_h$	$e\tau_h, \mu\tau_h$	
$N_b \geq 2$			$e\tau_h, \mu\tau_h$	$e\tau_h, \mu\tau_h$	$eh, \mu h$

reduce the W+jets contribution and are:

$$40 \text{ GeV} \leq m_{\ell\tau_h} \leq 100 \text{ GeV}, \quad \Delta\phi(\ell, \tau_h) > 2.5, \quad m_T^{\ell, MET} < 60 \text{ GeV},$$

where $m_T^{\ell, MET}$ is the transverse mass of the electron or muon,

$$m_T^{\ell, MET} = \sqrt{2p_T^\ell E_T^{\text{miss}}(1 - \cos \Delta\phi(p_T^\ell, E_T^{\text{miss}}))}. \quad (4.1)$$

4.2.2.1. Yields and Kinematics Distributions. For the shape analysis, the yields are shown in Tables 4.10 and 4.11. The kinematics distributions are included in Appendix ???. For counting analysis, the yields are shown in Table 4.12. The kinematics distributions are included in Appendix ???.

4.2.2.2. Leptons from Boson Decays and Tau Decays. Because the tau can decay to an electron, muon, or hadronically, each of these channels has some mixing between terms arising from $W \rightarrow \ell$ decays and $W \rightarrow \tau \rightarrow \ell$ decays. The mixing between the

selected final states and the underlying W boson decays are shown in Table 4.9. These numbers are estimated from simulated $t\bar{t}$ events and are consequently dependent on the values of branching fractions used in the simulation. The expected proportions of $W \rightarrow \ell$ decays and $W \rightarrow \tau \rightarrow \ell$ decay in the selected sample can be studied by calculating the signal-over-background ratio. For $\mu\mu$ channel, the distributions of the tailing muon p_T and impact parameter are shown in Figure 4.1. In the lower plots in Figure 4.1, the ratios between $t\bar{t}/tW \rightarrow \mu\tau \rightarrow \mu\mu$ and other simulations are shown as orange dots, while the ratios between $t\bar{t}/tW \rightarrow \mu\mu$ and other simulations are shown as blue dots. The ratios are calculated as function of the tailing muon p_T and impact parameter, shown on the left and right, respectively. Both the variables show significant discrimination of prompt muons directly from W decays against non-prompt muons from tau decays.

4.2.2.3. Trigger Status of Dilepton Events. In dilepton channels ee, $\mu\mu$, e μ , μ e, at least one of leading and trailing lepton is required to pass the single lepton trigger. It is possible that in some events, it is only the trailing lepton that fires the single lepton trigger, while the leading lepton does not. In such scenario, the modeling of trigger efficiencies has a more direct impact to the kinematics of the trailing lepton, which used for the shape analysis. To understand the contribution of such scenario in the selected dataset, a trigger test study is conducted to calculate the proportions of events with both leptons firing, only leading lepton firing, and only trailing lepton firing. Figure 4.2 shows the proportions as function of the trailing lepton p_T in the $\mu\mu$, ee, μ e, e μ channel. This is done by matching the leading and trailing lepton to the save triggering objects of single muon or electron HLT. The green lines and areas represent the data and simulation respectively of only trailing lepton firing the trigger, which have small contributions and good data-simulation agreements in ee, $\mu\mu$ channel.

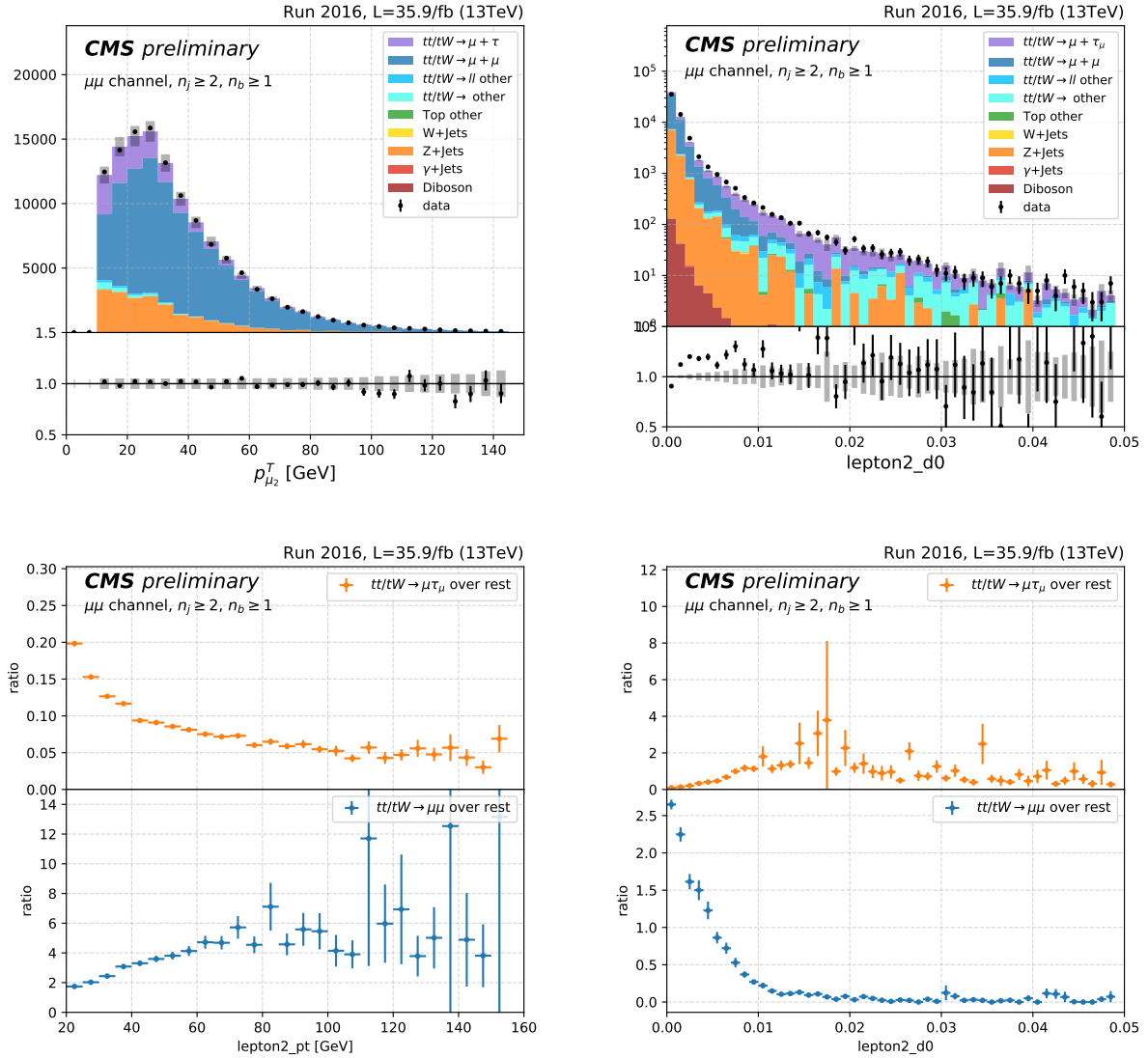


Figure 4.1. The distributions of the tailing muon p_T (*upper left*) and impact parameter (*upper right*). The ratios between $t\bar{t}/tW \rightarrow \mu\tau \rightarrow \mu\mu$ and other simulations are shown as orange dots, while the ratios between $t\bar{t}/tW \rightarrow \mu\mu$ and other simulations are shown as blue dots, as function of the tailing muon p_T (*lower left*) and impact parameter (*lower right*).

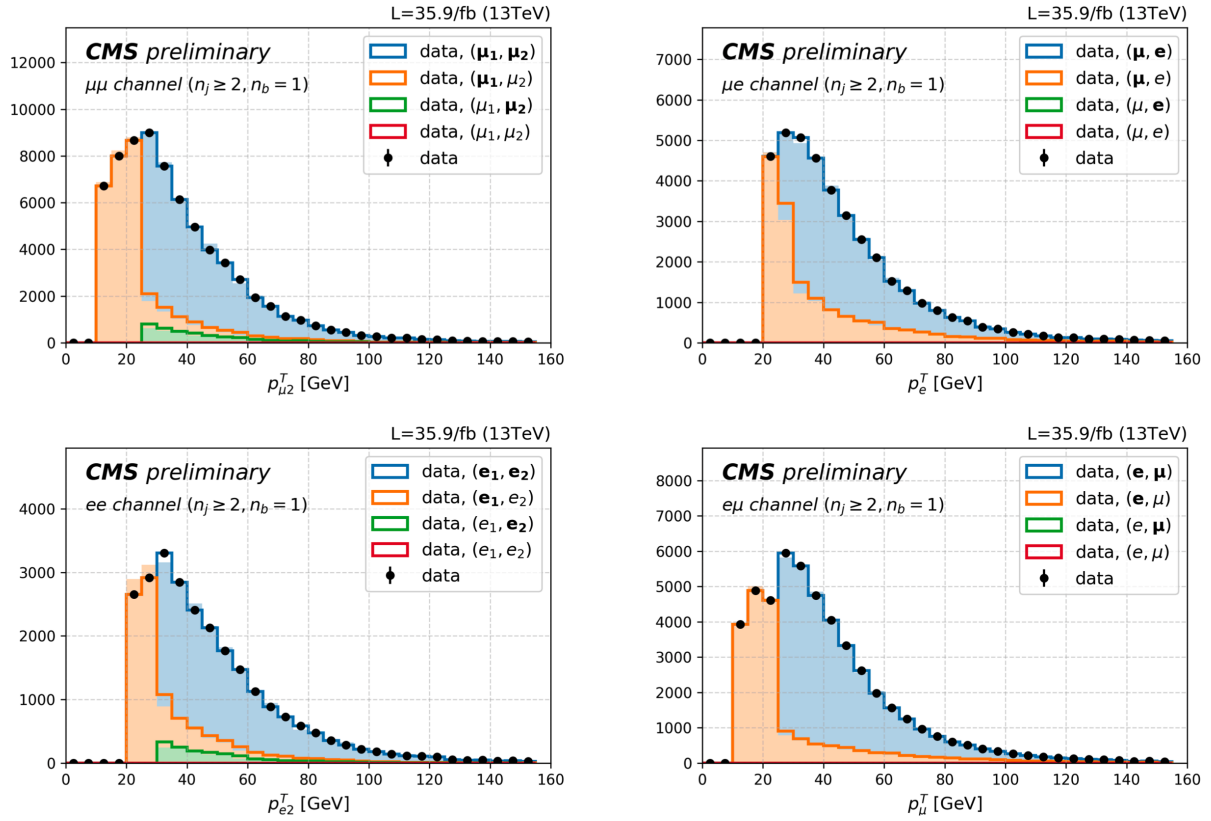


Figure 4.2. trailing lepton p_T in the $\mu\mu, ee, \mu e, e\mu$ channel. Data and MC events channel are split based on the trigger test of leading and trailing lepton: blue for both leptons firing trigger, orange for only leading lepton firing trigger, green for only trailing lepton firing trigger, red for neither leptons firing trigger. The lines are for data and the filled areas are for simulation.

Table 4.9. Composition of accepted $t\bar{t}$ and tW events, breakdown by 21 WW decay modes. Values are in percent.

Table 4.10. Estimates of the yields for various processes in the ee, $\mu\mu$, $e\mu$ and eh, μh final states broken down by the number of b tags. The estimate of the expected yield is compared to the yield observed from data. Uncertainties are statistical plus variation from luminosity and normalization uncertainties.

	QCD	Diboson (non-WW)	WW	Z	W	tW	t <bar>t</bar>	Expected	Observed
<i>ee</i>									
$N_j \geq 2, N_b = 0$	—	1014.2 ± 104.7	804.9 ± 46.8	55026.7 ± 5713.1	175.2 ± 25.0	854.4 ± 58.0	10865.1 ± 609.1	68740.4 ± 5747.0	68657
$N_j \geq 2, N_b = 1$	—	119.6 ± 12.4	51.2 ± 4.3	5207.9 ± 579.0	10.1 ± 4.8	1415.3 ± 89.8	24815.2 ± 1388.9	31619.1 ± 1507.5	30332
$N_j \geq 2, N_b \geq 2$	—	17.2 ± 1.8	3.3 ± 0.8	504.9 ± 86.2	5.2 ± 3.7	384.5 ± 30.8	14121.1 ± 791.1	15036.2 ± 796.4	14646
<i>$\mu\mu$</i>									
$N_j \geq 2, N_b = 0$	—	2628.2 ± 271.0	1944.1 ± 110.6	194725.6 ± 20123.0	455.9 ± 43.1	2081.2 ± 127.6	28399.5 ± 1589.3	230234.5 ± 20188.2	238485
$N_j \geq 2, N_b = 1$	—	324.9 ± 33.6	128.4 ± 8.9	19150.5 ± 2023.9	80.0 ± 16.4	3469.2 ± 205.5	64582.6 ± 3612.0	87735.6 ± 4145.7	86354
$N_j \geq 2, N_b \geq 2$	—	48.3 ± 5.0	5.8 ± 1.1	2028.9 ± 253.5	5.3 ± 3.8	976.6 ± 65.4	36916.5 ± 2065.4	39981.3 ± 2082.0	40011
<i>eμ</i>									
$N_j = 0, N_b = 0$	4264.9 ± 285.7	748.9 ± 77.6	17566.8 ± 983.8	49838.9 ± 5152.2	3713.1 ± 262.4	3305.7 ± 196.0	9606.0 ± 538.7	89044.3 ± 5291.3	90784
$N_j = 1, N_b = 0$	1907.5 ± 164.2	774.1 ± 80.2	7384.9 ± 414.6	13584.5 ± 1424.6	1700.9 ± 131.7	5413.8 ± 313.9	25755.0 ± 1441.5	56520.8 ± 2104.4	55427
$N_j = 1, N_b = 1$	279.7 ± 42.4	21.2 ± 2.5	173.9 ± 11.4	712.9 ± 98.8	95.5 ± 18.5	6330.4 ± 365.2	32341.1 ± 1809.6	39954.7 ± 1849.4	39021
$N_j \geq 2, N_b = 0$	737.0 ± 95.6	582.4 ± 60.4	2780.4 ± 157.3	5280.2 ± 574.9	710.3 ± 60.7	3117.8 ± 185.5	40246.2 ± 2251.5	53454.4 ± 2340.0	50301
$N_j \geq 2, N_b = 1$	403.7 ± 60.4	47.0 ± 5.2	185.6 ± 12.1	605.3 ± 89.0	64.9 ± 13.2	5127.5 ± 298.0	91534.6 ± 5118.7	97968.5 ± 5128.5	93440
$N_j \geq 2, N_b \geq 2$	203.0 ± 29.2	4.2 ± 0.6	13.1 ± 1.8	61.8 ± 23.9	14.7 ± 6.1	1510.7 ± 95.4	52409.1 ± 2931.1	54209.1 ± 2932.9	53859
<i>e + jets</i>									
$N_j \geq 2, N_b = 1$	13189.3 ± 740.4	578.8 ± 59.7	65.2 ± 5.2	13637.7 ± 1442.7	46769.4 ± 2037.7	17675.4 ± 999.7	37195.7 ± 20794.5	463867.6 ± 21047.6	468922
$N_j \geq 2, N_b \geq 2$	4665.8 ± 263.9	104.4 ± 10.8	7.1 ± 1.3	2367.0 ± 279.5	6359.5 ± 378.1	7591.6 ± 435.9	256643.9 ± 14348.6	277739.3 ± 14365.3	276116
<i>$\mu + \text{jets}$</i>									
$N_j \geq 2, N_b = 1$	42676.6 ± 2389.3	458.4 ± 47.3	90.1 ± 6.7	10504.3 ± 1123.2	71625.7 ± 4028.2	26161.6 ± 1474.4	572088.3 ± 31982.5	723605.0 ± 32376.7	710650
$N_j \geq 2, N_b \geq 2$	13244.3 ± 743.9	82.9 ± 8.6	9.0 ± 1.5	1738.4 ± 219.6	9522.0 ± 555.9	11251.4 ± 640.8	397617.9 ± 22229.3	433465.8 ± 22259.0	429861

Table 4.11. Estimates of the yields for various processes in the $e\tau_h$ and μh categories broken down by the number of b tags. The estimate of the expected yield is compared to the yield observed from data. Uncertainties are statistical only.

	QCD	Diboson (non-WW)	WW	Z	W	tW	t <bar>t</bar>	Expected	Observed
$e\tau$									
$N_j = 0, N_b = 0$	14609.7 ± 843.7	11.7 ± 1.4	102.2 ± 7.2	30670.4 ± 3175.9	9505.8 ± 594.4	11.1 ± 3.7	29.7 ± 2.8	54940.5 ± 3339.4	55591
$N_j = 1, N_b = 0$	1512.7 ± 125.2	10.0 ± 1.2	20.9 ± 2.3	3237.1 ± 355.2	1159.9 ± 98.0	20.8 ± 5.2	76.3 ± 5.7	6037.5 ± 389.2	6074
$N_j \geq 2, N_b = 0$	5519.7 ± 363.2	233.6 ± 24.3	269.8 ± 16.8	6721.8 ± 724.1	6906.0 ± 410.6	551.2 ± 40.4	5933.6 ± 333.3	26135.7 ± 968.7	25788
$N_j = 1, N_b = 1$	789.5 ± 77.4	8.0 ± 1.0	16.4 ± 2.0	725.6 ± 99.6	650.5 ± 60.3	675.5 ± 47.6	3381.9 ± 190.7	6247.5 ± 241.2	6256
$N_j = 2, N_b = 1$	421.6 ± 59.9	11.7 ± 1.3	10.8 ± 1.6	424.7 ± 69.2	305.0 ± 33.4	538.3 ± 39.7	5994.7 ± 336.8	7706.7 ± 352.8	7388
$N_j \geq 3, N_b = 1$	315.4 ± 56.0	13.1 ± 1.5	5.0 ± 1.0	212.1 ± 42.9	169.3 ± 23.1	302.1 ± 25.7	6021.4 ± 338.2	7038.5 ± 347.2	6660
$N_j = 2, N_b \geq 2$	48.4 ± 16.4	1.1 ± 0.2	0.3 ± 0.2	18.8 ± 15.9	10.6 ± 5.8	83.4 ± 11.1	2606.9 ± 147.4	2769.5 ± 149.7	2683
$N_j \geq 3, N_b \geq 2$	81.3 ± 28.8	1.8 ± 0.3	0.3 ± 0.2	55.2 ± 14.0	18.0 ± 6.9	87.8 ± 11.5	3574.9 ± 201.5	3819.4 ± 204.5	3704
$\mu\tau$									
$N_j = 0, N_b = 0$	19581.5 ± 1133.6	27.6 ± 3.1	244.6 ± 15.3	103926.9 ± 10727.5	20342.3 ± 1205.2	19.3 ± 5.0	66.2 ± 5.1	144208.5 ± 10854.4	146128
$N_j = 1, N_b = 0$	2255.6 ± 167.9	24.0 ± 2.6	37.0 ± 3.4	8216.3 ± 868.5	2470.3 ± 177.3	33.8 ± 6.8	162.4 ± 10.6	13199.4 ± 902.2	13293
$N_j \geq 2, N_b = 0$	5467.2 ± 372.9	313.5 ± 32.5	413.2 ± 24.9	10752.1 ± 1139.7	10989.1 ± 640.3	879.2 ± 59.4	9261.1 ± 519.4	38075.4 ± 1457.1	38184
$N_j = 1, N_b = 1$	1452.3 ± 113.6	12.3 ± 1.4	27.8 ± 2.8	1632.3 ± 193.8	1199.1 ± 96.4	1112.9 ± 72.6	5266.7 ± 296.1	10703.3 ± 390.8	10628
$N_j = 2, N_b = 1$	709.7 ± 75.4	17.6 ± 1.9	18.1 ± 2.1	708.4 ± 101.7	568.1 ± 50.5	769.3 ± 53.1	9493.5 ± 532.4	12284.6 ± 552.1	12048
$N_j \geq 3, N_b = 1$	438.5 ± 70.7	19.5 ± 2.1	9.7 ± 1.5	384.5 ± 62.6	292.9 ± 32.0	480.7 ± 36.5	9413.5 ± 527.9	11039.3 ± 538.5	10314
$N_j = 2, N_b \geq 2$	111.1 ± 19.9	1.7 ± 0.2	1.0 ± 0.4	58.6 ± 23.6	56.0 ± 16.9	153.8 ± 16.5	4157.7 ± 234.1	4539.9 ± 237.3	4321
$N_j \geq 3, N_b \geq 2$	117.5 ± 35.6	3.0 ± 0.4	1.4 ± 0.5	79.4 ± 22.2	18.1 ± 6.9	157.9 ± 16.7	5599.2 ± 314.7	5976.5 ± 318.0	5705

Table 4.12. Estimates of the yields. The estimate of the expected yield is compared to the yield observed from data. Uncertainties are statistical only.

		QCD	VV	γ	Z	W	t	tW	tt	total	data
$\mu e, n_b = 1$	- $\pm -$	90.3 \pm 4.2	0.9 \pm 0.9	202.7 \pm 37.6	13.4 \pm 5.1	9.5 \pm 2.6	2107.6 \pm 53.1	38871.4 \pm 87.5	41295.8 \pm 109.2	41047.0 \pm 202.6	
$\mu e, n_b \geq 2$	- $\pm -$	5.9 \pm 1.0	- $\pm -$	- $\pm -$	3.1 \pm 2.2	2.3 \pm 1.6	625.7 \pm 28.9	22647.7 \pm 66.8	23270.9 \pm 74.1	23918.0 \pm 154.7	
$\mu\mu, n_b = 1$	- $\pm -$	370.4 \pm 5.8	4.1 \pm 1.8	18046.9 \pm 455.4	52.4 \pm 11.7	55.8 \pm 6.7	3406.2 \pm 68.8	62266.6 \pm 112.4	84202.3 \pm 474.3	84284.0 \pm 290.3	
$\mu\mu, n_b \geq 2$	- $\pm -$	45.8 \pm 1.5	0.0 \pm 0.0	1945.7 \pm 142.0	3.6 \pm 2.6	3.9 \pm 1.8	959.3 \pm 36.2	35685.2 \pm 85.1	38643.4 \pm 169.6	39253.0 \pm 198.1	
$\mu\tau, n_b = 1$	1130.7 \pm 108.8	52.3 \pm 2.6	11.8 \pm 3.2	866.7 \pm 78.7	730.8 \pm 42.9	182.6 \pm 12.4	1291.0 \pm 41.9	18430.0 \pm 60.6	22695.9 \pm 159.6	21621.0 \pm 147.0	
$\mu\tau, n_b \geq 2$	346.6 \pm 51.5	5.5 \pm 0.7	0.9 \pm 0.8	103.6 \pm 29.6	56.9 \pm 14.4	36.8 \pm 5.6	322.6 \pm 21.0	9647.6 \pm 43.7	10520.4 \pm 78.3	9934.0 \pm 99.7	
$\mu + \text{jets}, n_b = 1$	24300.4 \pm 3404.9	371.0 \pm 5.2	1501.2 \pm 67.5	7533.2 \pm 265.9	49248.1 \pm 327.3	8484.6 \pm 85.3	24447.8 \pm 187.0	514064.6 \pm 327.2	629950.9 \pm 345.3	630704.0 \pm 794.2	
$\mu + \text{jets}, n_b \geq 2$	4650.7 \pm 1399.5	61.4 \pm 2.0	248.3 \pm 31.8	1331.9 \pm 114.0	6524.2 \pm 118.8	5172.2 \pm 66.7	10335.6 \pm 121.4	356185.1 \pm 272.2	384509.5 \pm 1442.2	385397.0 \pm 620.8	
$ee, n_b = 1$	- $\pm -$	138.2 \pm 3.6	2.8 \pm 1.2	4726.5 \pm 215.7	5.4 \pm 2.8	1.1 \pm 0.8	1382.0 \pm 42.7	23447.3 \pm 66.9	29703.3 \pm 229.9	29491.0 \pm 171.7	
$ee, n_b \geq 2$	- $\pm -$	16.2 \pm 0.9	0.1 \pm 0.1	500.5 \pm 67.8	3.7 \pm 2.6	2.1 \pm 1.2	371.4 \pm 22.1	13412.7 \pm 50.7	14306.6 \pm 87.5	14334.0 \pm 119.7	
$e\mu, n_b = 1$	- $\pm -$	127.2 \pm 4.9	25.5 \pm 13.2	411.9 \pm 52.7	32.8 \pm 7.2	37.6 \pm 5.4	2917.6 \pm 62.7	49878.6 \pm 99.2	53431.1 \pm 129.8	52362.0 \pm 228.8	
$e\mu, n_b \geq 2$	- $\pm -$	9.0 \pm 1.3	1.9 \pm 1.1	59.0 \pm 19.5	6.5 \pm 3.2	6.1 \pm 2.2	837.9 \pm 33.8	28374.1 \pm 74.9	29294.5 \pm 84.6	29860.0 \pm 172.8	
$e\tau, n_b = 1$	874.2 \pm 90.3	38.0 \pm 2.1	194.5 \pm 38.8	677.8 \pm 69.3	456.3 \pm 32.9	125.3 \pm 10.0	908.2 \pm 34.6	12884.7 \pm 49.7	16159.1 \pm 139.0	15309.0 \pm 123.7	
$e\tau, n_b \geq 2$	94.2 \pm 46.3	3.0 \pm 0.4	10.0 \pm 2.9	53.4 \pm 21.3	28.7 \pm 8.5	43.4 \pm 6.0	196.1 \pm 15.9	6682.4 \pm 35.8	7111.3 \pm 65.1	7006.0 \pm 83.7	
$e + \text{jets}, n_b = 1$	25625.1 \pm 29411.3	494.9 \pm 5.1	12035.7 \pm 173.0	13119.8 \pm 323.2	34481.3 \pm 266.1	5786.3 \pm 68.8	17454.7 \pm 154.8	360917.6 \pm 268.5	469915.4 \pm 2992.9	464543.0 \pm 681.6	
$e + \text{jets}, n_b \geq 2$	3327.4 \pm 1476.4	84.5 \pm 2.0	2095.3 \pm 78.4	2520.8 \pm 138.5	4696.3 \pm 98.0	3524.2 \pm 53.7	7616.3 \pm 102.3	249557.0 \pm 223.4	273421.8 \pm 1509.3	274162.0 \pm 523.6	

4.3. Calibrations and Corrections

4.3.1. Generator-Level Reweighting

4.3.1.1. Pile-up Reweighting. Differences between the pileup distribution used in simulation and data is corrected by reweighting the simulation according to the weights shown in Figure 4.3. The weights are calculated based on the distribution of the number of pileup (nPU), including out-of-time pileup, per event in the data and simulation, where the data is specially collected with least possible selection, so-called Minimum Bias Dataset (MinBias), and the simulation is from Z+jets events without any selection. The nPU distributions in data and simulation are shown in Figure 4.3 top. The ratio between the data and simulation is shown in Figure 4.3 bottom. The uncertainties correspond to the uncertainty of the cross-section of MinBias dataset, estimated by about 4.6% relative uncertainty of the total inelastic cross-section.

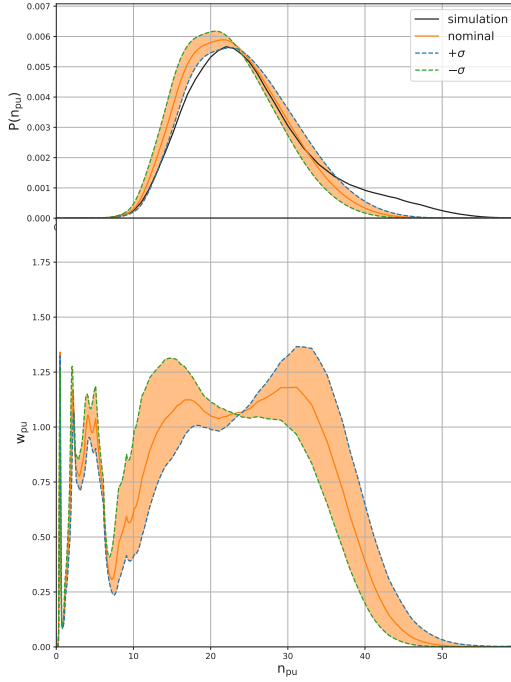


Figure 4.3. (*top*) Pileup distribution in data and simulation including the $\pm\sigma$ variation of the data pileup distributions. (*bottom*) The weights parameterized by number of simulated pileup resulting from taking the ratio of the pileup distribution in data and simulation.

4.3.1.2. Top p_T Reweighting. Additional corrections can be applied to the $t\bar{t}$ sample to account for generator level mismodeling of the top quark p_T spectrum [145, 146]. This is done by identifying the parton-level top quarks, and calculating a scale factor from the equation, $SF_t(p_T) = SF_{\bar{t}}(p_T) = e^{0.0615 - 0.0005p_T}$ [147]. The overall event weight is that is applied is $w = \sqrt{SF_t SF_{\bar{t}}}$. We do not apply the weight, but instead use it as the systematical uncertainties associated with the top p_T correction.

4.3.1.3. Z p_T Reweighting. Based on differences between the observed and predicted Z p_T spectrums, weights are derived to correct the p_T spectrum in simulation. The derivation

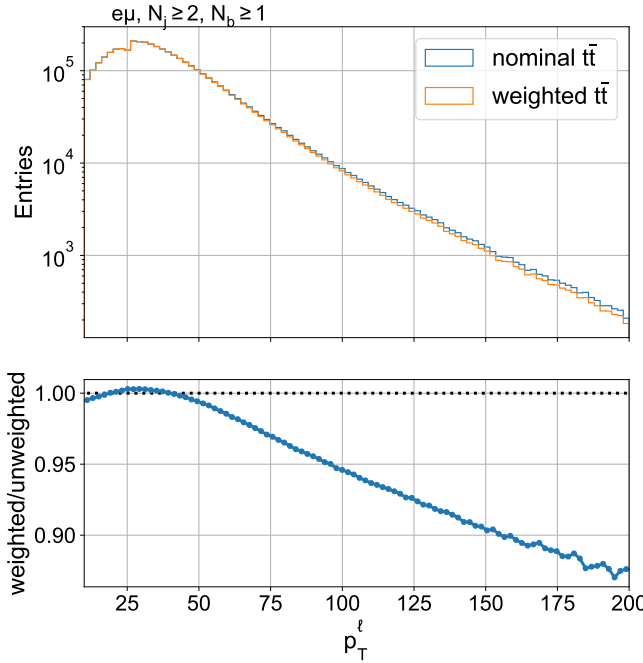


Figure 4.4. Comparison of the trailing lepton p_T distribution in $e\mu$ events with at least two jets and at least one b tag with top p_T weights applied and without the weights.

of the weights was done in the context of the $H \rightarrow WW$ analysis and is described in AN-2017-082. This correction does not have an associated uncertainty.

4.3.1.4. WW p_T Reweighting. Estimation of the WW process relies on the POWHEG MC generator which is a NLO fixed order generator. Higher order corrections are therefore not directly included, but have been calculated separately [148, 149, 150]. The estimation of uncertainty is based on the description in AN-2017-273. As mentioned there, the theoretical uncertainty associated with the corrections have not been provided so they are estimated by varying the renormalization, factorization, and the matching scale of the p_T resummation technique. The weights and their systematic variations, as well as the effect on the lepton p_T spectrum in the WW MC sample is shown in Figure 4.6.

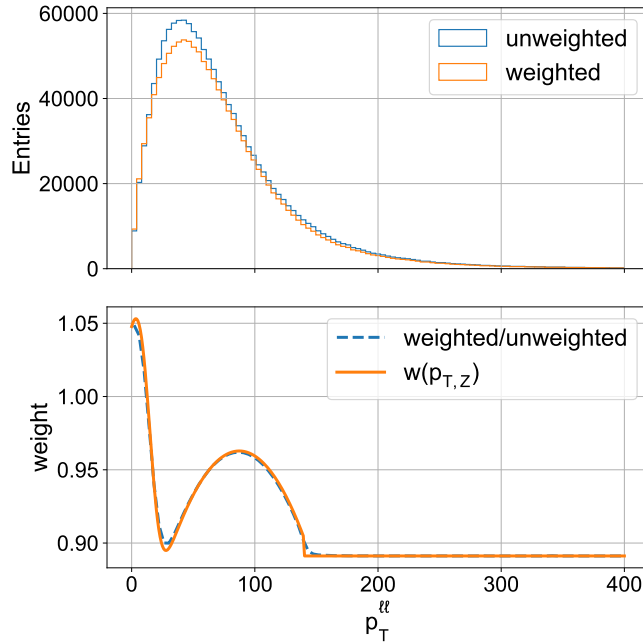


Figure 4.5. (top) Comparison of weighted and unweighted dilepton p_T spectrum for dimuon events with two jets and no b tags. (bottom) Comparison between ratio of distributions in the top distribution and the analytical function for generating weights.

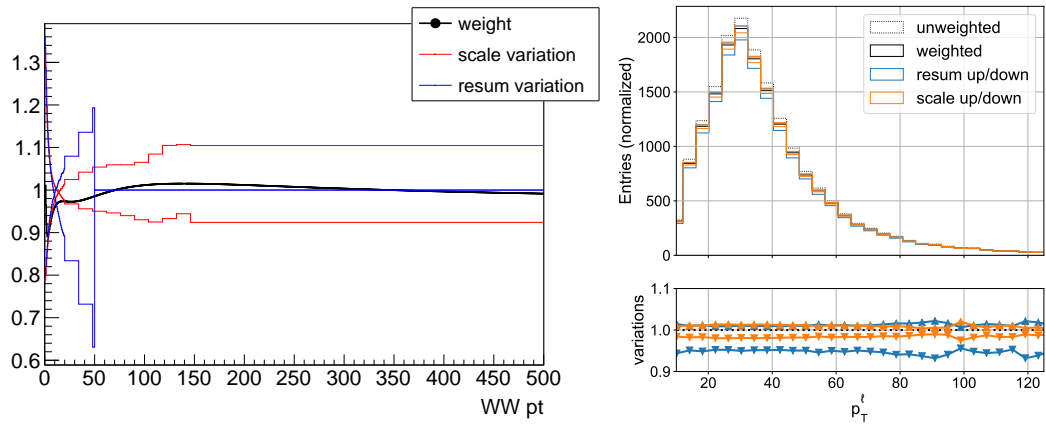


Figure 4.6. (left) Weights for the $qq \rightarrow WW$ process as a function of the $WW p_T$ and the two components of systematic variation. (right) Trailing lepton p_T from the $qq \rightarrow WW \rightarrow e\mu\nu\nu$ simulated sample when there are no reconstructed jets.

4.3.2. Corrections for Physics Objects

The some of the standard calibrations for the physics objects are provided by POGs and are applied to the selected objects in this analysis to account for potential mismodeling of the reconstruction and selection of physics objects in the simulation.

4.3.2.1. Muons. Muons in the simulation are corrected for the energy scale, identification, and isolation efficiencies.

4.3.2.2. Electrons. Electrons are corrected for the energy scale and resolution, reconstruction, and isolation efficiencies.

4.3.2.3. Hadronic Taus. The scale factor accounting for the difference of tau identification efficiencies in the simulation and data were measured in several control regions [140]. The measurement is carried out in both in two different control regions: one enriched in $Z \rightarrow \tau_\ell \tau_h$ production and one enriched in $t\bar{t}$. Because of the large overlap with our signal region in the case of the latter, the former measurement is used so that the datasets that are used are uncorrelated. For the selection algorithm and tight working point a scale factor of 0.95 ± 0.05 is used; for the very tight working point it is 0.92 ± 0.05 . The scale factors accounting for difference of tau energy in the simulation and data are measured by fitting to the sensitive variables. This energy correction is split into different τ_h decay modes. Two sensitive variables are considered. One is the visible mass m_{vis} of the $e\tau_h$ or $\mu\tau_h$ in the $Z \rightarrow \tau\tau$ region, the other is the visible mass of hadronic taus m_{τ_h} [140]. In this analysis, the energy scale factors measured with the former are applied to correct the simulation. The values of energy scale factors are

$$\tau \rightarrow h^\pm : 0.995(5), \quad \tau \rightarrow h^\pm \pi^0 : 1.011(3), \quad \tau \rightarrow h^\pm h^\mp h^\pm \pi^0 : 1.006(3)$$

Also corrections for $j \rightarrow \tau_h$ misidentification is applied, which is measured by us in a $j \rightarrow \tau_h$ fake-enriched region. More details about the measurement is presented in Section 4.3.4.

4.3.2.4. Jets and b tags. The measurement of jet energy in the detector has a small offset and spread comparing with the ground-truth of the original seeding gluons or quarks because of the noisy hadronic and pile-up environment and the nature of detector response. This effect is accounted for by the jet energy scale (JES) and jet energy resolution (JER).

To account for the difference in b tag efficiency in data and simulation, the b tag status of jets is modified based on a set of scale factors derived by the b tag POG. The method used for applying the b tag scale factors modifies the status of individual jets to either promote or demote their b tagging status [151]. The method relies on the user measuring the b tag efficiencies and mistag probabilities in the simulated samples. This is described further in Section 4.3.5.

4.3.3. Corrections for Trigger Efficiencies

4.3.3.1. Single Muon Trigger. The corrections of the single muon trigger efficiencies `HLT_IsoMu24` are applied as event weights calculated based on the presence of triggering muons in μe , $\mu\mu$, $\mu\tau_h$, μh channels. The scale factors are defined as the ratio between trigger efficiencies in the data over the efficiencies in the simulated dataset, and have a dependence on p_T and $|\eta|$. The Muon POG provides the scale factors for two separated periods, 2016 BCDEF and GH, shown in Figure 4.7.

4.3.3.2. Single Electron Trigger. The correctons of the single electron trigger efficiencies `HLT_Ele27_WPTight_Gsf` are applied as event weights calculated based on the presence of triggering electrons in ee , $e\mu$, $e\tau_h$, eh channels. The scale factors are defined as the ratio between trigger efficiencies in the data over the efficiencies in the simulated dataset, and have a dependence on p_T and $|\eta|$. The EGamma POG provides the scale factors, but the

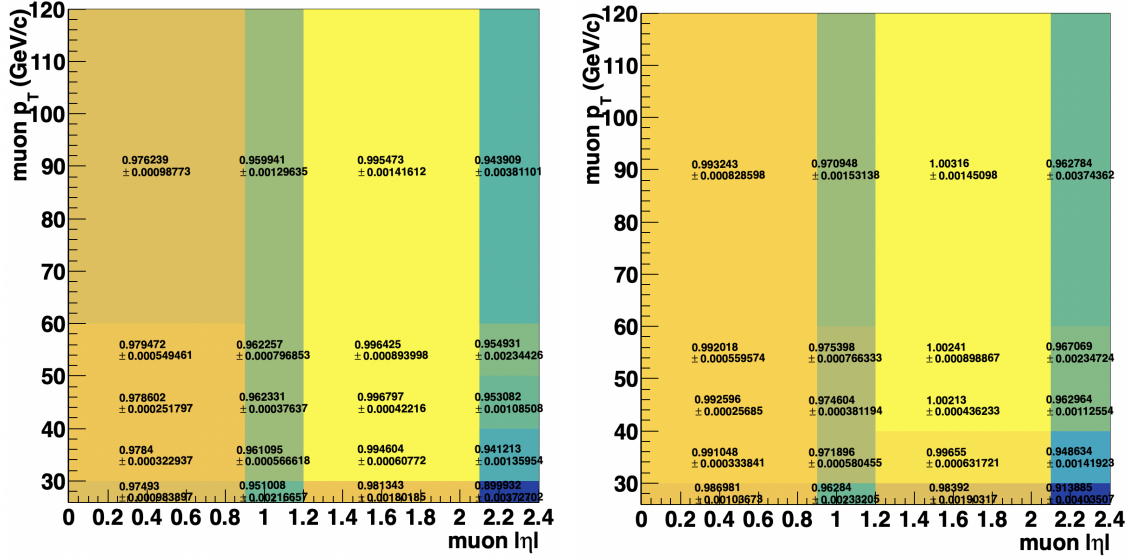


Figure 4.7. Scale factors for the single muon trigger efficiencies in run periods 2016 BCDEF (*left*) and GH (*right*). The uncertainties displayed are only statistical uncertainties.

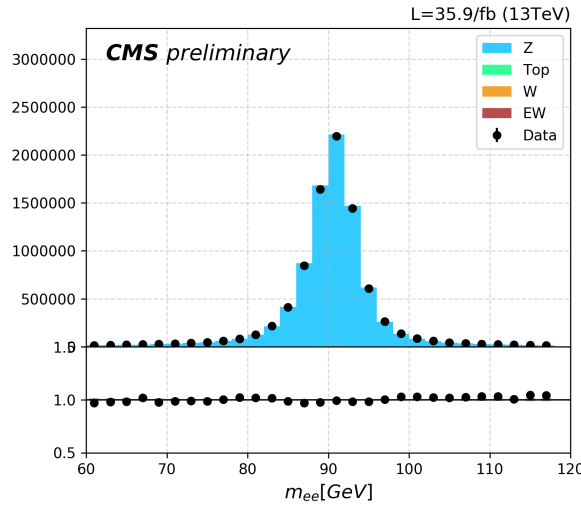


Figure 4.8. The m_{ee} distribution of the selected events for the measurement of the scale factors of single-electron trigger efficiencies.

uncertainties associated to the measurement are not included. In order to better account for the uncertainties of the scale factors, we have performed a dedicated measurement using the standard tag-and-prob approach recommended by the EGamma POG. In our SF

measurement, the dataset used is 2016 re-reco `SingleElectron` dataset with the golden certificate luminosity mask, while the simulations include `DYJETSToLL_M-10to50_amcatnlo`, `DYJETSToLL_M-50_amcatnlo` and `TT_powheg`, reweighted to pile-up $\sigma_{\text{mb}} = 69.2 \pm 2.3$ nb. The electrons are selected with tight identification and tight particle-flow isolation with $p_T > 20$ GeV and $|\eta| < 2.5$. Among selected electrons, tagged electrons are defined as $p_T > 30$ GeV and outside gap between barrel and endcap calorimeter $1.444 < |\eta| < 1.56$, and match with `HLT_Ele27_WPTight_Gsf` triggering objects. Events are selected by requiring exactly 2 opposite electrons with at least 1 tagged electron and $60 < m_{ee} < 120$ GeV. This event selection yields a sample of events significantly dominated by the Drell-Yan (DY) process. The distribution of m_{ee} is shown in Figure 4.8, where it can be seen that the purity of DY is very high in the selected ee events. Thus a signal-backgound fit is not necessary to obtain DY yields. In each event, if one electron is tagged, the other consequently become a probe. Each event provides either one or two tag-probe pairs. A probe is passing if it matches with `HLT_Ele27_WPTight_Gsf` triggering objects. The trigger efficiencies are calculated by the ratio between the number of passing probes over the total probes in $p_T - \eta$ bins,

$$\epsilon(p_T, \eta) = \frac{N_{\text{passing}}(p_T, \eta)}{N_{\text{total}}(p_T, \eta)}.$$

The scale factors are defined as the ratio between efficiencies in the data over efficiencies in the simulation,

$$SF(p_T, \eta) = \frac{\epsilon_{\text{Data}}(p_T, \eta)}{\epsilon_{\text{Simulation}}(p_T, \eta)}. \quad (4.2)$$

The measurement of the scale factors is divided for two run periods, 2016 BCDEF and GH. This is because in run 2016 BCDEF, the triggering efficiencies in the endcap suffers from a decrease of signal over noise ratio associated to the loss of tracking hits caused by problems in the pre-amplifier of the readout chips in the tracker's silicon microstrips. In mid August

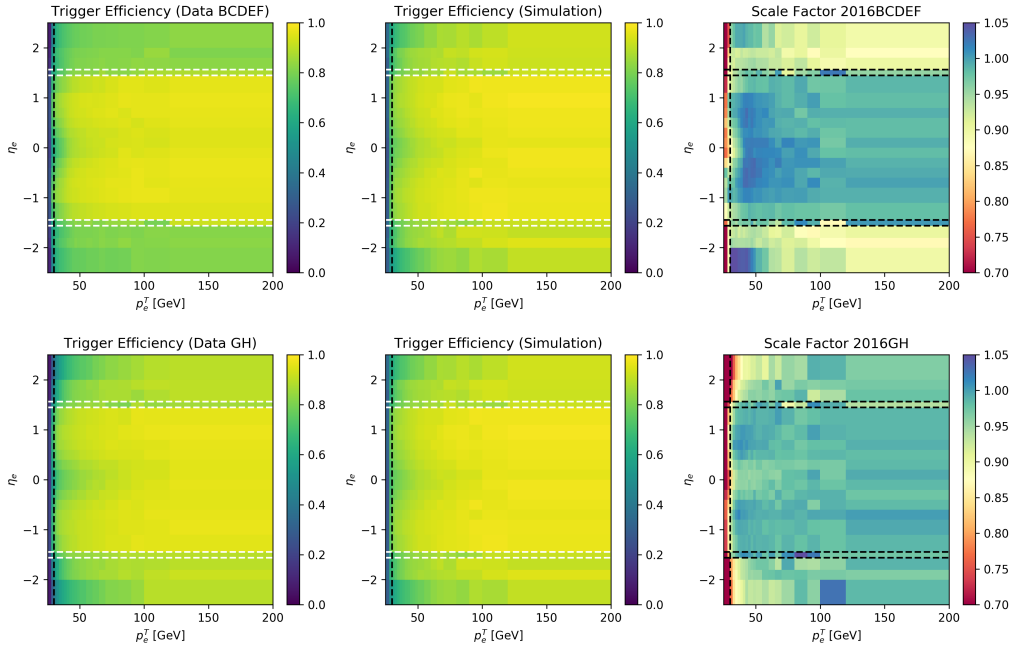


Figure 4.9. The 2D maps of ϵ_{data} , ϵ_{MC} and scale factors in run period 2016 BCDEF (*upper*) and 2016 GH (*lower*).

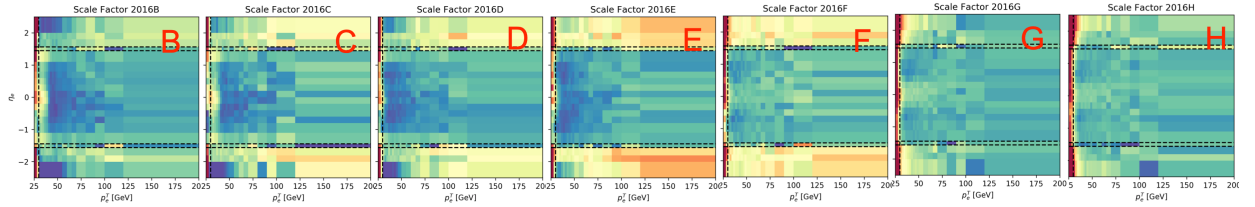


Figure 4.10. Scale factors in each 2016 data taking period.

2016, this problem of Si-strip in endcap region is fixed by increase the drain speed of the pre-amplifier. Thus the trigger efficiencies were improved in run 2016 GH. For the two run periods, Figure 4.9 shows the measured ϵ_{data} , ϵ_{MC} and SF . The SF for individual run periods are shown in Figure 4.10, where a clear improvement can be seen in period G with respective to period F. The systematical uncertainties of the scale factors are estimated by “two shifts” approach:

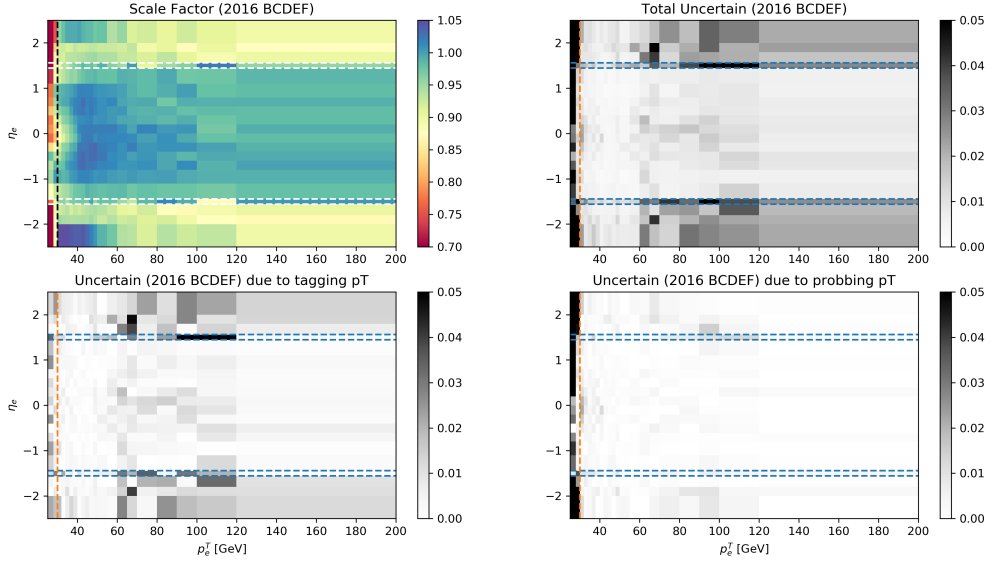


Figure 4.11. Scale factors and uncertainties in the 2016 BCDEF. Total uncertainties (*upper right*) combines the “two shifts” (*lower*) and statistical uncertainties.

- (1) shift up the p_T threshold for tagging electron by 10 GeV to simulate a different trigger. This estimates the systematical effect that some L1 seed could have a threshold of 32 GeV.
- (2) shift up and down the probing electron p_T by 0.5 GeV. This estimates the effect of the electron energy scale.

The systematical uncertainties are estimated by the ”two shifts” are shown in Figure 4.11 and 4.12.

4.3.3.3. Level-1 Trigger Prefiring in the Electromagnetic Calorimeter. In 2016, the gradual timing shift of ECAL was not properly propagated to L1 trigger primitives (TP) resulting in a significant fraction of high-eta L1 trigger primitives being mistakenly associated to the previous bunch crossing. Since Level-1 rules forbid two consecutive bunch crossings to fire, an unpleasant consequence of this (in addition to not finding the TP in the correct bunch crossing) is that events can self-veto if a significant amount of ECAL energy is found in

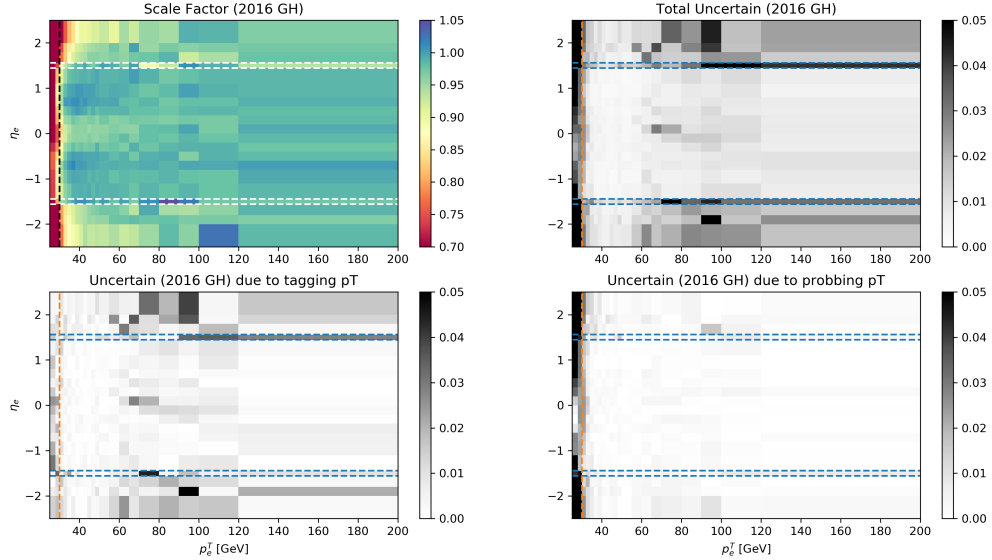


Figure 4.12. Scale factors and uncertainties in the 2016 GH. Total uncertainties (*upper right*) combines the “two shifts” (*lower*) and statistical uncertainties.

the region of $2.0 < |\eta| < 3.0$. This effect is not modeled by the simulations. Therefore scale factors are applied to reweight the events. The scale factors for ECAL prefire corrections is defined as

$$SF = \prod_{i=\gamma, jet} \left(1 - \epsilon_i(p_T, \eta) \right)$$

where $\epsilon_i(p_T, \eta)$ is the jet or photon prefire probability and the corresponding 2D maps are provided by the EGamma POG, shown in Figure 4.13. The prefire SF on average scales the simulated events down by about 1-2%.

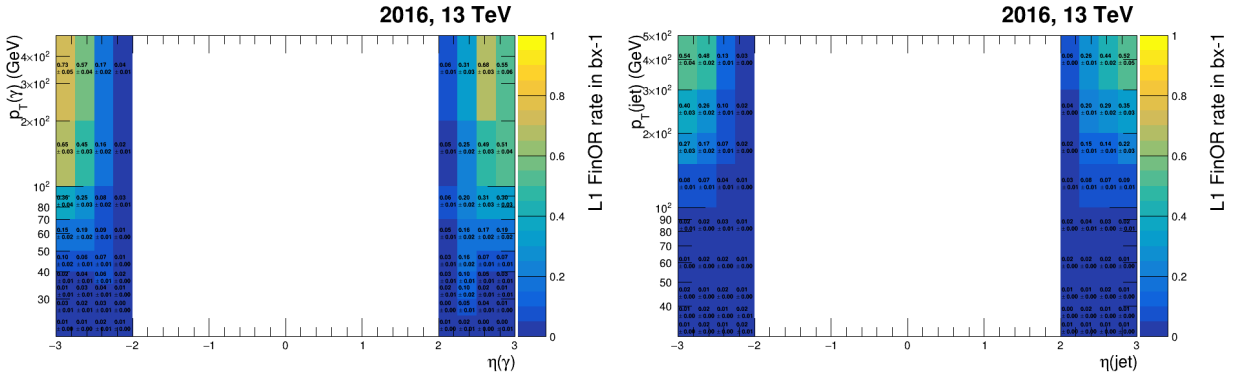


Figure 4.13. Prefiring probabilities $\epsilon_i(p_T, \eta)$ for photons (*left*) and jets (*right*).

4.3.4. Corrections for Jets Faking Hadronic Taus

To account for difference of the $j \rightarrow \tau_h$ faking probability in the data and simulation, scale factors are applied to simulated data based on the presence of $j \rightarrow \tau_h$ in the events. While the scale factors of τ_h identification is provided by the POG, the scale factors for the misidentification have to be measured by each analysis due to the potential different jet environments in different analysis. Here we present a measurement of $SF_{j \rightarrow \tau_h}$ using two side-band regions enriched with $j \rightarrow \tau_h$. The $SF_{j \rightarrow \tau_h}$ measurement is p_T and jet-favour dependent. Tight and VTight τ_h identification working points are considered. The two side-band regions are

- $t\bar{t}$ with $j \rightarrow \tau_h$ region: selected with $e\mu + \tau_h$ final state. The selection requires exactly one muon and one electron with tight identification and isolation, plus one hadronic tau passing Tight or VTight working point. Corrections to reconstruction and selection of electron and muon are applied. The events has to fire either single muon trigger or single electron trigger. The p_T threshold for triggering muon (electron) is 25 (30) GeV, while for non-triggering muon (electron) is 10 (20) GeV. This selects a sample enriched with $t\bar{t}$ with $b \rightarrow \tau_h$.

- Z+jets with $j \rightarrow \tau_h$ region: $\mu\mu + \tau_h$ and $ee + \tau_h$ final state are selected. The selection requires exactly two muons or two electrons with tight identification and isolation, plus one hadronic tau passing Tight or VTight working point. Corrections to reconstruction and selection of electron and muon are applied. The trigger and p_T thresholds of leptons are the same as $e\mu + \tau_h$ final state. This selects a sample enriched with Z+jets with a light jet misidentified as τ_h .

Note that the $e\mu + \tau_h$, $\mu\mu + \tau_h$, $ee + \tau_h$ channels are developed based on the $e\mu$, $\mu\mu$, ee channels in the $\mathcal{B}(W \rightarrow \ell\nu)$ measurement, using the same dilepton selection but replacing jet and b tag requirements with one additional Tight or VTight τ_h . The kinematics distribution of $e\mu + \tau_h$, $\mu\mu + \tau_h$, $ee + \tau_h$ channels are shown in Figure 4.14 and 4.15 for Tight and VTight working point, respectively.

The origins of selected τ_h are tagged based on generator-level truth. For each selected τ_h , if there is a gen-level τ_h found within $\Delta R = 0.3$, the τ_h is tagged as true identification. If not a true identification, we try to match it with jet in the vetoed-jet collection and tag it as $j \rightarrow \tau_h$, flavor of which equals to the simulated flavor of the jet correspondence. In the rare cases where multiple jet correspondences are found, the one with highest p_T is considered. Also in rare cases where neither gen-level τ_h match nor jet correspondence are found, the τ_h is tagged as null. The origins of τ_h is also included on the right column in Figure 4.14 and 4.15.

To measure $SF(q \rightarrow \tau_h)$ and $SF(b \rightarrow \tau_h)$, a template fit to the $\tau_h p_T$ is performed. The free parameters are $SF(q \rightarrow \tau_h)$ and $SF(b \rightarrow \tau_h)$ in 5 p_T bins from 20 GeV to 80 GeV. The systematical uncertainties, including cross sections, luminosity, electron/muon selection efficiencies, are taken into account as nuisance parameters in the fit. Because jet modeling of the Z+jets simulation is reported to be slightly off in $n_j = 0$ but good $n_j \geq 1$, the events are split into $n_j = 0$ and $n_j \geq 1$ to deal with jet modeling in the Z+jets simulation.

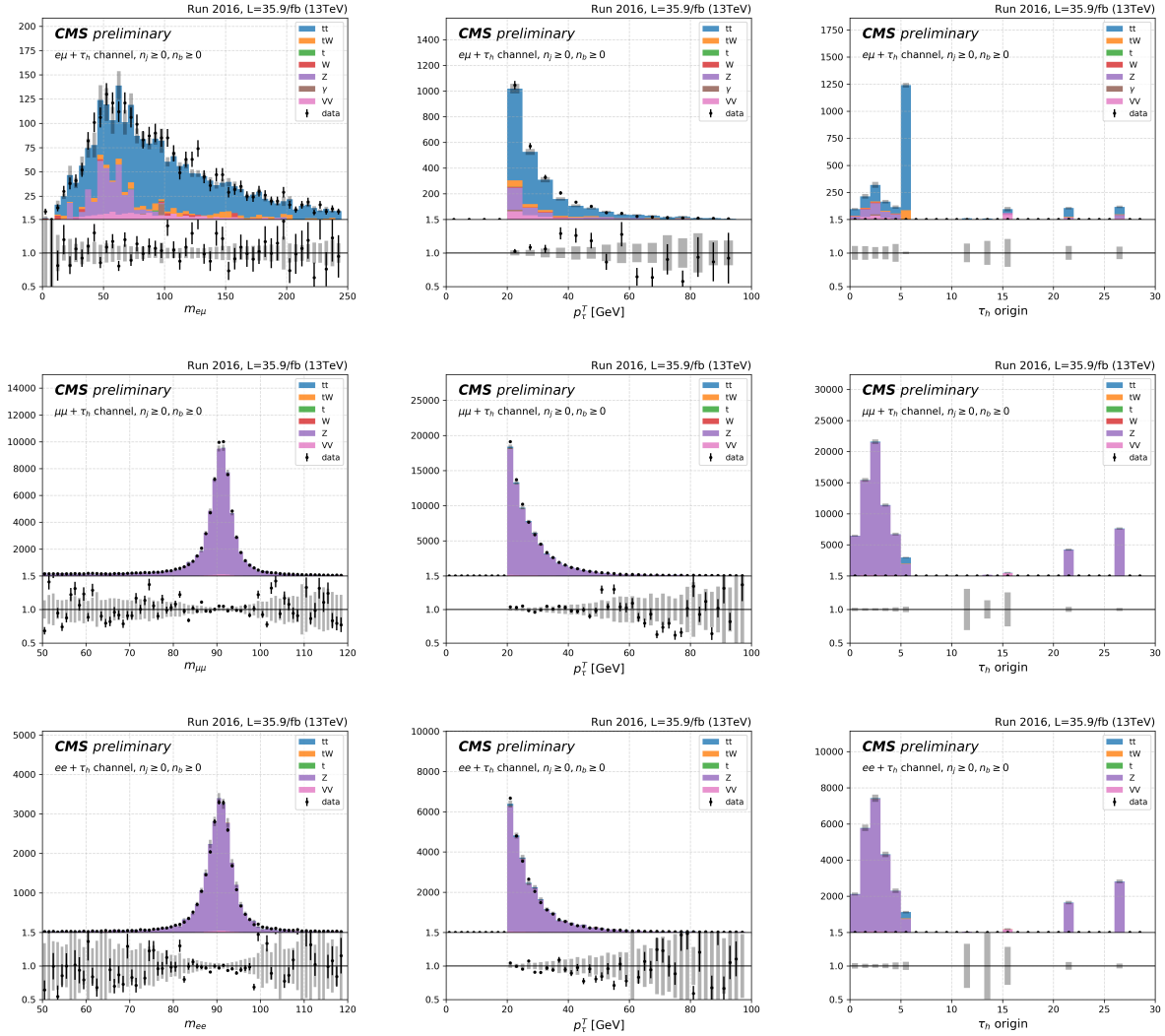


Figure 4.14. The kinematics distribution of $e\mu + \tau_h$, $\mu\mu + \tau_h$, $ee + \tau_h$ channels with Tight τ_h working point.

The result of $SF(j \rightarrow \tau_h)$ for Tight and VTight τ_h working points are listed in Table 4.13.

Figure 4.16 shows the measured $SF(j \rightarrow \tau_h)$ together with pulls and correlation matrix from the template fit. In the $\mathcal{B}(W \rightarrow \ell\nu)$ measurement, to correct the potential mis-modeling of $j \rightarrow \tau_h$ in the simulation, the origins of selected hadronic taus in the $e\tau_h$ and $\mu\tau_h$ channels are tagged with the gen-level truth in the simulated events. The approach of tagging τ_h origins is the same as described here. Based on the τ_h origins, corresponding scale factor in Table 4.13 is applied to reweight the simulated event.

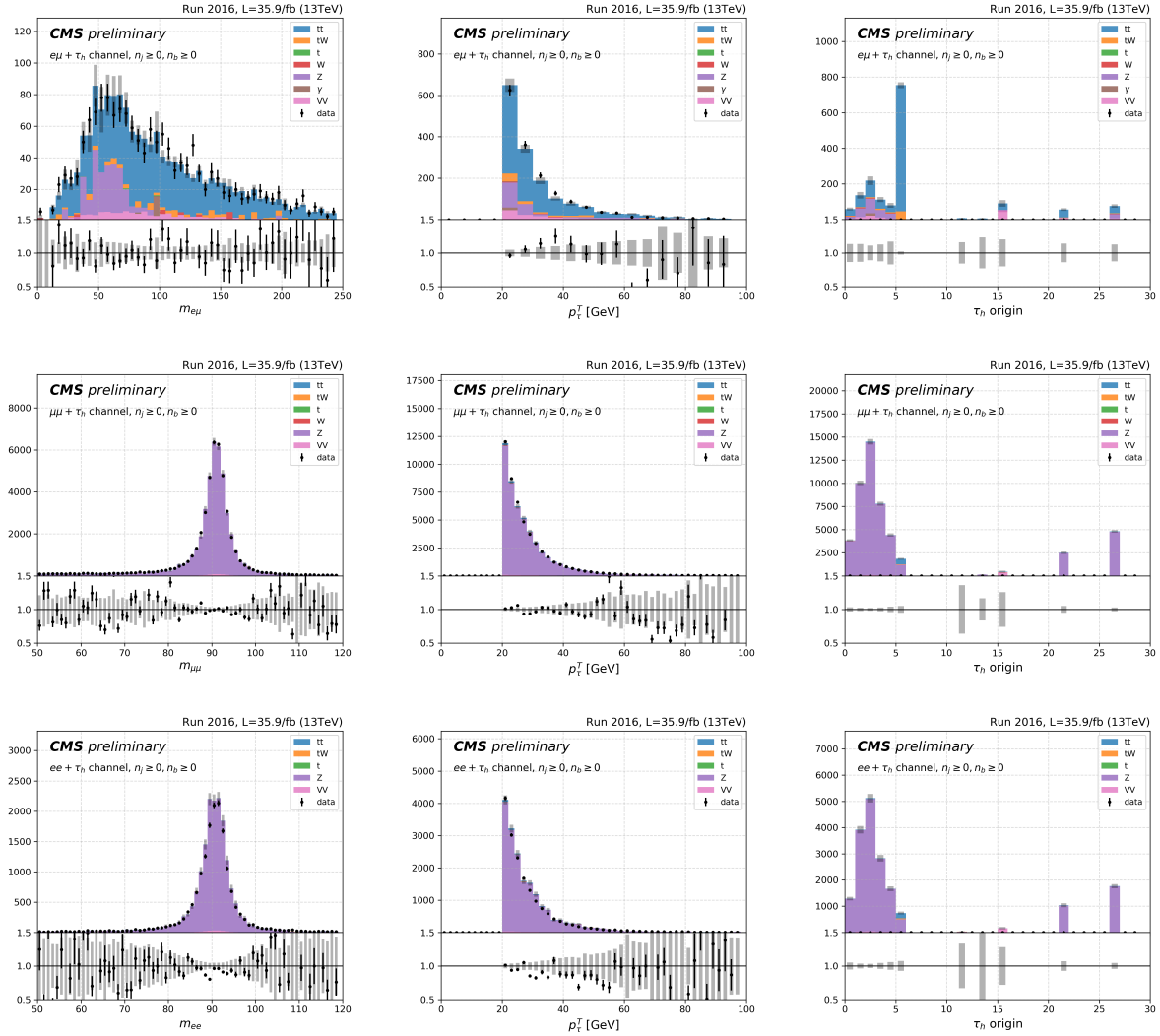


Figure 4.15. The kinematics distribution of $e\mu + \tau_h$, $\mu\mu + \tau_h$, $ee + \tau_h$ channels with Very Tight τ_h working point.

Table 4.13. Scale factors of $(j \rightarrow \tau_h)$ with Tight and Very Tight τ_h working point.

$p_{\tau_h}^T$ [GeV]	20-25	25-30	30-40	40-50	50-80
$SF(b \rightarrow \text{Tight } \tau_h)$	1.02 ± 0.12	1.16 ± 0.12	1.27 ± 0.11	1.21 ± 0.13	0.81 ± 0.13
$SF(q \rightarrow \text{Tight } \tau_h)$	1.04 ± 0.08	0.99 ± 0.07	0.99 ± 0.06	0.90 ± 0.06	0.91 ± 0.07
$SF(b \rightarrow \text{VTight } \tau_h)$	0.97 ± 0.14	1.19 ± 0.16	1.39 ± 0.15	0.96 ± 0.14	0.91 ± 0.17
$SF(q \rightarrow \text{VTight } \tau_h)$	1.02 ± 0.08	0.95 ± 0.07	0.94 ± 0.06	0.89 ± 0.07	0.86 ± 0.07

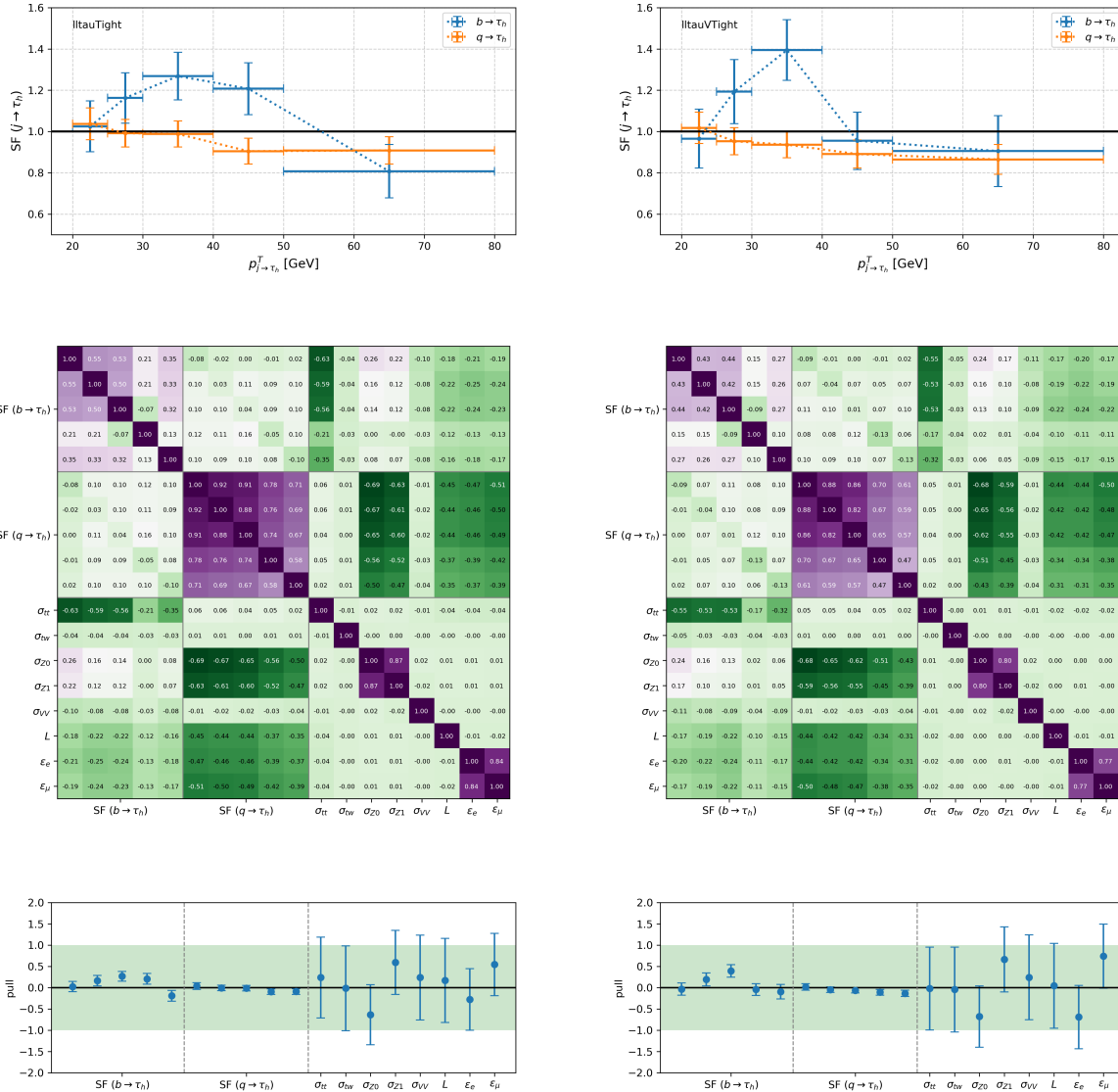


Figure 4.16. The correlation matrix and the pulls of the fitting parameters for Tight (left) and Very Tight (right) τ_h working point.

4.3.5. Corrections for b Tag Efficiency and Mistag Probability

To account for differences of the b tag efficiency in data and simulation, a method that modifies the b tag status of a jet is adopted in the simulation. In the method, the status is modified based on a set of data-to-simulation scale factors f_ϵ derived by the b tag and vertex

(BVT) POG, and the efficiencies for simulation ϵ measured independently in this section.

The method of the b tag correction for simulation works as follows:

- (1) Jets are identified as originating from the decay of a b quark, c quark, or “light” parton (u,s,d,g) from generator truth information. Depending on the parton flavor and jet p_T , the appropriate scale factor f_ϵ and efficiency from simulation ϵ are looked up from a map.
- (2) If $f_\epsilon < 1$, then a b tagged jet is downgraded to a non-b tagged jet with probability $p = 1 - f_\epsilon$. If it is not b tagged, nothing is changed.
- (3) If $f_\epsilon > 1$, then a non-b tagged jet is upgraded to a b tagged jet with probability $p = \frac{1-f_\epsilon}{1-\frac{1}{\epsilon}}$. If it is already b tagged, its status is unchanged.

The measurement of the b tag efficiency in simulation ϵ relies on knowing the flavor of the parton that gives rise to the jet. This is done with official CMS tools that assign a jet flavor based on the characteristics of the quark and gluon content of a jet [152]. The efficiencies are measured for the case of b, c, and light (u,s,d,g) flavor jets, and as a function of the jet p_T . That is,

$$\epsilon(p_T, \text{flavor}) = \frac{N_{\text{pass}}(p_T, \text{flavor})}{N(p_T, \text{flavor})}, \quad (4.3)$$

where the numerator is the number of jets passing the b tag working point, and the denominator is the total number of jets considered. These quantities are measured in both $t\bar{t}$ and Z plus jet samples. The CSVv2 discriminator value for the two samples are shown in figures 4.17 for the three jet flavor categories. The efficiency measurement uses the middle working point of CSVv2 discriminator, the same as the selection in the measurement of W branching fraction. The result of b tagging efficiencies is shown in Figure 4.18. There is some level of disagreement between the two samples for the b quark jets that likely could be attributed to the $t\bar{t}$ sample being generated with an NLO generator (POWHEG) and the Z plus jet sample being generated with a LO generator (MADGRAPH). The efficiencies from

$t\bar{t}$ sample is used for the b tag correction. The events used for the selection require at least one muon passing our analysis requirements, and the four leading p_T jets are considered in the measurement.

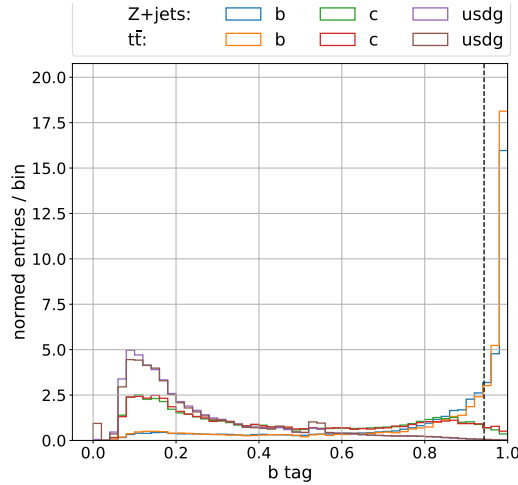


Figure 4.17. Distribution of the b tag score of the b, c and light quark jets in the Z+jets and $t\bar{t}$ simulated dataset.

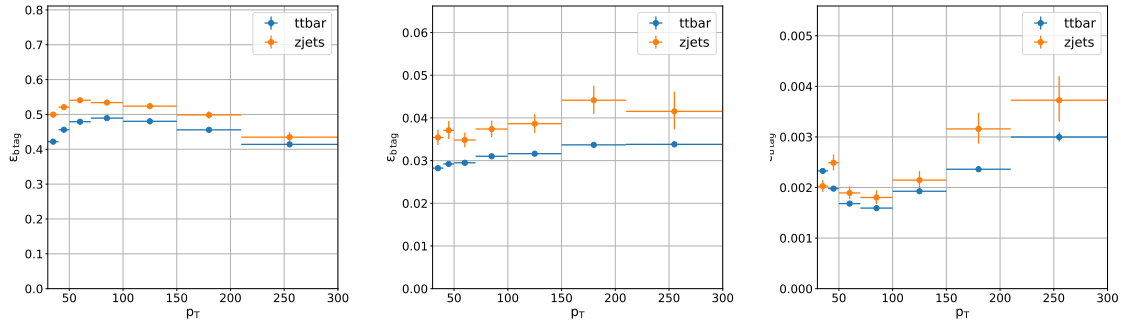


Figure 4.18. The b tag efficiencies for jets originating from b quark (left), c quark (middle), and light quark (right).

4.4. Background Estimation

The $\mathcal{B}(W \rightarrow \ell\nu)$ measurement has four sources of standard model backgrounds:

- vector boson plus jets ($W+jets$ in counting analysis, $Z+jets$)
- photon plus jets ($\gamma+jets$)

- diboson production (WW in counting analysis, ZZ, ZW)
- multijet QCD

It is worth pointing out that the W+jets and WW processes are treated as backgrounds in counting analysis, but the shape analysis treats them as signals. This is because the counting analysis uses only the $t\bar{t}$ enriched signal region, while the shape analysis includes extra control regions with relaxed jet multiplicities requirement. Overall, vector boson plus jets are the most prominent source of backgrounds. The contributions from γ +jets are much smaller and mainly in the eh channel. The contributions from diboson processes WW, ZZ, ZW are even smaller. In the $t\bar{t}$ regions, the contributions from these backgrounds are very small in comparison with the signals. The backgrounds from Z+jets, W+jets, γ +jets and diboson processes are all well modeled by the simulated datasets. Non-negligible contamination from QCD processes are found in $e\tau_h$, $\mu\tau_h$, eh, μh channels. The H_T -binned QCD simulations are evaluated, and turn out to be statistically sufficient at an acceptable level for the normalization in the eh and μh channels which requires high jet multiplicities $n_j \geq 4$. However, the number of simulated QCD events is insufficient for accurately modelling shape of kinematics distributions. Therefore, data-driven approaches are employed to estimate the QCD background in the $e\tau_h$, $\mu\tau_h$, eh, μh channels. For $e\tau_h$, $\mu\tau_h$ channel, a same-sign region is used. For eh, μh channel, the region with inverted lepton isolation is used.

4.4.1. QCD background in the $e\tau_h$ and $\mu\tau_h$ channels

This estimation relies on the dearth of standard model processes that can give rise to same-sign lepton pairs. It is expected that most events with same-sign lepton pairs are the result of at least one of the leptons coming from non-prompt decays. It is further assumed that this process will give rise to misidentifying hadronic jets as leptons in near equal measure between the same sign and opposite sign selections.

The process of deriving the estimate is simple enough: requiring the electron or muon having the same sign as the hadronic tau in the $e\tau_h$ and $\mu\tau_h$ channel. All other selection requirements are kept unchanged. The deficit between data and standard model simulation in the same-sign side-band region is multiplied by a transferring scale factor to estimate the QCD contamination in the signal region.

The same-sign (SS) to opposite-sign (OS) transfer scale factor transfer factor is calculated by

$$SF^{SS \rightarrow OS} = \frac{N_{\text{data}}^{\text{OS}} - \sum N_{\text{MC}}^{\text{OS}}}{N_{\text{data}}^{\text{SS}} - \sum N_{\text{MC}}^{\text{SS}}} \quad (4.4)$$

To determine $SF^{SS \rightarrow OS}$, the counting analysis uses $e\tau_h$ and $\mu\tau_h$ channels with $n_j = 2, n_b = 0$. The SS and OS regions of $e\tau_h$ and $\mu\tau_h$ channels with different n_j, n_b configurations are shown in Figure 4.20 and 4.21. The $SF^{SS \rightarrow OS}$ measured from $n_j = 2, n_b = 0$ is chosen because the jet and b tag configuration is closest to the signal region. The corresponding results of $SF^{SS \rightarrow OS}$ are 1.062 and 1.195 for $e\tau_h$ and $\mu\tau_h$ channel, respectively.

For shape analysis, this region is treated as a signal region. So the regions with anti-isolated electron or muon plus τ_h with $n_j = 0$ are used to measure $SF^{SS \rightarrow OS}$. Figure 4.19 shows the $m_{e\tau_h}$ and $m_{\mu\tau_h}$ distributions distributions in the same-sign and opposite-sign regions of $e\tau_h$ (on the right) and $\mu\tau_h$ (on the left) channel with the anti-isolated lepton and zero jets.

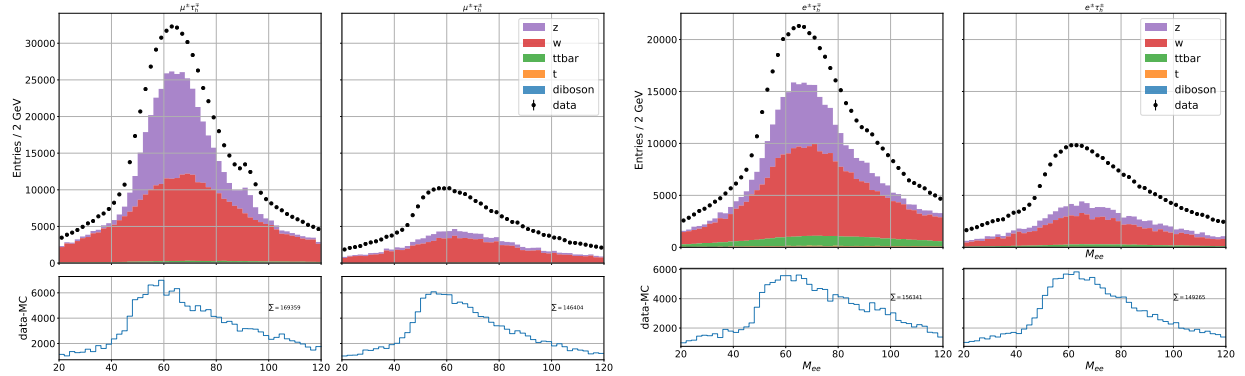


Figure 4.19. The $m_{e\tau_h}$ and $m_{\mu\tau_h}$ distributions in the same-sign and opposite-sign regions of $e\tau_h$ (on the right) and $\mu\tau_h$ (on the left) channel with the anti-isolated lepton and zero jets.

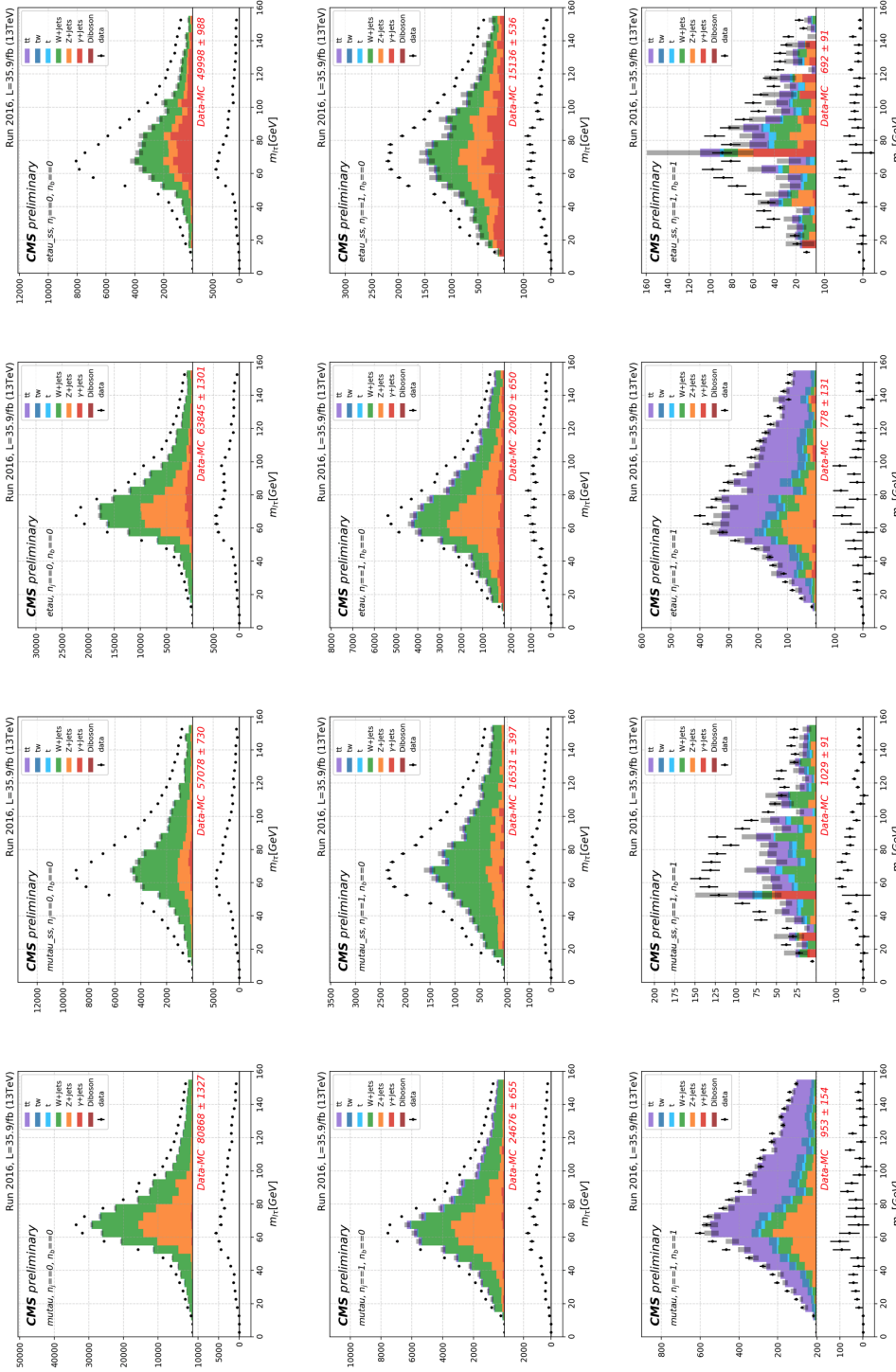


Figure 4.20. The $m_{\mu\tau_h}$ distributions in the same-sign and opposite-sign regions of $\mu\tau_h$ channel (left two columns). The $m_{e\tau_h}$ spectrum in the same-sign and opposite-sign regions of $e\tau_h$ channel (right two columns). Three rows correspond to $n_j = 0, n_b = 0, n_j = 1, n_b = 1$, respectively.

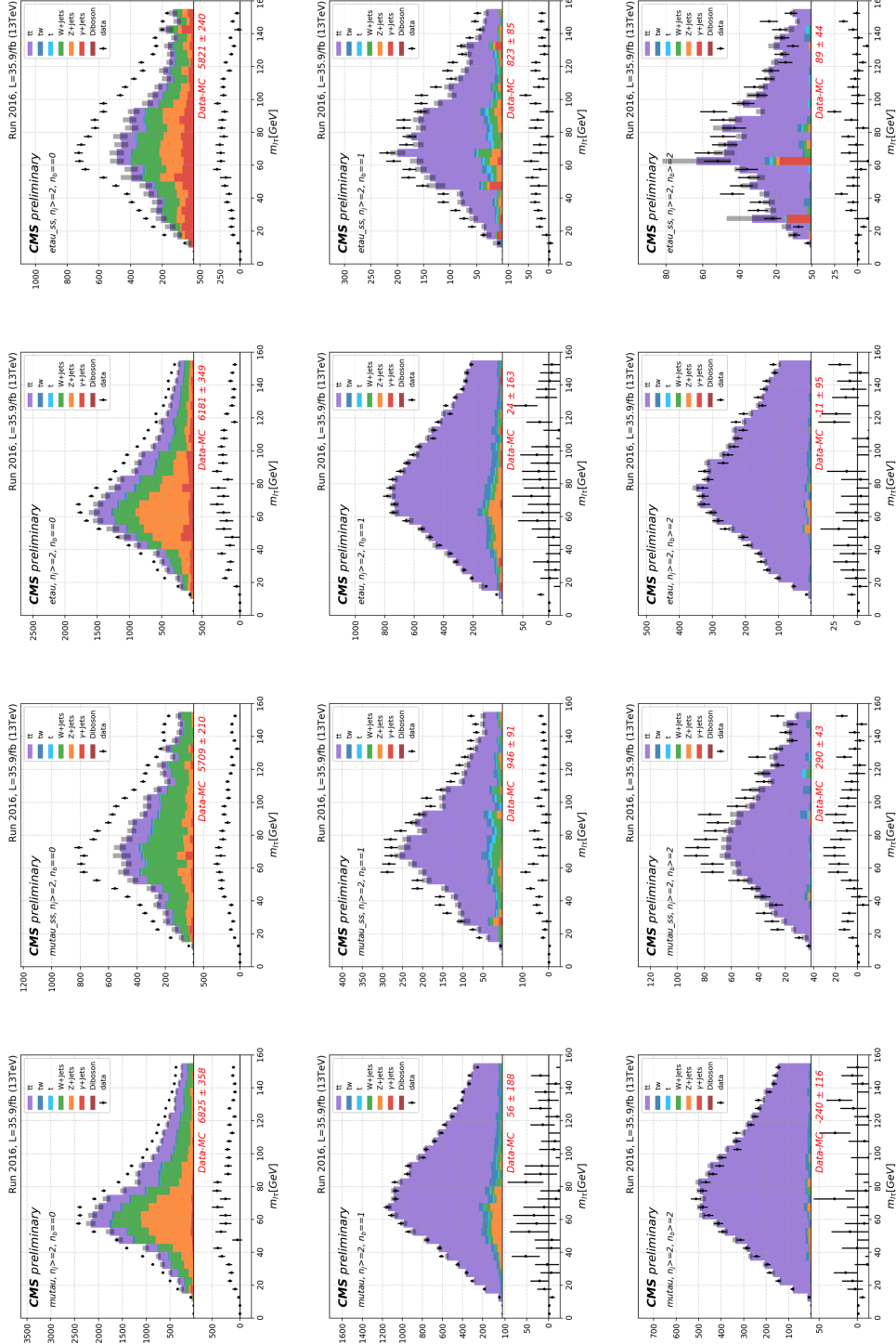


Figure 4.21. The $m_{\mu\tau_h}$ distributions in the same-sign and opposite-sign regions of $\mu\tau_h$ channel (left two columns). The $m_{e\tau_h}$ spectrum in the same-sign and opposite-sign regions of $e\tau_h$ channel (right two columns). Three rows correspond to $n_j \geq 2, n_b = 0, n_j \geq 2, n_b = 1, n_j \geq 2, n_b \geq 2$, respectively.

4.4.2. QCD background in the eh and μh channels

In the eh and μh channels, the QCD estimations are based on side-band regions with inverted lepton isolation, where the data excess with respect to the simulations are multiplied by an anti-isolation ($\overline{\text{iso}}$) to isolation (iso) transfer factor depending on the lepton p_T and η . When selecting anti-isolated electrons and muons, the isolation is required to pass loose working point but fail the tight working point. The requirement of single lepton trigger is the same as the isolated lepton cases.

The anti-isolation to isolation transfer factor is defined as

$$SF^{\overline{\text{iso}} \rightarrow \text{iso}}(p_T, \eta) = \frac{N_{\text{data}}^{\text{iso}}(p_T, \eta) - \sum N_{\text{MC}}^{\text{iso}}(p_T, \eta)}{N_{\text{data}}^{\overline{\text{iso}}}(p_T, \eta) - \sum N_{\text{MC}}^{\overline{\text{iso}}}(p_T, \eta)} \quad (4.5)$$

To measure $SF^{\overline{\text{iso}} \rightarrow \text{iso}}$, an orthogonal region with lepton plus $1 \leq n_j < 4$ and $n_b \geq 1$ is considered. To reduce the contamination for $W+jets$ and enhance the QCD purity, $m_T^{\ell, MET} < 40 \text{ GeV}$ is required. Figure 4.22 shows the isolated and anti-isolated lepton plus jet regions with $1 \leq n_j < 4$ and $n_b \geq 1$, μh in the left two columns and eh in the right two columns. The measured $SF^{\overline{\text{iso}} \rightarrow \text{iso}}$ result is shown in Figure 4.23.

Applying the measured $SF^{\overline{\text{iso}} \rightarrow \text{iso}}$ in the signal region (eh and μh channels with $n_j \geq 4$ and $n_b \geq 1$), the result QCD estimations obtained are shown in Figure 4.24. It is observed that the QCD estimation in the μh channel is reasonable, while that in the eh channel is over-estimated. The isolated and anti-isolated regions of eh and μh channels with $n_j \geq 4$ and $n_b \geq 1$ are shown in Figure 4.25, where the left and right two columns are for the μh channel and eh channel, respectively. Comparing the data-simulation difference in the isolated and anti-isolated regions, their shapes do demonstrate similarities. The over-estimation in the eh channel could come from the normalization of $SF^{\overline{\text{iso}} \rightarrow \text{iso}}$. In Figure 4.25, the QCD estimation from the H_T -binned QCD simulated datasets is shown as red lines, which gives a decent

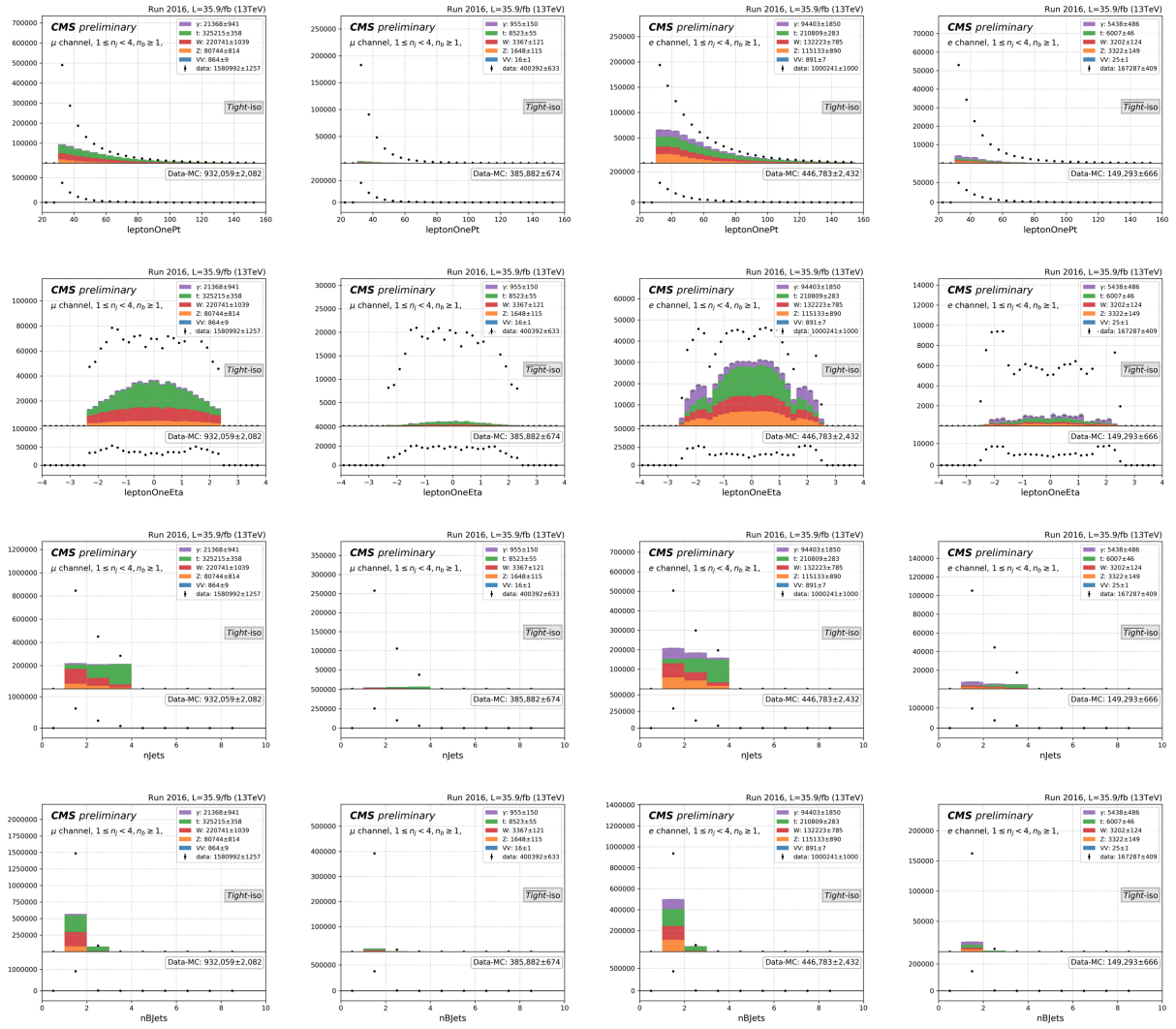


Figure 4.22. isolated and anti-isolated lepton plus jet regions with $1 \leq n_j < 4$ and $n_b \geq 1$, μh in the left two columns and eh in the right two columns.

estimation to the QCD normalization. If scale the anti-isolated region with the normalization of simulated dataset instead of the $SF^{\text{iso} \rightarrow \text{iso}}$, one gets a QCD estimation with data-driven shape and simulation-based normalization, shown in Figure 4.26.

For the counting analysis, the simulation-based normalization obtained from the HT-binned QCD simulated datasets is used. The statistical uncertainty of the simulation is about 4%. To be conservative, a 30% uncertainty is assigned to the QCD estimation. For

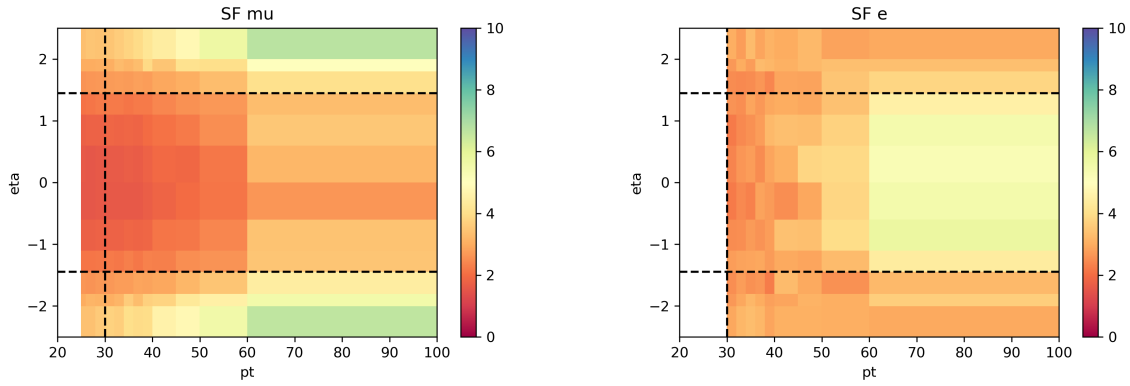


Figure 4.23. The $SF^{\text{iso} \rightarrow \text{iso}}$ measured in the lepton plus jet regions with $1 \leq n_j < 4$ and $n_b \geq 1$.

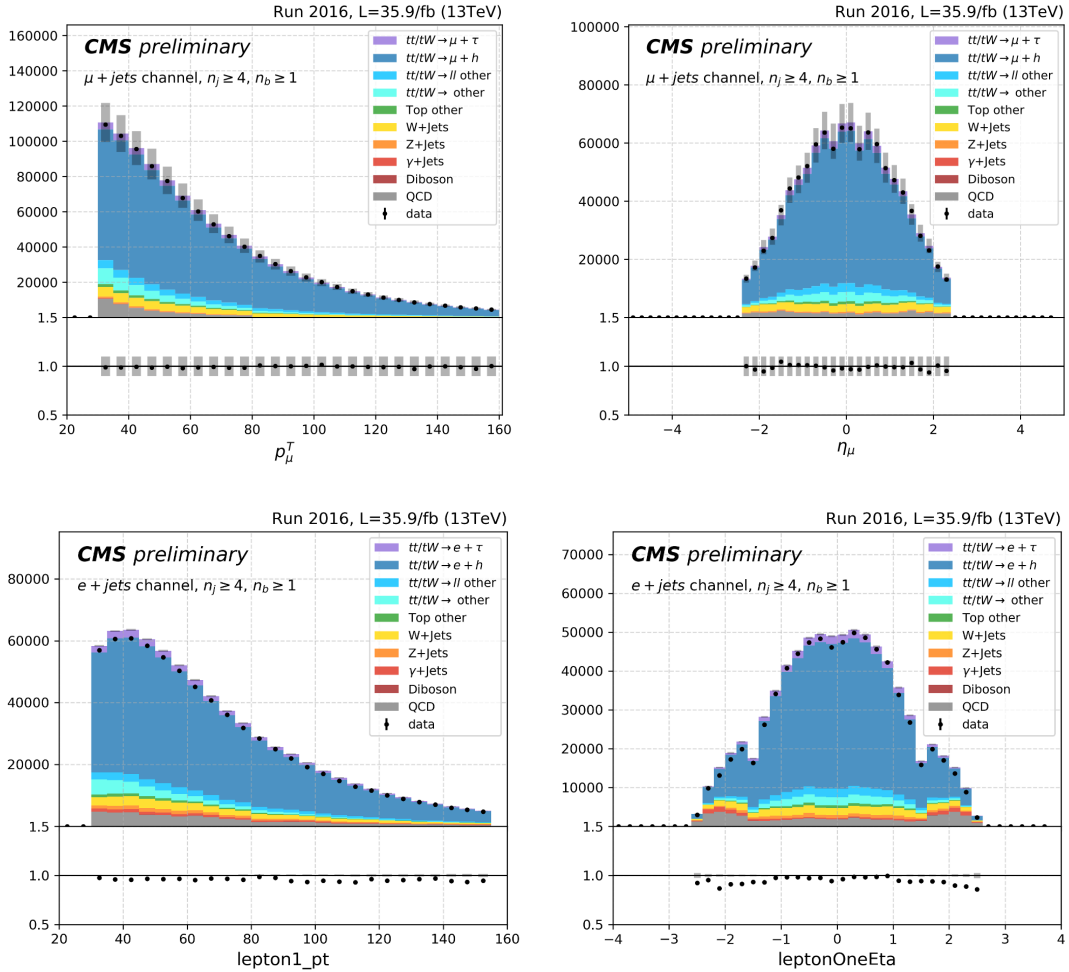


Figure 4.24. Fully data-driven QCD estimation in μh and eh signal regions with $n_j \geq 4$ and $n_b \geq 1$ based on the anti-isolation region with $SF^{\text{iso} \rightarrow \text{iso}}$.

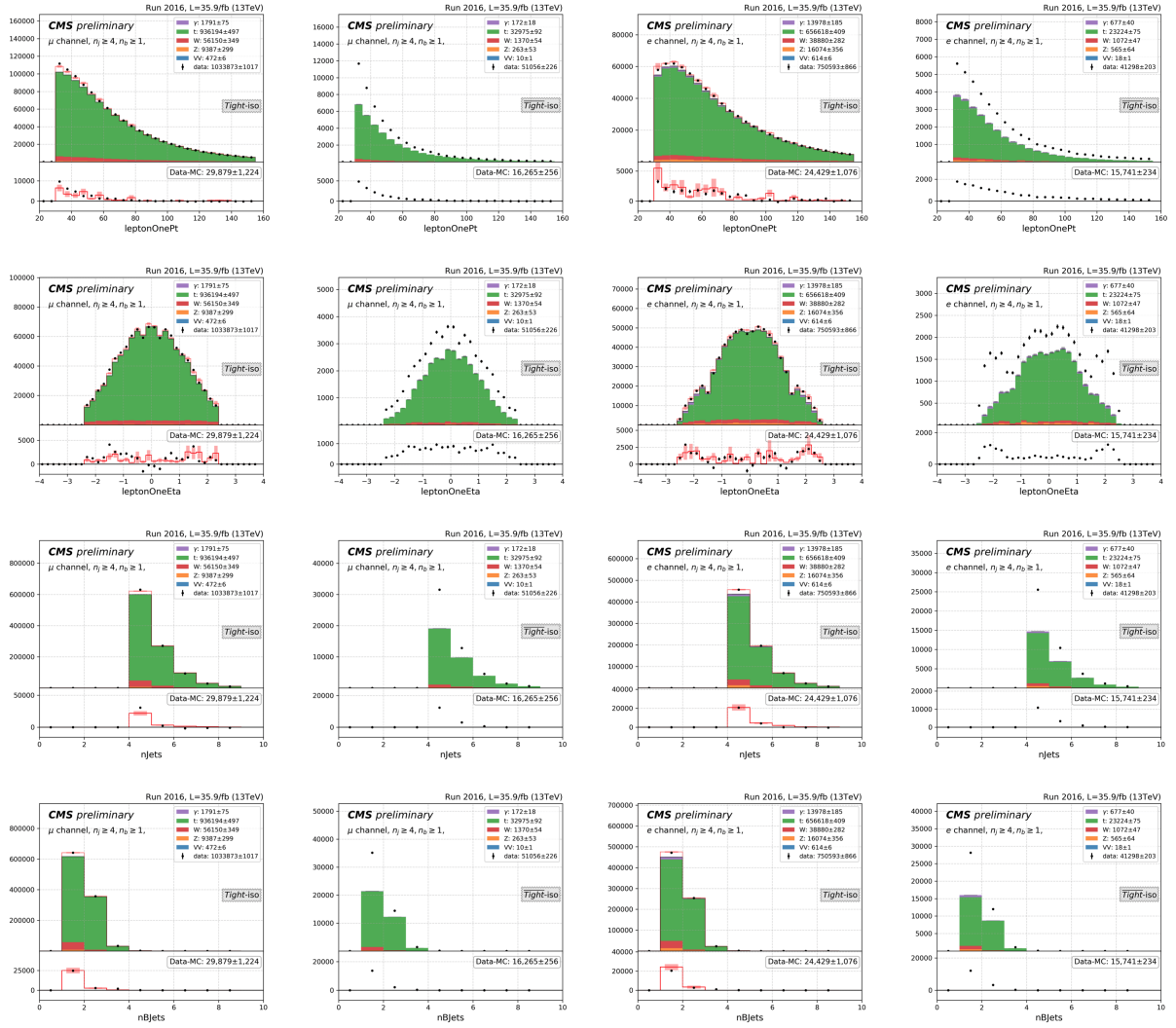


Figure 4.25. The isolated and anti-isolated regions of eh and μh channels with $n_j \geq 4$ and $n_b \geq 1$. The left and right two columns are for the μh channel and eh channel, respectively

the shape analysis, the shape of estimated QCD is from the anti-isolated region while the normalization is treated as a free parameters.

4.5. Statistical Analysis

Having carried out the event selection as described in Section 4.2, the estimation of the W branching fraction is carried out using two different approaches. Before describing the two approaches, it will be useful to describe the formalism that is common to both.

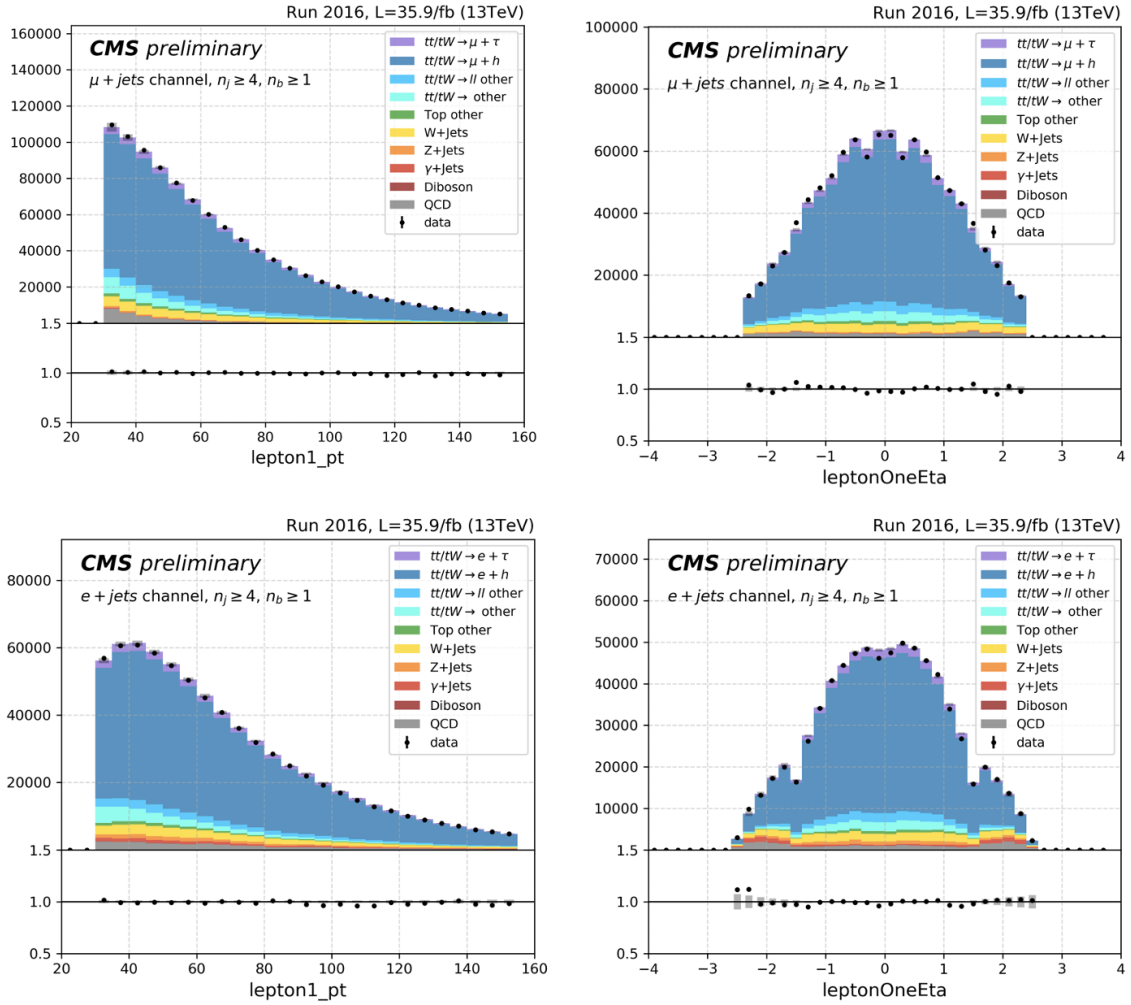


Figure 4.26. The QCD estimation in μh and eh signal regions with $n_j \geq 4$ and $n_b \geq 1$ based on data-driven shape and simulation-based normalization.

4.5.1. Modeling the Decays of WW Pairs

The quantities of interest are the four W branching fractions,

$$\boldsymbol{\beta} = \{\beta_e, \beta_\mu, \beta_\tau, \beta_h\}, \quad (4.6)$$

where the subscript indicates the decay mode of the W boson (hadronic decay modes, h, are grouped together). Because the τ can also decay to the other modes, the above vector can

be extended to include this,

$$\boldsymbol{\beta}' = \{\beta_e, \beta_\mu, \beta_\tau b_e^\tau, \beta_\tau b_\mu^\tau, \beta_\tau b_h^\tau, \beta_h\}. \quad (4.7)$$

Because this analysis is interested in final states with two W bosons, it is necessary to consider all possible decay combinations. This can be represented succinctly in matrix representation by taking the outer product of $\boldsymbol{\beta}'$ with itself,

$$\boldsymbol{B} = \boldsymbol{\beta}' \otimes \boldsymbol{\beta}' = \begin{bmatrix} \beta_e \beta_e & \beta_e \beta_\mu & \beta_e \beta_\tau b_e^\tau & \beta_e \beta_\tau b_\mu^\tau & \beta_e \beta_\tau b_h^\tau & \beta_e \beta_h \\ \beta_\mu \beta_e & \beta_\mu \beta_\mu & \beta_\mu \beta_\tau b_e^\tau & \beta_\mu \beta_\tau b_\mu^\tau & \beta_\mu \beta_\tau b_h^\tau & \beta_\mu \beta_h \\ \beta_\tau b_e^\tau \beta_e & \beta_\tau b_e^\tau \beta_\mu & \beta_\tau b_e^\tau \beta_\tau b_e^\tau & \beta_\tau b_e^\tau \beta_\tau b_\mu^\tau & \beta_\tau b_e^\tau \beta_\tau b_h^\tau & \beta_\tau b_e^\tau \beta_h \\ \beta_\tau b_\mu^\tau \beta_e & \beta_\tau b_\mu^\tau \beta_\mu & \beta_\tau b_\mu^\tau \beta_\tau b_e^\tau & \beta_\tau b_\mu^\tau \beta_\tau b_\mu^\tau & \beta_\tau b_\mu^\tau \beta_\tau b_h^\tau & \beta_\tau b_\mu^\tau \beta_h \\ \beta_\tau b_h^\tau \beta_e & \beta_\tau b_h^\tau \beta_\mu & \beta_\tau b_h^\tau \beta_\tau b_e^\tau & \beta_\tau b_h^\tau \beta_\tau b_\mu^\tau & \beta_\tau b_h^\tau \beta_\tau b_h^\tau & \beta_\tau b_h^\tau \beta_h \\ \beta_h \beta_e & \beta_h \beta_\mu & \beta_h \beta_\tau b_e^\tau & \beta_h \beta_\tau b_\mu^\tau & \beta_h \beta_\tau b_h^\tau & \beta_h \beta_h \end{bmatrix}. \quad (4.8)$$

This is a 36 term symmetric matrix containing 21 unique terms. The signal samples are constructed from a combination of $t\bar{t}$ and tW final states, and are divided into 21 categories based on the decay modes identified by inspecting generator-level truth information. The efficiencies for these signal samples can be summarized in matrix notation,

$$\boldsymbol{E} = \begin{bmatrix} \epsilon_{ee} & \epsilon_{e\mu} & \epsilon_{e\tau_e} & \epsilon_{e\tau_\mu} & \epsilon_{e\tau_h} & \epsilon_{eh} \\ \epsilon_{e\mu} & \epsilon_{\mu\mu} & \epsilon_{\mu\tau_e} & \epsilon_{\mu\tau_\mu} & \epsilon_{\mu\tau_h} & \epsilon_{\mu h} \\ \epsilon_{e\tau_e} & \epsilon_{\mu\tau_e} & \epsilon_{\tau_e\tau_e} & \epsilon_{\tau_e\tau_\mu} & \epsilon_{\tau_e\tau_h} & \epsilon_{\tau_e h} \\ \epsilon_{e\tau_\mu} & \epsilon_{\mu\tau_\mu} & \epsilon_{\tau_e\tau_\mu} & \epsilon_{\tau_\mu\tau_\mu} & \epsilon_{\tau_\mu\tau_h} & \epsilon_{\tau_\mu h} \\ \epsilon_{e\tau_h} & \epsilon_{\mu\tau_h} & \epsilon_{\tau_e\tau_h} & \epsilon_{\tau_\mu\tau_h} & \epsilon_{\tau_h\tau_h} & \epsilon_{\tau_h h} \\ \epsilon_{eh} & \epsilon_{\mu h} & \epsilon_{\tau_e h} & \epsilon_{\tau_\mu h} & \epsilon_{\tau_h h} & \epsilon_{hh} \end{bmatrix}, \quad (4.9)$$

where the subscript on the τ indicates its decay mode. This matrix is constructed for each signal process in each channel and $n_j n_b$ category, and, in the case of the shape analysis, the fitted p_T observable. The value of the efficiencies are calculated based on the ratio,

$$\epsilon_{ij} = \frac{\sum_k w_{ij}^k}{N_{ij}^{\text{gen}}}, \quad (4.10)$$

where w^k is the weight for event k and N_{gen} is the total number of events generated for a given process. Based on this, the estimated number of events for a signal process, s , that produces two W bosons can be written,

$$N_s = \sigma_s L \sum_{ij} \mathbf{E}_{s,ij} \mathbf{B}_{ij}, \quad (4.11)$$

where σ_s is the cross-section for process under consideration, L is the integrated luminosity. Having established these preliminaries, the particulars of the twoanalysis approaches will be described in detail in the next two sections.

4.5.2. Shape Analysis

In this approach, a maximum likelihood estimation of the branching fractions is carried out. The data is divided into categories based on the multiplicity and flavor of leptons, jet multiplicity, and b tag multiplicities as described in Section 4.2.2. Additional discriminating information is included by further binning the data according to a single kinematic observable in each category category. The observable is selected to enhance the discrimination between decay products that come directly from the W boson decay and decay products where a tau lepton is an intermediate product. The variables that are selected by each lepton flavor category are as follows:

- ee, $\mu\mu$, e μ : the trailing lepton p_T

- $e\tau_h$ and $\mu\tau_h$: the hadronic tau p_T
- eh and μh : the triggering lepton p_T

These distributions are shown in Figures 4.27 through 4.31. Histogram templates are generated for each category by binning using the Bayesian Block algorithm [153]. The binning is calculated independently for each category based on $\sim 10^4$ simulated events.

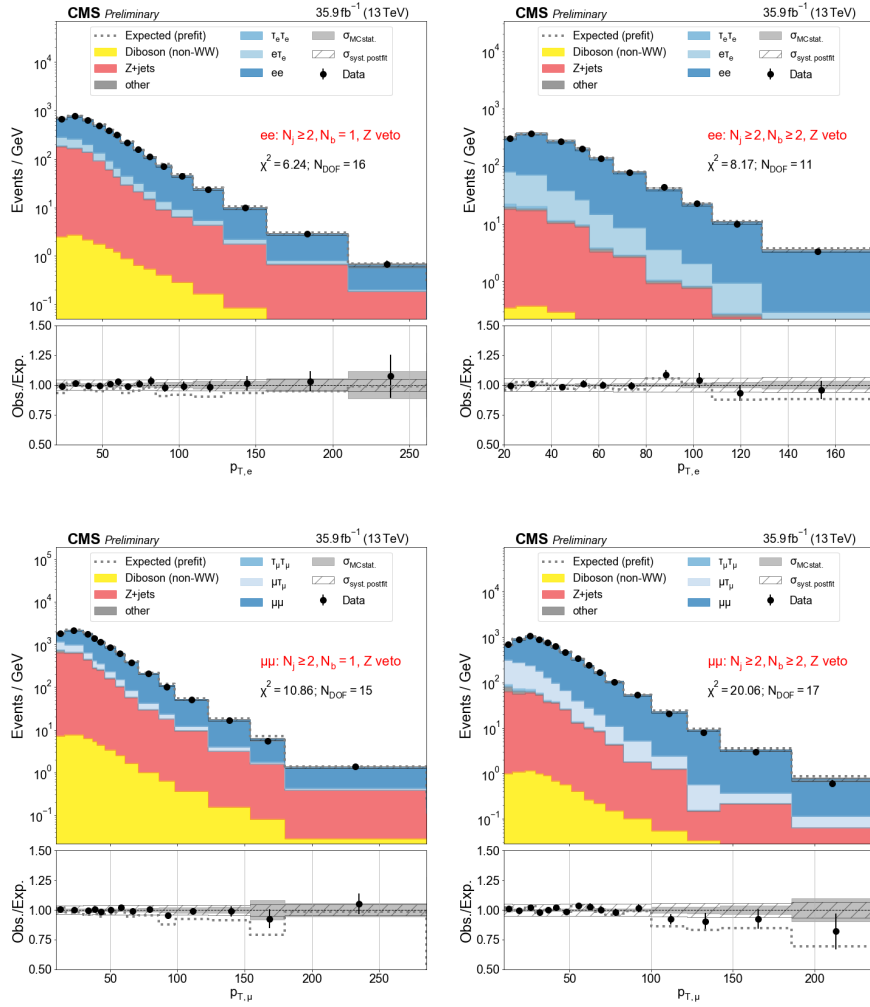


Figure 4.27. Templates used as inputs to the fit for the ee and $\mu\mu$ channels.

Effectively, this parameterizes the efficiency matrix in Equation 4.9 by the observables listed above, the number of jets, and the number of b tags. Having constructed the data

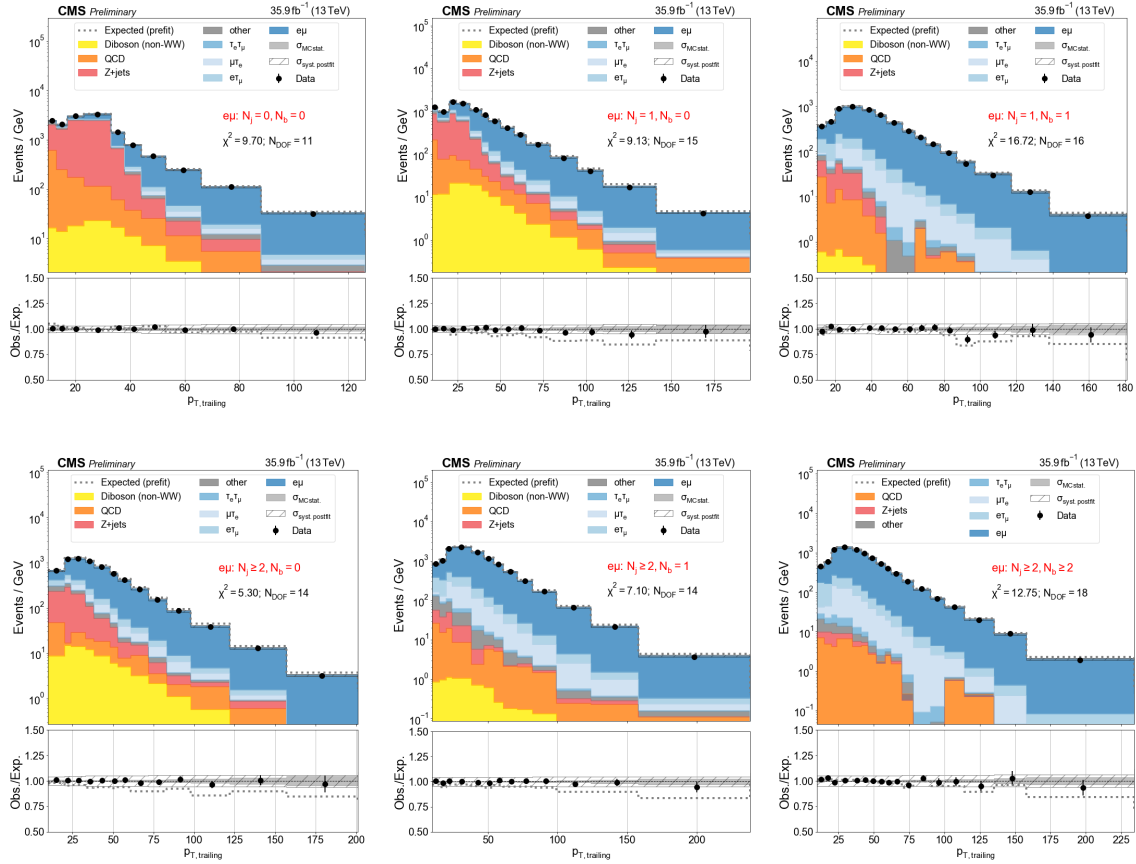


Figure 4.28. Templates used as inputs to the fit for the $e\mu$ channel.

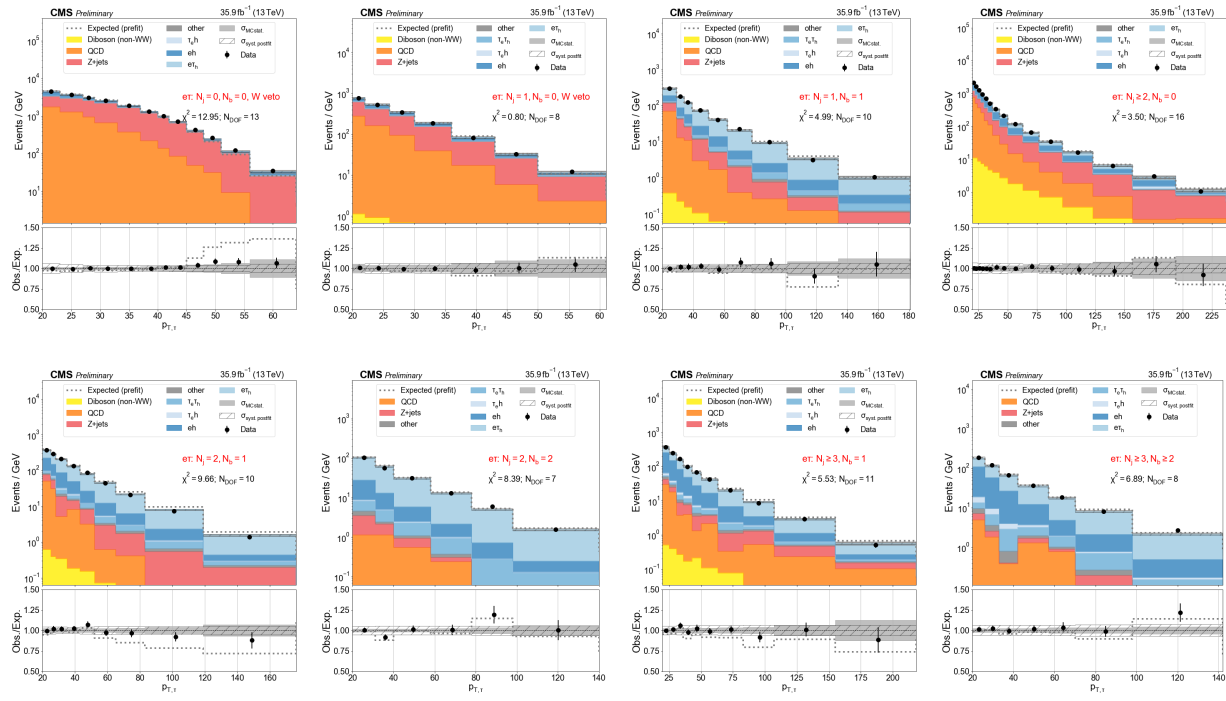
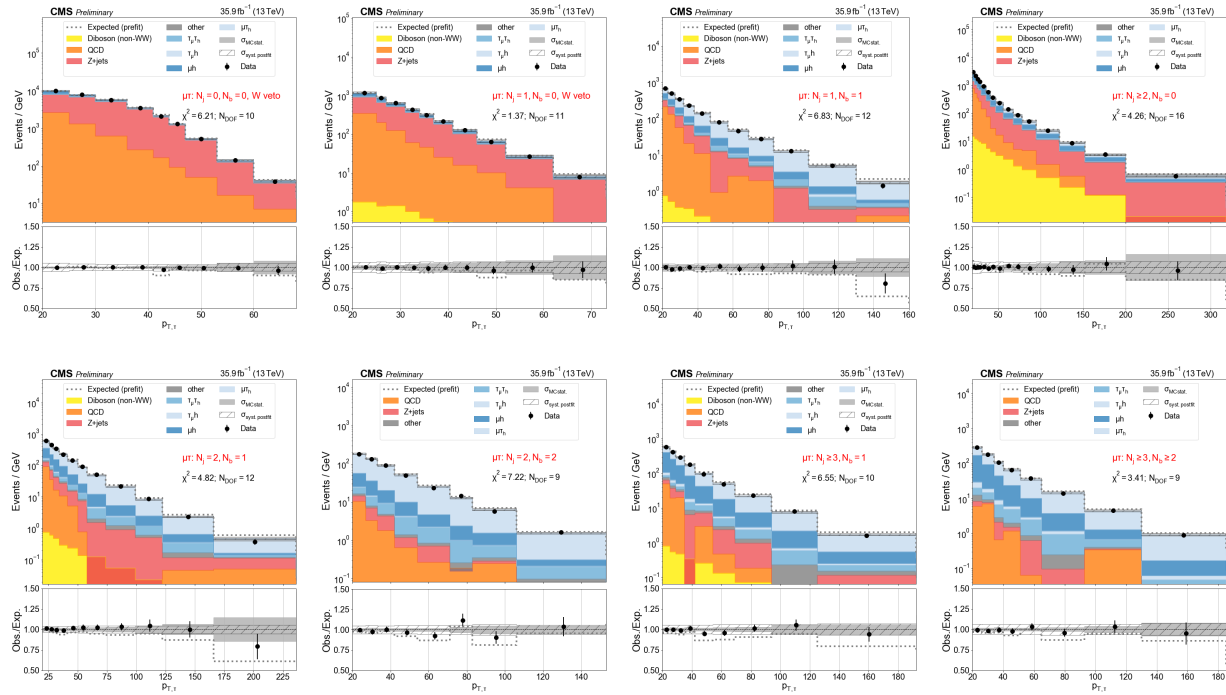
model, the negative log likelihood can be calculated,

$$NLL(\boldsymbol{\beta}) = \sum_{i \in \text{bin}} [-y_i \ln f_i(\boldsymbol{\beta}) + f_i(\boldsymbol{\beta})], \quad (4.12)$$

where y_i is the data yield in bin i . The predicted yields, f_i are a sum of signal and background templates,

$$f_i(\boldsymbol{\beta}) = \sum_{\text{sig.}} s_i(\boldsymbol{\beta}) + \sum_{\text{bkg.}} b_i. \quad (4.13)$$

where the signal term, $s(\boldsymbol{\beta})$ is as written in Equation 4.11 and the background term b is estimated by either simulated dataset or data driven approach described in Section 4.4.

Figure 4.29. Templates used as inputs to the fit for the $e\tau_h$ channel.Figure 4.30. Templates used as inputs to the fit for the $\mu\tau_h$ channel.

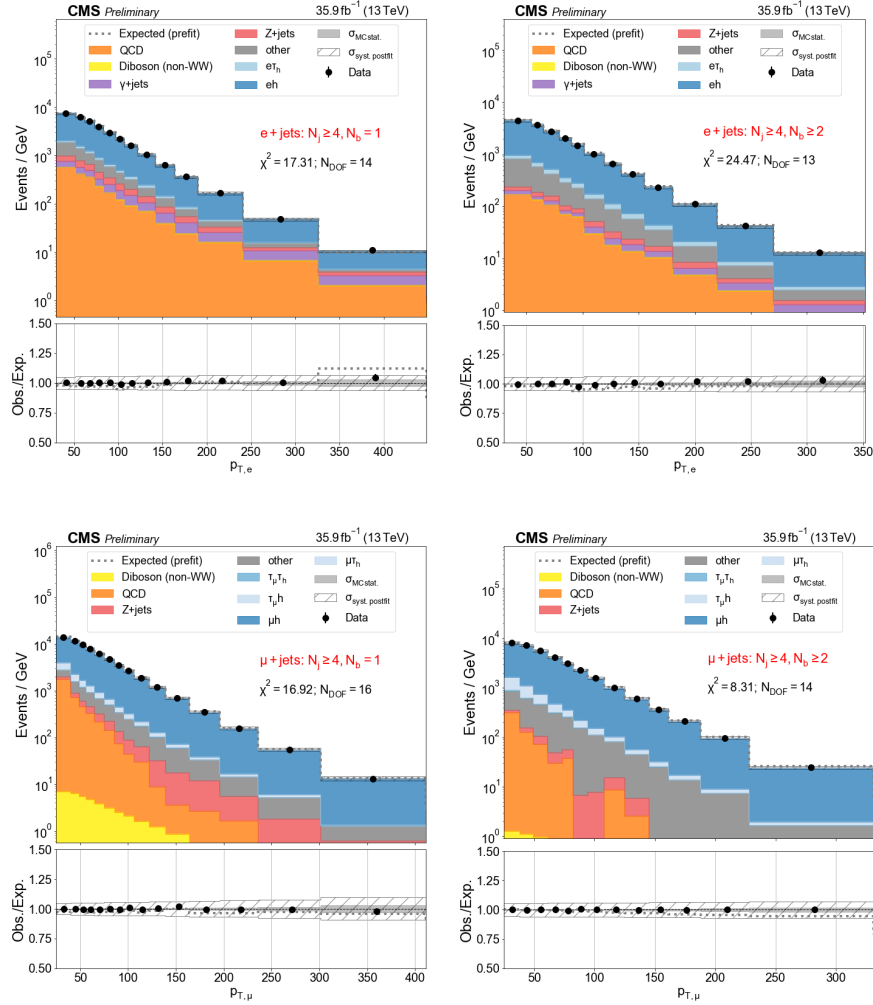


Figure 4.31. Templates used as inputs to the fit for the eh and μh channels.

4.5.2.1. Assessment of Systematic Uncertainties. The shape analysis accounts for the effects of various sources of systematic uncertainties by incorporating nuisance parameters into the fit [154]. The individual sources of systematics uncertainties are described in Section 4.6. This approach to the systematic uncertainties has the benefit that all correlations between the various nuisance parameters that exist in the model definition are accounted for when the fit is carried out. In some cases, the nuisance parameters can become constrained by the fit. Additionally, it is straight forward to incorporate auxiliary control regions ($Z \rightarrow \tau_\ell \tau_h$)

to improve the constraints on background normalizations and uncertainties on the modeling of physics objects in simulation.

The modification to the objective function follows the approach recommended by Conway, i.e., adding additional terms, $\pi(\boldsymbol{\theta})$, to the cost function to account for the priors on the nuisance parameters, θ ,

$$NLL(\boldsymbol{\beta}, \boldsymbol{\theta}) = \sum_{i \in \text{bins}} [-y_i \ln f_i(\boldsymbol{\beta}, \boldsymbol{\theta}) + f_i(\boldsymbol{\beta}, \boldsymbol{\theta})] + \pi(\boldsymbol{\theta}). \quad (4.14)$$

Nuisance parameters are assumed to be Gaussian constrained unless otherwise noted. Thus the corresponding negative log likelihood term takes the form of L2 regularization $\pi(\boldsymbol{\theta}) = \frac{1}{2}|\boldsymbol{\theta}|^2$. In the predictive model $f_i(\boldsymbol{\beta}, \boldsymbol{\theta})$, the nuisance parameters are treated either as normalization parameters (multiplicative factors which are bin independent) or shape nuisance parameters which vary depending on the bin they are applied to. In the latter case, morphing templates are generated for the cases that the nuisance parameters are shifted up and down by one standard deviation. The details for each source of systematic uncertainty is described in Section 4.6. A quadratic morphing of the bin content as a function of a nuisance parameter is used for values $\theta \in [-1, 1]$,

$$f(\theta) = \frac{\theta(\theta - 1)}{2}f^- - (\theta - 1)(\theta + 1)f^0 + \frac{\theta(\theta + 1)}{2}f^+, \quad (4.15)$$

with f^0 corresponding to the nominal prediction in a given bin, and f^- and f^+ correspond to the down and up variations of the relevant source of uncertainty. In the circumstance that the variation in yield is symmetric about nominal value as a function of θ , the quadratic term becomes unimportant. Outside the range $[-1, 1]$, the bin content varies linearly with the value of θ .

The branching fraction estimates are determined by minimizing the NLL Equation 4.14 with respect to all parameters. This is done for all final state channels and b tag bins

simultaneously which accounts for correlations between common nuisance parameters and the W branching fractions.

4.5.2.2. Assessment of Statistical Uncertainty. In addition to various sources of uncertainty associated with the detector and with the modeling of physical processes, there is a non-negligible uncertainty arising from the finite and limited statistics of the simulated samples used to model the data. Ideally, the simulated samples would have > 5 times the number of events collected in data for each process. This is generally not the case, and in some cases, the number of simulated events is less than the number of corresponding events collected in data. With this in mind, the Barlow-Beeston lite method [155] is adopted to account for the resulting uncertainty. In brief, this method entails introducing a nuisance parameter for each bin in the analysis that controls the normalization of that bin and is constrained according to the variance associated with the statistics of the simulated samples. Because these nuisance parameters are to the first order not correlated across bins, they can be solved for analytically as described in Section 5 of Conway [154].

4.5.2.3. Bias Study of Parameter Extraction. It is desirable that the method produces an unbiased measurement of the W branching fractions. Even though it is not expected that bias should arise, it is important to verify no bias with a toy Monte Carlo study. This study is carried out by generating 10^4 pseudo-datasets from the nominal data model templates with values of the branching fractions samples in the ranges $\beta_e, \beta_\mu, \beta_\tau \in [0.1, 0.12]$ with $\beta_h = 1 - (\beta_e + \beta_\mu + \beta_\tau)$. For each of the 10^4 quadruplets, a pseudo-dataset is generated accounting for Poisson statistics of each individual signal and background template, and the search procedure is carried out, i.e., Equation 4.12 is minimized to determine the observed estimator. From this, the bias can be determined,

$$\text{bias} = \frac{\beta_{\text{true}} - \beta_{\text{obs}}}{\beta_{\text{true}}}. \quad (4.16)$$

The results of this study are shown in Figures 4.32 and 4.33. The mean value of the bias shows no deviation from zero within a standard deviation. There is also no indication that there is a dependence of the bias on the true value of the branching fraction used to generate the data.

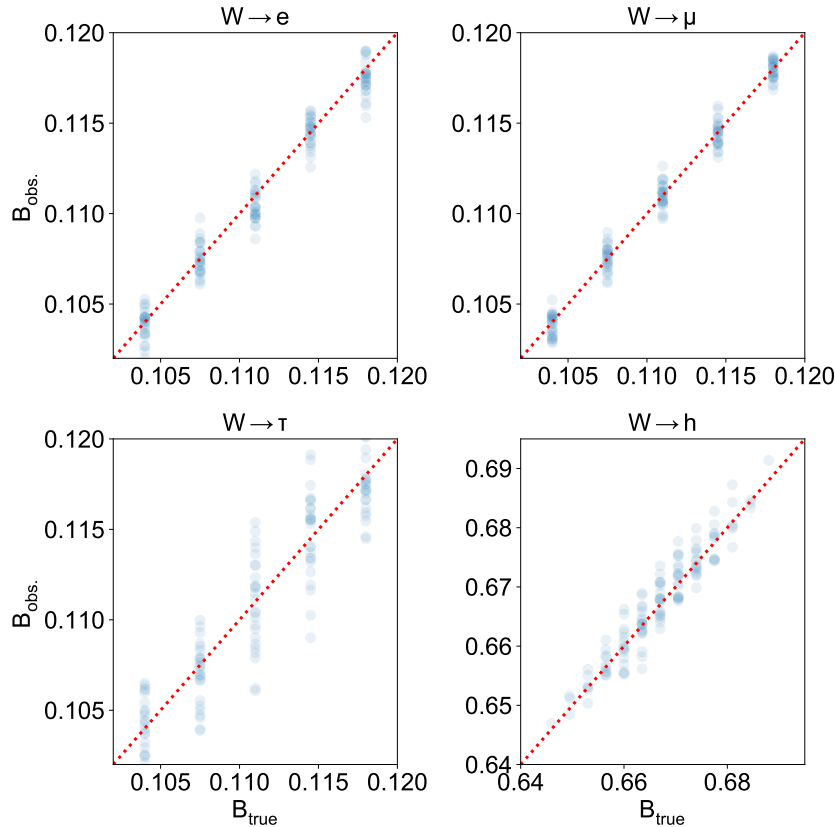


Figure 4.32. Results of bias test showing the value of each of the four branching fractions determined from the fit versus the value used to generate the pseudo-dataset. The red dashed line indicates a line of slope one passing through the origin.

This study also allows for an independent estimation of the uncertainty on each of the parameters. The resulting uncertainties estimated from the toy Monte Carlo datasets are found to be close to the values calculated by carrying out a numerical estimation of the NLL Hessian about its minimum. This comparison is shown in Figure 4.34.

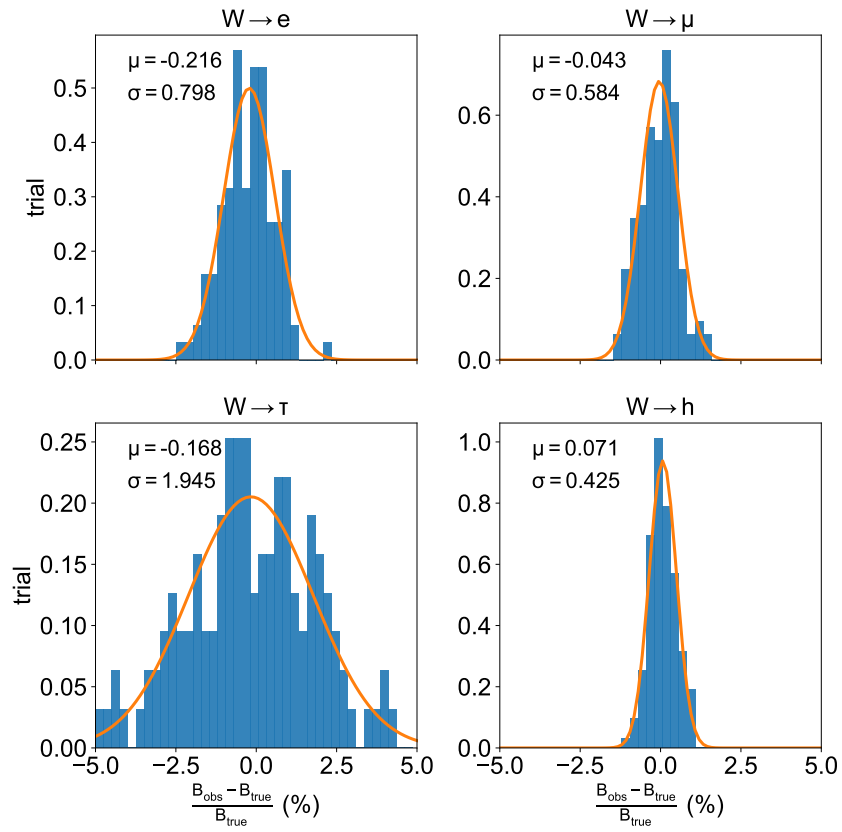


Figure 4.33. Histogrammed values of the bias measured for each of the scan points. The values of μ and σ denote the mean and standard error for each distribution.

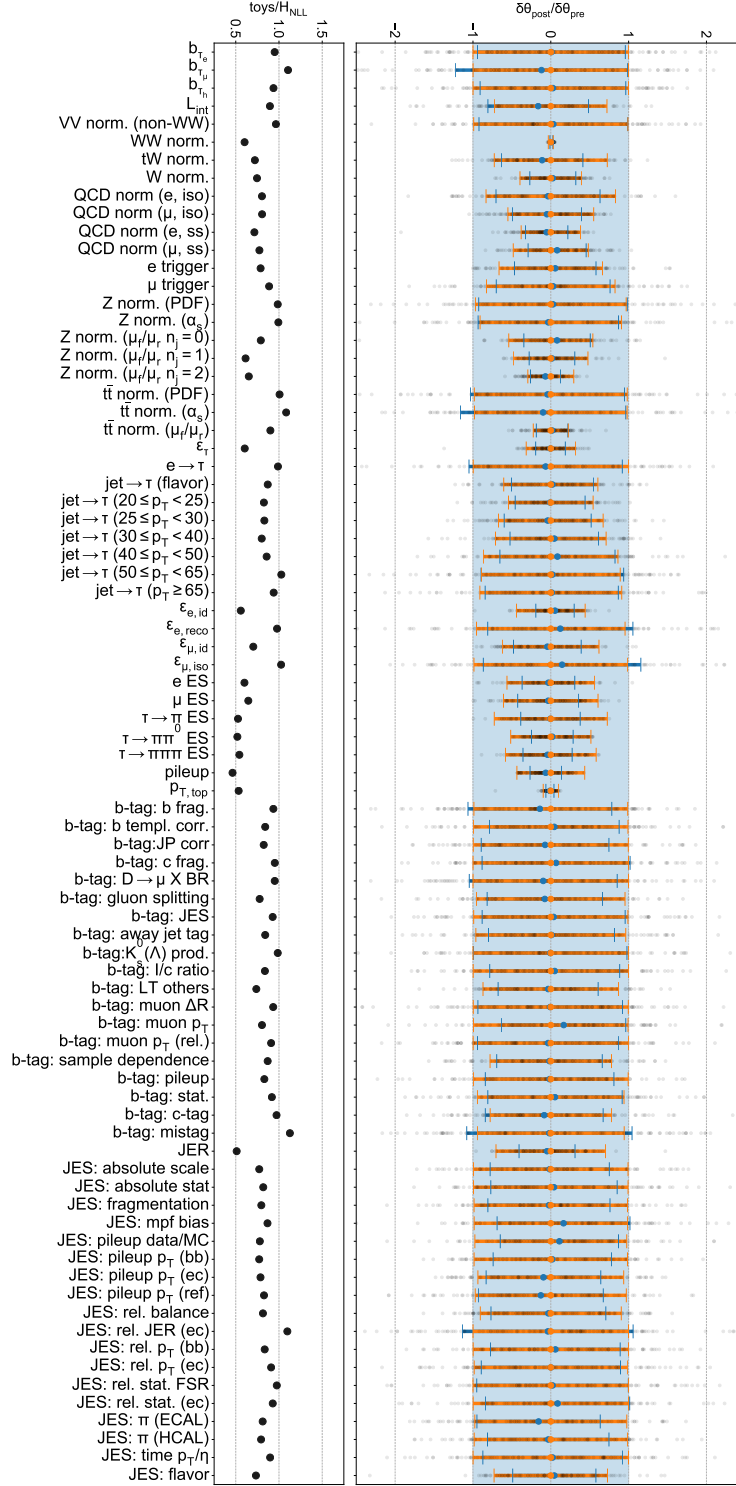


Figure 4.34. Pulls for nuisance parameters based on toy data while scanning the W boson leptonic branching fractions. The black dots indicate the values for individual trials, the blue bars show the standard error estimated from those trials, and the orange bar are the values estimated from the Hessian of the negative log-likelihood NLL .

4.5.2.4. Profile Likelihood Scans. The covariance matrix associated with the likelihood is estimated using numerical differentiation tools [156]. In addition to this, the variance associated with each parameter can be estimated by scanning over values of the parameter near its minimum and minimizing the likelihood while holding the parameter's value fixed. The resulting values of the NLL can then be fitted with a parabola to get the associated standard deviation. Because the full likelihood is just a sum of the Poisson likelihoods for each bin, the likelihood associated with each bin can also be studied. This is useful for analyzing which categories and which parts of the kinematic space are more sensitive to different fit parameters.

The result of scanning over the three leptonic branching fractions is shown in Figure 4.35. Curvatures of the NLL in each bin of the analysis are estimated in the same way and presented in Figures 4.36, 4.37, 4.38. The figure shows the estimated curvature (variance) in each bin normalized to the total variance. The simplest way to interpret what is shown is that a larger bar corresponds to a more significant contribution to the sensitivity to the parameter under consideration.

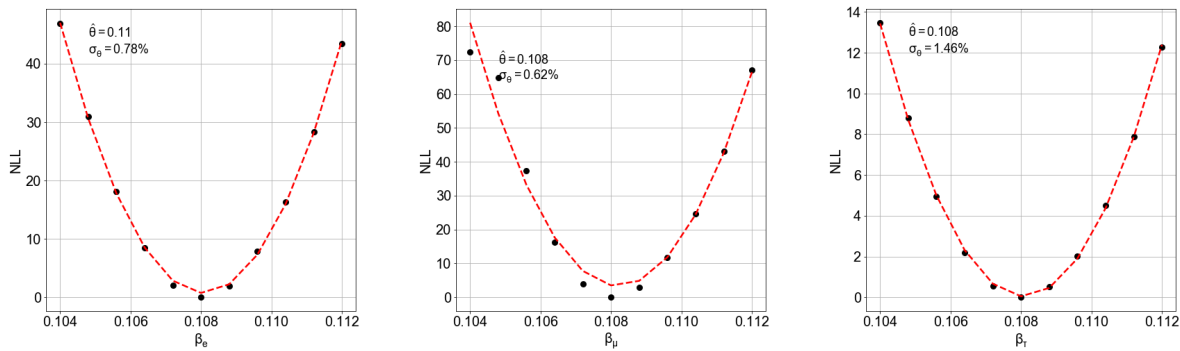


Figure 4.35. Values for the negative log-likelihood while scanning over the leptonic branching fractions of the W.

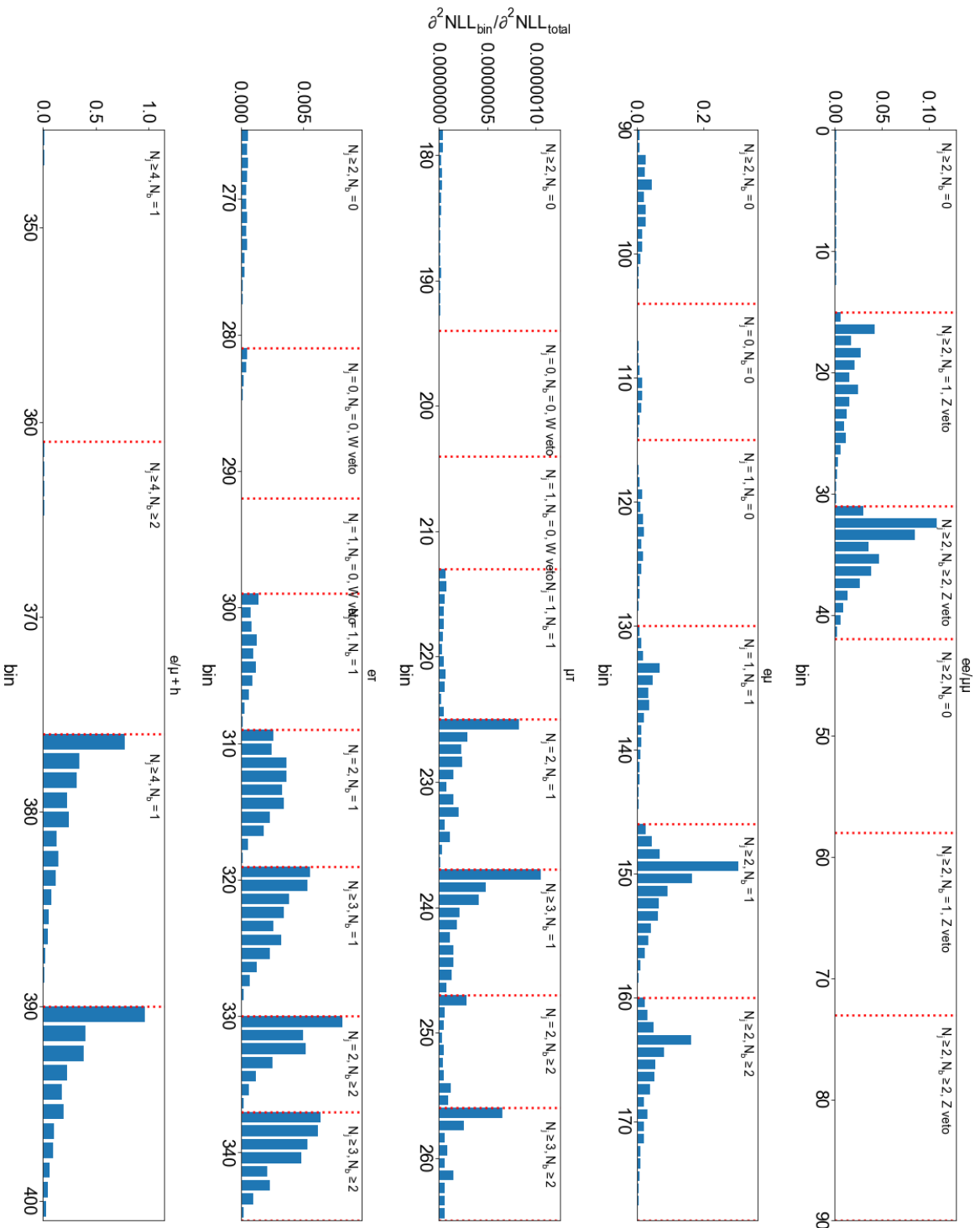


Figure 4.36. Bin-by-bin sensitivity for the electronic branching fraction.

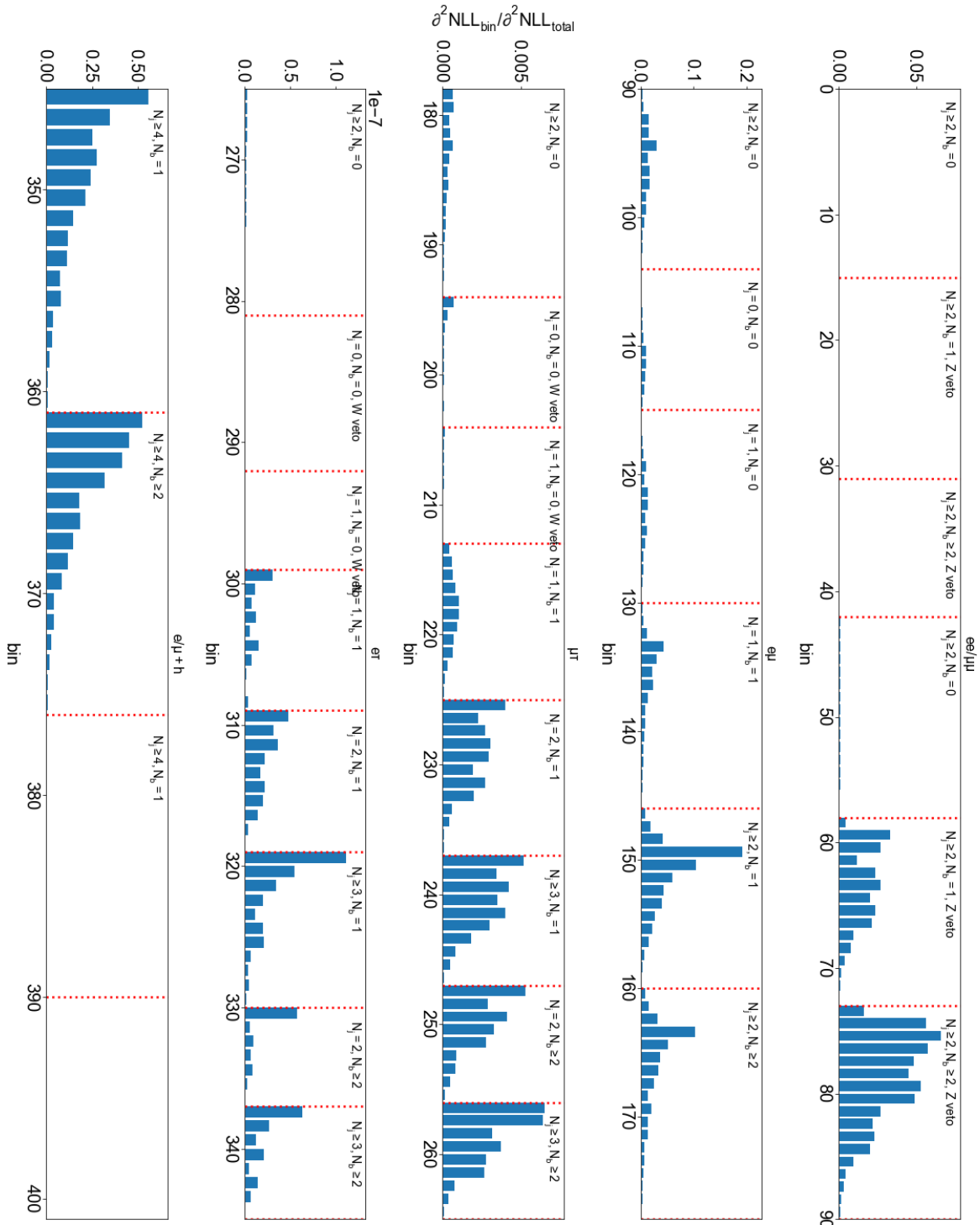


Figure 4.37. Bin-by-bin sensitivity for the muonic branching fraction.

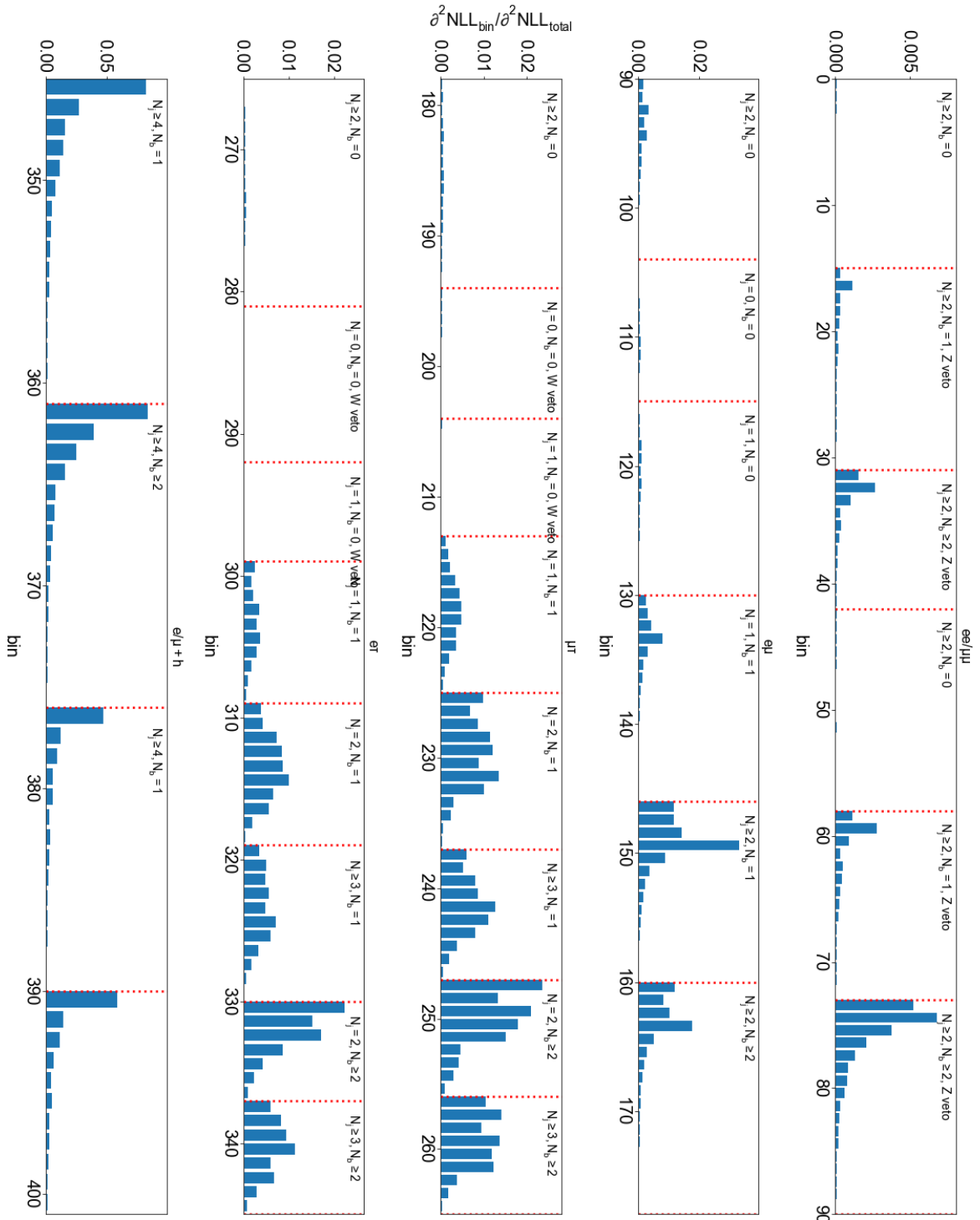


Figure 4.38. Bin-by-bin sensitivity for the tauonic branching fraction.

4.5.3. Counting Analysis

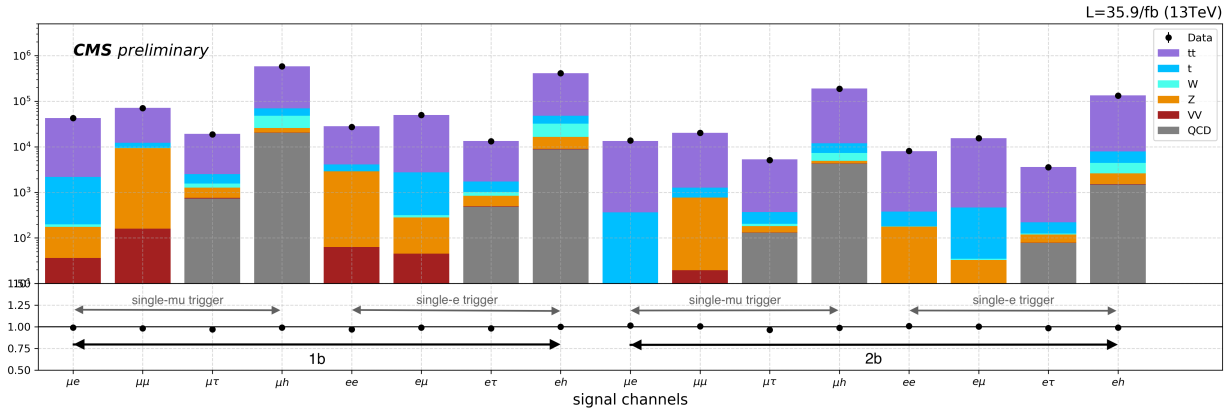


Figure 4.39. Channels are organized into four groups based on trigger type and b tag multiplicity. Counting analysis extracts W branching fractions from the yields of grouped channels.

In this approach, channels are divided into four mutually-exclusive groups based on the trigger types and the b tag multiplicities. The trigger types include the single-muon and the single-electron trigger. The b tag multiplicity can be either $n_b = 1$ or $n_b \geq 2$. The configuration of four channel groups is shown in Figure 4.39. Namely,

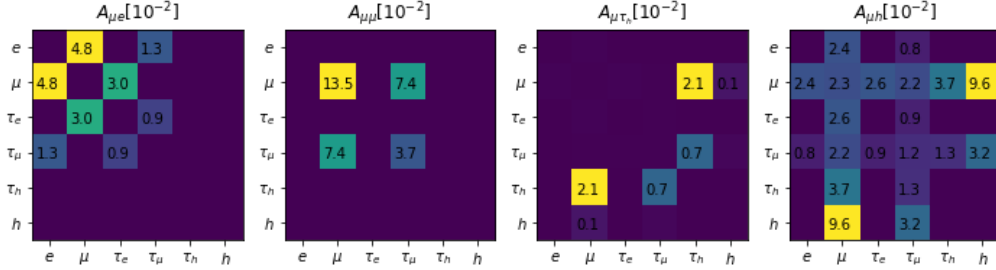
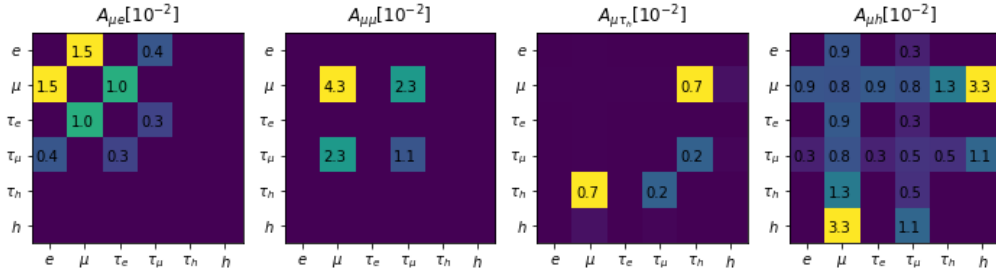
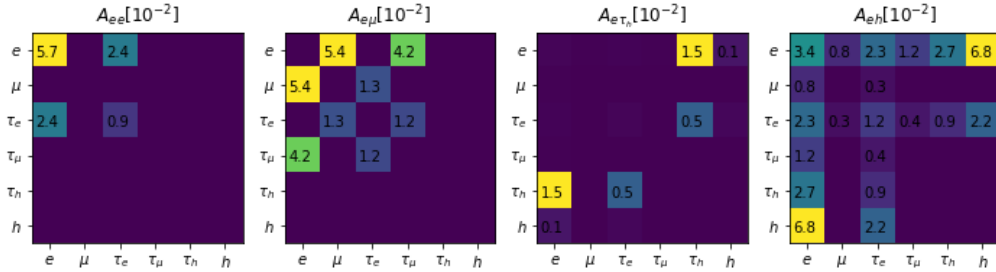
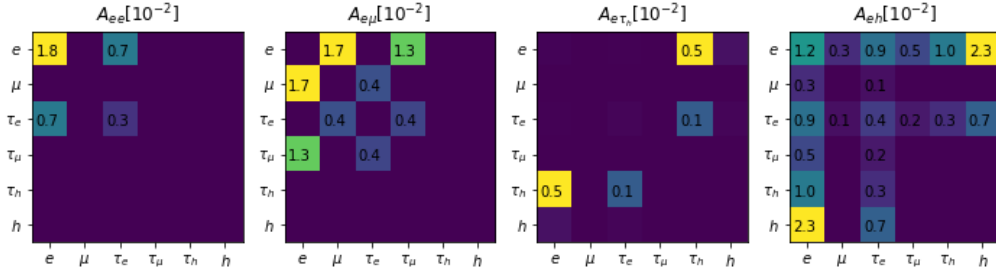
- single- μ trigger with $n_b = 1$ or $n_b \geq 2$: $\{\mu e, \mu \mu, \mu \tau, \mu h\}$.
- single-e trigger with $n_b = 1$ or $n_b \geq 2$: $\{ee, e\mu, e\tau, eh\}$.

where $e\mu$ and μe are mutually exclusive – $e\mu$ channel requires single-e trigger with $p_T^e > p_T^\mu$, while μe channel requires μ -trigger with $p_T^\mu < p_T^e$.

To reduce contamination from $j \rightarrow \tau$ fakes and QCD background, in the counting analysis, the thresholds of leptons' p_T and working point for the hadronic tau isolation are slightly tighten. This results in slightly different signal efficiencies comparing with the shape analysis. For the eight channels under consideration, the signal efficiencies determined from simulated $t\bar{t}$ and tW events are shown in Tables 4.14 and Figure 4.40.

4.5.3.1. Parameter Extraction. In each of the groups above, three branching fractions $\beta_e, \beta_\mu, \beta_\tau$ are extracted by solving a set of three quadratic equations. Then the results from

Table 4.14. Efficiency of $t\bar{t}+tW$ events, breakdown by 21 WW decay. Values are in percent.

channels with μ -trigger-1bchannels with μ -trigger-2bchannels with e -trigger-1bchannels with e -trigger-2bFigure 4.40. Efficiency matrices of eight channels with $n_b = 1$ and $n_b \geq 2$. The channels are grouped based on trigger types and b tag multiplicities.

all four groups are combined taking into account the uncorrelated statistical uncertainties and full-correlated systematic uncertainties. The details of the combination is described in

Section 4.6. Here we give the method of parameter extraction by establishing and solving quadratic equations.

The normalized yield X , which is constructed in a similar manner to the branching fractions, is the ratio of yield in one channel over the sum of yields in the channel group. For channel groups using single-electron and single-muon trigger, denoting the triggering lepton as $t \in \{\mu, e\}$, the normalized yields X 's are defined as

$$X_e = \frac{n^{te}}{n^{te} + n^{t\mu} + n^{t\tau_h} + n^{th}}, X_\mu = \frac{n^{t\mu}}{n^{te} + n^{t\mu} + n^{t\tau_h} + n^{th}}, X_\tau = \frac{n^{t\tau_h}}{n^{te} + n^{t\mu} + n^{t\tau_h} + n^{th}}, \quad (4.17)$$

where $n \equiv N - \sum_b N_b$ is the data yield with background subtracted. Based on Equation 4.11, the normalized yields $\{X_e, X_\mu, X_\tau\}$ from data should equal to the same calculation based on the efficiency \mathbf{E} matrix and the branching fraction matrix \mathbf{B} :

$$\begin{aligned} X_e &= \frac{\mathbf{E}_{ij}^{te} \mathbf{B}_{ij}}{\mathbf{E}_{ij}^{te} \mathbf{B}_{ij} + \mathbf{E}_{ij}^{t\mu} \mathbf{B}_{ij} + \mathbf{E}_{ij}^{t\tau_h} \mathbf{B}_{ij} + \mathbf{E}_{ij}^{th} \mathbf{B}_{ij}}, \\ X_\mu &= \frac{\mathbf{E}_{ij}^{t\mu} \mathbf{B}_{ij}}{\mathbf{E}_{ij}^{te} \mathbf{B}_{ij} + \mathbf{E}_{ij}^{t\mu} \mathbf{B}_{ij} + \mathbf{E}_{ij}^{t\tau_h} \mathbf{B}_{ij} + \mathbf{E}_{ij}^{th} \mathbf{B}_{ij}}, \\ X_\tau &= \frac{\mathbf{E}_{ij}^{t\tau_h} \mathbf{B}_{ij}}{\mathbf{E}_{ij}^{te} \mathbf{B}_{ij} + \mathbf{E}_{ij}^{t\mu} \mathbf{B}_{ij} + \mathbf{E}_{ij}^{t\tau_h} \mathbf{B}_{ij} + \mathbf{E}_{ij}^{th} \mathbf{B}_{ij}}. \end{aligned} \quad (4.18)$$

Plugging in the explicit form of \mathbf{E} and \mathbf{B} matrices in Equation 4.8 and 4.9 and the unitarity condition $\beta_h = 1 - \beta_e - \beta_\mu - \beta_\tau$, Equation 4.18 can be written as a set of three quadratic

equations with three unknowns $\{\beta_e, \beta_\mu, \beta_\tau\}$.

$$\begin{aligned}
 F_e(\beta_e, \beta_\mu, \beta_\tau) &= c_{e1}\beta_e^2 + c_{e2}\beta_\mu^2 + c_{e3}\beta_\tau^2 + c_{e4}\beta_e\beta_\mu + c_{e5}\beta_e\beta_\tau + c_{e6}\beta_\mu\beta_\tau \\
 &\quad + c_{e7}\beta_e + c_{e8}\beta_\mu + c_{e9}\beta_\tau + c_{e0} = 0, \\
 F_\mu(\beta_e, \beta_\mu, \beta_\tau) &= c_{\mu1}\beta_e^2 + c_{\mu2}\beta_\mu^2 + c_{\mu3}\beta_\tau^2 + c_{\mu4}\beta_e\beta_\mu + c_{\mu5}\beta_e\beta_\tau + c_{\mu6}\beta_\mu\beta_\tau \\
 &\quad + c_{\mu7}\beta_e + c_{\mu8}\beta_\mu + c_{\mu9}\beta_\tau + c_{\mu0} = 0, \\
 F_\tau(\beta_e, \beta_\mu, \beta_\tau) &= c_{\tau1}\beta_e^2 + c_{\tau2}\beta_\mu^2 + c_{\tau3}\beta_\tau^2 + c_{\tau4}\beta_e\beta_\mu + c_{\tau5}\beta_e\beta_\tau + c_{\tau6}\beta_\mu\beta_\tau \\
 &\quad + c_{\tau7}\beta_e + c_{\tau8}\beta_\mu + c_{\tau9}\beta_\tau + c_{\tau0} = 0,
 \end{aligned} \tag{4.19}$$

where the coefficients c_{lk} , with the index $l \in \{e, \mu, \tau\}$ corresponding to the three equations $F_e = 0, F_\mu = 0, F_\tau = 0$ and the index $k \in \{0, 1, 2, \dots, 9\}$, are fully determined by efficiency matrix \mathbf{E} and normalized yields $\{X_e, X_\mu, X_\tau\}$. The analytical result of c_{lk} is listed in Table 4.15.

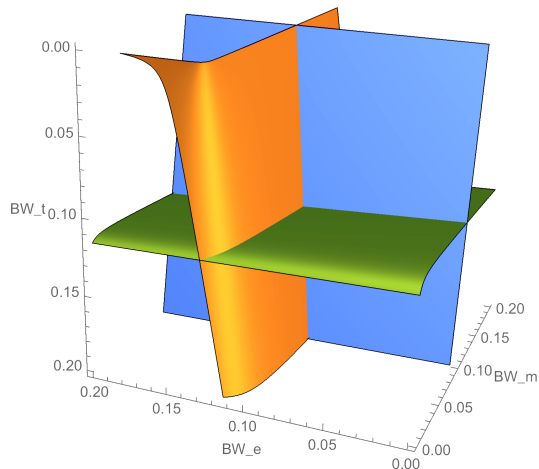


Figure 4.41. Visualization of Equation 4.19 in the $\{\beta_e, \beta_\mu, \beta_\tau\}$ parameter space. Each equation is a hyperbolic plane, while their intersection is the solution. Mathematically, there are 8 possible solutions. However, only one solution is physical, located with $\beta \in (0, 1)$.

Table 4.15. Coefficients of quadratic equations c_{lk} in terms of efficiency matrix E and normalized yields $\{X_e, X_\mu, X_\tau\}$, where the index $l \in \{e, \mu, \tau\}$ and the index $k \in \{0, 1, 2, \dots, 9\}$. In the table, $\Delta_{ij} \equiv E_{ij}^{tl} - X_l \times (E_{ij}^{\text{te}} + E_{ij}^{\text{t}\mu} + E_{ij}^{\text{t}\tau_h} + E_{ij}^{\text{th}})$ is a 6×6 matrix, where the lower index i, j are for the 6×6 elements.

c_{l0}	Δ_{66}
c_{l1}	$\Delta_{11} - 2\Delta_{16} + \Delta_{66}$
c_{l2}	$\Delta_{22} - 2\Delta_{26} + \Delta_{66}$
c_{l3}	$b_e^\tau b_e^\tau \Delta_{33} + b_\mu^\tau b_\mu^\tau \Delta_{44} + b_h^\tau b_h^\tau \Delta_{55} + 2b_e^\tau b_\mu^\tau \Delta_{34} + 2b_e^\tau b_h^\tau \Delta_{35} + 2b_\mu^\tau b_h^\tau \Delta_{45} - 2b_e^\tau \Delta_{15} - 2b_\mu^\tau \Delta_{25} - 2b_h^\tau \Delta_{56} + \Delta_{66}$
c_{l4}	$2\Delta_{12} - 2\Delta_{16} - 2\Delta_{26} + 2\Delta_{66}$
c_{l5}	$2b_e^\tau \Delta_{13} + 2b_\mu^\tau \Delta_{14} + 2b_h^\tau \Delta_{15} - 2b_e^\tau \Delta_{36} - 2b_\mu^\tau \Delta_{46} - 2b_h^\tau \Delta_{56} - 2\Delta_{16} + 2\Delta_{66}$
c_{l6}	$2b_e^\tau \Delta_{23} + 2b_\mu^\tau \Delta_{24} + 2b_h^\tau \Delta_{25} - 2b_e^\tau \Delta_{36} - 2b_\mu^\tau \Delta_{46} - 2b_h^\tau \Delta_{56} - 2\Delta_{26} + 2\Delta_{66}$
c_{l7}	$2\Delta_{16} - 2\Delta_{66}$
c_{l8}	$2\Delta_{26} - 2\Delta_{66}$
c_{l9}	$2b_e^\tau \Delta_{36} + 2b_\mu^\tau \Delta_{46} + 2b_h^\tau \Delta_{56} - 2\Delta_{66}$

In the $\{\beta_e, \beta_\mu, \beta_\tau\}$ parameter space, Equation 4.19 represents three hyperbolic planes. Figure 4.41 shows a visualization of the three hyperbolic planes in the $\{\beta_e, \beta_\mu, \beta_\tau\}$ parameter space. The intersection of the three planes is the solution to the three quadratic equations, which presents the measurement of branching fractions. Namely,

$$\begin{bmatrix} \beta_e \\ \beta_\mu \\ \beta_\tau \end{bmatrix} = \text{Solution} \begin{bmatrix} F_e(\beta_e, \beta_\mu, \beta_\tau) = 0 \\ F_\mu(\beta_e, \beta_\mu, \beta_\tau) = 0 \\ F_\tau(\beta_e, \beta_\mu, \beta_\tau) = 0 \end{bmatrix} \quad (4.20)$$

4.5.3.2. Assessment of Statistical Uncertainties. The statistical uncertainties of data are propagated to the branching fraction via the numerically calculated partial derivatives

$\partial_N \beta$. The statistical uncertainties of yields in different channels are treated as uncorrelated, and are summed in quadrature after being propagated to β .

The statistical uncertainties due to the simulation are estimated by the same error propagation approach. For $t\bar{t}$ and tW simulation, the statistical uncertainties are embedded in the statistical uncertainties of the E matrix based on Equation 4.10. The statistical uncertainty of efficiency, obtained by an integral of beta distribution, the conjugate of the binomial distribution, is propagated to the branching fractions via their partial derivatives with respect to efficiency, $\partial_\epsilon \beta$. The statistical uncertainties of 21 efficiencies in the E matrix are treated as uncorrelated and their impacts to β are summed in quadrature. For other background simulation, the statistical uncertainties are propagated to β via partial derivatives $\partial_{N_{\text{bkg}}} \beta$ similar to that of data.

4.5.3.3. Assessment of Systematic Uncertainties. The systematic uncertainties are estimated by varying the systematic parameters up and down, and then repeating the same process of parameter extraction. The corresponding deviations with respect to the nominal β represent the systematic uncertainties. Different systematic sources are treated as independent. The systematic uncertainties in different trigger- n_b groups are fully correlated.

4.5.3.4. Bias Study of Parameter Extraction. A test of parameter extraction is performed using toy MC datasets. In toy MC datasets, the yield N follows the normal distribution with a mean value equal to the expected yield based on simulated datasets and QCD estimation, and the standard deviation equals $\delta N = \sqrt{N}$. The branching fractions β are extracted from each toy MC dataset. In total, 2000 toy MC datasets are generated. The W to lepton branching fractions in the simulation is 10.8%, which is the ground truth to compare the extracted parameters. The distribution of 2000 $\{\beta_e, \beta_\mu, \beta_\tau\}$ extracted are shown in Figure 4.42. The centers of the distributions are consistent with the assumed

branching fraction in the simulation, while widths of distributions are consistent with the data statistical uncertainty calculated by error propagation.

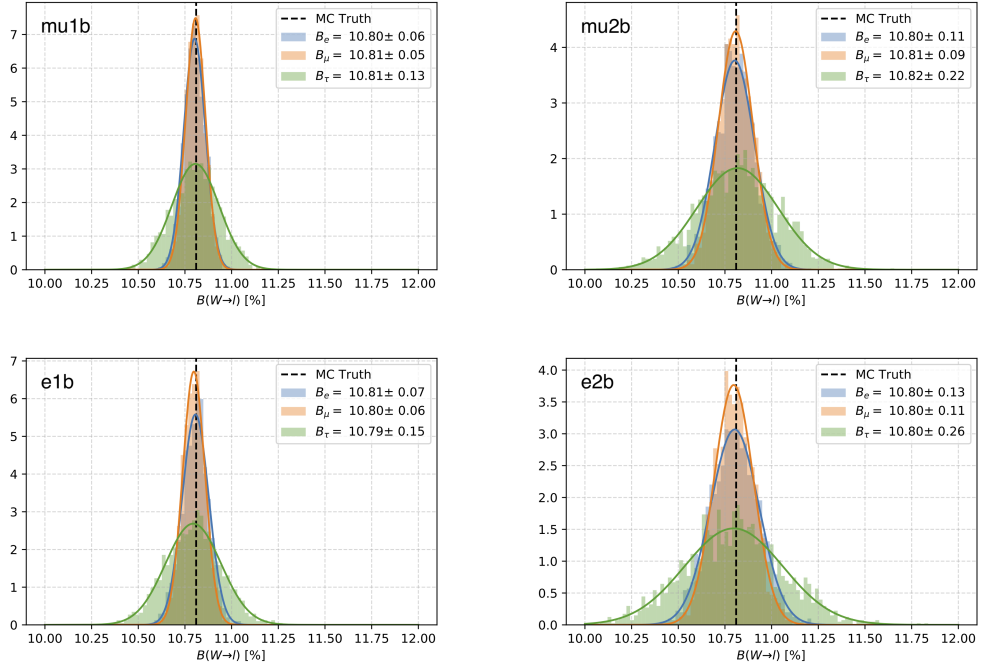


Figure 4.42. Distribution of $\{\beta_e, \beta_\mu, \beta_\tau\}$ extracted from 2000 toy MC datasets. The curves are Gaussian fit to the distributions.

4.6. Systematic Uncertainties

Various sources of systematic uncertainties are described in this sections. As discussed in Section 4.5, the treatment of systematics differs between the two analysis approaches: the shape analysis makes use of nuisance parameters; the counting analysis is carried out varying each systematic individually and assessing the variation on the estimates of the branching fractions. This section first presents the sources of systematic uncertainties and then estimates their impacts to the measurement in shape and counting analysis.

4.6.1. Sources of Systematic Uncertainties

4.6.1.1. Luminosity. The uncertainty on the CMS luminosity measurement is taken to be 2.5% for the 2016 run [157]. This uncertainty effects the overall scale of all predicted yields in a fully correlated manner.

4.6.1.2. Data-driven estimations for QCD background. The uncertainty is split into four normalization parameters: one for each of the final states $e\tau_h$, $\mu\tau_h$, eh , and μh .

4.6.1.3. Cross section for simulated processes. We assign the following uncertainties to the cross sections for simulated processes.

- $t\bar{t}$: 5%, (and PDF, α_s , μ_R/μ_F in shape analysis)
- tW : 5%
- $Z+jets$: 10%, (and PDF, α_s , μ_R/μ_F in shape analysis)
- $W+jets$: 10%
- $\gamma+jets$: 10%
- diboson: 10%

Since shape analysis also incorporates $Z+jets$ control regions and is sensitive to the $t\bar{t}$ cross-section, the cross-section of $Z+jets$ and $t\bar{t}$ is further decomposed into extra nuisance parameters, including PDF, α_s , μ_R/μ_F . The counting analysis does not have $Z+jets$ control regions and is insensitive to $t\bar{t}$ cross-section due to the construction of ratio of channels. So overall uncertainties of $t\bar{t}$ and $Z+jets$ are used.

4.6.1.4. WW p_T reweighting. The shape analysis treats WW as a signal. The reweighting of the WW p_T is accounted for by including two nuisance parameter for the resummation and factorization variations as described in Section 4.3.1. In the $t\bar{t}$ signal region employed by the counting analysis, there is little contamination from WW process. Thus the WW p_T reweighting and associated systematic effects are neglected.

4.6.1.5. top p_T reweighting. Top p_T reweighting is applied in nominal case because it is observed as unnecessary, but is used to estimate the associated uncertainties. In shape analysis, the uncertainty on the top p_T scale is included as a one-sided morphing templates generated based on previous top studies in shape analysis and it turns out to be highly constrained. In counting analysis, the construction of ratios allow cancellations of $t\bar{t}$ related systematics and 1% of the top p_T scale is used as the size of uncertainty, which gets propagated through the parameter extraction.

4.6.1.6. Pileup. Each event is weighted with a scale factor to account for differences in the pileup spectrum between data and simulation. The uncertainty on the event weights is mainly due to the uncertainty on the minimum bias cross section. The nominal minimum bias cross section is 69.2 ± 3.18 mb. The effect of the uncertainty is propagated through the analysis by calculating the distribution of pileup in data while varying the cross section up and down by one standard deviation.

4.6.1.7. Trigger efficiency.

- *single muon:* 0.5% normalization uncertainty on all categories where the triggering lepton is a muon.
- *single electron:* a p_T and η dependent correction is applied to events triggered with single electron trigger. The correction and uncertainty is measured with tag-and-prob approach described in 4.3.3. The uncertainty accounts for the statistical uncertainty, the variation due the triggering of the tag lepton, and variation due to the probe electron.

4.6.1.8. Muon reconstruction.

- *identification/isolation:* the uncertainties are accounted for each muon and are based on values provided by the POG.

- *energy scale*: to account for the muon energy scale, the muon p_T is varied by $\pm 1\sigma$ (0.2%).

4.6.1.9. Electron reconstruction.

- *identification/isolation*: the uncertainties provided per electron are taken from values provided by the POG.
- *reconstructions*: treated the same as the identification uncertainty. Scale factors and their uncertainties are only η dependent.
- *energy scale*: The electron energy scale is assumed to be known at the 0.5% level, and is assigned a nuisance parameter that modifies the change to the shape of the relevant kinematic quantity.

4.6.1.10. Tau reconstruction.

- *identification*: the τ_h POG recommends a 5% uncertainty on the scale factor applied to simulation. In shape analysis, because a control region is included to provide an *in situ* evaluation of the τ_h efficiency scale factor, the scale factors are included as p_T -dependent nuisance parameter in seven p_T bins.
- *jet $\rightarrow \tau_h$* : scale factors and uncertainties for jets faking taus were derived based on a dilepton plus reconstructed tau control region. A nuisance parameter is assigned to each p_T bin used to measure the scale factor and an overall normalization nuisance parameter is assigned to account for any difference in rate between light and heavy jets.
- *$e \rightarrow \tau_h$* : a single normalization nuisance parameter is included to templates where an electron is misreconstructed as a hadronically decaying tau. The counting analysis neglects this uncertainty because the contribution of electron faking τ_h is only sizable in $Z \rightarrow \tau_e \tau_h$ control region, not considered by the counting analysis.

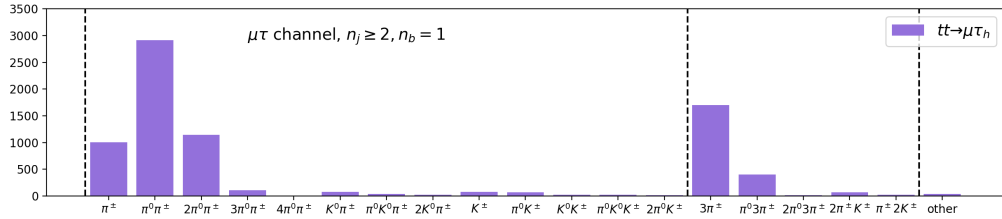


Figure 4.43. Distribution of gen-level τ_h decay modes of $t\bar{t} \rightarrow \mu\tau_h$ simulated events selected in the $\mu\tau_h$ channel.

- *energy scale*: the tau energy scale is corrected in correspondence with POG recommendations and an uncertainty of 1.2% per decay mode is assigned. These are included as three shape uncertainties depending on the reconstructed decay mode of the hadronically decaying tau.

In addition, the uncertainties of different τ_h decay widths are investigated. Currently the world average of the major τ_h decay widths have about 0.5-1.0% uncertainties. Five highest τ_h branching fractions include

$$\mathcal{B}(\tau_h \rightarrow \pi^\pm) = 0.1082(5), \quad \mathcal{B}(\tau_h \rightarrow \pi^\pm \pi^0) = 0.2549(9), \quad \mathcal{B}(\tau_h \rightarrow \pi^\pm 2\pi^0) = 0.0926(10),$$

$$\mathcal{B}(\tau_h \rightarrow 3\pi^\pm) = 0.0931(5), \quad \mathcal{B}(\tau_h \rightarrow 3\pi^\pm \pi^0) = 0.0462(5).$$

Since different decay modes are reconstructed separately by the CMS τ_h identification and thus have different efficiencies. The uncertainties of different τ_h widths could propagate to the τ_h identification efficiencies and lead to some impacts on the final results. To decide the impact, we tag the generator-level decay mode of reconstructed τ_h and vary the event weight accounting to the relative uncertainty of the tau decay branching fraction. Figure 4.43 shows the distribution of gen-level τ_h decay modes of $t\bar{t} \rightarrow \mu\tau_h$ simulated events selected in the $\mu\tau_h$ channel. Considering the above five major τ_h decay mode, the corresponding uncertainties on the $\mathcal{B}(W \rightarrow \ell\nu)$ are found to be less than 0.1% relatively, small enough to neglect.

4.6.1.11. Jet reconstruction. Jet systematics impact the analysis by modifying the acceptance of events in the various jet multiplicity categories. With that in mind, the uncertainty is taken into account by varying the various sources of jet uncertainties and assessing the resulting effect on the jet and b tag multiplicities.

- *energy scale:* the jet energy scale is varied by the various uncertainty sources on the jet energy corrections provided by the JetMET POG. These are included as 18 shape nuisance parameters (the lepton kinematic quantities which are fit are generally not affected by variation of the jet energy scale, but migration between different b tag categories does happen)
- *resolution:* the jet energy is corrected in simulation to account for the difference in resolution between data and simulation. The correction is applied per jet and is dependent on the jet p_{T} . Consequently, there is an associated uncertainty. The overall effect of this is estimated by varying the scale factor up and down one standard deviation and propagating the effect to the morphing templates.

4.6.1.12. b-tagging. The b tag modelling in simulation is corrected to better describe the data based on scale factors. The uncertainty on the correction is assessed based on up and down variations of b tagging and mistagging scale factors supplied by the b tag POG. The b tag uncertainties are factorized based on the various sources of uncertainty considered in the calculation of the scale factors. The variation is propagated through the analysis through the inclusion of shape nuisance parameters for both b tagging and mistagging variation.

4.6.1.13. Theory/simulation modelling. In addition to the normalization uncertainties coming from PDF, QCD scale, and uncertainty on α_s , several other theory uncertainties are accounted for. These are only included for $t\bar{t}$ processes and are applied as recommended by TOP PAG.

- *ISR/FSR*: variations to α_S affecting both ISR and FSR are evaluated based on dedicated $t\bar{t}$ MC samples. This is done for ISR and FSR independently. These variations are propagated through the analysis through morphing templates.
- *ME-PS matching scale*: matrix element to parton shower matching is regulated at the generator level by the *hdamp* parameter. This parameter is varied from the nominal value of $1.58^{+0.66}_{-0.59}$ in dedicated MC samples and propagated through morphing templates.
- *Underlying event*: modelling of the underlying event is dependent on the Pythia tune that is used (in the case of this analysis, CUETP8M2T4) [158]. Dedicated samples are generated varying the appropriate parameters and the variation in efficiency is propagated through the analysis with morphing templates.

There are two issues with these uncertainty sources that are worth considering. The first is that the variations due to these sources of uncertainty are estimated from dedicated MC samples. This leads to a fairly sizeable statistical uncertainty, and can lead to exaggerated uncertainties and strange behavior in the morphing templates (e.g., both the up and down variation will predict yields below/above the nominal sample). Also, the size of the uncertainty resulting from the FSR variation is very large (up to 20%) in the eh categories. This level of variation would be corrected for in the scale factors accounting for the difference in ID/misID efficiency for identified τ_h candidates, and that uncertainty in general would be much smaller, below 5%.

To derive the correction for these dedicated MC samples, we calculate the probabilities of reconstructing taus in the nominal and dedicated $t\bar{t}$ events. The origins of the reconstructed taus are tagged based on the matching to the gen-level particles. Both Tight and VTight WP of tau identification are considered. The changes in the tau id and misid due to the FSR up and down variation are shown in Figure 4.44. The changes due to the ISR, MEPS, UE

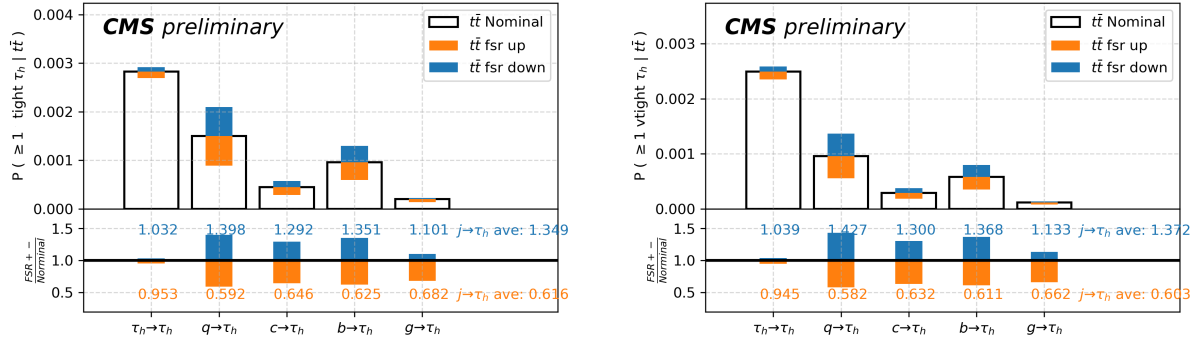


Figure 4.44. Effect of final state radiation on the τ_h identification and $j \rightarrow \tau_h$ misidentification obtained from the dedicated and the nominal $t\bar{t}$ samples. The Tight and VTight WP are shown on the left and right, respectively.

up and down variations are shown in Figure 4.45. It is clear that the FSR has a considerable impact on the τ_h id and misid that needs removal, while the effect from the ISR, MEPS and UE are neglectable.

The FSR dedicated $t\bar{t}$ samples are corrected using the SF in Figure 4.44. The up and down variations given by the dedicated MC samples lead to envelopes on the $t\bar{t}$ event efficiencies. As discussed in Section 4.5, there are 21 $t\bar{t}$ event efficiencies corresponding to 21 different WW decay scenarios. For VTight WP, the 21 envelopes on efficiencies due to FSR, ISR, MEPS, and UE variations are shown in Figure 4.46-4.49. Due to the finite statistics of the dedicated MC samples, the envelopes edges are smeared by the MC statistics, which are also shown in the Figure 4.46 - 4.49.

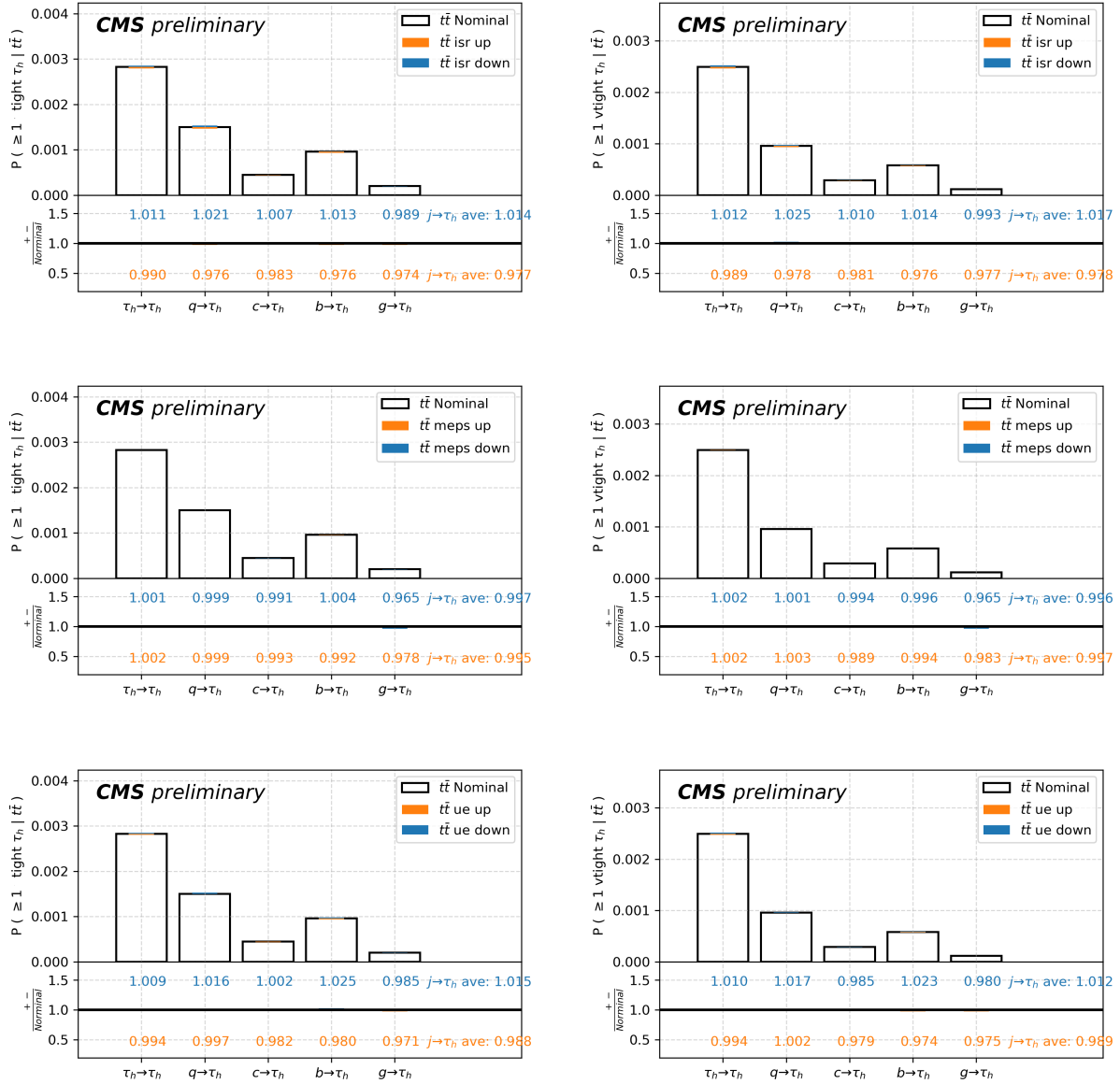


Figure 4.45. ISR, MEPS, UE effect on the τ_h identification and $j \rightarrow \tau_h$ misidentification obtained from the dedicated and the nominal $t\bar{t}$ samples. The Tight and VTight WP are shown on the left and right, respectively.

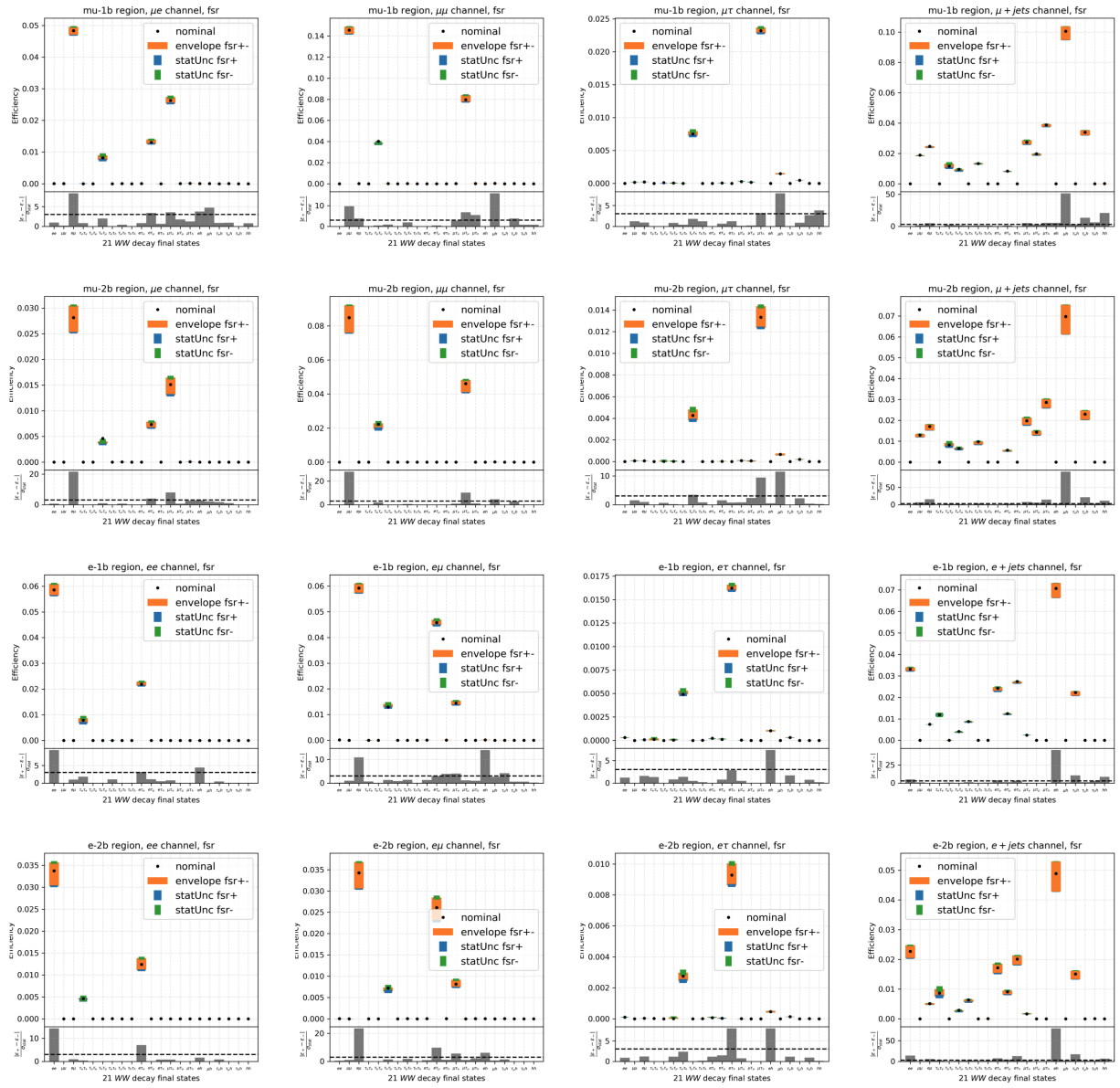


Figure 4.46. envelopes on 21 efficiencies due to final state radiation (FSR) uncertainty. VTight WP is shown.

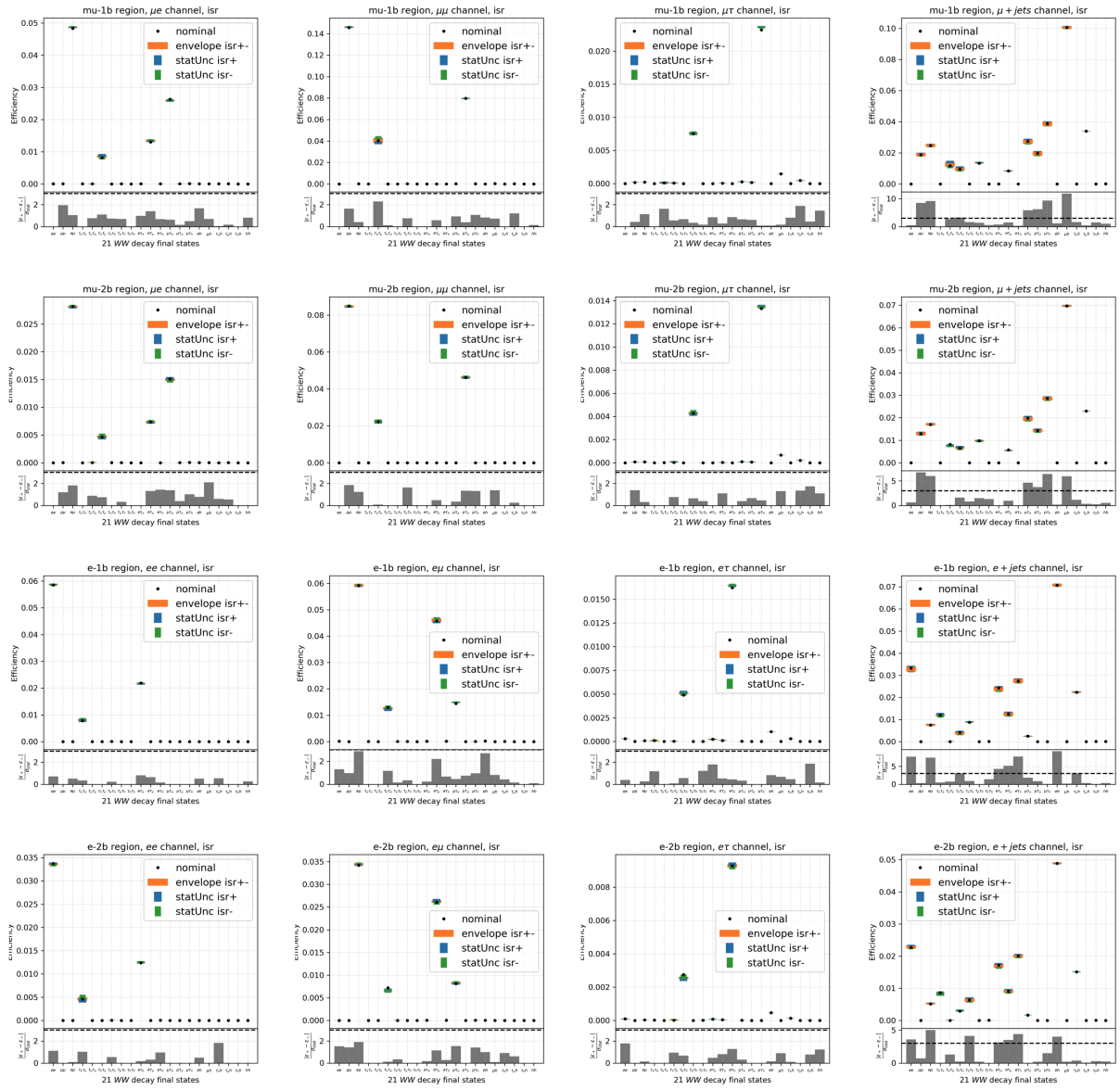


Figure 4.47. Envelopes on 21 efficiencies due to initial state radiation (ISR) uncertainty. VTight WP is shown.

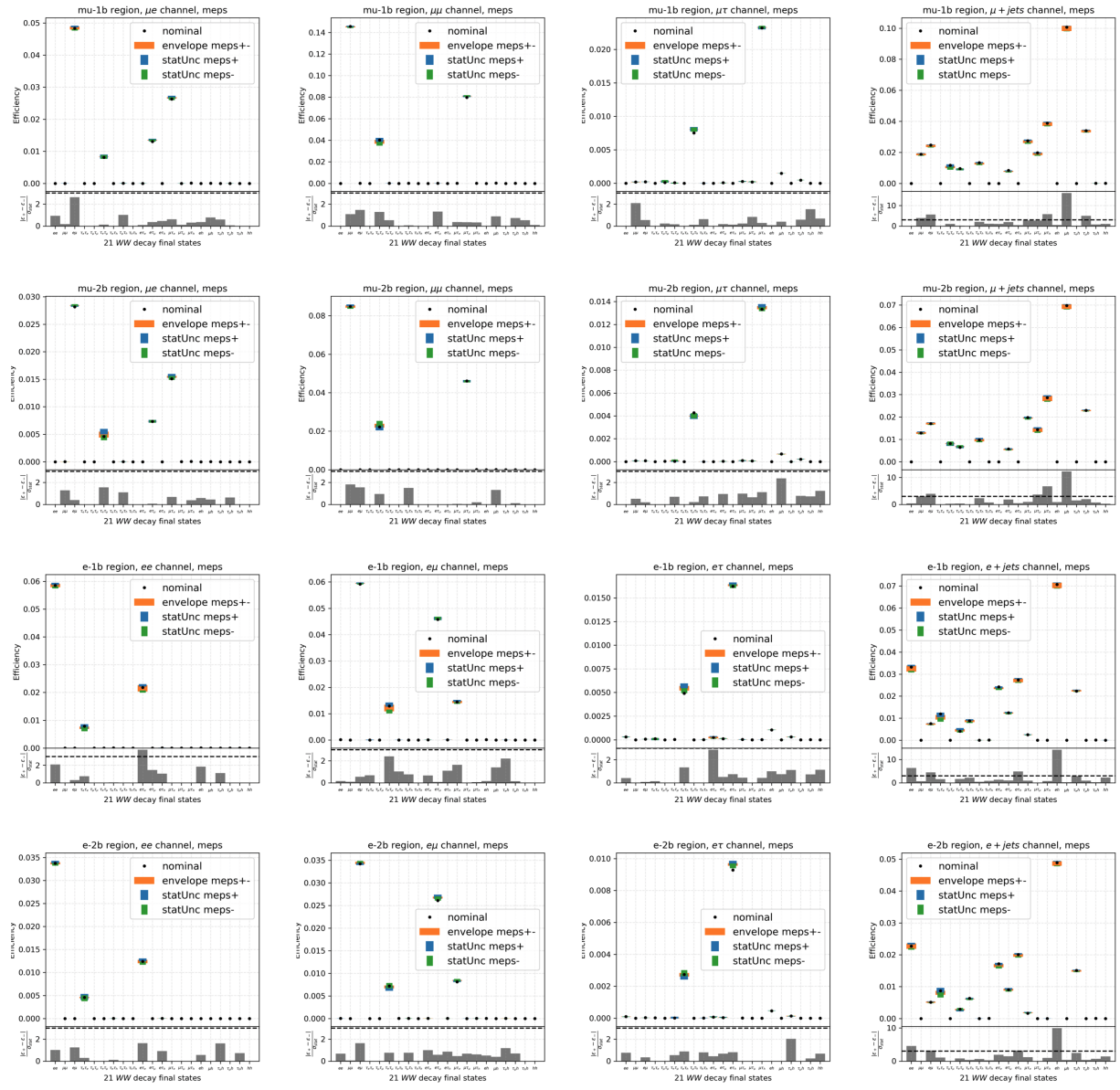


Figure 4.48. Envelopes on 21 efficiencies due to parton shower matching (ME-PS) uncertainty. VTight WP is shown.

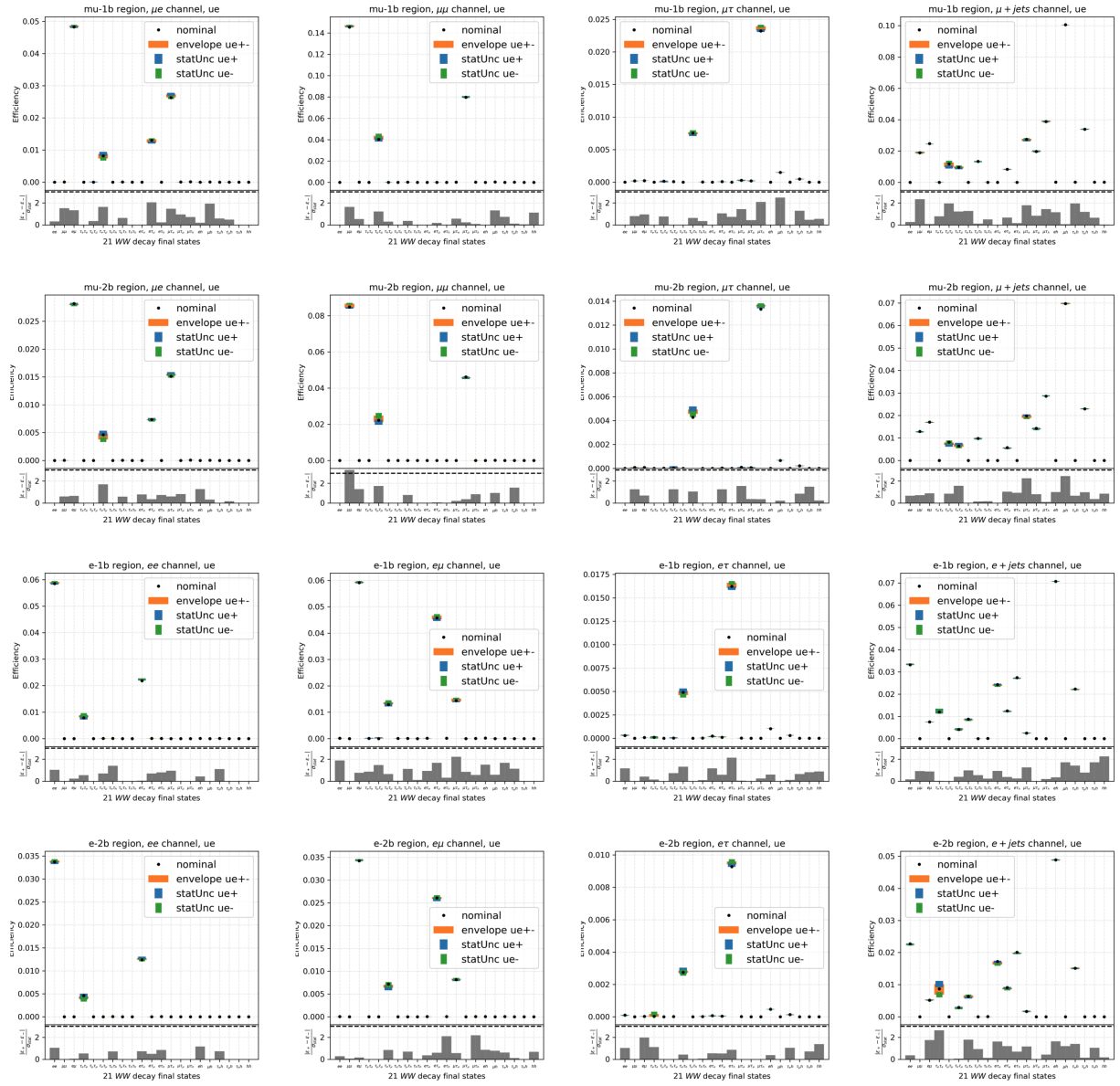


Figure 4.49. Envelopes on 21 efficiencies due to underline event (UE) uncertainty. VTight WP is shown.

4.6.2. Shape Analysis

As described previously, each source of uncertainty is accounted for in the shape analysis by including one or more associated nuisance parameters. After minimizing the likelihood, post-fit values for the nuisance parameters and their associated uncertainties are obtained. This is illustrated in Figure 4.53. In general, the pulls on the nuisance parameters do not exceed two standard deviations of their initial uncertainty, but many of the nuisance parameters do become constrained. Additionally, the correlations for each parameter can be obtained and are displayed in Figure 4.51. In order to isolate the effect of each nuisance parameter on the uncertainty of the branching fractions, the minimization is repeated while individually fixing each nuisance parameter either to its post-fit value plus or minus the post-fit uncertainty. The result of this process is shown in Figure 4.53.

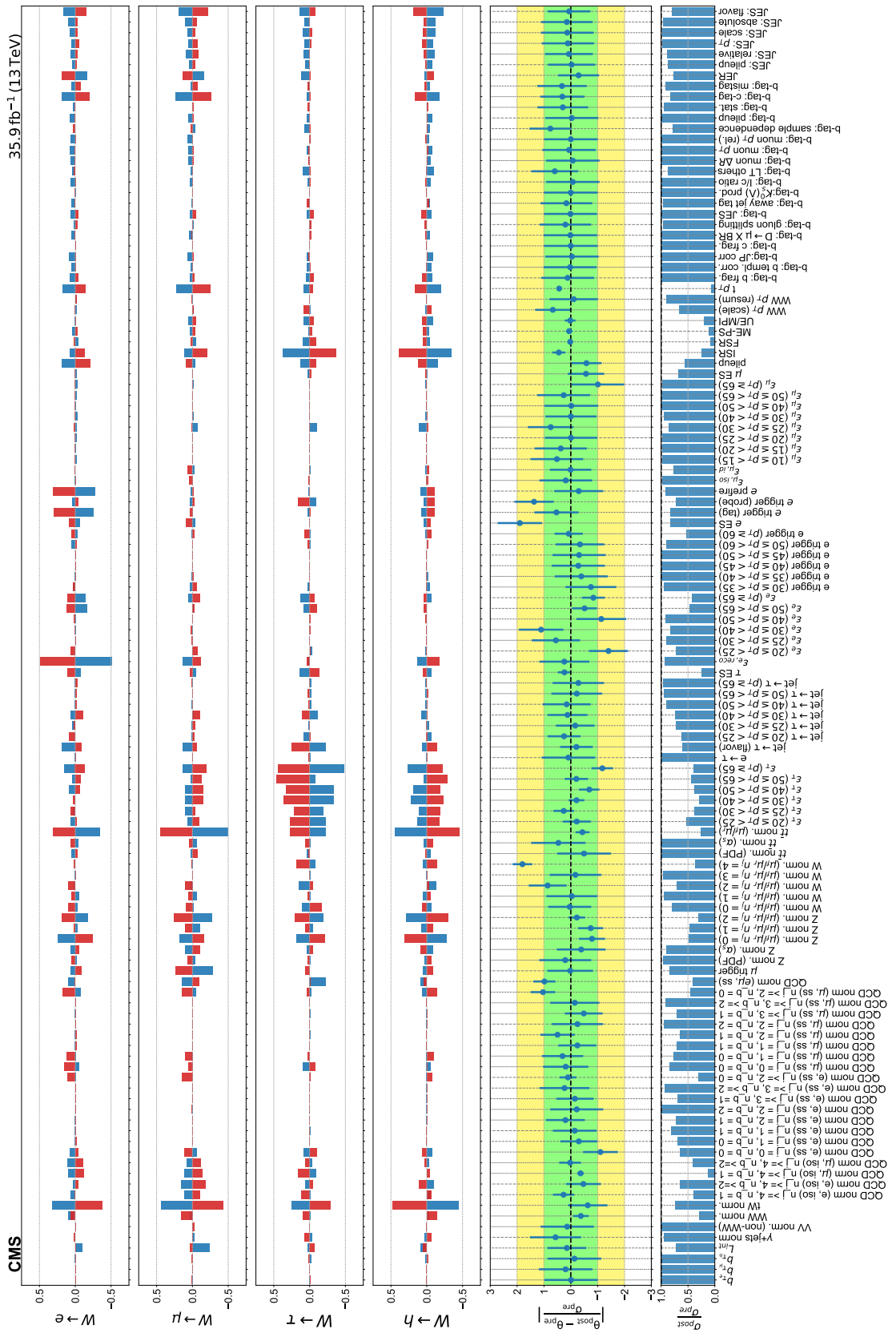


Figure 4.50. Pulls and constrain of all non-MC statistic nuisance parameters after minimizing the likelihood.

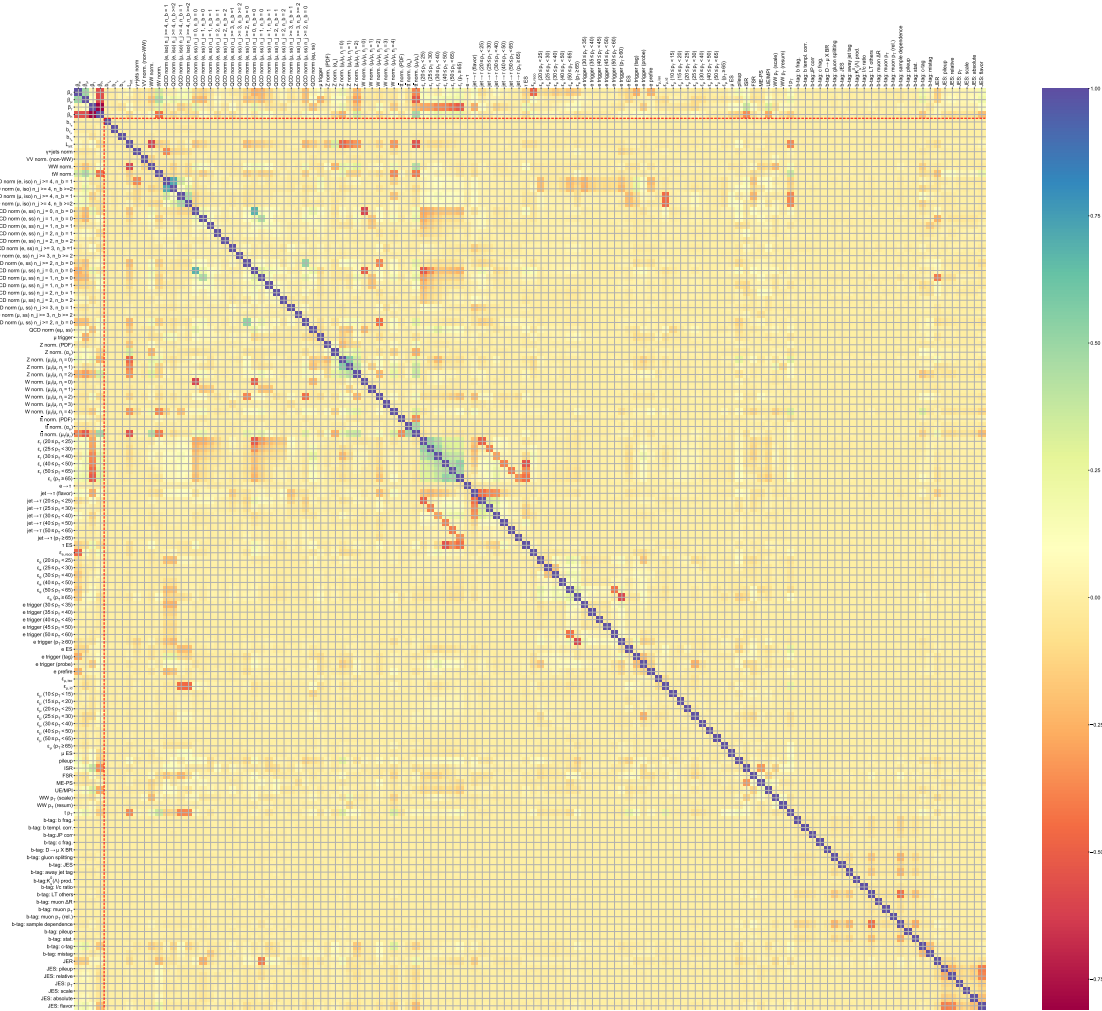


Figure 4.51. Correlation matrix for branching fractions and nuisance parameters. This does not include the nuisance parameters associated with bin-by-bin MC statistical uncertainty.

4.6.3. Counting Analysis

For the counting analysis, the systematics are assessed individually by varying up and down the sources of systematic uncertainties. The same branching fraction extraction is repeated with the variated systematic parameter. The change in the branching fractions with respect to the nominal value is treated as the systematic uncertainty resulting from a given source of systematics.

Recall that channels are divided into four groups based on the trigger types and b tag multiplicities, $(\mu 1b, \mu 2b, e 1b, e 2b)$, each of which produces one $\mathcal{B}(W \rightarrow \ell\nu)$ measurement. Table 4.16 shows the uncertainties of $\mathcal{B}(W \rightarrow \ell\nu)$ in these four groups due to each individual source of systematics. The combine of the four groups assumes

- (1) one single source of systematics is fully correlated among the four groups.
- (2) different sources of systematics are mutually independent.

Therefore, the chi-squared in the combine can be written as

$$\chi^2(\beta) = (\beta_0 - \mathbf{A}\beta)^T \mathbf{V}^{-1} (\beta_0 - \mathbf{A}\beta) \quad (4.21)$$

where $\beta = [\beta_e, \beta_\mu, \beta_\tau]^T$ is the combined branching fraction, and β_0 is the nominal value of the four measurements in the $\mu 1b, \mu 2b, e 1b, e 2b$ group, defined as

$$\beta_0 = \left[\beta_e^{\mu 1b}, \beta_\mu^{\mu 1b}, \beta_\tau^{\mu 1b}, \quad \beta_e^{\mu 2b}, \beta_\mu^{\mu 2b}, \beta_\tau^{\mu 2b}, \quad \beta_e^{e 1b}, \beta_\mu^{e 1b}, \beta_\tau^{e 1b}, \quad \beta_e^{e 2b}, \beta_\mu^{e 2b}, \beta_\tau^{e 2b} \right]^T, \quad (4.22)$$

and $\mathbf{A} = [I_{3 \times 3}, I_{3 \times 3}, I_{3 \times 3}, I_{3 \times 3}]^T$ is a 12×3 matrix consist of four 3×3 identity matrices. \mathbf{V} is the variance matrix for the 12 elements in β_0 , which combines the various sources of statistical and the systematic uncertainties.

$$\mathbf{V} = \sum_{n \in \text{data, MC}} (\Delta_n \beta_0) \otimes (\Delta_n \beta_0) + \sum_{\theta \in \text{syst}} (\Delta_\theta \beta_0) \otimes (\Delta_\theta \beta_0). \quad (4.23)$$

where $\Delta_\theta \beta_0$ is the variation of $\mathcal{B}(W \rightarrow \ell\nu)$ with respect to one sigma of systematic parameter θ , and the absolute value of $\Delta_\theta \beta_0$ are shown as rows in Table 4.16. The statistical and systematic part of the \mathbf{V} matrix is shown in Figure 4.52. The combined β_ℓ can be analytically calculated:

$$\beta = (\mathbf{A}^T \mathbf{V}^{-1} \mathbf{A})^{-1} (\mathbf{A}^T \mathbf{V}^{-1}) \beta_0, \quad \text{with } \text{Var}[\beta] = (\mathbf{A}^T \mathbf{V}^{-1} \mathbf{A})^{-1}. \quad (4.24)$$

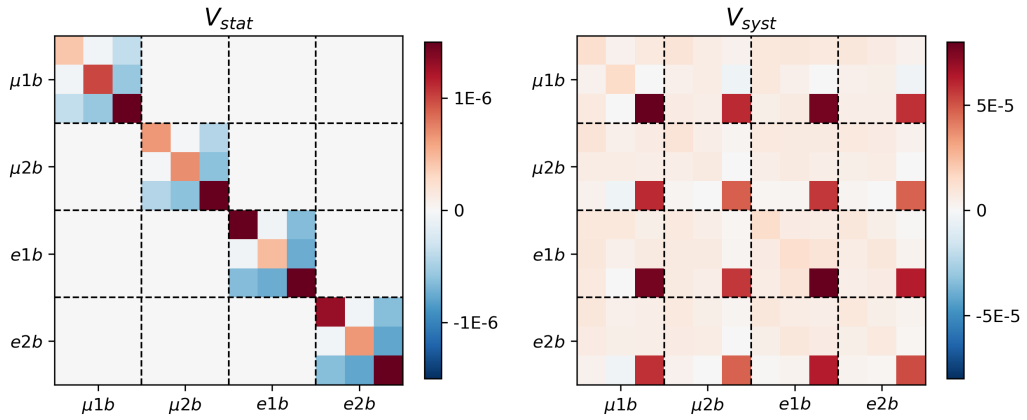


Figure 4.52. The statistical and systematic part of the \mathbf{V} matrix.

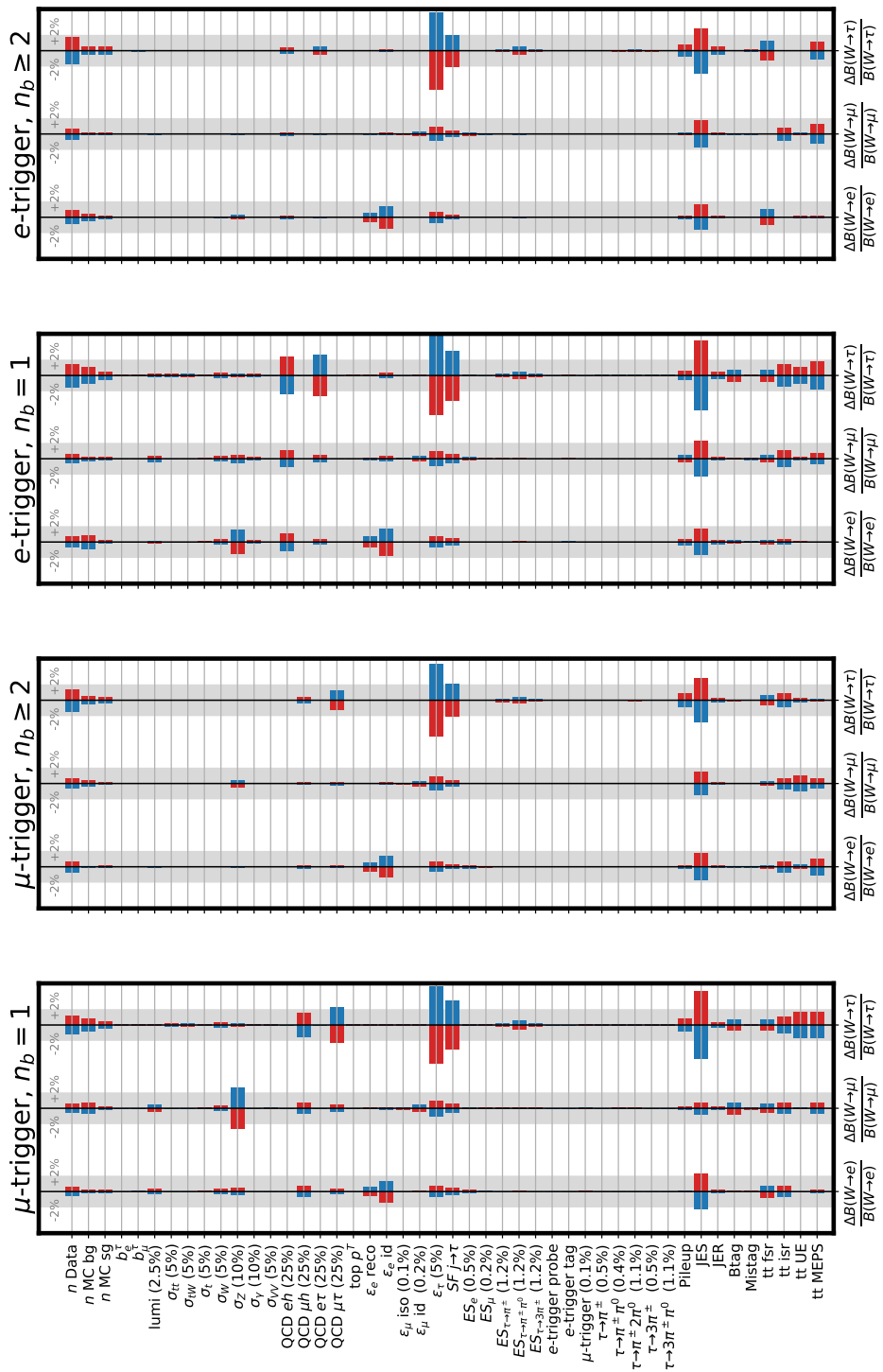


Figure 4.53. Statistical uncertainties and impacts of systematic parameters in counting analysis.

Table 4.16. Statistical and systematic uncertainties in counting analysis.

Error Source	μ -1b			μ -2b			e -1b			e -2b		
	B_e	B_μ	B_τ	B_e	B_μ	B_τ	B_e	B_μ	B_τ	B_e	B_μ	B_τ
StatErr of Data	0.543	0.533	1.243	0.714	0.637	1.492	0.743	0.557	1.520	0.904	0.707	1.807
StatErr of bg MC	0.178	0.745	0.767	0.110	0.411	0.501	0.897	0.257	1.065	0.494	0.137	0.521
StatErr of sg MC	0.168	0.151	0.415	0.189	0.165	0.428	0.217	0.176	0.503	0.233	0.192	0.520
PDG err of Br_e^τ	0.002	0.019	0.029	0.002	0.019	0.029	0.003	0.019	0.029	0.003	0.020	0.030
PDG err of Br_μ^τ	0.047	0.017	0.098	0.047	0.017	0.099	0.041	0.013	0.101	0.043	0.013	0.106
2.5% err of luminosity	0.330	0.461	0.120	0.093	0.064	0.049	0.135	0.390	0.204	0.002	0.101	0.092
5% err of tt XS	0.002	0.000	0.151	0.009	0.015	0.032	0.021	0.011	0.148	0.011	0.002	0.003
5% err of tW XS	0.002	0.001	0.157	0.010	0.015	0.033	0.022	0.012	0.155	0.011	0.002	0.004
5% err of t XS	0.062	0.062	0.033	0.053	0.052	0.058	0.063	0.060	0.032	0.052	0.054	0.040
5% err of W+Jets XS	0.343	0.354	0.325	0.068	0.068	0.066	0.349	0.347	0.366	0.065	0.066	0.084
10% err of Z+Jets XS	0.495	2.655	0.237	0.122	0.491	0.055	1.576	0.501	0.173	0.275	0.104	0.041
10% err of γ +Jets XS	0.020	0.019	0.029	0.005	0.005	0.007	0.249	0.247	0.213	0.058	0.058	0.081
10% err of VV XS	0.004	0.044	0.027	0.001	0.010	0.005	0.038	0.003	0.021	0.008	0.001	0.001
25% err of QCD in $e4j$	0.000	0.000	0.000	0.000	0.000	0.000	1.164	1.118	2.410	0.219	0.218	0.406
25% err of QCD in $\mu4j$	0.742	0.737	1.562	0.223	0.214	0.384	0.000	0.000	0.000	0.000	0.000	0.000
25% err of QCD in $e\tau$	0.000	0.000	0.000	0.000	0.000	0.000	0.372	0.498	2.651	0.069	0.092	0.503
25% err of QCD in $\mu\tau$	0.345	0.465	2.360	0.185	0.250	1.285	0.000	0.000	0.000	0.000	0.000	0.000
top pT reweighting	0.000	0.000	0.032	0.002	0.003	0.007	0.004	0.002	0.031	0.002	0.000	0.001
0.6% err of ϵ_e reco	0.575	0.054	0.042	0.583	0.055	0.042	0.709	0.160	0.103	0.574	0.084	0.069
1.4% err of ϵ_e id	1.386	0.129	0.101	1.410	0.133	0.101	1.766	0.335	0.275	1.456	0.163	0.197
0.1% err of ϵ_μ reco	0.015	0.125	0.016	0.008	0.095	0.011	0.009	0.078	0.008	0.008	0.077	0.008
0.2% err of ϵ_μ id	0.052	0.496	0.066	0.021	0.370	0.045	0.033	0.299	0.029	0.032	0.299	0.031
5% err of ϵ_τ	0.745	1.004	5.091	0.694	0.937	4.823	0.723	0.967	5.146	0.700	0.937	5.111
4.7% err of $\epsilon_{j \rightarrow \tau}$	0.460	0.620	3.145	0.307	0.414	2.129	0.458	0.613	3.260	0.290	0.388	2.115
0.5% err of ES_e	0.249	0.023	0.018	0.228	0.022	0.016	0.008	0.171	0.061	0.010	0.247	0.017
0.2% err of ES_μ	0.095	0.092	0.033	0.093	0.092	0.035	0.013	0.116	0.011	0.012	0.114	0.012
1.2% err of $ES_{\tau \rightarrow \pi^\pm}$	0.034	0.046	0.232	0.035	0.047	0.244	0.034	0.046	0.245	0.030	0.040	0.216
1.2% err of $ES_{\tau \rightarrow \pi^\pm \pi^0}$	0.086	0.116	0.587	0.069	0.093	0.477	0.066	0.088	0.469	0.075	0.100	0.548
1.2% err of $ES_{\tau \rightarrow 3\pi^\pm}$	0.026	0.035	0.175	0.026	0.034	0.177	0.024	0.032	0.172	0.024	0.032	0.176
Single-e Trigger (probe syst)	0.000	0.000	0.000	0.000	0.000	0.000	0.029	0.032	0.004	0.036	0.004	0.009
Single-e Trigger (tag syst)	0.000	0.000	0.000	0.000	0.000	0.000	0.063	0.088	0.080	0.037	0.013	0.038
Single-mu Trigger (0.1%)	0.086	0.099	0.008	0.076	0.072	0.004	0.000	0.000	0.000	0.000	0.000	0.000
0.5% err of $Br_{\tau \rightarrow \pi^\pm}$	0.008	0.011	0.046	0.009	0.012	0.049	0.008	0.011	0.046	0.009	0.011	0.054
0.4% err of $Br_{\tau \rightarrow \pi^\pm \pi^0}$	0.017	0.023	0.099	0.018	0.025	0.105	0.018	0.024	0.106	0.019	0.025	0.113
1.1% err of $Br_{\tau \rightarrow \pi^\pm 2\pi^0}$	0.021	0.028	0.121	0.021	0.028	0.117	0.021	0.027	0.118	0.024	0.030	0.139
0.5% err of $Br_{\tau \rightarrow 3\pi^\pm}$	0.015	0.020	0.092	0.016	0.022	0.099	0.016	0.020	0.097	0.016	0.021	0.102
1.1% err of $Br_{\tau \rightarrow 3\pi^\pm \pi^0}$	0.008	0.011	0.042	0.009	0.012	0.045	0.008	0.010	0.041	0.009	0.011	0.045
Pileup	0.041	0.183	0.777	0.231	0.026	0.891	0.428	0.474	0.592	0.248	0.137	0.835
JES	2.300	0.750	4.421	1.823	1.543	2.968	1.681	2.370	4.577	1.681	1.773	2.993
JER	0.238	0.180	0.265	0.143	0.146	0.356	0.259	0.249	0.406	0.148	0.138	0.538
Btag	0.098	0.772	0.643	0.111	0.023	0.114	0.181	0.091	0.762	0.024	0.109	0.088
Mistag	0.100	0.141	0.035	0.100	0.056	0.090	0.077	0.142	0.124	0.030	0.096	0.135
tt fsr	0.760	0.583	0.743	0.236	0.253	0.643	0.289	0.473	0.756	1.029	0.065	1.337
tt isr	0.724	0.747	1.105	0.720	0.723	0.876	0.317	1.060	1.414	0.043	0.830	0.062
tt UE	0.021	0.037	1.665	0.306	1.017	0.266	0.122	0.177	1.060	0.172	0.133	0.053
tt MEPS	0.198	0.653	1.699	1.117	0.645	0.129	0.033	0.743	1.812	0.163	1.279	1.196
Total	3.335	3.647	8.655	2.998	2.579	6.609	3.643	3.459	9.135	2.884	2.728	6.966

4.7. Results

This section presents results of the measurements of the branching fractions using the two methods described earlier. The two approaches yield consistent result. Then, the ratios of branching fractions and the derived SM quantities are presented based on the branching fractions measured by the shape analysis, the more precise approach.

4.7.1. W branching fractions

The values of the branching fractions measured using the two approaches are shown in Table 4.17 and Figure 4.54. These plots also show the current, best measured values of the W branching fractions based on a combination of the measurements done by each of the LEP experiments [16]. The measured values are strongly correlated because of the construction of the model and because of the constraint that the sum of branching fractions for leptonic and hadronic decay modes be equal to one. To demonstrate this, two dimensional contours have been drawn and are shown in Figure 4.55.

Table 4.17. Values of branching fractions determined in both analysis approaches and the PDG values. The errors include statistical (first) and systematic (second) uncertainties.

	counting	shape	LEP
w/o LFU			
$\mathcal{B}(W \rightarrow e\nu)$	$(11.16 \pm 0.04 \pm 0.27)\%$	$(10.83 \pm 0.01 \pm 0.10)\%$	$(10.71 \pm 0.14 \pm 0.07)\%$
$\mathcal{B}(W \rightarrow \mu\nu)$	$(11.13 \pm 0.03 \pm 0.21)\%$	$(10.94 \pm 0.01 \pm 0.08)\%$	$(10.63 \pm 0.13 \pm 0.07)\%$
$\mathcal{B}(W \rightarrow \tau\nu)$	$(10.64 \pm 0.08 \pm 0.65)\%$	$(10.77 \pm 0.05 \pm 0.21)\%$	$(11.38 \pm 0.17 \pm 0.11)\%$
$\mathcal{B}(W \rightarrow h)$	$(67.08 \pm 0.07 \pm 0.72)\%$	$(67.46 \pm 0.04 \pm 0.28)\%$	$(-- \pm --)\%$
w/ LFU			
$\mathcal{B}(W \rightarrow \ell\nu)$	$(-- \pm --)\%$	$(10.89 \pm 0.01 \pm 0.08)\%$	$(10.86 \pm 0.06 \pm 0.09)\%$
$\mathcal{B}(W \rightarrow h)$	$(-- \pm --)\%$	$(67.32 \pm 0.02 \pm 0.23)\%$	$(67.41 \pm 0.18 \pm 0.20)\%$

Table 4.18. Correlation matrix of leptonic branching fractions.

$$\begin{array}{c}
 \text{counting} & \text{shape} & \text{LEP} \\
 \left[\begin{array}{ccc} 1 & +0.59 & -0.06 \\ +0.59 & 1 & -0.27 \\ -0.06 & -0.27 & 1 \end{array} \right] & \left[\begin{array}{ccc} 1 & +0.47 & +0.09 \\ +0.47 & 1 & +0.14 \\ +0.09 & +0.14 & 1 \end{array} \right] & \left[\begin{array}{ccc} 1 & +0.17 & -0.20 \\ +0.17 & 1 & -0.12 \\ -0.20 & -0.12 & 1 \end{array} \right]
 \end{array}$$

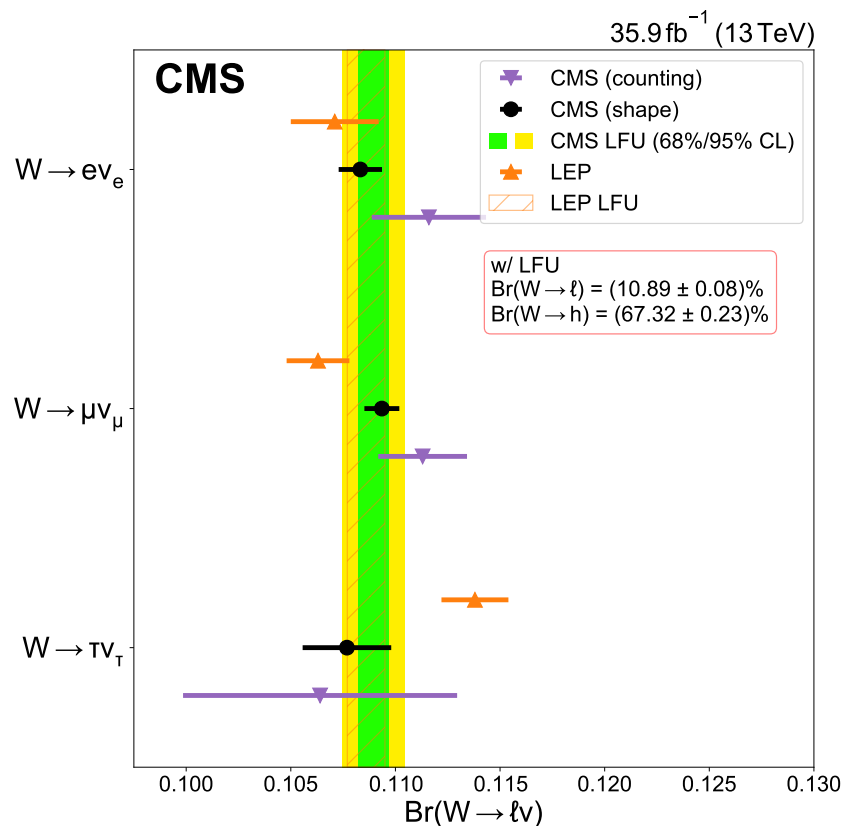


Figure 4.54. Summary of measured values of leptonic branching fractions.

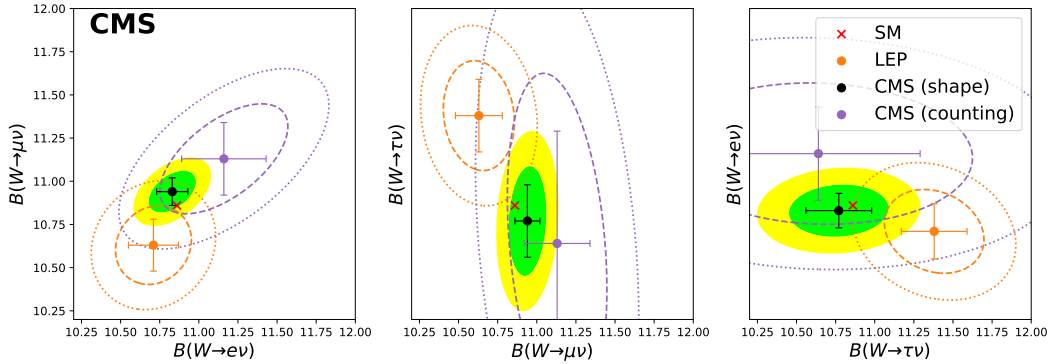


Figure 4.55. Two dimensional comparisons of leptonic branching fractions. For each pair shown in the panels, the branching fraction that is not shown has been marginalized over. The dashed lines correspond to 68% and 95% contour levels for the resulting two dimensional Gaussian distribution.

4.7.2. Ratios of Branching Fractions and Derived Quantities

Having measured the branching fractions, it is of interest to calculate the ratios between branching fractions and their probability distribution functions to compare to values obtained at other experiments where only ratios are measured. To transform the likelihood of the branching fractions to the likelihood for ratios, the following integral transformation is evaluated[159],

$$f(r_{\tau/e}, r_{\tau/\mu}) = \int_{-\infty}^{\infty} |\beta_\tau| g(r_{\tau/e}\beta_\tau, r_{\tau/\mu}\beta_\tau, \beta_\tau) d\beta_\tau \quad (4.25)$$

where $r_{\tau/e} = \beta_\tau/\beta_e$ and $r_{\tau/\mu} = \beta_\tau/\beta_\mu$ and $g(\beta_e, \beta_\mu, \beta_\tau)$ is the PDF of the branching fractions which is normal distribution with parameters determined from the $\mathcal{B}(W \rightarrow \ell\nu)$ measurement. The resulting ratios are shown in Figure 4.56. Table 4.19 shows comparisons between the ratios constructed from the measurements described above, and those measured by LEP and ATLAS.

Table 4.19. Ratios of branching fractions.

	CMS	LEP	ATLAS
$\mathcal{B}(W \rightarrow \mu\nu)/\mathcal{B}(W \rightarrow e\nu)$	1.013 ± 0.009	0.993 ± 0.019	–
$\mathcal{B}(W \rightarrow \tau\nu)/\mathcal{B}(W \rightarrow e\nu)$	1.011 ± 0.020	1.063 ± 0.027	–
$\mathcal{B}(W \rightarrow \tau\nu)/\mathcal{B}(W \rightarrow \mu\nu)$	0.998 ± 0.019	1.070 ± 0.026	0.992 ± 0.013
$2\mathcal{B}(W \rightarrow \tau\nu)/(\mathcal{B}(W \rightarrow e\nu) + \mathcal{B}(W \rightarrow \mu\nu))$	1.002 ± 0.019	1.066 ± 0.025	–

The values of the leptonic branching fractions can also be used as a check of the unitarity of the CKM matrix elements and calculating the least well measured of the matrix elements, $|V_{cs}|$. To do both of these calculations, the following relation between the leptonic branching fractions and CKM matrix elements is useful,

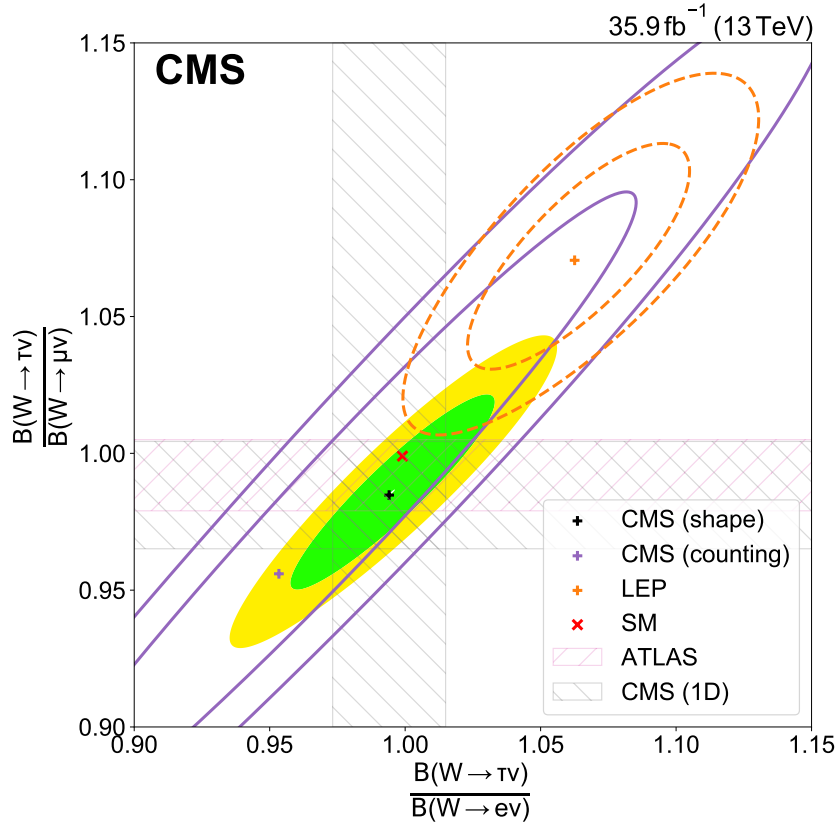


Figure 4.56. Two dimensional distributions of the ratios $\mathcal{B}(W \rightarrow \tau\nu)/\mathcal{B}(W \rightarrow e\nu)$ vs $\mathcal{B}(W \rightarrow \tau\nu)/\mathcal{B}(W \rightarrow \mu\nu)$ with comparisons of the CMS result to LEP and ATLAS measurements.

$$R_{h/\ell}^W = \frac{\mathcal{B}(W \rightarrow h)}{1 - \mathcal{B}(W \rightarrow h)} = \left(1 + \frac{\alpha_S(m_W)}{\pi}\right) \sum_{d,s,b}^{u,c} |V_{ij}|^2, \quad (4.26)$$

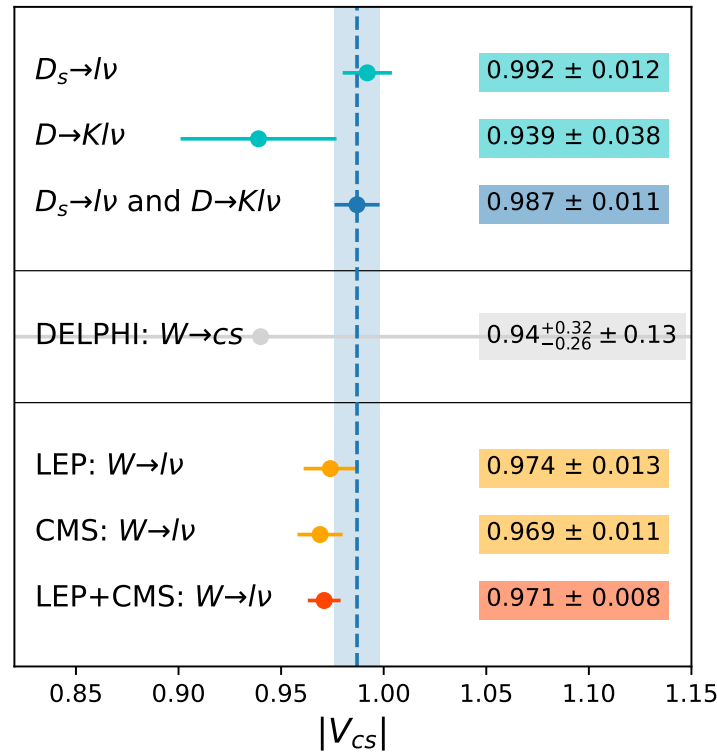
where $\alpha_S(m_W)$ is the strong coupling constant at the W pole. The CMS value for the ratio of total hadronic and total leptonic branching fraction is

$$R_{h/\ell}^W = 2.060 \pm 0.021, \quad (4.27)$$

which leads to the following derived value for $\alpha_S(m_W)$, $\sum_{d,s,b}^{u,c} |V_{ij}|^2$ and $|V_{cs}|$.

Table 4.20. SM quantities can be derived from the CMS measured $R_{h/\ell}^W$.

Assumption	Quantity	CMS	LEP	CMS+LEP
	$R_{h/\ell}^W$	2.060 ± 0.021	2.068 ± 0.025	2.063 ± 0.016
CKM Unitarity: $\sum_{d,s,b}^{u,c} V_{ij} ^2 = 2$ $\implies \alpha_S(m_W)$		0.094 ± 0.033	0.108 ± 0.040	0.099 ± 0.026
PDG [27] $\alpha_S(m_W) = 1.1200 \pm 0.010$ $\implies \sum_{d,s,b}^{u,c} V_{ij} ^2$		1.985 ± 0.021	1.997 ± 0.025	1.992 ± 0.016
PDG [27]: $\alpha_S(m_W) = 1.1200 \pm 0.010$ $\implies V_{cs} $		0.969 ± 0.011	0.974 ± 0.013	0.971 ± 0.008
PDG [27]: $\sum_{ud,us,ub}^{cd,cb} V_{ij} ^2 = 1.0490(18)$				

Figure 4.57. The $|V_{cs}|$ derived from the $\mathcal{B}(W \rightarrow \ell\nu)$ measurement by CMS, LEP and CMS+LEP, in comparison with the direct measurements [27].

CHAPTER 5

Clustering Algorithms for the Reconstruction of the CMS High Granularity Calorimeter (HGCAL)

The luminosity of the future High Luminosity Large Hadron Collider (HL-LHC) is going to achieve up to $7.5 \times 10^{34} \text{ cm}^{-2}\text{s}^{-1}$ [160] in its ultimate scenario, which is 5 times that delivered at present. This leads to the production of high pile-up events containing up to 200 interactions in each bunch crossing (PU200). Current CMS endcap calorimeters [161] are designed with a lifetime radiation limit of 500 fb^{-1} [29], which will be reached at the end of LHC Run-III in 2023. During the third long shutdown period of LHC from 2024 to 2026, the CMS Collaboration is going to conduct the Phase-II upgrade of the CMS detector [29]. One of the major tasks in the CMS Phase-II upgrade is to replace the current endcap calorimeters, including both endcap electromagnetic and hadronic calorimeters, with a new high granularity calorimeter system (HGCAL) which is based on highly-segmented Silicon sensors and plastic scintillators.

The $\mathcal{B}(W \rightarrow \ell\nu)$ measurement presented in this thesis achieves 2% relative uncertainty on the $\mathcal{B}(W \rightarrow \tau\nu)$ result. One of the most offending systematic uncertainties that limit the precision is the efficiency of hadronic identification, which has a 5% relative uncertainty, about 1% coming from the statistics of the measurement, 4% coming from the systematics related to the track cuts of $p_T > 0.5 \text{ GeV}$. HGCAL is designed to make the most advantage of its fine channels to achieve the best possible spatial resolution, energy resolution and particle identification efficiency. It is able to detect photons and charged hadrons at much smaller separation, which is one of the key steps to reconstruct τ_h decay mode in the

hadron-plus-strip algorithm. Furthermore, novel computer vision (CV) based deep learning particle identification is under developing, which aims at identifying particles directly from the images of candidate jets. Therefore, in the HL-LHC era, HGCAL is able to bring a noticeable improvement of $\mathcal{B}(W \rightarrow \ell\nu)$ precision.

In parallel with the $\mathcal{B}(W \rightarrow \ell\nu)$ analysis, I have been highly involved in the clustering algorithm of the HGCAL reconstruction. This chapter summarizes my R&D works for the HGCAL clustering algorithm, based on our existing publications [162, 163, 164, 165]

5.1. Design and Reconstruction of HGCAL

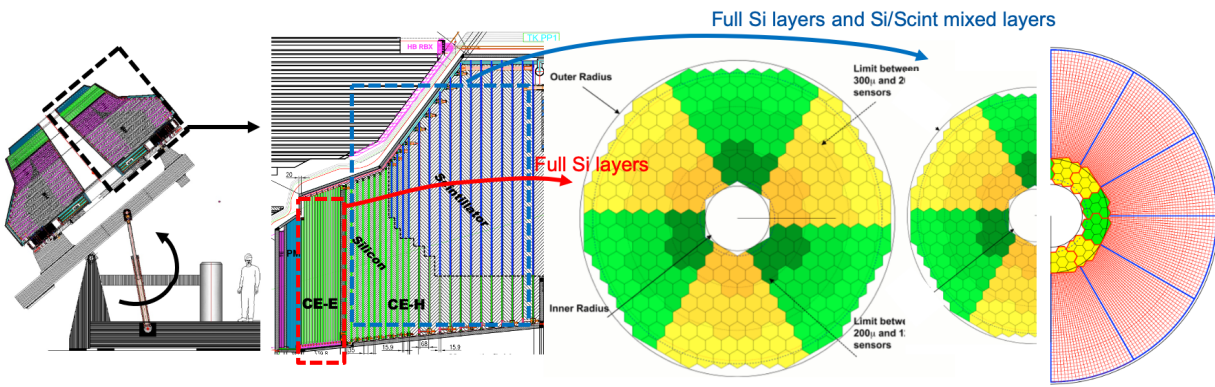


Figure 5.1. The design of HGCAL [31]. (left) Sketch of HGCAL endcap. (mid-left) The internal structure on the longitudinal-radial (z-r) plane. Red and blue rectangles indicate regions of CE-E (for calorimeter endcap electromagnetic) and CE-H (for calorimeter endcap hadronic), respectively, where CE-E has 28 full Si layers and CE-H has 8 full Si layers plus 14 Si-scintillators hybrid layers. (mid-right, right) Layouts of CE-E and CE-H layer. Silicon wafers are shown as yellow and green hexagons and scintillators are shown as red mesh. Darker, medium and lighter shades of hexagons represent silicon wafers with thickness of 120, 200 and 300 μm , respectively.

The design of HGCAL [31] is shown in Figure 5.1. Two HGCAL endcaps will be mounted on both sides of the CMS detector. Each endcap weighs about 215 tons and measures about 2 m in longitudinal direction and 2.3 m in radial direction, covering $1.5 < |\eta| < 3.0$. The full system operates at a temperature of -35°C maintained by a CO₂ cooling system. Each

endcap consists of 50 layers, each of which combines passive absorber material and active sensor material. The front 28 layers are the electromagnetic part (CE-E), which uses Cu, CuW and Pb as absorber and Si wafers with 120, 200, 300 μm thickness as sensors. The back 22 layers are the hadronic part (CE-H), which uses stainless steel and Cu as absorber and includes 8 full Silicon layers plus 14 hybrid layers of Si sensors and plastic scintillators with SiPM readout. The electromagnetic radiation thickness and hadronic interaction thickness of CE-E are $25X_0$ and 1.3λ respectively, while the hadronic interaction thickness of CE-H is 8.2λ . In total, The full HGCAL system has 620 m^2 of Silicon and about 400 m^2 of plastic scintillators. The size of each Si sensor is $0.5\text{-}1.0 \text{ cm}^2$ and the number of Si channels is about 6 million. The size of the scintillators is $4\text{-}30 \text{ cm}^2$ and the number of scintillator channels is about 240 thousand.

As a consequence of both high pile-up in the HL-LHC and enormous number of channels in the HGCAL, the number of input hits to HGCAL clustering algorithm is huge, usually in the order of $n \sim O(10^5)$ in PU200 events, where n denotes the number of hits. The clustering algorithm aggregates hits in 2D clusters layer by layer, producing about $k \sim O(10^4)$ clusters, where k denotes number of clusters. The average number of hits in a cluster is about $m = n/k \sim 10$; therefore HGCAL clustering task is characterized by $n > k \gg m$. Since cells are small compared to shower lateral size, an "energy density" is defined to better hint regional energy blobs in the HGCAL clustering. After 2D clustering algorithm, 3D showers in HGCAL are reconstructed by collecting and associating 2D clusters on different layers using TICL algorithms [166].

The current trigger system in CMS consists of two levels: Level 1 Trigger (L1T) and High Level Trigger (HLT). L1T utilizes customized ASICs and FPGAs to reduce the event rate from 40 MHz LHC collision frequency to 100 kHz within a 4 μs time budget for decision; HLT is fully based on C++ software running on CPUs and further reduces event rate from

100 kHz to 1 kHz with a 300 ms time budget for decision. However, in the era of HL-LHC, CMS HLT expects 30 times more computing load: 1.3x from upgraded detectors with more channels; 3x from increased number of pile-up interactions; 7.5x from improved L1T output rate. Among this 30x surge of the computing demand, improvement in the CPU performance by 2026 is expected to account for only 4x. Therefore, there will be a considerable deficit of computing power if the HLT architecture remains unchanged in 2026. In the HL-LHC era, the HLT time budget for CMS HGCAL clustering is roughly estimated to be less than a few tens of milliseconds. It is particularly a huge challenge of computing for the HGCAL clustering algorithm to process $n \sim 5 \times 10^5$ hits within such a limited time budget. To cope with this computing challenge, CMS is studying the feasibility of heterogeneous computing in HLT and offline reconstruction. With the support of CUDA [167] in the CMS software framework (CMSSW), it is possible to accelerate the HGCAL reconstruction with GPUs.

5.2. Cluster of Energy (CLUE) Clustering Algorithm

The input to the clustering algorithm is a set of n hits, whose number varies from a few thousands to a few millions, depending on the longitudinal and transverse granularity of the calorimeter as well as on the number of particles entering the detector. The output is a set of k clusters whose number is usually one or two order of magnitudes smaller than n and in principle depends on both the number of incoming particles and the number of layers. Assuming that the lateral granularity of sensors is constant and finite, the average number of hits in clusters ($m = n/k$) is also constant and finite. For example, in the CMS HGCAL, m is in the order of 10. This leads to the relation among the number of hits n , the number of clusters k , and the average number of hits in clusters m as $n > k \gg m$.

Most well-known algorithms do not simultaneously satisfy the requirements on linear scalability and easy parallelization for applications like clustering hits in high granularity

calorimeters, which is characterized by low dimension and $n > k \gg m$. It is therefore important to investigate new, fast and parallelizable clustering algorithms, as well as their optimized accompanying spatial index that can be conveniently constructed and queried in parallel.

5.2.1. Algorithm Description

Clustering data is one of the most challenging tasks in several scientific domains. The definition of cluster is itself not trivial, as it strongly depends on the context. Many clustering methods have been developed based on a variety of induction principles [168]. Currently popular clustering algorithms include (but are not limited to) partitioning, hierarchical and density-based approaches [168, 169]. Partitioning approaches, such as k-mean [170], compose clusters by optimizing a dissimilarity function based on distance. However, in the application to high granularity calorimeters, partitioning approaches are prohibitive because the number of clusters k is not known a priori. Hierarchical methods make clusters by constructing a dendrogram with a recursion of splitting or merging. However, hierarchical methods do not scale well because each decision to merge or split needs to scan over many objects or clusters [169]. Therefore, they are not suitable for our application. Density-based methods, such as DBSCAN [171], OPTICS [172] and Clustering by Fast Search and Find Density Peak (CFSFDP) [173], group points by detecting continuous high-density regions. They are capable of discovering clusters of arbitrary shapes and are efficient for large spatial database. If a spatial index is used, their computational complexity is $O(n \log n)$ [169]. However, one of the potential weaknesses of the currently well-known density-based algorithms is that they intrinsically include serial processes which are hard to parallelize: DBSCAN has to iteratively visit all points within an enclosure of density-connectedness before working on the next cluster [171]; OPTICS needs to sequentially add points in an ordered list to

obtain a dendrogram of reachability distance [172]; CFSFDP needs to sequentially assign points to clusters in order of decreasing density [173]. In the application to high granularity calorimeters, as discussed in Section 1, linear scalability and fully parallelization are essential to handle a huge dataset efficiently by means of heterogeneous computing.

In order to satisfy these requirements, we propose a fast and fully-parallelizable density-based algorithm (CLUE) inspired by CFSFDP. For the purpose of the algorithm, each sensor cell on a layer with its energy deposit is taken as a 2D point with an associated weight equaling to its energy value. As in CFSFDP, two key variables are calculated for each point: the local density ρ and the separation δ defined in Equation 5.3 and 5.4, where δ is the distance to the nearest point with higher density (“nearest-higher”) which is slightly adapted from that in CFSFDP in order to take advantage of the spatial index. Then cluster seeds and outliers are identified based on thresholds on ρ and δ . Differing from cluster assignment in CFSFDP, which sorts density and adds points to clusters in order of decreasing density, CLUE first builds a list of followers for each point by registering each point as a follower to its nearest-higher. Then it expands clusters by passing cluster indices from the seeds to their followers iteratively. Since such expansion of clusters is fully independent from each others, it not only avoids the costly density sorting in CFSFDP, but also enables a k -way parallelization. Unlike the noise identification in CFSFDP, CLUE rejects noise by identifying outliers and their iteratively descendant followers, as discussed in Section 5.2.3.1.

5.2.1.1. Spatial index with fixed-grid. Query of neighborhood, which retrieves nearby points within a distance, is one of the most frequent operations in density-based clustering algorithms. CLUE uses a spatial index to access and query spatial data points efficiently. Given that the physical layout of sensor cells is a multi-layer tessellation, it is intuitive to index its data with a fixed-grid, which divides the space into fixed rectangular bins [174, 175]. Comparing with the data-driven structures such as KD-Tree [176] and R-Tree [177], space

partition in fixed-grid is independent of any particular distribution of data points [178], thus can be explicitly predefined before loading data points. In addition, both construction and query with a fixed-grid are computationally simple and can be easily parallelized. Therefore, CLUE uses a fixed-grid as spatial index for efficient neighborhood queries.

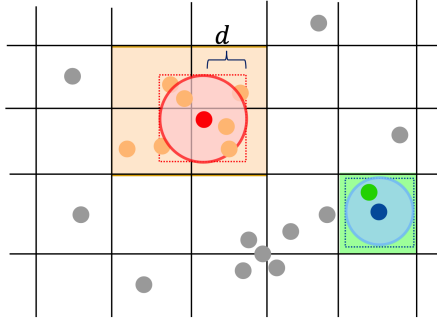


Figure 5.2. 2D points are indexed with a grid for fast neighborhood query in CLUE. Construction of this spatial index only involves registering the indices of points into the bins of the grid according to points' 2D spatial positions. To query d -neighborhood $N_d(i)$ defined in Equation 5.2, taking the red point for example, we first locate its $\Omega_d(i)$ defined in Equation 5.1, a set of all points in the bins touched by a square window $[x_i \pm d, y_i \pm d]$. The $[x_i \pm d, y_i \pm d]$ window is shown as the orange square while $\Omega_d(i)$ is shown as orange points. Then we examine points in $\Omega_d(i)$ to identify those within a distance d from point i , shown as the ones contained in the red circle.

For each layer of the calorimeter, a fixed-grid spatial index is constructed by registering the indices of 2D points into the square bins in the grid according to the 2D coordinates of the points. When querying $N_d(i)$, the d -neighborhood of point i , CLUE only needs to loop over points in the bins touched by the square window $(x_i \pm d, y_i \pm d)$ as shown in Fig. 5.2. We denote those points as $\Omega_d(i)$, defined as:

$$\Omega_d(i) = \{j : j \in \text{tiles touched by the square window } [x_i \pm d, y_i \pm d]\}. \quad (5.1)$$

where $\Omega_d(i)$ is guaranteed to include all neighbors within a distance d from the point i . Namely,

$$N_d(i) = \{j : d_{ij} < d, j \in \Omega_d(i)\} \subseteq \Omega_d(i). \quad (5.2)$$

Without any spatial index, the query of $N_d(i)$ requires a sequential scan over all points. In contrast, with the grid spatial index, CLUE only needs to loop over the points in $\Omega_d(i)$ to acquire $N_d(i)$. Given that d is small and the maximum granularity of points is constant, the complexity of querying $N_d(i)$ with a fixed-grid is $O(1)$.

5.2.1.2. Clustering procedure of CLUE. CLUE requires the following four parameters: d_c is the cutoff distance in the calculation of local density; ρ_c is the minimum density to promote a point as a seed or the maximum density to demote a point as an outlier; δ_c and δ_o are the minimum separation requirements for seeds and outliers, respectively. The choice of these four parameters can be based on physics: for example, d_c can be chosen based on the shower size and the lateral granularity of detectors; ρ_c can be chosen to exclude noise; δ_c and δ_o can be chosen based on the shower sizes and separations. These four parameters allow more degrees of freedom to tune CLUE for the desired goals of physics.

Figure 5.3 illustrates the main steps of CLUE algorithm. The local density ρ in CLUE is defined as:

$$\rho_i = \sum_{j:j \in N_{d_c}(i)} \chi(d_{ij}) w_j, \quad (5.3)$$

where w_j is the weight of point j , $\chi(d_{ij})$ is a convolution kernel, which can be optimized according to specific applications. Obvious possible kernel options include flat, Gaussian and exponential functions.

The nearest-higher and the distance to it δ (separation) in CLUE are defined as:

$$nh_i = \begin{cases} \arg \min_{j \in N'_{d_m}(i)} d_{ij}, & \text{if } |N'_{d_m}(i)| \neq 0 \\ -1, & \text{otherwise} \end{cases}, \quad \delta_i = \begin{cases} d_{i,nh_i}, & \text{if } |N'_{d_m}(i)| \neq 0 \\ +\infty, & \text{otherwise} \end{cases}, \quad (5.4)$$

where $d_m = \max(\delta_o, \delta_c)$ and $N'_{d_m}(i) = \{j : \rho_j > \rho_i, j \in N_{d_m}(i)\}$ is a subset of $N_{d_m}(i)$, where points have higher local densities than ρ_i .

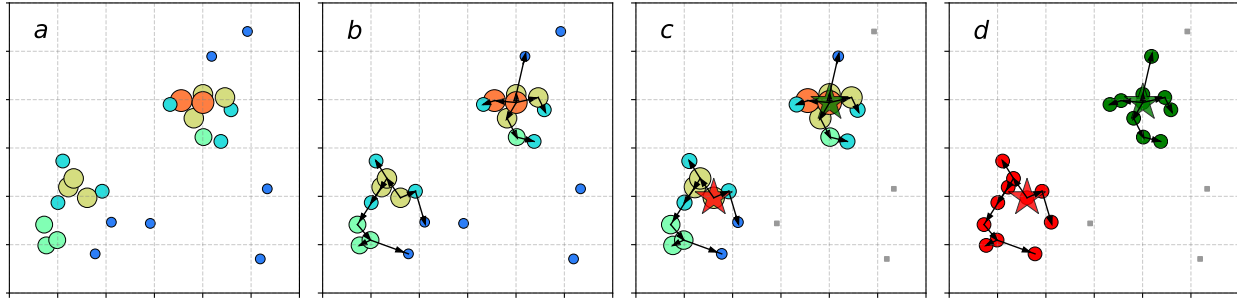


Figure 5.3. Demonstration of CLUE algorithm. Points are distributed inside a 6×6 2D area and CLUE parameters are set to $d_c = 0.5$, $\rho_c = 3.9$, $\delta_c = \delta_o = 1$. Before the clustering procedure starts, a fixed-grid spatial index is constructed. In the first step, shown in Fig. 5.3 (a), CLUE calculates the local density ρ for each point, defined in Equation 5.3. The color and size of points represent their local densities. In the second step, shown in Fig. 5.3 (b), CLUE calculates the nearest-higher (nh) and the separation (δ) for each point, defined in Equation 5.4. The black arrows represent the relation from the nearest-higher of a point to the point itself. If the nearest-higher of a point is -1, there is no arrow pointing to it. In the third step, in as Fig. 5.3 (c), CLUE promotes a point as a seed if ρ, δ are both large, or demote it to an outlier if ρ is small and δ is large. Promoted seeds and demoted outliers are shown as stars and grey squares, respectively. In the fourth step, shown in Fig. 5.3 (d), CLUE propagates the cluster indices from seeds through their chains of followers defined in Equation 5.5. Noise points, which are outliers and their descendant followers, are guaranteed not to receive any cluster indices from any seeds. The color of points represents the cluster indices. A grey square means its cluster index is undefined and the point should be considered as noise.

After ρ and δ are calculated, points with density $\rho > \rho_c$ and large separation $\delta > \delta_c$ are promoted as cluster seeds, while points with density $\rho < \rho_c$ and large separation $\delta > \delta_o$ are demoted to outliers. For each point, there is a list of followers defined as:

$$F_i = \{j : nh_j = i\}. \quad (5.5)$$

The lists of followers are built by registering the points which are neither seeds nor outliers to the follower lists of their nearest-highe. The cluster indices, associating a follower with

a particular seed, are passed down from seeds through their chains of followers iteratively. Outliers and their descendant followers are guaranteed not to receive any cluster indices from seeds, which grants a noise rejection as shown in Fig. 5.5. The calculation of ρ, δ and the decision of seeds and outliers both support n -way parallelization, while the expansion of clusters can be done with k -way parallelization. Pseudocode of CLUE is included in Appendix C.1.

5.2.2. GPU Implementation

To parallelize CLUE on GPU, one GPU thread is assigned to each point, for a total of n threads, to construct spatial index, calculate ρ and δ , promote (demote) seeds (outliers) and register points to the corresponding lists of followers of their nearest-higthers. Next, one thread is assigned to each seed, for a total of k threads, to expand clusters iteratively along chains of followers. The block size of all kernels, which in practice does not have a remarkable impact on the speed performance, is set to 1024. In the test in Table 5.2, changing the block size from 1024 to 256 on GPU leads to only about 0.14 ms decrease in the sum of kernel execution times. The details of parallelism for each kernel are listed in Table 5.1. Since the results of a CLUE step are required in the following steps, it is necessary to guarantee that all the threads are synchronized before moving to the next stage. Therefore, each CLUE step can be implemented as a separate kernel. To optimize the performance of accessing the GPU global memory with coalescing, the points on all layers are stored as a single structure-of-array (SoA), including information of their layer numbers and 2D coordinates and weights. Thus points on all layers are input into kernels in one shot.

When parallelizing CLUE on GPU, thread conflicts to access and modify the same memory address in global memory could happen in the following three cases:

- multiple points need to register to the same bin simultaneously;

Table 5.1. Kernels and Parallelism

Kernels	parallelism	total threads	block size
build fixed-grid spatial index	1 point/thread	n	1024
calculate local density	1 point/thread	n	1024
calculate nearest-higher and separation	1 point/thread	n	1024
decide seeds/outliers, register followers	1 point/thread	n	1024
expand clusters	1 seed/thread	k	1024

- multiple points need to register to the list of seeds simultaneously;
- multiple points need to register as followers to the same point simultaneously.

Therefore, atomic operations are necessary to avoid the race conditions among threads in the global memory. During an atomic operation, a thread is granted with an exclusive access to read from and write to a memory location which is inaccessible to other concurrent threads until the atomic operation finishes. This inevitably leads to some microscopic serialization among threads in race. The serialization in cases (i) and (iii) is negligible because bins are usually small as well as the number of followers of a given point. In contrast, serialization in case (ii) can be costly because the number of seeds k is large. This can cause delays in the execution of kernel responsible for seed promotion. Since the atomic pushing back to the list of seeds is relatively fast in GPU memory comparing to the data transportation between host and device, the total execution time of CLUE still does not suffer significantly from the serialization in case (ii). The speed performance is further discussed in Section 5.2.3.

5.2.3. Performance Evaluation

5.2.3.1. Clustering results. We demonstrate the clustering results of CLUE with a set of synthetic datasets, shown in Fig. 5.4. Each example has 1000 2D points and includes spatially uniform noise points. The datasets in Fig. 5.4 (a) and (c) are from the scikit-learn package [179]. The dataset in Fig. 5.4 (b) is taken from [173]. Fig 5.4 (a) and (b) include

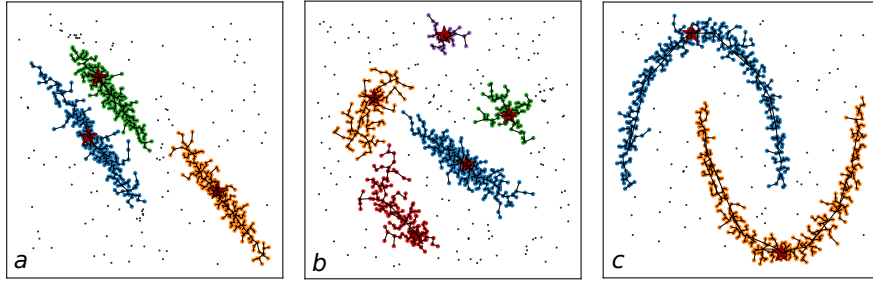


Figure 5.4. Examples of CLUE clustering on synthetic datasets. Each sample includes 1000 2D points with the same weight generated from certain distributions, including uniform noise points. The color of points represent their cluster indices. Black points represent outliers detached from any clusters. The links between pairs of points illustrate the relationship between nearest-higher and follower. The red stars highlight the cluster seeds.

elliptical clusters and Fig 5.4 (c) contains two parabolic arcs. CLUE successfully detects density peaks in Figs. 5.4 (a), (b), and (c).

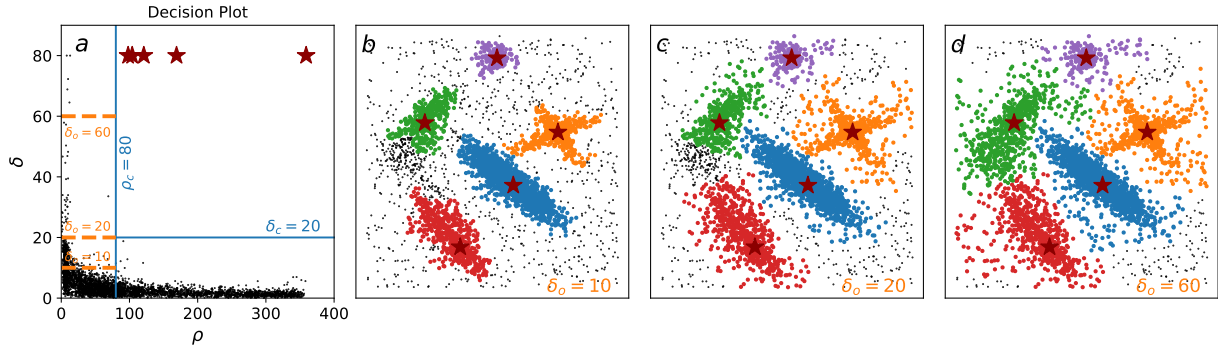


Figure 5.5. Noise rejection using different values of δ_o . Noise is either an outlier or a descendant follower of an outlier. In this dataset [173], 4000 points are distributed in 500×500 2D square area. Figure 5.5 (a) represents the decision plot on the $\rho - \delta$ plane, where fixed $\rho_c = 80$ and $\delta_c = 40$ values are shown as vertical and horizontal blue lines, respectively. Three different values of δ_o (10,20,60) are shown as orange dash lines. Figures 5.5 (b), (c) and (d) show the results with $\delta_o = 10, 20, 60$, respectively, illustrating how increasing δ_o loosens the continuity requirement and helps to demote outliers. The level of noise rejection should be chosen according to the user's needs.

In the induction principle of density-based clustering, the confidence of assigning a low density point to a cluster is established by maintaining the continuity of the cluster. Low density points with large separation should be deprived of association to any clusters. CFSFDP

uses a rather costly technique, which calculates a boarder region of each cluster and defines core-halo points in each cluster, to detach unreliable assignments from clusters [173]. In contrast, CLUE achieves this using cuts on δ_o and ρ_c while expanding a cluster, as described in Section 5.2.1. The example in Fig. 5.5 shows how cutting at different separation values helps to demote outliers. Figure 5.5 (a) represents the decision plot on the $\rho - \delta$ plane. Points with density below $\rho_c = 80$, shown on the left side of the vertical blue line, could be demoted as outliers if their δ are larger than a threshold. Once an outlier is demoted, all its descendant followers are disallowed from attaching to any clusters. While keeping $\rho_c = 80$ fixed, the effect of using three different values of δ_o (10, 20, 60), shown as orange dash lines in Fig. 5.5 (a), has been investigated. The corresponding results are shown in Fig. 5.5 (b), (c) and (d), respectively.

5.2.3.2. Execution time and scalability. We tested the computational performance of CLUE using a synthetic dataset that resembles high occupancy events in high granularity calorimeters operated at HL-LHC. The dataset represents a calorimeter with 100 sensor layers. A fixed number of points on each layer are assigned a unit weight in such a way that the density represents circular clusters of energy whose magnitude decreases radially from the centre of the cluster according to a Gaussian distribution with the standard deviation, σ , set to 3 cm. 5% of the points represent noise distributed uniformly over the layers. When clustering with CLUE, the bin size is set to 5 cm comparable with the width of the clusters and the algorithm parameters are set to $d_c = 3$ cm, $\delta_o = \delta_c = 5$ cm, $\rho_c = 8$. To test CLUE's linear scalability, the number of points on each layer is incremented from 1000 to 10000 in 10 equaling steps. A total of 100 layers are input to CLUE simultaneously which simulates the proposed CMS HGCAL design [31]. Therefore the total number of points in the test ranges from 10^5 to 10^6 . The linear scalability of execution time are validated in Fig. 5.6.

Table 5.2. Decomposition of CLUE execution time in the case of 10^4 points per layer with 100 layers. The time of sub-processes on GPU is measured with NVIDIA profiler, while on CPU is measured with `std::chrono` timers in the C++ code. The uncertainties are the standard deviations of 200 trial runs of the same event (10000 trial runs if GPU). The uncertainties of sub-processes on GPU are neglectable given that the maximum and minimum kernel execution time measured by NVIDIA Profiler are very close. With respect to the single-threaded CPU, the speed up factors of the multi-threaded CPU with TBB and the GPU are given in the bracket. “other” represents the difference between total execution time and the sum of the execution time of CLUE steps, and major CUDA API calls in the case of GPU.

CLUE Step	CPU [1T] (baseline)	CPU TBB [10T]	GPU
build fixed-grid spatial index	59.3 ± 1.6 ms	117.7 ± 6.4 ms (0.50x)	0.28 ms (208.63x)
calculate local density	218.4 ± 2.5 ms	33.7 ± 2.6 ms (6.48x)	0.51 ms (430.57x)
calculate nearest-higher and separation	326.9 ± 2.9 ms	45.5 ± 2.5 ms (7.19x)	0.89 ms (368.54x)
decide seeds/outliers, register followers	54.4 ± 2.5 ms	109.4 ± 7.7 ms (0.50x)	0.34 ms (162.38x)
expand clusters	17.4 ± 1.5 ms	6.1 ± 1.3 ms (2.86x)	0.35 ms (49.74x)
cuda memcpy	—	—	2.87 ms
cuda memset	—	—	0.10 ms
other	29.1 ± 1.7 ms	44.9 ± 15.7 ms	1.30 ms
TOTAL (10000 points per layer)	705.49 ± 7.93 ms	357.24 ± 19.68 ms (1.97x)	6.63 ± 0.63 ms (106.42x)

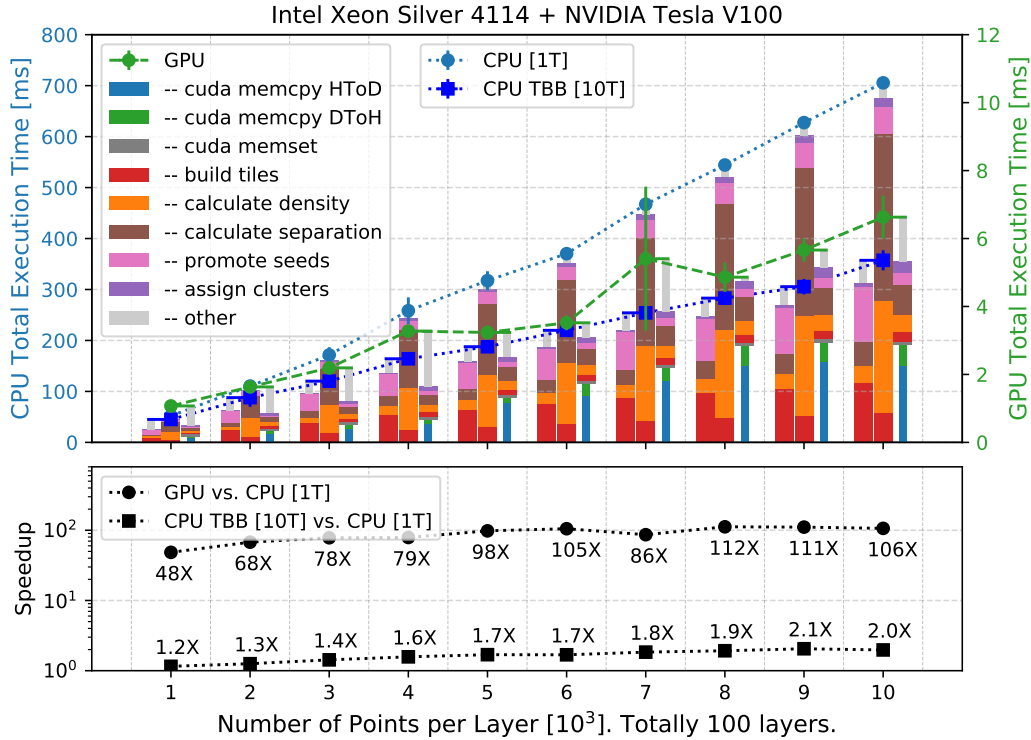


Figure 5.6. (*upper*) Execution time of CLUE on the single-threaded CPU, multi-threaded CPU with TBB and GPU scale linearly with number of input points, ranging from 10^5 to 10^6 in total. Execution time on single-threaded CPU is shown as blue circles and on 10 multi-threaded CPU with Thread Building Blocks (TBB) is shown as blue squares, while the time on GPU is shown as green circles. The stacked bars represent the decomposition of execution time. The green and blue narrower bars are latency for data traffic between host memory and device memory; wider bars represent time of essential CLUE steps; light grey narrower bars labelled as “other” are the difference between the total execution time and the sum of major CLUE steps (and major CUDA API calls if GPU). (*lower*) Comparing with the single-threaded CPU, the speed up factors of the GPU range from 48 to 112, while the speed up factors of the multi-threaded CPU with TBB range from 1.2 to 2.0, which is less than the number of concurrent threads on CPU because of atomic pushing to the data containers discussed in Section 5.2.2. Table 5.2 shows the details of the decomposition of the execution time in the case of 10^4 points per layer.

The single-threaded version of the CLUE algorithm on CPU has been implemented in C++, while the one on GPU has been implemented in C with CUDA [167]. The multi-threaded version of CLUE on CPU uses the Thread Building Block (TBB) library [180]

and has been implemented using the Abstraction Library for Parallel Kernel Acceleration (Alpaka) [181]. The test of the execution time is performed on an Intel Xeon Silver 4114 CPU and NVIDIA Tesla V100 GPU connected by PCIe Gen-3 link. The time of each GPU kernel and CUDA API call is measured using the NVIDIA profiler. The total execution time is averaged over 200 identical events (10000 identical events if GPU). Since CLUE is performed event by event and it is not necessary to repeat memory allocation and release for each event when running on GPU, we perform a one-time allocation of enough GPU memory before processing events and a one-time GPU memory deallocation after finishing all events. Therefore, the one-time *cudaMalloc* and *cudaFree* are not included in the average execution time. Such exclusion is legit because the number of events is extremely massive in high energy physics experiments and the execution time of the one-time *cudaMalloc* and *cudaFree* reused by each individual event is negligible.

In Fig. 5.6 (*upper*), the scalability of CLUE is linear, consistent with the expectation. The execution time on the single-threaded CPU, multi-threaded CPU with TBB and GPU increases linearly with the total number of points. The stacked bars represent the decomposition of execution time. In the decomposition, unique to the GPU implementation is the latency of data transfer between host and device, which is shown as blue and green narrower bars, while common to all the three implementations are the five CLUE steps. Comparing with the single-threaded CPU, when building spatial index and deciding seeds, shown as red and pink bars, the multi-threaded CPU using TBB does not give a notable speed up due to the implementation of atomic operations in Alpaka [181] as discussed in Section 5.2.2, while the GPU has a prominent outperformance thanks to its larger parallelization scale. For GPU, the kernel of seed promotion in which serialization exists due to atomic appending of points in the list of seeds, does not affect the total execution time significantly if compared with other sub-processes. In the two most computing-intense steps, calculating density and

separation, there are no thread conflicts or inevitable atomic operations. Therefore, both the multi-threaded CPU using TBB and the GPU provide a significant speed up. The details of the decomposition of execution time in the case of 10^4 points per layer are listed in Table 5.2.

Fig. 5.6 (*lower*) shows the speed up factors. Compared to the single-threaded CPU, the CUDA implementation on GPU is 48-112 times faster, while the multi-threaded version using TBB via Alpaka with 10 threads on CPU is about 1.2-2.0 times faster. The speed up factors are constrained to be smaller than the number of concurrent threads because of the atomic operations. In Table 5.2, the speed up factors of multi-threaded CPU using TBB reduce to less than 1 in the sub-process steps of building spatial index and promoting seeds and registering followers, where atomic operations happen and bottleneck the overall speed up factor.

5.3. CLUE in the CMS Software Framework (CMSSW)

In this section, we present both CPU and GPU implementations of CLUE in the application of HGCAL clustering in the CMS Software framework (CMSSW). Comparing with the previous HGCAL clustering algorithm, CLUE on CPU (GPU) in CMSSW is 30x (180x) faster in processing PU200 events while outputting almost the same clustering results.

5.3.1. Integration in the CMSSW

The previous clustering algorithm [165] used in the CMS HGCAL reconstruction was based on Clustering by Fast Search and Find Density Peak (CFSFDP) [173] and exploited a KD-Tree spatial index [176]. In the step of calculating local density ρ , KD-Tree provides a significant speedup comparing with not using any spatial index [165]. However, it has three crucial computing weaknesses: first, KD-Tree does not provide the optimal spatial index for HGCAL, because its window-query is of $O(n \log n)$ complexity and it is hard to construct

or query on the GPUs; second, the calculation of separation δ does not take advantage of spatial index but still relies on a costly $O(n^2)$ loop; third, the expansion of clusters happens in sequential order of decreasing density, which is not only costly because of sorting but also hard to parallelize.

CLUsters of Energy (CLUE) [162] is a recently-proposed parallelizable high-speed clustering algorithm. It overcomes the above three computing weaknesses and achieves an average $O(n)$ computational complexity in the applications like HGCAL where $n > k \gg m$. CLUE uses a spatial index [174] for fast querying of neighbours. Figure 5.3 is a demonstration of CLUE procedure provided in [162]. Both the CPU and the GPU version of CLUE, referred as CLUE-CPU and CLUE-GPU in this paper, have been implemented in CMSSW for HGCAL reconstruction. CLUE-CPU is implemented in C++, while CLUE-GPU is implemented using CUDA. Figure 5.7 shows the workflow of CLUE-GPU within CMSSW: hits are offloaded from CPU to GPU after energy calibration; then CLUE steps are carried out on GPU; in the end, the clustering results are transported back to CPU for post processing and other downstream HGCAL reconstruction related to 3D linkage of CLUE clusters.

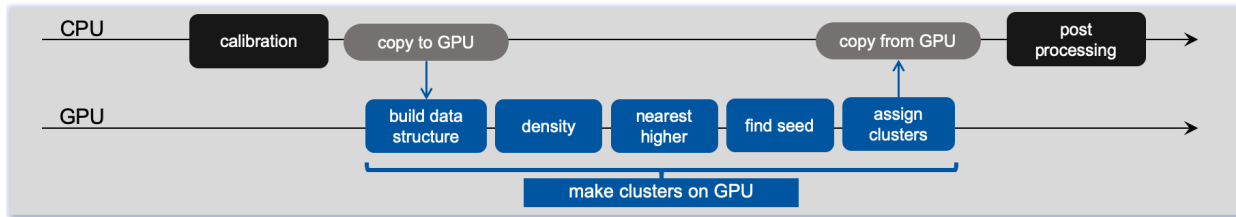


Figure 5.7. Workflow of CLUE-GPU in CMS Software framework (CMSSW). Hits are offloaded from CPU to GPU after energy calibration. Then CLUE process are carried out on GPU. In the end, the cluster indices of all hits are transported back to CPU for post processing.

To validate the implementation of CLUE in CMSSW, results of CLUE-CPU and CLUE-GPU are compared with the previous clustering algorithm in CMSSW version 10.6, referred

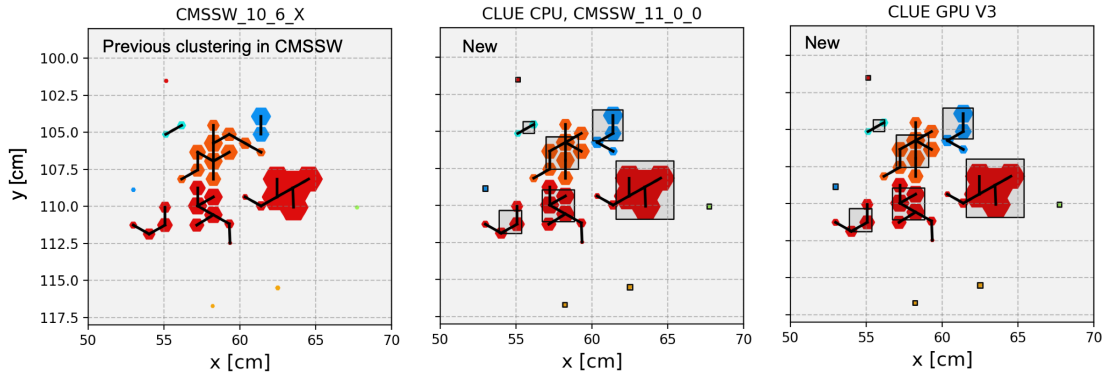


Figure 5.8. Example of clustering result from previous algorithm in CMSSW version 10.6.X (*left*) and CLUE-CPU (*middle*) and CLUE-GPU (*right*). The example shows a small region on the 12th layer of a simulated of $t\bar{t}$ event.

as CMSSW_10_6_X. Based on the simulated $t\bar{t}$ events, CLUE-CPU and CLUE-GPU completely agree with each other, while both of them show some rare disagreements with the previous clustering algorithm implemented in CMSSW_10_6_X. Such disagreements are caused by the different ordering of hits with exactly equal ρ or equal δ when using different data structures, namely grid in CLUE and KD-Tree in CMSSW_10_6_X. An example of clustering result is shown in Figure 5.8, where from left to right are results from CMSSW_10_6_X, CLUE-CPU and CLUE-GPU. In this example, CLUE-CPU and CLUE-GPU provide almost the same result as the clusters in CMSSW_10_6_X. However, a small notable difference is the blue cluster, which includes 4 hits in CMSSW_10_6_X but 2 in CLUE. This is because the hit at about (x=60, y=106) cm is equally close to the two neighbouring hits in orange cluster and blue cluster, and its two different assignments, caused by different ordering of these two neighbors in spatial index, are equally correct. The topology of blue cluster in both cases are acceptable. Therefore, it is reasonable to conclude that CLUE in CMSSW gives almost the same clustering result as CMSSW_10_6_X with neglectable differences.

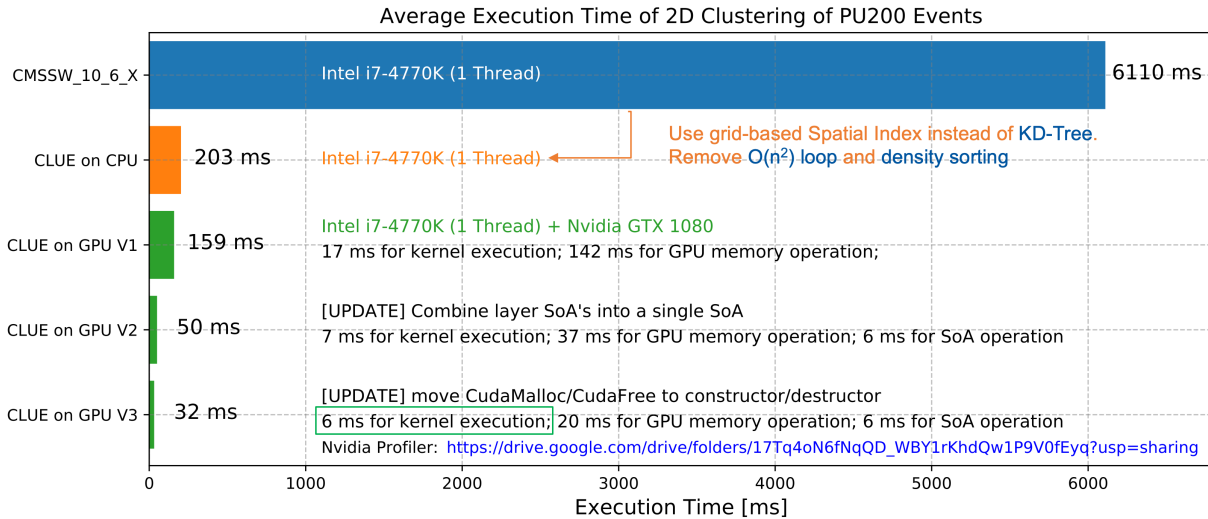


Figure 5.9. Average execution time of HGCAL clustering for PU200 events. The testing platform is based on Intel i7-4770K CPU and NVIDIA GTX 1080 GPU. Blue, orange and green bars represent execution time of CMSSW_10_6_X, CLUE-CPU and CLUE-GPU respectively. Both CMSSW_10_6_X and CLUE-CPU use a single CPU thread. Three green bars are three evolving versions of CLUE-GPU.

5.3.2. Performance in the CMSSW

The execution time of HGCAL clustering are tested using PU200 events. The testing platform is based on Intel i7-4770K CPU and NVIDIA GTX 1080 GPU. The average execution time is shown in Figure 5.9, where measured time includes all clustering steps and all necessary data transfer between CPU and GPU.

The previous clustering algorithm in CMSSW_10_6_X using a single thread CPU takes 6110 ms on average. In comparison, CLUE-CPU takes only 203 ms using the same single thread CPU, producing almost the same result but 30x faster. The GPU implementation in CMSSW includes three versions. The first version is a plain CUDA implementation of CLUE-CPU and average execution time is 159 ms. The second version combines the data of all hits in the entire HGCAL as a single Structure of Array (SoA) to improve access to global memory and to allow parallelization of hits on different layers. The average execution time of the second version is reduced to 50 ms. The third version uses one-time GPU memory

allocation and memory release before and after processing all events respectively. It further reduces execution time to 32 ms, which is decomposed into 6 ms for kernel execution, 20 ms for host-device data transportation and 6 ms for SoA conversion. The 6 ms total kernel execution time is comparable with that in [162]. The speedup factor of CLUE-GPU over CLUE-CPU is about 6x.

In the future, the latency due to data traffic and SoA conversion can be shared with other reconstruction processes if more processes are also offloaded to GPU. Such latency can also be partially hidden if multiple CUDA streams work on different events simultaneously to keep the GPU occupied.

CHAPTER 6

Conclusion

A precision measurement of three individual leptonic branching fractions and the inclusive hadronic branching fraction of W boson has been performed using the LHC $\sqrt{s} = 13$ TeV proton-proton collision data collected by the CMS detector during run 2016. Dataset are triggered with single electron and single muon trigger. The final states corresponding the topology of leptonic and semileptonic $t\bar{t}$ are selected. The selected sample is split into mutually-exclusive channels based on the multiplicity of electron, muon and hadronic tau, requiring at least one muon or one electron that enables trigger. For each channel, further partition relying on the jet and b tag multiplicities is designed to separate regions with different signal purity.

Two approaches are developed for this measurement. The shape analysis fits the p_T distribution of the sensitive leptons in different channels. It exploits the WW and W+jets regions for more W statistics, and Z+jets regions for controlling the systematics related to the identification of hadronic tau. The counting analysis constructs ratios of yields for channels with the same trigger and analytically solves three leptonic branching fractions from a set of quadratic equations. It eliminates the shape information and uses only the $t\bar{t}$ concentrated regions. It is designed to cross-check the shape analysis.

From shape analysis, the W branching fractions $\mathcal{B}(W \rightarrow e\nu)$, $\mathcal{B}(W \rightarrow \mu\nu)$, $\mathcal{B}(W \rightarrow \tau\nu)$ and $\mathcal{B}(W \rightarrow h)$ are 10.83(10)%, 10.94(08)%, 10.77(21)% and 67.46(28)%, respectively. From counting analysis, the W branching fractions $\mathcal{B}(W \rightarrow e\nu)$, $\mathcal{B}(W \rightarrow \mu\nu)$, $\mathcal{B}(W \rightarrow \tau\nu)$ and $\mathcal{B}(W \rightarrow h)$ are 11.16(27)%, 11.13(22)%, 10.64(65)% and 67.08(72)%, respectively. The values from the two approaches consistent with each other in one sigma. The shape analysis

is about 3 times more precise than the counting analysis, owing to the sensitivity from the p_T spectrum, controlling the τ_h systematics and wider selection regions embracing WW and W+jets events.

Based on the more precise result from the shape analysis, the ratios between pair-wised leptonic channels are calculated. Assuming universality between electron and muon, the ratio between tauonic branching fraction and the average of electronic and muonic branching fraction is determined as

$$R_{\tau/(e,\mu)} = \frac{2B_\tau^W}{B_e^W + B_\mu^W} = 1.002 \pm 0.019,$$

consistent with the standard model lepton flavor universality. This resolves the LEP's tension with the standard model, which has been an open issue for more than a decade. Assuming lepton flavor universality among three generations, the leptonic and total hadronic branching fraction is estimated as 10.89(08)% and 67.32(23)% respectively, leading to the ratio of the total leptonic and total hadronic branching fractions as $R_{h/l}^W = 2.060 \pm 0.021$. With $R_{h/\ell}^W = \mathcal{B}(W \rightarrow h)/(1 - \mathcal{B}(W \rightarrow h)) = (1 + \alpha_S(m_W)/\pi) \sum_{d,s,b}^{u,c} |V_{ij}|^2$, three standard model quantities are subsequently derived: the sum square of elements in the first two rows of the Cabibbo–Kobayashi–Maskawa (CKM) matrix $\sum |V_{ij}|^2 = 1.991 \pm 0.019$, the CKM element $V_{cs} = 0.970 \pm 0.008$, and the strong coupling constant at the W mass pole $\alpha_S(m_W) = 0.099 \pm 0.026$.

This CMS measurement of W branching fraction successfully improves upon the experimental precision from LEP. In addition, give the a good agreement with the standard model lepton flavor universality, it clearly resolves LEP's tension with the SM LU.

APPENDIX A

An Outline of the Quantum Field Theory of the Standard Model

Quantum Field Theory combines special relativity and quantum mechanics to describe the Lorentz invariant rules for fields representing particles and forces. The foundation of QFT is the principle of least action.

$$\delta s = \delta \int \mathcal{L}(\phi, \partial_\mu \phi) dx = 0, \quad (\text{A.1})$$

which leads to the Euler-Lagrange equation of motion for the fields:

$$\frac{\partial}{\partial x_\mu} \left(\frac{\partial \mathcal{L}}{\partial (\partial \phi / \partial x_\mu)} \right) - \frac{\partial \mathcal{L}}{\partial \phi} = 0, \quad (\text{A.2})$$

where $\mathcal{L}(\phi, \partial_\mu \phi)$ is the Lagrangian of the quantum fields. In such a framework, the behaviors of the quantum fields are then fully dictated by their Lagrangian via the Euler-Lagrangian Equation of Motion in Equation A.2. Therefore, this allows us to encode our understanding of the dynamics and interactions of field into the Lagrangian. For example, Klein-Gordon Equations and Dirac Equations, which are two versions of the generalization of Schrodinger Equation in the special relativity domain, can be derived from the Lagrangian of the massive scalar field ϕ and massive spinor filed ψ , as shown in Equation A.3 and A.4. Another example is the electromagnetic field. Based on the Gauss's Law $\nabla \cdot \vec{E} = 0$ and $\nabla \cdot \vec{B} = 0$, Faraday's law of induction $\nabla \times \vec{E} = -\partial_t \vec{B}$ and Ampere's circuital law $\nabla \times \vec{B} = (1/c)\partial_t \vec{E}$, the Maxwell equations for electromagnetic field in the free space can be achieved by defining a Lagrangian

of a massless vector field A_μ , as shown in Equation A.5.

$$\text{scalar: } \mathcal{L}_\phi = \frac{1}{2}\partial_\mu\phi\partial^\mu\phi - \frac{1}{2}m^2\phi^2 \implies \text{Klein-Gordon Equation: } \partial_\mu\partial^\mu\phi + m^2\phi = 0 \quad (\text{A.3})$$

$$\text{spinor: } \mathcal{L}_\psi = i\bar{\psi}\gamma^\mu\partial_\mu\psi - m\bar{\psi}\psi \implies \text{Dirac Equation: } (i\gamma^\mu\partial_\mu - m)\psi = 0 \quad (\text{A.4})$$

$$\text{vector: } \mathcal{L}_A = -\frac{1}{4}F_{\mu\nu}F^{\mu\nu} \implies \text{Maxwell Equations: } \partial_\mu\partial^\mu A_\mu = 0 \quad (\text{A.5})$$

The first well-established quantum field theory is Quantum Electrodynamics (QED). Its formulation in the early 20th century was a joint effort from many great physicists such as Paul Dirac, Wolfgang Pauli, Werner Heisenberg, and Enrico Fermi. Since its establishment, QED was able to successfully explain many atomic phenomena that involve photon and charged particles, such as spontaneous photon emission in the atoms. However, in the late 1930s, physicists realized that QED calculation could diverge during the next-to-leading order. This causes skepticism to QED to make meaningful predictions when involving loops. This problem was solved by proving that the divergence in the fermion vacuum polarization and interaction vertices can exactly cancel out each other. Therefore QED is renormalizable. 1965 Nobel Prize in Physics was awarded to Shinichiro Tomonaga, Julian Schwinger, and Richard Feynman for their contributions to the QED renormalization. SM is an extension based on QED, which extends the gauge symmetry in QED from $U(1)$ to $U(1)_Y \times SU(2)_L \times SU(3)_c$, including electroweak and strong force. Several milestones along the establishment of SM involves

- **Yang-Mills Theory.** In 1954, Chen-Ning Yang and Robert Mills described the gauge theory for the non-abelian group [182]. It serves as one of the most important theoretical frameworks for SM. Based on Yang-Mills Theory, SM QCD is developed and Electroweak force is unified.

- **Higgs mechanism.** In 1964, the Higgs mechanism to generate the mass of gauge field via spontaneous symmetry breaking was proposed by three independent groups: Robert Brout and François Englert [183]; by Peter Higgs [184]; and by Gerald Guralnik, C. R. Hagen, and Tom Kibble [185].
- **GWS Model.** In 1961 Gheldon Glashow combines the electromagnetic and weak force based on Yang-Mills gauge field [186]; then in 1967, Steven Weinberg and Abdus Salam incorporated the Higgs Mechanism into Glashow's electroweak theory [187]. In 1972, the massive Yang-mills gauge fields with gauge boson mass generated by the Higgs mechanism is proven renormalizable by Gerard 't Hooft and Martinus Veltman [188]. In 1973, CKM matrix was added to GWS theory to allow quark mixing and CP violation.
- **Quark Model and QCD.** In 1964, the quark model was proposed by Murray Gell-Mann in order to classify a increasing number of newly discovered mesons and baryons. Quark model soon obtained supports from experiments, such as deep inelastic scattering experiments at SLAC starting in 1969, the discoveries of $J/\psi(c\bar{c})$ at Brookhaven National Laboratory and SLAC in 1974, Upsilon $\Upsilon(b\bar{b})$ at Fermilab in 1977, and top quark at Fermilab in 1995. In 1973, asymptotic freedom was proposed by David Gross and Frank Wilczek, and independently by David Politzer, to explain the quark confinement: strong interaction allows perturbation calculation at high energy while confined at low energy.

This section gives a brief summary of SM skeleton in aspect of the Yang-Mills theory, higgs mechanism, GWS Theory, Quark asymptotic freedom in QCD. Before starting, we may remind ourselves the final form of the SM Lagrangian:

$$\begin{aligned}
\mathcal{L}_{U(1) \times SU(2) \times SU(3)} = & -\frac{1}{4}B_{\mu\nu}B^{\mu\nu} - \frac{1}{4}W_{\mu\nu}^a W_a^{\mu\nu} - \frac{1}{4}G_{\mu\nu}^a G_a^{\mu\nu} \\
& + \bar{\chi}_L \gamma^\mu (i\partial_\mu - g \frac{\tau_a}{2} W_\mu^a - g' \frac{Y}{2} B_\mu) \chi_L + \bar{\psi}_R \gamma^\mu (i\partial_\mu - g' \frac{Y}{2} B_\mu) \psi_R - g_s (\bar{q} \gamma^\mu T_a q) G_\mu^a \\
& + \left| (i\partial_\mu - g \frac{\tau_a}{2} W_\mu^a - g' \frac{Y}{2} B_\mu) \phi \right|^2 - V(\phi) \\
& - (y_1 \bar{\chi}_L \phi \psi_R + y_2 \bar{\chi}_L \phi_c \psi_R + \text{hermitian conjugate}),
\end{aligned} \tag{A.6}$$

where the first to the forth row represents the gauge sector, fermion sector, higgs sector and fermion mass sector respectively. This total SM Lagrangian functions as an indexing map of the discussion in this section. One of the beauty of SM is its minimality. We can count the number of free parameters in the SM Lagrangian. Thanks to the symmetries imposed in the SM, only 18 basic free parameters to begin with are needed in the model.

- 3 gauge coupling strength for hypercharge, isospin and color. g, g', g_s .
- 2 parameters μ and λ in the higgs potential field $V(\phi) = \frac{1}{2}\mu^2\bar{\phi}\phi + \frac{1}{4}\lambda(\bar{\phi}\phi)^2$
- 9 Yukawa couplings between higgs and 9 charged fermions: $y_e, y_\mu, y_\tau, y_u, y_d, y_c, y_s, y_t, y_b$
- 4 parameters in the CKM matrix, 3 Euler angles $\theta_{12}, \theta_{23}, \theta_{31}$ and CP violating phase δ .

The values of these free SM parameters are determined from the experiments. In addition to the above 18 basic parameters, neutrino oscillation indicates neutrinos are not massless and their flavor eigenstates are a mixing of the mass eigenstates. Accordingly, three additional Yukawa couplings are needed for neutrino mass. Analogical to the CKM matrix for the quark mixing, the neutrino mixing is described by PMNS matrix which has 4 free parameters corresponding to three rotation angles and a CP violation phase. Moreover, the CP violation in QCD could also be allowed by adding an extra parameter δ_{CP} . However, in the experiment,

the QCD CP violation is not observed in contrast with the considerable CP violation observed in the weak interaction. This CP conservation in QCD is often referred to as "strong CP problem". So δ_{CP} could be treated as a free SM parameter with a very small value yet to be measured.

A.1. Yang-Mills Gauge Theory

Gauge theory is a type of quantum field theory, the Lagrangian of which is invariant under local phase transformations or gauge transformations. The term "gauge" should be understood as the regularization of the redundant degrees of freedom in the Lagrangian. The transformations between different gauges form a Lie group, which characterizes this gauge theory. Yang-Mills gauge theory is the gauge theory for the non-abelian Lie groups. ("abelian" or "non-abelian" tells whether two gauge transformations in the group are commutable or not.) The standard model is built based on the Yang-Mills gauge theory. But why does SM have to respect the gauge symmetry? The primordial reason is that by enhancing the global phase symmetry to local phase symmetry, we can introduce massless gauge bosons and consequently obtain the couplings between the fermions and the gauge boson. Another benefit anchors in the renormalization. A QFT is useful only if it is renormalizable to make finite meaningful predictions. And gauge theory is proven renormalizable. Besides obtaining force and renormalization, a relatively modern understanding of gauge symmetry is that it is not a symmetry in nature but an artificial consequence of the redundant degree of freedom in the theory. According to Noether's theorem, a nature symmetry corresponds to a conservation law. For example, the global gauge symmetry of QED gives rise to the conservation of electric charge. But the local symmetry in the QED, which is related to the redundant degree of freedom in the mathematical description of the photo polarization, does not lead to any corresponding conserved current. The thinking about the essence of

the gauge symmetry is nicely presented in Schwartz's book, *Quantum Field Theory and the Standard Model* [189]. Here provide a description of the gauge symmetry of the abelian U(1) group and the non-abelian SU(2), SU(3) groups, which is crucial for SM electroweak and QCD, as well as beyond SM models for lepton non-universality in Section 2.3.

A.1.1. U(1) Gauge Symmetry

The Lagrangian of a U(1) gauge theory with spinor field ψ and the associated gauge vector field B_μ is

$$\mathcal{L}_{U(1)} = i\bar{\psi}\gamma^\mu D_\mu\psi - m\bar{\psi}\psi - \frac{1}{4}B_{\mu\nu}B^{\mu\nu}, \quad (\text{A.7})$$

where the covariant derivative D_μ and covariant field strength tensor $B_{\mu\nu}$ defined as

$$D_\mu \equiv \partial_\mu + ig'\frac{Y}{2}B_\mu, \quad B_{\mu\nu} \equiv \partial_\mu B_\nu - \partial_\nu B_\mu. \quad (\text{A.8})$$

$\mathcal{L}_{U(1)}$ is invariant under U(1) local transformation

$$\psi \mapsto e^{i\alpha(x_\mu)}\psi, \quad B_\mu \mapsto B_\mu - \frac{1}{g'\frac{Y}{2}}\partial_\mu\alpha(x_\mu). \quad (\text{A.9})$$

The interaction between the U(1) charge current $j^\mu \equiv g'\bar{\psi}\gamma^\mu\psi$ and the gauge field B_μ is $-j^\mu A_\mu$ and is embedded in the covariant derivative D_μ . The QED is a U(1) Gauge theory. So the QED Lagrangian takes the form of Equation A.7. If we choose $g'\frac{Y}{2} = -e$ and use the conventional notation A_μ for the QED gauge field, Equation A.7 becomes the common form of QED Lagrangian.

A.1.2. SU(2) Gauge Symmetry

The three generators of SU(2) group T_a with $a \in 1, 2, 3$ are usually represented by the half of Pauli Matrices $T_a = \frac{1}{2}\tau_a = \frac{1}{2}\sigma_a$, where the Pauli Matrices are

$$\sigma_1 = \begin{bmatrix} 0 & 1 \\ 1 & 0 \end{bmatrix}, \quad \sigma_2 = \begin{bmatrix} 0 & -i \\ i & 0 \end{bmatrix}, \quad \sigma_3 = \begin{bmatrix} 1 & 0 \\ 0 & -1 \end{bmatrix}. \quad (\text{A.10})$$

The commutation relation of the group generators can be represented as $[T_a, T_b] = if_{abc}T_c$, where f_{abc} is the structure constant of the group. For SU(2) group, the structure constant is the Levi-Civita symbol $f_{abc} = \epsilon_{abc}$. In SM, the left-handed neutrino and charged lepton in the same generation form a doublets described by $SU(2)$ group. The same scenario is for the up and down type left-handed quark in the same generation. The higgs doublet in the SM also transforms as a global $SU(2)$ group. Other than the applications in the SM, SU(2) group is also useful in the description of nucleons with proton-neutron doublet $[n, p]$.

Now we consider a SU(2) gauge theory. Suppose there are two spinor fields ψ_1 and ψ_2 , which compose a spinor doublet $\chi = [\psi_1, \psi_2]^T$. the Lagrangian of the spinnor doublet χ and the gauge vector triplet W^a is

$$\begin{aligned} \mathcal{L}_{SU(2)} &= (i\bar{\psi}_1\gamma^\mu D_\mu\psi_1 - m_1\bar{\psi}_1\psi_1) + (i\bar{\psi}_2\gamma^\mu D_\mu\psi_2 - m_2\bar{\psi}_2\psi_2) - \frac{1}{4}W_{\mu\nu}^a W_a^{\mu\nu} \\ &= i\bar{\chi}\gamma^\mu D_\mu\chi - m\bar{\chi}\chi - \frac{1}{4}W_{\mu\nu}^a W_a^{\mu\nu}, \end{aligned} \quad (\text{A.11})$$

where the covariant derivative D_μ and covariant field strength tensor $W_{\mu\nu}^a$ defined as

$$D_\mu \equiv \partial_\mu + ig\frac{\tau_a}{2}W_\mu^a, \quad W_{\mu\nu}^a \equiv \partial_\mu W_\nu^a - \partial_\nu W_\mu^a - gf_{abc}W_\mu^b W_\nu^c \quad (\text{A.12})$$

$\mathcal{L}_{SU(2)}$ is invariant under SU(2) local transformation

$$\chi \mapsto e^{i\alpha^a(x_\mu)\frac{\tau_a}{2}}\chi, \quad W_\mu^a \mapsto W_\mu^a - \frac{1}{g}\partial_\mu\alpha^a(x_\mu) - f_{abc}\alpha^b(x_\mu)W_\mu^c \quad (\text{A.13})$$

Because SU(2) group is non-abelian, the nontrivial group structure f_{abc} has its contribution to the covariant field strength tensor $W_{\mu\nu}^a$. This leads to the fact that the term $\frac{1}{4}W_{\mu\nu}^a W_a^{\mu\nu}$ in the Equation A.11 not only involves the kinetic energy of the gauge field but also includes WWW and $WWWW$ terms representing three points and four-point self-interaction of the gauge field. The gauge boson can self interact when gauge symmetry is imposed on a non-abelian group, a unique feature of the non-abelian gauge theories. As we will see in the GWS theory in Section A.3, this leads to the Triple-Gauge-Coupling (TGC) and Quatic-gauge-coupling (QGC) in the SM.

A.1.3. SU(3) Gauge Symmetry

The eight generators of SU(3) group T_a with $a \in 1, 2, \dots, 8$ are usually represented by the half of Gell-mann Matrices $T_a = \frac{1}{2}\lambda_a$, where the Gell-mann Matrices are

$$\begin{aligned} \lambda_1 &= \begin{bmatrix} 0 & 1 & 0 \\ 1 & 0 & 0 \\ 0 & 0 & 0 \end{bmatrix}, & \lambda_2 &= \begin{bmatrix} 0 & -i & 0 \\ i & 0 & 0 \\ 0 & 0 & 0 \end{bmatrix}, & \lambda_3 &= \begin{bmatrix} 1 & 0 & 0 \\ 0 & -1 & 0 \\ 0 & 0 & 0 \end{bmatrix}, & \lambda_8 &= \begin{bmatrix} 1 & 0 & 0 \\ 0 & 1 & 0 \\ 0 & 0 & -2 \end{bmatrix}, \\ \lambda_4 &= \begin{bmatrix} 0 & 0 & 1 \\ 0 & 0 & 0 \\ 1 & 0 & 0 \end{bmatrix}, & \lambda_5 &= \begin{bmatrix} 0 & 0 & -i \\ 0 & 0 & 0 \\ i & 0 & 0 \end{bmatrix}, & \lambda_6 &= \begin{bmatrix} 0 & 0 & 0 \\ 0 & 0 & 1 \\ 0 & 1 & 0 \end{bmatrix}, & \lambda_7 &= \begin{bmatrix} 0 & 0 & 0 \\ 0 & 0 & -i \\ 0 & i & 0 \end{bmatrix}. \end{aligned} \tag{A.14}$$

The SU(3) group has non-trivial structure constants which are $f_{123} = 1$, $f_{147} = f_{246} = f_{257} = f_{345} = f_{516} = f_{637} = \frac{1}{2}$, $f_{458} = f_{678} = \frac{\sqrt{3}}{2}$. Besides the structure constant f_{abc} , there are also three useful group constants T_R, C_F, C_A defined as below, with their values for SU(3) group

on the right side

$$Tr(T^a T^b) = T_R \delta^{ab} \longrightarrow T_R^{SU(3)} = \frac{1}{2} \quad (\text{A.15})$$

$$T_a^{i,k} T_{k,j}^a = C_F \delta_{ij} \longrightarrow C_F^{SU(3)} = \frac{N_c^2 - 1}{2N_c} = \frac{4}{3} \quad (\text{A.16})$$

$$f_{acd} f^{bcd} = C_A \delta_{ab} \longrightarrow C_A^{SU(3)} = N_c = 3 \quad (\text{A.17})$$

where N_c is the number of charges or colors. These constants often appear in the calculation of the renormalization of the group. In the SM, SU(3) group is used to describe the triplet of three colors r, g, b in the QCD. In addition to the application in SM, SU(3) group is also useful to describe light mesons and baryons which consist of $[u, d, s]$ quarks. For light mesons, two light quarks form $SU(3) \times SU(3)$ group, while for light baryon, three light quarks form $SU(3) \times SU(3) \times SU(3)$ group.

Now we consider SU(3) gauge theory. Suppose there are three spinor fields ψ_r, ψ_g, ψ_b , which compose a spinor triplet $q = [\psi_r, \psi_g, \psi_b]^T$. Lagrangian of the spinor triplet q and the gauge field octolet G^a is

$$\begin{aligned} \mathcal{L}_{SU(3)} &= \sum_{k \in \{r,g,b\}} (i\bar{\psi}_k \gamma^\mu D_\mu \psi_k - m\bar{\psi}_k \psi_k) - \frac{1}{4} G_{\mu\nu}^a G_a^{\mu\nu} \\ &= i\bar{q} \gamma^\mu D_\mu q - m\bar{q} q - \frac{1}{4} G_{\mu\nu}^a G_a^{\mu\nu} \end{aligned} \quad (\text{A.18})$$

where the covariant derivative D_μ and covariant field strength tensor $G_{\mu\nu}^a$ defined as

$$D_\mu \equiv \partial_\mu + igT_a G_\mu^a, \quad G_{\mu\nu}^a \equiv \partial_\mu G_\nu^a - \partial_\nu G_\mu^a - g_s f_{abc} G_\mu^b G_\nu^c \quad (\text{A.19})$$

$\mathcal{L}_{SU(3)}$ is invariant under SU(3) local transformation

$$q \longmapsto e^{ia_a(x_\mu)T^a} q, \quad G_\mu^a \longmapsto G_\mu^a - \frac{1}{g''} \partial_\mu \alpha^a(x_\mu) - f_{abc} \alpha^b(x_\mu) G_\mu^c \quad (\text{A.20})$$

The same as the $SU(2)$ scenario, the covariant field strength tensor $G_{\mu\nu}^a$ in Equation A.19 has contributions from the non-trivial group structure f_{abc} of $SU(3)$ group, so the kinematic term of gauge field $\frac{1}{4}G_{\mu\nu}^a G_a^{\mu\nu}$ in the Lagrangian in Equation A.18 not only involves the kinematic energy of the gauge field but also include GGG and $GGGG$ terms representing the three-point and four-point self-interaction of the gauge field. For QCD in SM, gluon's self-interaction leads to many unique phenomenologies in the strong interactions, such as quark confinement, evolution of the parton distribution functions and final state ration, which will be discussed in Section A.4.

A.2. The Higgs Mechanism

One might notice that the gauge fields discussed above in Section A.1 are all massless: the Lagrangians do not have any terms for the gauge fields' mass because directly adding such mass terms breaks the gauge symmetry. The massless gauge field does not cause problems in the QED and QCD, where photon and gluon are indeed massless. But for weak interaction, it is known that weak force is short-range, and thus the weak bosons must be massive. But if we naively add a mass term for the weak boson by hand, e.g. $mW_\mu W^\mu$, and give up the gauge symmetry, we will come across divergence in the loop integrals related to the propagator and end up with an un-renormalizable theory failing to make any meaningful predictions at high energy scale. The way to get around is the “higgs mechanism” which generates mass for gauge bosons via spontaneous symmetry breaking while maintaining the gauge symmetry. It first introduces a scalar field ϕ with spontaneously-broken global symmetry. ϕ has gauge charge, and thus couples via the covariant derivative with the gauge field that desires mass. Eventually, it is the gauge covariant derivatives of a spontaneously-broken ϕ that provides the mass for the gauge field. For this reason, the mass of the gauge particle is often intuitively interpreted as the “resistance” when the gauge boson moves in the ϕ field and interacts with

it. In this subsection, the higgs mechanism with $U(1)$ and $SU(2)$ spontaneously broken symmetry are illustrated.

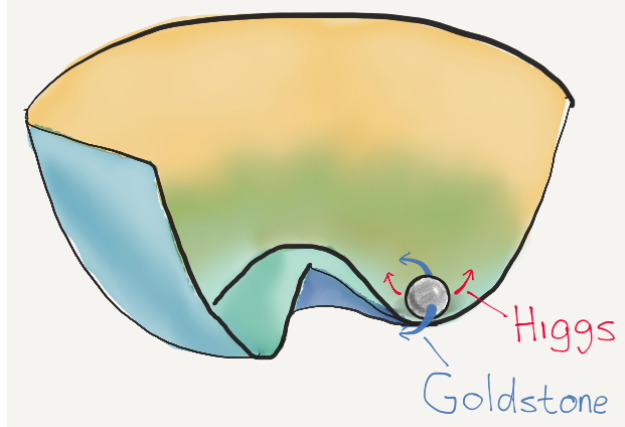


Figure A.1. Spontaneous symmetry breaking of the scalar field ϕ with a $U(1)$ global symmetric potential. The shape of potential on the complex plane looks like a Mexican hat. The scalar field's minimum potential shifts from the origin by the amount of Higgs vacuum expectation value, forming a ring of positions with minimal potential. The scalar field has to choose one of the positions on the ring to settle down. Such a choice is so-called spontaneous symmetry breaking. The radial and lateral perturbation mode around this minimal position gives rise to the Higgs field and the Goldstone field.

A.2.1. $U(1)$ Spontaneous Symmetry Breaking

Consider a $U(1)$ gauge theory with a scalar field ϕ , which has a $U(1)$ global symmetric potential

$$V(\phi) = \frac{1}{2}\mu^2\phi^*\phi + \frac{1}{4}\lambda(\phi^*\phi)^2. \quad (\text{A.21})$$

When engaging local symmetry, we introduce the associated gauge field B_μ . The total Lagrangian for the scalar field and the gauge field is

$$\begin{aligned} \mathcal{L} &= D^\mu\phi^*D_\mu\phi - V(\phi) - \frac{1}{4}B_{\mu\nu}B^{\mu\nu} \\ &= D^\mu\phi^*D_\mu\phi - \left(\frac{1}{2}\mu^2\phi^*\phi + \frac{1}{4}\lambda(\phi^*\phi)^2\right) - \frac{1}{4}B_{\mu\nu}B^{\mu\nu}, \end{aligned} \quad (\text{A.22})$$

where the covariant derivative D_μ and covariant field strength tensor $B_{\mu\nu}$ defined as

$$D_\mu \equiv \partial_\mu + ig' \frac{Y}{2} B_\mu, \quad B_{\mu\nu} \equiv \partial_\mu B_\nu - \partial_\nu B_\mu, \quad (\text{A.23})$$

and the gauge transformation of the scalar field and gauge field is

$$\phi \mapsto e^{i\alpha(x_\mu)} \phi, \quad B_\mu \mapsto B_\mu - \frac{1}{g' \frac{Y}{2}} \partial_\mu \alpha(x_\mu). \quad (\text{A.24})$$

The Lagrangian in Equation is invariant under $U(1)$ gauge transformation in Equation . At this moment, B_μ is massless. The spontaneous symmetry breaking is concerning the scalar's potential $V(\phi)$. When $\mu^2 < 0$, the scalar field's potential $V(\phi)$ on the complex plane looks like a Mexican hat, shown in Figure A.1. It has an infinite number of positions with minimal potential on a ring with $|\phi|^2 = -\frac{\mu^2}{\lambda} = \nu^2$, where ν is the vacuum expectation value or VEV of the scalar ϕ . Because of nontrivial vev, nature has to choose one of these ground states for ϕ instead of the complete vacuum $\phi = 0$. This choice is the so-called spontaneous symmetry break. The term "symmetry break" implies that choosing one specific VEV breaks the $U(1)$ global symmetry of the scalar potential; the term "spontaneous" suggests that the symmetry breaking is induced completely by the scalar itself when $\mu^2 < 0$. During the SSB, it turns out that it does not matter which one of the VEV's is chosen because the complex phase of ϕ will eventually be absorbed by the gauge field B_μ . For convenience, we could choose a VEV $\phi_0 = \nu e^{i0/\nu}$. The scalar field ϕ can be treated as the vibration around ϕ_0 :

$$\phi = \frac{\nu + h}{\sqrt{2}} e^{i\theta/\nu}, \quad (\text{A.25})$$

where the h is the real scalar field for the perturbation in the radial direction, while θ is the real scalar field for the perturbation in the lateral direction. The radial and lateral vibration h and θ is the Higgs and Goldstone field respectively, which transform under the

gauge transformation as following

$$h \mapsto h, \quad \theta \mapsto \theta + \alpha(x_\mu). \quad (\text{A.26})$$

Rewrite Lagrangian in the Equation ?? in terms of the Higgs field h and Goldstone field θ , one gets

$$\begin{aligned} \mathcal{L} &= D^\mu \phi^* D_\mu \phi - \left(\frac{1}{2} \mu^2 \phi^* \phi + \frac{1}{4} \lambda (\phi^* \phi)^2 \right) - \frac{1}{4} B_{\mu\nu} B^{\mu\nu} \\ &= (\partial_\mu + ig' \frac{Y}{2} B_\mu) \phi^* (\partial_\mu + ig' \frac{Y}{2} B_\mu) \phi - \left(\frac{1}{2} \mu^2 \phi^* \phi + \frac{1}{4} \lambda (\phi^* \phi)^2 \right) - \frac{1}{4} B_{\mu\nu} B^{\mu\nu} \\ &= -\frac{1}{4} \mathcal{B}_{\mu\nu} \mathcal{B}^{\mu\nu} + \frac{Y^2}{8} g'^2 \nu^2 \mathcal{B}^\mu \mathcal{B}_\mu \quad (\text{Gauge boson kinetics and mass}) \\ &\quad + \left(\frac{1}{2} (\partial_\mu h)^2 - \lambda \nu^2 h^2 \right) \quad (\text{Higgs kinetics and mass}) \\ &\quad - \left(\lambda \nu h^3 + \frac{1}{4} \lambda h^4 \right) \quad (\text{Higgs self-coupling}) \\ &\quad + \left(\frac{Y^2}{8} 2\nu g'^2 \mathcal{B}^\mu \mathcal{B}_\mu h + \frac{Y^2}{8} g'^2 \mathcal{B}^\mu \mathcal{B}_\mu h^2 \right) \quad (\text{coupling between Higgs and Gauge boson}) \end{aligned} \quad (\text{A.27})$$

where

$$\mathcal{B}_\mu = B_\mu - \frac{1}{g' \frac{Y}{2}} \partial_\mu \theta / \nu \quad (\text{A.28})$$

is the gauge field after absorbing the Goldstone field. Intuitively, it means the gauge boson eats the Goldstone boson. Comparing with Equation ??, this Lagrangian also invariant under $U(1)$ gauge transformation, but the gauge field become massive. It is straight-forward to identify the mass term of the gauge field in the Lagrangian and the mass of the gauge boson and higgs boson turn out to be

$$m_B = g' \frac{Y}{2} \nu, \quad m_h = \sqrt{2\lambda\nu^2} \quad (\text{A.29})$$

Now, the gauge boson acquires its mass! To summary, what is happening is the following: because of the non-trivial vev of the scalar field, SSB happens and produces the Higgs field and the Goldstone field; the Goldstone boson is eaten by the the gauge boson; the gauge boson then become massive and digest the degree of freedom of the Goldstone boson into the transverse polarization which is necessary for massive particles; the higgs field is revealed after the SSB, which predicts a new massive scalar higgs boson.

A.2.2. SU(2) Spontaneous Symmetry Breaking

The Higgs mechanism with SSB for $SU(2)$ symmetry is similar to $U(1)$ breaking but requires two scalar fields forming a scalar doublet. This is the same structure as the scalar field in the SM with $U(1) \times SU(2) \rightarrow U(1)$ SSB discussed in Section A.3. Therefore, $SU(2)$ breaking in this section provides an illustration of SSB with the scalar doublet. More complex scalar structures, such as 2 higgs doublets (2HDM) considered in Section 2.3.4 or higgs triplet, break following the same principle. Here we illustrate the Higgs mechanism with $SU(2)$ SSB by considering a doublet of two complex scalar fields, $\phi = (\phi^+, \phi^0)^T$, which has a $SU(2)$ global symmetric potential as

$$V(\phi) = \frac{1}{2}\mu^2\phi^\dagger\phi + \frac{1}{4}\lambda(\phi^\dagger\phi)^2. \quad (\text{A.30})$$

SSB happens when $\mu < 0$. For convenience, we choose a specific VEV $\phi = (0, \nu/\sqrt{2})^T$ for the SSB and expend the scalar fields around this VEV

$$\phi = \begin{bmatrix} \phi^+ \\ \phi_0 \end{bmatrix} = \begin{bmatrix} 0 \\ (\nu + h)/\sqrt{2} \end{bmatrix} e^{i\frac{\tau_a}{2}\theta^a/\nu} \simeq \begin{bmatrix} \theta_2/2 + i\theta_1/2 \\ \nu + h - i\theta_3/2 \end{bmatrix} / \sqrt{2}, \quad (\text{A.31})$$

where the Higgs field h corresponds to the radial oscillation around the VEV, while three Goldstone field $\theta_1, \theta_2, \theta_3$ corresponds to the three oscillation components in the three rotational direction around $\frac{\tau_a}{2}$ generator axes. The Higgs field and three Goldstone fields transforms under the gauge transformation as

$$h \mapsto h, \quad \theta_a \mapsto \theta_a + \alpha_a(x_\mu). \quad (\text{A.32})$$

Then we can write the SU(2) Lagrangian for the scalar doublet ϕ in terms of Higgs field using the expansion of ϕ around VEV in Equation

$$\begin{aligned} \mathcal{L} &= (D^\mu \phi)^\dagger D_\mu \phi - \left(\frac{1}{2} \mu^2 \phi^\dagger \phi + \frac{1}{4} \lambda (\phi^\dagger \phi)^2 \right) - \frac{1}{4} W_{\mu\nu}^a W_a^{\mu\nu} \\ &= ((\partial_\mu + ig \frac{\tau_a}{2} W_\mu^a) \phi)^\dagger (\partial_\mu + ig \frac{\tau_a}{2} W_\mu^a) \phi - \left(\frac{1}{2} \mu^2 \phi^\dagger \phi + \frac{1}{4} \lambda (\phi^\dagger \phi)^2 \right) - \frac{1}{4} W_{\mu\nu}^a W_a^{\mu\nu} \\ &= -\frac{1}{4} \mathcal{W}_{\mu\nu}^a \mathcal{W}_a^{\mu\nu} + \frac{1}{8} g^2 \nu^2 \mathcal{W}_a^\mu \mathcal{W}_\mu^a \quad (\text{Gauge boson kinematics and mass}) \\ &\quad + \left(\frac{1}{2} (\partial_\mu h)^2 - \lambda \nu^2 h^2 \right) \quad (\text{Higgs kinematics and mass}) \\ &\quad - \left(\lambda \nu h^3 + \frac{1}{4} \lambda h^4 \right) \quad (\text{Higgs self coupling}) \\ &\quad + \left(\frac{1}{8} 2\nu g^2 \mathcal{W}_a^\mu \mathcal{W}_\mu^a h + \frac{1}{8} g^2 \mathcal{W}_a^\mu \mathcal{W}_\mu^a h^2 \right) \quad (\text{coupling between Higgs and Gauge boson}) \end{aligned} \quad (\text{A.33})$$

where $\mathcal{W}_\mu^a = W_\mu^a - \frac{1}{g} \partial_\mu \theta^a / \nu - f_{abc} \theta^b W_\mu^c$ are three massive gauge bosons after absorbing three Goldstone bosons.

A.3. Glashow-Weinberg-Salam Electroweak Model

The $U(1) \times SU(2)$ gauge symmetric Lagrangian of GWS model for the SM electroweak unification reads

$$\begin{aligned} \mathcal{L}_{U(1) \times SU(2)} = & -\frac{1}{4}W_{\mu\nu}^a W_a^{\mu\nu} - \frac{1}{4}B_{\mu\nu}B^{\mu\nu} \\ & + \bar{\chi}_L \gamma^\mu (i\partial_\mu - g \frac{\tau_a}{2} W_\mu^a - g' \frac{Y}{2} B_\mu) \chi_L + \bar{\psi}_R \gamma^\mu (i\partial_\mu - g' \frac{Y}{2} B_\mu) \psi_R \\ & + \left| (i\partial_\mu - g \frac{\tau_a}{2} W_\mu^a - g' \frac{Y}{2} B_\mu) \phi \right|^2 - V(\phi) \\ & - (G_1 \bar{\chi}_L \phi \psi_R + G_2 \bar{\chi}_L \phi_c \psi_R + \text{hermitian conjugate}), \end{aligned} \quad (\text{A.34})$$

where the left-handed leptons and quarks in the same family form isospin doublets χ_L with isospin $\frac{1}{2}$, while all right-handed fermions are isospin singlet ψ_R with isospin 0

$$\begin{aligned} \text{leptons: } \chi_L &= \begin{pmatrix} \nu_{e,L} \\ e_L^- \end{pmatrix}, \begin{pmatrix} \nu_{\mu,L} \\ \mu_L^- \end{pmatrix}, \begin{pmatrix} \nu_{\tau,L} \\ \tau_L^- \end{pmatrix}, \quad \psi_R = e_R^-, \mu_R^-, \tau_R^- \\ \text{quarks: } \chi_L &= \begin{pmatrix} u_L \\ d_L \end{pmatrix}, \begin{pmatrix} c_L \\ s_L \end{pmatrix}, \begin{pmatrix} t_L \\ b_L \end{pmatrix}, \quad \psi_R = u_R, d_R, c_R, s_R, t_R, b_R \end{aligned} \quad (\text{A.35})$$

The Lagrangian in Equation A.34 contains many crucial ideas to realize the unification of electromagnetic and weak interaction. Here list three of the most fundamental ideas. First, the electroweak mixing angle mixes the $U(1)$ and $SU(2)$ gauge bosons. Second, the Higgs mechanism with $U(1) \times SU(2) \rightarrow U(1)$ breaking generates mass for gauge bosons under the electroweak mixing angle. Third, the Yukawa couplings generate the fermion mass and result in the fixing between the fermions' flavor eigenstates and mass eigenstates.

A.3.1. Electroweak Mixing Angle

GWS model allows an electroweak mixing angle θ_W in the $\mathcal{L}_{U(1) \times SU(2)}$ such that

$$g \sin(\theta_W) = g' \cos(\theta_W) = e. \quad (\text{A.36})$$

As consequences, the mixing angle leads to rotated gauge boson fields and mixing features in the gauge-fermion coupling and gauge self-coupling. With the electroweak mixing angle θ_W , the electroweak gauge field B and W^a can be rewritten as a set of new gauge fields A, Z, W^\pm :

$$A_\mu = (g' W_\mu^3 + g B_\mu) / \sqrt{g^2 + g'^2} = \cos\theta_W B_\mu + \sin\theta_W W_\mu^3 \quad (\text{A.37})$$

$$Z_\mu = (g' W_\mu^3 - g B_\mu) / \sqrt{g^2 + g'^2} = \cos\theta_W B_\mu - \sin\theta_W W_\mu^3 \quad (\text{A.38})$$

$$W_\mu^\pm = (W_\mu^1 \mp i W_\mu^2) / \sqrt{2}. \quad (\text{A.39})$$

Similarly, the hypercharge current $J_Y^\mu = \bar{\psi} \gamma^\mu \frac{Y}{2} \psi$ and three isospin current $J_\tau^{\mu,a} = \bar{\chi}_L \gamma^\mu \frac{\tau_a}{2} \chi_L$ can be rewritten as four new currents of electroweak quantum number: the electromagnetic current J_{EM} , the weak neutral current J_{NC} and the two weak charge current J_\pm defined as:

$$J_{EM}^\mu = \bar{\chi}_L \gamma^\mu \frac{\tau_3}{2} \chi_L + \bar{\psi} \gamma^\mu \frac{Y}{2} \psi \quad (\text{A.40})$$

$$J_{NC}^\mu = \cos^2\theta_W \bar{\chi}_L \gamma^\mu \frac{\tau_3}{2} \chi_L - \sin^2\theta_W \bar{\psi} \gamma^\mu \frac{Y}{2} \psi \quad (\text{A.41})$$

$$J_\pm^\mu = \bar{\chi}_L \gamma^\mu \frac{\tau_\pm}{2} \chi_L, \quad (\text{A.42})$$

where the charge raising and lowering matrix τ_\pm are linear combination of Pauli matrices:

$$\tau_+ = (\tau_1 + i\tau_2) / \sqrt{2} = \sqrt{2} \begin{bmatrix} 0 & 1 \\ 0 & 0 \end{bmatrix}, \quad \tau_- = (\tau_1 - i\tau_2) / \sqrt{2} = \sqrt{2} \begin{bmatrix} 0 & 0 \\ 1 & 0 \end{bmatrix}. \quad (\text{A.43})$$

By adding the EW mixing angle and work with the EW mixed gauge fields and currents, the Lagrangian of interaction between fermion and gauge boson can be rewritten as the sum of electromagnetic coupling, weak neutral and weak charge current gauge coupling.

$$\begin{aligned}
\mathcal{L}_{U(1) \times SU(2)}^{\psi\text{-gauge int}} &= -ig\bar{\chi}_L\gamma^\mu\frac{\tau_a}{2}W_\mu^a\chi_L - ig'\bar{\psi}\gamma^\mu\frac{Y}{2}B_\mu\psi \\
&= -ig\bar{\chi}_L\gamma^\mu\frac{\tau_+}{2}\chi_L W_\mu^+ - ig\bar{\chi}_L\gamma^\mu\frac{\tau_-}{2}\chi_L W_\mu^- \quad (\text{Change Current Gauge coupling}) \\
&\quad - i(g\cos\theta_W\bar{\chi}_L\gamma^\mu\frac{\tau_3}{2}\chi_L - g'\sin\theta_W\bar{\psi}\gamma^\mu\frac{Y}{2}\psi)Z_\mu \quad (\text{Neutral Current Gauge coupling}) \\
&\quad - i(g\sin\theta_W\bar{\chi}_L\gamma^\mu\frac{\tau_3}{2}\chi_L + g'\cos\theta_W\bar{\psi}\gamma^\mu\frac{Y}{2}\psi)A_\mu \quad (\text{EM Current Gauge coupling}) \\
&= -igJ_\pm^\mu W_\mu^\pm - \frac{ig}{\cos\theta_W}J_{NC}^\mu Z_\mu - ieJ_{EM}^\mu A_\mu
\end{aligned} \tag{A.44}$$

The QED electric charge can be composed by the hypercharge and the third isospin value as $Q = T_3 + \frac{Y}{2}$. In Equation A.44, on one hand, the electromagnetic current J_{EM} couples with photon field A with a coupling strength constant e , which is exactly the component corresponding to the QED gauge interaction. On the other hand, the weak neutral current J_{NC} couples with Z boson with a coupling constant $g/\cos\theta_W$ and the weak charged current couples with W^\pm with coupling constant g , which corresponds to the weak gauge interaction. Therefore, in this way, the electroweak interaction is comprised of the QED and weak components.

Besides a mixing pattern in the fermion-gauge couplings in Equation A.44, the electroweak mixing angle also leads to a mixing in the gauge self-couplings. As discussed in the Section A.1, the non-abelian group has non-trivial structure constant f_{abc} built into the gauge fields, which results in the gauge self-couplings among $W^{a=1,2,3}$ in the gauge kinematic energy term. Due to electroweak mixing θ_W , the self-gauge coupling in the $W^{a=1,2,3}$ basis can be transformed into $W^\pm Z\gamma$ basis and takes a slightly more complex form, which includes

2 vertices of triple-gauge-coupling shown in Figure ?? and 4 vertices of four-quatic-gauge couplings shown in Figure A.3

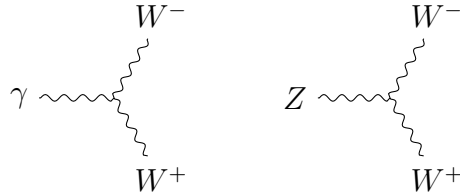


Figure A.2. Vertices of SM electroweak Triple-Gauge-Couplings. WW pairs couple to Z/γ because of the electroweak mixing θ_W . The Triple-Gauge-Couplings is one of the major process of WW pair production in the electron-positron collider $e^-e^+ \rightarrow Z/\gamma \rightarrow W^+W^-$ such as LEP2 which is discussed in Section ??.

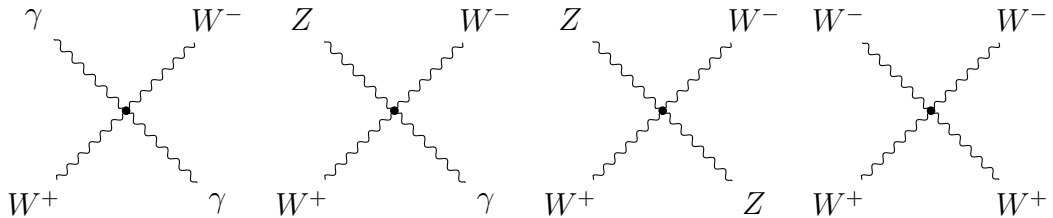


Figure A.3. Vertices of SM electroweak Quatic-Gauge-Couplings.

A.3.2. Gauge Boson Mass

The weak gauge boson must be massive since the weak force is indicated short-ranged by the experiments. Nowadays, the masses of W , Z boson have been measured as $M_W = 80.379 \pm 0.012$ GeV and $M_Z = 91.1876 \pm 0.0021$ GeV, which in the GWS model is generated by the Higgs mechanism with $U(1)_Y \times SU(2)_L \rightarrow U(1)_{EM}$ spontaneous symmetry breaking. The breaking is implemented by a complex scalar doublet field $\phi = [\phi^+, \phi^0]$, the same structure as the Higgs mechanism with $SU(2)$ breaking. While the isospin of the scalar doublet is determined by the $SU(2)$ generators, the choice of the doublet's hypercharge determines the mass of Z and A field after the breaking. To obtain massless photon, the

hypercharge of ϕ is therefore chosen to be $Y_\phi = 1$. The derivation of the photon mass and weak boson mass with $Y_\phi = 1$ is as following

$$\begin{aligned}
\mathcal{L}_{U(1) \times SU(2)}^{\text{gauge mass}} &= \left| \left(-ig \frac{\tau_a}{2} W_\mu^a - ig' \frac{Y}{2} B_\mu \right) \phi \right|^2 \\
&= \frac{1}{8} \left| \begin{bmatrix} gW_\mu^3 + g'B_\mu & g(W_\mu^1 - iW_\mu^2) \\ g(W_\mu^1 + iW_\mu^2) & -gW_\mu^3 + g'B_\mu \end{bmatrix} \begin{bmatrix} 0 \\ \nu \end{bmatrix} \right|^2 \\
&= \frac{1}{8} \nu^2 g^2 (W_\mu^1 W_1^\mu + W_\mu^2 W_2^\mu) + \frac{1}{8} \nu^2 (g'B_\mu - gW_\nu^3)(g'B^\mu - gW^{3\nu}) \\
&= (\frac{1}{2} \nu g)^2 W_\mu^+ W^{-\mu} + \frac{1}{2} (\frac{1}{2} \nu \sqrt{g'^2 + g^2})^2 Z_\mu Z^\mu + 0 A_\mu A^\mu,
\end{aligned} \tag{A.45}$$

where shown is the Lagrangian terms about the gauge boson mass, the term with gauge field squares coming from the squared covariant derivative of the scalar doublet $|D_\mu \phi|^2$ in the Higgs sector. The VEV $(0, \nu/\sqrt{2})^T$ is used for the scalar doublet and the underline gauge fields W^a, B are replaced with the physical gauge field W^\pm, Z, A with final mass of

$$M_W = \frac{1}{2} \nu g, \quad M_Z = \frac{1}{2} \nu \sqrt{g'^2 + g^2} = \frac{1}{2} \nu \frac{g}{\cos \theta_W}, \quad M_A = 0. \tag{A.46}$$

One of the immediate consequences of the choice of $Y_\phi = 1$ for massless photon is that the ratio between W and Z boson is related to the electroweak mixing angle θ_W :

$$\frac{M_W}{M_Z} = \cos \theta_W \tag{A.47}$$

While Equation A.45 shows a part of the Lagrangian in the Higgs sector that only have gauge field, the full Lagrangian in the Higgs sector with $\phi = (0, (\nu + h)/\sqrt{2})^T$ and $Y_\phi = 1$

reads as

$$\begin{aligned}
\mathcal{L}_{U(1) \times SU(2)}^{\text{higgs}} &= \left| \left(i\partial_\mu - g \frac{\tau_a}{2} W_\mu^a - g' \frac{Y}{2} B_\mu \right) \phi \right|^2 - \left(\frac{1}{2} \mu^2 \phi^\dagger \phi + \frac{1}{4} \lambda (\phi^\dagger \phi)^2 \right) \\
&= \left(\frac{1}{2} \nu g \right)^2 W_\mu^+ W^{-\mu} + \frac{1}{2} \left(\frac{1}{2} \nu \sqrt{g'^2 + g^2} \right)^2 Z_\mu Z^\mu + 0 A_\mu A^\mu \quad (\text{gauge mass}) \\
&\quad + \left(2 \frac{h}{\nu} + \frac{h^2}{\nu^2} \right) \left(\left(\frac{1}{2} \nu g \right)^2 W_\mu^+ W_\mu^- + \frac{1}{2} \left(\frac{1}{2} \nu \sqrt{g'^2 + g^2} \right)^2 Z_\mu Z_\mu \right) \quad (\text{Higgs-gauge coupling}) \\
&\quad + \left(\frac{1}{2} (\partial_\mu h)^2 - \lambda \nu^2 h^2 \right) - \left(\lambda \nu h^3 + \frac{1}{4} \lambda h^4 \right) \quad (\text{Higgs and self-coupling})
\end{aligned} \tag{A.48}$$

where the first row corresponds to the gauge boson mass; the second row is responsible for the couplings between gauge bosons; the third row describes the kinematic energy, mass, and self-coupling of Higgs boson. The mass of Higgs boson can be identified as $M_h = \sqrt{2\lambda\nu^2}$. The coupling strength between the gauge boson and the Higgs boson exactly equals the gauge boson mass. Since the photon is massless, it does not couple to the Higgs. As will be discussed in the following paragraph, the coupling strength between the fermion and the Higgs boson is proportional to the fermion mass. Therefore, this property of the Higgs boson is often described as “higgs couples to mass”, which is essentially an experimental observable of the theory that “ particle mass originates from interacting with higgs”. The SM vertices for the Higgs coupling to gauge boson and fermions are shown in Figure A.4.

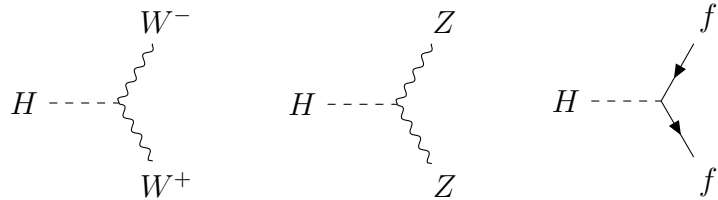


Figure A.4. Vertices of SM Higgs-gauge couplings and Higgs-fermion coupling. The coupling strength is proportional to the mass of the coupled gauge boson or fermion.

A.3.3. Fermion Mass and Fermion Mixing

In GWS model, the fermion mass is allowed by introducing Yukawa coupling between the fermion and the scalar doublet ϕ with the coupling constant y_f . After the spontaneous symmetry breaking $U(1)_Y \times SU(2)_L \rightarrow U(1)_{EM}$, ϕ is expended around its VEV as $\phi = (0, (\nu + h)/\sqrt{2})^T$. Accordingly, the Lagrangian of the Yukawa coupling between the fermion and the scalar doublet ϕ is transformed into the terms for fermion mass and terms for Higgs-fermion interaction. For example, considering only the first family of leptons and quarks, the Lagrangian in the Yukawa coupling sector reads as

$$\begin{aligned} \mathcal{L}_{U(1) \times SU(2)}^{\text{yukawa}} &= [-y_e(\bar{\nu}_e, \bar{e})_L \phi e_R - y_d(\bar{u}, \bar{d})_L \phi d_R - y_u(\bar{u}, \bar{d})_L \phi_c u_R] + h.c. \\ &= -\frac{y_e}{\sqrt{2}}\nu(\bar{e}_L e_R + \bar{e}_R e_L) - \frac{y_u}{\sqrt{2}}\nu(\bar{u}_L u_R + \bar{u}_R u_L) - \frac{y_d}{\sqrt{2}}\nu(\bar{d}_L d_R + \bar{d}_R d_L) \\ &\quad - \frac{y_e}{\sqrt{2}}h(\bar{e}_L e_R + \bar{e}_R e_L) - \frac{y_u}{\sqrt{2}}h(\bar{u}_L u_R + \bar{u}_R u_L) - \frac{y_d}{\sqrt{2}}h(\bar{d}_L d_R + \bar{d}_R d_L) \quad (\text{A.49}) \\ &= -\frac{y_e\nu}{\sqrt{2}}\bar{e}e - \frac{y_u\nu}{\sqrt{2}}\bar{u}u - \frac{y_d\nu}{\sqrt{2}}\bar{d}d \quad (\text{fermion mass}) \\ &\quad - \frac{y_e}{\sqrt{2}}h\bar{e}e - \frac{y_u}{\sqrt{2}}h\bar{u}u - \frac{y_d}{\sqrt{2}}h\bar{d}d \quad (\text{Higgs-fermion coupling}), \end{aligned}$$

where the fermion mass is then proportional to the Yukawa coupling strength y_f

$$M_f = \frac{y_f v}{\sqrt{2}}, \quad (\text{A.50})$$

and ϕ_c is the charge conjugate of the scalar doublet

$$\phi_c = -i\tau_2\phi^* = -i\tau_2 \begin{bmatrix} \phi^+ \\ \phi^0 \end{bmatrix}^* = -i\tau_2 \begin{bmatrix} \phi^- \\ \bar{\phi}^0 \end{bmatrix} = \begin{bmatrix} -\bar{\phi}^0 \\ \phi^- \end{bmatrix}. \quad (\text{A.51})$$

From Equation A.49, the coupling strength between fermion and Higgs boson is proportional to the fermion mass $\frac{y_f}{\sqrt{2}} = \frac{M_f}{\nu}$. Here χ_L and ψ denote the mass eigenstates of the fermions.

It turns out that for quarks, the flavor eigenstates participating in the weak interaction is a linear mixing of mass eigenstates. Such mixing allows the quark transition between two different generations in the flavor changing charged current (FCCC) weak process, confirmed in many experiments. The quark mixing is mathematically expressed as a 3x3 unitary matrix known as the CKM matrix. For down-type quarks, the CKM matrix composes their weak flavor eigenstates (d', s', b') by linear combining their mass eigenstate (d, s, b) . For up-type quarks (up, charm, top), their flavor eigenstates are set equal to their mass eigenstates. By rotating (d, s, b) with CKM matrix, the weak coupling strengths between d, s, b quark and u, c, t quark are scaled by the nine elements in the CKM matrix. The CKM rotation from mass eigenstates (d, s, b) to flavor eigenstates (d', s', b') can be expressed as

$$\begin{bmatrix} d' \\ s' \\ b' \end{bmatrix} = \begin{bmatrix} V_{ud} & V_{us} & V_{ub} \\ V_{cd} & V_{cs} & V_{cb} \\ V_{td} & V_{ts} & V_{tb} \end{bmatrix} \begin{bmatrix} d \\ s \\ b \end{bmatrix} \quad (\text{A.52})$$

Similar to quark mixing, the discovery of the neutrino oscillation implies that three neutrinos should also be mixed by a 3x3 unitary matrix. More specifically, the neutrinos oscillation is a consequence of the two facts: firstly, they are massive; secondly, their flavor eigenstates are a mixture of their mass eigenstates. Thus SM is modified accordingly to cope with the neutrino oscillation: three Yukawa coupling constants for neutrino are added for neutrino mass; the 3x3 PMNS matrix is postulated to implement the neutrino mixing. Analogical to the quark mixing, the neutrino flavor eigenstates are “PMNS-rotated” mass eigenstates

$$\begin{bmatrix} \nu_e \\ \nu_\mu \\ \nu_\tau \end{bmatrix} = \begin{bmatrix} U_{e1} & U_{e2} & U_{e3} \\ U_{\mu 1} & U_{\mu 2} & U_{\mu 3} \\ U_{\tau 1} & U_{\tau 2} & U_{\tau 3} \end{bmatrix} \begin{bmatrix} \nu_1 \\ \nu_2 \\ \nu_3 \end{bmatrix} \quad (\text{A.53})$$

For both CKM and PMNS matrix, though there are 9 elements in the matrix, only four independent parameters are needed to fully parametrize the matrix. The parameters include $\theta_{12}, \theta_{13}, \theta_{23}$, for the rotation angle along third, second, and first axis, respectively, and δ_{13} for the CP violation during the weak interaction between the first and the third family. Sometimes, Wolfenstein parameters $[A, \lambda, \rho, \eta]$ are used instead of $[\theta_{12}, \theta_{13}, \theta_{23}, \delta_{13}]$ for a polynomial parametrization. The two parametrizations of the CKM and PMNS matrix can be expressed as

$$\begin{aligned}
V, U &= \begin{bmatrix} 1 & 0 & 0 \\ 0 & c_{23} & s_{23} \\ 0 & -s_{23} & c_{23} \end{bmatrix} \begin{bmatrix} c_{13} & 0 & s_{13}e^{-i\delta_{13}} \\ 0 & 1 & 0 \\ -s_{13}e^{i\delta_{13}} & 1 & c_{13} \end{bmatrix} \begin{bmatrix} c_{12} & s_{12} & 0 \\ -s_{12} & c_{13} & 0 \\ 0 & 0 & 1 \end{bmatrix} \\
&= \begin{bmatrix} c_{12}c_{13} & s_{12}c_{13} & s_{13}e^{-i\delta} \\ -s_{12}c_{23} - c_{12}s_{23}s_{13}e^{i\delta} & c_{12}c_{23} - s_{12}s_{23}s_{13}e^{i\delta} & s_{23}c_{13} \\ s_{12}s_{23} - c_{12}c_{23}s_{13}e^{i\delta} & -c_{12}s_{23} - s_{12}c_{23}s_{13}e^{i\delta} & c_{23}c_{13} \end{bmatrix} \quad (\text{A.54}) \\
&= \begin{bmatrix} 1 - \lambda^2/2 & \lambda & A\lambda^3(\rho - i\eta) \\ -\lambda & 1 - \lambda^2/2 & A\lambda^2 \\ A\lambda^3(1 - \rho - i\eta) & -A\lambda^2 & 1 \end{bmatrix} + O(\lambda^4)
\end{aligned}$$

where the parameters are determined by the experiments. For parametrization with rotation angle $[\theta_{12}, \theta_{13}, \theta_{23}, \delta_{13}]$, the world average experimental measurements are

$$\text{CKM: } \theta_{12} = 13.04 \pm 0.15, \theta_{13} = 0.201 \pm 0.011, \theta_{23} = 1.23 \pm 0.06, \delta = 68.8 \pm 4.6 \quad (\text{A.55})$$

$$\text{PMNS: } \theta_{12} = 33.62^{+0.78}_{-0.76}, \theta_{13} = 47.2^{+1.9}_{-3.9}, \theta_{23} = 8.54^{+0.15}_{-0.15}, \delta = 234^{+43}_{-31}. \quad (\text{A.56})$$

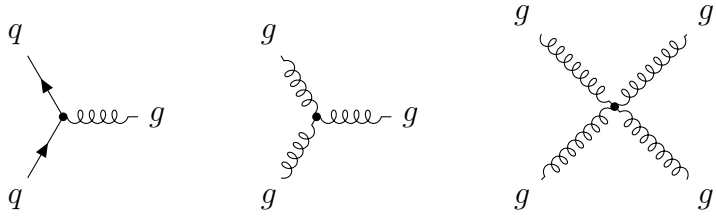


Figure A.5. Vertices of the SM QCD interaction. Quarks and gluons both carry colors allowing quark-gluon interaction and gluon self-interaction.

A.4. Quantum Chromodynamics

QCD assumes three color charges with three anti-colors, analogical to the QED's positive and negative electric charge. The potential between two color charges can be attractive or repulsive in the short-distance range, depending on the state of the two-color system:

$$V(r)_{\text{singlet}} = -\frac{4\alpha_s}{3r} + \lambda r \quad (\text{attractive in short-distance range}) \quad (\text{A.57})$$

$$V(r)_{\text{octet}} = \frac{\alpha_s}{6r} + \lambda r \quad (\text{repulsive in short-distance range}), \quad (\text{A.58})$$

where the $\frac{1}{r}$ term dominates in the short-distance range, and λr term dominates in the long-distance range. In the short-distance range, if the two interacting colors form a color singlet state, the strong force between them is attractive; but repulsive if the two form a color octet state. For example, the two quarks in a meson form a color singlet state, and thus the strong force between them is attractive. In contrast, in the quark-quark scattering process where gluons are exchanged, the two quarks form a color octet state with a repulsive strong force. In the long-distance range, when two colors split far from each other, the strong force potential increases linearly with the separation, creating cylindrical "color tubes" in the space in between. When the separation become large, the potential energy in the "color tube" will be enough to create new quark-antiquark pairs from the vacuum, guaranteeing that quarks cannot be separated and no quarks exist alone. This is an intuitive approach to understand quark confinement. A formal derivation of the QCD quark confinement is

through the running of couplings presented in the next paragraph in Equation A.59. Though color charge and gluon in the QCD can be analogical to electric charge and photons in the QED in many ways, QCD has many unique phenomena, such as asymptotic freedom, quark confinement, color anti-screening. Theoretically speaking, these unique figures is essentially originated from two facts:

- The SU(3) group is non-abelian.
- the number of quarks is $n_f = 6$

Non-trivial f_{abc} of SU(3) group leads to the gluon self-coupling, which together with $n_f = 6$ further determines the unique running of the QCD coupling: the QCD coupling increases when the energy scale goes low; meanwhile, it decreases in the high-energy region. This can be demonstrated by the calculation of the beta function in the QCD renormalization group equation. The SU(3) gauge symmetric Lagrangian for QCD is

$$\mathcal{L}_{SU(3)}^{QCD} = i\bar{q}\gamma^\mu D_\mu q - m\bar{q}q - \frac{1}{4}G_{\mu\nu}^a G_a^{\mu\nu}, \quad (\text{A.59})$$

where the first term expresses the quark kinematic energy and interaction with gluons, the third term $\frac{1}{4}G_{\mu\nu}^a G_a^{\mu\nu}$ gives gluon kinematic energy and self-interaction. The gluon self-coupling plays a core role in the QCD running couplings: the running coupling is driven by the vacuum polarization; the QCD vacuum polarization of the gluon propagator includes not only the quark bubbles but also has a large contribution from the gluon bubbles. The general form of renormalization group equation (RGE) is

$$\mu \frac{\partial}{\partial \mu} \alpha(\mu) \equiv \beta(\alpha) = -2\alpha \left[\left(\frac{\alpha}{4\pi}\right) \beta_0 + \left(\frac{\alpha}{4\pi}\right)^2 \beta_1 + \left(\frac{\alpha}{4\pi}\right)^3 \beta_2 + \dots \right], \quad (\text{A.60})$$

where the running of coupling with respect to the energy scale $\mu \frac{\partial}{\partial \mu} \alpha(\mu)$ is represented as “beta function” $\beta(\alpha)$ which can be expanded as a power series of the coupling α . The

coefficiencies of the power series $\beta_0, \beta_1, \beta_2, \beta_3 \dots$ are calculated from the considering 1-loop, 2-loop, 3-loop ... vacuum polarization of the gluon. If only considering the leading order beta function by taking into account only the 1-loop contribution, the renormalization group equation reduces to a simple first-order linear differential equation $\mu \frac{\partial \alpha(\mu)}{\partial \mu} = \frac{\beta_0}{2\pi} \alpha^2$, which is easily solved by

$$\alpha(\mu) = \frac{\alpha(\mu_0)}{1 + \alpha(\mu_0) \frac{\beta_0}{2\pi} \ln\left(\frac{\mu}{\mu_0}\right)} = \frac{1}{\frac{\beta_0}{4\pi} \ln\left(\frac{\mu^2}{\Lambda^2}\right)}, \quad (\text{A.61})$$

where μ is the running scale, μ_0 is a reference scale and Λ is the energy scale which diverges coupling $\alpha(\Lambda) \gg 1$ and the condition for power expansion of beta function breaks. The energy scale Λ is called “Landau Pole” and is a constant fixed by the boundary condition of the RGE. The β_0 is obtained by evaluating and summing 1-loop diagrams contributing to the vacuum polarization.

For QED, photon’s vacuum polarization only includes fermion bubbles, and summing all 1-loop diagrams yields $\beta_0 = -4/3$. This is a negative number, which means the QED coupling strength increases as the energy scale μ increases. Phenomenologically speaking, the closer one gets to the bare electric charge, the larger the effective electric charge he will be able to feel. In other words, the photon’s vacuum polarization creates a charge “screening” effect for the bare charge. The screening effect is analogical to charge screening effect created by the electric polarization in the dielectric media surrounding an electric charge. The Landau pole of QED can be estimated from $\alpha(m_e = 511\text{keV}) = \frac{1}{137}$ which gives $\Lambda_{QED} = 10^{286} \text{ eV}$, a very large energy scale much beyond the Planck scale. So QED is valid and renormalizable in a vast range of energy scales.

For QCD, the gluon’s vacuum polarization includes both the fermion bubble and the gluon bubble. Summing all 1-loop diagrams yields

$$\beta_0 = \frac{11C_A}{3} - \frac{2n_f}{3} = 7, \quad (\text{A.62})$$

where $n_f = 6$ is the number of quarks. The sign of β_0 in QCD is positive, opposite to β_0 in the QED. Therefore the QCD coupling α_s increases when approaching to lower energy scale. When energy is low, α_s is large, and quarks are confined; when energy is high, α_s is small, and quarks get asymptotic freedom. The screening effect in the QCD is opposite to that in the QED. When going away from a bare color charge, one feels a larger effective color charge. In other words, the gluon's vacuum polarization creates a color “anti-screening” effect on the bare color. In fact, the effect is anti-screening as long as the number of quarks is less than $n_f < 17$. The QCD's Landau pole Λ_{QCD} thereby sets a lower limit for the energy scale, which is approximated by experiments to be around 200 GeV. For energy scale below Λ_{QCD} , perturbative approach no longer works and Lattice QCD is invented to solve the related problems at the low energy scale.

Beyond the 1-loop diagram, the running of coupling can be determined by solving higher order RGE and evaluating $\beta_1, \beta_2, \beta_3$ with the higher-order loops diagrams. The higher-order up to $O(\alpha^3)$ solution to the RGE in Equation A.60 reads as [189]

$$\alpha_s(\mu) = \alpha_s(\mu_R) - \frac{\alpha_s^2(\mu_R)}{2\pi} \beta_0 \ln \frac{\mu}{\mu_R} + \frac{\alpha_s^3(\mu_R)}{8\pi^2} \left[-\beta_1 \ln \frac{\mu}{\mu_R} + 2\beta_0^2 \ln^2 \frac{\mu}{\mu_R} \right] + O(\alpha_s^4(\mu_R)), \quad (\text{A.63})$$

where the higher order of beta coefficients $\beta_1, \beta_2, \beta_3$ are calculated by summing higher-order up to four-loop diagrams

$$\begin{aligned} \beta_1 &= 102 - 10n_f - \frac{8}{3}n_f, & \beta_2 &= \frac{325}{54}n_f^2 - \frac{5033}{18}n_f + \frac{2857}{2} \\ \beta_3 &= \frac{1093}{729}n_f^3 + \left(\frac{50065}{162} + \frac{6472}{81}\zeta_3 \right)n_f^2 - \left(\frac{1078361}{162} + \frac{6508}{27}\zeta_3 \right)n_f + 3564\zeta_3 + \frac{149753}{6} \end{aligned}$$

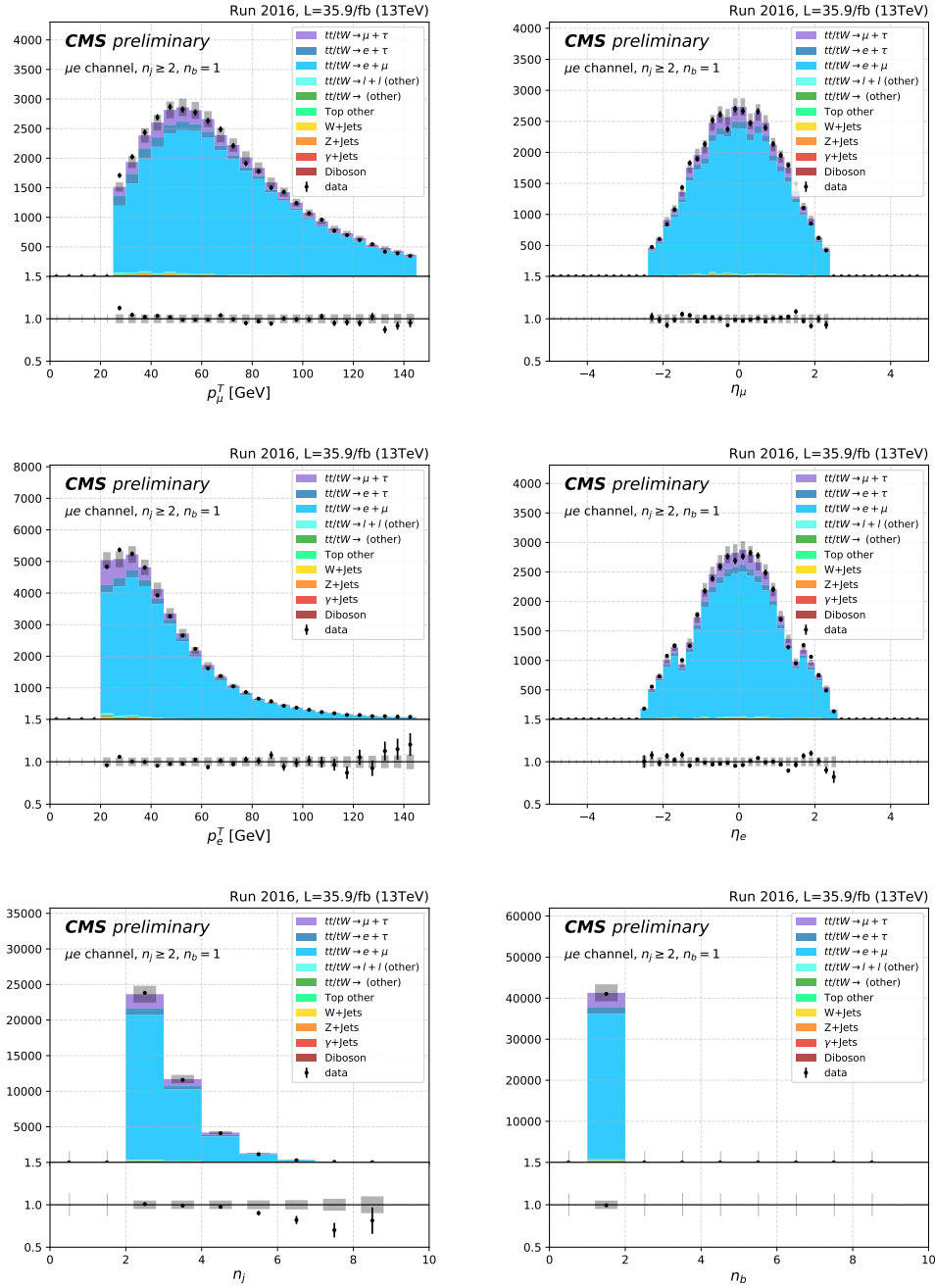
APPENDIX B

Plots for the Analysis of W Branching Fractions

??

B.1. Kinematics Plots in Counting Analysis

??

$\mu e - 1b$ Figure B.1. μe channel with $n_j \geq 2, n_b = 1$.

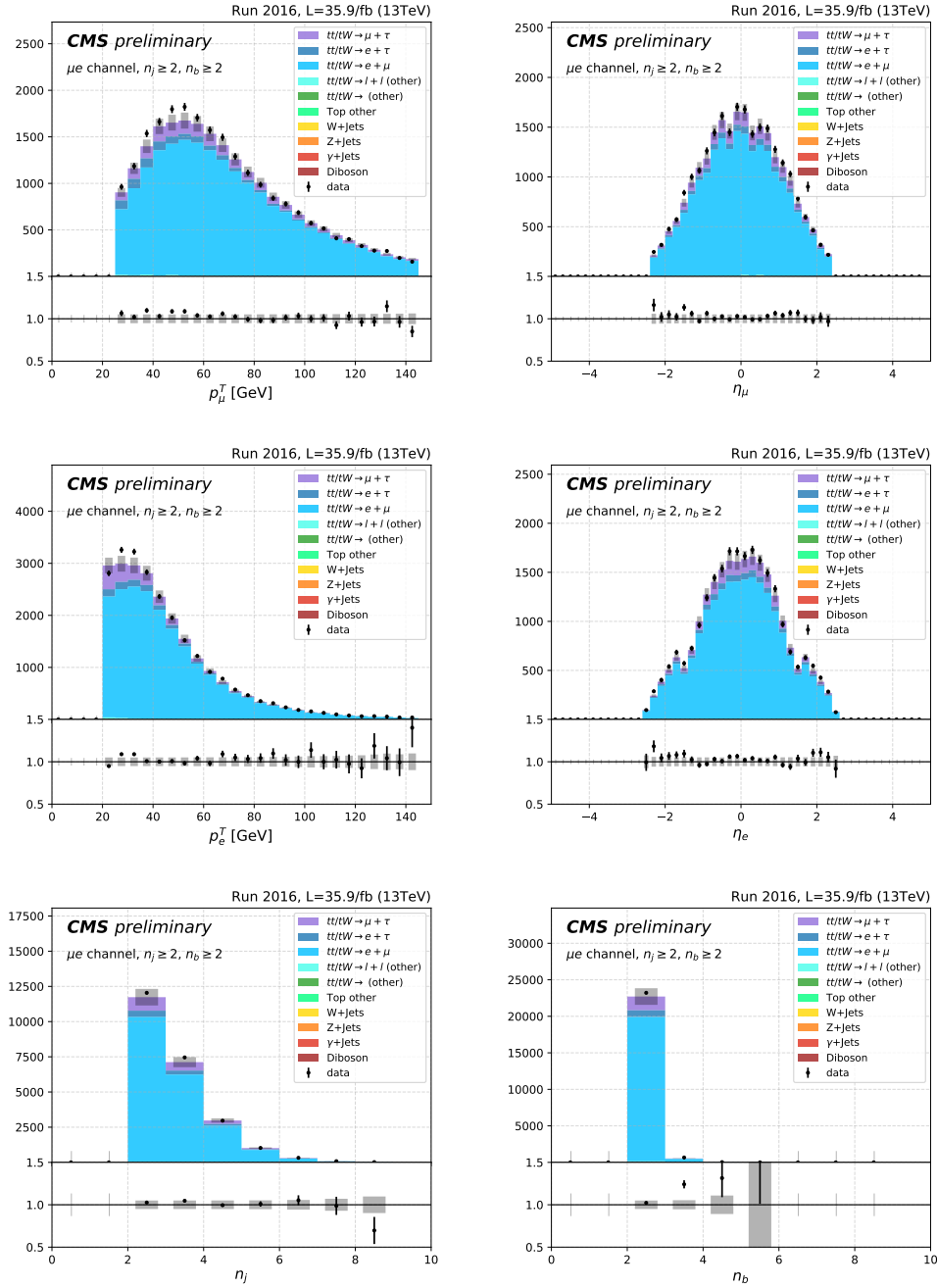
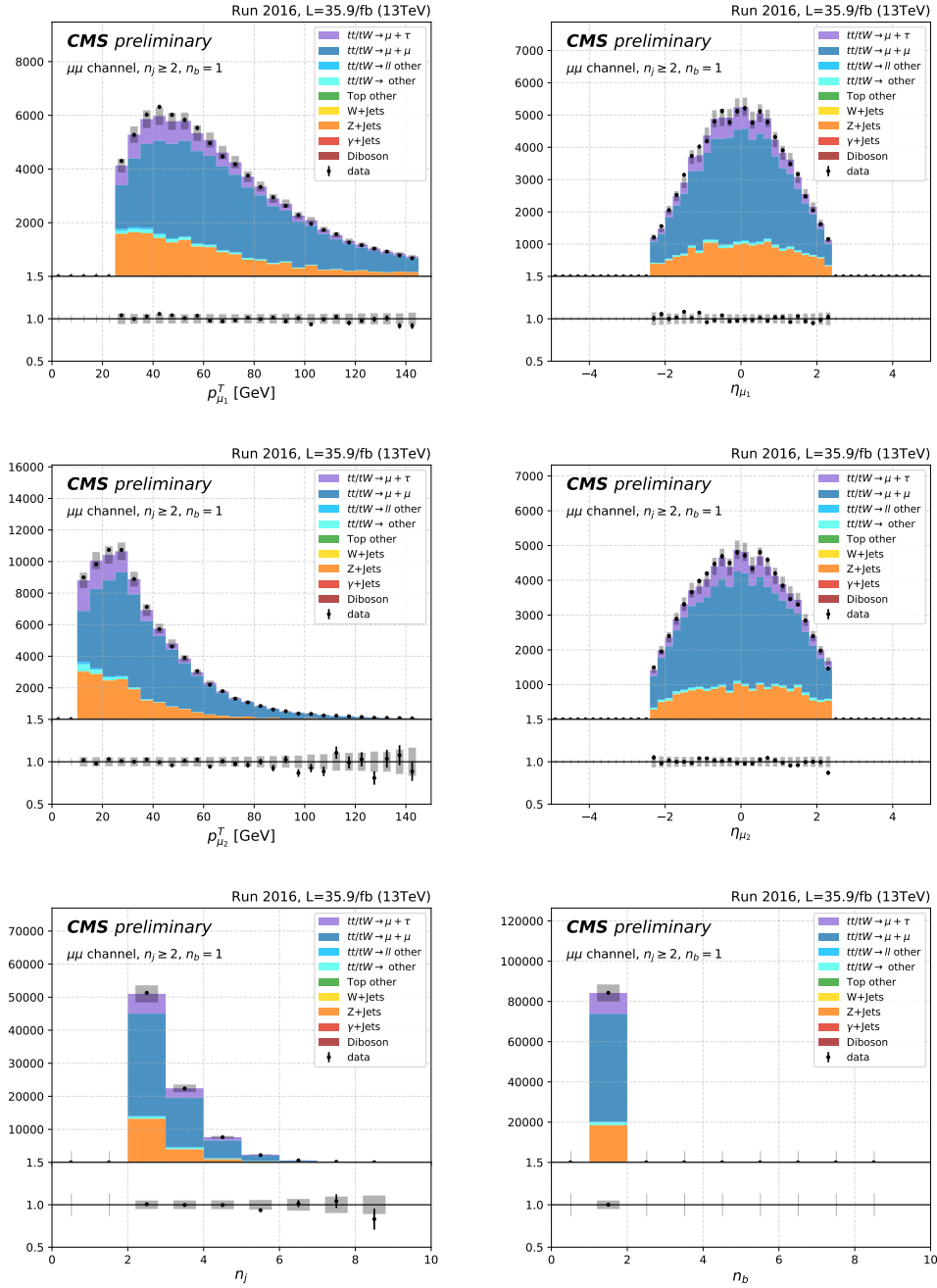
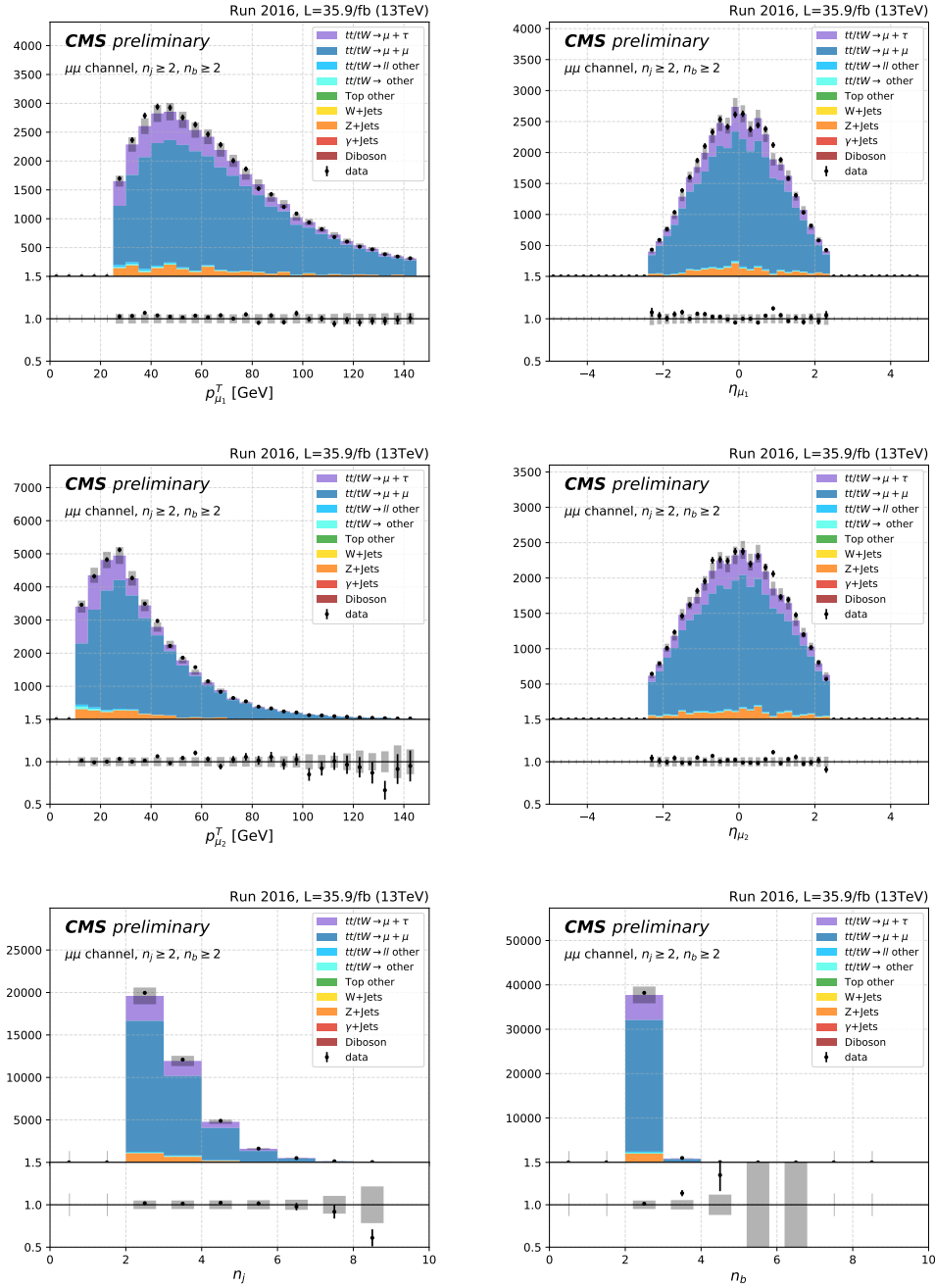
$\mu e - 2b$


Figure B.2. μe channel with $n_j \geq 2$, $n_b \geq 2$.

$\mu\mu - 1b$ Figure B.3. $\mu\mu$ channel with $n_j \geq 2, n_b = 1$.

$\mu\mu - 2b$ Figure B.4. $\mu\mu$ channel with $n_j \geq 2, n_b \geq 2$.

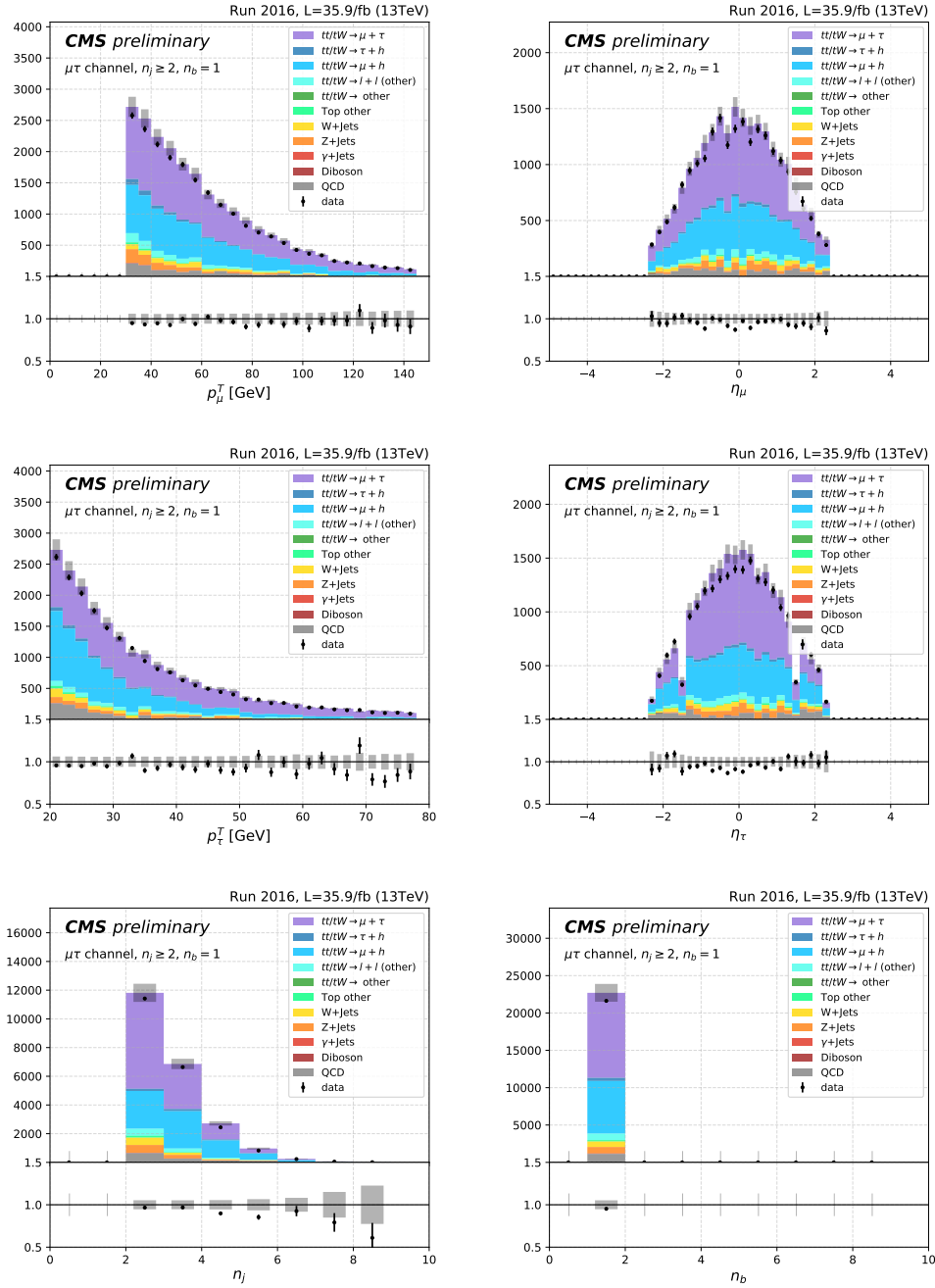
$\mu\tau - 1b$


Figure B.5. $\mu\tau$ channel with $n_j \geq 2$, $n_b = 1$.

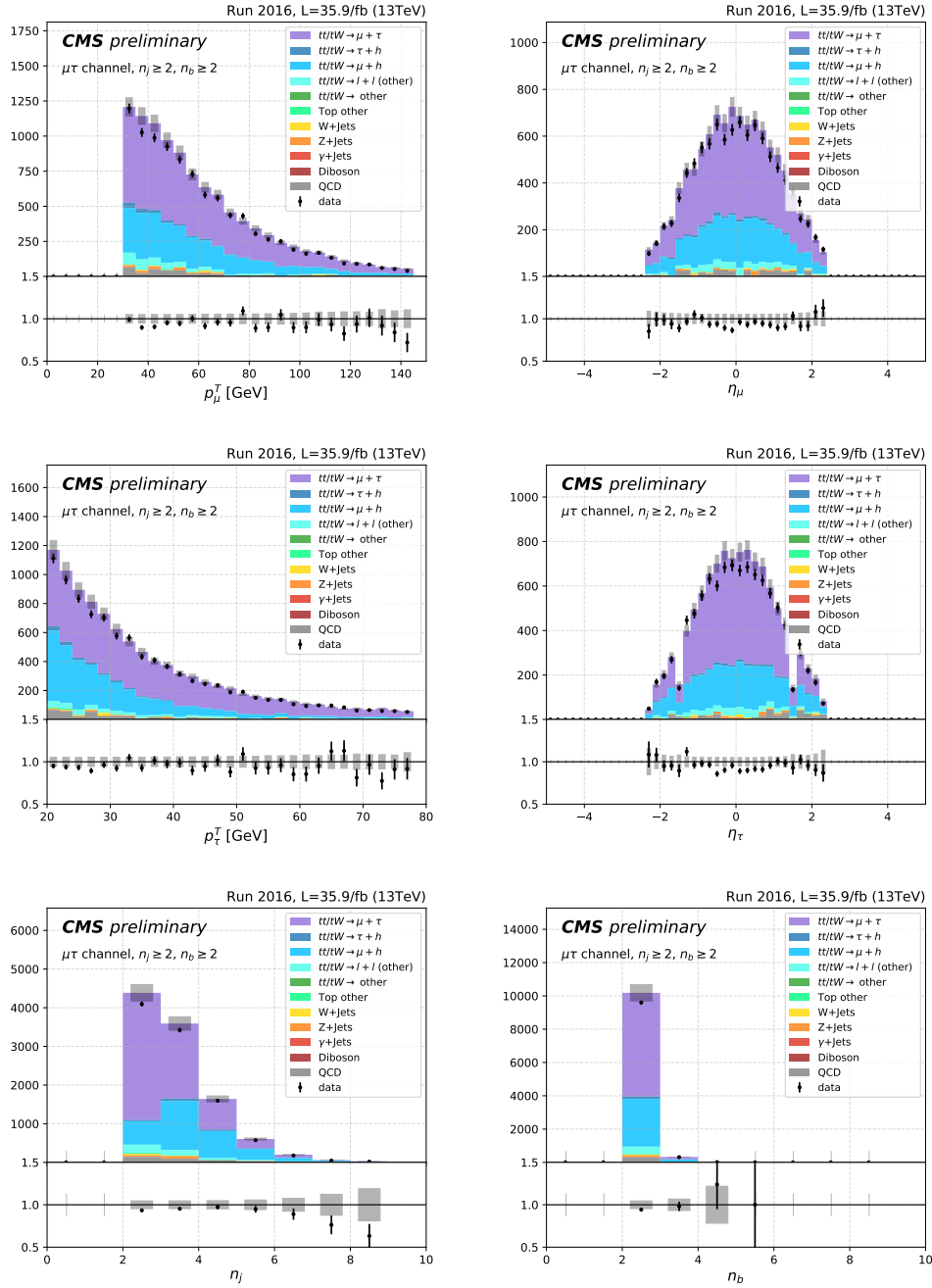
$\mu\tau - 2b$


Figure B.6. $\mu\tau$ channel with $n_j \geq 2, n_b \geq 2$.

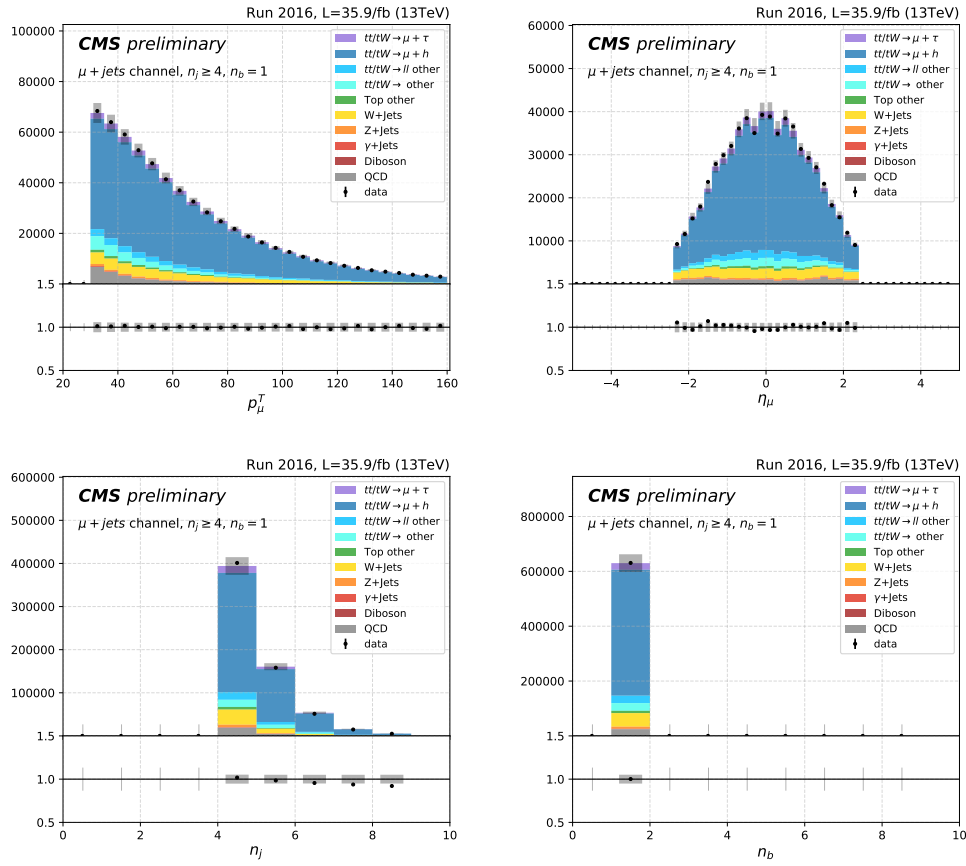
$\mu j - 1b$


Figure B.7. μ jet channel with $n_j \geq 4, n_b = 1$.

$$\mu j - 2b$$

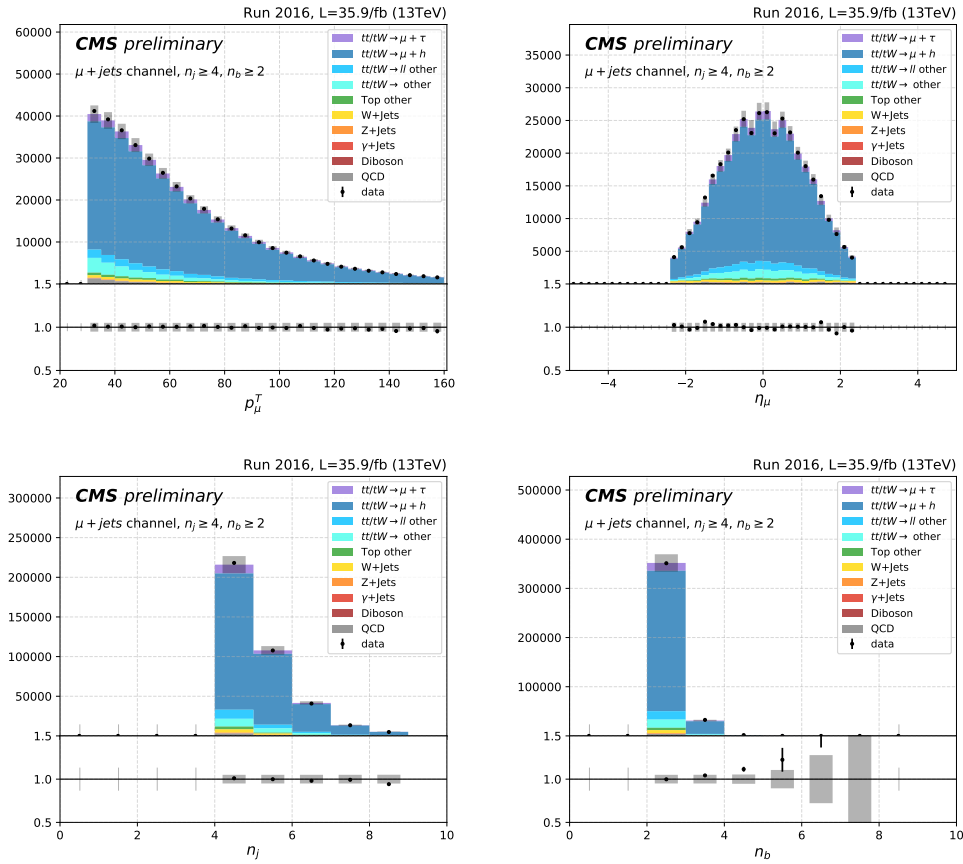
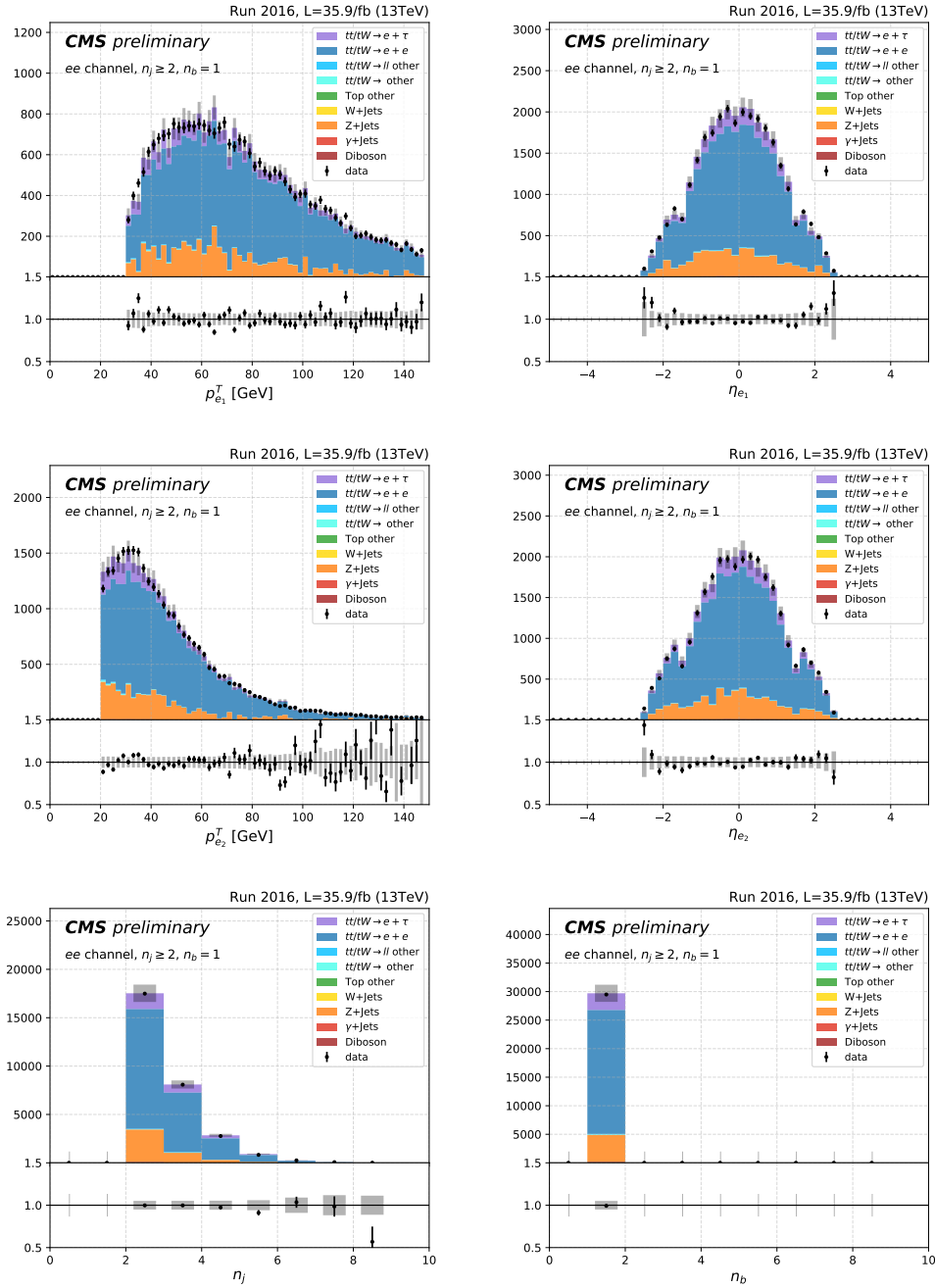
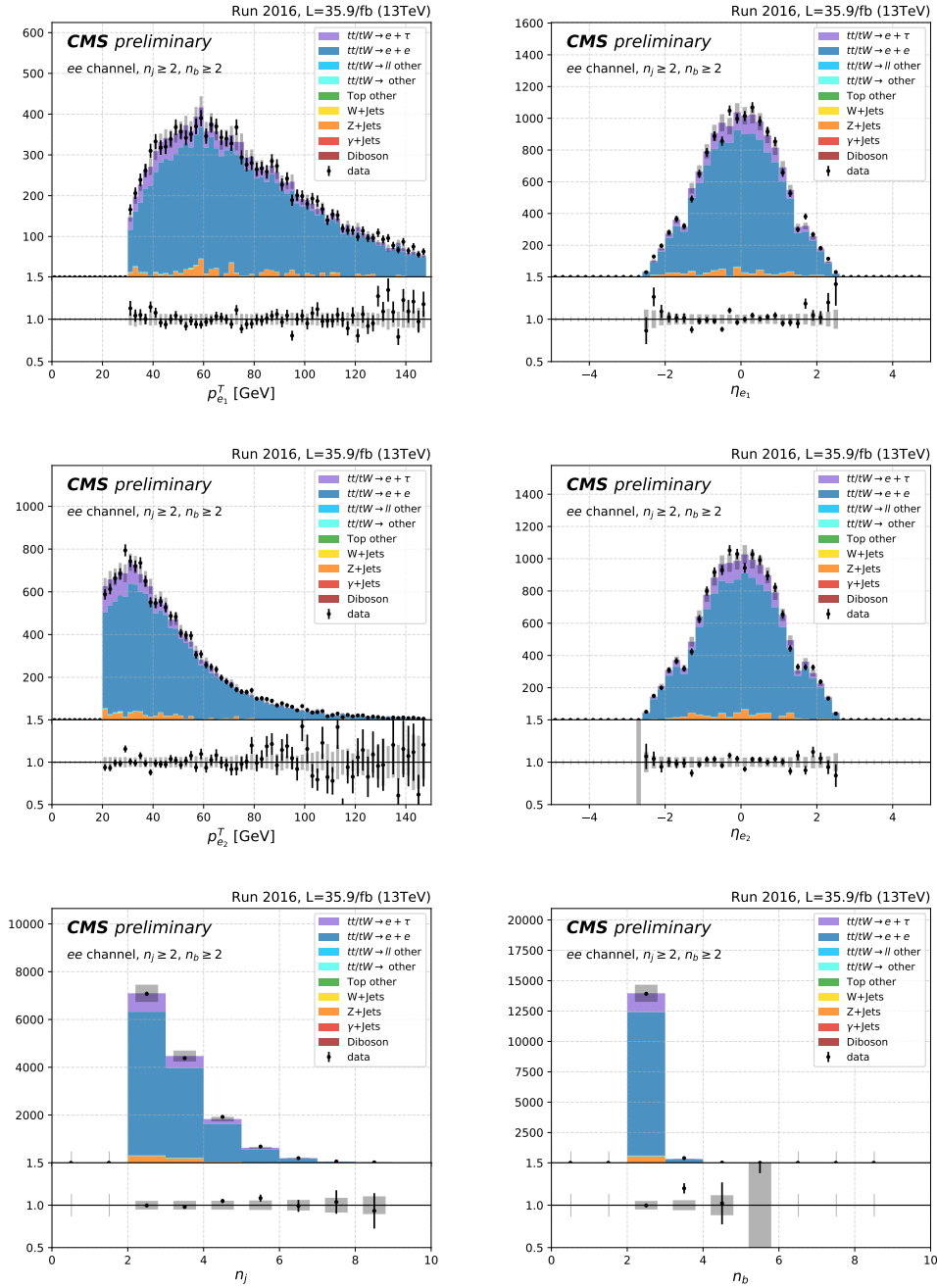
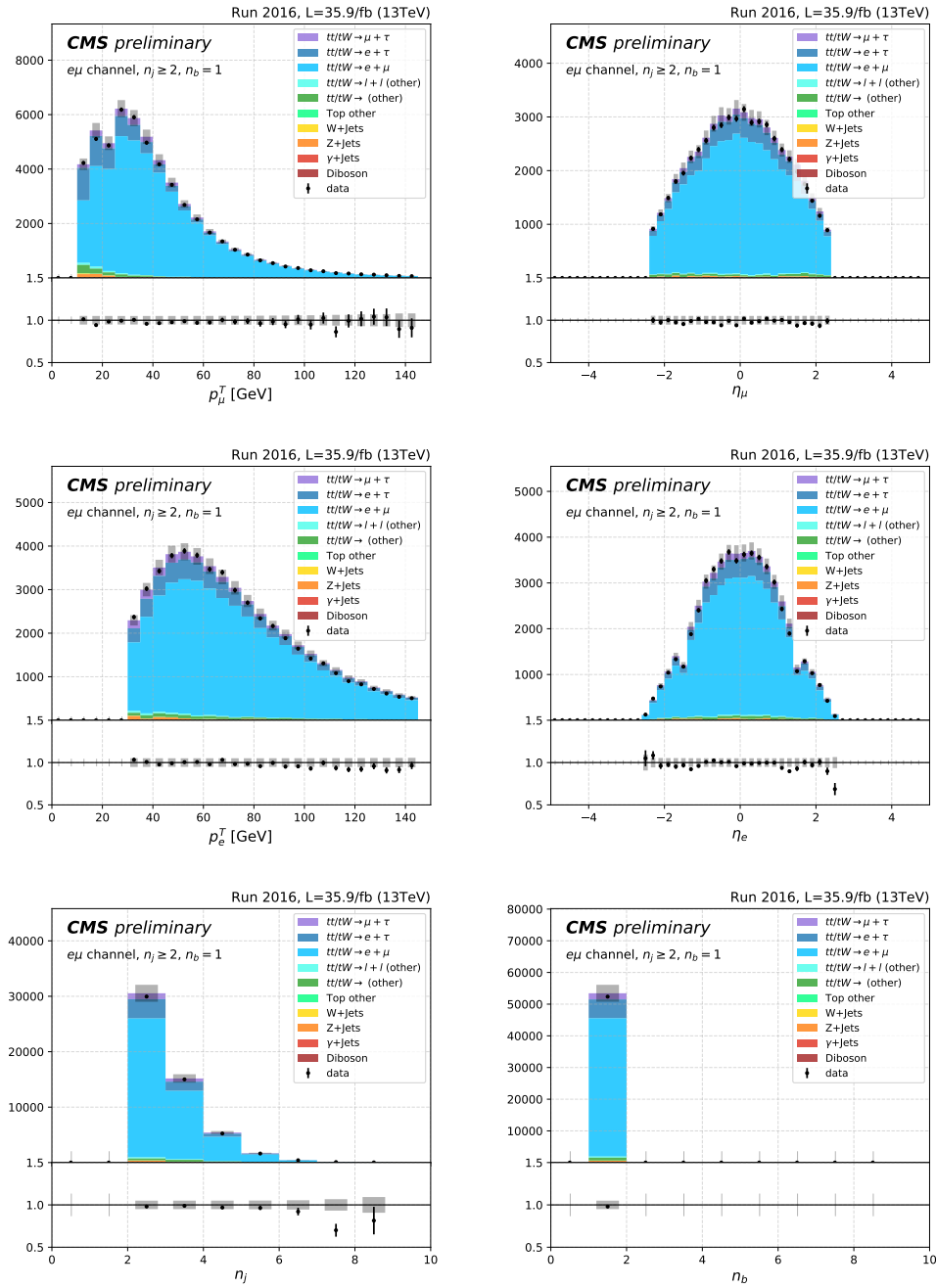


Figure B.8. μ jet channel with $n_j \geq 4, n_b \geq 2$.

$ee - 1b$ Figure B.9. ee channel with $n_j \geq 4, n_b = 1$.

$ee - 2b$ Figure B.10. ee channel with $n_j \geq 2, n_b \geq 2$.

$e\mu - 1b$ Figure B.11. $e\mu$ channel with $n_j \geq 4$, $n_b = 1$.

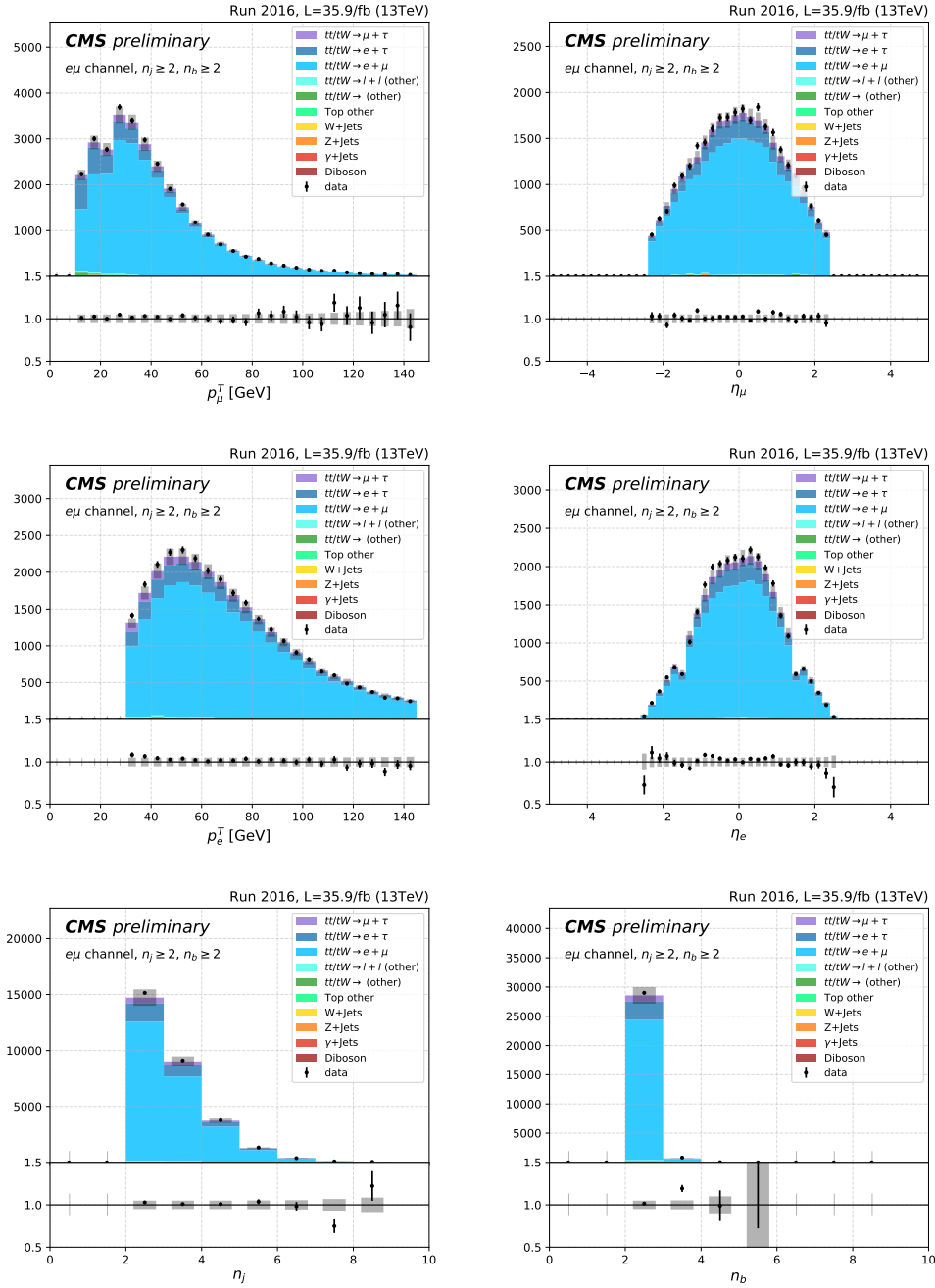
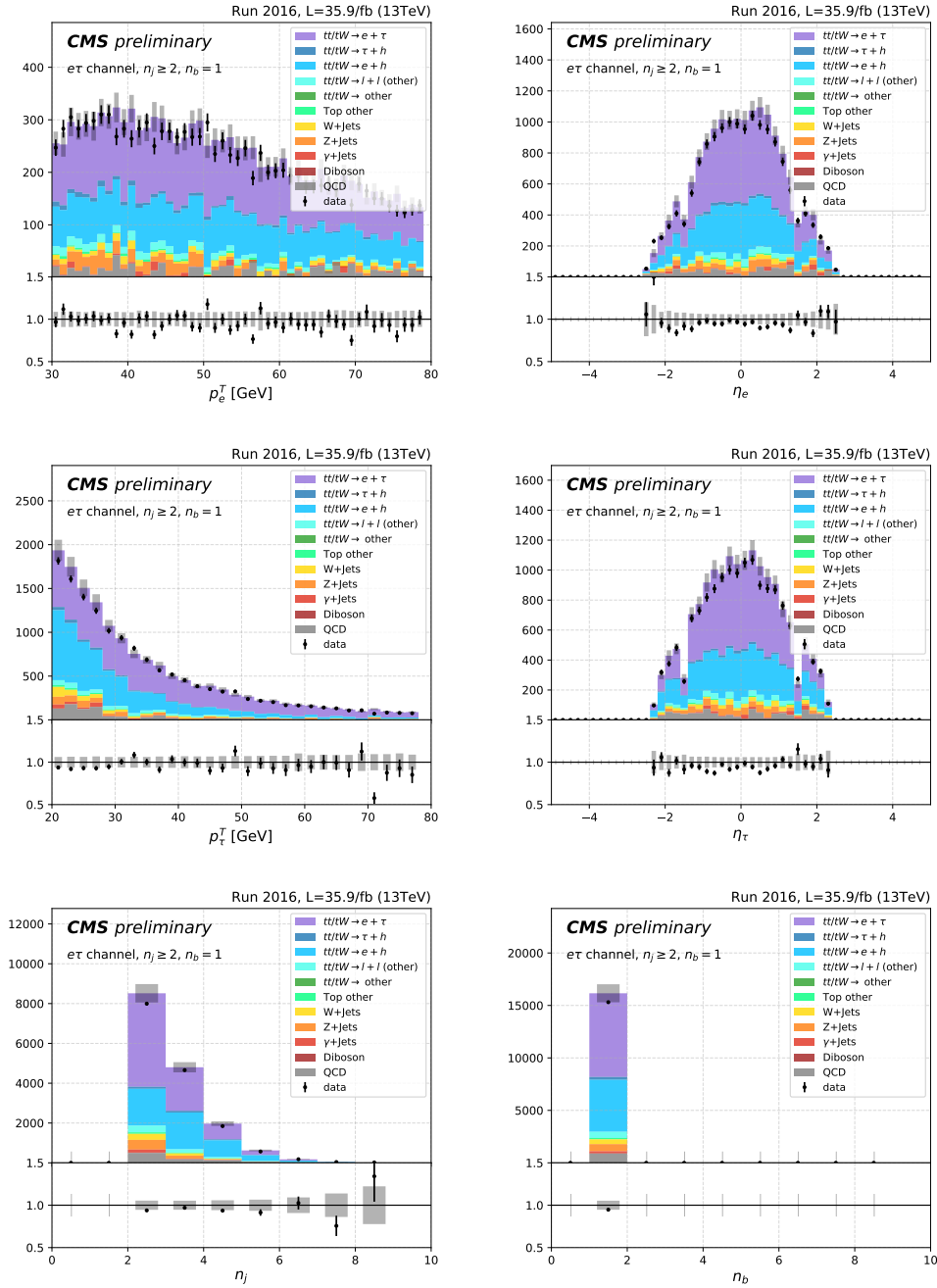
$e\mu - 2b$


Figure B.12. $e\mu$ channel with $n_j \geq 2$, $n_b \geq 2$.

$e\tau - 1b$ Figure B.13. $e\tau$ channel with $n_j \geq 4, n_b = 1$.

$$e\tau - 2b$$

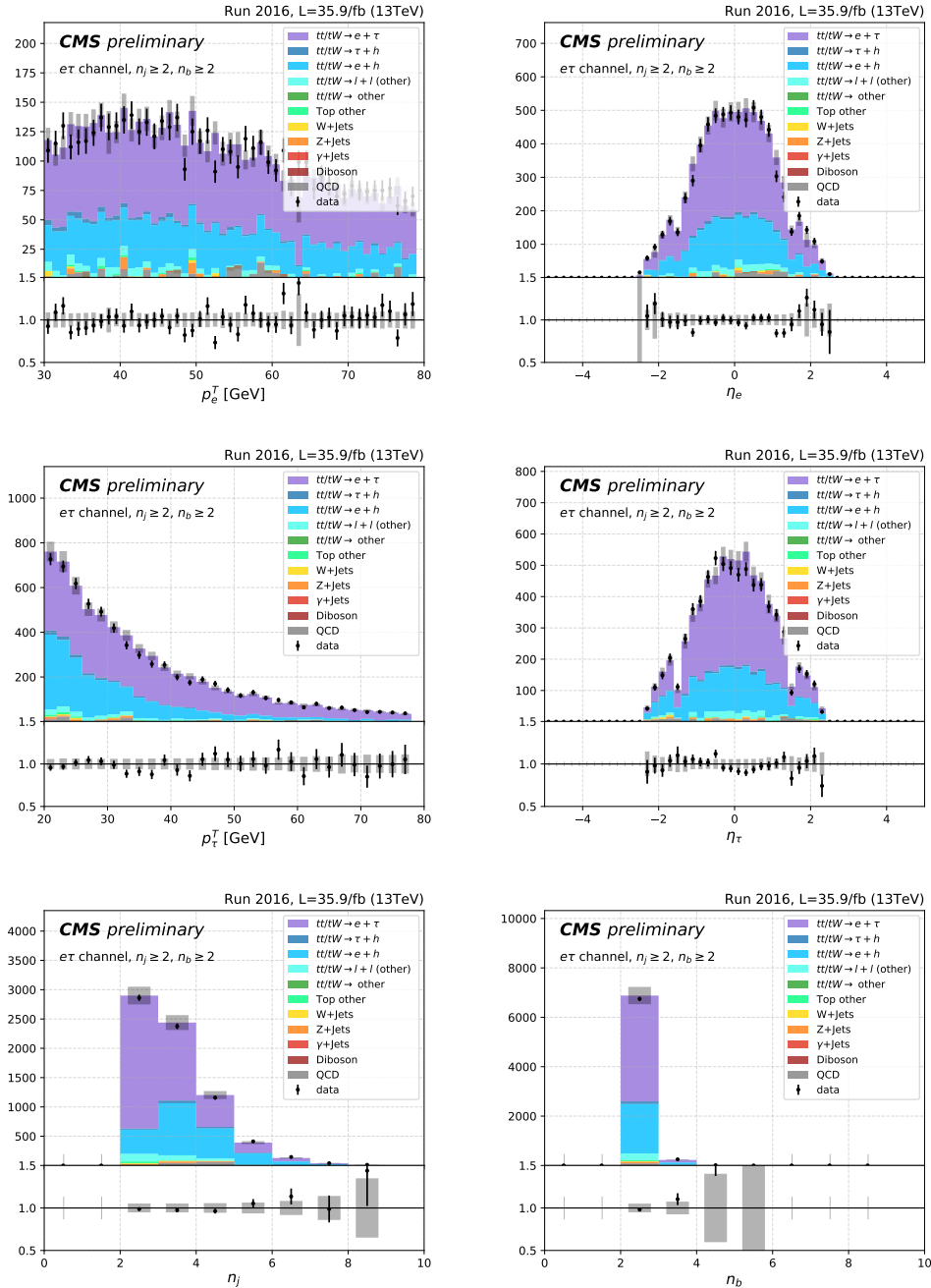
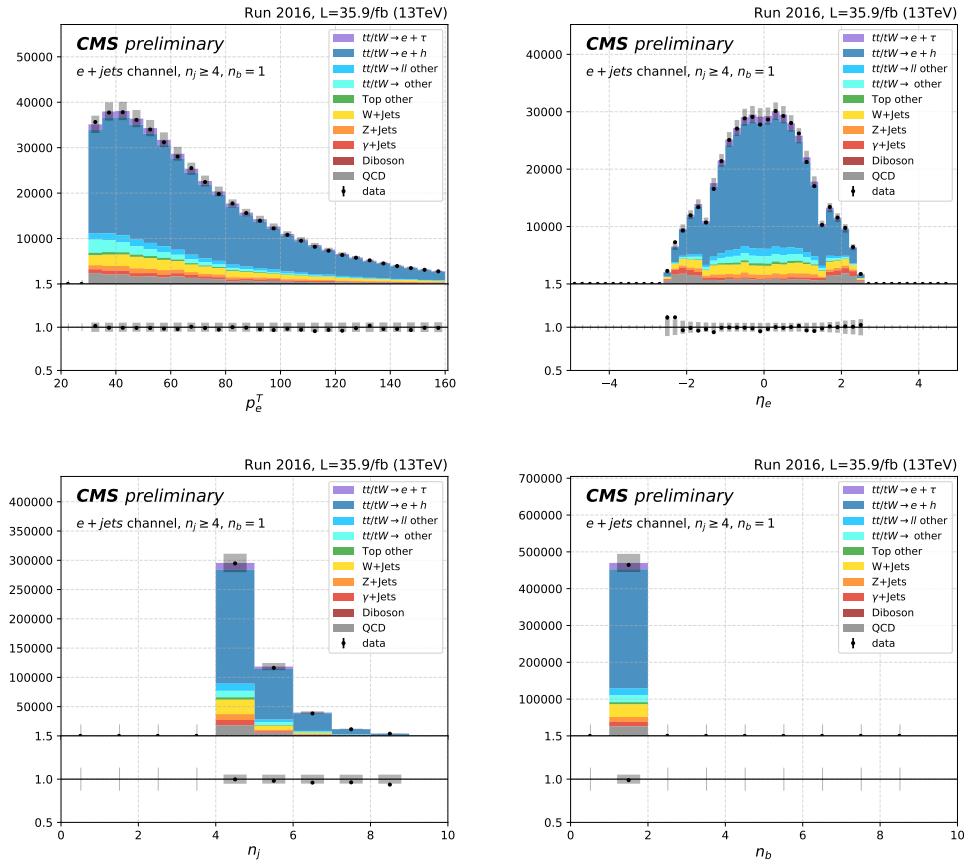
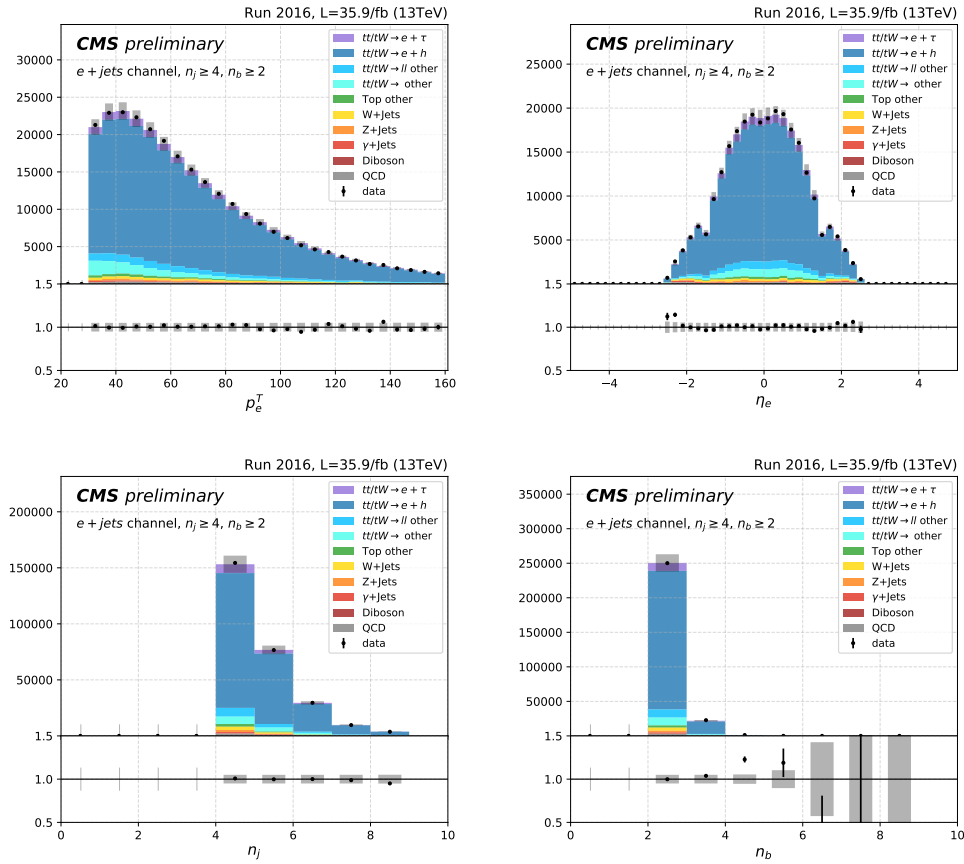


Figure B.14. $e\tau$ channel with $n_j \geq 2, n_b \geq 2$.

$e j - 1b$ Figure B.15. $e j$ channel with $n_j \geq 4, n_b = 1$.

$e j - 2b$ Figure B.16. $e j$ channel with $n_j \geq 2$, $n_b \geq 2$.

B.2. Kinematics Plots in Shape Analysis

??

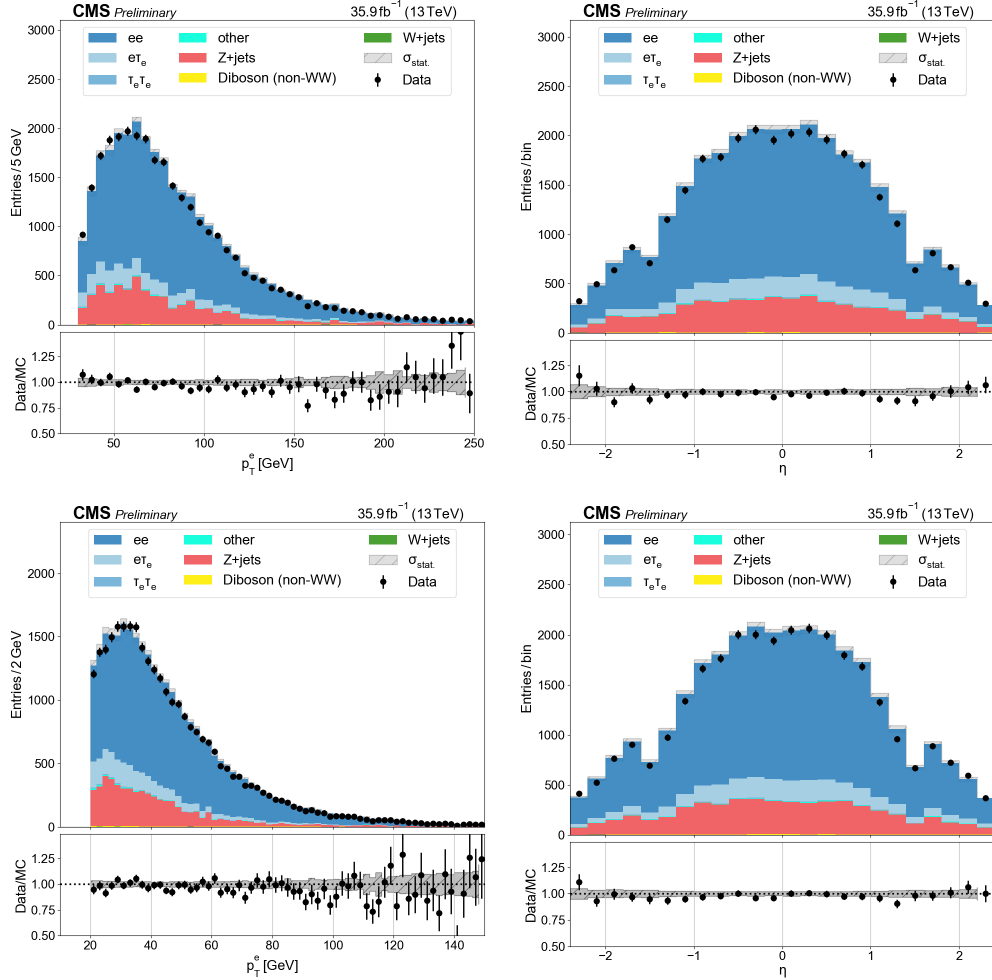


Figure B.17. p_T and η distributions for leading (top) and trailing (bottom) electrons in the ee channel with $N_j \geq 2$, $N_b = 1$, and Z boson veto.

B.2.0.1. ee.

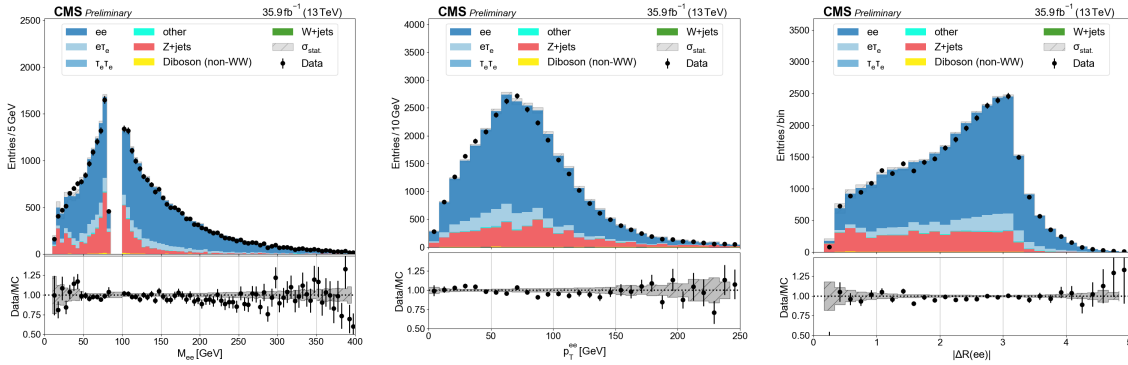


Figure B.18. Dielectron mass, p_T , and ΔR in the ee channel with $N_j \geq 2$, $N_b = 1$, and Z boson veto.

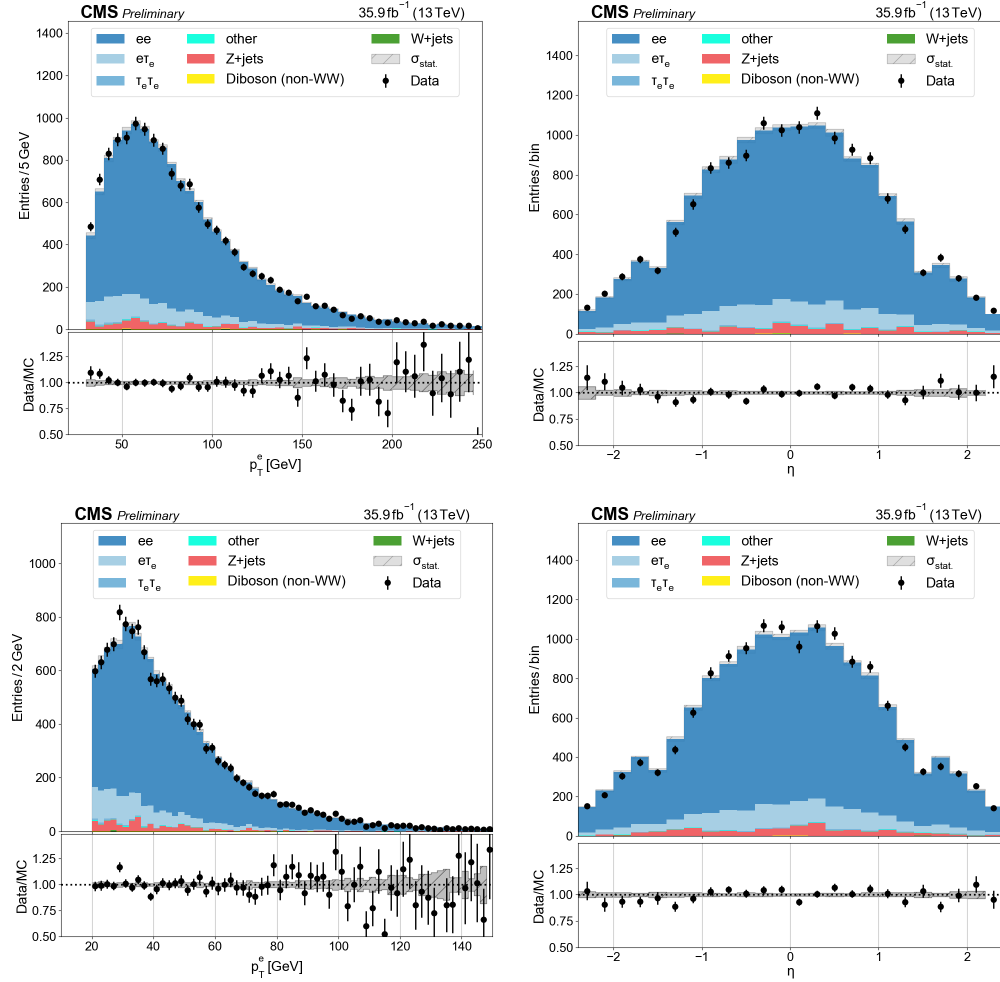


Figure B.19. p_T and η distributions for leading (top) and trailing (bottom) electrons in the ee channel with $N_j \geq 2$, $N_b \geq 2$, and Z boson veto.

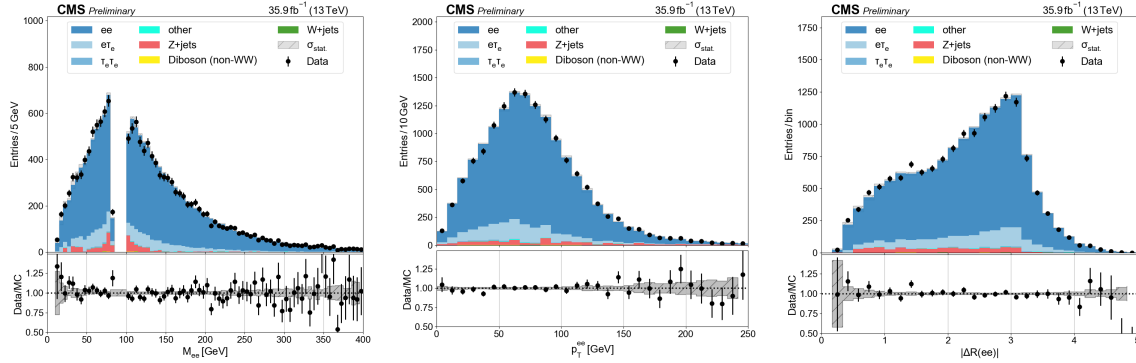


Figure B.20. Dielectron mass, p_T , and ΔR in the ee channel with $N_j \geq 2$, $N_b \geq 2$, and Z boson veto.

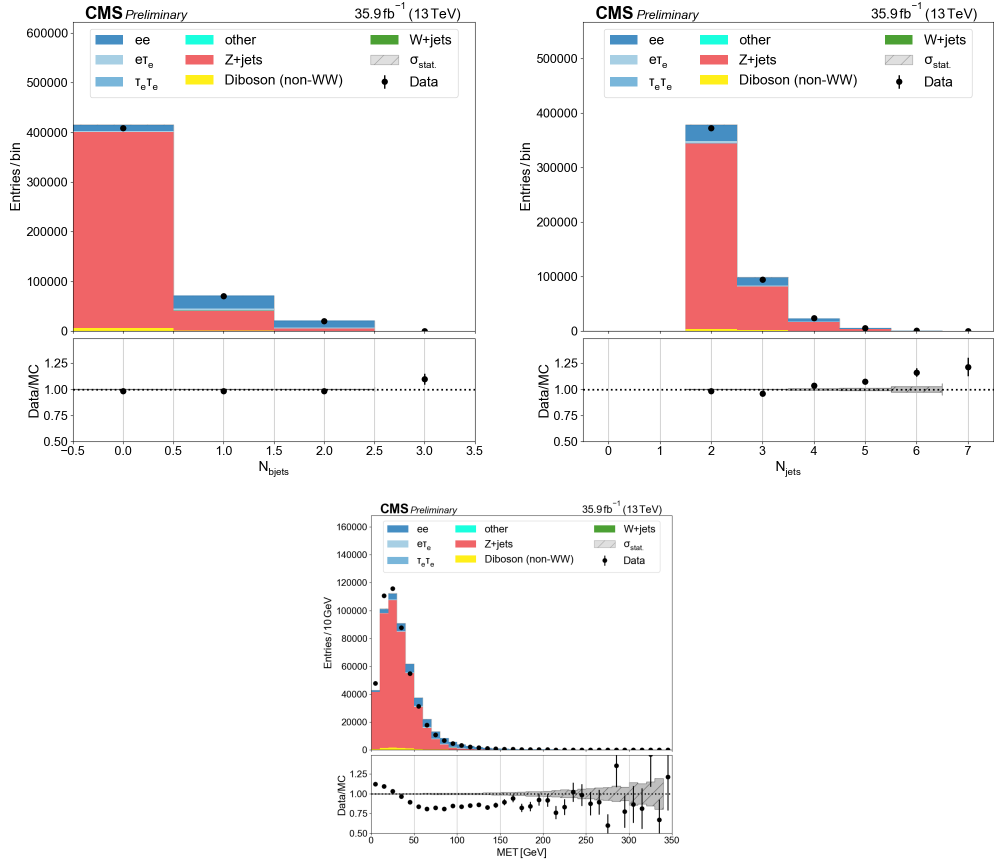


Figure B.21. Multiplicity of b tagged jets, non-tagged jets, and MET in ee channel with $N_j \geq 2$.

B.2.0.2. mumu.

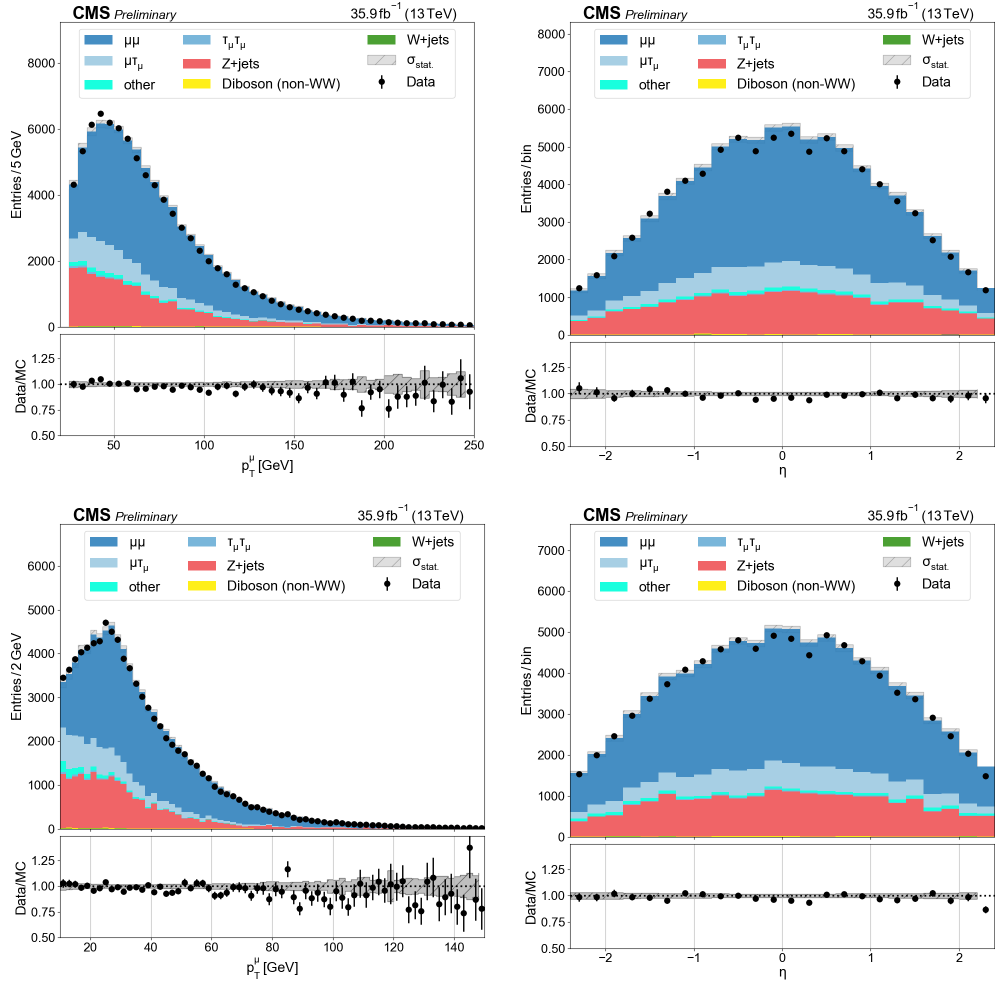


Figure B.22. p_T and η distributions for leading (top) and trailing (bottom) electrons in the $\mu\mu$ channel with $N_j \geq 2$, $N_b = 1$, and Z boson veto.

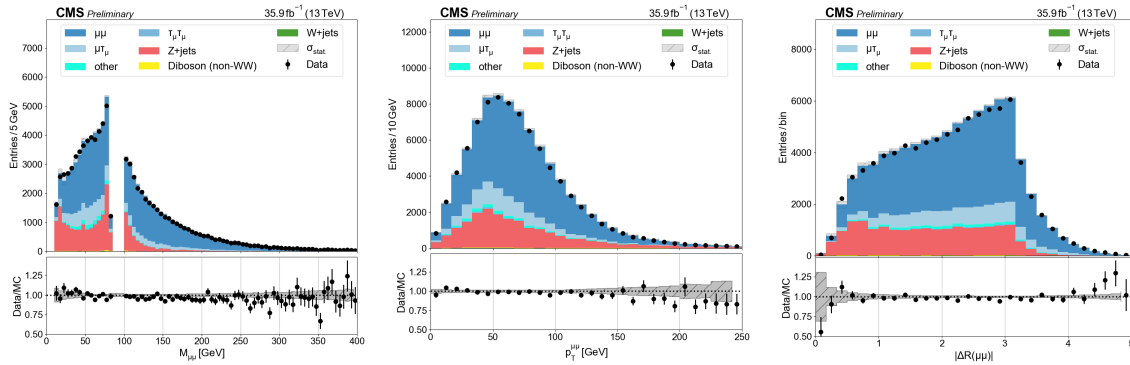


Figure B.23. Dielectron mass, p_T , and ΔR in the $\mu\mu$ channel with $N_j \geq 2$, $N_b = 1$, and Z boson veto.

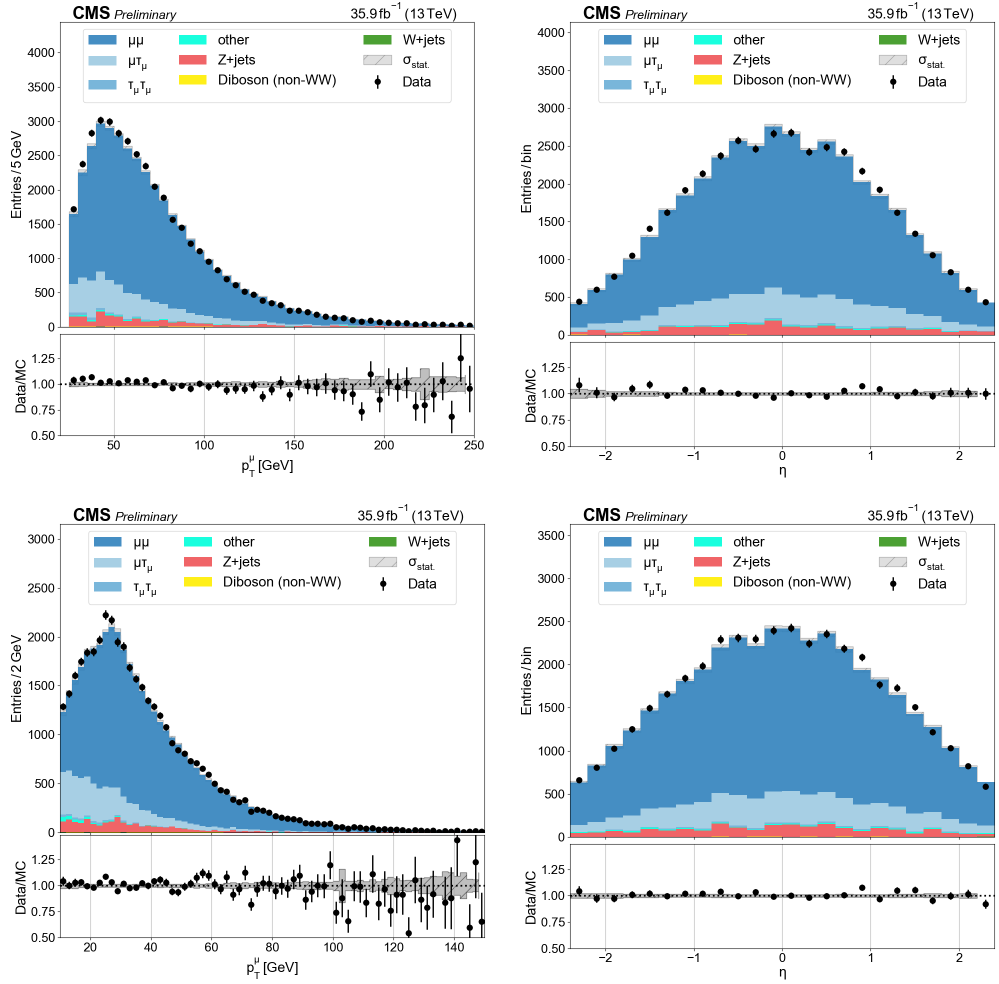


Figure B.24. p_T and η distributions for leading (top) and trailing (bottom) electrons in the $\mu\mu$ channel with $N_j \geq 2$, $N_b \geq 2$, and Z boson veto.

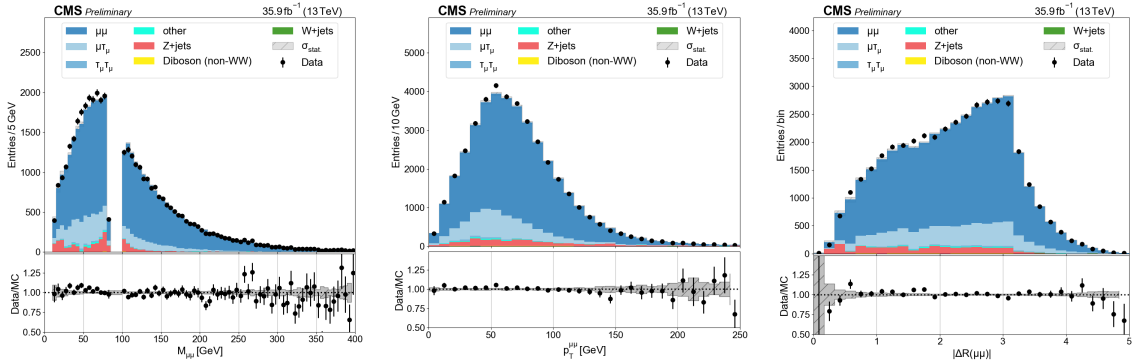


Figure B.25. Dielectron mass, p_T , and ΔR in the $\mu\mu$ channel with $N_j \geq 2$, $N_b \geq 2$, and Z boson veto.

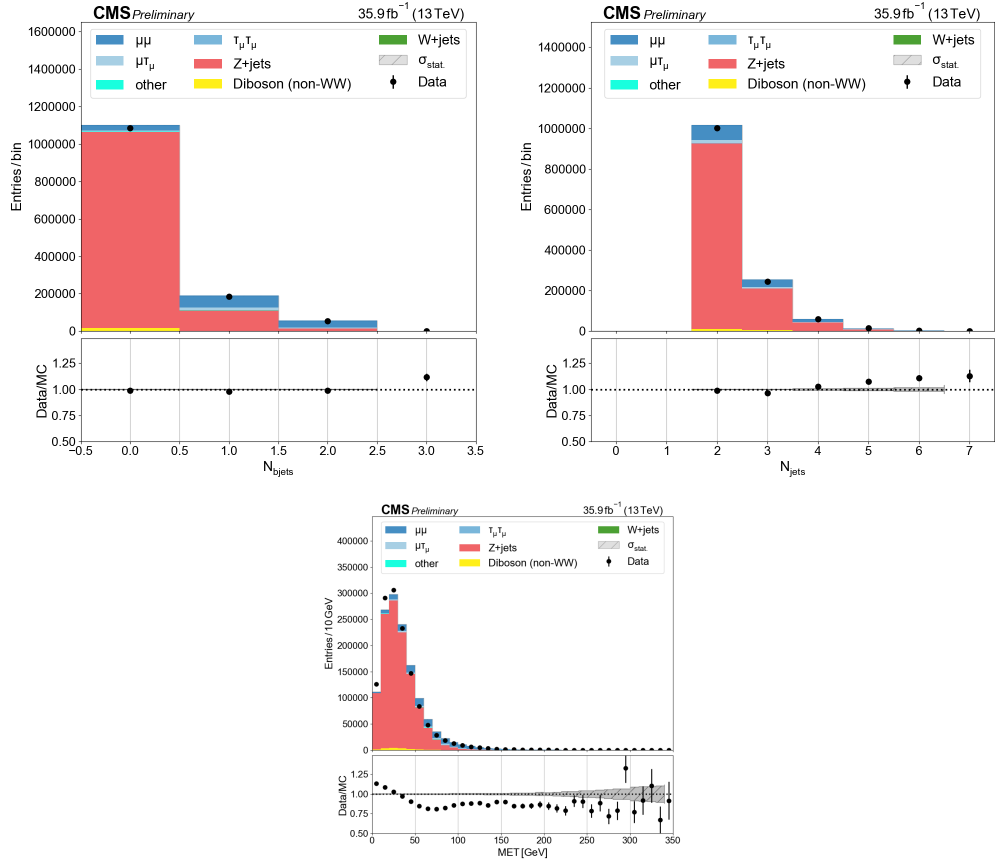


Figure B.26. Multiplicity of b tagged jets, non-tagged jets, and MET in $\mu\mu$ channel with $N_j \geq 2$.

B.2.0.3. emu.

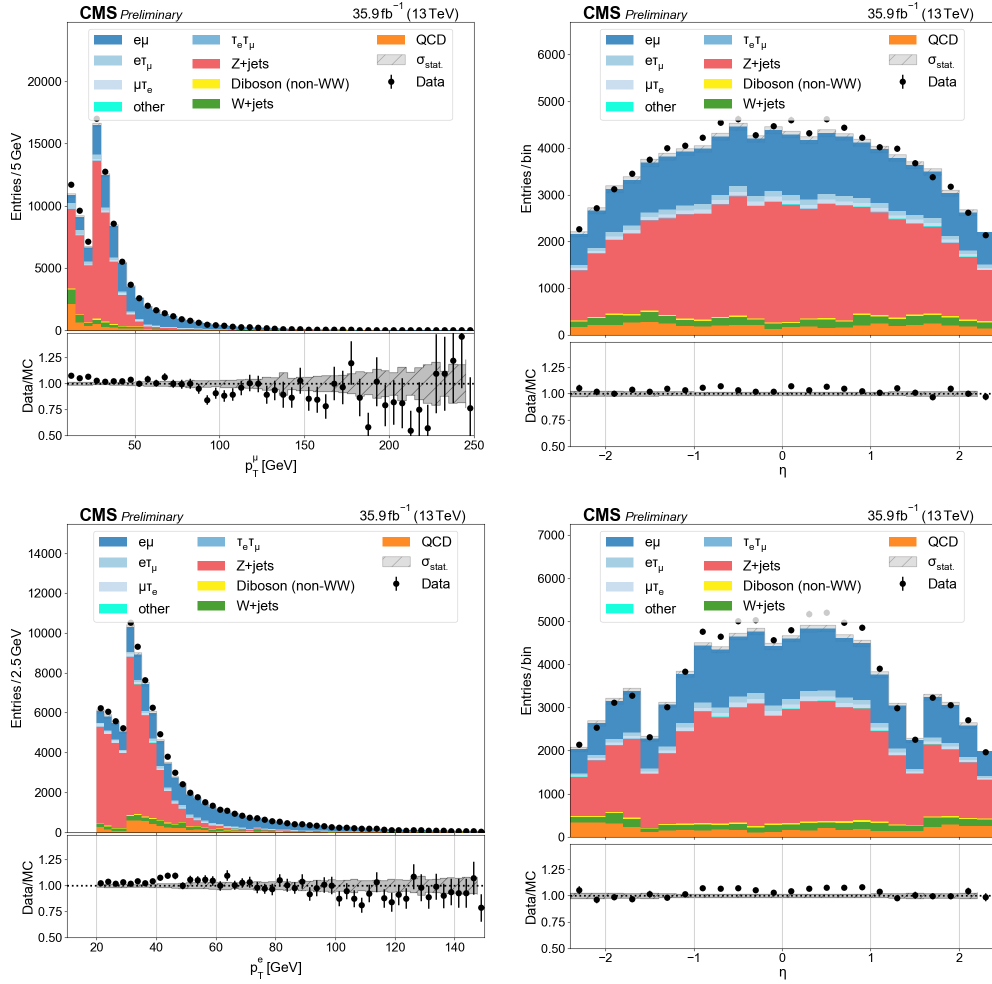


Figure B.27. p_T and η distributions for leading (top) and trailing (bottom) electrons in the $e\mu$ channel with $N_j = 0$.

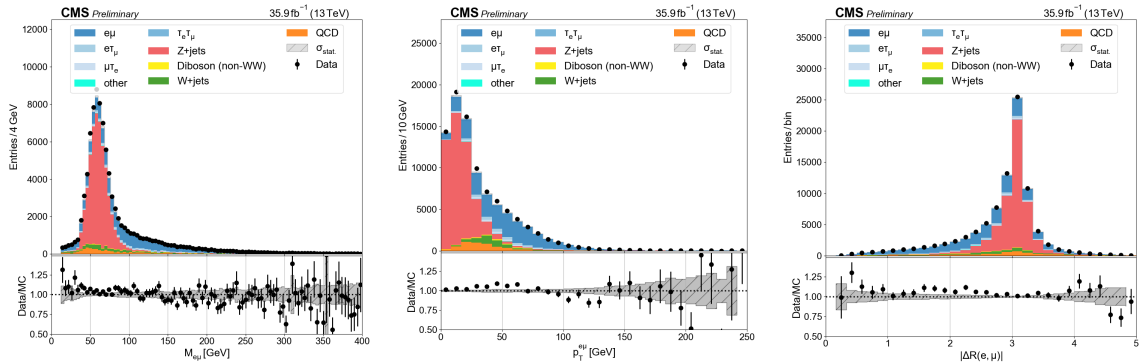


Figure B.28. Dielectron mass, p_T , and ΔR in the $e\mu$ channel with $N_j = 0$.

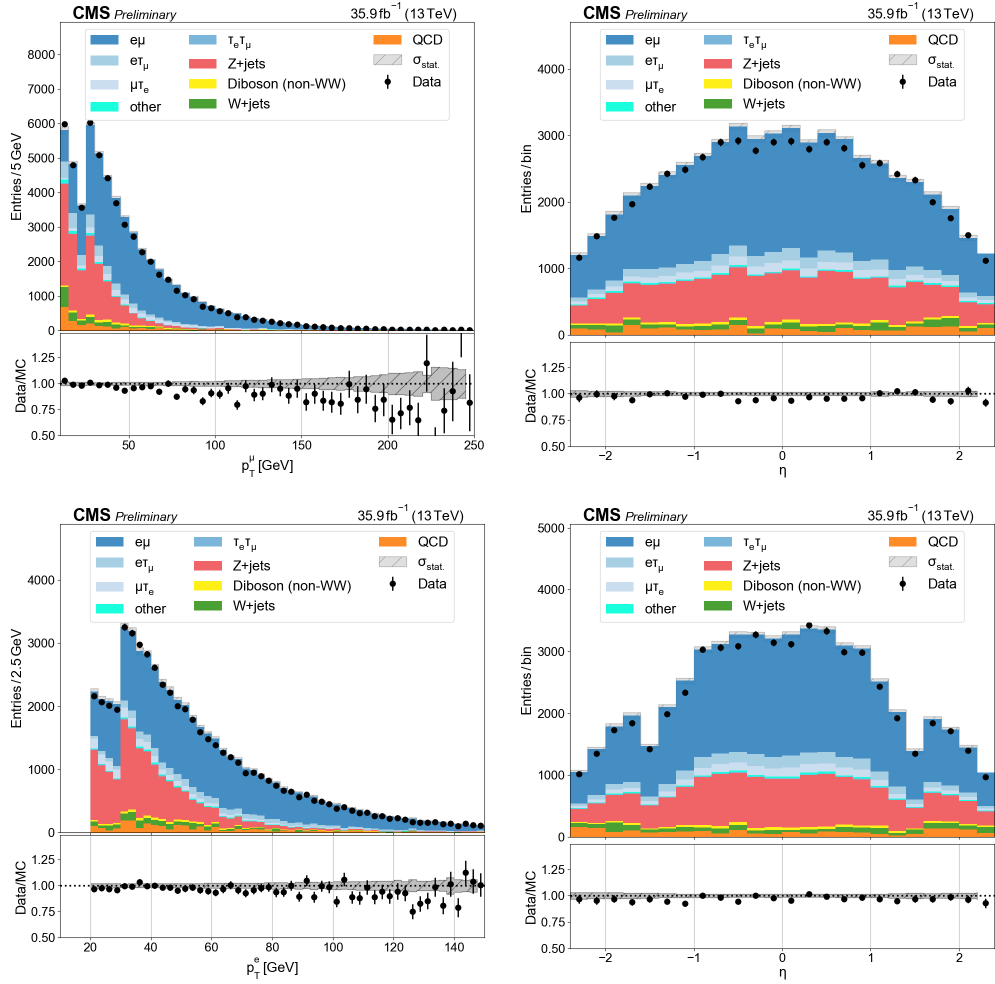


Figure B.29. p_T and η distributions for leading (top) and trailing (bottom) electrons in the $e\mu$ channel with $N_j = 1$ and $N_b = 0$.

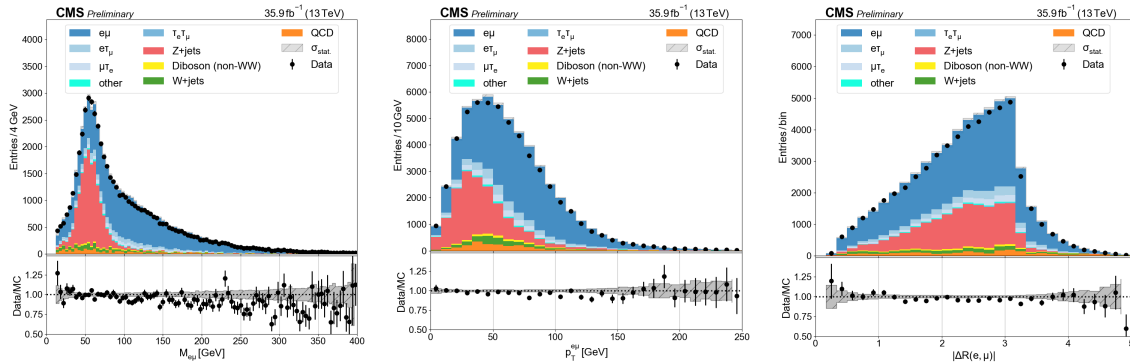


Figure B.30. Dielectron mass, p_T , and ΔR in the $e\mu$ channel with $N_j = 0$ and $N_b = 0$.

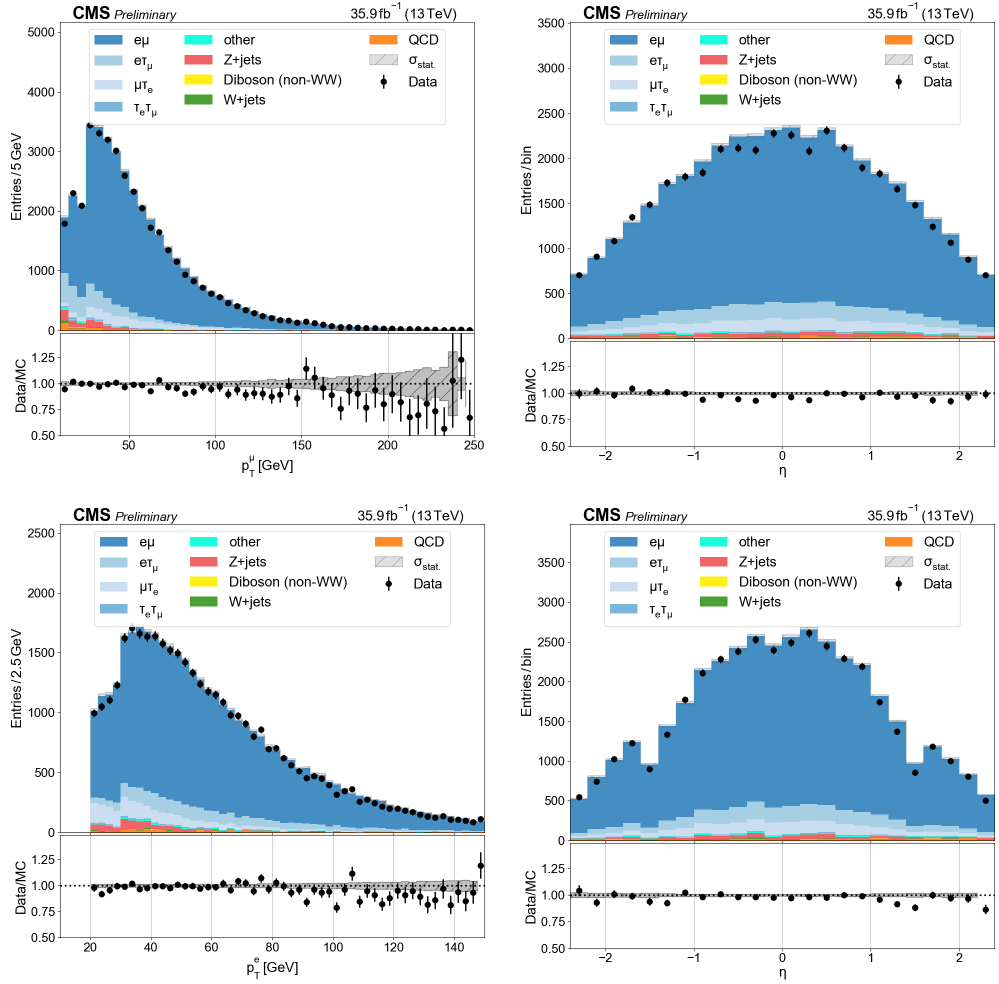


Figure B.31. p_T and η distributions for leading (top) and trailing (bottom) electrons in the $e\mu$ channel with $N_j = 1$ and $N_b = 1$.

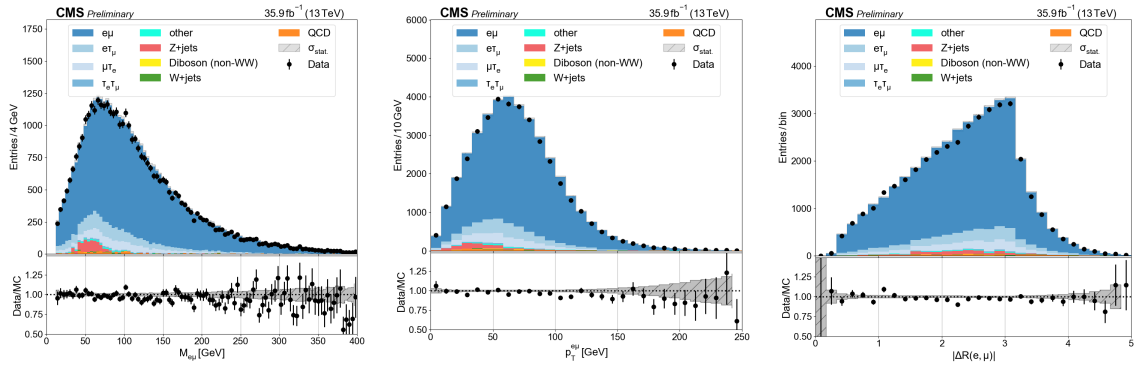


Figure B.32. Dielectron mass, p_T , and ΔR in the $e\mu$ channel with $N_j = 1$ and $N_b = 1$.

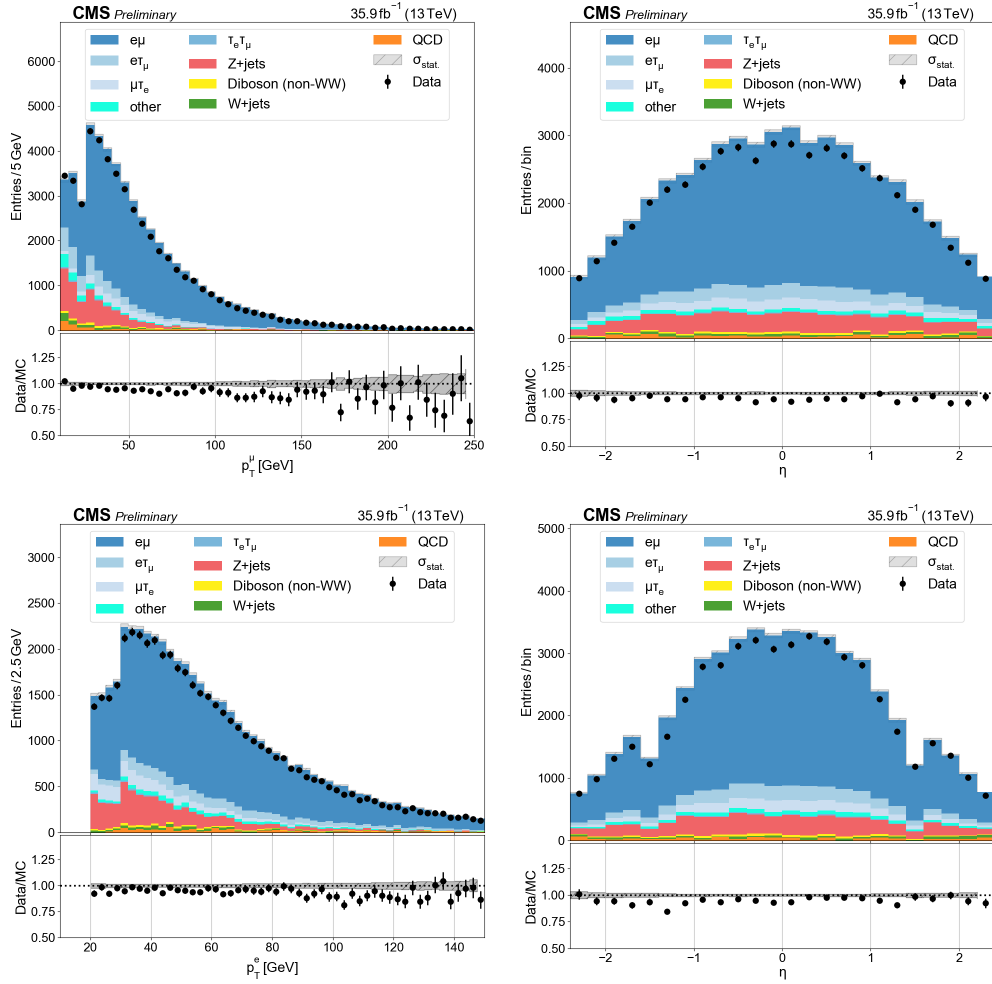


Figure B.33. p_T and η distributions for leading (top) and trailing (bottom) electrons in the $e\mu$ channel with $N_j \geq 2$ and $N_b = 0$.

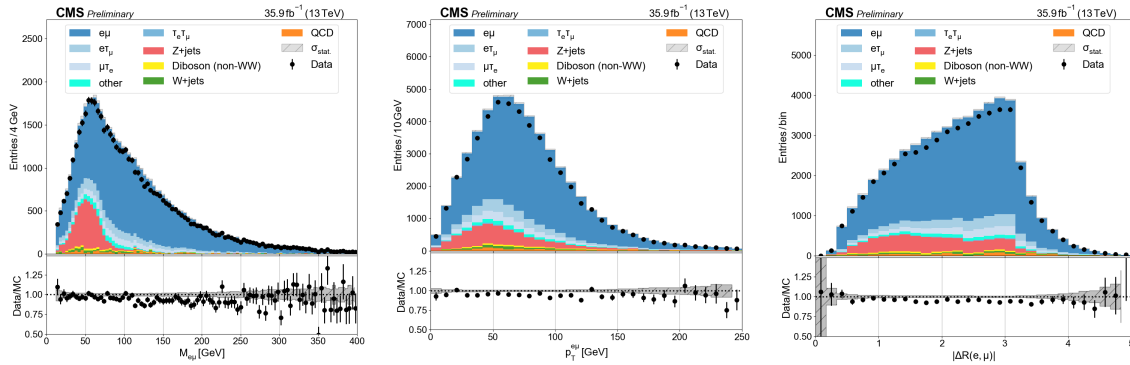


Figure B.34. Dielectron mass, p_T , and ΔR in the $e\mu$ channel with $N_j \geq 2$ and $N_b = 0$.

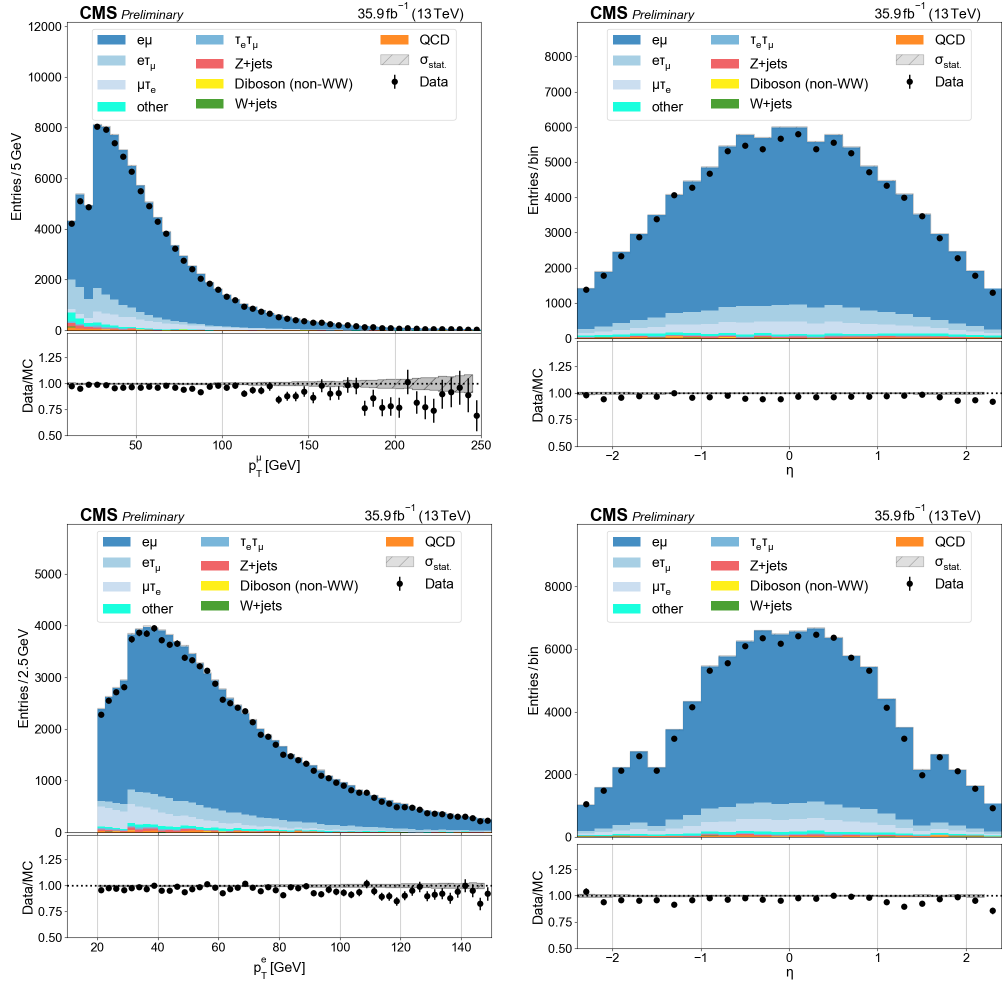


Figure B.35. p_T and η distributions for leading (top) and trailing (bottom) electrons in the $e\mu$ channel with $N_j \geq 2$ and $N_b = 1$.

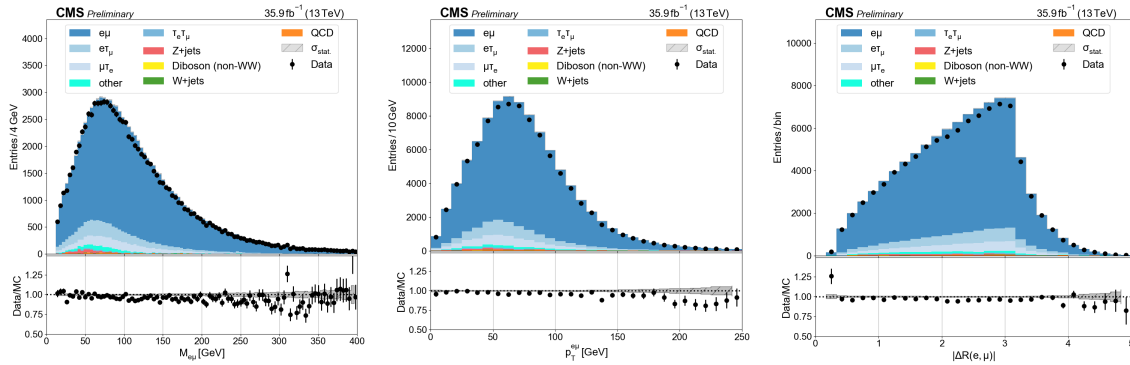


Figure B.36. Dielectron mass, p_T , and ΔR in the $e\mu$ channel with $N_j \geq 2$ and $N_b = 1$.

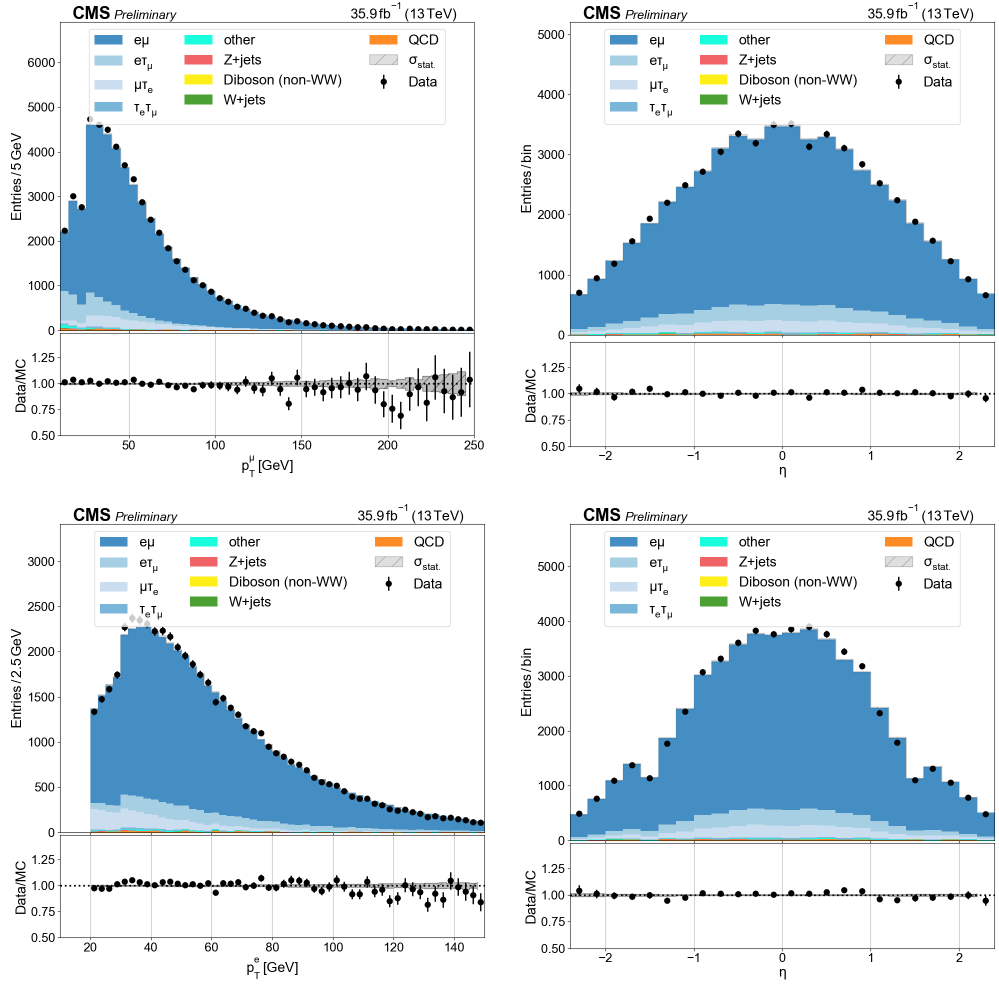


Figure B.37. p_T and η distributions for leading (top) and trailing (bottom) electrons in the $e\mu$ channel with $N_j \geq 2$ and $N_b = 1$.

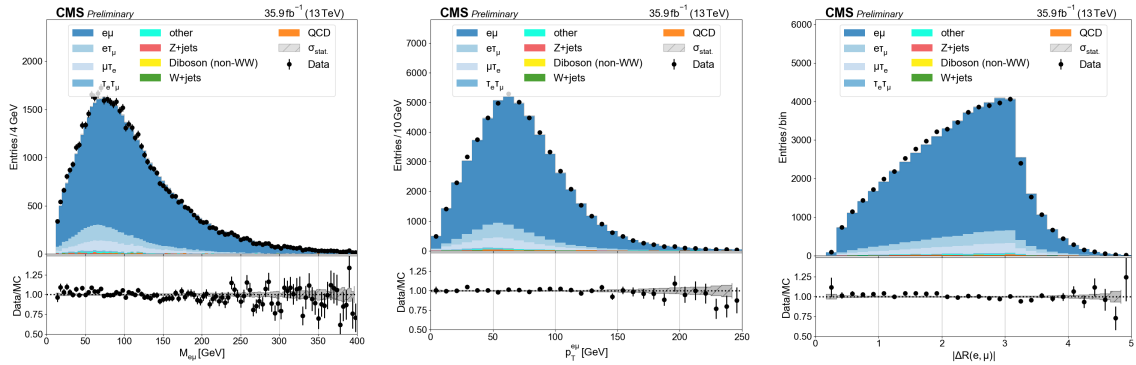


Figure B.38. Dielectron mass, p_T , and ΔR in the $e\mu$ channel with $N_j \geq 2$ and $N_b = 1$.

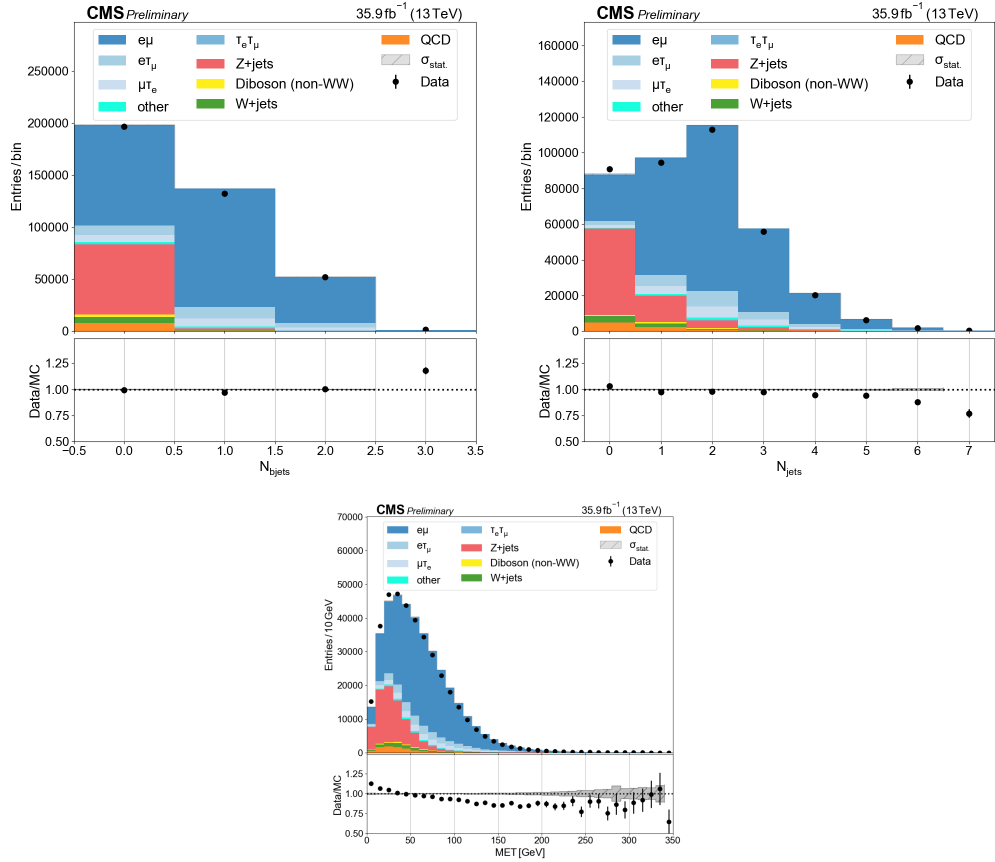


Figure B.39. Multiplicity of b tagged jets, non-tagged jets, and MET in $e\mu$ channel.

B.2.0.4. etau.

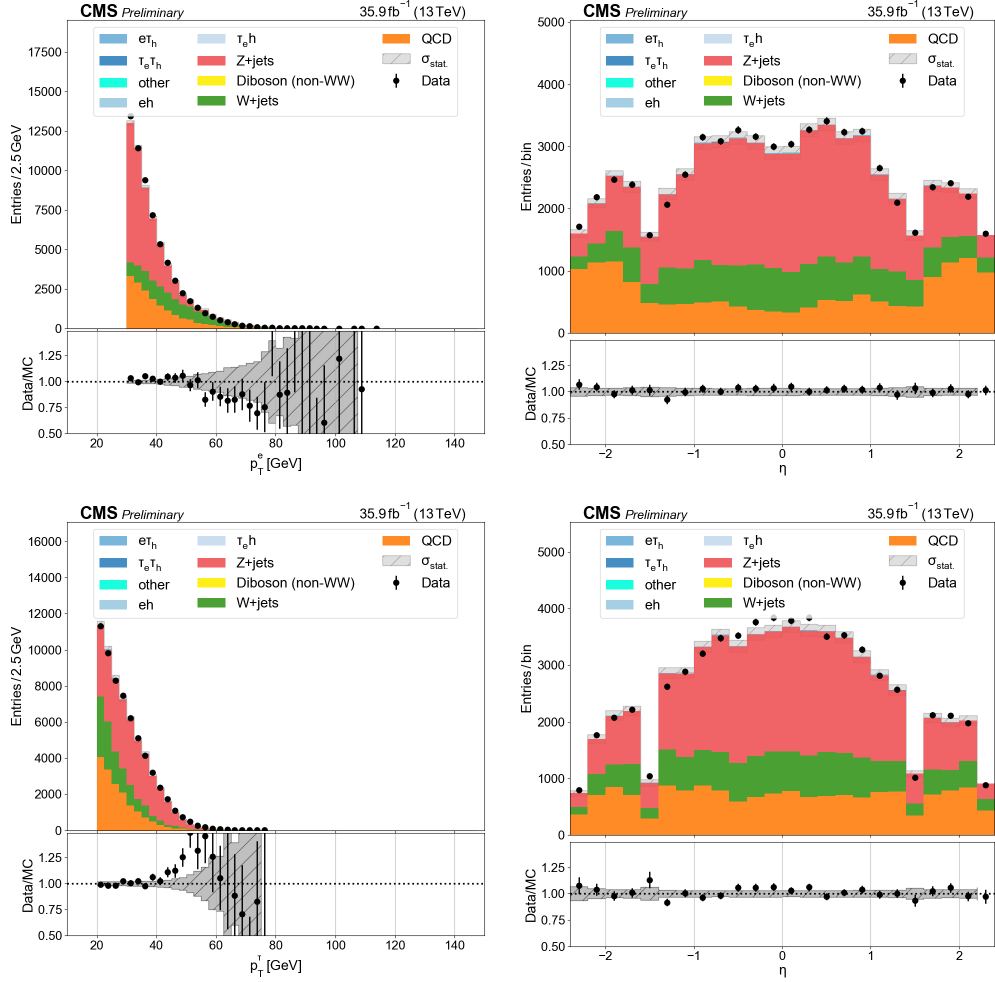


Figure B.40. p_T and η distributions for leading (top) and trailing (bottom) electrons in the $e\tau$ channel with $N_j = 0$.

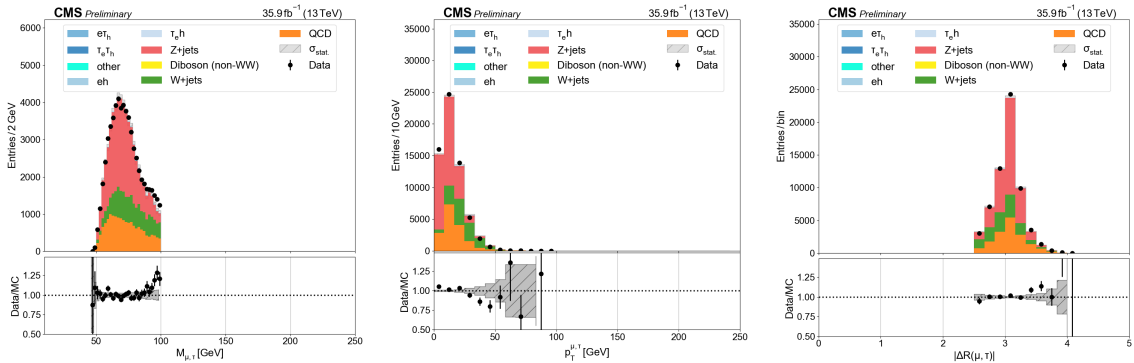


Figure B.41. Dielectron mass, p_T , and ΔR in the $e\tau$ channel with $N_j = 0$.

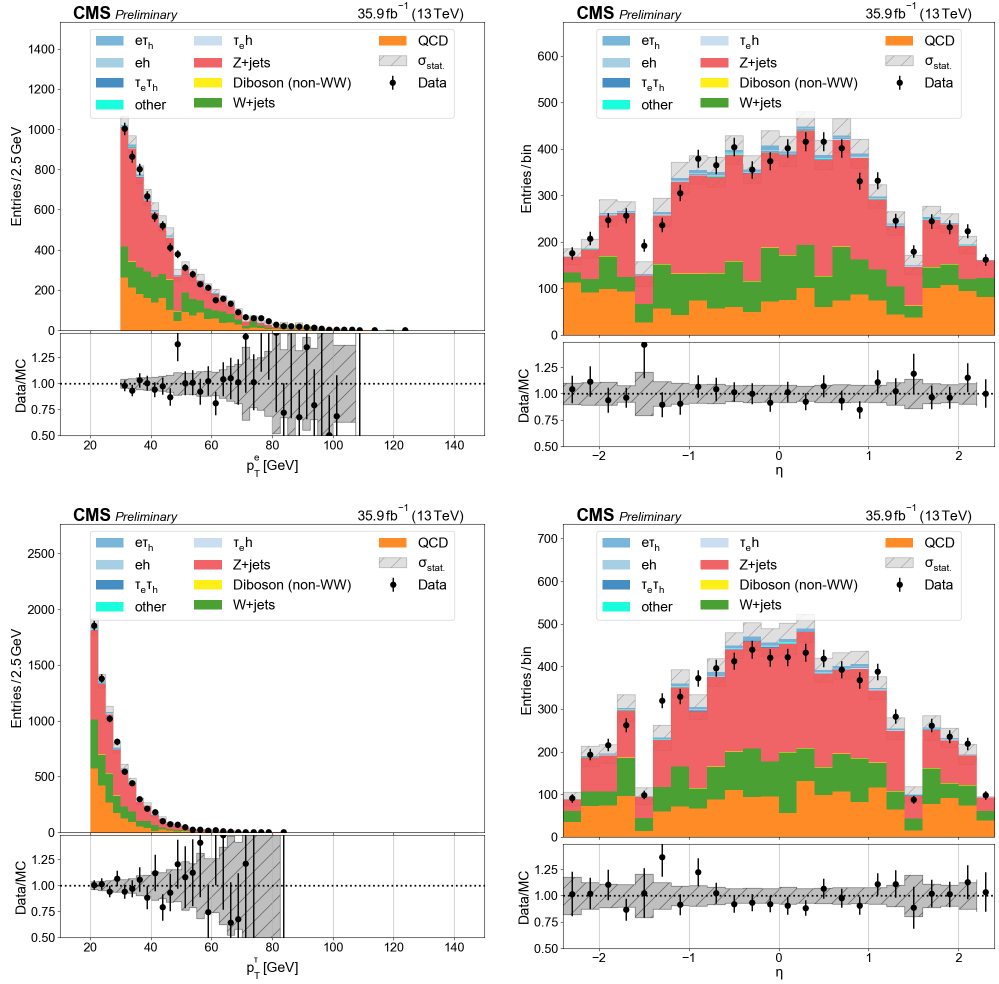


Figure B.42. p_T and η distributions for leading (top) and trailing (bottom) electrons in the $e\tau$ channel with $N_j = 1$ and $N_b = 0$.

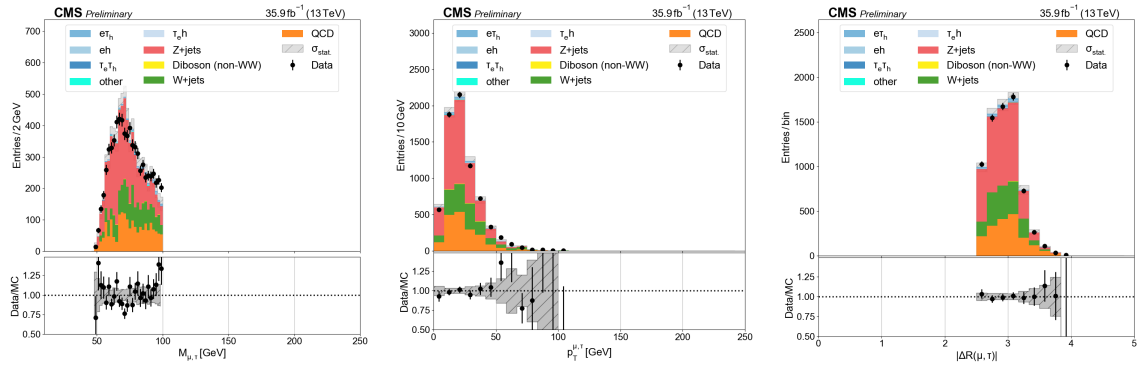


Figure B.43. Dielectron mass, p_T , and ΔR in the $e\tau$ channel with $N_j = 0$ and $N_b = 0$.

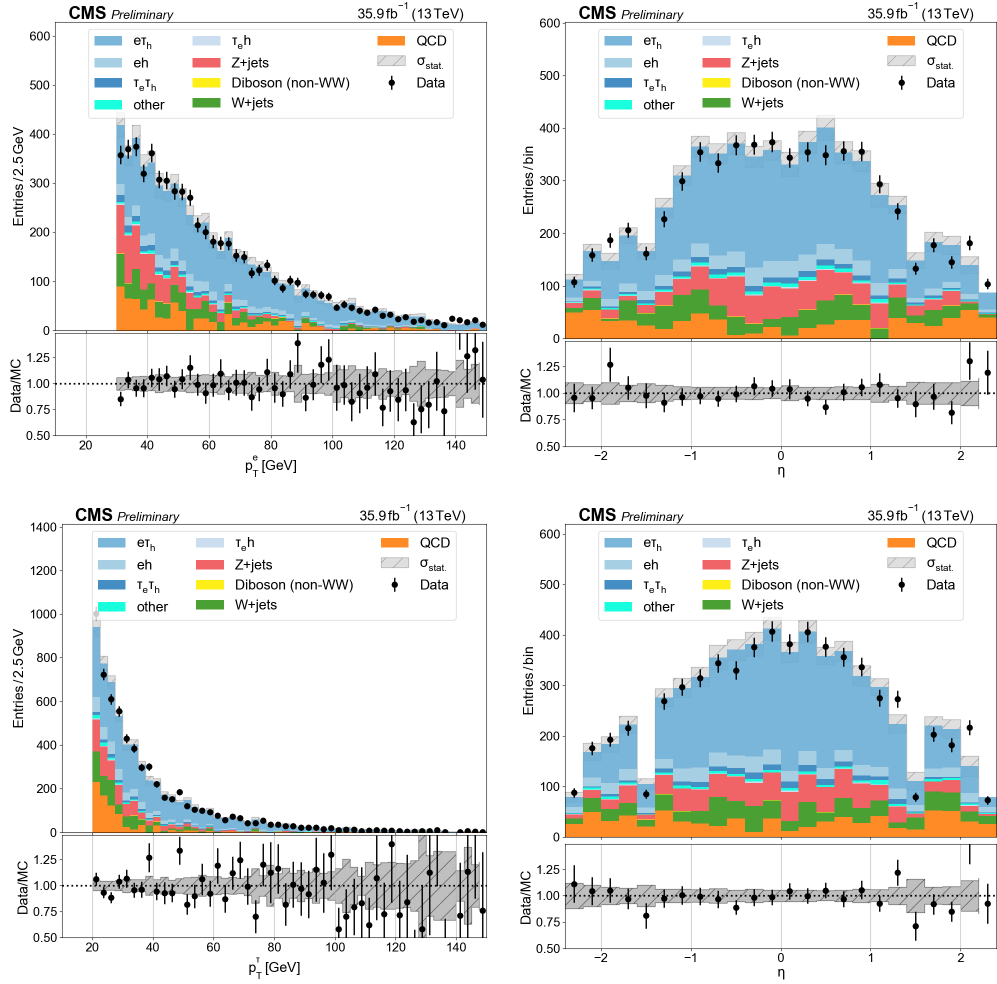


Figure B.44. p_T and η distributions for leading (top) and trailing (bottom) electrons in the $e\tau$ channel with $N_j = 1$ and $N_b = 1$.

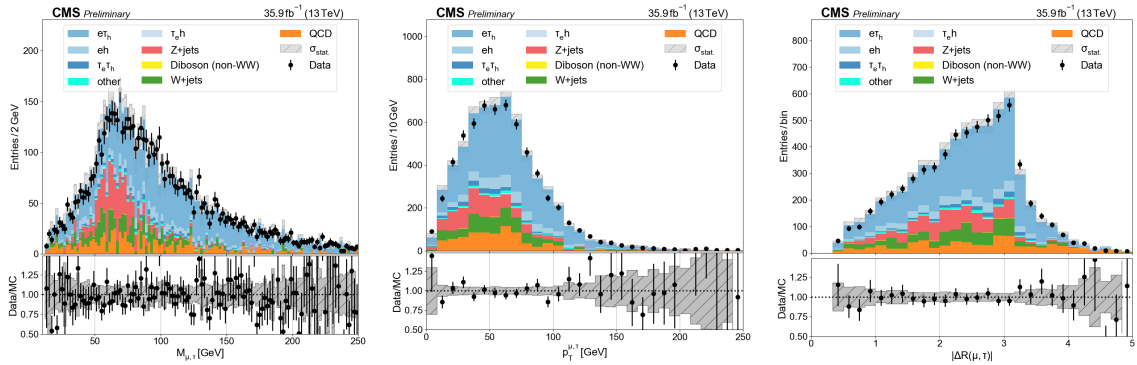


Figure B.45. Dielectron mass, p_T , and ΔR in the $e\tau$ channel with $N_j = 1$ and $N_b = 1$.

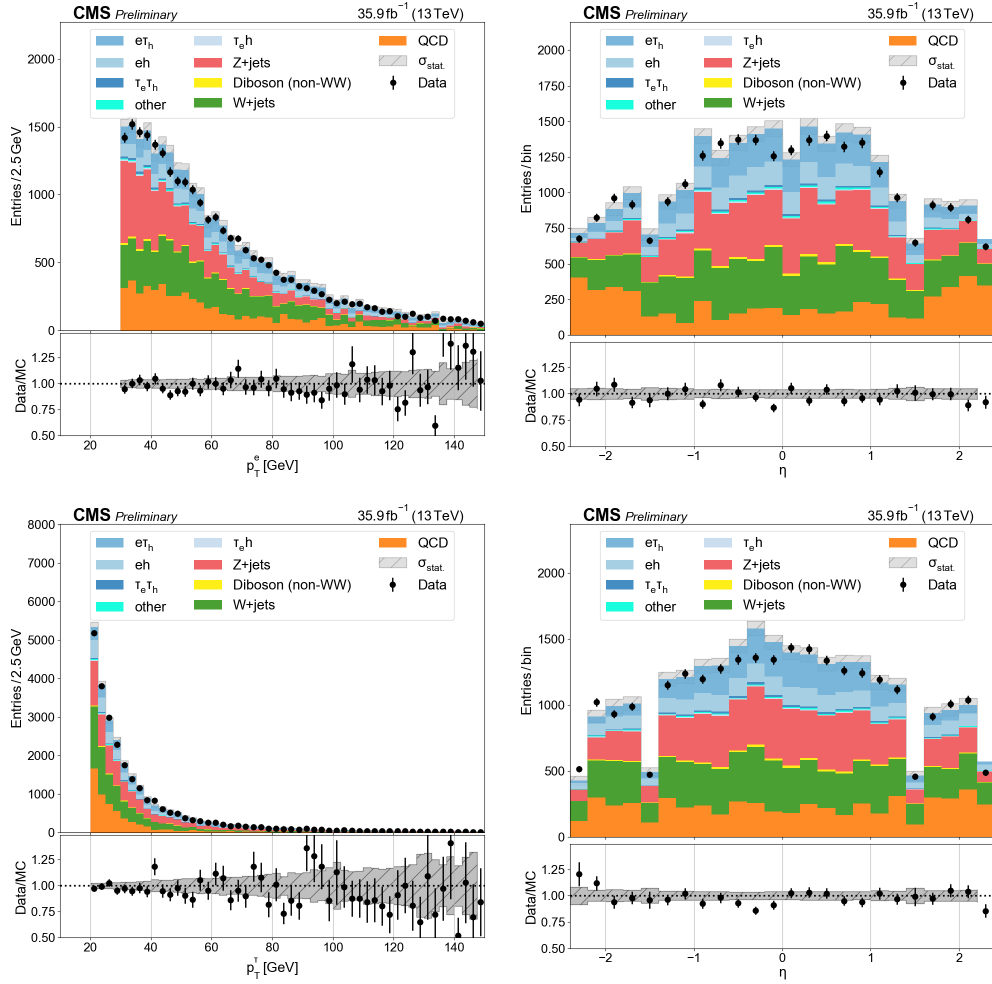


Figure B.46. p_T and η distributions for leading (top) and trailing (bottom) electrons in the $e\tau$ channel with $N_j \geq 2$ and $N_b = 0$.

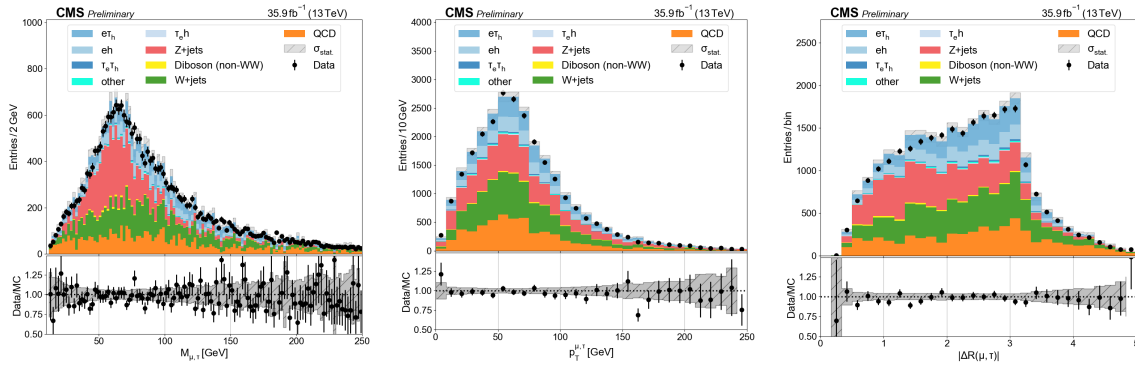


Figure B.47. Dielectron mass, p_T , and ΔR in the $e\tau$ channel with $N_j \geq 2$ and $N_b = 0$.

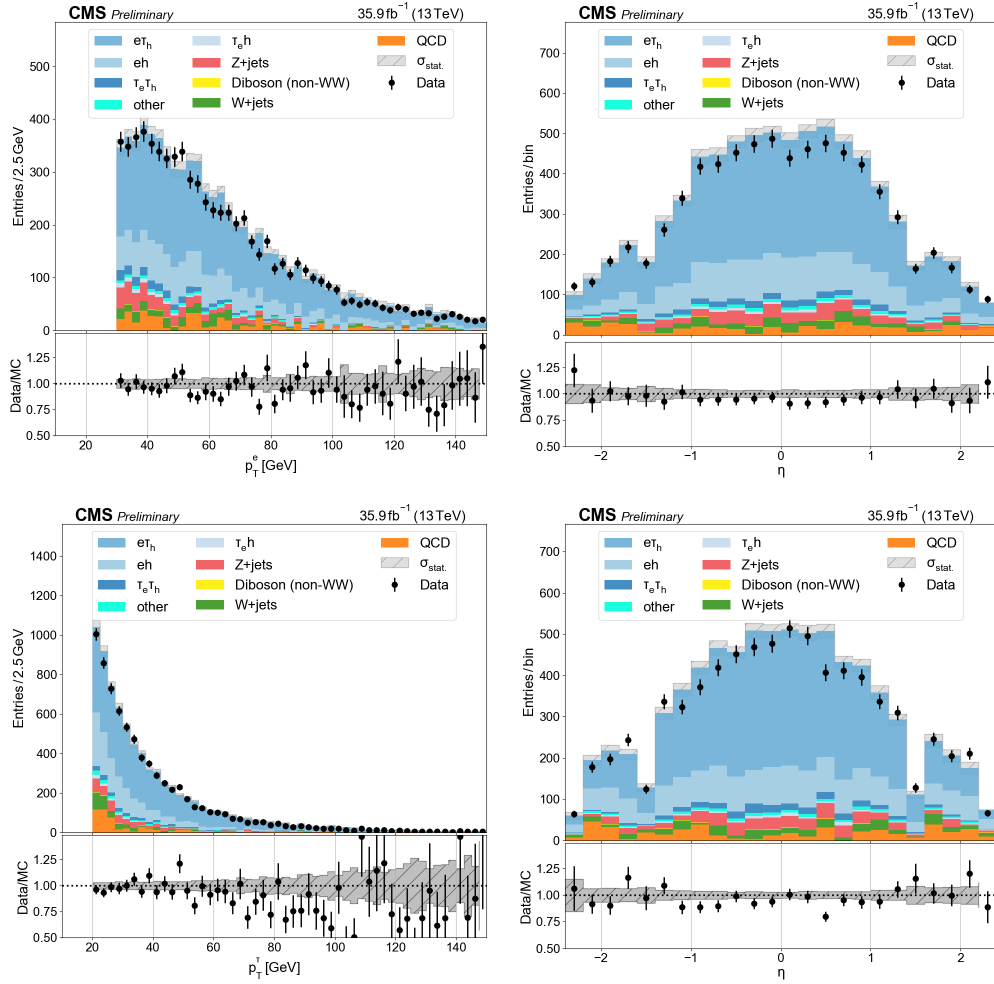


Figure B.48. p_T and η distributions for leading (top) and trailing (bottom) electrons in the $e\tau$ channel with $N_j = 2$ and $N_b = 1$.

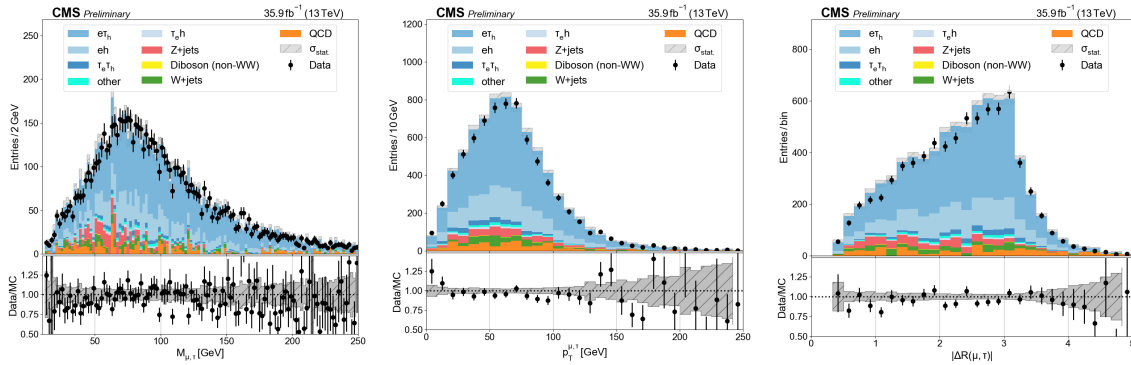


Figure B.49. Dielectron mass, p_T , and ΔR in the $e\tau$ channel with $N_j = 2$ and $N_b = 1$.

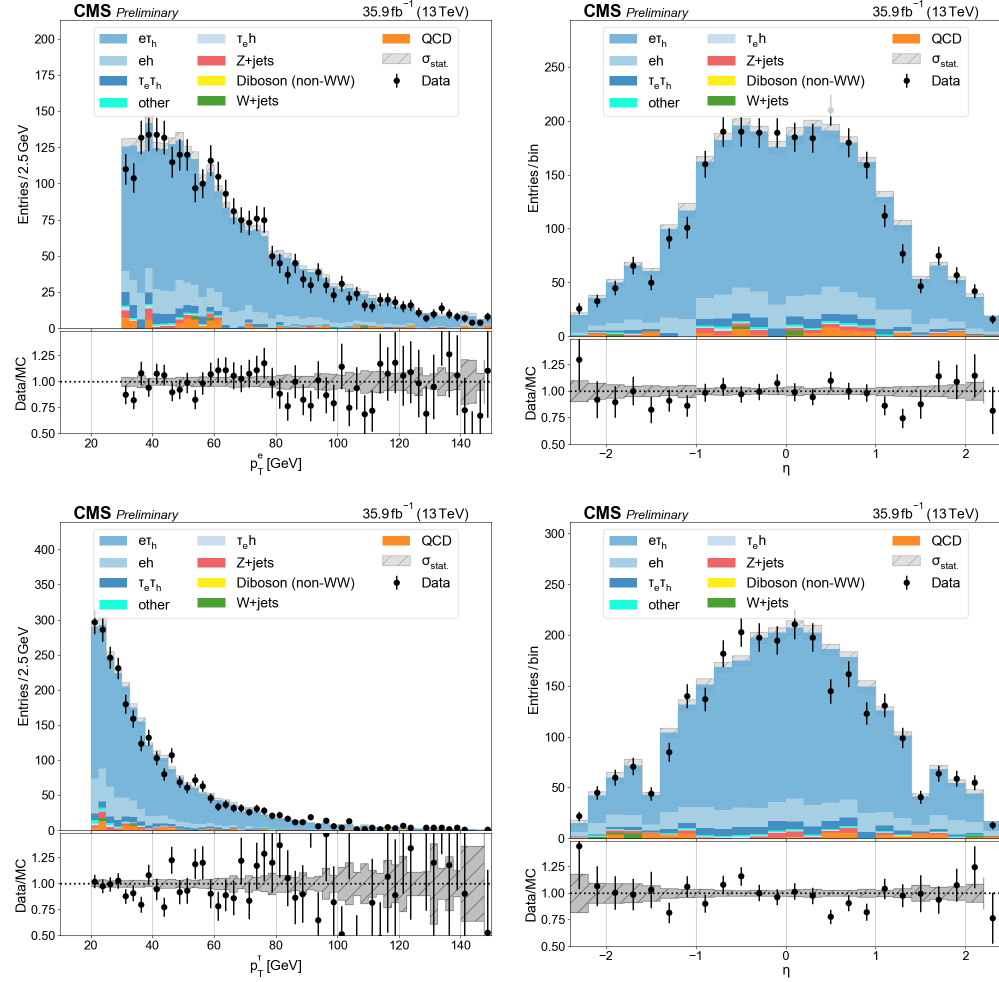


Figure B.50. p_T and η distributions for leading (top) and trailing (bottom) electrons in the $e\tau$ channel with $N_j = 2$ and $N_b = 2$.

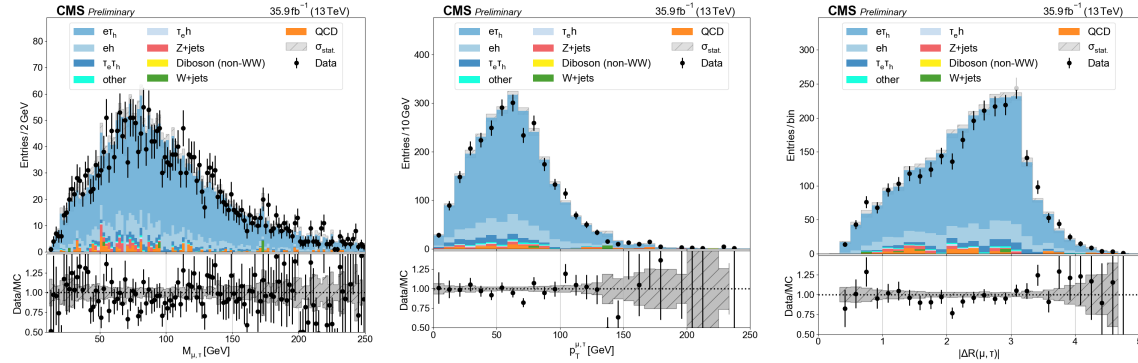


Figure B.51. Dielectron mass, p_T , and ΔR in the $e\tau$ channel with $N_j = 2$ and $N_b = 2$.

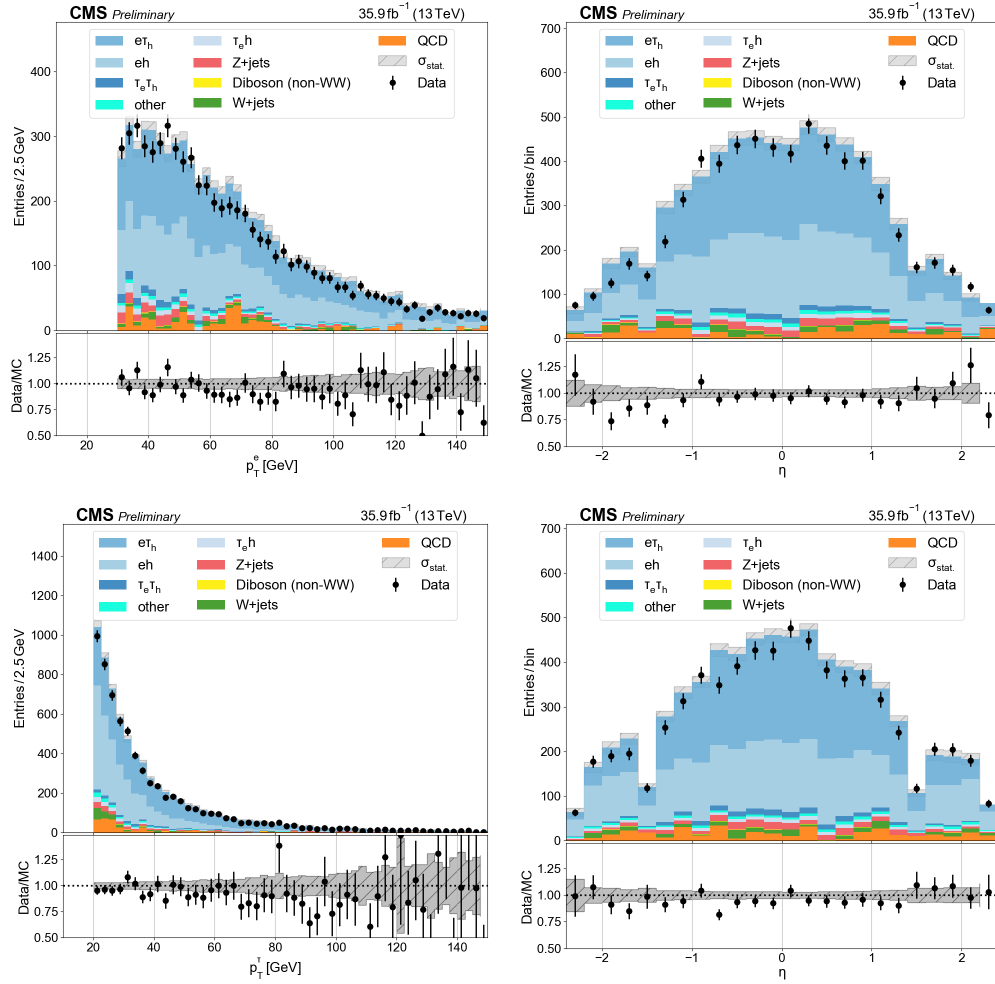


Figure B.52. p_T and η distributions for leading (top) and trailing (bottom) electrons in the $e\tau$ channel with $N_j \geq 3$ and $N_b = 1$.

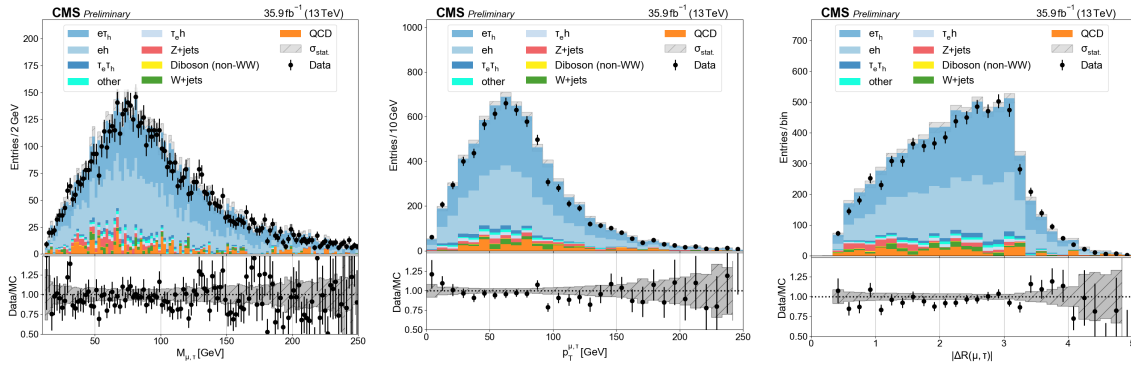


Figure B.53. Dielectron mass, p_T , and ΔR in the $e\tau$ channel with $N_j \geq 3$ and $N_b = 1$.

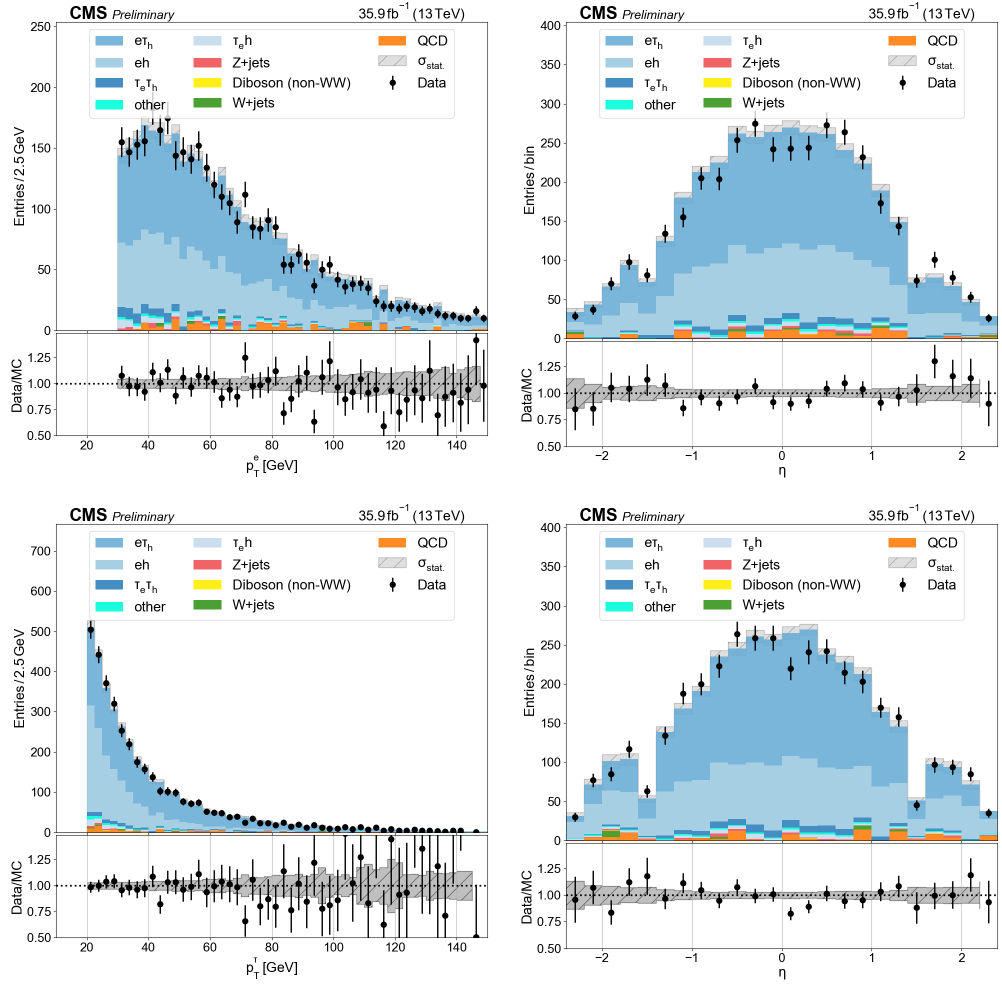


Figure B.54. p_T and η distributions for leading (top) and trailing (bottom) electrons in the $e\tau$ channel with $N_j \geq 3$ and $N_b \geq 2$.

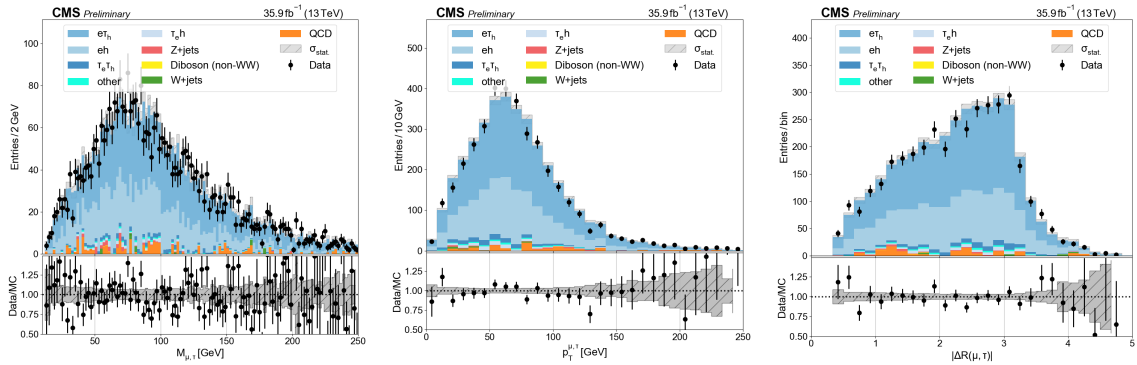


Figure B.55. Dielectron mass, p_T , and ΔR in the $e\tau$ channel with $N_j \geq 3$ and $N_b \geq 2$.

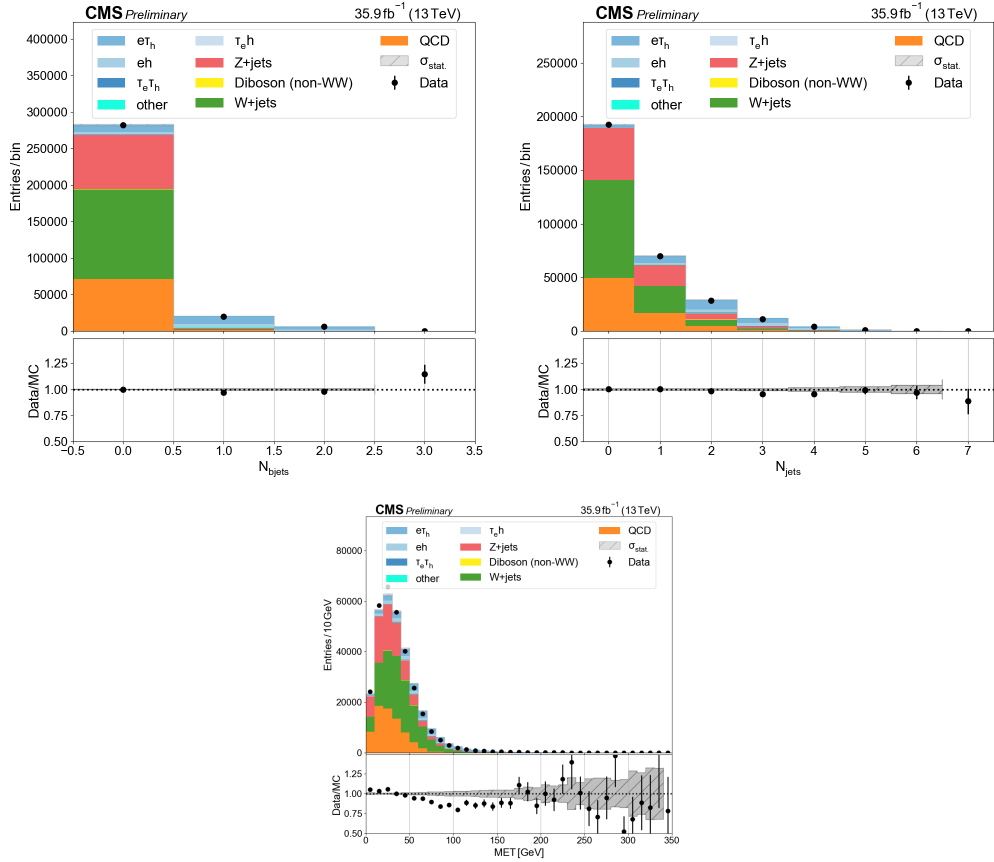


Figure B.56. Multiplicity of b tagged jets, non-tagged jets, and MET in $e\tau$ channel.

B.2.0.5. mutau.

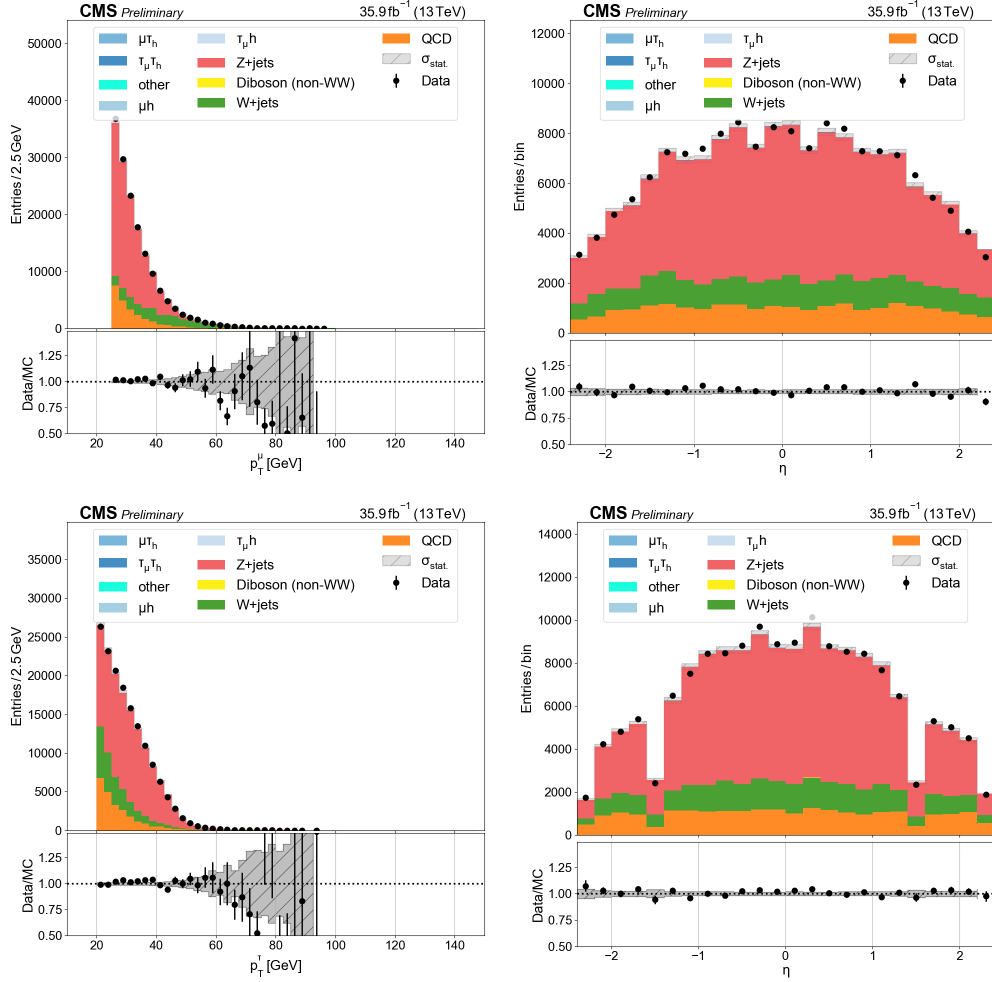


Figure B.57. p_T and η distributions for leading (top) and trailing (bottom) electrons in the $\mu\tau$ channel with $N_j = 0$.

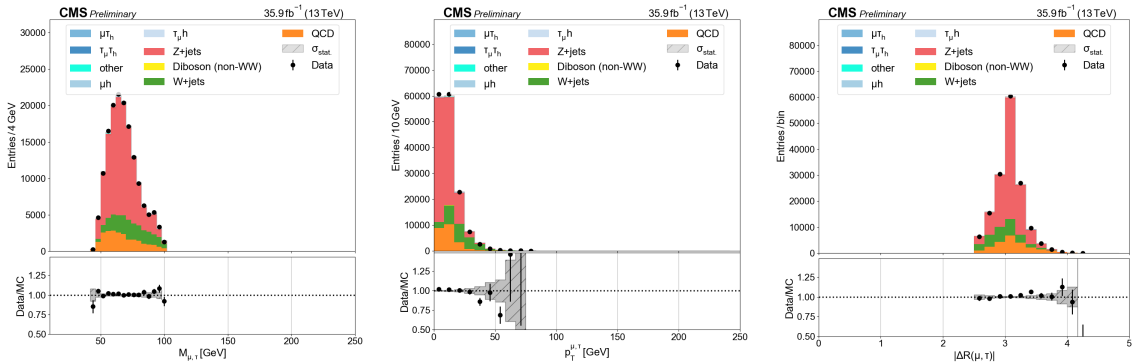


Figure B.58. Dielectron mass, p_T , and ΔR in the $\mu\tau$ channel with $N_j = 0$.

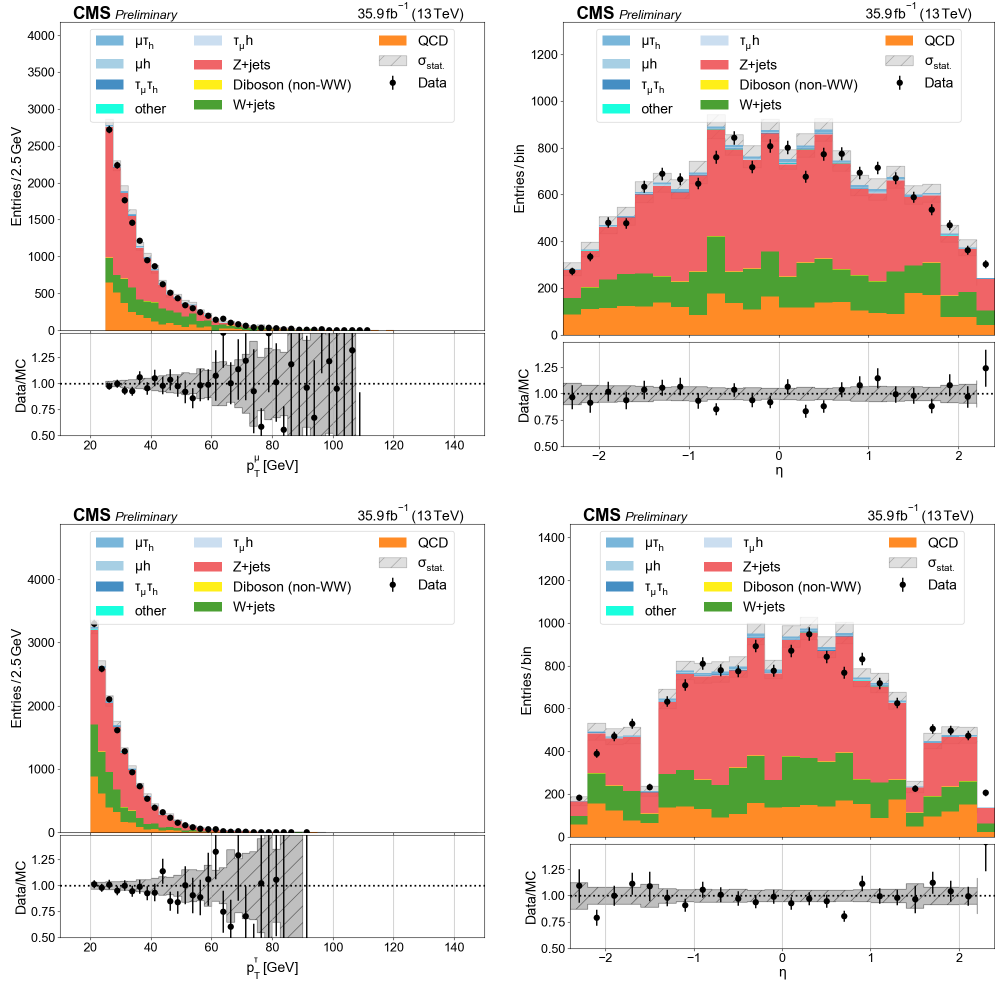


Figure B.59. p_T and η distributions for leading (top) and trailing (bottom) electrons in the $\mu\tau$ channel with $N_j = 1$ and $N_b = 0$.

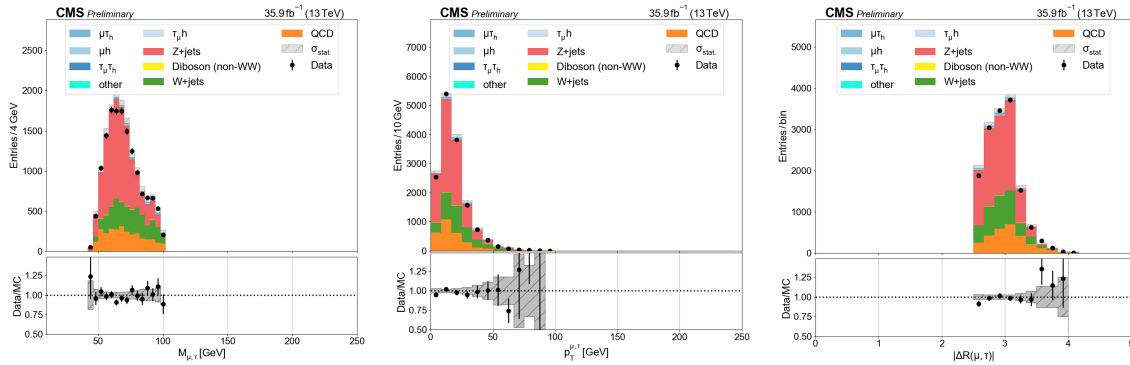


Figure B.60. Dielectron mass, p_T , and ΔR in the $\mu\tau$ channel with $N_j = 0$ and $N_b = 0$.

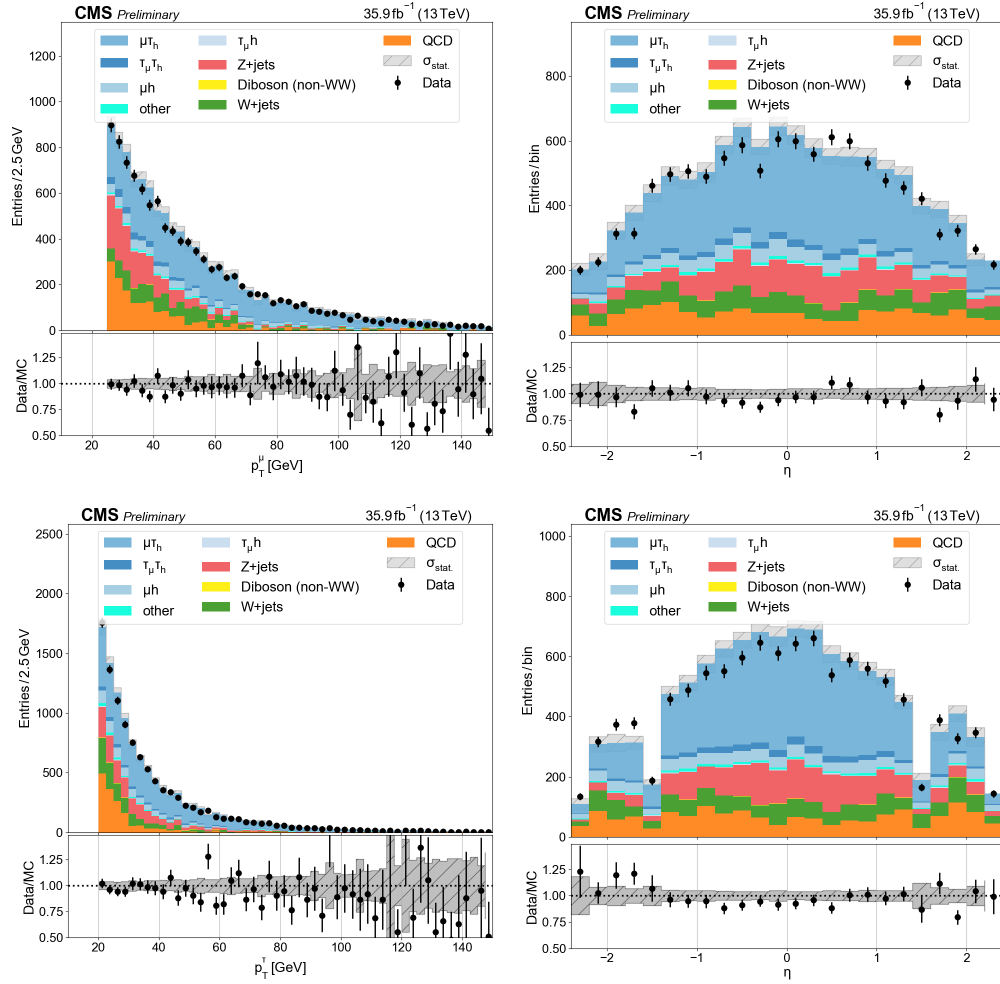


Figure B.61. p_T and η distributions for leading (top) and trailing (bottom) electrons in the $\mu\tau$ channel with $N_j = 1$ and $N_b = 1$.

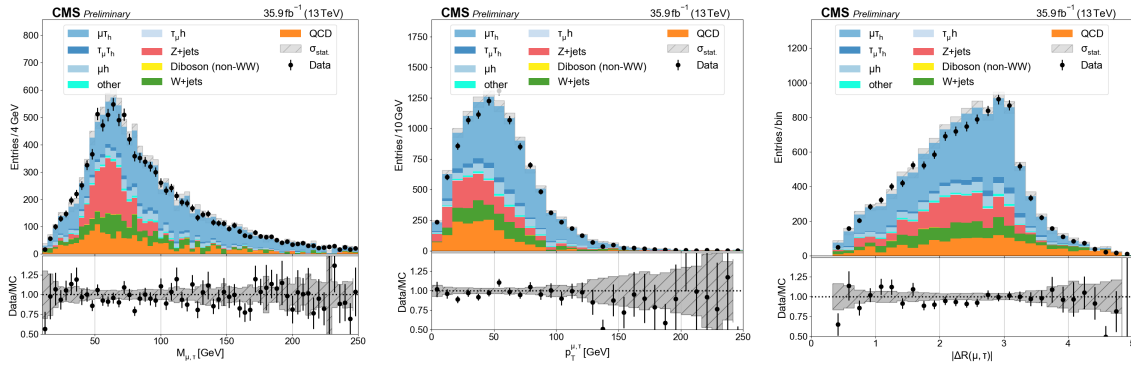


Figure B.62. Dielectron mass, p_T , and ΔR in the $\mu\tau$ channel with $N_j = 1$ and $N_b = 1$.

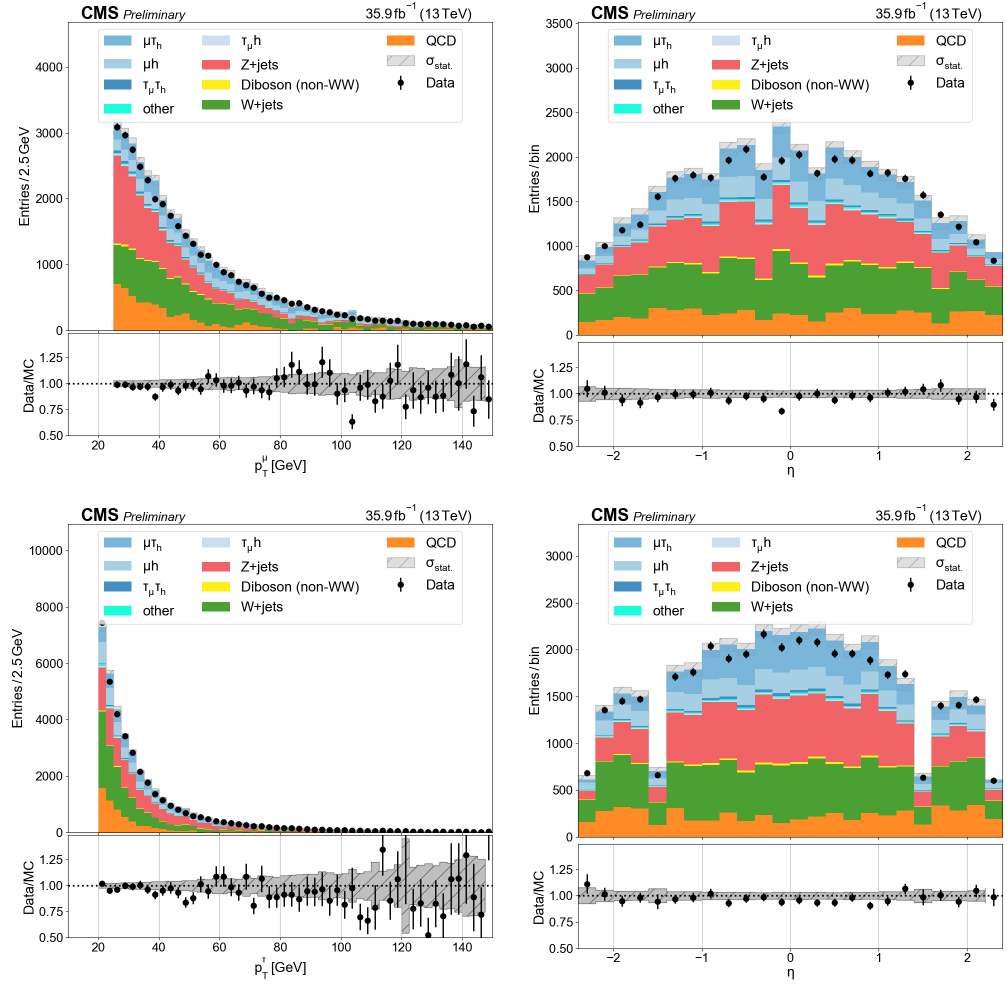


Figure B.63. p_T and η distributions for leading (top) and trailing (bottom) electrons in the $\mu\tau$ channel with $N_j \geq 2$ and $N_b = 0$.

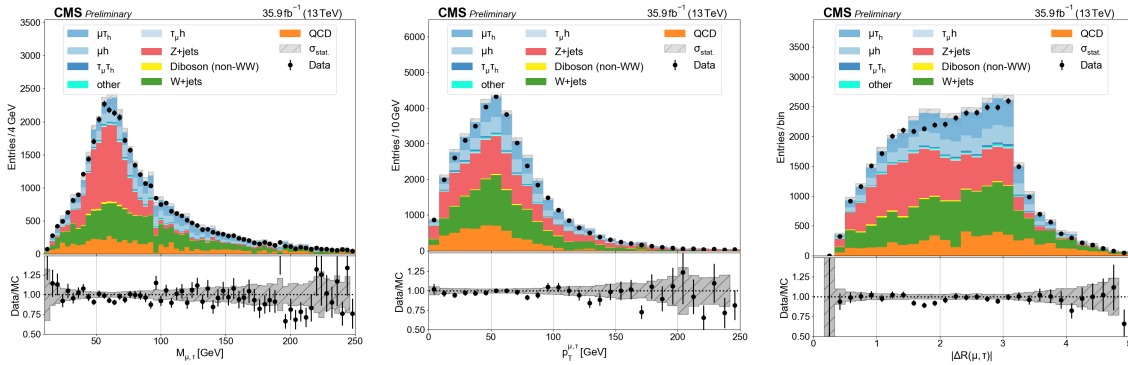


Figure B.64. Dielectron mass, p_T , and ΔR in the $\mu\tau$ channel with $N_j \geq 2$ and $N_b = 0$.

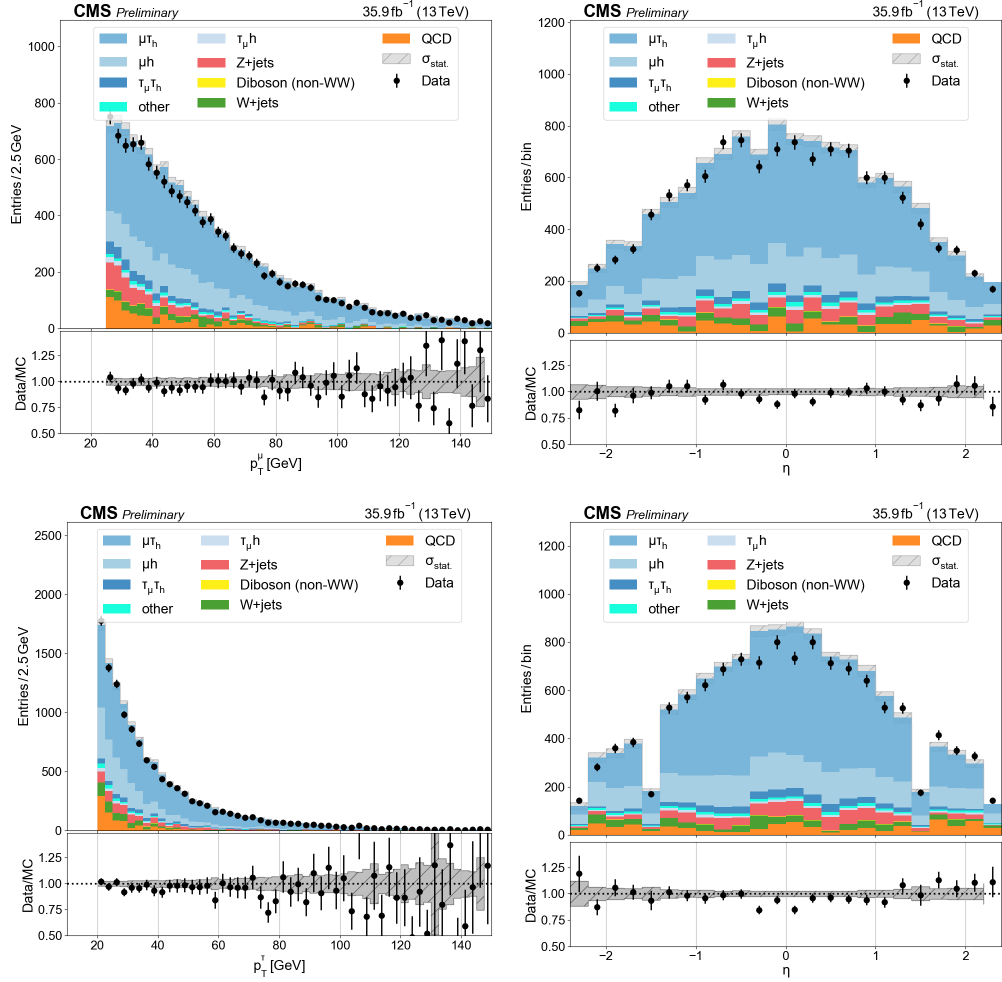


Figure B.65. p_T and η distributions for leading (top) and trailing (bottom) electrons in the $\mu\tau$ channel with $N_j = 2$ and $N_b = 1$.

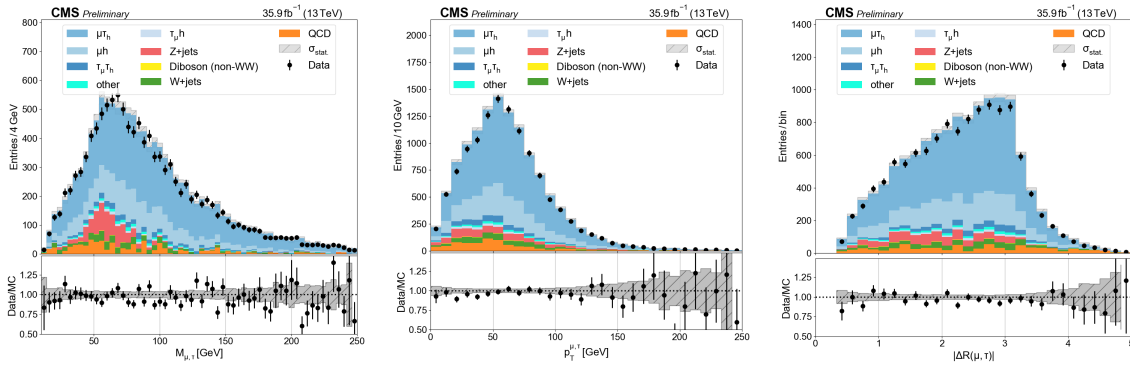


Figure B.66. Dielectron mass, p_T , and ΔR in the $\mu\tau$ channel with $N_j = 2$ and $N_b = 1$.

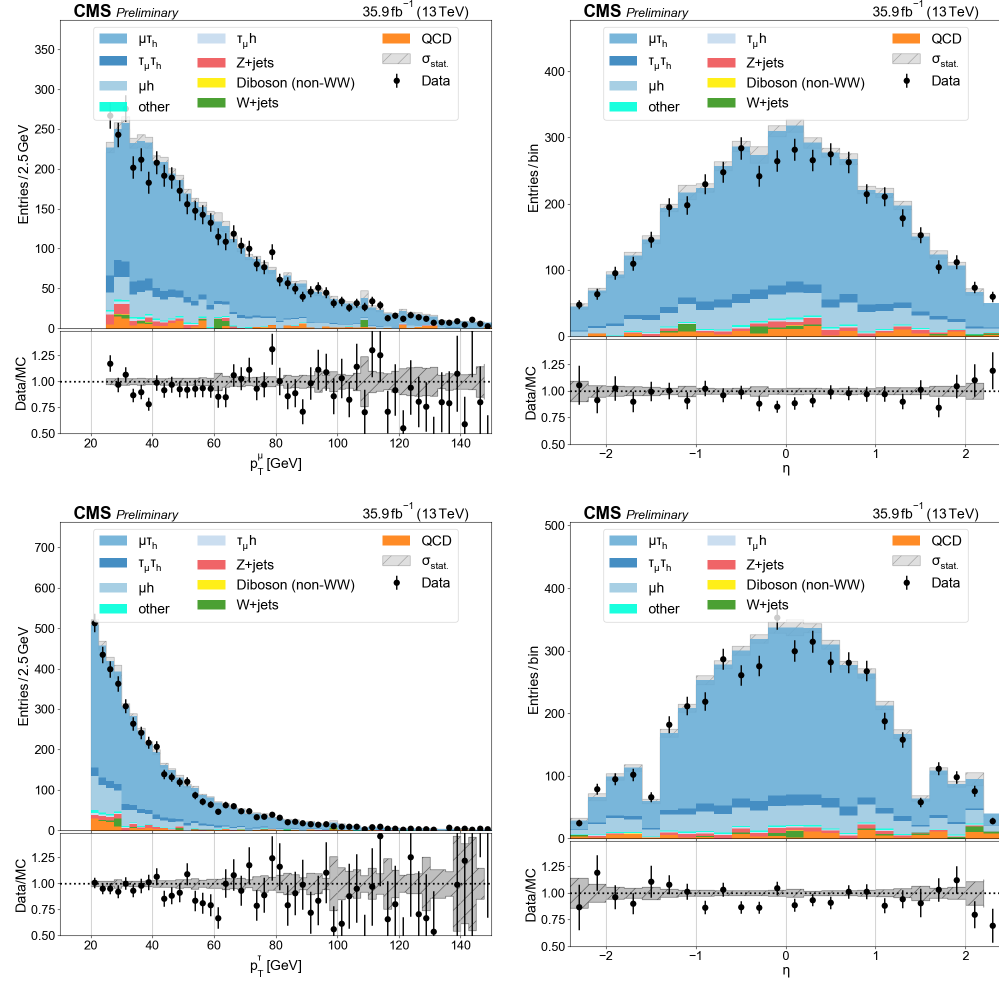


Figure B.67. p_T and η distributions for leading (top) and trailing (bottom) electrons in the $\mu\tau$ channel with $N_j = 2$ and $N_b = 2$.

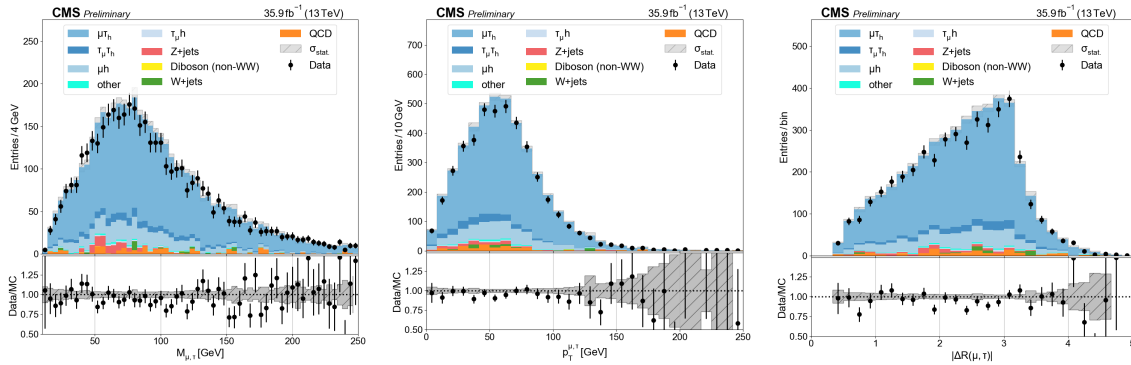


Figure B.68. Dielectron mass, p_T , and ΔR in the $\mu\tau$ channel with $N_j = 2$ and $N_b = 2$.

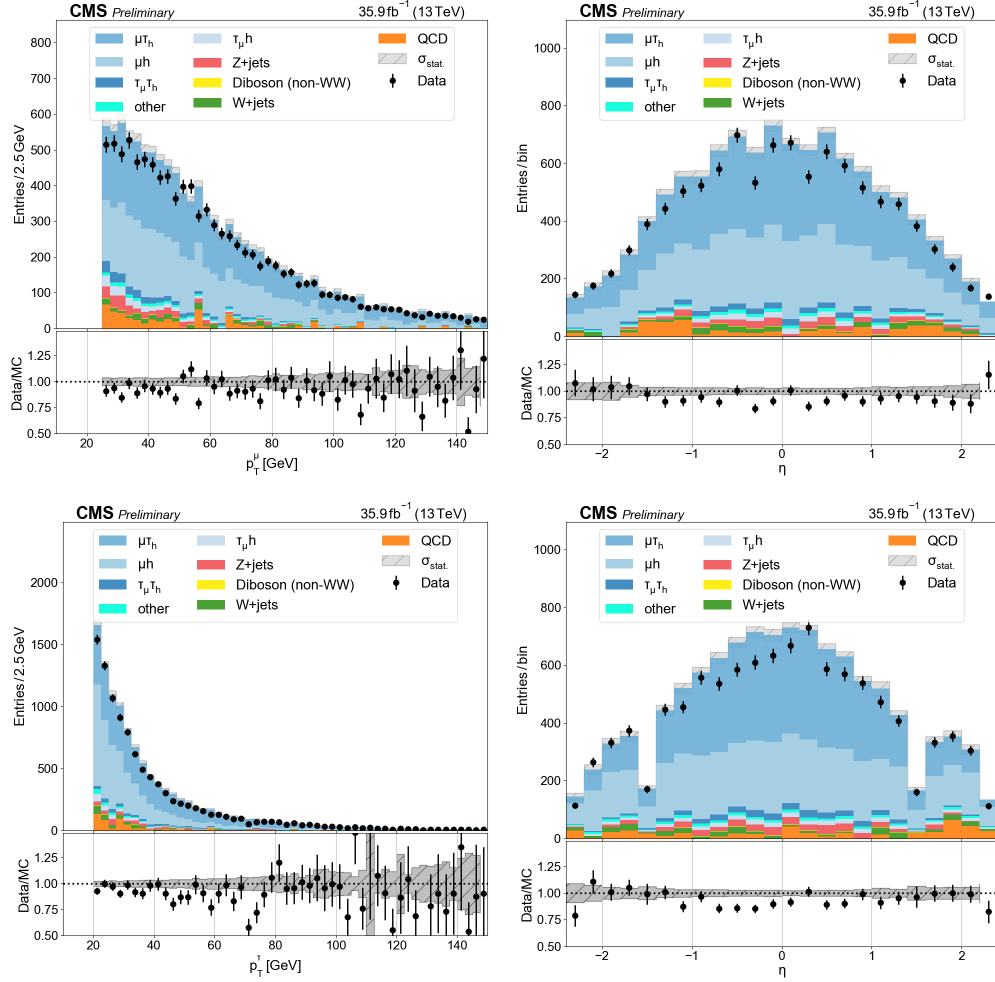


Figure B.69. p_T and η distributions for leading (top) and trailing (bottom) electrons in the $\mu\tau$ channel with $N_j \geq 3$ and $N_b = 1$.

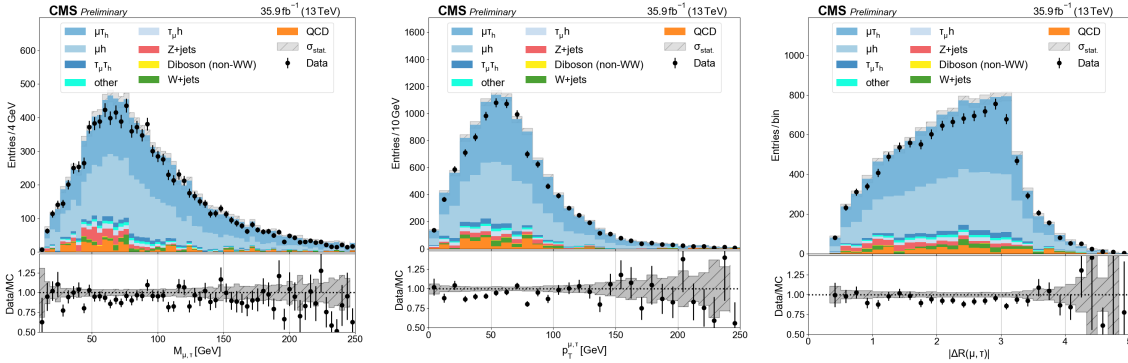


Figure B.70. Dielectron mass, p_T , and ΔR in the $\mu\tau$ channel with $N_j \geq 3$ and $N_b = 1$.

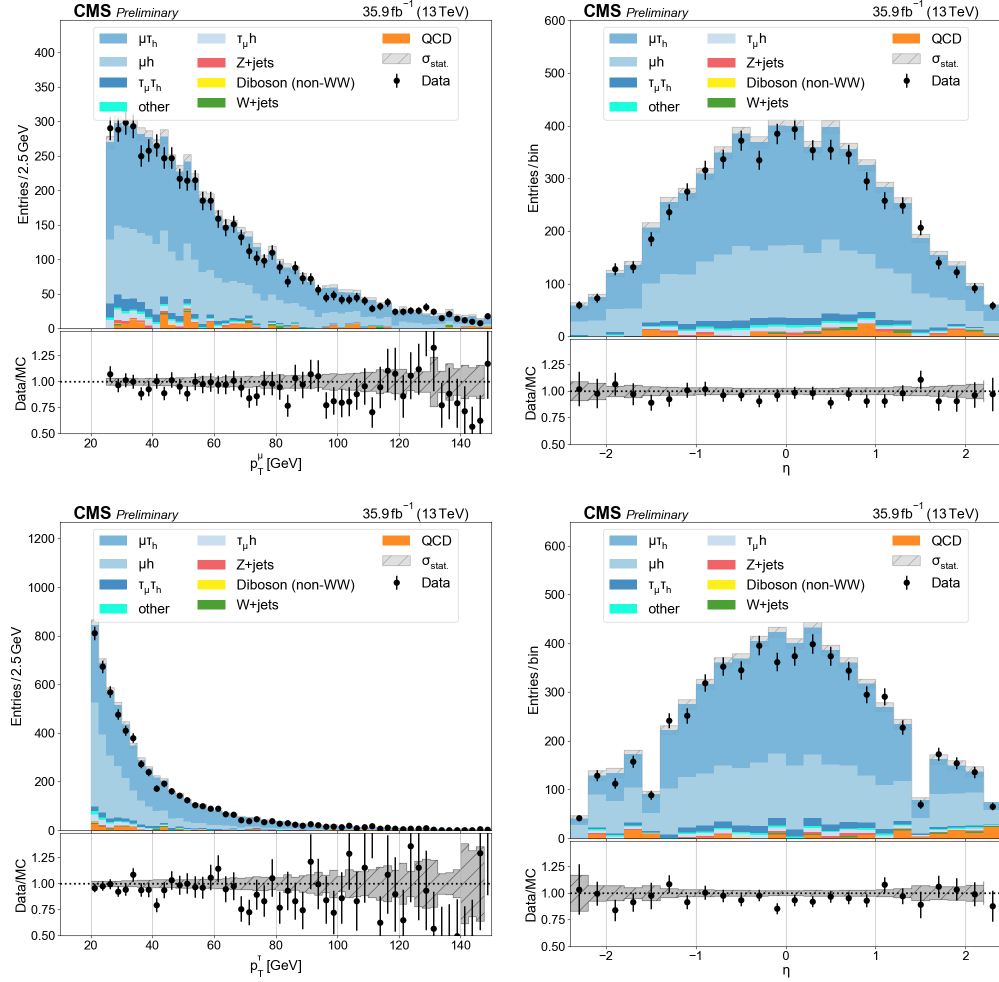


Figure B.71. p_T and η distributions for leading (top) and trailing (bottom) electrons in the $\mu\tau$ channel with $N_j \geq 3$ and $N_b \geq 2$.

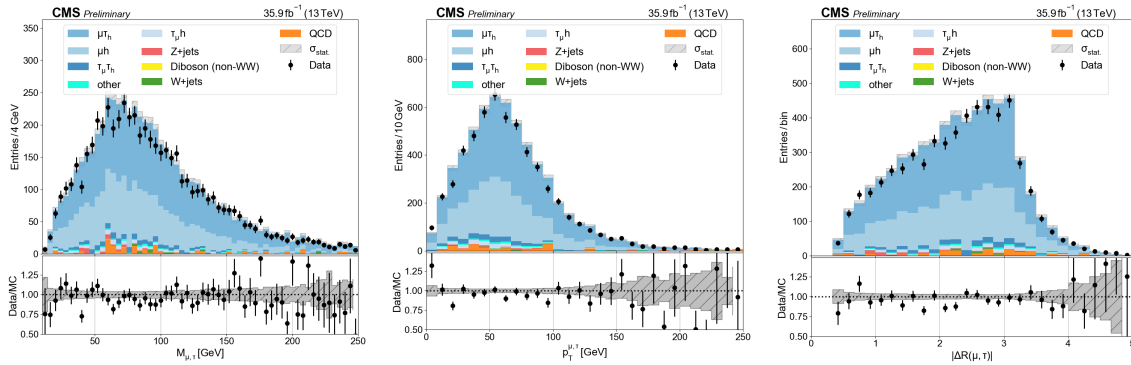


Figure B.72. Dielectron mass, p_T , and ΔR in the $\mu\tau$ channel with $N_j \geq 3$ and $N_b \geq 2$.

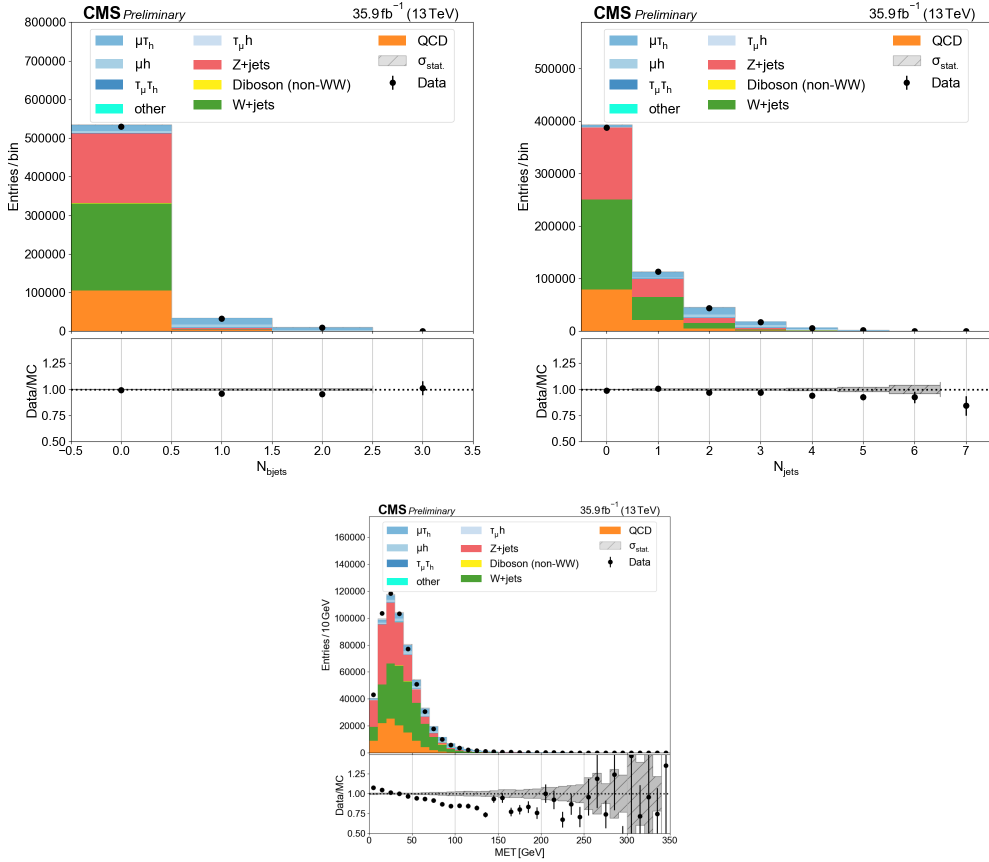


Figure B.73. Multiplicity of b tagged jets, non-tagged jets, and MET in $\mu\tau$ channel.

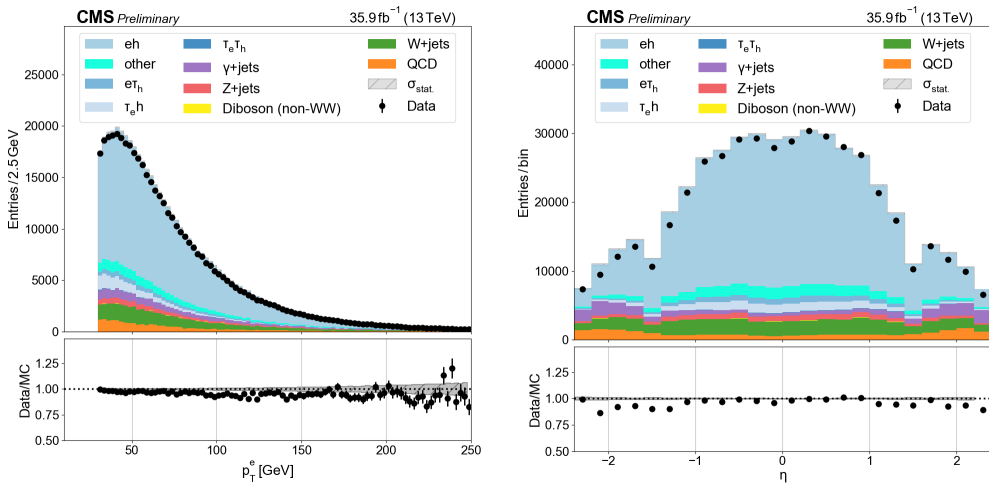


Figure B.74. p_T and η distributions for the muon in the $e + \text{jets}$ channel with $N_j \geq 4$ and $N_b = 1$.

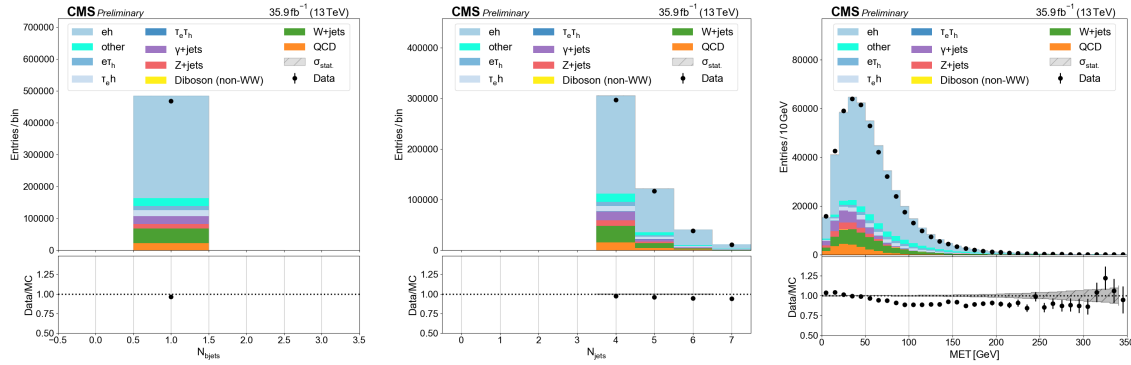


Figure B.75. Multiplicity of b tagged jets, non-tagged jets, and MET in $e +$ jets channel with $N_j \geq 4$ and $N_b = 1$.

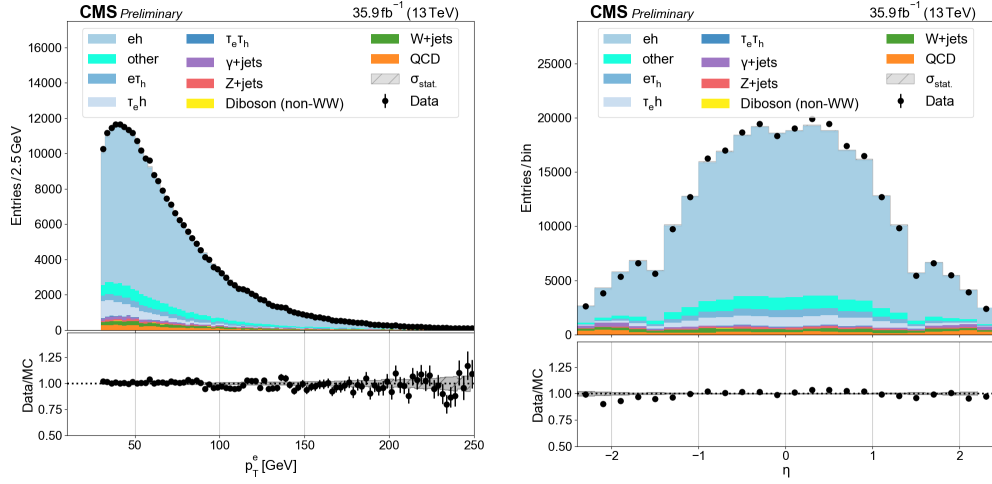


Figure B.76. p_T and η distributions for the muon in the $e +$ jets channel with $N_j \geq 2$ and $N_b \geq 2$.

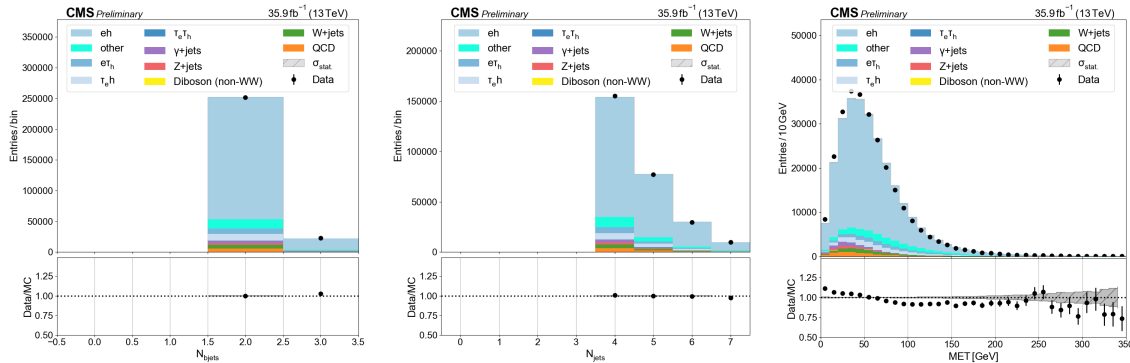


Figure B.77. Multiplicity of b tagged jets, non-tagged jets, and MET in $e +$ jets channel with $N_j \geq 4$ and $N_b \geq 2$.

B.2.0.6. ejet.

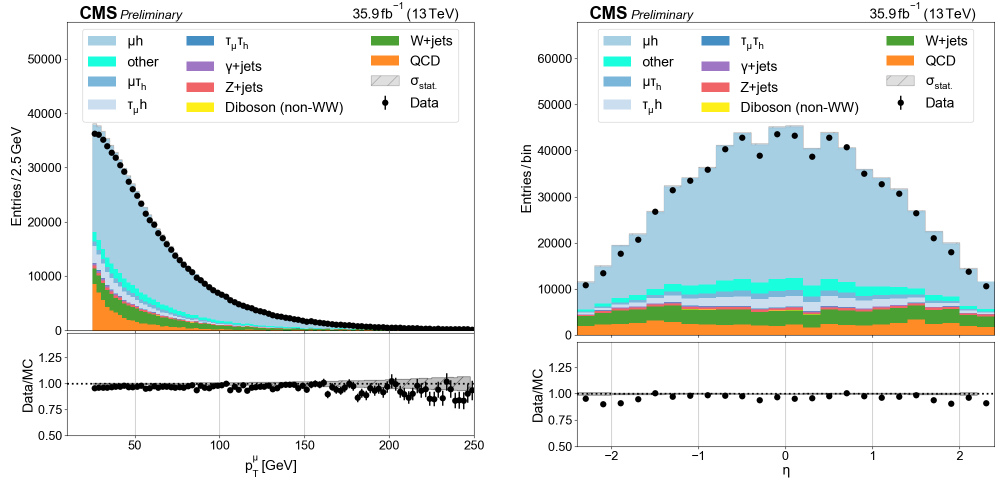


Figure B.78. p_T and η distributions for the muon in the $\mu + \text{jets}$ channel with $N_j \geq 4$ and $N_b = 1$.

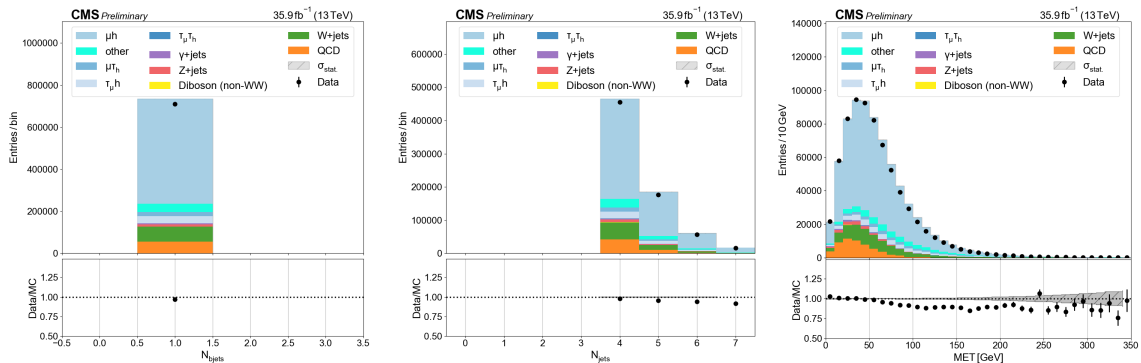


Figure B.79. Multiplicity of b tagged jets, non-tagged jets, and MET in $\mu + \text{jets}$ channel with $N_j \geq 4$ and $N_b = 1$.

B.2.0.7. mujet.

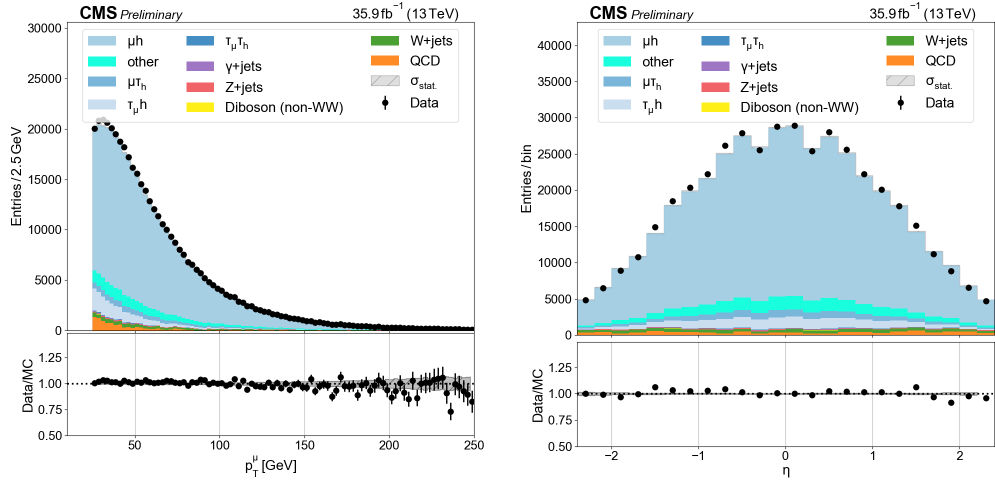


Figure B.80. p_T and η distributions for the muon in the $\mu + \text{jets}$ channel with $N_j \geq 2$ and $N_b \geq 2$.

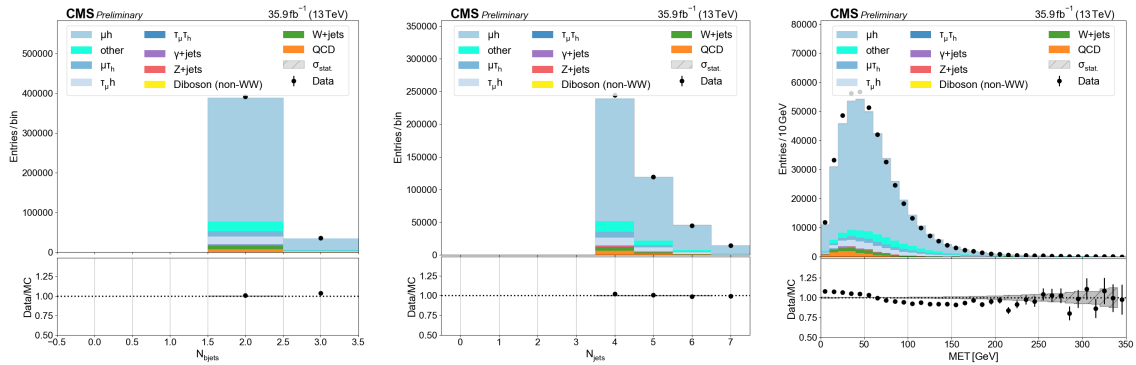


Figure B.81. Multiplicity of b tagged jets, non-tagged jets, and MET in $\mu + \text{jets}$ channel with $N_j \geq 4$ and $N_b \geq 2$.

APPENDIX C

Supplement Materials for CLUE clustering algorithm**C.1. Pseudocode**

Pseudocode of CLUE in serialized implementation. Parallelization is discussed in Section 5.2.2.

Algorithm 1: calculate ρ

```

for  $i \in points$  do
     $\rho_{[i]} = 0$ 
    for  $j \in \Omega_{d_c}(i)$  do
        if  $dist(i, j) < d_c$  then
             $\rho_{[i]} += w_{[j]}$ 

```

Algorithm 2: calculate δ

```

for  $i \in points$  do
     $\delta_{[i]} = +\infty$ 
     $nh_{[i]} = -1$ 
    for  $j \in \Omega_{d_m}(i)$  do
        if  $dist(i, j) < d_m$  and  $\rho_{[j]} > \rho_{[i]}$  then
            if  $dist(i, j) < \delta_{[i]}$  then
                 $nh_{[i]} = j$ 
                 $\delta_{[i]} = d_{ij}$ 

```

Algorithm 3: find seeds and outliers, assign clusters

```

k = 0;
stack = [] ;
for  $i \in points$  do
     $isSeed = \rho_{[i]} > \rho_c$  and  $\delta_{[i]} > \delta_c$ 
     $isOutlier = \rho_{[i]} < \rho_c$  and  $\delta_{[i]} > \delta_o$ 
    if  $isSeed$  then
         $clusterId_{[i]} = k$ 
        k++
        stack.pushback(i)
    else
        if not  $isOutlier$  then
             $followers_{[nh_{[i]}]}$ .pushback( $i$ )
while  $stack.size > 0$  do
    i = stack.back
    stack.popback
    for  $j \in followers_{[i]}$  do
         $clusterId_{[j]} = clusterId_{[i]}$ 
        stack.pushback(j)

```

C.2. Extra Performance Tests

Ryzen

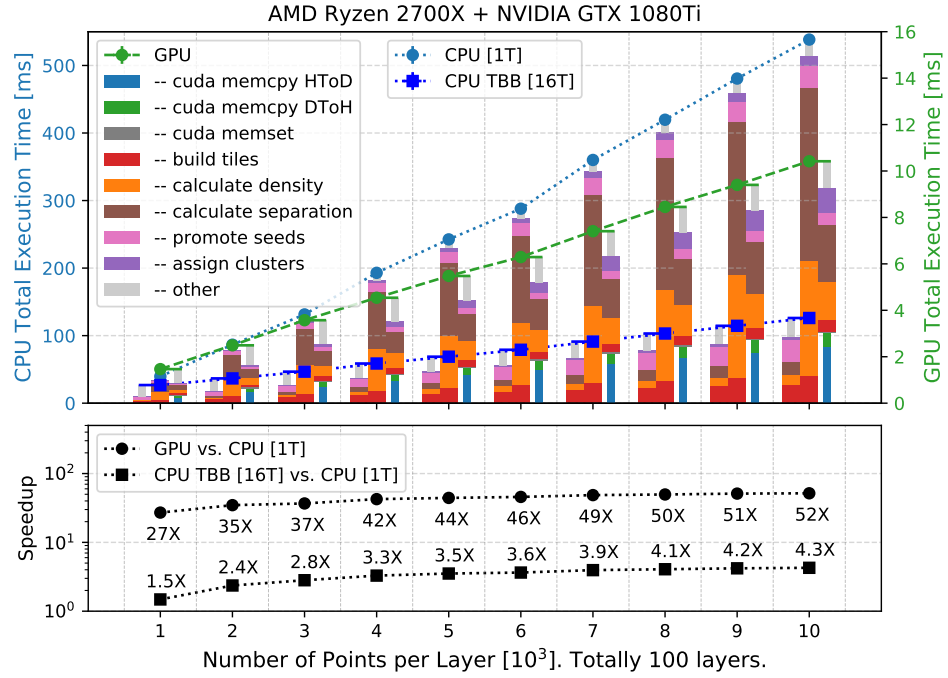


Figure C.1. Execution time of CLUE on CPU and GPU both scale linearly with number of input points, ranging from 10^5 to 10^6 in total on 100 layers. Mean and standard deviation are based on 200 trial runs. AMD Ryzen 2700X and NVIDIA GTX 1080Ti.

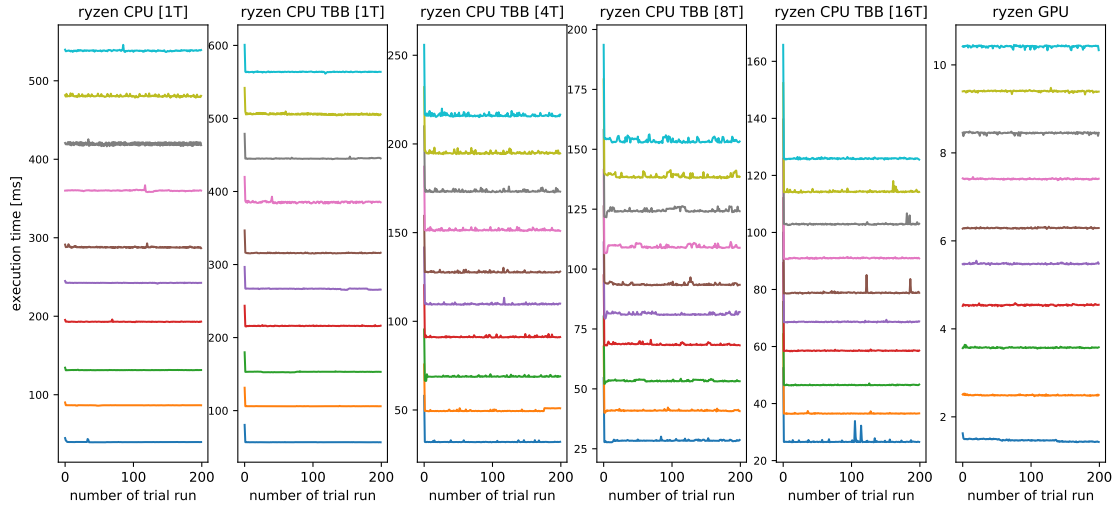


Figure C.2. Stability during 200 trial runs

CLUE Step	CPU [1T] (baseline)	CPU TBB [1T]	CPU TBB [4T]	CPU TBB [8T]	CPU TBB [16T]	CPU TBB [32T]	GPU
build fixed-grid spatial index	5.38 ± 0.09 ms	6.45 ± 0.05 ms (0.85x)	3.79 ± 0.10 ms (1.45x)	3.41 ± 0.12 ms (1.61x)	3.25 ± 0.46 ms (1.69x)	0.06 ms (89.15x)	
calculate local density	10.91 ± 0.07 ms	11.98 ± 0.02 ms (0.93x)	3.20 ± 0.10 ms (3.40x)	1.86 ± 0.08 ms (5.87x)	1.20 ± 0.05 ms (9.10x)	0.15 ms (70.40x)	
calculate nearest-higher and separation	14.37 ± 0.07 ms	16.26 ± 0.01 ms (0.88x)	4.18 ± 0.09 ms (3.43x)	2.35 ± 0.12 ms (6.11x)	1.47 ± 0.08 ms (9.70x)	0.20 ms (70.81x)	
decide seeds/outliers, register followers	2.39 ± 0.14 ms	3.45 ± 0.02 ms (0.87x)	3.12 ± 0.03 ms (0.96x)	3.20 ± 0.19 ms (0.94x)	3.14 ± 0.41 ms (0.95x)	0.04 ms (70.48x)	
expand clusters	0.30 ± 0.03 ms	2.14 ± 0.01 ms (0.14x)	0.52 ± 0.01 ms (0.58x)	0.33 ± 0.02 ms (0.90x)	0.27 ± 0.01 ms (1.10x)	0.04 ms (6.90x)	
cuda memcpy, memset	—	—	—	—	—	—	0.31 ms, 0.06 ms
other	5.66 ± 0.28 ms	16.58 ± 1.67 ms	17.29 ± 1.62 ms	17.38 ± 1.65 ms	17.48 ± 1.62 ms	0.60 ms	
TOTAL (1000 points per layer)	39.71 ± 0.54 ms	56.86 ± 1.67 ms (0.70x)	32.12 ± 1.84 ms (1.24x)	28.53 ± 1.86 ms (1.39x)	26.81 ± 1.94 ms (1.48x)	1.47 ± 0.03 ms (27.09x)	
CLUE Step	CPU [1T] (baseline)	CPU TBB [1T]	CPU TBB [4T]	CPU TBB [8T]	CPU TBB [16T]	CPU TBB [32T]	GPU
build fixed-grid spatial index	10.21 ± 0.05 ms	12.14 ± 0.05 ms (0.84x)	7.04 ± 0.22 ms (1.45x)	6.34 ± 0.13 ms (1.61x)	5.88 ± 0.17 ms (1.73x)	0.12 ms (84.32x)	
calculate local density	26.51 ± 0.05 ms	28.54 ± 0.03 ms (0.93x)	7.33 ± 0.09 ms (3.62x)	4.04 ± 0.12 ms (6.56x)	2.49 ± 0.07 ms (10.66x)	0.28 ms (94.16x)	
calculate nearest-higher and separation	34.56 ± 0.04 ms	37.12 ± 0.02 ms (0.93x)	9.48 ± 0.03 ms (3.65x)	5.12 ± 0.10 ms (6.75x)	3.13 ± 0.03 ms (11.04x)	0.40 ms (87.20x)	
decide seeds/outliers, register followers	6.24 ± 0.05 ms	6.98 ± 0.03 ms (0.89x)	6.49 ± 0.33 ms (0.96x)	6.44 ± 0.17 ms (0.97x)	5.99 ± 0.03 ms (1.04x)	0.09 ms (71.07x)	
expand clusters	1.44 ± 0.01 ms	3.69 ± 0.01 ms (0.39x)	1.02 ± 0.02 ms (1.41x)	0.68 ± 0.03 ms (2.12x)	0.58 ± 0.02 ms (2.47x)	0.08 ms (17.05x)	
cuda memcpy, memset	—	—	—	—	—	—	0.61 ms, 0.08 ms
other	7.61 ± 0.16 ms	17.68 ± 1.79 ms	18.44 ± 1.74 ms	18.45 ± 1.78 ms	18.57 ± 1.74 ms	0.83 ms	
TOTAL (2000 points per layer)	86.57 ± 0.28 ms	106.15 ± 1.79 ms (0.82x)	49.79 ± 1.91 ms (1.74x)	41.08 ± 1.90 ms (2.11x)	36.65 ± 1.96 ms (2.36x)	2.49 ± 0.01 ms (34.48x)	
CLUE Step	CPU [1T] (baseline)	CPU TBB [1T]	CPU TBB [4T]	CPU TBB [8T]	CPU TBB [16T]	CPU TBB [32T]	GPU
build fixed-grid spatial index	14.79 ± 0.08 ms	17.44 ± 0.16 ms (0.85x)	11.11 ± 0.22 ms (1.35x)	9.43 ± 0.16 ms (1.57x)	8.78 ± 0.20 ms (1.69x)	0.18 ms (88.24x)	
calculate local density	41.04 ± 0.04 ms	44.54 ± 0.04 ms (0.93x)	11.41 ± 0.10 ms (3.64x)	6.05 ± 0.14 ms (6.87x)	3.77 ± 0.02 ms (11.03x)	0.47 ms (89.11x)	
calculate nearest-higher and separation	53.70 ± 0.04 ms	57.14 ± 0.06 ms (0.93x)	14.54 ± 0.11 ms (3.68x)	7.62 ± 0.19 ms (7.05x)	4.70 ± 0.03 ms (11.42x)	0.65 ms (82.77x)	
decide seeds/outliers, register followers	9.30 ± 0.09 ms	10.25 ± 0.08 ms (0.91x)	10.77 ± 0.25 ms (0.80x)	9.66 ± 0.29 ms (0.96x)	8.84 ± 0.03 ms (1.05x)	0.13 ms (69.24x)	
expand clusters	2.55 ± 0.02 ms	5.01 ± 0.03 ms (0.51x)	1.53 ± 0.04 ms (1.67x)	1.00 ± 0.05 ms (2.54x)	0.89 ± 0.03 ms (2.86x)	0.13 ms (19.99x)	
cuda memcpy, memset	—	—	—	—	—	—	0.91 ms, 0.08 ms
other	9.51 ± 0.08 ms	18.78 ± 1.88 ms	19.62 ± 1.86 ms	19.75 ± 1.85 ms	19.67 ± 1.86 ms	1.02 ms	
TOTAL (3000 points per layer)	131.40 ± 0.24 ms	153.16 ± 1.92 ms (0.86x)	68.99 ± 1.91 ms (1.90x)	53.51 ± 1.92 ms (2.46x)	46.65 ± 2.06 ms (2.82x)	3.57 ± 0.01 ms (36.75x)	
CLUE Step	CPU [1T] (baseline)	CPU TBB [1T]	CPU TBB [4T]	CPU TBB [8T]	CPU TBB [16T]	CPU TBB [32T]	GPU
build fixed-grid spatial index	18.33 ± 0.09 ms	22.95 ± 0.17 ms (0.80x)	15.00 ± 0.13 ms (1.22x)	12.99 ± 0.20 ms (1.41x)	12.14 ± 0.21 ms (1.51x)	0.22 ms (81.71x)	
calculate local density	61.94 ± 0.14 ms	64.51 ± 0.04 ms (0.90x)	16.41 ± 0.08 ms (3.77x)	8.62 ± 0.19 ms (7.18x)	5.22 ± 0.04 ms (11.86x)	0.63 ms (99.09x)	
calculate nearest-higher and separation	84.05 ± 0.22 ms	86.08 ± 0.04 ms (0.98x)	21.84 ± 0.29 ms (3.85x)	11.35 ± 0.29 ms (7.40x)	6.85 ± 0.04 ms (12.26x)	0.95 ms (88.33x)	
decide seeds/outliers, register followers	13.11 ± 0.13 ms	15.44 ± 0.18 ms (0.85x)	15.13 ± 0.14 ms (0.87x)	13.37 ± 0.31 ms (0.98x)	12.27 ± 0.04 ms (1.07x)	0.19 ms (68.13x)	
expand clusters	4.12 ± 0.02 ms	7.18 ± 0.02 ms (0.57x)	2.25 ± 0.04 ms (1.83x)	1.56 ± 0.07 ms (2.64x)	1.37 ± 0.03 ms (3.00x)	0.23 ms (17.69x)	
cuda memcpy, memset	—	—	—	—	—	—	1.21 ms, 0.08 ms
other	11.43 ± 0.03 ms	19.95 ± 1.99 ms	20.71 ± 1.94 ms	20.84 ± 1.97 ms	20.84 ± 1.97 ms	1.03 ms	
TOTAL (4000 points per layer)	192.97 ± 0.32 ms	216.12 ± 1.97 ms (0.89x)	91.34 ± 2.09 ms (2.11x)	68.73 ± 2.06 ms (2.81x)	58.69 ± 2.17 ms (3.29x)	4.54 ± 0.01 ms (42.50x)	
CLUE Step	CPU [1T] (baseline)	CPU TBB [1T]	CPU TBB [4T]	CPU TBB [8T]	CPU TBB [16T]	CPU TBB [32T]	GPU
build fixed-grid spatial index	22.48 ± 0.11 ms	27.53 ± 0.24 ms (0.82x)	18.13 ± 0.21 ms (1.24x)	15.50 ± 0.26 ms (1.45x)	14.47 ± 0.18 ms (1.55x)	0.27 ms (82.06x)	
calculate local density	77.69 ± 0.07 ms	81.28 ± 0.12 ms (0.96x)	20.64 ± 0.22 ms (3.70x)	10.74 ± 0.23 ms (7.25x)	6.52 ± 0.05 ms (11.91x)	0.82 ms (94.31x)	
calculate nearest-higher and separation	107.57 ± 0.05 ms	109.03 ± 0.12 ms (0.98x)	27.62 ± 0.16 ms (3.90x)	14.31 ± 0.36 ms (7.52x)	8.67 ± 0.05 ms (12.40x)	1.18 ms (91.42x)	
decide seeds/outliers, register followers	16.26 ± 0.16 ms	19.08 ± 0.15 ms (0.85x)	18.82 ± 0.15 ms (0.80x)	16.88 ± 0.51 ms (0.96x)	15.40 ± 0.05 ms (1.06x)	0.24 ms (66.83x)	
expand clusters	5.28 ± 0.02 ms	8.90 ± 0.04 ms (0.59x)	2.83 ± 0.04 ms (1.87x)	1.96 ± 0.08 ms (2.69x)	1.72 ± 0.02 ms (3.08x)	0.33 ms (15.97x)	
cuda memcpy, memset	—	—	—	—	—	—	1.51 ms, 0.08 ms
other	13.22 ± 0.08 ms	21.01 ± 2.11 ms	21.83 ± 2.07 ms	21.98 ± 2.07 ms	22.02 ± 2.04 ms	1.04 ms	
TOTAL (5000 points per layer)	242.50 ± 0.24 ms	266.83 ± 2.18 ms (0.91x)	109.85 ± 2.28 ms (2.21x)	81.38 ± 2.16 ms (2.98x)	68.80 ± 2.21 ms (3.52x)	5.48 ± 0.01 ms (44.26x)	

CLUE Step	CPU [1T] (baseline)	CPU TBB [1T]	CPU TBB [4T]	CPU TBB [8T]	CPU TBB [16T]	CPU TBB [32T]	CPU TBB [64T]	CPU TBB [128T]	CPU TBB [256T]	CPU TBB [512T]	CPU TBB [1024T]	CPU TBB [2048T]	CPU TBB [4096T]	CPU TBB [8192T]	CPU TBB [16384T]	CPU TBB [32768T]	CPU TBB [65536T]	CPU TBB [131072T]	CPU TBB [262144T]	CPU TBB [524288T]	CPU TBB [1048576T]	CPU TBB [2097152T]	CPU TBB [4194304T]	CPU TBB [8388608T]	CPU TBB [16777216T]	CPU TBB [33554432T]	CPU TBB [67108864T]	CPU TBB [134217728T]	CPU TBB [268435456T]	CPU TBB [536870912T]	CPU TBB [1073741840T]	CPU TBB [2147483680T]	CPU TBB [4294967360T]	CPU TBB [8589934720T]	CPU TBB [17179869440T]	CPU TBB [34359738880T]	CPU TBB [68719477760T]	CPU TBB [13743895520T]	CPU TBB [27487781040T]	CPU TBB [54975562080T]	CPU TBB [109951124160T]	CPU TBB [219902248320T]	CPU TBB [439804496640T]	CPU TBB [879608993280T]	CPU TBB [175921798640T]	CPU TBB [351843597280T]	CPU TBB [70368719440T]	CPU TBB [14073743880T]	CPU TBB [28147487760T]	CPU TBB [56294975520T]	CPU TBB [11258995080T]	CPU TBB [22517990160T]	CPU TBB [45035980320T]	CPU TBB [90071960640T]	CPU TBB [180143921280T]	CPU TBB [360287842560T]	CPU TBB [720575685120T]	CPU TBB [144115137040T]	CPU TBB [288230274080T]	CPU TBB [576460548160T]	CPU TBB [1152921096320T]	CPU TBB [2305842192640T]	CPU TBB [4611684385280T]	CPU TBB [9223368770560T]	CPU TBB [18446737541120T]	CPU TBB [36893475082240T]	CPU TBB [73786950164480T]	CPU TBB [147573900328960T]	CPU TBB [295147800657920T]	CPU TBB [590295601315840T]	CPU TBB [1180591202631680T]	CPU TBB [2361182405263360T]	CPU TBB [4722364810526720T]	CPU TBB [9444729621053440T]	CPU TBB [1888945924210680T]	CPU TBB [3777891848421360T]	CPU TBB [7555783696842720T]	CPU TBB [15111567393685440T]	CPU TBB [30223134787370880T]	CPU TBB [60446269574741760T]	CPU TBB [12089253914948320T]	CPU TBB [24178507829896640T]	CPU TBB [48357015659793280T]	CPU TBB [96714031319586560T]	CPU TBB [193428062638573120T]	CPU TBB [386856125277146240T]	CPU TBB [773712250554292480T]	CPU TBB [1547424501108584960T]	CPU TBB [3094849002217169920T]	CPU TBB [6189698004434339840T]	CPU TBB [12379396008868679680T]	CPU TBB [24758792017737359360T]	CPU TBB [49517584035474718720T]	CPU TBB [99035168070949437440T]	CPU TBB [19807033614189887480T]	CPU TBB [39614067228379774960T]	CPU TBB [79228134456759549920T]	CPU TBB [15845626891359889960T]	CPU TBB [31691253782719779920T]	CPU TBB [63382507565439559840T]	CPU TBB [12676501513087911960T]	CPU TBB [25353003026175823920T]	CPU TBB [50706006052351647840T]	CPU TBB [1014120121047032960T]	CPU TBB [2028240242094065920T]	CPU TBB [4056480484188131840T]	CPU TBB [8112960968376263680T]	CPU TBB [16225921936732527360T]	CPU TBB [32451843873465054720T]	CPU TBB [64903687746930109440T]	CPU TBB [12980737549386021880T]	CPU TBB [25961475098772043760T]	CPU TBB [51922950197544087520T]	CPU TBB [10384590039508817040T]	CPU TBB [20769180079017634080T]	CPU TBB [41538360158035268160T]	CPU TBB [83076720316070536320T]	CPU TBB [166153440632141072640T]	CPU TBB [332306881264282145280T]	CPU TBB [664613762528564290560T]	CPU TBB [1329227525057128581120T]	CPU TBB [2658455050114257162240T]	CPU TBB [531691010022854332480T]	CPU TBB [106338202004578866480T]	CPU TBB [212676404009157732960T]	CPU TBB [425352808018315465920T]	CPU TBB [850705616036630931840T]	CPU TBB [170141123207326186320T]	CPU TBB [340282246414652372640T]	CPU TBB [680564492829304745280T]	CPU TBB [1361128985658609490560T]	CPU TBB [2722257971317218981120T]	CPU TBB [5444515942634437962240T]	CPU TBB [1088903188528875592480T]	CPU TBB [2177806377057751184960T]	CPU TBB [4355612754115502369920T]	CPU TBB [871122550823100473880T]	CPU TBB [1742245101646200947680T]	CPU TBB [3484490203292401895360T]	CPU TBB [6968980406584803790720T]	CPU TBB [13937960813169607581440T]	CPU TBB [27875921626339215162880T]	CPU TBB [55751843252678430325760T]	CPU TBB [111503686505356860651520T]	CPU TBB [223007373010713721303040T]	CPU TBB [446014746021427442606080T]	CPU TBB [892029492042854885212160T]	CPU TBB [1784058984085709770424320T]	CPU TBB [3568117968171419540848640T]	CPU TBB [7136235936342839081697280T]	CPU TBB [14272471872685678163394560T]	CPU TBB [28544943745371356326789120T]	CPU TBB [57089887490742712653578240T]	CPU TBB [11417977498148542530755680T]	CPU TBB [22835954996297085061511360T]	CPU TBB [45671909992594170123022720T]	CPU TBB [91343819985188340246045440T]	CPU TBB [18268763997037668049209080T]	CPU TBB [36537527994075336098418160T]	CPU TBB [73075055988150672196836320T]	CPU TBB [146150111976301344393672640T]	CPU TBB [292300223952602688787345280T]	CPU TBB [584600447905205377574690560T]	CPU TBB [1169200898510406755149381120T]	CPU TBB [2338401797020813510298762240T]	CPU TBB [4676803594041626720585524480T]	CPU TBB [9353607188083253441170548960T]	CPU TBB [1870721437616646688234097760T]	CPU TBB [3741442875233293376468195520T]	CPU TBB [7482885750466586752936391040T]	CPU TBB [14965771500933173505872782080T]	CPU TBB [29931543001866347011745564160T]	CPU TBB [59863086003733294023491128320T]	CPU TBB [119726172007465880446982256640T]	CPU TBB [239452344014931760893964513280T]	CPU TBB [478904688029863521787929026560T]	CPU TBB [957809376059727043575858053120T]	CPU TBB [191561875211945408715171610640T]	CPU TBB [383123750423890817430343221280T]	CPU TBB [766247500847781634860686442560T]	CPU TBB [1532495001695563269721372885120T]	CPU TBB [3064990003391126539442745770240T]	CPU TBB [6129980006782253078885491540480T]	CPU TBB [12259960013564506157770983080960T]	CPU TBB [24519920027129012315541966161920T]	CPU TBB [49039840054258024631083932323840T]	CPU TBB [98079680108516049262167864647680T]	CPU TBB [19615936021703209852433572929520T]	CPU TBB [3923187204340641970486714585840T]	CPU TBB [7846374408681283940973429117680T]	CPU TBB [15692748017362567881946858235360T]	CPU TBB [31385496034725135763893716470720T]	CPU TBB [62770992069450271527787432941440T]	CPU TBB [125541984138900543055574865882880T]	CPU TBB [251083968277801086111149731765760T]	CPU TBB [502167936555602172222299463531520T]	CPU TBB [100433973311120434444459892706320T]	CPU TBB [200867946622240868888919785412640T]	CPU TBB [40173589324448173777783957082520T]	CPU TBB [80347178648896347555567914165040T]	CPU TBB [160694357297792695111135828330080T]	CPU TBB [321388714595585390222271656660160T]	CPU TBB [642777429191170780444543313320320T]	CPU TBB [1285554858382341560889086626640640T]	CPU TBB [2571109716764683121778173253281280T]	CPU TBB [5142219433529366243556346506562560T]	CPU TBB [1028443886705873248711269301312560T]	CPU TBB [2056887773411746497422538602625120T]	CPU TBB [4113775546823492994845077205250240T]	CPU TBB [8227541093646985989690154410500480T]	CPU TBB [1645508218729397197938030882000960T]	CPU TBB [3291016437458794395876061764001920T]	CPU TBB [6582032874917588791752123528003840T]	CPU TBB [13164065749835177583504247056007680T]	CPU TBB [26328131499670355167008494012015360T]	CPU TBB [52656262999340710334016988024030720T]	CPU TBB [1053125259868014206680339760480640T]	CPU TBB [2106250519736028403360679520801280T]	CPU TBB [4212501039472056806721359041602560T]	CPU TBB [8425002078944113613442718083205120T]	CPU TBB [16850041577888227226845560166410240T]	CPU TBB [33700083155776454453691120332820480T]	CPU TBB [67400166311552908907382400665640960T]	CPU TBB [134800332757058578014764801331281920T]	CPU TBB [269600665514117156029529602662563840T]	CPU TBB [539201331028342312058592053251327680T]	CPU TBB [107840266205668462411784010650265440T]	CPU TBB [215680532111336924823568021300530880T]	CPU TBB [431361064222673849647136042601061760T]	CPU TBB [862722128445347699294272085202123520T]	CPU TBB [172544425689069539858854417040425040T]	CPU TBB [345088851378139079717708834080850880T]	CPU TBB [690177702756278159435417668161711680T]	CPU TBB [138035540551356238867335333633423360T]	CPU TBB [27607108110271247773467066726684720T]	CPU TBB [5521421622054249554693413345339440T]	CPU TBB [11042843241088891109386826690678880T]	CPU TBB [22085686482177782218773653381357760T]	CPU TBB [44171372964355564437547306762715520T]	CPU TBB [8834274592871112887509461352543040T]	CPU TBB [1766854118574224177501892270508080T]	CPU TBB [3533708237148448355003784541016160T]	CPU TBB [7067416474296896710007569082032320T]	CPU TBB [14134832985593793420015138164064640T]	CPU TBB [28269665971187586840030276328129280T]	CPU TBB [56539331942375173680060552656258560T]	CPU TBB [11307866388475034736012110531317120T]	CPU TBB [22615732776950069472024221066634240T]	CPU TBB [45231465553900138944048442133268480T]	CPU TBB [90462931107800277888096884466536960T]	CPU TBB [18092586221560055577619376893307920T]	CPU TBB [36185172443120111155238753786615840T]	CPU TBB [72370344886240222310477507573231680T]	CPU TBB [14474068977248044462095501514663360T]	CPU TBB [2894813795449608892419000302932720T]	CPU TBB [5789627590899217784838000605865440T]	CPU TBB [11579255181798355569676001211730880T]	CPU TBB [2315851036359671113935200242346160T]	CPU TBB [4631702072719342227870400484692320T]	CPU TBB [9263404145438684455740800969384640T]	CPU TBB [1852680829087736891148160193876920T]	CPU TBB [3705361658175473782296320387753840T]	CPU TBB [7410723316350947564592640775507680T]	CPU TBB [14821446632701895129185281551015360T]	CPU TBB [29642893265403790258370563102030720T]	CPU TBB [59285786530807580516741126204061440T]	CPU TBB [11857157306161516023348251240812280T]	CPU TBB [23714314612323032046696502481625560T]	CPU TBB [47428629224646064093393004963251120T]	CPU TBB [94857258449292128186786009926502240T]	CPU TBB [18971451689584245637357201985304480T]	CPU TBB [37942903379168491274714403970608960T]	CPU TBB [75885806758336982549428807941217920T]	CPU TBB [15177161351667396509885761588243520T]	CPU TBB [3035432270333479301977132317648640T]	CPU TBB [6070864540666958603954464635297280T]	CPU TBB [12141729081339172079189293270594560T]	CPU TBB [24283458162678344158378586541189120T]	CPU TBB [4856691632535668831675717308237240T]	CPU TBB [9713383265071337663351434606474480T]	CPU TBB [1942676653014275332672869241298960T]	CPU TBB [3885353306028550665345738482597280T]	CPU TBB [7770706612057101330691476965194560T]	CPU TBB [1554141322410402666182953931389120T]	CPU TBB [3108282644820805332365867862778240T]	CPU TBB [6216565289641610664731735772556480T]	CPU TBB [124331305792832212483407154461120T]	CPU TBB [24866261158566442496681428710240T]	CPU TBB [49732522317132884993362828404080T]	CPU TBB [99465044634265769986725656808160T]	CPU TBB [19893008926853153997345113616320T]	CPU TBB [39786017853706307994680227232640T]	CPU TBB [79572035707412615989360454465280T]	CPU TBB [159144070014252311978720898980560T]	CPU TBB [318288140028464623957441797761120T]	CPU TBB [63657628005692924781488359562240T]	CPU TBB [12731525601185849956296711912480T]	CPU TBB [25463051202371899912593423824960T]	CPU TBB [50926102410327895624960T]	CPU TBB [1018481001012410327895624960T]	CPU TBB [203696200202410327895624960T]	CPU TBB [40739240040410327895624960T]	CPU TBB [814784800808210327895624960T]	CPU TBB [1629569601616420327895624960T]	CPU TBB [325913920323280327895624960T]	CPU TBB [651827840646560327895624960T]	CPU TBB [1303655681280640327895624960T]	CPU TBB [2607311362561280640327895624960T]	CPU TBB [521462264160327895624960T]	CPU TBB [104292432320640327895624960T]	CPU TBB [208584864641280640327895624960T]	CPU TBB [41616972929280640327895624960T]	CPU TBB [83233945858560327895624960T]	CPU TBB [166467891717120327895624960T]	CPU TBB [33293578343440327895624960T]	CPU TBB [66587156686880327895624960T]	CPU TBB [13317431373760327895624960T]	CPU TBB [26634862747520327895624960T]	CPU TBB [53269725450400327895624960T]	CPU TBB [106539450802000327895624960T]	CPU TBB [213078901604000327895624960T]	CPU TBB [426157803208000327895624960T]	CPU TBB [852315606416000327895624960T]	CPU TBB [170463120832000327895624960T]	CPU TBB [340926241664000327895624960T]	CPU TBB [681852483328000327895624960T]	CPU TBB [136370566656000327895624960T]	CPU TBB [272741133312000327895624960T]	CPU TBB [545482266624000327895624960T]	CPU TBB [1090964533288000327895624960T]	CPU TBB [2181929066576000327895624960T]	CPU TBB [4363858133152000327895624960T]

Patatrack02

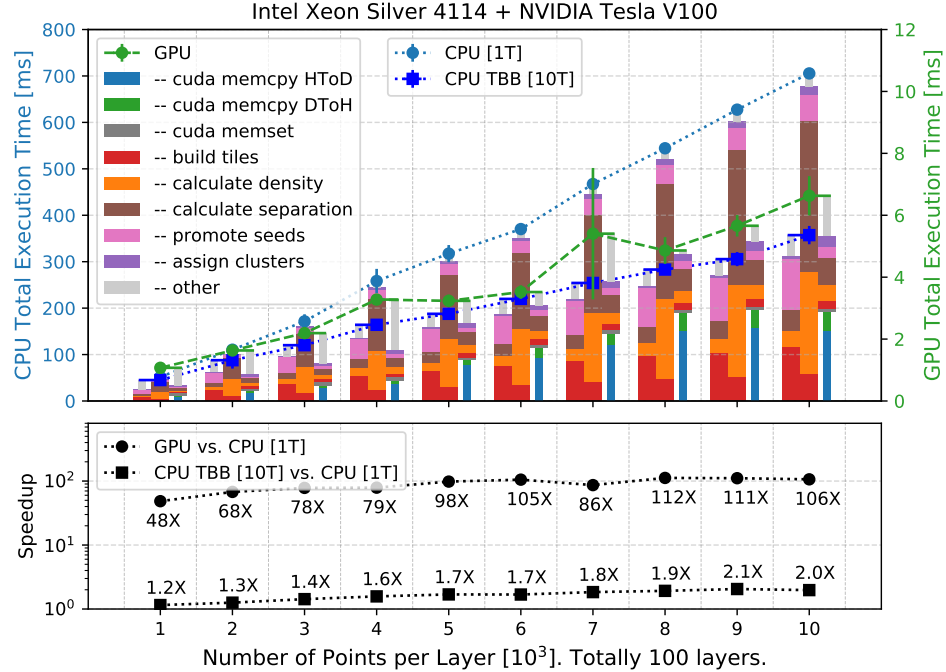


Figure C.3. Execution time of CLUE on CPU and GPU both scale linearly with number of input points, ranging from 10^5 to 10^6 in total on 100 layers. Mean and standard deviation are based on 200 trial runs. (10000 trial runs if GPU of Patatrack02) Intel Xeon Silver 4114 and NVIDIA Tesla V100

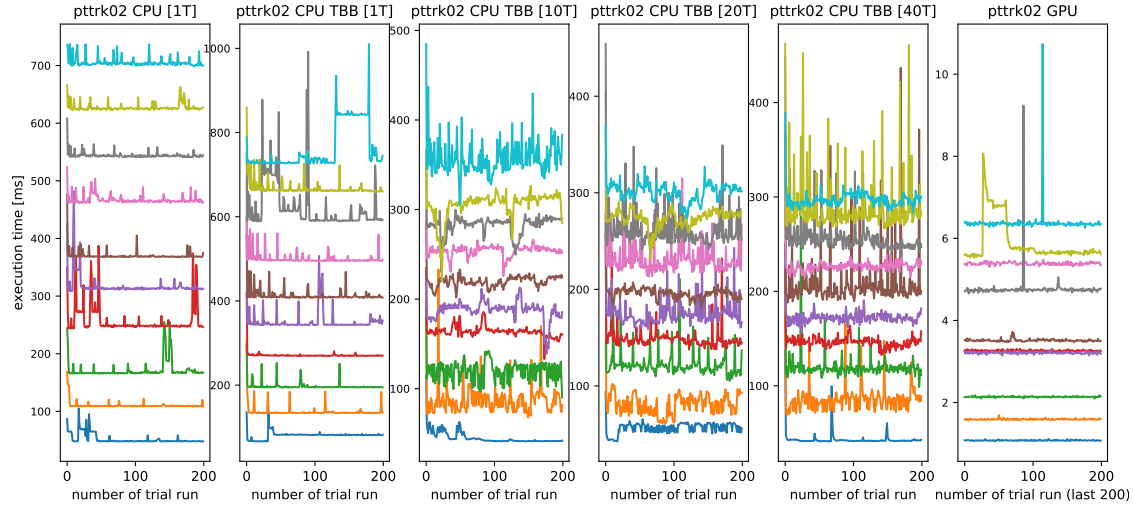


Figure C.4. Stability during 200 trial runs

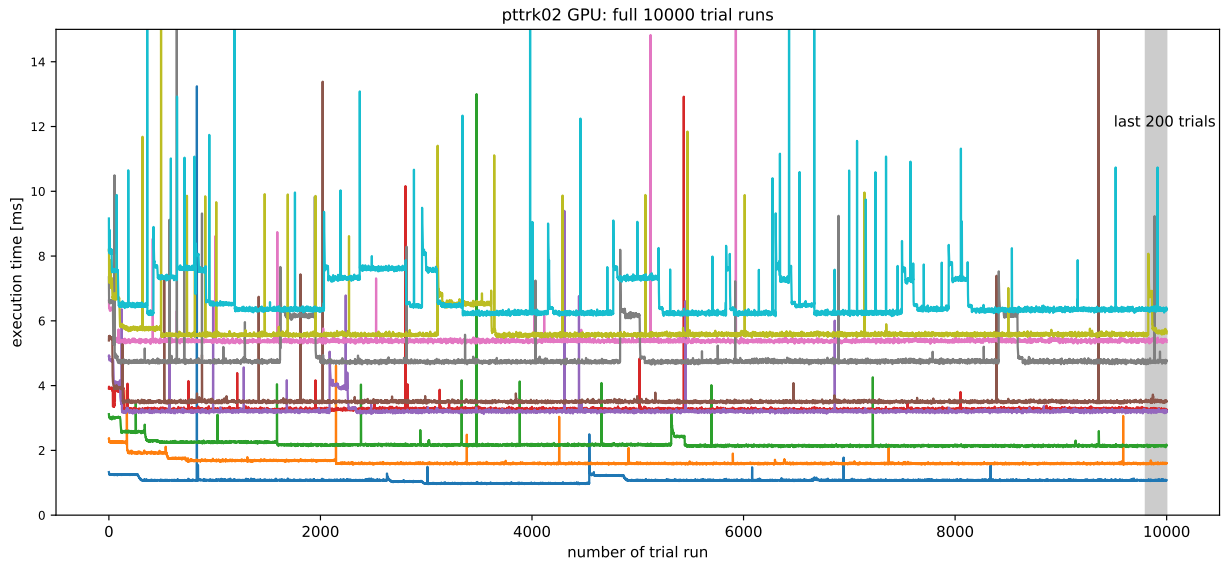


Figure C.5. On GPU of Patatrack02, 10000 trials are performed

CLUE Step	CPU [1T] (baseline)	CPU TBB [1T]	CPU TBB [10T]	CPU TBB [20T]	CPU TBB [40T]	CPU TBB [80T]	GPU
build fixed-grid spatial index	5.50 ± 0.82 ms	6.87 ± 0.98 ms (0.80x)	9.38 ± 1.70 ms (0.59x)	14.44 ± 2.05 ms (0.38x)	10.40 ± 2.64 ms (0.53x)	0.03 ms (18.74x)	
calculate local density	15.58 ± 2.53 ms	19.42 ± 2.27 ms (0.80x)	2.61 ± 0.65 ms (5.97x)	2.27 ± 0.40 ms (6.86x)	0.93 ± 0.46 ms (16.77x)	0.06 ms (278.53x)	
calculate nearest-higher and separation	19.92 ± 4.06 ms	24.70 ± 2.13 ms (0.81x)	3.11 ± 0.79 ms (6.40x)	2.70 ± 0.45 ms (7.38x)	1.09 ± 0.33 ms (18.33x)	0.08 ms (238.02x)	
decide seeds/outliers, register followers	4.20 ± 0.82 ms	4.98 ± 0.47 ms (0.84x)	9.15 ± 1.33 ms (0.46x)	13.25 ± 1.35 ms (0.32x)	9.65 ± 0.69 ms (0.43x)	0.02 ms (202.73x)	
expand clusters	0.47 ± 0.11 ms	2.43 ± 0.25 ms (0.19x)	0.43 ± 0.10 ms (1.10x)	0.36 ± 0.03 ms (1.30x)	0.22 ± 0.02 ms (2.11x)	0.05 ms (9.26x)	
cuda memory, memset	—	—	—	—	—	—	0.17 ms, 0.08 ms
other	6.31 ± 2.57 ms	22.32 ± 4.19 ms	20.38 ± 3.76 ms (1.15x)	23.61 ± 2.58 ms	20.84 ± 5.08 ms	0.58 ms	0.17 ms, 0.08 ms
TOTAL (1000 points per layer)	51.98 ± 8.94 ms	80.72 ± 8.43 ms (0.64x)	45.06 ± 7.25 ms (1.15x)	56.63 ± 5.69 ms (0.92x)	43.13 ± 8.20 ms (1.21x)	1.07 ± 0.14 ms (48.47x)	
CLUE Step	CPU [1T] (baseline)	CPU TBB [1T]	CPU TBB [10T]	CPU TBB [20T]	CPU TBB [40T]	CPU TBB [80T]	GPU
build fixed-grid spatial index	11.01 ± 0.67 ms	12.89 ± 0.99 ms (0.85x)	23.52 ± 4.06 ms (0.47x)	24.77 ± 4.16 ms (0.44x)	29.30 ± 6.06 ms (0.38x)	0.07 ms (167.61x)	
calculate local density	35.98 ± 1.77 ms	41.51 ± 2.90 ms (0.87x)	7.51 ± 1.30 ms (4.79x)	4.15 ± 0.65 ms (8.08x)	2.78 ± 2.26 ms (12.94x)	0.11 ms (318.84x)	
calculate nearest-higher and separation	45.00 ± 2.30 ms	50.14 ± 4.23 ms (0.90x)	8.83 ± 1.43 ms (5.09x)	5.01 ± 0.73 ms (8.98x)	3.22 ± 0.52 ms (13.97x)	0.14 ms (320.98x)	
decide seeds/outliers, register followers	8.39 ± 0.60 ms	9.00 ± 0.69 ms (0.93x)	21.76 ± 2.50 ms (0.39x)	22.51 ± 2.67 ms (0.37x)	23.95 ± 2.29 ms (0.35x)	0.06 ms (145.20x)	
expand clusters	1.63 ± 0.13 ms	3.61 ± 0.15 ms (0.45x)	0.88 ± 0.17 ms (1.86x)	0.61 ± 0.04 ms (2.08x)	0.46 ± 0.10 ms (3.53x)	0.08 ms (21.75x)	
cuda memory, memset	—	—	—	—	—	—	0.33 ms, 0.09 ms
other	8.45 ± 1.58 ms	19.80 ± 10.11 ms	25.36 ± 14.49 ms	24.11 ± 4.43 ms	26.29 ± 9.01 ms	0.76 ms	0.33 ms, 0.09 ms
TOTAL (2000 points per layer)	110.45 ± 6.22 ms	136.95 ± 14.78 ms (0.81x)	87.86 ± 18.09 ms (1.26x)	81.15 ± 10.80 ms (1.36x)	86.01 ± 13.72 ms (1.28x)	1.63 ± 0.12 ms (67.66x)	
CLUE Step	CPU [1T] (baseline)	CPU TBB [1T]	CPU TBB [10T]	CPU TBB [20T]	CPU TBB [40T]	CPU TBB [80T]	GPU
build fixed-grid spatial index	17.82 ± 1.88 ms	19.68 ± 1.08 ms (0.91x)	37.75 ± 4.77 ms (0.47x)	43.22 ± 5.46 ms (0.41x)	46.26 ± 6.08 ms (0.39x)	0.10 ms (184.57x)	
calculate local density	56.15 ± 4.39 ms	62.31 ± 3.40 ms (0.90x)	11.11 ± 1.42 ms (5.05x)	6.67 ± 1.11 ms (8.42x)	4.06 ± 1.01 ms (13.83x)	0.14 ms (415.21x)	
calculate nearest-higher and separation	71.16 ± 4.71 ms	76.14 ± 3.79 ms (0.93x)	13.11 ± 1.42 ms (5.43x)	7.81 ± 0.47 ms (9.15x)	4.90 ± 0.41 ms (14.53x)	0.21 ms (343.11x)	
decide seeds/outliers, register followers	12.63 ± 1.68 ms	13.50 ± 1.25 ms (0.94x)	32.54 ± 2.13 ms (0.39x)	34.89 ± 2.24 ms (0.36x)	35.23 ± 1.51 ms (0.30x)	0.09 ms (142.97x)	
expand clusters	2.47 ± 0.34 ms	5.06 ± 0.09 ms (0.49x)	1.19 ± 0.05 ms (2.07x)	0.81 ± 0.15 ms (3.07x)	0.73 ± 1.07 ms (3.37x)	0.08 ms (30.39x)	
cuda memory, memset	—	—	—	—	—	—	0.51 ms, 0.10 ms
other	11.27 ± 1.78 ms	20.76 ± 7.07 ms	24.48 ± 4.21 ms	29.02 ± 12.28 ms	28.85 ± 11.58 ms	0.97 ms	1.63 ms
TOTAL (3000 points per layer)	171.50 ± 15.29 ms	197.45 ± 10.59 ms (0.87x)	120.18 ± 11.08 ms (1.43x)	122.41 ± 15.98 ms (1.40x)	120.03 ± 16.28 ms (1.43x)	2.19 ± 0.17 ms (78.21x)	
CLUE Step	CPU [1T] (baseline)	CPU TBB [1T]	CPU TBB [10T]	CPU TBB [20T]	CPU TBB [40T]	CPU TBB [80T]	GPU
build fixed-grid spatial index	24.92 ± 3.97 ms	25.17 ± 0.82 ms (0.99x)	55.06 ± 2.77 ms (0.45x)	53.85 ± 3.04 ms (0.46x)	58.18 ± 2.91 ms (0.43x)	0.13 ms (195.20x)	
calculate local density	83.62 ± 9.08 ms	86.14 ± 2.17 ms (0.97x)	16.10 ± 0.67 ms (5.18x)	8.67 ± 1.54 ms (9.63x)	5.12 ± 0.35 ms (16.44x)	0.20 ms (413.61x)	
calculate nearest-higher and separation	111.91 ± 11.02 ms	111.97 ± 2.84 ms (1.00x)	19.50 ± 0.62 ms (5.74x)	10.75 ± 0.75 ms (10.11x)	6.90 ± 0.49 ms (16.23x)	0.30 ms (369.89x)	
decide seeds/outliers, register followers	18.50 ± 2.46 ms	19.26 ± 0.46 ms (0.96x)	44.05 ± 1.74 ms (0.42x)	44.40 ± 1.91 ms (0.42x)	45.22 ± 1.54 ms (0.41x)	0.12 ms (149.11x)	
expand clusters	4.97 ± 0.72 ms	7.72 ± 0.19 ms (0.64x)	1.90 ± 0.10 ms (2.61x)	1.15 ± 0.13 ms (4.31x)	1.05 ± 0.04 ms (4.71x)	0.12 ms (40.35x)	
cuda memory, memset	—	—	—	—	—	—	0.67 ms, 0.10 ms
other	14.49 ± 3.37 ms	20.97 ± 4.58 ms	27.48 ± 4.34 ms	30.24 ± 11.54 ms	30.11 ± 4.34 ms	0.97 ms	1.63 ms
TOTAL (4000 points per layer)	258.41 ± 26.14 ms	271.23 ± 10.62 ms (0.93x)	164.08 ± 7.61 ms (1.57x)	149.07 ± 13.18 ms (1.73x)	146.58 ± 7.21 ms (1.76x)	3.28 ± 0.14 ms (75.88x)	
CLUE Step	CPU [1T] (baseline)	CPU TBB [1T]	CPU TBB [10T]	CPU TBB [20T]	CPU TBB [40T]	CPU TBB [80T]	GPU
build fixed-grid spatial index	30.44 ± 2.04 ms	33.77 ± 3.01 ms (0.90x)	63.89 ± 5.23 ms (0.48x)	64.53 ± 5.32 ms (0.47x)	70.36 ± 3.08 ms (0.43x)	0.16 ms (191.80x)	
calculate local density	102.24 ± 4.98 ms	111.40 ± 7.26 ms (0.92x)	18.78 ± 0.79 ms (5.44x)	10.27 ± 1.32 ms (9.95x)	5.99 ± 0.29 ms (17.07x)	0.25 ms (411.02x)	
calculate nearest-higher and separation	139.52 ± 9.76 ms	145.92 ± 9.00 ms (0.96x)	22.96 ± 0.71 ms (6.08x)	12.75 ± 0.71 ms (10.94x)	8.35 ± 0.41 ms (16.71x)	0.41 ms (342.51x)	
decide seeds/outliers, register followers	23.19 ± 2.01 ms	25.69 ± 2.93 ms (0.90x)	51.20 ± 3.66 ms (0.45x)	53.37 ± 2.50 ms (0.43x)	54.61 ± 1.34 ms (0.42x)	0.15 ms (150.13x)	
expand clusters	5.89 ± 0.45 ms	10.10 ± 1.33 ms (0.58x)	2.28 ± 0.11 ms (2.58x)	1.48 ± 0.23 ms (3.97x)	1.36 ± 0.03 ms (4.34x)	0.14 ms (41.11x)	
cuda memory, memset	—	—	—	—	—	—	1.31 ms, 0.09 ms
other	16.09 ± 1.77 ms	24.58 ± 11.43 ms	28.63 ± 3.42 ms	33.26 ± 13.64 ms	31.55 ± 4.34 ms	0.72 ms	1.63 ms
TOTAL (5000 points per layer)	317.37 ± 18.46 ms	351.46 ± 25.59 ms (0.90x)	187.74 ± 10.64 ms (1.69x)	175.67 ± 16.69 ms (1.81x)	172.21 ± 6.79 ms (1.84x)	3.24 ± 0.20 ms (98.09x)	

References

- [1] C. Albajar et al. Studies of Intermediate Vector Boson Production and Decay in UA1 at the CERN Proton - Antiproton Collider. *Z. Phys. C*, 44:15–61, 1989.
- [2] JA Appel, P Bagnaia, M Banner, R Battiston, K Bernlöhr, K Borer, M Borghini, G Carboni, Vincenzo Cavasinni, P Cenci, et al. Measurement of w \pm and z0 properties at the cern pp collider. *Zeitschrift für Physik C Particles and Fields*, 30(1):1–22, 1986.
- [3] J. Alitti et al. A Measurement of electron - tau universality from decays of intermediate vector bosons at the CERN anti-p p collider. *Z. Phys. C*, 52:209–218, 1991.
- [4] J. Alitti et al. A Search for charged Higgs from top quark decay at the CERN $\bar{p}p$ collider. *Phys. Lett. B*, 280:137–145, 1992.
- [5] V.M. Abazov et al. Combination of CDF and D0 Results on W Boson Mass and Width. *Phys. Rev. D*, 70:092008, 2004.
- [6] F. Abe et al. A Measurement of $\sigma B(W \rightarrow e\nu)$ and $\sigma B(Z^0 \rightarrow e^+e^-)$ in $p\bar{p}$ collisions at $\sqrt{s} = 1800$ GeV. *Phys. Rev. D*, 44:29–52, 1991.
- [7] F. Abe et al. A Measurement of the production and muonic decay rate of W and Z bosons in $p\bar{p}$ collisions at $\sqrt{s} = 1.8$ TeV. *Phys. Rev. Lett.*, 69:28–32, 1992.
- [8] F. Abe et al. Measurement of the ratio $\sigma B(W \rightarrow \nu_\tau)/\sigma B(W \rightarrow e\nu)$, in $p\bar{p}$ collisions at $\sqrt{s} = 1.8$ TeV. *Phys. Rev. Lett.*, 68:3398–3402, 1992.
- [9] B. Abbott et al. Extraction of the width of the W boson from measurements of $\sigma(p\bar{p} \rightarrow W + X) \times B(W \rightarrow e\nu)$ and $\sigma(p\bar{p} \rightarrow Z + X) \times B(Z \rightarrow ee)$ and their ratio. *Phys. Rev. D*, 61:072001, 2000.
- [10] S. Abachi et al. W and Z boson production in $p\bar{p}$ collisions at $\sqrt{s} = 1.8$ -TeV. *Phys. Rev. Lett.*, 75:1456–1461, 1995.
- [11] B. Abbott et al. A measurement of the $W \rightarrow \tau\nu$ production cross section in $p\bar{p}$ collisions at $\sqrt{s} = 1.8$ TeV. *Phys. Rev. Lett.*, 84:5710–5715, 2000.
- [12] A. Heister et al. Measurement of W-pair production in e+ e- collisions at centre-of-mass energies from 183-GeV to 209-GeV. *Eur. Phys. J. C*, 38:147–160, 2004.
- [13] J. Abdallah et al. Measurement of the W pair production cross-section and W branching ratios in e+ e- collisions at $s^{**}(1/2) = 161$ -GeV to 209-GeV. *Eur. Phys. J. C*, 34:127–144, 2004.
- [14] G. Abbiendi et al. Measurement of the e+ e- \rightarrow W+ W- cross section and W decay branching fractions at LEP. *Eur. Phys. J. C*, 52:767–785, 2007.
- [15] P. Achard et al. Measurement of the cross section of W-boson pair production at LEP. *Phys. Lett. B*, 600:22–40, 2004.
- [16] S. Schael et al. Electroweak Measurements in Electron-Positron Collisions at W-Boson-Pair Energies at LEP. *Phys. Rept.*, 532:119–244, 2013.
- [17] Ansgar Denner. Techniques for calculation of electroweak radiative corrections at the one loop level and results for W physics at LEP-200. *Fortsch. Phys.*, 41:307, 1993.

- [18] Bernd A. Kniehl, Fantina Madricardo, and Matthias Steinhauser. Gauge independent W boson partial decay widths. *Phys. Rev. D*, 62:073010, 2000.
- [19] David d'Enterria and Matej Srebre. α_s and V_{cs} determination, and CKM unitarity test, from W decays at NNLO. *Phys. Lett. B*, 763:465, 2016.
- [20] Serguei Chatrchyan et al. Identification of b-Quark Jets with the CMS Experiment. *JINST*, 8:P04013, 2013.
- [21] A.M. Sirunyan et al. Identification of heavy-flavour jets with the CMS detector in pp collisions at 13 TeV. *JINST*, 13(05):P05011, 2018.
- [22] Emil Bols, Jan Kieseler, Mauro Verzetti, Markus Stoye, and Anna Stakia. Jet Flavour Classification Using DeepJet. *JINST*, 15(12):P12012, 2020.
- [23] Georges Aad et al. Test of the universality of τ and μ lepton couplings in W-boson decays from $t\bar{t}$ events with the ATLAS detector. 7 2020.
- [24] Serguei Chatrchyan et al. Performance of tau-lepton reconstruction and identification in CMS. *JINST*, 7:P01001, 2012.
- [25] Vardan Khachatryan et al. Reconstruction and identification of τ lepton decays to hadrons and ν at CMS. *JINST*, 11(01):P01019, 2016.
- [26] A.M. Sirunyan et al. Performance of reconstruction and identification of τ leptons decaying to hadrons and ν_τ in pp collisions at $\sqrt{s} = 13$ TeV. *JINST*, 13(10):P10005, 2018.
- [27] Particle Data Group, P A Zyla, R M Barnett, J Beringer, O Dahl, D A Dwyer, D E Groom, C J Lin, K S Lugovsky, E Pianori, D J Robinson, C G Wohl, W M Yao, K Agashe, G Aielli, B C Allanach, C Amsler, M Antonelli, E C Aschenauer, D M Asner, H Baer, Sw Banerjee, L Baudis, C W Bauer, J J Beatty, V I Belousov, S Bethke, A Bettini, O Biebel, K M Black, E Blucher, O Buchmuller, V Burkert, M A Bychkov, R N Cahn, M Carena, A Ceccucci, A Cerri, D Chakraborty, R Sekhar Chivukula, G Cowan, G D'Ambrosio, T Damour, D de Florian, A de Gouv  a, T De-Grand, P de Jong, G Dissertori, B A Dobrescu, M D'Onofrio, M Doser, M Drees, H K Dreiner, P Eerola, U Egede, S Eidelman, J Ellis, J Erler, V V Ezhela, W Fetscher, B D Fields, B Foster, A Freitas, H Gallagher, L Garren, H J Gerber, G Gerbier, T Gershon, Y Gershtein, T Gherghetta, A A Godizov, M C Gonzalez-Garcia, M Goodman, C Grab, A V Gritsan, C Grojean, M Grunewald, A Gurtu, T Gutsche, H E Haber, C Hanhart, S Hashimoto, Y Hayato, A Hebecker, S Heinemeyer, B Heltsley, J J Hern  ndez-Rey, K Hikasa, J Hisano, A H  cker, J Holder, A Holtkamp, J Huston, T Hyodo, K F Johnson, M Kado, M Karliner, U F Katz, M Kenzie, V A Khoze, S R Klein, E Klemp, R V Kowalewski, F Krauss, M Kreps, B Krusche, Y Kwon, O Lahav, J Laiho, L P Lelloch, J Lesgourgues, A R Liddle, Z Ligeti, C Lippmann, T M Liss, L Littenberg, C Lourenco, S B Lugovsky, A Lusiani, Y Makida, F Maltoni, T Mannel, A V Manohar, W J Marciano, A Masoni, J Matthews, U G Meissner, M Mikhasenko, D J Miller, D Milstead, R E Mitchell, K M  nig, P Molaro, F Moortgat, M Moskovic, K Nakamura, M Narain, P Nason, S Navas, M Neubert, P Nevski, Y Nir, K A Olive, C Patrignani, J A Peacock, S T Petcov, V A Petrov, A Pich, A Piepke, A Pomarol, S Profumo, A Quadt, K Rabbertz, J Rademacker, G Raffelt, H Ramani, M Ramsey-Musolf, B N Ratcliff, P Richardson, A Ringwald, S Roesler, S Rolli, A Romanouk, L J Rosenberg, J L Rosner, G Rybka, M Ryskin, R A Ryutin, Y Sakai, G P Salam, S Sarkar, F Sauli, O Schneider, K Scholberg, A J Schwartz, J Schwiening, D Scott, V Sharma, S R Sharpe,

- T Shutt, M Silari, T Sjöstrand, P Skands, T Skwarnicki, G F Smoot, A Soffer, M S Sozzi, S Spanier, C Spiering, A Stahl, S L Stone, Y Sumino, T Sumiyoshi, M J Syphers, F Takahashi, M Tanabashi, J Tanaka, M Taševský, K Terashi, J Terning, U Thoma, R S Thorne, L Tiator, M Titov, N P Tkachenko, D R Tovey, K Trabelsi, P Urquijo, G Valencia, R Van de Water, N Varelas, G Venanzoni, L Verde, M G Vincter, P Vogel, W Vogelsang, A Vogt, V Vorobyev, S P Wakely, W Walkowiak, C W Walter, D Wands, M O Wascko, D H Weinberg, E J Weinberg, M White, L R Wiencke, S Willocq, C L Woody, R L Workman, M Yokoyama, R Yoshida, G Zanderighi, G P Zeller, O V Zenin, R Y Zhu, S L Zhu, F Zimmermann, J Anderson, T Basaglia, V S Lugovsky, P Schaffner, and W Zheng. Review of Particle Physics. *Progress of Theoretical and Experimental Physics*, 2020(8), 08 2020. 083C01.
- [28] G. Apollinari, I. Béjar Alonso, O. Brüning, P. Fessia, M. Lamont, L. Rossi, and L. Tavian. *High-Luminosity Large Hadron Collider (HL-LHC): Technical Design Report V. 0.1*. CERN Yellow Reports: Monographs. CERN, Geneva, 2017.
 - [29] D. Contardo, M. Klute, J. Mans, L. Silvestris, and J. Butler. Technical proposal for the phase-ii upgrade of the cms detector. 2015.
 - [30] Armen Tumasyan et al. The Phase-2 Upgrade of the CMS Tracker. 6 2017.
 - [31] CMS Collaboration. The Phase-2 Upgrade of the CMS Endcap Calorimeter. Technical Report CERN-LHCC-2017-023. CMS-TDR-019, CERN, Geneva, Nov 2017.
 - [32] G. Arnison, A. Astbury, B. Aubert, C. Bacci, G. Bauer, A. Bézaguet, R. Böck, T.J.V. Bowcock, M. Calvetti, T. Carroll, P. Catz, P. Cennini, S. Centro, F. Ceradini, S. Cittolin, D. Cline, C. Cochet, J. Colas, M. Corden, D. Dallman, M. DeBeer, M. Della Negra, M. Demoulin, D. Denegri, A. Di Ciaccio, D. DiBitonto, L. Dobrzynski, J.D. Dowell, M. Edwards, K. Eggert, E. Eisenhandler, N. Ellis, P. Erhard, H. Faissner, G. Fontaine, R. Frey, R. Frühwirth, J. Garvey, S. Geer, C. Ghesquière, P. Ghez, K.L. Giboni, W.R. Gibson, Y. Giraud-Héraud, A. Givernaud, A. Gonidec, G. Grayer, P. Gutierrez, T. Hansl-Kozanecka, W.J. Haynes, L.O. Hertzberger, C. Hodges, D. Hoffmann, H. Hoffmann, D.J. Holthuizen, R.J. Homer, A. Honma, W. Jank, G. Jorat, P.I.P. Kalmus, V. Karimäki, R. Keeler, I. Kenyon, A. Kernan, R. Kinnunen, H. Kowalski, W. Kozanecki, D. Krym, F. Lacava, J.-P. Laugier, J.-P. Lees, H. Lehmann, K. Leuchs, A. Lévêque, E. Linglin, E. Locci, M. Loret, J.-J. Malosse, T. Markiewicz, G. Maurin, T. McMahon, J.-P. Mendiburu, M.-N. Minard, M. Moricca, H. Muirhead, F. Muller, A.K. Nandi, L. Naumann, A. Norton, A. Orkin-Lecourtois, L. Paoluzi, G. Petrucci, G. Piano Mortari, M. Pimiä, A. Placci, E. Radermacher, J. Ransdell, H. Reithler, J.-P. Revol, J. Rich, M. Rijssenbeek, C. Roberts, J. Rohlf, P. Rossi, C. Rubbia, B. Sadoulet, G. Sajot, G. Salvi, J. Salvini, J. Sass, A. Saudraix, A. Savoy-Navarro, D. Schinzel, W. Scott, T.P. Shah, M. Spiro, J. Strauss, K. Sumorok, F. Szoncso, D. Smith, C. Tao, G. Thompson, J. Timmer, E. Tscheslog, J. Tuominiemi, S. Van der Meer, J.-P. Vialle, J. Vrana, V. Vuillemin, H.D. Wahl, P. Watkins, J. Wilson, Y.G. Xie, M. Yvert, and E. Zurfluh. Experimental observation of isolated large transverse energy electrons with associated missing energy at $s=540$ gev. *Physics Letters B*, 122(1):103–116, 1983.
 - [33] M. Banner, R. Battiston, Ph. Bloch, F. Bonaudi, K. Borer, M. Borghini, J.-C. Chollet, A.G. Clark, C. Conta, P. Darriulat, L. Di Lella, J. Dines-Hansen, P.-A. Dorsaz, L. Fayard, M. Fraternali, D. Froidevaux, J.-M. Gaillard, O. Gildemeister, V.G. Goggi, H. Grote, B. Hahn, H. Hänni, J.R. Hansen, P. Hansen, T. Himel, V. Hungerbühler,

- P. Jenni, O. Kofoed-Hansen, E. Lançon, M. Livan, S. Loucas, B. Madsen, P. Mani, B. Mansoulie, G.C. Mantovani, L. Mapelli, B. Merkel, M. Mermikides, R. Møllerud, B. Nilsson, C. Onions, G. Parrou, F. Pastore, H. Plothow-Besch, M. Polverel, J.-P. Repellin, A. Rothenberg, A. Roussarie, G. Sauvage, J. Schacher, J.L. Siegrist, H.M. Steiner, G. Stimpfl, F. Stocker, J. Teiger, V. Vercesi, A. Weidberg, H. Zaccone, and W. Zeller. Observation of single isolated electrons of high transverse momentum in events with missing transverse energy at the cern pp collider. *Physics Letters B*, 122(5):476–485, 1983.
- [34] Morad Aaboud et al. Precision measurement and interpretation of inclusive W^+ , W^- and Z/γ^* production cross sections with the ATLAS detector. *Eur. Phys. J. C*, 77(6):367, 2017.
- [35] Roel Aaij et al. Measurement of forward $W \rightarrow e\nu$ production in pp collisions at $\sqrt{s} = 8$ TeV. *JHEP*, 10:030, 2016.
- [36] Roel Aaij et al. Measurement of forward W and Z boson production in pp collisions at $\sqrt{s} = 8$ TeV. *JHEP*, 01:155, 2016.
- [37] Simone Bifani, Sébastien Descotes-Genon, Antonio Romero Vidal, and Marie-Hélène Schune. Review of Lepton Universality tests in B decays. *J. Phys. G*, 46(2):023001, 2019.
- [38] Vincenzo Cirigliano and Ignasi Rosell. Two-loop effective theory analysis of pi (K) —> e anti-nu/e [gamma] branching ratios. *Phys. Rev. Lett.*, 99:231801, 2007.
- [39] Toshio Numao. Precise tests of $e - \mu$ universality. *Mod. Phys. Lett. A*, 7:3357–3364, 1992.
- [40] D.I. Britton et al. Measurement of the $\pi^+ \rightarrow e^+$ neutrino branching ratio. *Phys. Rev. Lett.*, 68:3000–3003, 1992.
- [41] A. Aguilar-Arevalo et al. Improved Measurement of the $\pi \rightarrow e\nu$ Branching Ratio. *Phys. Rev. Lett.*, 115(7):071801, 2015.
- [42] G. Czapek et al. Branching ratio for the rare pion decay into positron and neutrino. *Phys. Rev. Lett.*, 70:17–20, 1993.
- [43] C. Lazzeroni et al. Precision Measurement of the Ratio of the Charged Kaon Leptonic Decay Rates. *Phys. Lett. B*, 719:326–336, 2013.
- [44] F. Ambrosino et al. Precise measurement of $\Gamma(K \rightarrow e\nu(\gamma))/\Gamma(K \rightarrow \mu\nu(\gamma))$ and study of $K \rightarrow e\nu\gamma$. *Eur. Phys. J. C*, 64:627–636, 2009. [Erratum: Eur.Phys.J. 65, 703 (2010)].
- [45] Bogdan A. Dobrescu and Andreas S. Kronfeld. Accumulating evidence for nonstandard leptonic decays of D_s mesons. *Phys. Rev. Lett.*, 100:241802, 2008.
- [46] Y. Amhis et al. Averages of b -hadron, c -hadron, and τ -lepton properties as of summer 2016. *Eur. Phys. J. C*, 77(12):895, 2017.
- [47] J.P. Lees et al. Evidence for an excess of $\bar{B} \rightarrow D^{(*)}\tau^-\bar{\nu}_\tau$ decays. *Phys. Rev. Lett.*, 109:101802, 2012.
- [48] J.P. Lees et al. Measurement of an Excess of $\bar{B} \rightarrow D^{(*)}\tau^-\bar{\nu}_\tau$ Decays and Implications for Charged Higgs Bosons. *Phys. Rev. D*, 88(7):072012, 2013.
- [49] M. Huschle et al. Measurement of the branching ratio of $\bar{B} \rightarrow D^{(*)}\tau^-\bar{\nu}_\tau$ relative to $\bar{B} \rightarrow D^{(*)}\ell^-\bar{\nu}_\ell$ decays with hadronic tagging at Belle. *Phys. Rev. D*, 92(7):072014, 2015.

- [50] Y. Sato et al. Measurement of the branching ratio of $\bar{B}^0 \rightarrow D^{*+}\tau^-\bar{\nu}_\tau$ relative to $\bar{B}^0 \rightarrow D^{*+}\ell^-\bar{\nu}_\ell$ decays with a semileptonic tagging method. *Phys. Rev. D*, 94(7):072007, 2016.
- [51] S. Hirose et al. Measurement of the τ lepton polarization and $R(D^*)$ in the decay $\bar{B} \rightarrow D^*\tau^-\bar{\nu}_\tau$. *Phys. Rev. Lett.*, 118(21):211801, 2017.
- [52] Roel Aaij et al. Measurement of the ratio of branching fractions $\mathcal{B}(\bar{B}^0 \rightarrow D^{*+}\tau^-\bar{\nu}_\tau)/\mathcal{B}(\bar{B}^0 \rightarrow D^{*+}\mu^-\bar{\nu}_\mu)$. *Phys. Rev. Lett.*, 115(11):111803, 2015. [Erratum: *Phys. Rev. Lett.* 115, 159901 (2015)].
- [53] R. Aaij et al. Measurement of the ratio of the $B^0 \rightarrow D^{*-}\tau^+\nu_\tau$ and $B^0 \rightarrow D^{*-}\mu^+\nu_\mu$ branching fractions using three-prong τ -lepton decays. *Phys. Rev. Lett.*, 120(17):171802, 2018.
- [54] R. Aaij et al. Test of Lepton Flavor Universality by the measurement of the $B^0 \rightarrow D^{*-}\tau^+\nu_\tau$ branching fraction using three-prong τ decays. *Phys. Rev. D*, 97(7):072013, 2018.
- [55] Yasmine Sara Amhis et al. Averages of b -hadron, c -hadron, and τ -lepton properties as of 2018. 9 2019.
- [56] Antonio Pich. Precision Tau Physics. *Prog. Part. Nucl. Phys.*, 75:41–85, 2014.
- [57] A. Zupanc et al. Measurements of branching fractions of leptonic and hadronic D_s^+ meson decays and extraction of the D_s^+ meson decay constant. *JHEP*, 09:139, 2013.
- [58] J.P. Alexander et al. Measurement of $B(D_s^+ \rightarrow e^+\nu)$ and the Decay Constant $f_{D_s^+}$ From 600 $/pb^{-1}$ of e^\pm Annihilation Data Near 4170 MeV. *Phys. Rev. D*, 79:052001, 2009.
- [59] P.U.E. Onyisi et al. Improved Measurement of Absolute Branching Fraction of $D(s) + \rightarrow \text{tau}^+ \nu(\text{tau})$. *Phys. Rev. D*, 79:052002, 2009.
- [60] P. Naik et al. Measurement of the Pseudoscalar Decay Constant $f(D(s))$ Using $D(s) + \rightarrow \text{tau}^+ \nu, \text{tau}^+ \rightarrow \rho^+ \text{anti-}\nu$ Decays. *Phys. Rev. D*, 80:112004, 2009.
- [61] P. del Amo Sanchez et al. Measurement of the Absolute Branching Fractions for $D_s^- \rightarrow \ell^-\bar{\nu}_\ell$ and Extraction of the Decay Constant $f_{D_s^-}$. *Phys. Rev. D*, 82:091103, 2010. [Erratum: *Phys. Rev. D* 91, 019901 (2015)].
- [62] Medina Ablikim et al. Measurement of the $D_s^+ \rightarrow \ell^+\nu_\ell$ branching fractions and the decay constant $f_{D_s^+}$. *Phys. Rev. D*, 94(7):072004, 2016.
- [63] Medina Ablikim et al. Determination of the pseudoscalar decay constant $f_{D_s^+}$ via $D_s^+ \rightarrow \mu^+\nu_\mu$. *Phys. Rev. Lett.*, 122(7):071802, 2019.
- [64] D. Besson et al. Improved measurements of D meson semileptonic decays to π and K mesons. *Phys. Rev. D*, 80:032005, 2009.
- [65] L. Widhalm et al. Measurement of $D0 \rightarrow \pi l \nu$ ($Kl \nu$) Form Factors and Absolute Branching Fractions. *Phys. Rev. Lett.*, 97:061804, 2006.
- [66] Bernard Aubert et al. Measurement of the hadronic form-factor in $D^0 \rightarrow K^-e^+\nu_e$. *Phys. Rev. D*, 76:052005, 2007.
- [67] M. Ablikim et al. Study of Dynamics of $D^0 \rightarrow K^-e^+\nu_e$ and $D^0 \rightarrow \pi^-e^+\nu_e$ Decays. *Phys. Rev. D*, 92(7):072012, 2015.
- [68] Medina Ablikim et al. Study of the $D^0 \rightarrow K^-\mu^+\nu_\mu$ dynamics and test of lepton flavor universality with $D^0 \rightarrow K^-\ell^+\nu_\ell$ decays. *Phys. Rev. Lett.*, 122(1):011804, 2019.
- [69] P. Abreu et al. Measurement of $|V(\text{cs})|$ using W decays at LEP-2. *Phys. Lett. B*, 439:209–224, 1998.

- [70] Serguei Chatrchyan et al. Observation of a New Boson at a Mass of 125 GeV with the CMS Experiment at the LHC. *Phys. Lett. B*, 716:30–61, 2012.
- [71] Georges Aad et al. Observation of a new particle in the search for the Standard Model Higgs boson with the ATLAS detector at the LHC. *Phys. Lett. B*, 716:1–29, 2012.
- [72] B. Andersson, G. Gustafson, G. Ingelman, and T. Sjöstrand. Parton fragmentation and string dynamics. *Physics Reports*, 97(2):31–145, 1983.
- [73] Albert M Sirunyan et al. Search for a W' boson decaying to a τ lepton and a neutrino in proton-proton collisions at $\sqrt{s} = 13$ TeV. *Phys. Lett. B*, 792:107–131, 2019.
- [74] Vardan Khachatryan et al. Search for W' decaying to tau lepton and neutrino in proton-proton collisions at $\sqrt(s) = 8$ TeV. *Phys. Lett. B*, 755:196–216, 2016.
- [75] Morad Aaboud et al. Search for High-Mass Resonances Decaying to $\tau\nu$ in pp Collisions at 13 TeV with the ATLAS Detector. *Phys. Rev. Lett.*, 120(16):161802, 2018.
- [76] Albert M Sirunyan et al. Search for high-mass resonances in final states with a lepton and missing transverse momentum at $\sqrt{s} = 13$ TeV. *JHEP*, 06:128, 2018.
- [77] Morad Aaboud et al. Search for a new heavy gauge boson resonance decaying into a lepton and missing transverse momentum in 36 fb^{-1} of pp collisions at $\sqrt{s} = 13$ TeV with the ATLAS experiment. *Eur. Phys. J. C*, 78(5):401, 2018.
- [78] Albert M Sirunyan et al. Search for a heavy resonance decaying into a Z boson and a vector boson in the $\nu\bar{\nu}q\bar{q}$ final state. *JHEP*, 07:075, 2018.
- [79] Morad Aaboud et al. Search for diboson resonances with boson-tagged jets in pp collisions at $\sqrt{s} = 13$ TeV with the ATLAS detector. *Phys. Lett. B*, 777:91–113, 2018.
- [80] Albert M Sirunyan et al. Search for dijet resonances in proton–proton collisions at $\sqrt{s} = 13$ TeV and constraints on dark matter and other models. *Phys. Lett. B*, 769:520–542, 2017. [Erratum: *Phys.Lett.B* 772, 882–883 (2017)].
- [81] Morad Aaboud et al. Search for new phenomena in dijet events using 37 fb^{-1} of pp collision data collected at $\sqrt{s} = 13$ TeV with the ATLAS detector. *Phys. Rev. D*, 96(5):052004, 2017.
- [82] Albert M Sirunyan et al. Search for heavy resonances decaying to a top quark and a bottom quark in the lepton+jets final state in proton–proton collisions at 13 TeV. *Phys. Lett. B*, 777:39–63, 2018.
- [83] Morad Aaboud et al. Search for $W' \rightarrow tb$ decays in the hadronic final state using pp collisions at $\sqrt{s} = 13$ TeV with the ATLAS detector. *Phys. Lett. B*, 781:327–348, 2018.
- [84] Ken Hsieh, Kai Schmitz, Jiang-Hao Yu, and C.-P. Yuan. Global Analysis of General $SU(2) \times SU(2) \times U(1)$ Models with Precision Data. *Phys. Rev. D*, 82:035011, 2010.
- [85] R. N. Mohapatra and J. C. Pati. "natural" left-right symmetry. *Phys. Rev. D*, 11:2558–2561, May 1975.
- [86] R.S. Chivukula, Elizabeth H. Simmons, and J. Terning. Limits on the ununified standard model. *Phys. Lett. B*, 346:284–290, 1995.
- [87] Howard Georgi, Elizabeth E. Jenkins, and Elizabeth H. Simmons. The un-unified standard model. *Nuclear Physics B*, 331(3):541 – 555, 1990.
- [88] Xiao-yuan Li and Ernest Ma. Gauge model of generation nonuniversality. *Phys. Rev. Lett.*, 47:1788–1791, Dec 1981.
- [89] D.J. Muller and S. Nandi. A separate $su(2)$ for the third family: Topflavor. *Nuclear Physics B - Proceedings Supplements*, 52(1):192 – 194, 1997.

- [90] Cheng-Wei Chiang, N. G. Deshpande, Xiao-Gang He, and J. Jiang. Family $su(2)_l \times su(2)_h \times u(1)$ model. *Phys. Rev. D*, 81:015006, Jan 2010.
- [91] Lisa Edelhäuser and Alexander Knochel. Observing nonstandard W' and Z' through the third generation and Higgs lens. 8 2014.
- [92] Yeong Gyun Kim and Kang Young Lee. Early lhc bound on the w boson mass in the non-universal gauge interaction model. *Physics Letters B*, 706(4):367 – 370, 2012.
- [93] G.C. Branco, P.M. Ferreira, L. Lavoura, M.N. Rebelo, Marc Sher, and João P. Silva. Theory and phenomenology of two-higgs-doublet models. *Physics Reports*, 516(1):1 – 102, 2012. Theory and phenomenology of two-Higgs-doublet models.
- [94] H.E. Haber and G.L. Kane. The search for supersymmetry: Probing physics beyond the standard model. *Physics Reports*, 117(2):75 – 263, 1985.
- [95] Jihn E. Kim. Light pseudoscalars, particle physics and cosmology. *Physics Reports*, 150(1):1 – 177, 1987.
- [96] R. D. Peccei and Helen R. Quinn. CP conservation in the presence of pseudoparticles. *Phys. Rev. Lett.*, 38:1440–1443, Jun 1977.
- [97] Mark Trodden. Electroweak baryogenesis: A Brief review. In *33rd Rencontres de Moriond: Electroweak Interactions and Unified Theories*, pages 471–480, 1998.
- [98] Neil Turok and John Zadrozny. Electroweak baryogenesis in the two-doublet model. *Nuclear Physics B*, 358(2):471 – 493, 1991.
- [99] Michael Joyce, Tomislav Prokopec, and Neil Turok. Nonlocal electroweak baryogenesis. Part 2: The Classical regime. *Phys. Rev. D*, 53:2958–2980, 1996.
- [100] G. Abbiendi et al. Search for Charged Higgs bosons: Combined Results Using LEP Data. *Eur. Phys. J. C*, 73:2463, 2013.
- [101] Vardan Khachatryan et al. Search for a charged Higgs boson in pp collisions at $\sqrt{s} = 8$ TeV. *JHEP*, 11:018, 2015.
- [102] Georges Aad et al. Search for charged Higgs bosons decaying via $H^\pm \rightarrow \tau^\pm \nu$ in fully hadronic final states using pp collision data at $\sqrt{s} = 8$ TeV with the ATLAS detector. *JHEP*, 03:088, 2015.
- [103] Morad Aaboud et al. Search for charged Higgs bosons decaying via $H^\pm \rightarrow \tau^\pm \nu_\tau$ in the $\tau+$ jets and $\tau+$ lepton final states with 36 fb^{-1} of pp collision data recorded at $\sqrt{s} = 13$ TeV with the ATLAS experiment. *JHEP*, 09:139, 2018.
- [104] V. Barger, J. L. Hewett, and R. J. N. Phillips. New constraints on the charged higgs sector in two-higgs-doublet models. *Phys. Rev. D*, 41:3421–3441, Jun 1990.
- [105] S. Mohammad Moosavi Nejad, S. Abbaspour, and R. Farashahian. Interference effects for the top quark decays $t \rightarrow b + W^+/H^+(\rightarrow \tau^+ \nu_\tau)$. *Phys. Rev. D*, 99:095012, May 2019.
- [106] David d'Enterria and Villads Jacobsen. Improved strong coupling determinations from hadronic decays of electroweak bosons at N^3LO accuracy. 5 2020.
- [107] Lyndon Evans and Philip Bryant. LHC Machine. *JINST*, 3:S08001, 2008.
- [108] Stephen Myers. The LEP collider, from design to approval and commissioning. 10 1991.
- [109] S. Chatrchyan et al. The CMS Experiment at the CERN LHC. *JINST*, 3:S08004, 2008.
- [110] G. Aad et al. The ATLAS Experiment at the CERN Large Hadron Collider. *JINST*, 3:S08003, 2008.

- [111] Jr. Alves, A.Augusto et al. The LHCb Detector at the LHC. *JINST*, 3:S08005, 2008.
- [112] K. Aamodt et al. The ALICE experiment at the CERN LHC. *JINST*, 3:S08002, 2008.
- [113] CERN. Facts and figures about the lhc.
- [114] LHC Design Report. 3. The LHC injector chain. 12 2004.
- [115] The CMS Collaboration. Public cms luminosity information.
- [116] Georges Aad et al. Observation of a new particle in the search for the Standard Model Higgs boson with the ATLAS detector at the LHC. *Phys. Lett. B*, 716:1–29, 2012.
- [117] Serguei Chatrchyan et al. Observation of a New Boson at a Mass of 125 GeV with the CMS Experiment at the LHC. *Phys. Lett. B*, 716:30–61, 2012.
- [118] Michael Benedikt, Alain Blondel, Patrick Janot, Michelangelo Mangano, and Frank Zimmermann. Future Circular Colliders succeeding the LHC. *Nature Phys.*, 16(4):402–407. 6 p, 2020.
- [119] G.L. Bayatian et al. CMS technical design report, volume II: Physics performance. *J. Phys. G*, 34(6):995–1579, 2007.
- [120] The CMS Collaboration. About cms detector.
- [121] G. Acquistapace et al. CMS, the magnet project: Technical design report. 5 1997.
- [122] V. Karimäki. The CMS tracker system project: Technical Design Report. 1997.
- [123] The CMS Collaboration. Performance of the cms muon detectors in early 2016 collision runs.
- [124] The CMS electromagnetic calorimeter project: Technical Design Report. 1997.
- [125] The CMS hadron calorimeter project: Technical Design Report. 1997.
- [126] The CMS muon project: Technical Design Report. 1997.
- [127] Vardan Khachatryan et al. The CMS trigger system. *JINST*, 12(01):P01020, 2017.
- [128] Daniele Trocino. The CMS High Level Trigger. *J. Phys. Conf. Ser.*, 513:012036, 2014.
- [129] A.M. Sirunyan et al. Particle-flow reconstruction and global event description with the CMS detector. *JINST*, 12(10):P10003, 2017.
- [130] R. Fruhwirth. Application of Kalman filtering to track and vertex fitting. *Nucl. Instrum. Meth. A*, 262:444–450, 1987.
- [131] G. L. Bayatian et al. CMS Physics: Technical Design Report Volume 1: Detector Performance and Software. 2006.
- [132] Wolfgang Adam, R. Frühwirth, Are Strandlie, and T. Todor. Reconstruction of Electrons with the Gaussian-Sum Filter in the CMS Tracker at the LHC. 1 2005.
- [133] Matteo Cacciari, Gavin P. Salam, and Gregory Soyez. The anti- k_t jet clustering algorithm. *JHEP*, 04:063, 2008.
- [134] Albert M Sirunyan et al. Extraction and validation of a new set of CMS PYTHIA8 tunes from underlying-event measurements. *Eur. Phys. J. C*, 80(1):4, 2020.
- [135] CMS Luminosity Measurements for the 2016 Data TakingPeriod. Technical Report CMS-PAS-LUM-17-001, CERN, Geneva, 2017.
- [136] Serguei Chatrchyan et al. Performance of CMS muon reconstruction in pp collision events at $\sqrt{s} = 7$ TeV. *JINST*, 7:P10002, 2012.
- [137] A. M. Sirunyan et al. Performance of the CMS muon detector and muon reconstruction with proton-proton collisions at $\sqrt{s} = 13$ TeV. *JINST*, 13(06):P06015, 2018.
- [138] S. Baffioni, C. Charlot, F. Ferri, D. Futyan, P. Meridiani, I. Puljak, C> Rovelli, R. Salerno, and Y. Sirois. Electron reconstruction in CMS. *Eur. Phys. J. C*, 49:1099, 2007.

- [139] The CMS collaboration. Reconstruction and identification of lepton decays to hadrons and at cms. *Journal of Instrumentation*, 11(01):P01019, 2016.
- [140] Tau ID Performance at CMS in Run II with the 2016 pp Dataset. Technical Report CMS-TAU-16-003-001, CERN, Geneva, 2018.
- [141] CMS Collaboration. Particle-flow event reconstruction in CMS and performance for jets, taus, and E_T^{miss} . CMS Physics Analysis Summary CMS-PAS-PFT-09-001, CERN, 2009.
- [142] Matteo Cacciari, Gavin P. Salam, and Gregory Soyez. The anti- k_t jet clustering algorithm. *JHEP*, 04:063, 2008.
- [143] Serguei Chatrchyan et al. Determination of jet energy calibration and transverse momentum resolution in CMS. *JINST*, 6:11002, 2011.
- [144] Identification of heavy-flavour jets with the CMS detector in pp collisions at 13 TeV. *JINST*, 13(CMS-BTV-16-002. CMS-BTV-16-002-004. 05):P05011. 114 p, Dec 2017. Replaced with the published version. Added the journal reference and the DOI. All the figures and tables can be found at <http://cms-results.web.cern.ch/cms-results/public-results/publications/BTV-16-002> (CMS Public Pages).
- [145] Measurement of the differential cross section for $t\bar{t}$ production in the dilepton final state at $\sqrt{s} = 13$ TeV. Technical Report CMS-PAS-TOP-16-011, CERN, Geneva, 2016.
- [146] Measurement of the inclusive and differential $t\bar{t}$ production cross sections in lepton + jets final states at 13 TeV. Technical Report CMS-PAS-TOP-16-008, CERN, Geneva, 2016.
- [147] The modeling of the top quark transverse momentum. https://twiki.cern.ch/twiki/bin/view/CMS/TopPtReweighting#TOP_PAG_corrections_based_on_dat.
- [148] Patrick Meade, Harikrishnan Ramani, and Mao Zeng. Transverse momentum resummation effects in W^+W^- measurements. *Phys. Rev.*, D90(11):114006, 2014.
- [149] Prerit Jaiswal and Takemichi Okui. Explanation of the WW excess at the LHC by jet-veto resummation. *Phys. Rev.*, D90(7):073009, 2014.
- [150] Massimiliano Grazzini, Stefan Kallweit, Dirk Rathlev, and Marius Wiesemann. Transverse-momentum resummation for vector-boson pair production at NNLL+NNLO. *JHEP*, 08:154, 2015.
- [151] b tag scale factor methods. https://twiki.cern.ch/twiki/bin/view/CMS/BTagSFMethods#2a_Jet_by_jet_updating_of_the_b. accessed: 2018-07-16.
- [152] jet flavor matching. https://twiki.cern.ch/twiki/bin/view/CMSPublic/SWGuideBTagMCTools#Jet_flavour_in_PAT. accessed: 2018-07-26.
- [153] Brian Pollack, Saptaparna Bhattacharya, and Michael Schmitt. Bayesian Blocks in High Energy Physics: Better Binning made easy! 2017.
- [154] J. S. Conway. Incorporating Nuisance Parameters in Likelihoods for Multisource Spectra. In *Proceedings, PHYSTAT 2011 Workshop on Statistical Issues Related to Discovery Claims in Search Experiments and Unfolding, CERN, Geneva, Switzerland 17-20 January 2011*, pages 115–120, 2011.
- [155] Roger Barlow and Christine Beeston. Fitting using finite monte carlo samples. *Computer Physics Communications*, 77(2):219–228, 1993.
- [156] numdifftools. <https://pypi.org/project/numdifftools/>.
- [157] CMS Luminosity Measurements for the 2016 Data Taking Period. Technical Report CMS-PAS-LUM-17-001, CERN, Geneva, 2017.

- [158] Investigations of the impact of the parton shower tuning in Pythia 8 in the modelling of $t\bar{t}$ at $\sqrt{s} = 8$ and 13 TeV. Technical Report CMS-PAS-TOP-16-021, CERN, Geneva, 2016.
- [159] D. V. Hinkley. On the ratio of two correlated normal random variables. *Biometrika*, 56:635, 1969.
- [160] Large Hadron Collider. Schedules and luminosity forecasts, 2015.
- [161] S. Chatrchyan et al. The CMS Experiment at the CERN LHC. volume 3, page S08004, 2008.
- [162] Marco Rovere, Ziheng Chen, Antonio Di Pilato, Felice Pantaleo, and Chris Seez. Clue: A fast parallel clustering algorithm for high granularity calorimeters in high energy physics. 2020.
- [163] Ziheng Chen, Antonio Di Pilato, Felice Pantaleo, and Marco Rovere. GPU-based Clustering Algorithm for the CMS High Granularity Calorimeter. *EPJ Web Conf.*, 245:05005, 2020.
- [164] Antonio Di Pilato, Ziheng Chen, Felice Pantaleo, and Marco Rovere. Reconstruction in an imaging calorimeter for HL-LHC. *JINST*, 15(06):C06023, 2020.
- [165] Ziheng Chen, Clemens Lange, Emilio Meschi, Edward Scott, and Chris Seez. Offline Reconstruction Algorithms for the CMS High Granularity Calorimeter for HL-LHC. In *Proceedings, 2017 IEEE Nuclear Science Symposium and Medical Imaging Conference and 24th international Symposium on Room-Temperature Semiconductor X-Ray & Gamma-Ray Detectors (NSS/MIC 2017): Atlanta, Georgia, USA, October 21-28, 2017*, page 8532605, 2018.
- [166] CMS HGCAL DPG. Hgcal reconstruction website ticl, 2020.
- [167] NVIDIA Corporation. Nvidia cuda c programming guide, 2010. Version 10.0.
- [168] Oded Maimon and Lior Rokach. *Data Mining and Knowledge Discovery Handbook*. Springer, 2005.
- [169] Jiawei Han, Jian Pei, and Micheline Kamber. *Data mining: concepts and techniques*. Elsevier, 2012.
- [170] Stuart Lloyd. Least squares quantization in pcm. *IEEE transactions on information theory*, 28(2):129–137, 1982.
- [171] Martin Ester, Hans-Peter Kriegel, Jörg Sander, and Xiaowei Xu. A density-based algorithm for discovering clusters a density-based algorithm for discovering clusters in large spatial databases with noise. In *Proceedings of the Second International Conference on Knowledge Discovery and Data Mining*, KDD’96, pages 226–231. AAAI Press, 1996.
- [172] Mihael Ankerst, Markus M. Breunig, Hans-Peter Kriegel, and Jörg Sander. Optics: Ordering points to identify the clustering structure. In *Proceedings of the 1999 ACM SIGMOD International Conference on Management of Data*, SIGMOD ’99, pages 49–60, New York, NY, USA, 1999. ACM.
- [173] Alex Rodriguez and Alessandro Laio. Clustering by fast search and find of density peaks. volume 344, pages 1492–1496. American Association for the Advancement of Science, 2014.
- [174] Jon Louis Bentley and Jerome H Friedman. Data structures for range searching. *ACM Computing Surveys (CSUR)*, 11(4):397–409, 1979.
- [175] Cyrus Levinthal. Molecular model-building by computer. *Scientific american*, 214(6):42–53, 1966.

- [176] Jon Louis Bentley. Multidimensional binary search trees used for associative searching. *Commun. ACM*, 18(9):509–517, September 1975.
- [177] Antonin Guttman. R-trees: A dynamic index structure for spatial searching. *SIGMOD Rec.*, 14(2):47–57, June 1984.
- [178] Philippe Rigaux, Michel Scholl, and Agnes Voisard. *Spatial databases: with application to GIS*. Elsevier, 2001.
- [179] F. Pedregosa, G. Varoquaux, A. Gramfort, V. Michel, B. Thirion, O. Grisel, M. Blondel, P. Prettenhofer, R. Weiss, V. Dubourg, J. Vanderplas, A. Passos, D. Cournapeau, M. Brucher, M. Perrot, and E. Duchesnay. Scikit-learn: Machine learning in Python. *Journal of Machine Learning Research*, 12:2825–2830, 2011.
- [180] James Reinders. *Intel threading building blocks: outfitting C++ for multi-core processor parallelism.* ”O’Reilly Media, Inc.”, 2007.
- [181] Erik Zenker, Benjamin Worpitz, René Widera, Axel Huebl, Guido Juckeland, Andreas Knüpfer, Wolfgang E Nagel, and Michael Bussmann. Alpaka—an abstraction library for parallel kernel acceleration. In *2016 IEEE International Parallel and Distributed Processing Symposium Workshops (IPDPSW)*, pages 631–640. IEEE, 2016.
- [182] C. N. Yang and R. L. Mills. Conservation of isotopic spin and isotopic gauge invariance. *Phys. Rev.*, 96:191–195, Oct 1954.
- [183] F. Englert and R. Brout. Broken symmetry and the mass of gauge vector mesons. *Phys. Rev. Lett.*, 13:321–323, Aug 1964.
- [184] Peter W. Higgs. Broken symmetries and the masses of gauge bosons. *Phys. Rev. Lett.*, 13:508–509, Oct 1964.
- [185] G. S. Guralnik, C. R. Hagen, and T. W. B. Kibble. Global conservation laws and massless particles. *Phys. Rev. Lett.*, 13:585–587, Nov 1964.
- [186] S.L. Glashow. Partial Symmetries of Weak Interactions. *Nucl. Phys.*, 22:579–588, 1961.
- [187] Steven Weinberg. A model of leptons. *Phys. Rev. Lett.*, 19:1264–1266, Nov 1967.
- [188] Gerard ’t Hooft and M.J.G. Veltman. Regularization and Renormalization of Gauge Fields. *Nucl. Phys. B*, 44:189–213, 1972.
- [189] M.D. Schwartz. *Quantum Field Theory and the Standard Model*. Quantum Field Theory and the Standard Model. Cambridge University Press, 2014.